Transactions of the ASME®

FLUIDS ENGINEERING DIVISION
Technical Editor
DEMETRI P. TELIONIS (1999)
Executive Secretary
PAT WHITE (1999)
Assistant to the Editor
N. W. SCHAEFFLER
Calendar Editor
M. F. ACKERSON

Associate Technical Editors
P. R. BANDYOPADHYAY (1997)
S. BANERJEE (1999)
P. W. BEARMAN (1998)
M. N. DHAUBHADEL (1999)
J. EATON (1999)
F. GIRALT (1997)
J. A. C. HUMPHREY (1997)
F. HUSSAIN (1998)
J. KATZ (1998)
C. MERKLE (2000)
B. SCHIAVELLO (1999)
O. SIMONIN (1998)
P. M. SOCKOL (1998)
M. W. SINDIR (1997)
M. SOMMERFELD (1999)
M. S. TRIANTAFYLLOU (1998)

BOARD ON COMMUNICATIONS
Chairman and Vice-President
R. MATES

OFFICERS OF THE ASME
President, **KEITH B. THAYER**
Exec. Director
D. L. BELDEN
Treasurer
J. A. MASON

PUBLISHING STAFF
Managing Director, Engineering
CHARLES W. BEARDSLEY
Director, Technical Publishing
PHILIP DI VIETRO
Managing Editor, Technical Publishing
CYNTHIA B. CLARK
Managing Editor, Transactions
CORNELIA MONAHAN
Production Assistant
MARISOL ANDINO

Transactions of the ASME, Journal of Fluids Engineering (ISSN 0098-2202) is published quarterly (Mar., June, Sept., Dec.) for $195.00 per year by The American Society of Mechanical Engineers, 345 East 47th Street, New York, NY 10017. Periodicals postage paid at New York, NY and additional mailing offices. POSTMASTER: Send address changes to Transactions of the ASME, Journal of Fluids Engineering, c/o THE AMERICAN SOCIETY OF MECHANICAL ENGINEERS, 22 Law Drive, Box 2300, Fairfield, NJ 07007-2300.
CHANGES OF ADDRESS must be received at Society headquarters seven weeks before they are to be effective. Please send old label and new address.
PRICES: To members, $40.00, annually: to nonmembers, $195.00. Add $40.00 for postage to countries outside the United States and Canada.
STATEMENT from By-Laws. The Society shall not be responsible for statements or opinions advanced in papers or . . . printed in its publications (B7.1, Par. 3).

INDEXED by Applied Mechanics Reviews and Engineering Information, Inc. Canadian Goods & Services Tax Registration #126148048.

Journal of Fluids Engineering

Published Quarterly by The American Society of Mechanical Engineers

VOLUME 119 • NUMBER 4 • DECEMBER 1997

741 **Editorial**

742 **Industrial Perspective**

744 **Dynamical Nuclei Measurement: On the Development and the Performance Evaluation of an Optimized Center-Body Meter**
T. M. Pham, J. M. Michel, and Y. Lecoffre

752 **Tip Vortex Cavitation on an Oscillating Hydrofoil**
O. Boulon, J. P. Franc, and J. M. Michel

759 **Equilibrium of Ventilated Cavities in Tip Vortices**
F. Castro, A. Crespo, F. Manuel, and D. H. Fruman

768 **Rotordynamic Forces in Cavitating Inducers**
A. Bhattacharyya, A. J. Acosta, C. E. Brennen, and T. K. Caughey

775 **Observations of Oscillating Cavitation of an Inducer**
Yoshinobu Tsujimoto, Yoshiki Yoshida, Yasukazu Maekawa, Satoshi Watanabe, and Tomoyuki Hashimoto

782 **Diffusion Induced Bubble Populations Downstream of a Partial Cavity**
Po-Wen Yu and Steven L. Ceccio

788 **Mechanism and Control of Cloud Cavitation**
Y. Kawanami, H. Kato, H. Yamaguchi, M. Tanimura, and Y. Tagaya

795 **Uncertainties and CFD Code Validation**
H. W. Coleman and F. Stern

804 **A Perspective on the Construction of Nonsymmetric Uncertainty Intervals**
Paul K. Maciejewski

808 **Interaction of a Steady Approach Flow and a Circular Cylinder Undergoing Forced Oscillation**
Jianfeng Zhang and Charles Dalton

814 **State Estimator of Flow as an Integrated Computational Method With the Feedback of Online Experimental Measurement**
Toshiyuki Hayase and Satoru Hayashi

823 **On Oscillatory Instability of Convective Flows at Low Prandtl Number**
A. Yu. Gelfgat, P. Z. Bar-Yoseph, and A. L. Yarin

831 **Parametric Studies on a Numerical, Nonlinear Pulse Tube Flow**
C. S. Kirkconnell and G. T. Colwell

838 **Numerical Simulation of Drag Reducing Turbulent Flow in Annular Conduits**
Idir Azouz and Siamack A. Shirazi

847 **Friction Factor Determination for Flow Through Finite Wire-Mesh Woven-Screen Matrices**
J. R. Sodré and J. A. R. Parise

852 **Linear Feedback Control of Boundary Layer Using Electromagnetic Microtiles**
S. N. Singh and P. R. Bandyopadhyay

859 **Application of Turbulence Models to Bypass Transition**
K. J. A. Westin and R. A. W. M. Henkes

867 **A Modified Low-Reynolds-Number k-ω Model for Recirculating Flows**
Shia-Hui Peng, Lars Davidson, and Sture Holmberg

876 **Eddy Viscosity Transport Equations and Their Relation to the k-ϵ Model**
F. R. Menter

885 **Numerical Simulation of Channel Flows by a One-Equation Turbulence Model**
V. I. Vasiliev, D. V. Volkov, S. A. Zaitsev, and D. A. Lyubimov

893 **Multigrid Computation of Incompressible Flows Using Two-Equation Turbulence Models: Part I—Numerical Method**
X. Zheng, C. Liao, C. Liu, C. H. Sung, and T. T. Huang

900 **Multigrid Computation of Incompressible Flows Using Two-Equation Turbulence Models: Part II—Applications**
X. Zheng, C. Liao, C. Liu, C. H. Sung, and T. T. Huang

906 **Open Channel Flow Over Submerged Obstructions: An Experimental and Numerical Study**
Dani Fadda and Peter E. Raad

(Contents continued on p. 803)

(Contents continued)

911 Correlated Compressible and Incompressible Channel Flows
C. Crnojević and V. D. Djordjević

916 Interfacial Area Concentration and Void Fraction of Two-Phase Flow in Narrow Rectangular Vertical Channels
T. Wilmarth and M. Ishii

923 A Study on Converging Thin Annular Jets
D. Sivakumar and B. N. Raghunandan

929 Jet-Plate Interaction for Wedge-Shaped Plates of Arbitrary Angles
S. S. Chu and W. L. Chow

934 Nearfield Evolution of a Longitudinal Vortex Generated by an Inclined Jet in a Turbulent Boundary Layer
X. Zhang and M. W. Collins

940 Chebyshev Collocation Analysis of Axisymmetric Flow and Heat Transfer Between Counter-Rotating Disks
R. W. Hill and K. S. Ball

948 Wall Pressure and Effective Wall Shear Stresses in Heat Exchanger Tube Inlets With Application to Erosion-Corrosion
D. G. Elvery and K. Bremhorst

954 Experimental Comparison of Flow Fields at the Inlet and the Outlet of an Inducer With Shrouded and Unshrouded Configurations
C. Offtinger, C. Henry, R. Morel, and F. Spettel

960 Numerical Study of Sail Aerodynamics
Michel Guilbaud and D. R. Rajaona

968 Flow Analysis in a Pump Diffuser—Part 1: LDA and PTV Measurements of the Unsteady Flow
K. Eisele, Z. Zhang, M. V. Casey, J. Gülich, and A. Schachenmann

978 Flow Analysis in a Pump Diffuser—Part 2: Validation and Limitations of CFD for Diffuser Flows
F. A. Muggli, K. Eisele, M. V. Casey, J. Gülich, and A. Schachenmann

985 Unsteady Total Pressure Field Downstream of an Embedded Stator in a Multistage Axial Flow Compressor
N. Suryavamshi, B. Lakshminarayana, J. Prato, and J. R. Fagan

995 A Generalized Gas-Liquid-Solid Three-Phase Flow Analysis for Airlift Pump Design
D. P. Margaris and D. G. Papanikas

1003 Perturbation Solution for Flow in Two-Cavity Dies
K. J. Ruschak and S. J. Weinstein

Technical Brief

1009 On the Accuracy of Wall Similarity Methods in Determining Friction Velocity Over Smooth and Ribletted Surfaces
A. Baron and M. Quadrio

1012 Fluids Engineering Calendar

Announcements and Special Notices

787 Transactions Change of Address Form

1018 Call for Symposium Papers—1999 ASME/JSME Fluids Engineering Conference

1028 Statement of Numerical Accuracy

1028 Statement of Experimental Uncertainty

1028 Access to the Electronic JFE

1028 Submission of Papers

Journal of Fluids Engineering

Editorial

Cavitation Phenomena and Their Impact on the Flow, Noise, and Performance of Hydraulic Machines

The theme of the present issue of JFE is cavitation. Several contributed papers that address a variety of cavitation phenomena, as well as their impact on the flow and performance of hydraulic machines, have been selected and published at the beginning of this issue. These complex, partially understood and typically poorly predicted phenomena have several adverse effects. They are primary contributors to noise, unsteady loading and vibration in hydraulic machines, cause erosion and modify the performance of pump and propellers, in some cases to the level of complete failure. Thus, prevention of cavitation, or at least its prediction, are critical and in certain situations the primary design parameter. As the papers in this issue demonstrate, we still have a long way to go before such design tools are available.

It is well established that cavitation inception occurs when a nucleus, typically a free stream bubble or a gas pocket on a surface, is exposed to a sufficiently low pressure to cause its unstable growth. The required tension depends on the characteristics of nuclei in the water, typically referred to in the cavitation literature as "water quality," and the type of cavitation involved. Since there is no consensus at the present time on how to quantify the water quality, it is difficult to interpret results of tests performed in different facilities. Consequently, substantial effort has already been invested in developing means for quantifying the water quality, either by measuring the distribution of bubbles in the water, or by measuring the tension required to cause a known form of cavitation in a device with calibrated pressure distributions. The Venturix, described in the paper by Pham et al., is the latest development in this area. It involves a carefully designed flow chamber with a center body and acoustic means for measuring the rate of cavitation events. The operational range of this device and the acoustic sensors are addressed. Due to the simplicity in implementing the Venturix, we may at some point use such a method as a standard.

The second condition for cavitation inception, i.e., having a sufficiently low pressure, requires knowledge of the unsteady, instantaneous pressure. In vortex dominated flows, at the present time, we do not have reliable data or means to determine the instantaneous pressure within the vortex core and its relationship to the gross flow structure. This problem is particularly difficult when tip vortex cavitation is concerned, since the core size is the order of 1% of the characteristic length scales (e.g., chordlength) and it tends to migrate, i.e., its exact location is unknown. Turbulence modeling in the vicinity of such concentrated vortices is also an unresolved issue. Thus, design of devices involving tip vortex cavitation is based on empirical data. The present issue contains two papers that deal with tip vortex cavitation. In the first paper, by Boulon et al., the focus is on measurements of tip vortex cavitation on oscillating foils, where the core pressure varies due to the changes in the incidence angle. The ratio between two time scales, the capture time of nuclei, that depends on their distributions, and the period of oscillations dominates the impact of the unsteady vortex strength. When these time scales are comparable, the nuclei distribution has a substantial effect on the conditions for cavitation inception. The second paper, by Castro et al., deal with the structure of ventilated cavities within tip vortices, where the gas phase is intentionally introduced to the vortex core. The resulting flow consists of a leading bubble with a re-entrant, reverse-flow jet, followed by a satellite cavity. The flow structure and stability strongly depend on the wing geometry.

The problem is exasperated further in the complex geometry of hydraulic turbomachines, where our understanding of the flow is limited. Two papers in the present issue deal with cavitation and its impact on inducer pumps. The first, by Bhattacharyya et al., deals with the effect of cavitation on rotor dynamic forces in a whirling axial flow inducer. They measure large destabilizing force peaks that increase with decreasing cavitation indices. The trends do not exhibit the typically assumed quadratic functional behavior, which complicates the modeling, based on matrices of stiffness, damping and inertia. The second paper, by Tsujimoto et al., focuses on oscillating cavitation on inducers. In doing so, the authors provide a demonstration of the complexity of cavitating flows as well as our limited ability to predict their occurrence. They confirm, using pressure measurements and high speed photography, that the cavitation on the blades of inducer pumps oscillates and rotates from blade to blade. The rotation speed can be either faster or slower than the blade speed. Some phenomena are associated with backflow vortices and others involve surge mode oscillations. The paper discusses these phenomena and attempts to identify a specific mode that was previously predicted.

When attached sheet cavitation occurs, the process involves shedding of predominantly noncondensable gas bubbles behind the cavity. The paper by Yu and Ceccio compares measured concentrations of bubbles to several models of gas diffusion into the attached cavity. The results demonstrate our level of understanding of the physical phenomena involved. A model based on a laminar boundary layer underpredicts and models based on turbulent boundary layers overpredict the gas diffusion into the cavity. In both cases, the discrepancies are substantial. When the pressure decrease is well below the inception conditions, the attached sheet cavitation becomes increasingly unsteady and starts shedding increasingly larger fractions of the cavity. This process, typically referred to as cloud cavitation, is the most destructive form of cavitation, both in terms of noise as well as in its ability to cause massive damage to lifting surfaces. The paper by Kawanami et al. focuses on this phenomenon. The experiments demonstrate the existence of a reentrant jet, a thin, reversed liquid flow under the cavity that causes the shedding. By installing thin obstacles on the surface, the authors demonstrate substantial changes to the stability of the cavitation, surface pressure fluctuations and noise. They attribute this substantial effect to prevention of the re-entrant flow.

J. Katz
Department of Mechanical Engineering
The Johns Hopkins University

Journal of Fluids Engineering

Industry Perspective

Observations of Oscillating Cavitation of an Inducer[1]

Philippe Geai.[2] The market of civil space launchers has become more and more competitive, and providing weight-optimized propulsion systems is an all days challenge for SEP, the European leader in Space Propulsion. This optimization includes the minimization of the propellant tanks wall thickness and involves the design of high-suction performance pumps to feed the combustion chamber of the rocket engine. Such pumps have generally an inducer located upstream of the centrifugal impeller(s). The normal operating region of inducers is such that rotating cavitation is a well known problem which has been encountered during the developments of American, Japanese and European modern turbopumps.

This cavitation instability may involve the turbopump with detrimental consequences to pump bearing radial loads, and a potential excitation of a rotor mode within the operating range. Moreover, as shown in the paper, the super-synchronous rotating cavitation component may also interact with the rotational frequency, and then excite some sub-synchronous modes close to the well-known "cavitation surge" mode. We must be careful not to get confused by this interaction, and distinguish: (1) rotating cavitation which is a local flow instability, and (2) auto-oscillations of cavitation, which is a system-dependent axial flow instability.

Each of these modes can appear independently from the other. The former strongly depends on the choice of design parameters for the inducer itself, while the latter depends on the whole system (pump + lines), and can be controlled by vapour "capacities" judiciously located upstream of the pump.

It is interesting to point that both existing modelizations of local and global instabilities are based on the knowledge of the total volume of vapour V_c (cavities, rip vortex and recirculation vortices), and the evolution of V_c with respect to inlet pressure and flow rate $\delta V_c/\delta P$, $\delta V_c/\delta Q$. That's why exhaustive experimental investigation using visualizations such as described in the paper, may be useful in helping us

(1) determine these parameters (and find a correlation between $\delta V_c/\delta P$, $\delta V_c/\delta Q$ and Tsujimoto's K and M Parameters),

(2) understand the physical phenomena of interactions between the different patterns of vapour, to bring reliable information for the development of more detailed predicting models.

Furthermore, the (inlet pressure, flow rate) mapping of the occurrence of the different types of cavitation may give some trends to the engineer for its main functional design choices. Tsujimoto's work has largely contributed to the development of modelization tools for rotating cavitation, but their application to the determination of detailed design rules requires much more work. That's why an interesting follow-up of this work could be an experimental investigation of the influence of some major geometrical design parameters, such as the inducer leading edge shape.

Tip Vortex Cavitation on an Oscillating Hydrofoil[1]

D. H. Fruman.[2] Vortex cavitation, and Tip Vortex Cavitation (TVC) in particular, is a very challenging problem, which concerns all hydraulic machinery operating either in open or confined spaces. In the case of screw propellers for naval operation, TVC has been a subject of much attention because of its impact on the acoustic discretion of submarines. A considerable amount of work has been devoted to determine the conditions for cavitation onset and development in a laboratory environment and to set up the strategy to extrapolate the results to prototype situations. In this respect, due account has to be taken of the impact of Reynolds numbers, water quality, turbulence, etc. on the data analysis and extrapolation. Another important aspect is related to the effect of non-permanent situations due, for example, to the modification of the instantaneous incidence of and pressure on the blades of a propeller during its rotation in the wake of the ship or submarine. The work presented in this paper is a contribution to the understanding of this very important problem. It has a profound impact on many practical situations, even if it cannot be summarized in a simple handbook type formulation.

[1] By Y. Tsujimoto, Y. Yoshida, Y. Maekawa, S. Watanabe, and T. Hashimoto published in this issue pp. 775–781.

[2] Head of Turbomachinery Fluid Dynamics Department, SEP, Foret de Vernon, 27207 Vernon Cedex, France.

[1] By O. Boulon, J. P. Franc, and J. M. Michel published in this issue pp. 752–758.

[2] Head, Interfacial Phenomena Group, ENSTA, 91120 Palaiseau, France. Scientific Advisor, Hydrodynamics Laboratory, Ecoole navale, 29240 Brest naval, France and Program Director, Action Concertée Cavitation.

T. M. Pham
Research Assistant.

J. M. Michel
Research Director.

Laboratoire des Ecoulements
Géophysiques et Industriels,
BP 53, 38041 Grenoble,
Cedex 9, France

Y. Lecoffre
Head of Ylec Consultants,
Allée des Dauphins,
38330 Saint Ismier, France

Dynamical Nuclei Measurement: On the Development and the Performance Evaluation of an Optimized Center-Body Meter

This work is concerned with the development of a center-body venturi for nuclei measurements of novel design, the Venturix. Our project aims to: 1. Define a specially tailored geometry for cavitation nuclei measurement. This design study takes into consideration the following main aspects: the venturi mean flow in subcavitating regime, the viscous effects, the bubble dynamics. 2. Evaluate the performance of the meter: After testing the proposed design concepts, the venturi operating characteristics, in particular its operational limits, are assessed. Finally, the performance of the acoustic method used for detecting and counting the active nuclei in the venturi is discussed.

1 Introduction

The concentration and susceptibility of nuclei contained in water, collectively called water quality, profoundly affect the inception, development, and scaling of cavitation. Controlling these parameters in experimental facilities is necessary during cavitation tests on models. In particular, a similarity law in "λ^3" on the nuclei concentrations (λ is the geometrical scale) must be respected in order to properly predict prototype performance from model tests (Holl et al., 1961). This control can be achieved by injecting an adjustable amount of microbubbles in the test water and determining the spectra of the injected nuclei. The accuracy of the latter measurement is of major importance in order to inject a proper nuclei content or, at least, to know the real test conditions.

We may roughly distinguish two main classes of measuring techniques: the optical methods (Holography, Phase Doppler . . .), and the hydrodynamic method using venturi-type devices. For our purposes, we will focus on the venturi's use. Indeed, compared with the other nuclei detection techniques, the venturi system presents several advantages: it provides a direct measurement of the nuclei critical pressure, there is no limitation on the size of the smallest detectable nuclei, the liquid sample volumes are significant. Real possibilities lie in this technique, but we do not yet completely understand discrepancies observed with optical measurement results. All this motivates an accurate investigation of the venturi's performance.

The operating principle of the venturi is the following: the internal flow inside a venturi is used to make nuclei unstable by exposing them to a low pressure field. The minimal pressure level which monitors the meter operation is induced at the throat. Any nucleus whose critical tension is higher than this value will be activated and will create a cavitation bubble. The latter is detected either optically or acoustically by the noise generated during its collapse inside the diffuser. The first nuclei venturi-type meter was designed by Oldenziel (1972). It consisted of a glass venturi tube with optical detection of cavitation bubbles. The original design was then subject to various design modifications. In 1975, the Neyrtec company developed its own venturi-type meter using plexiglass and stainless steel venturi tubes. Neyrtec opted in 1982 for an axisymmetric geometry: the Nuclei Center-Body Meter (patent no. 84/18 820).

We propose to develop a center-body venturi of novel design, named Venturix, whose operating characteristics and performance will be known as accurately as possible. This research project was initiated in 1991 by Ylec Consultants in collaboration with the Laboratoire des Ecoulements Géophysiques et Industriels. The basic idea is to define a simple general design of the meter, which makes studying of the internal flow all the more easier, experimentally as well as numerically. The main innovation consists in the cylindrical shape of the outer flow surface. This simple geometry is then "optimized" so as to take into consideration the viscous effects on the venturi internal pressure distribution and to prevent any separation-induced cavitation in the diffuser. Next, we check that the proposed design concepts actually meet the design requirements and we evaluate the meter performance with regard to its operation limits and to nuclei measurement precision. It should be noted that we opted for an acoustic detection of nuclei in the Venturix. Therefore, we will restrict our discussion to the nuclei measurement by venturi meter with acoustic detection. Moreover, as our primary objective is to characterize the Venturix operation from the hydrodynamic point of view, we do not estimate the performance of the signal processing system. We used a data acquisition and processing system which was commercially available.

2 Design and Optimization of the Venturix

We address in this section the main aspects for the rational design of the instrument according to the proposed concepts.

2.1 Design Requirements—Objectives of the Optimization Procedure. The determination of the pressure field inside the Venturix is essential for accurate measurements with the meter. The knowledge of the minimal pressure value is actually necessary to determine the nuclei critical tension. Hence, we aim to design the Venturix so that:

- The nuclei are exposed to a well-defined pressure field inside the venturi. A sine qua non condition to estimate that pressure field is to evaluate the viscous effects on the pressure distribution.
- All sources of perturbation of the pressure distribution are controlled. In particular, laminar flow separation in the diffuser, which dramatically brings about sheet cavitation, must be avoided. Indeed, the development of sheet cavitation limits the

Contributed by the Fluids Engineering Division for publication in the JOURNAL OF FLUIDS ENGINEERING. Manuscript received by the Fluids Engineering Division June 3, 1996; revised manuscript received May 6, 1997. Associate Technical Editor: J. Katz.

minimum throat pressure to the value of the pressure inside the attached cavity (Briançon-Marjollet, 1987).

2.2 General Design. The general design of the Venturix comes from a simplification of the internal geometry of the Neyrtec's center-body venturi. Both devices consist of two coaxial elements which set the boundaries of an axisymmetric flow. The basic asset of this configuration lies in the annular flow cross-section which notably limits the occurrence of nuclei mutuel interference. In the initial design, the flow was confined between an external cone and a central body. In the Venturix, the flow is bounded by:

- A cylindrical pipe segment which we will call hereafter the external cylinder,
- A central body made up of an ellipsoidal section, followed by a cylindrical section and a conical section.

These sections, respectively, define the contraction, the throat, and a first diffuser, the prediffuser. A second divergence of the flow is achieved by increasing the internal pipe diameter, the diameter of the central body remaining constant. The Venturix geometry and dimensions are shown in Fig. 1.

The spacing between the central body and the external cylinder is equal to one millimeter. The throat section is ten millimeters long. The choice of these values results from a previous design study lead by Lecoffre and Marcoz (1978) and are in good agreement with the works of d'Agostino and Acosta (1991). The pressure recovery in the venturi is performed in two steps. First, the flow passes through the prediffuser where only small adverse pressure gradients are allowed. The prediffuser has been accordingly designed: the slope angle is equal to 1.9 degree; the matching radius to the cylindrical section is 200 mm. Secondly, the flow passes through a steeper diffuser as the danger of separation is mitigated. A honey comb located upstream the Venturix (not shown in Fig. 1) ensures regular inlet flow conditions independent of the upstream flow conditions. On the basis of this general design, we "optimize" the designs of the throat section and the expansion area by application of the inverse-type procedure presented in Sections 2.3 and 2.4.

2.3 Optimization of the Throat Section. The aim is that the monitoring pressure remains constant throughout the throat section for a reference flow rate. This allows to minimize the pressure gradients over the whole operational range of flow rates.

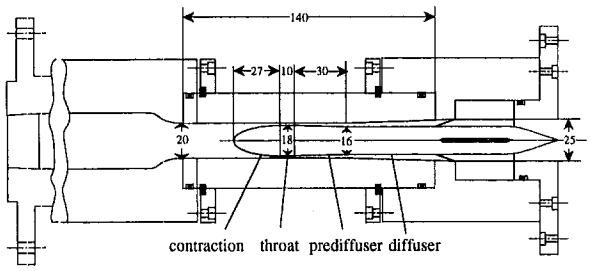

Fig. 1 Venturix geometry and dimensions (in mm)

Our present design work is essentially concerned with the estimate of the viscous effects. Indeed, one effect of the boundary layer is the reduction of the flux-averaged cross-sectional area of the venturi with respect to its geometrical value. Our aim is to compensate the flow acceleration due to the boundary layer development and therefore meet the design requirement presented above. Our investigative procedure consists in:

- *Calculating the venturi potential mean flow*

A boundary integral method is implemented under the assumption of an inviscid and incompressible fluid. The spacing between the central body and the external cylinder is supposed to remain constant and equal to 1 mm throughout the throat section. The velocity field is induced by source and vortex distributions spread over the surfaces of the central body and the external cylinder. The singularity densities are determined by least square minimization of source/vortex pseudo-error using an iterative process (T. M. Pham et al., 1992). This enables us to calculate the pressure field inside the venturi.

- *Predicting the boundary layer behavior*

Using the pressure distributions previously determined, a boundary layer computation is run for a reference flow rate of 1.2 l/s (i.e., a throat velocity equal to 20 m/s for a 1 mm spacing between the external cylinder and the central body). The displacement thicknesses on the ogive and the external cylinder walls are computed.

- *Correcting accordingly the venturi geometry*

The radius of the central ogive is diminished by the cumulated displacement thicknesses. This provides a constant flux-averaged cross-sectional area (i.e., a constant pressure) for the reference flow rate, the boundary layer effects being taken into account. It corresponds to a minimum spacing between the exter-

Nomenclature

c_o = sound velocity, m/s
$C_{\text{acous/opt}}$ = correlation factor between acoustic, and optical nuclei countings —
C_f = friction coefficient, —
C_p = pressure coefficient, $C_p = 2 \cdot ((P - P_{up})/\rho \cdot (Q/S_{\text{ref}})^2)$
k = pressure loss coefficient, —
M = corrective factor, —
N_{acoustic} = number of acoustically detected nuclei —
N_{opt} = number of optically detected nuclei —
P_a = acoustic pressure, Pa
P_{cr} = critical pressure of a nucleus, Pa
P_{th} = average pressure in the throat section, Pa
P_{up} = pressure at the Venturix upstream, Pa
P_∞ = ambiant pressure, Pa
Q = flow rate, l/s
r = distance from the bubble center, m
R_{cr} = critical radius of a nucleus, μm
R_o = initial bubble radius, μm
R_{eq} = equivalent bubble radius, μm
R_{match} = matching radius, cylindrical/conical sections, mm
R_∞ = maximum bubble radius given by the Rayleigh-Plesset equation, μm
S_{ref} = minimal cross-sectional area, mm^2
S_{up} = cross-sectional area of the inlet duct, mm^2
$S(z)$ = flow cross-sectional area at the abscissa z, mm^2
t = time, s
$\mathcal{V}$ = bubble volume, mm^3
V_{th} = average flow velocity in the throat section, m/s
z = abscissa along the axis of the central body, mm ($z = 0$ at the nose of the ogive)
α = slope angle of the prediffuser, degree
ΔP = pressure loss in the Venturix, Pa
σ_{vent} = cavitation venturi parameter $\sigma_{\text{vent}} = 2((P_{up} - P_v)/\rho V_{th}^2)$

Operators

$\ddot{}$ = derivative with respect to time
$''$ = derivative with respect to z

nal cylinder and the central body equal to 1.057 mm instead of 1 mm.

It should be noted that the precision on the central ogive radius must be compatible with the order of magnitude of the calculated displacement thicknesses. This implies very strict construction tolerances and makes necessary the use of stainless steel for constructing the external cylinder and the central ogive. In addition, we defined a mounting procedure in order to minimize the misalignment errors and achieve a coaxiality as good as possible.

2.4 Optimization of the Expansion Area. We conducted preliminary venturi flow visualizations under stroboscopic lightening through a plexiglass external cylinder. They pointed out the occurrence of a laminar flow separation in the prediffuser for a wide range of flow rates. Indeed, we observed that an attached cavity was formed on the central body at the immediate downstream of the prediffuser inlet. This was an evidence for a boundary layer separation (Arakeri et al., 1973, Franc et al., 1985). The initial design of the prediffuser must therefore be reconsidered. Two options are possible:

- Modifying the prediffuser geometrical definition (slope angle α, matching radius to the cylindrical section R_{match});
- Inducing the boundary layer transition to turbulence.

Boundary layer computations, using an integral method and the Habiballah and Arnal's criterion to predict the transition to turbulence (1984), lead to the following conclusions:

- For turbulence ratios lower than 1 percent, a boundary layer laminar separation is systematically predicted no matter what the values of α and R_{match} are. The use of a less steep prediffuser only slightly delays flow separation occurrence; it has no significant effect.
- For a turbulence ratio of 1 percent, considering the initial geometrical definition of the prediffuser (α = 1.9 deg, R_{match} = 200 mm), no separation is predicted.

In view of these results, it has been decided to control the turbulence intensity at the inlet by adding "turbulence generators" to trip the boundary layers. These turbulence generators consist of two rings. One ring (Ring no. 1) is mounted on the external cylinder wall at the immediate upstream of the venturi, the other one (Ring no. 2) is mounted on the central body nose. The location and dimensions of the rings are chosen in order to strike a balance between two opposite requirements:

- the turbulence intensity which is created must be strong enough to avoid laminar separation in the expansion area;
- the head loss due to the rings must remain in an admissible range.

Ring no. 1 is located 20 mm upstream the contraction inlet; its thickness and protruding height are respectively equal to 2 mm and 0.75 mm. Ring no. 2 has a 1 mm thickness.

The use of turbulence generators appears to be very efficient, as will be shown in Section 3.1.1.

The Venturix being designed and constructed according to the study described above, we must now evaluate its performance. One may address the following questions:

- Does the Venturix meet the design requirements with regard to the control of laminar flow separation and to the optimum pressure distribution inside the venturi?
- Because of the relatively high reflection coefficient of the couple (water, stainless steel), does the use of an external cylinder in stainless steel induce any problem for acoustically detecting the nuclei?
- Is the acoustic method adapted for correctly detecting and counting the active nuclei?

We present hereafter the experimental and numerical activities we carried out for validating the proposed design concepts (Section 3) and assessing the performance of the acoustic detection method, theoretically (Section 4) and experimentally (Section 5).

3 Validation of the Proposed Design Concepts

3.1 Boundary Layer Control by Means of Turbulence Generators

3.1.1 Flow Regimes in the Venturix—Operation Limits We carry out flow visualizations under stroboscopic lightening through a plexiglass external cylinder. The Venturix is equipped with the boundary layer control facility described above. Flow visualizations point out the existence of two main flow regimes:

- *Travelling bubble flow regime*

It is the nominal operational regime of the venturi. It is characterized by the random occurrence of cavitation bubbles in the venturi. Each nucleus evolves quite individually. Its collapse in the diffuser does not induce any significant perturbation of the subcavitating pressure distribution.

- *Patch cavitation*

As the flow rate is increased (i.e., the pressure in the throat section is decreased), more and more nuclei are activated and begin to interact with each other. The explosive bubbles growth leads to the formation of unstable, intermittent structures of cavitation in the expansion area. As the flow rate still increases, the cavitation patches become bigger and partially "obstruct" the cross-sectional area of the throat section. They induce significant perturbations of the venturi mean flow which can no longer be considered as a non cavitating flow. This phenomenon which affects the venturi operation is called saturation or choking. The consequence of saturation is a general increase of the pressure with respect to its steady non cavitating value.

Note that no attached cavity has been observed, which shows that the danger of flow separation is totally erased by inducing the boundary layer transition to turbulence. Thus, the proposed design concept to avoid flow separation has been successfully demonstrated: the Venturix operation is only limited by the occurrence of saturation at high nuclei concentrations.

A chart defining the Venturix operation limits is experimentally established and compares favourably with the results of a theoretical estimate (see Fig. 2). V_{th} is deduced from flow rate measurement. P_{th} is determined by application of the Bernoulli's theorem, the pressure upstream the venturi being measured. In Fig. 2, the triangles denote the venturi operating points for which the inception of patch cavitation is observed. The solid line shows an estimate of the minimum attainable throat pressure. It is given by the expression: $(P_{th})_{min} = P_{up} - 0.5 \cdot \rho(k -$

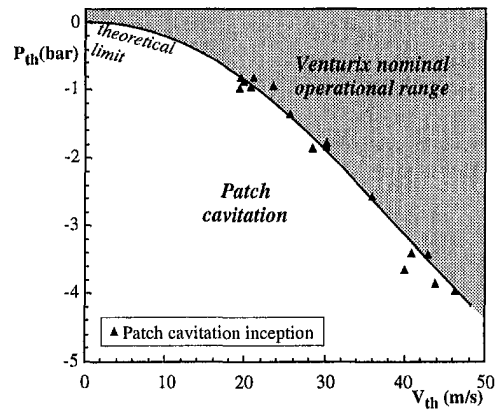

Fig. 2 Venturix operation limits: minimum throat pressure as a function of throat velocity

$1) \cdot V_{in}^2$, assuming that the Venturix is inoperant when the pressure in the exhaust duct is equal to P_v, for a measured pressure loss coefficient k equal to 0.55. This leads to an average critical value of the venturi parameter without saturation equal to $[\sigma_{vent}] = 0.6$.

The use of turbulence generators appears to significantly widen the operational range of the Venturix. However, we should check that it does not introduce any change in the dynamics of the nuclei crossing the Venturix.

3.1.2 Turbulence Intensity Effects on the Measurement of the Nuclei Critical Pressure. The use of turbulence generators raises the question whether the turbulent pressure fluctuations which are created upstream the venturi inlet can modify the nuclei dynamics, that is:

- Can the nuclei critical pressure be modified by a rectified diffusion effect?
- Can a nuclei resonance be induced by the turbulent pressure fluctuations?
- Is it possible that nuclei are activated upstream the throat section?

To answer those questions, we must characterize the pressure fluctuations created by the turbulence generators. To this end, a fluctuating pressure transducer PCB 105B02 is flush mounted on the cylinder wall at the immediate downstream of Ring no. 1; the diameter of the sensitive element is equal to 3 mm; its sensibility is equal to 0.005 psi; its resonance frequency is 250 kHz. We perform pressure measurements for flow rates from 0.3 l/s to 2.1 l/s. The fluctuating pressure signals are captured and stored by means of a numerical oscilloscope. Their spectral analysis leads to a mean characteristic frequency ranging from 500 to 3000 Hz and to a maximal mean amplitude varying from 350 to 1700 Pa. In view of those results, we conclude that, for the whole range of flow rates:

- A nuclei resonance is unlikely. Indeed, the observed pressure fluctuations frequencies are far smaller than typical values of the natural frequency of air bubbles in water.
- By comparing the transit time of a nucleus in the oscillating pressure field with the period of the pressure oscillations, it appears that it is submitted to a maximum of ten or so pressure oscillations. Consequently, the modification of the nuclei critical pressure by rectified diffusion is not significant.
- The maximal amplitude of the pressure perturbations represents less than 0.6 percent of the pressure drop induced in the venturi, the turbulence effects on nuclei growth are negligible.

All this validates the accuracy of the nuclei critical pressure measurement against the effects of turbulence intensity.

3.2 The Pressure Distribution in the Venturi. We analyze in the present section the Reynolds number effect on the pressure distribution, according to a numerical estimate compared with experimental results. The objective is to validate the proposed throat design. All our results will be presented in terms of the adimensionnel pressure coefficient C_p defined in the nomenclature.

To estimate the Reynolds number effect, we implement a procedure similar to the one used to "optimize" the meter's internal geometry:

The displacement thicknesses on the venturi walls are computed for different Reynolds number values (i.e., for different flow rates), assuming a constant pressure in the throat section;

For each considered Reynolds number, the central body radius is increased by the cumulated displacement thicknesses. We then determine the corresponding flow cross-sectional areas at different abcissas in the venturi. The C_p distribution is deduced from Bernoulli's equation by

$$C_p(z) = S_{ref}^2 \left\{ \frac{1}{S_{up}^2} - \frac{1}{S(z)^2} \right\}$$

with

$C_p(z)$	pressure coefficient at the abscissa z
S_{up}	cross-sectional area of the inlet duct
$S(z)$	flow cross-sectional area at the abscissa z

For measuring the pressure distribution inside the venturi, a stainless-steel external cylinder is equipped with eleven static pressure taps helicoidly distributed along the cylinder. The diameter of the holes is equal to 0.3 mm. Three pressure tabs are located in the throat section.

Pressure distributions are experimentally established for flow rates of 0.6 l/s to 1.9 l/s. The C_p distributions in the throat section for the considered flow rates are presented in Fig. 3, compared with our numerical estimate results. The corresponding minimum pressure coefficients C_{pmin} are plotted in Fig. 4 versus the flow rate. The estimated C_{pmin} values are compared with two sets of experimental data.

We note in Fig. 3 that the pressure distribution curves which are experimentally established are very close in shape and in magnitude to the curves obtained from our numerical estimate of the Reynolds number effect. A practically constant pressure in the throat section is actually obtained, but for a flow rate approximately equal to 0.9 l/s instead of 1.2 l/s. The corresponding minimum C_p value is equal to -1.1075 which is near to the expected value -1.1032. According to Fig. 4, the predicted and experimental evolutions of C_{pmin} with flow rate compare very favorably. It must be emphasized that differences of C_{pmin} up to 13 percent occur, which shows that the Reynolds number effect cannot be neglected.

Hence, the agreement between measurements and numerical estimates validates the proposed design concepts concerning the viscous effects compensation. Moreover, the very small scattering of the experimental results (the maximum standard deviation on C_p is equal to 5.10^{-3}) demonstrates conclusively that it is possible to calibrate the venturi by direct pressure measurements, in spite of the difficulties associated with this type of measurements.

3.3 Study of the Acoustic Signal Received in the Stainless-Steel External Cylinder. As previously addressed, we decided to construct the external cylinder in stainless steel due to the strict dimensional tolerances implied by our design study. However, regarding the acoustic nuclei detection, the use of

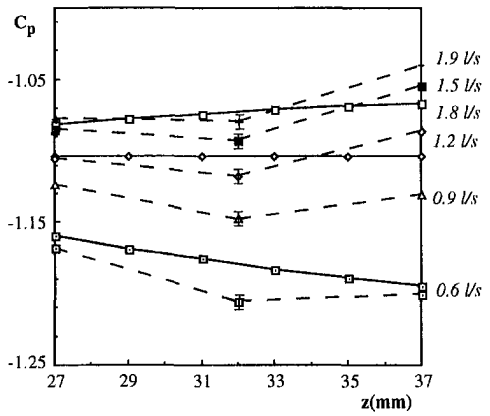

Fig. 3 Measured and estimated C_p distibutions in the throat section for different flowrate values (solid lines: numerical estimates—broken lines: experimental results)

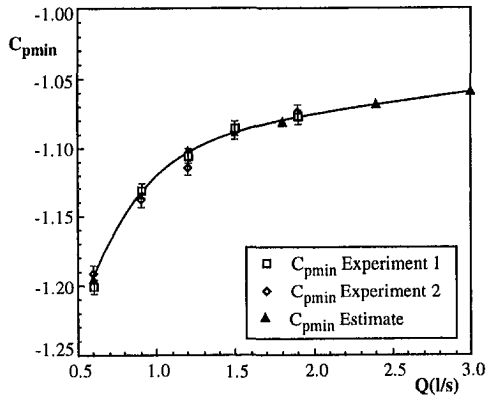

Fig. 4 Minimum pressure coeficient in the venturi throat *v/s* flow rate

stainless steel may be unappropriate due to the relatively high reflection coefficient of the couple (water, stainless steel). Indeed, bubble collapses are acoustically detected in the Venturix by means of a piezo-electric transducer mounted in the diffuser's walls: the pressure wave generated during collapse reflects on the venturi walls, resulting in an oscillating damped acoustic signal (or burst) registered by the ceramic cell. And the discrimination between cavitation events is possible if the typical duration of the acoustic burst from a single collapse is shorter than the average time between cavitation events. The use of stainless steel may give rise to problems, in that the duration of the bursts increases with the reflection coefficient at the boundary water/solid walls. Using a numerical oscilloscope, we examined the acoustic signals received in a stainless steel external cylinder in travelling bubble regime, in order to estimate the typical duration of the acoustic bursts. The measurements led to a mean duration of the bursts in the order of the millisecond, which corresponds to a maximum rate of a thousand discernable events per second. It corresponds to a maximum concentration of 0.3 nuclei/cm^3 for a 3 l/s flow rate, of 1 nuclei/cm^3 for a 1 l/s flow rate. This shows that the use of a stainless steel external cylinder does not give rise to any problem with regard to the acoustic detection of nuclei.

4 Bubble Dynamics and Acoustic Nuclei Detection

The objective of the present numerical investigation is to improve our understanding of bubble dynamics and acoustics in the Venturix. Particularly, we want to assess the consequences of the flow confinement on the acoustic detection of nuclei: the dynamic response of individual bubbles throughout the venturi is evaluated in order to assess the impact of their size on their acoustic signature.

4.1 The Numerical Model. Let us consider a single spherical gas bubble, initially at equilibrium, with a radius R_o under upstream conditions, and which enters into the venturi. We assume that the mass flow through the bubble wall is negligible and that the gas within the bubble has an isothermal behavior. We assume also that there is no slip between the bubble and the surrounding liquid. The external pressure driving the bubble size change is supposed to be equal to the liquid pressure in absence of the bubble at the location of its center.

Up to the throat entrance, the assumption is made that the bubble remains spherical, its radius $R(t)$ obeying the classical Rayleigh-Plesset equation. We solve it by a Runge-Kutta type integration. The Rayleigh-Plesset equation is invalidated when the bubble reaches the throat entrance: the vicinity of the walls must be taken into account as the bubble radius is expected to be of the same order as the transverse dimension of the throat. This influence shifts the form of the bubble from a spherical one to a nonspherical one. We consider a simple physical model to approach this confinement effect: the bubble is transported by a one-directional mean flow bounded by two parallel plates. Its center is located in the middle plan of the channel. The spacing between the plates may remain constant to simulate the throat section or be increased to simulate the prediffuser. A boundary integral method allows us to determine the bubble wall motion and shape distortion during its journey through the throat and the prediffuser. An indirect formulation of the integral problem is used: a single-layer potential is created by source distributions placed on the bubble interface and on the solid walls. A complete description of the method for tracking the moving interface is given by Canot et al. (1991).

4.2 Computer Run Cases. A series of computer runs are made using the method above described. The set of cases which are treated are shown in Table 1.

In Table 1:

- R_o is the initial bubble radius under the upstream pressure P_{up};
- P_{th} is the minimum pressure imposed in the throat;

P_{cr}, R_{cr} are the critical pressure and radius with respect to quasi-static stability;

- R_∞ is the maximal bubble radius given by the Rayleigh-Plesset equation for the same imposed pressure field.

With the static approach, from comparing P_{th} and P_{cr} values, R_∞ and R_{cr} values, we can infer that the calculation cases illustrate two typical situations:

—Cases 1, 2, 3: $P_{th} \leq P_{cr}$ $R_\infty \geq R_{cr}$

The bubble experiences an explosive growth up until it reaches the venturi expansion area. This is followed by a violent implosion. For the present considered cases, the nucleus will be surely detected.

—Case 4: $P_{th} \leq P_{cr}$ $R_\infty \leq R_{cr}$

The pressure in the throat drops below the critical pressure but the bubble does not remain long enough in this region to achieve its critical size. In this case, we can wonder if this bubble is actually activated or not.

In the following section the results obtained are presented and discussed with respect to bubble dynamics and acoustics.

4.3 Computer Run Results and Interpretations. Examples of bubble size and shape histories are illustrated in Fig. 5 and Fig. 6 for case 1 and case 4. In Fig. 5, the bubble size curves are compared with results obtained from integration of the Rayleigh-Plesset equation.

For a detailed description of bubble dynamics in the venturi, we refer the reader to Pham et al. (1995). For present purposes, we focus on the implosion phase. Our goal is to evaluate the amplitude of the acoustic pressure P_a developed during the collapse of different-sized bubbles, P_a being calculated as:

$$\frac{1}{\rho} \cdot [P_a(r, t) - P_\infty(t)] = \frac{1}{4\pi \cdot r} \cdot \ddot{\mathcal{V}}(t - r/c_o)$$

We aim to assess the average $\ddot{\mathcal{V}}(t)$ value during collapse, that is for $z \in [38, 43\ \text{mm}]$. Using an interpolation procedure of the second order, the numerically calculated curves $\ddot{\mathcal{V}}(z)$ are approximated as parabolas. The parabolas equations provide the

Table 1 Calculation cases

	R_o (μm)	P_{up} (Bar)	P_{th} (Pa)	P_{cr} (Pa)	R_{cr} (μm)	R_∞ (μm)
1	10.	1.9278	1.	831.	65.	620.
2	20.	1.9278	0.	1771.	181.	740.
3	50.	1.9278	0.	2164.	706.	955.
4	100.	1.9378	1000.	2252.	2000.	1100.

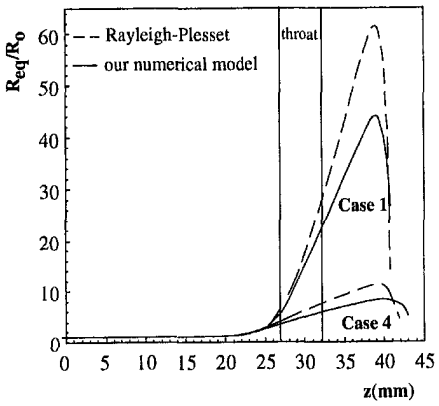

Fig. 5 Bubble size history during venturi traverse (R_{eq} is the radius that a spherical bubble of same volume would have)

average values of the second derivative of the bubble volume with respect to z. The flow velocity is practically constant in the short duct section which is considered; therefore, the second derivative of $\mathcal{V}$ with respect to z is directly proportional to the second derivative of $\mathcal{V}$ with respect to time, then to P_a. The calculated average $\mathcal{V}''(z)$ values are summarized for cases 1 to 4 in Table 2.

In view of these values, we can infer that two antagonistic mechanisms occur:

1 The acoustic pressure amplitude increases with the bubble volume.
2 The bubble implosion is inhibited by the solid boundaries; the restricted mean flow effect being all the more important as the collapsing bubble is large.

Mechanism 1 prevails over mechanism 2. Thereby, bubble acoustics in the Venturix shows up in a similar way as in unbounded liquid: sound emission during collapse increases with bubble size.

According to our analysis, the Venturix is capable of detecting nuclei of all range of sizes, even for a particularly "difficult" situation with respect to acoustic detection (case 4). This conclusion is in disagreement with Ligneul and Bovis' numerical and theoretical work results based on energetic considerations (1986), but compares favourably with Ceccio, Gowing, and Gindroz's results (1995).

5 Investigation of the Venturix Operation by Fast Cinematography

We report in the present section the results and conclusions of an investigation of the Venturix operation by fast cinematography. The primary objective of the study is to correlate the optical and acoustic observations of cavitation, in order to validate the nuclei

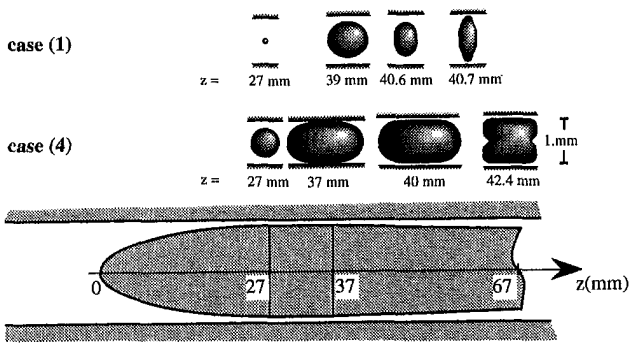

Fig. 6 Bubble shape history during venturi traverse

Table 2 Average value of the second derivative of the bubble volume with respect to z

	R_o (μm)	$R-P$	Our numerical model	Difference $R-P$/our numerical model
1	10	0.480	0.153	0.327
2	20	0.604	0.221	0.383
3	50	0.970	0.309	0.661
4	100	1.192	0.393	0.799

detection method. For this purpose, we carried out nuclei measurements in a venturi, using a plexiglass external cylinder equipped with a piezo-electric cell, and we compared the acoustic and optical nuclei counting results. Seven high-speed movies have been shot using a PHOTEC camera of maximum cadence equal to 10,000 frames per second. The venturi operation conditions which were considered are illustrated in Fig. 7. The corresponding values of the venturi parameter are also specified.

As previously said, the collapse noises are detected by means of a piezo-electric transducer located midway in the diffuser. The piezo-electric cell signal is processed by the electronic signal processor commercialized by the ACB-cerg company. The electronic board delivers normalized squared signals which are then counted. The PHOTEC camera is equipped with a LED system, which can be triggered by an external source. In our case, the monitoring source is the analogical output of the venturi electronic signal processor: the LED marks the film as long as the voltage output of the venturi electronic signal processor is non-zero, which allows to "visualize" on the film the squared signals delivered by the electronic board. By this means, we can simultaneously visualize the hydrodynamic events which take place in the venturi and the output of the venturi electronic board.

5.1 Comparison Between Optical and Acoustic Nuclei Counting Results. We analyze each film frame by frame. This enables us to correlate the number of bubbles crossing the venturi at a given time t, $N_{opt}(t)$, with the number of nuclei, which are acoustically detected at the same moment, $N_{acoustic}(t)$. To take into account the fact that all bubbles are not visible due to the venturi axisymmetric configuration, we introduce a corrective term M. This term is empirically determined based on the occurrence frequency of the following event: a nucleus is acoustically detected but no bubble is visible on the film. M varies from 1.1 to 1.85 depending on the σ_{vent}, values. For each film and corresponding σ_{vent}, we determine an average correlation factor defined as:

$$C_{acous/opt} = \frac{1}{M} \cdot \left(\sum_t N_{acoustic}(t) / \sum_t N_{opt}(t) \right)$$

The evolution of the correlation factor as a function of the venturi parameter is plotted in Fig. 8.

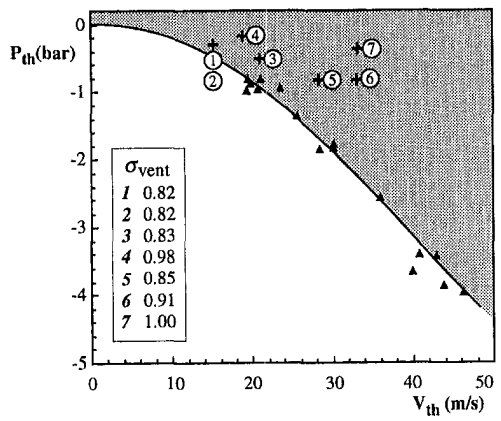

Fig. 7 Venturix operation conditions investigated by fast cinematography

As shown in Fig. 8, the acoustic detection and signal processing system overestimates the nuclei number by a multiplying factor up to seven. The nuclei overcounting is all the more important as the venturi parameter is smaller. More particularly, the venturi parameter must be superior to about 0.9 so that the overcounting factor remains inferior to two. As compared with the value of $[\sigma_{vent}]_{sat}$ determined in Section 3.1.1, it seems that this overcounting phenomenom constitutes a strict limitation to the venturi operation.

5.2 Interpretation With Regard to Bubble Dynamics in the Venturi. According to the flow visualizations by fast cinematography, the discrepancies between optical and acoustic nuclei counting results are due at least in part to bubble splittings occurring in the venturi. We observed, in effect, that important deviations from the bubble single-collapse case occurred as the venturi parameter is decreased:

- Toroidal bubbles formation: during explosion, the bubble takes the shape of a torus of axis normal to the solid walls. When collapsing, the toroidal bubble breaks up into small parts. It is likely that these small bubbles collapse non simultaneously and generate distinct acoustic signals. Previous experimental works (Blake et al., 1987, Vogel et al., 1989) reported similar behavior of bubbles near a solid boundary. They highlighted their instable feature.
- Bubble splitting: during collapse, the bubble splits up into smaller bubbles which collapse non-simultaneously. This observation is in agreement with the results of our numerical modelling of bubble dynamics in the venturi, as well as with previous studies of the dynamics of bubbles located between two solid boundaries (Pham et al., 1992, 1995; Chahine, 1982).
- Bubble rebounds were also observed.

- Toroidal bubbles formation and bubble splitting phenomena are essentially related to the solid walls presence and to the induced deformation of the bubble interface. The confinement effect is all the more important as the cavitation bubble is larger, that is as the venturi parameter is smaller. Accordingly, when the venturi parameter is decreased under a critical value, the excessive growth of the cavitation bubbles in the venturi leads to their division into smaller bubbles which collapse non simultaneously. In others words, a nucleus gives birth to one bubble which breaks up into smaller bubbles which generate during their collapse distinct acoustic signals. As a result, the number of active nuclei is overestimated.

6 Summary and Conclusions

We have reported in the present paper the current results of a work concerned with the development of a new type of CSM. They can be summarized as follows:

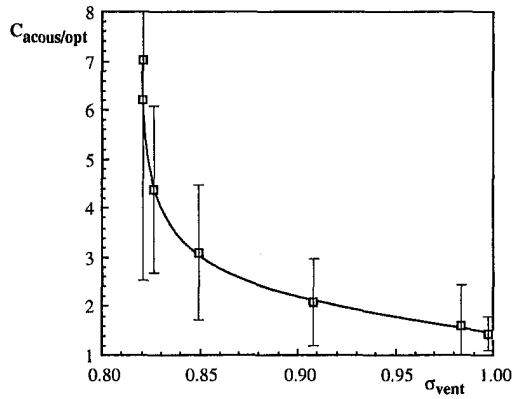

Fig. 8 Correlation factor between acoustic and optical nuclei countings as a function of the venturi parameter

- The Venturix was designed so as to limit the occurrence of choking and flow separation. In particular, we recommend the use of "turbulence generators" in order to trip the boundary layer and avoid flow separation. The internal geometry was accurately defined to obtain, for a reference flow rate, an optimum pressure distribution in the venturi. The latter is characterized in subcavitating regime by a constant pressure in the throat section.
- The proposed design concepts were successfully demonstrated:

According to flow vizualizations, the "turbulence generators" appeared to be very efficient to avoid laminar flow separation. They do not introduce any perturbation in the measurement of the nuclei critical pressure and the Venturix operation is only limited by the occurrence of saturation at high nuclei concentrations.

Measured pressure distributions inside the venturi showed good agreement with numerical predictions.

We examined the acoustic signals received in a stainless steel external cylinder. The use of stainless steel appeared not to give rise to any problem as regards nuclei acoustic detection.

- We carried out a numerical analysis of bubble dynamics and acoustics in the Venturix. The results of this analysis indicate that the Venturix is capable of detecting nuclei of all range of sizes. Indeed, even if the inhibiting effect of restricted mean flow on bubble growth and collapse is more strongly felt by the larger nuclei, acoustic emission increases with bubble size. Thus, large nuclei are as well acoustically detectable as small nuclei.
- An investigation of the meter operation by fast cinematography pointed out the existence of a critical value of the venturi parameter equal to about 0.9. For lower σ_{vent} values, the number of active nuclei which are acoustically detected is overestimated. This overcounting phenomenon is mainly due to bubbles splittings which occur in the venturi. We suggest to modify the signal processing system in order to take this phenomenom into account.

Uncertainties

The error on the pressure is related on the one hand to the size of the pressure tabs (Shaw, 1960), on the other hand to the performance specifications and the accuracy of the pressure transducers. Using a chart given by Barat (1973), we can evaluate the measurements errors due to the tab dimension influence. The estimated maximum error on pressure is equal to 15 mbar. Considering our experimental conditions (3 Bar $\leq P_{up} \leq$ 4.5 Bar), the corresponding relative errors on pressure are less than 1 percent for flow rates lower than 1.9 l/s: for Q = 1.2 l/s the maximum error is equal to 0.2 percent of the throat pressure, for Q = 1.9 l/s it is increased up to 0.8 percent. The maximum standard deviation on C_p is equal to 5.10^{-3}. This establishes the feasability of measuring the static pressure inside the venturi with an acceptable precision. Concerning the transducers' precision, the pressure transducers as well as the flowmeter can be recalibrated during the measurements, which permits to minimize the measurement errors.

Acknowledgments

We would like to thank the Direction des Recherches, Etudes, et Techniques and the Bassin d'Essais des Carènes for their financial support.

References

Arnal, D., Habiballah, M., and Coustols, E., 1984, "Théorie de l'instabilité laminaire—critères de transition en écoulements bidimensionnel et tridimensionnel," *La Recherche Aérospatiale* 2.

Arakeri, V. H., and Acosta, A. J., 1973, "Viscous Effects on the Inception of Cavitation on Axisymmetric Bodies," Part I and II, ASME JOURNAL OF FLUIDS ENGINEERING, Vol. 95, pp. 519–527.

d'Agostino, L., and Acosta, A. J. 1991, "A Cavitation Susceptibility Meter with Optical Cavitation Monitoring Parts I and II," ASME JOURNAL OF FLUIDS ENGINEERING, Vol. 113, pp. 261–277.

Barat, M., 1973, "Les mesures de pression à l'aide de prises à la paroi," Cycle de conférences sur les techniques de mesure dans les écoulements—24–28 September.

Blake, J. R., and Gibson, D. C., 1987, "Cavitation Bubbles Near Boundaries," *Ann. Rev. Fluid Mech.,* Vol. 19, pp. 99–123.

Briançon-Marjollet, L., 1987, "Couche limites, germes et cavités en interaction," Thesis, Grenoble.

Canot, E., and Achard, J. L., 1991, "An Overview of Boundary Integral Formulations for Potential Flows for Fluid-Fluid Systems," *Arc. Mec., Warzawa,* Vol. 43, pp. 453–498.

Ceccio, S. L., Gowing, S., and Gindroz, B., 1995, "A Comparison of CSM Bubble Detection Methods," ASME *Symposium on Gas-Liquid Flows in Fluid Machinery and Devices,* FED Vol. 226, pp. 43–49.

Chahine, G. L., 1982, "Experimental and Asymptotic Study of Nonspherical Bubble Collapse," *Appl. Scient. Res.,* Vol. 45, pp. 187–197.

Franc, J. P., and Michel, J. M., 1985, "Attached Cavity and the Boundary Layer: Experimental Investigation and Numerical Treatment," *Journal of Fluid Mechanics,* Vol. 154, pp. 63–90.

Holl, J. W., and Wislicenus, G. F., 1961, "Scale Effects of Cavitation Phenomena," ASME *Journal of Basic Engineering,* pp. 385–395.

Lecoffre, Y., and Marcoz, J., 1978, "Separate Bubble Cavitation Tests, Control-Method, Nuclei Measurement by Venturi Tube," *La Houille Blanche,* No. 5.

Ligneul, P., and Bovis, A., 1986, "The Use and Limitations of the Venturi Tube as a Cavitation Susceptibility Meter," *International Symposium on Cavitation in Sendai, Japan.*

Oldenziel, D. M., 1982, "A New Instrument in Cavitation Research: The Cavitation Susceptibility Meter," ASME JOURNAL OF FLUIDS ENGINEERING, Vol. 104, pp. 136–142.

Pham, T. M., Michel, J. M., and Lecoffre, Y., 1992, "A New Design of the Cavitation Susceptibility Meter: The Venturix," *International Symposium on Bubble Dynamics and Interface Phenomena,* Birmingham, U.K.

Pham, T. M., Michel, J. M., and Lecoffre, Y., 1995, "Development of a New Type of CSM: Design Concepts and Investigation of Performance Characteristics," *International Symposium on Cavitation,* CAV'95, Deauville, France.

Plesset, M. S., and Chapman, R. B., 1971, "Collapse of an Initial Spherical Vapour Cavity in the Neighbourhood of a Solid Boundary," *Journal of Fluid Mechanics,* Vol. 47, Part 2, pp. 283–290.

Shaw, R., 1960, "The Influence of Hole Dimensions on Static Pressure Measurements," *Journal of Fluid Mechanics,* Vol. 7, pp. 550–564.

Vogel, A., Lauterborn, W., and Timm, R., 1989, "Optical and Acoustic Investigations of the Dynamics of Laser-Produced Cavitation Bubbles Near a Solid Boundary," *Journal of Fluid Mechanics,* Vol. 206, pp. 299–338.

O. Boulon
PhD. Student.

J. P. Franc
Research Assistant.

J. M. Michel
Research Director.

Laboratoire des Ecoulements
Géophysiques et Industriels,
Institut de Mécanique de Grenoble, BP 53,
38041 Grenoble Cedex 9, France

Tip Vortex Cavitation on an Oscillating Hydrofoil

This paper discusses tests conducted in the hydrodynamic tunnel of the University of Grenoble on a 3D oscillating hydrofoil. Visualization of unsteady tip vortex cavitation indicates a strong influence of the water nuclei content. The investigation was focused on the influence of the oscillation frequency on tip vortex cavitation inception. For very low nuclei content, cavitation inception is strongly delayed as compared to the steady-state results at very small oscillation frequencies. This delay is significantly reduced by nuclei seeding. The results can be explained by assuming that the time required for the inception of cavitation in the tip vortex corresponds to the time necessary for a cavitation nucleus to be captured by the vortex core.

1 Introduction

Marine propellers generally operate under unsteady conditions. During one revolution, a propeller blade experiences varying pressure and velocity conditions because of a number of phenomena, such as the wake of the hull or the variation in submersion depth. Therefore, it is important to know the influence of unsteadiness on the inception and the development of cavitation, especially the tip vortex cavitation which generally appears first.

Tip vortex cavitation is still extensively studied (see in particular, Arndt et al., 1991, Fruman, 1995), but only a very few number of results are related to tip vortex cavitation under unsteady conditions. To our knowledge, the only results available on the subject are those of Hart et al. (1991, 1992) and McKenney and Hart (1993). They conducted experiments on a NACA 64A309 cross section hydrofoil of rectangular planform, oscillating sinusoidally in pitch about the center of pressure at frequencies varying between 0 and 50 Hz, this corresponding to a reduced frequency f^* ranging from 0 to 2. The mean angle of attack was 5 or 7 degrees and the oscillation amplitude ± 2 or ± 5 degrees. Their visualization show an intricate vortex chain resulting from the interaction between the tip vortex and the spanwise vortices shed from the trailing edge by the oscillating foil.

The present study, which is also relative to an oscillating hydrofoil, is part of a French program on tip vortex cavitation involving several laboratories. Main results in steady flow were presented by Fruman et al. (1992). Because of the large number of parameters involved in the unsteady configuration (σ, Re, V, nuclei content, f, α_0, $\Delta\alpha$), it is difficult to conduct a comprehensive research program. We focused our attention on a few typical questions, mainly the influence of nuclei content and oscillation frequency on the inception of tip vortex cavitation. It allowed us to analyze this type of unsteady cavitation in terms of the three characteristic times important in this problem: the oscillation period, the nucleus capture time, and the transit time c/V. A few additional conditions were examined briefly and are the effects of mean angle of attack and Reynolds number.

2 Experimental Facilities

The tests were conducted in the free surface channel of the hydrodynamic tunnel of the University of Grenoble (Briançon-Marjollet and Michel, 1990). The flow velocity can vary between 3 and 12 m/s and the turbulence intensity is about 1.5‰.

Contributed by the Fluids Engineering Division for publication in the JOURNAL OF FLUIDS ENGINEERING. Manuscript received by the Fluids Engineering Division July 5, 1995; revised manuscript received December 3, 1996. Associate Technical Editor: Jong H. Kim.

The hydrofoil has a symmetrical NACA 16-020 cross-section and an elliptical planform. The maximum chord length is $c = 60$ mm, the span length is $b/2 = 90$ mm and the aspect ratio is $A = 3.8$. The dimensions of the test section and the foil arrangement are shown in Fig. 1.

The foil is oscillating sinusoidally in pitch around its mid-chord. The instantaneous angle of attack $\alpha(t)$ is given by $\alpha(t) = \alpha_0 + \Delta\alpha \sin 2\pi ft$. All the results presented here correspond to an oscillation amplitude $\Delta\alpha$ equal to 5 degrees. The mean angle of attack is generally kept constant at 10 degrees, although a few tests were conducted for other values to analyse the effect of this parameter (see Section 5). The oscillation frequency f is systematically increased from 0 to 24 Hz; the maximum value of the reduced frequency f^*, obtained for the minimum flow velocity of 3 m/s, is about 0.5. Most tests were carried out at a Reynolds number equal to 4.5×10^5, i.e., at a flow velocity of about 7 m/s; the influence of Reynolds number is analyzed in Section 6.

A fundamental parameter to be controlled during the tests is the water quality which is characterized by the nuclei content. The hydrodynamic tunnel of the University of Grenoble is equipped with a nuclei seeding device which is done by the injection of water saturated with air at high pressure, and a classical cavitation susceptibility meter for nuclei measurement (Briançon-Marjollet and Michel, 1990). In the present study, two water qualities were considered: one corresponds to normal operating conditions without nuclei injection, whereas the other one corresponds to maximum nuclei injection. They are characterised by the histograms of critical pressure presented in Fig. 2. We can roughly consider that, without nuclei seeding, there is almost no cavitation nucleus in the water, in comparison to the case with nuclei injection.

Visualization were systematically obtained for various operating conditions either by high-speed movies or by video recording under stroboscopic lighting at a frequency slightly different than the oscillation frequency.

From visualization obtained by video recording, it is possible to determine the inception of tip vortex cavitation. In the case of an oscillating foil, tip vortex cavitation appears during the oscillation cycle and, for any value of the cavitation parameter, inception is characterized by a critical value of the angle of attack.

Cavitation inception is detected visually. It is known that such a procedure may be lacking in accuracy, especially in the case of high nuclei contents for which it may be difficult to distinguish between actual cavitation and a simple migration of nuclei toward the vortex core with a limited growth. To limit the subjectivity of inception measurements, two inception criteria were defined:

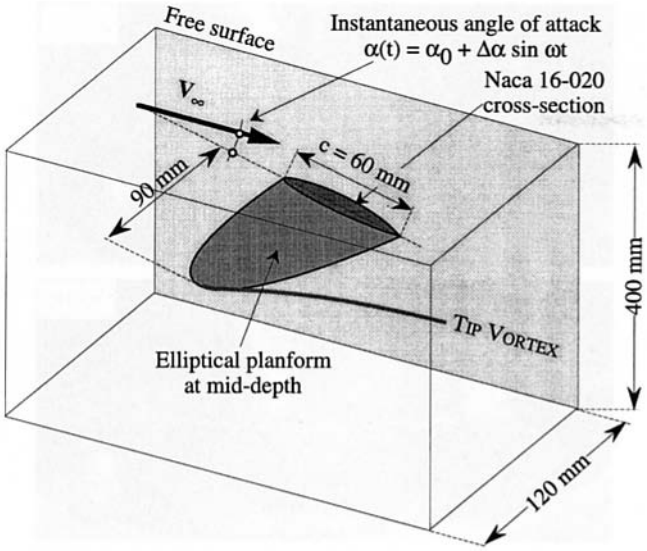

Fig. 1 Test section and foil arrangement

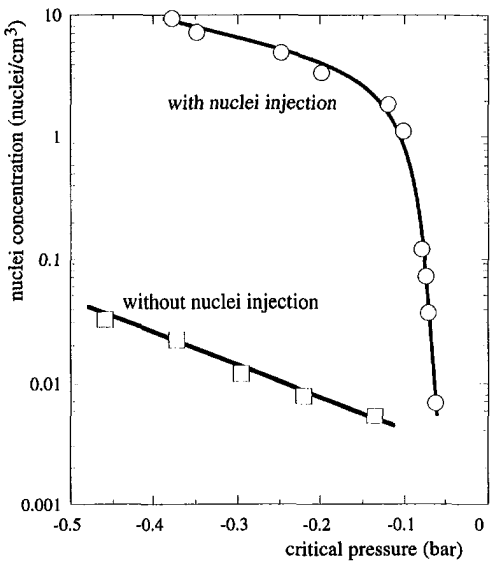

Fig. 2 Histograms of critical pressure presenting the difference in water nuclei content with and without nuclei injection for σ = 1.2 and V = 7.7 m/s

- *the occurrence of intermittent cavitation along the vortex path* which consists in determining the "first" cavitation bubble;

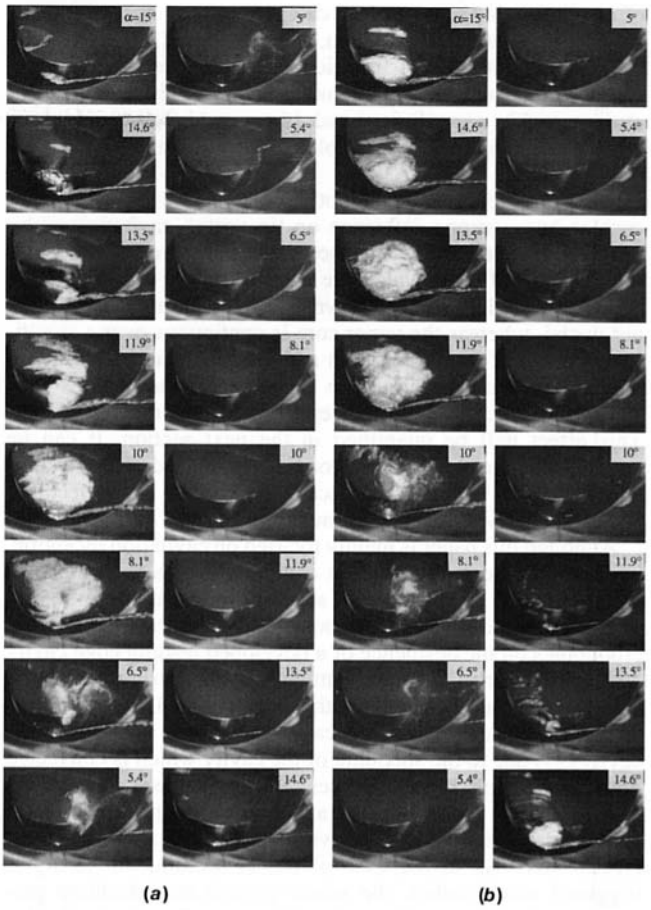

Fig. 3 Visualization of tip vortex cavitation during one period of oscillation for σ = 1.2, α_0 = 10 deg, $\Delta\alpha$ = 5 deg, f = 23.3 Hz, with and without nuclei injection, at Re = 4.5 10^5. The origin of time t/T = 0 for the first image (upper left) of both cycles corresponds to the maximum angle of attack. The time interval between two consecutive images is $\Delta t/T = \frac{1}{16}$. (*a*) Without nuclei injection; (*b*) with nuclei injection

- the occurrence of a permanent vapour core *attached* to the tip.

It was noticed that the second criterion was much easier to observe and much more reproducible than the first one, especially under unsteady conditions. Consequently, all the inception measurements presented are relative to this second criterion, except in Section 4.1, where a comparison of both criteria is presented under steady conditions.

3 Visualization

Figure 3 presents an example of visualization obtained from high-speed movies at a rate of 4000 frames/s. A whole period

Nomenclature

a = viscous core radius m
A = aspect ratio $A = 4b/\pi c = 3.8$
$b/2$ = span length $b/2$ = 90 mm
c = chord length c = 60 mm
f = oscillation frequency Hz
f^* = reduced oscillation frequency $f^* = fc/V$
n = nuclei density nuclei/cm^3
p = pressure Pa
p_{ref} = reference hydrostatic pressure at foil tip Pa
p_v = vapor pressure Pa
r = radial distance m
R = microbubble radius m
Re = Reynolds number —
t = time s
T = oscillation period $T = 1/f$ s
T_ν = viscous time $T_\nu = R^2/4\nu$ s
V = flow velocity m/s
$\dot{W}$ = bubble velocity m/s
α = instantaneous angle of attack degree
α_0 = mean angle of attack degree
Γ = vortex strength m^2/s
$\Delta\alpha$ = oscillation amplitude degree
ν = liquid kinematic viscosity m^2/s
ρ = liquid density kg/m^3
σ = cavitation parameter $\sigma = (p_{ref} - p_v)/(\frac{1}{2}\rho V^2)$
τ = radial capture time s
τ' = axial feeding time s
ω = vortex rotational speed rd/s

of oscillation is shown in two cases: Fig. 3(a) corresponds to the case without nuclei injection, whereas Fig. 3(b) corresponds to the case with nuclei injection, all other parameters being unchanged. The presence of nuclei in case 3(b) is confirmed on images 13 (α = 10 deg) and 14 (α = 11.9 deg) on which we can observe cavitation bubbles exploding on the upper-side of the foil.

A careful comparison of both cases shows that the nuclei content has a strong influence on tip vortex cavitation under unsteady conditions. For instance, if we compare images 14 (α = 11.9 deg) of both cycles, we observe only a cavitation spot approximately half a chord downstream the tip in the case without nuclei, whereas the vapor core is continuous over a significant portion of the vortex path and already attached to the tip in the case with seeding. The presence of nuclei leads to a significant advance in the inception of tip vortex cavitation. This effect will be quantified in the next section. It can be noticed that the development of the leading edge cavity also experiences a significant advance in the case of nuclei seeding, compared to the case without nuclei injection.

Although this paper is mainly focused on cavitation inception, we can observe on Fig. 3 that cavitation desinence is also in advance in the case of nuclei seeding. Whereas the influence of nuclei on inception is commonly accepted, the effect of microbubbles on the desinence of a developed leading edge cavity and on tip vortex cavitation might appear intriguing at first sight. If we observe in detail both cycles of Fig. 3, the disappearance of cavitation—tip vortex cavitation as well as leading edge cavity—is due to the shedding of the cavity which is convected downstream and then collapses. For both cases, the cavity growth process is very similar and the shedding process seems to take place as soon as the cavity has reached about the same critical size. As in the case of nuclei seeding the cavity is triggered much earlier, the whole growth and shedding processes are in advance. Thus, the desinence of cavitation is also in advance in the case of nuclei seeding.

At high reduced oscillation frequencies, the tip vortex path has a clear sinusoidal shape characterized by a wavelength $\lambda = V/f$ or a reduced wavelength $\lambda/c = 1/f^*$ as shown on Fig. 4. It is made of a sequence of noncavitating and cavitating pieces according to the phase of their emission in the oscillation cycle. If we look at the vortex tip in more details, we can observe that the cavitating vortex becomes thicker near the tip and changes into a twisted ribbon (Fig. 5, α = 14 deg). Then it seems to split (Fig. 5, α = 15 deg) and to give birth to a secondary cavitating vortex (Fig. 5, α = 12, 10 and 6 deg) of rather spanwise nature, contrary to the tip vortex which is fundamentally a streamwise structure.

The formation of this secondary vortex is difficult to interpret. According to Arndt et al. (1991), who reported similar observations in the steady case, it may originate in a difference of vorticity associated to a separation bubble of varying length. It may also be connected to the classical mechanism of shedding

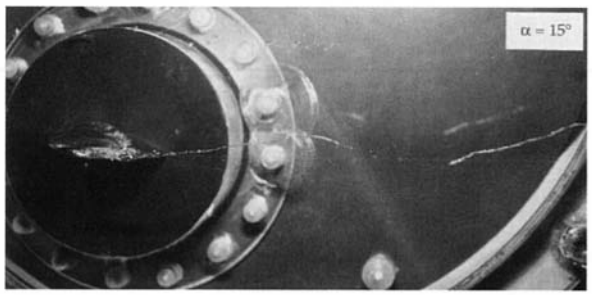

Fig. 4 Overall view of the sinusoidal tip vortex path downstream the oscillating hydrofoil at high reduced oscillation frequency with nuclei injection. σ = 1, Re = 2 10^5, f = 23.3 Hz, f^* = 0.4, α_0 = 10 deg, $\Delta\alpha$ = 5 deg

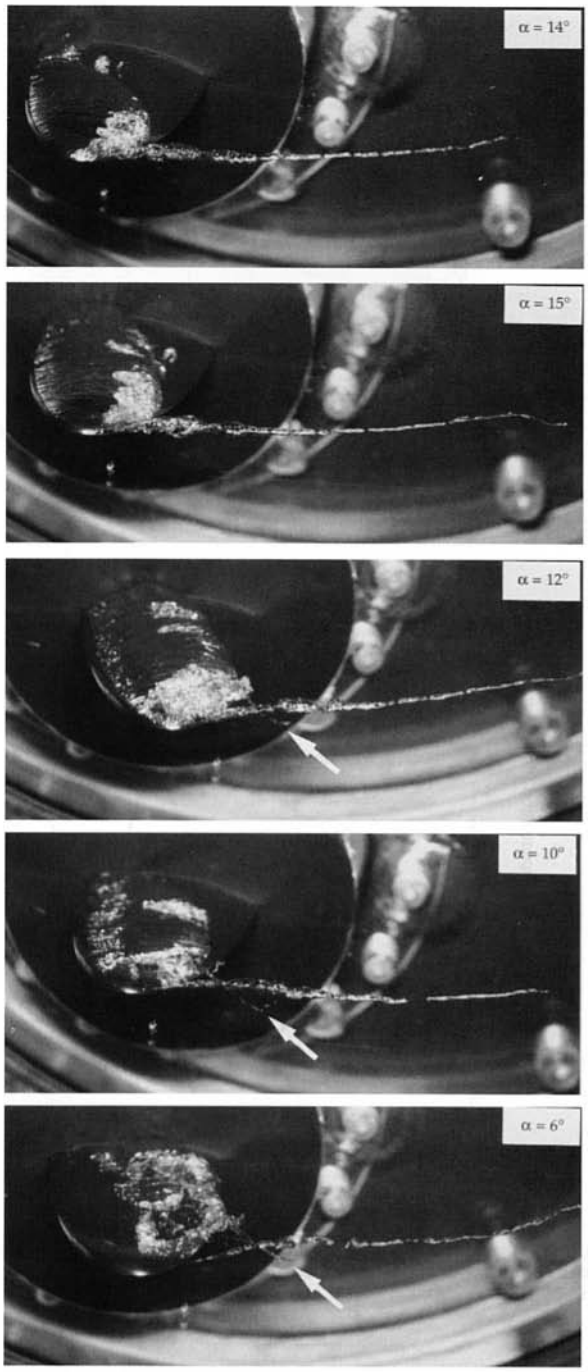

Fig. 5 Visualization of tip vortex cavitation at high reduced oscillation frequency, with nuclei injection, σ = 1, Re = 2 10^5, f = 23.3 Hz, f^* = 0.4, α_0 = 10 deg, $\Delta\alpha$ = 5 deg

of spanwise vortices by a partial cavity. Anyhow, the greatest care must be taken in the interpretation of visualization by cavitation in so far as a non cavitating—and so invisible—vortex is very likely to pre-exist to the vapor structure.

4 Tip Vortex Cavitation Inception

4.1 Steady Case. Figure 6 shows that, in steady flow, the incipient cavitation number defined on the basis of the vapor core getting attached to the tip does not depend upon the nuclei content. On the contrary, in the case of nuclei injection, the "first" bubble appears before the case without nuclei injection.

Results presented in Fig. 6 are independent of the experimental procedure i.e., operating either at fixed σ and increasing α

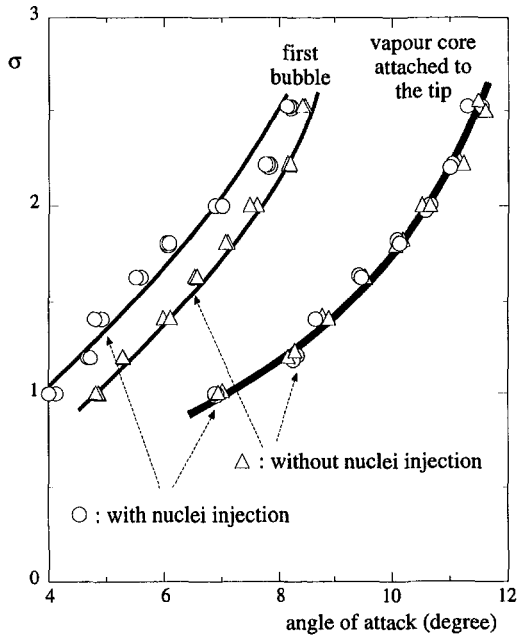

Fig. 6 Incipient cavitation numbers versus the angle of attack for Re = 4.5 10^5 with and without nuclei injection

or at fixed α and decreasing σ. In addition, no hysteresis is observed between inception and desinence.

4.2 Unsteady Case. Figure 7 presents the angle of attack for which the vapor core gets attached to the tip (called incipient angle of attack α_i) versus the reduced frequency for $\sigma = 1.6$ and for the two water qualities considered in the present study. The case $f^* = 0$ corresponds to the steady state for which we already noticed that no nuclei effect exists if the second inception criterion is used. For this reason both curves start from the same point.

In the case of nuclei seeding, when the reduced oscillation frequency increases, the incipient angle of attack gradually increases. For the higher reduced frequency $f^* = 0.2$ considered in Fig. 7, the inception of tip vortex cavitation is delayed about 3 degrees in comparison with the quasi-steady case and is about 2 degrees in advance with respect to the case without nuclei seeding at the same frequency.

Without nuclei injection, we observe on Fig. 7 a strong unsteady effect for very small values of the reduced frequency $f^* < 0.01$, characterized by an inception delay of more than 4 degrees. On the contrary, for values of the reduced frequency greater than about 0.05, no unsteady effect is visible on tip

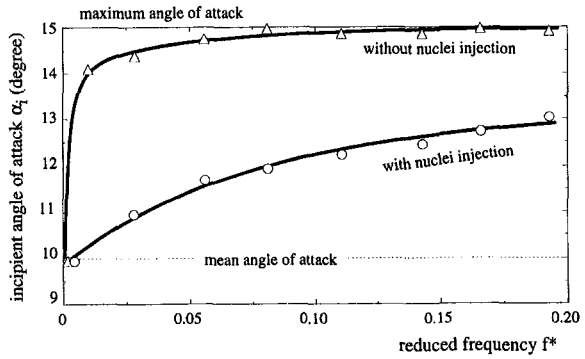

Fig. 7 Incipient angle of attack as a function of reduced frequency for $\sigma = 1.6$, $\alpha_0 = 10$ degrees, $\Delta\alpha = 5$ degrees, with and without nuclei injection, at Re = 4.5 10^5

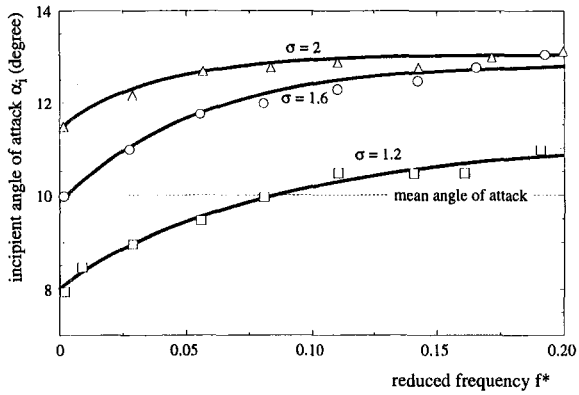

Fig. 8 Incipient angle of attack as a function of reduced frequency for $\sigma = 2$, 1.6, and 1.2, $\alpha_0 = 10$ degrees, $\Delta\alpha = 5$ degrees, with nuclei injection, at Re = 4.5 10^5—Influence of cavitation number.

vortex cavitation; it always occurs around the maximum angle of attack.

For a higher value of the cavitation parameter equal to 2, the incipient angle of attack also increases gradually with the oscillation frequency in the case of nuclei seeding. The difference is that the tip vortex does not cavitate without nuclei injection. A synthesis of the values of the incipient angle of attack versus the reduced frequency for various values of the cavitation number is given on Fig. 8. Lower values of the cavitation number ($\sigma < 1$) were not investigated in detail because cavitation is much more developed and a leading edge cavity strongly interacts with the tip vortex.

We emphasize on the observation that, as soon as the foil oscillates, i.e., for an oscillation frequency as small as 1 Hz, an important delay of about 4 degrees is observed without nuclei injection. This delay is considerably reduced if the flow contains a high enough nuclei concentration. Therefore, the effect of the reduced frequency on the incipient angle of attack, which is shown in Fig. 7, appears to be a combined effect of unsteadiness and water quality. This question will be discussed in more details in Section 7.

5 Effect of Mean Angle of Attack

Figure 9 illustrates the influence of the mean value of the angle of attack α_0 on tip vortex cavitation inception. Two different values of α_0 were chosen and the oscillation amplitude was kept constant at 5 degrees.

For a given water quality, cavitation inception appears to be delayed by an increase of the mean angle of attack. It is satisfactory to find out that this delay vanishes as the reduced oscillation frequency approaches zero, i.e. under quasi-steady conditions.

6 Effect of Reynolds Number

The effect of Reynolds number was investigated by varying the flow velocity. Table 1 gives a few results in a particular case. It clearly appears that the Reynolds number has no significant influence on the inception of tip vortex cavitation under unsteady conditions, at least in its limited range of variation presently investigated.

7 Discussion of Results

Let us consider again the results related to the case without nuclei injection presented in Section 4.2 (in particular Fig. 7). The question is to interpret why there is such an important influence of the oscillation for reduced frequencies as small as 0.01.

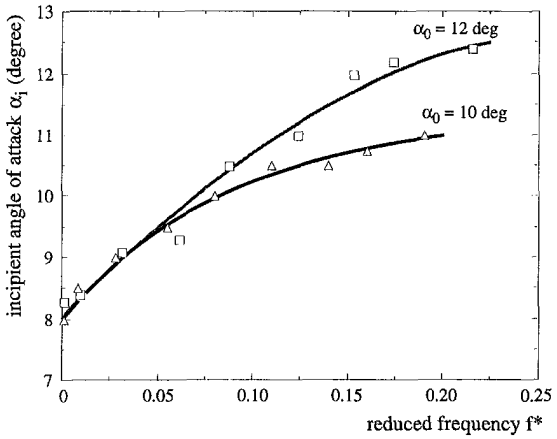

Fig. 9 Incipient angle of attack as a function of reduced frequency for $\sigma = 1.2$, $\Delta\alpha = 5$ degrees, with nuclei injection, at Re = 4.5 10^5—Influence of mean angle of attack.

A priori, we could suspect a purely unsteady effect affecting, in particular, the setting of the vortex strength. The reduced frequency, which is defined by:

$$f^* = \frac{fc}{V} = \frac{c/V}{T}$$

measures the ratio of the time required for a fluid particle to go over the chord length, to the period of oscillation. If $f^* = 0.01$, the displacement of the foil can be neglected during the transit time $T/100$ of a particle along the chord length: the fluid particle will indeed not feel the foil movement during its travel. We can then expect that quasi-steady conditions are achieved, and tip vortex cavitation should appear for a value of the angle of attack close to the one corresponding to the steady case. Then, unsteadiness cannot be the major reason for such an inception delay at very low reduced frequencies.

Furthermore, in steady flow and without nuclei seeding, if the foil is rapidly moved from 0 degree to the angle of attack corresponding to tip vortex cavitation inception (for a given σ value), we observe the inception of cavitation after a delay, which is variable and of the order of a few seconds, and in any case much larger than c/V. Then, it is clear that tip vortex cavitation requires some time to appear after the flow is settled.

Considering present experimental results on the influence of water quality in unsteady flow, we are led to conjecture that this inception time is the time required for a nucleus to enter the vortex core. According to this interpretation, the effect of the reduced frequency presented in Section 4.2 appears to be a combined effect of water quality and unsteadiness.

Two different mechanisms are possible, for a nucleus to reach the vortex core. A nucleus can be radially captured by the tip vortex because of its rotational speed, or, it can feed the vortex core from upstream in an axial way. Both assumptions are examined hereafter.

7.1 Radial Capture. A microbubble of constant radius R moves toward the vortex core with a velocity $\vec{W}$ according to the classical Johnson and Hsieh equation (Ligneul and Latorre, 1989):

$$\frac{d\vec{W}}{dt} = -3\,\frac{\text{grâd}\,p}{\rho} - 9\,\frac{\nu}{R^2}(\vec{W} - \vec{V}). \qquad (1)$$

This equation of motion of the microbubble takes into account the added mass of the bubble, the pressure forces exerted by the rotating flow and the drag evaluated on the basis of the Stokes formula. $\vec{V}$ is the purely tangential flow velocity induced by the tip vortex and $|\text{grâd}\,p| = \rho V^2/r$ the corresponding pressure gradient at a radial distance r from the core.

We suppose that the nucleus radius R is small enough, so that the term on the left-hand side can be neglected in comparison with the second term on the right-hand side. It is equivalent to suppose that the viscous time T_ν defined by $T_\nu = R^2/4\nu$ is much smaller than the nucleus capture time denoted by τ. This assumption, which will be checked a posteriori, leads to the following simplified equation:

$$\vec{W} - \vec{V} = -\frac{R^2}{3\nu}\,\frac{\text{grâd}\,p}{\rho}. \qquad (2)$$

Equation (2) simply means that the pressure forces exactly balance the viscous drag at any time. As a result, the microbubble has a tangential velocity component equal to the flow tangential velocity, and a centripetal velocity component given by:

$$-\frac{dr}{dt} = \frac{R^2}{3\nu}\,\frac{V^2}{r}. \qquad (3)$$

The tangential flow velocity in the tip vortex is given by:

$$V = \frac{\Gamma}{2\pi r} \qquad (4)$$

where Γ denotes the vortex strength. By integrating Eq. (3) we get the instantaneous radial position r of the micro bubble as a function of time t and of its initial position r_0:

$$r_0^4 - r^4 = \frac{4}{3}\,\frac{R^2}{\nu}\,\frac{\Gamma^2}{4\pi^2}\,t. \qquad (5)$$

The capture time τ is the time necessary for the bubble to reach the vortex core $r = 0$. We get from Eq. (5):

$$\tau = \frac{3}{4}\,\frac{\nu}{R^2}\,\frac{4\pi^2}{\Gamma^2}\,r_0^4. \qquad (6)$$

If we consider a classical Rankine vortex of core radius, a, and rotational speed, ω, the vortex strength is given by $\Gamma = 2\pi\omega a^2$ and finally, the capture time is:

$$\tau = \frac{3\nu r_0^4}{4\omega^2 R^2 a^4}. \qquad (7)$$

The parameters a and ω can be estimated from LDV measurements. Typical values in the present case (Fruman et al., 1992) are $a = 0.9$ mm and $\omega = 10000$ rd/s. These values are characteristic of the steady case and are used in the present unsteady configuration to get estimates of capture times.

The distance r_0 between the vortex centre and the nearest nucleus highly depends upon the nuclei density. Cavitation inception generally occurs on a limited part of the vortex, in the vicinity of the tip. For a rough estimate, we shall suppose that inception can occur on a length of the order of the chord length c. If the nuclei density is n, a cylinder of length c and radius r_{max} defined by:

Table 1 Influence of Reynolds number on tip vortex cavitation inception for $\sigma = 1.6$, $\alpha_0 = 10$ degrees, $\Delta\alpha = 5$ degrees, $f^* = 0.1$, with nuclei injection

Re	1.8 10^5	4.6 10^5	7.4 10^5
V (m/s)	2.7	6.7	10.8
f (Hz)	4.5	11.1	18.1
α at inception (°)	11.1	11.4	11.2

Table 2 Estimates of the capture time for two different water qualities

	Without nuclei injection	With nuclei injection
n (nuclei/cm^3)	0.05	10
r_0 (mm)	6.8	0.49
τ	0.98 s	26 μs

$$r_{max} = \frac{1}{\sqrt{\pi n c}} \tag{8}$$

contains, on an average, one nucleus. Then, the mean value of the distance of a nuclei to the vortex core is $r_0 \approx \frac{2}{3} r_{max}$.

From Fig. 2, the nuclei concentrations can be chosen equal to about 0.05 and 10 for the two water qualities. If we consider a typical nucleus radius $R = 5$ μm, we get the rough estimates presented in Table 2.

As the nuclei moves toward the vortex core, it goes through decreasing pressures and grows. The present computation does not take into account this phenomenon as the nucleus radius is supposed constant in Eq. (1).

Let us notice that the viscous time given as $T_\nu = R^2/4\nu$ is equal to 6 μs and is smaller than the capture time τ, as assumed a priori. The assumption is less proper in the case of nuclei seeding.

7.2 Axial Feeding. In the case of an axial feeding, the nucleus enters the vortex core from upstream through a circular section of radius a. If the nuclei density is n, a cylinder of radius a and length l defined by:

$$l = \frac{1}{n\pi a^2} \tag{9}$$

contains, on an average, one nucleus. Then, the mean time τ' for a nucleus to axially feed the vortex core is of the order of:

$$\tau' = \frac{l}{V} = \frac{1}{n\pi a^2 V} \tag{10}$$

Considering again the orders of magnitude of nuclei concentrations given in Table 2, we get, for $a = 0.9$ mm and $V = 7.7$ m/s:

- $\tau' \approx 1$ s without nuclei injection
- $\tau' \approx 5$ ms with nuclei injection.

7.3 Interpretation of Experimental Results. Whatever may be the feeding mechanism (radial or axial), the orders of magnitude presented in Sections 7.1 and 7.2 show that, without nuclei injection, the time required for a microbubble to reach the vortex core and initiate cavitation is of the order of one second whereas it is much smaller in the case of nuclei injection, due to the large increase in nuclei concentration.

If the period of oscillation is small with respect to this capture time, there will not be enough time for a nucleus to reach the vortex core and trigger cavitation during each cycle of oscillation. In that case, a significant deviation from the quasi-steady case is expected. On the contrary, if the period of oscillation is much larger than the capture time, cavitation is quasi instantaneously triggered.

Even though some very crude assumptions were made, the above-mentioned values give a satisfactory account of the experimental results presented in Section 4.2. It can be noticed that, in the case of nuclei seeding, the capture times τ and τ' are so small that no nuclei effect is expected in practice; nevertheless, a purely unsteady effect (i.e., not connected with the water quality but affecting for instance the instantaneous vortex strength) is expected for reduced oscillation frequencies getting near one. It is the reason for the progressive increase in cavitation inception delay observed for $f^* < 0.2$, which is quite different in nature for the one observed for $f^* \cong 0.01$ without nuclei injection.

8 Conclusions

The inception of tip vortex cavitation on an oscillating hydrofoil strongly depends upon the oscillation frequency and the nuclei concentration.

- For very low nuclei content, an important delay (in comparison with the steady flow) is observed for reduced oscillation frequencies as small as 0.01. At higher frequencies, this delay tends to become independent of the oscillation frequency, cavitation inception occurring close to the maximum angle of attack.
- The injection of nuclei significantly decreases the delay observed for $f^* \cong 0.01$ without nuclei seeding. In addition, the delay increases much more gradually as the reduced oscillation frequency increases.

The unsteady effect discussed in the present study is closely correlated to the nuclei concentration. More precisely, cavitation will occur in the core of the tip vortex only if a nucleus has enough time to reach the core during the period of oscillation and trigger cavitation.

- If the nuclei concentration is so small that the capture time is much higher than the period of oscillation, a combined effect of water quality and unsteadiness is expected. It generates a significant delay at reduced oscillation frequencies, much smaller than one.
- On the contrary, if the nuclei concentration is so high that the capture time is negligible in comparison with the period of oscillation, we have to do with a purely unsteady effect which becomes significant when the period of oscillation approaches the transit time c/V ($f^* \approx 1$).

In conclusion, from a fundamental viewpoint, tip vortex cavitation inception on an oscillating hydrofoil is essentially controlled by three characteristic times: the oscillation period, the nucleus capture time, and the transit time c/V. In particular, the delay in the inception of cavitation strongly depends upon the relative orders of magnitude of these three characteristic times. From an experimental viewpoint, the present study confirms the fundamental importance of controlling the water quality, especially for the investigation of unsteady cavitating flows.

Acknowledgments

This work was conducted with the financial support of the "Direction des Recherches, Etudes et Techniques" (DRET) and is part of a program "Action Concertée Cavitation", headed by DRET (contract No 92-080).

Experimental Uncertainties

The uncertainties on incipient cavitation numbers and incipient angles of attack are respectively of the order of ± 0.05 and ± 0.2 deg. These estimates result from various series of tests carried out independently by several experimentators. The uncertainties on the determination of flow parameters (as flow velocity and pressure) are negligible in comparison with differences of visual appreciation of cavitation inception or defaults of reproducibility.

References

Arndt R. E. A. and Keller A. P., 1991, "Water Quality Effect on Cavitation Inception on a Trailing Vortex," ASME-JSME Fluids Engineering Conference, Portland, Oregon, June 23–27, FED-Vol. 116, pp. 1–9.

Arndt R. E. A., Arakeri V. H. and Higuchi H., 1991, "Some Observations of Tip-Vortex Cavitation," *Journal of Fluid Mechanics,* Vol. 229, pp. 269–289.

Briançon-Marjollet L., and Michel J. M., 1990, "The Hydrodynamic Tunnel of I.M.G.: Former and Recent Equipments," ASME JOURNAL OF FLUIDS ENGINEERING, Vol. 112, pp. 338–342.

Fruman D. H., 1995, "The ⟨⟨Action Concertée Cavitation⟩⟩ Program and Accomplishments," *International Symposium on Cavitation,* 2–5 May, Deauville, France.

Fruman D. H., Dugué C., Pauchet A., Cerrutti P., and Briançon-Marjollet L., 1992, "Tip Vortex Roll-Up and Cavitation," *19th Symposium on Naval Hydrodynamics,* Seoul, Korea, Aug.

Hart D. P., 1991, "Cavitation Inception in the Tip Vortex Region of an Oscillating Hydrofoil," 1991 ASME *Cavitation and Multiphase Flow Forum,* FED-Vol. 109, pp. 35–41.

Hart D. P., Acosta A., and Leonard A., 1992, "Observation of Cavitation and Wake Structure of Unsteady Tip Vortex Flows," *International STG Symposium on Propulsors and Cavitation,* June 22–24, Hamburg, Germany.

Ligneul P., and Latorre R., 1989, "Study on the Capture and Noise of Spherical Nuclei in the Presence of the Tip Vortex of Hydrofoils and Propellers," *Acoustica,* Vol. 68, pp. 1–14.

McKenney E. A. and Hart D. P., 1993, "Experimental Determination of Bound Circulation and Shed Vorticity Induced by an Oscillating Hydrofoil," 1993 ASME *Cavitation and Multiphase Flow Forum,* FED-Vol. 153, pp. 87–91.

F. Castro
Professor of Fluid Mechanics,
Departamento de Ingeniería
Energética y Fluidomecánica,
Universidad de Valladolid,
47011 Valladolid, Spain

A. Crespo

F. Manuel

Professors of Fluid Mechanics,
Departamento de Ingeniería
Energética y Fluidomecánica,
E.T.S.I.I., Universidad
Politécnica de Madrid,
28006 Madrid, Spain

D. H. Fruman
Professor of Fluid Mechanics,
Groupe Phénomènes d'Interface. ENSTA,
Palaiseau, 91120 France

Equilibrium of Ventilated Cavities in Tip Vortices

The behavior of air cavities formed in the tip vortex trailing from rectangular and elliptical planform hydrofoils has been examined both theoretically and experimentally. These cavities have some peculiarities, in particular their ability to move upstream and reach a stable position near the hydrofoil. Detailed measurements of the velocity components and the cavity characteristics have been made. The results are compared with the predictions of a theoretical model based on the equilibrium balance of a cavity developing in a Lamb vortex.

1 Introduction

It is well known that a finite span wing generates a tip vortex with a low pressure region in its inner core. Vapor cavities can occur depending on the value of the minimum pressure reached on the vortex axis. However, since rotating flows are extremely effective in capturing nuclei (free small air or noncondensable gas bubbles), vapor cavities occurrence is often, especially for large air contents in the water, very difficult to distinguish from partially or totally ventilated cavities. This situation is particularly evident when critical (inception) cavitation numbers for different air contents are plotted as a function of Reynolds numbers (Arndt et al., 1991). Indeed, for increasing air content the inception cavitation number tends to become nearly independent of the Reynolds numbers. Moreover, for large air content values (termed weak water), the inception cavitation numbers at a given Reynolds number become weakly dependent on the lift coefficient (Arndt and Keller, 1992). Assuming that the tangential velocity distribution of the tip vortex behaves as a Rankine or Lamb model, it is easy to show that the pressure prevailing in the vortex core decreases as the square of the lift coefficient and the power 0.4 of the Reynolds number. Incipient cavitation numbers that are weakly dependent on both the lift coefficient and the Reynolds numbers are characteristic of gaseous cavitation; the effect of dissolved air on cavitation characteristics has been reviewed by Arndt (1981). Therefore, it appears that, for water containing large amounts of free air, capture of nuclei is the dominant effect and that ventilated cavities are formed prior to the occurrence of vapor cavities. It has been noted by Arndt and Keller (1992) that in weak water the inception phenomenon is highly intermittent. To explain this intermittence, these authors proposed a simple model based on the tangential velocity distribution of a Rankine type vortex showing that two vortex structures, one single phase, and the other two-phase, can exist.

If a finite span hydrofoil is tested in a cavitation tunnel and if the water circulating in the tunnel is well deaerated, when the pressure is reduced below the one for tip vortex cavitation inception, the diameter of the natural (vapor) cavity within the vortex will increase. However, the growth of the diameter of the cavity is limited by the fact that, at a certain point, surface cavitation will develop on the low pressure surface of the hydrofoil. This will cause, at first, extraneous effects on the tip vortex cavity and, at last, the disappearance of the cavity. Therefore, very large (as compared to the foil dimensions) natural (vapor) cavities are very unlikely to be experimental, or even practically, achieved. Ventilation can artificially generate large cavities without being concerned by surface cavitation. Thus, the investigation of the behavior of ventilated cavity shapes and intermittence is interesting from three points of view: First, there is no need to operate under reduced pressure conditions; second, interesting information can be gathered to understand the behavior of large natural (vapor) cavities; and third, ventilated cavity behavior can be associated with some aspects of the vortex breakdown process. Besides, ventilated cavities occur very often in blades and hub vortices of propellers operating near the free surface, surface-piercing propellers, turbine hubs, etc., Arndt (1995).

In a water tunnel operating at pressures and velocities such that natural (vapor) tip vortex cavitation cannot occur, the air in the liquid may be captured by the tip vortex and a ventilated cavity can be formed, Fig. 1, whose shape and kinematics are determined by the flow conditions: liquid velocity, foil shape, incidence angle, the turbulence intensity level, and occasionally air flow rate. These cavities have been observed by Meijer (1981) in an open-channel, and Manuel et al. (1987, 1992) in a closed-channel of circular cross-section; Meijer (1981) termed them swimming cavities because of their ability to move upstream. Escudier and Keller (1983) associated these cavities to the vortex-breakdown phenomenon, and obtained analogous shapes by pumping air in the region downstream of the vortex-breakdown. Recent experiments conducted in the Grand Tunnel Hydrodynamique of the Bassin d'Essais des Carènes with a very large elliptical foil and a large air content have shown that the shape of the cavities occurring near the vortex tip, Fig. 2, is similar to that of Fig. 1. This relates to what has been said in the previous paragraph and shows that, under precise conditions, ventilated tip vortex cavities, detached from the tip of the wing,

Contributed by the Fluids Engineering Division for publication in the JOURNAL OF FLUIDS ENGINEERING. Manuscript received by the Fluids Engineering Division May 22, 1995; revised manuscript received June 3, 1997. Associate Technical Editor: R. E. A. Arndt.

can exist. Vapor cavities obtained by Maines and Arndt (1993) with an elliptical foil of a different cross section under specific test conditions and by Dugué and Fruman (1992) when a tip vortex is subjected to an appropriate longitudinal pressure gradient, show also detached cavities having very analogous shapes.

Ventilated cavities are generally constituted by a leading cavity of nearly elliptical cross section (see Fig. 1(*a*), Manuel, 1981; Manuel et al., 1987; and Escudier and Keller, 1983), and have two characteristic transition regions that can be identified in the cavity of Fig. 1. The first region contains the stagnation point at the front, and can be considered as a transition from the unperturbed flow to a uniform cylindrical cavity. The second region is a sudden constriction of the first cavity, followed by a wavy pattern. The second transition region has been studied by Castro (1987) and Manuel et al. (1987) using an analogy with water wave theory in which hydraulic jumps, progressive waves, and solitary waves move along the interface; similar results for progressive waves were obtained by Ackerett (1930), Uberoi et al. (1972), and Keller and Escudier (1980).

Although the cavities described here have some relationship with vortex breakdown, there are some fundamental differences. First, this is a two-phase phenomenon, whereas the vortex breakdown, as it is usually described, occurs in a single phase. On the other hand, if air is not injected, or the air content of the water is low enough, nothing resembling vortex breakdown appears in the single phase flow for the same kinematic conditions under which the cavity is present. As discussed by Althaus et al. (1995) there are several types of vortex breakdown: the double-helix, spiral, and bubble type breakdown, the last two are the most common. It is difficult in principle to associate our phenomena to any of these breakdown types. Jumper et al. (1993) indicate that the spiral form occurs most often, and that it can be better observed using stroboscopic lighting or if photographs were taken using a fast shutter speed. A high speed photograph of the cavity is shown in Fig. 1(*b*), and apparently there is an structure resembling spiral vortices. However, as Escudier (1988) indicates, whether the spiral and bubble forms of breakdown are fundamentally different remains a controversial issue, and the axisymmetric or bubble form is basic and the spiral form a consequence of the instability of the bubble form.

Experiments have been conducted in two water tunnels with circular and rectangular test sections, respectively, using hydrofoils of rectangular and elliptic planforms. Both axial and azimuthal velocities of the tip vortex for the critical conditions under which the cavity is either stable in the test section, or moves back and forth have been measured. The experiments have been made both with and without cavitation; and the change of the flow field due to the presence of a cavity has been estimated.

A simple model, that assumes inviscid flow and small bubble size, gives the flow conditions that allow for cavity stability. Under these assumptions, the cavity pressure is equal to the pressure of the wall of the test section, and the leading point of the cavity is a stagnation point, where the head of the axial velocity just cancels the pressure minimum of the vortex. Comparison of the model predictions and experimental results shows a good agreement and can explain some aspects of the observed behavior. Although, as stated before, the phenomena presented here are not exactly vortex breakdown; the predictions of the model are also compared with those of other authors for vortex

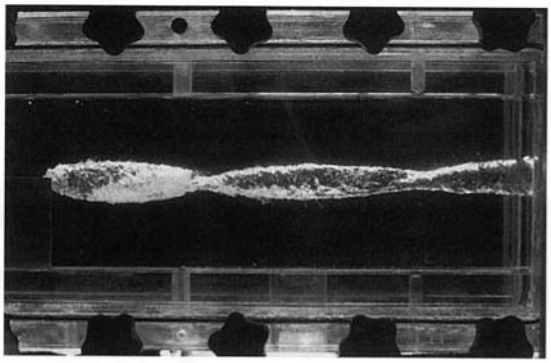

Fig. 1(*a*) Cavity at three different times (I: 1′06″ II: 2′30″ and III: 6′) after stopping the air supply. Rectangular planform, 10 deg incidence angle, W_1 = 5 m/s. ENSTA tunnel.

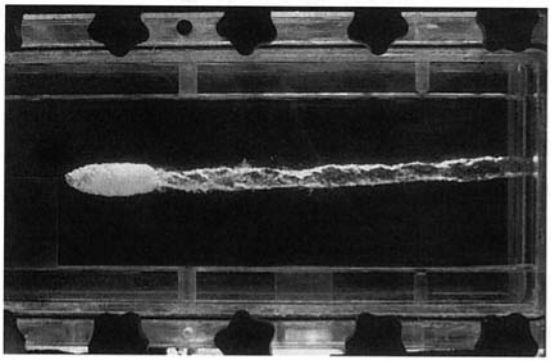

Fig. 1(*a*) Cont.

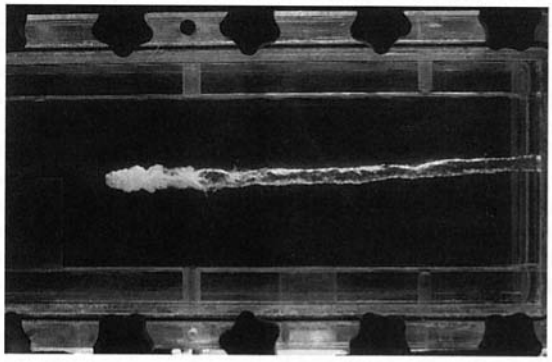

Fig. 1(*a*) Cont.

Nomenclature

c = foil chord
$E_1(x)$ = exponential integral $E_1(x) = \int_x^\infty (e^{-x}/x)dx$
i = incidence angle of the airfoil
k = ratio between maximum swirl velocity and maximum axial velocity (overshoot)
p = pressure
p_o = pressure in the axis upstream
p_∞ = pressure for large r
p_c = cavity pressure
R = radius of upstream section
R_2 = cavity radius
r = radial distance
V = azimuthal component of velocity
V_{MAX} = maximum of V
W = axial component of velocity
W_o = axial velocity in the axis
W_1 = velocity far from the axis in the upstream section
W_2 = velocity far from the axis in the downstream section
x = downstream distance
X = non dimensional radial distance: $X = r/\delta$
δ = radius of the vortex core
Γ = vortex intensity
ρ = density
ν = kinematic viscosity

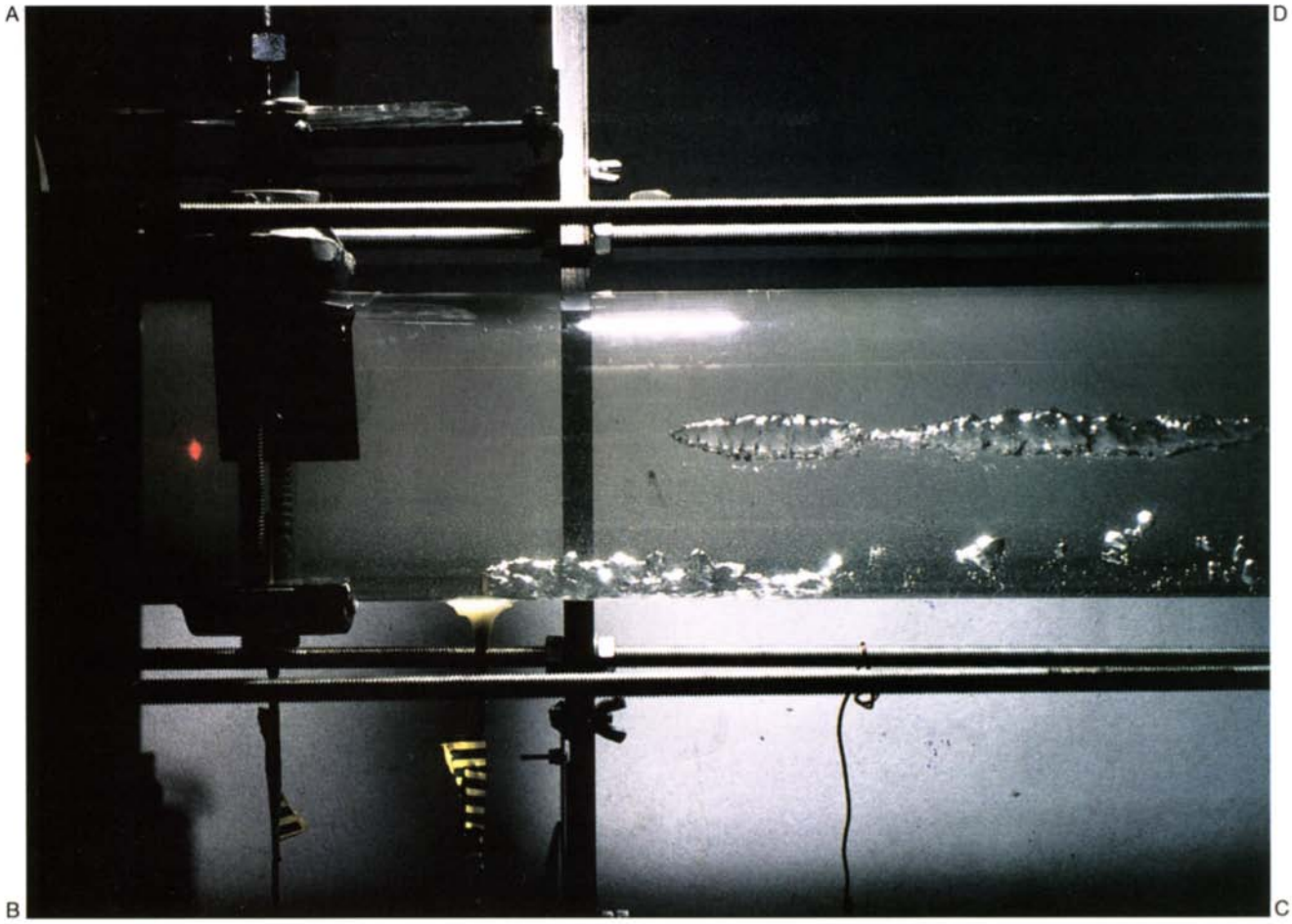

Fig. 1(*b*) High speed photography of the cavity. Rectangular planform, 10 deg incidence angle, W_1 = 3, 1 m/s. ETSII tunnel.

Fig. 1 Photographs of the cavity

breakdown (Squire, 1962; Escudier and Keller, 1983; Spall et al., 1987; Escudier, 1988; and Jumper et al., 1993). The fundamental difference, between our result and those of vortex breakdown, is that we predict a fixed value of the nondimensional vortex intensity for which the cavity is in a stable position, whereas the other studies predict the minimum value of the nondimensional vortex intensity that will result in vortex breakdown.

2 Experimental

The ENSTA cavitation tunnel has a rectangular test section 800 mm long, 80 mm wide, and 150 mm high where a hydrofoil can be mounted vertically on the lower horizontal surface. Three hydrofoils were tested: one of elliptical planform (E) 40 mm maximum chord, a 80 mm half span and a NACA 16020 cross section; another has the shape of a quarter of an ellipse with a straight trailing edge (STE) 40 mm maximum chord, a 60 mm half span and a NACA 16020 cross section; and third one of rectangular planform (RY) having a Clark Y cross section of 7 percent relative thickness, a 115 mm chord and 80 mm half span. Velocities were measured along horizontal lines centered on the vortex for different downstream distances, using a DANTEC two component back scattering fiber optics laser velocimetry system (estimated velocity error 5 percent). The three-dimensional traversing system has a precision of ±0.2 mm. The velocity in the test section can be varied between 3 and 10 m/s and the upstream turbulence level is about 1 percent. Air was injected from a pressure tap situated downstream of the hydrofoil in the lower horizontal wall of the test section.

The test section of the ETSII (UPM) water tunnel is circular and has a diameter of 94 mm and a length of 500 mm. The hydrofoil has a rectangular planform (R), the chord is 45 mm and the span is 52 mm, that has been adjusted so that the resulting tip vortex will be centered. The axial velocities are in the range of 1 to 5 m/s and the blade incidence angle changes from −5 to 15 deg, the corresponding circulation varies from −0.01 to 0.04 m^2/s. The free turbulence intensity is of the order of 5 percent. The elliptical planform hydrofoil of ENSTA has also been installed in the ETSII water tunnel using a specially designed support so that the protruding length of the foil can be changed to maintain the vortex centered along the axis of the test section. Air is injected through a tube located either opposite of the blade or 40 mm downstream. Axial velocities are measured with a laser Doppler anemometer operating in the backscatter mode (velocity error 8 percent). The azimuthal velocities have to be measured in forward-scatter mode (5 percent velocity error). The two-dimensional traversing system has a precision of ±0.5 mm and of ±2 mm in the radial and the axial directions, respectively.

Both measurements of the axial and tangencial velocities conducted with a laser anemometer are affected by an spatial bias incorporating the effect of the finite size of the measuring volume and the vortex wandering. The Reynolds number based on the chord are in the range 10^5–10^6 and those based on the vortex core radius are in the range 2×10^3–2×10^4.

3 Results

3.1 Cavity Observations. When the flow is established in the tunnel and the injection of air is initiated, the bubbles

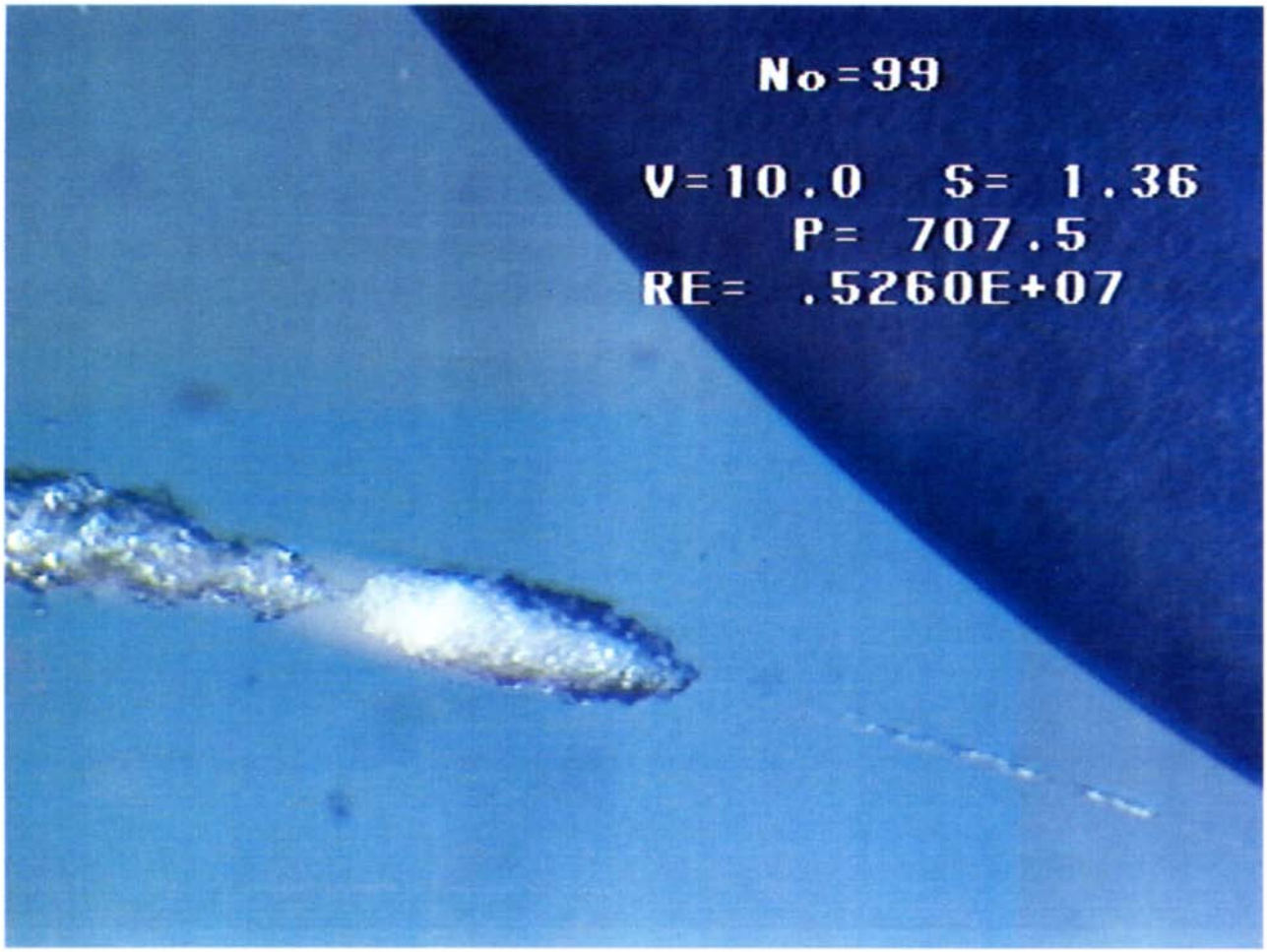

Fig. 2 Tip vortex cavity with injection of nuclei, photograph obtained at the Bassin d'Essais des Carènes, Val de Reuil (France), with a 475 mm maximum chord elliptical foil, a velocity of 10 m/s and a Reynolds number of 5.26 10^6. Notice the analogy between the leading cavity of Figs. 1 and 2.

entering the test section from the tap situated on the lower horizontal wall are convected downstream by the main current, rise because of buoyancy forces and are finally trapped by the vortex. Soon, a cavity, whose leading edge nearly coincides with the transition between the test section (of constant area) and the diffuser (of variable area and adverse pressure gradient) develops. In the case of an elliptical planform the bubble remains in the diffuser, whatever the flow conditions. However, if the incidence angle of the foil is above a critical value, the cavity can occasionally move back and forth from the diffuser to the wing in a fraction of a second. This situation is very unstable and the cavity never remains attached to the foil or remains in equilibrium in the test section. For rectangular planforms and large enough values of water velocity, air flow rate, and angle of attack, the bubble is able to move upstream in the main test section, and, under some circumstances, to get in contact with the foil. By modifying the test conditions, the leading edge of the cavity can be stabilized directly in contact with the foil or at a short distance downstream. However, the range of flow conditions necessary to maintain the cavity at a certain distance from the wing is very narrow. For example, changes in the incidence angle of the order of 1 deg can either make the cavity to travel downstream or get attached to the wing. The leading cavity has a re-entrant jet downstream and it is followed by an air column with a wavy interface, that in some cases becomes highly disturbed. These waves may be analogous to water waves, as interpreted by Manuel et al. (1987), or caused by a Kelvin-Helmholtz instability originated by the shear near the interface. Under some circumstances the successive waves pinch off and another reentering jet occurs. When the cavity is stabilized in the main test section the air entrainment seems to take place essentially in the diffuser.

The cavity in the tip vortex of the rectangular foil can be maintained within the test section even if the air supply is stopped. For a test performed in the ENSTA water tunnel this process lasted for about ten minutes. Without injected air, the size of the leading bubble and the satellite cavity decrease and the leading edge moves downstream in a quasi-steady manner, as shown by the three photographs of Fig. 1(a). The reduction of the size of the cavities is related to the continuous draining of the air inside the cavity. The leading edge of the cavity oscillates with increasing amplitude and decreasing frequency as the cavity becomes smaller and moves downstream. At the ETSII water tunnel, when the air supply is stopped, the bubble disappears in about ten seconds. This is probably due to the higher than ENSTA upstream turbulence leading to an increased air entrainment from the cavity surface. Experiments conducted with the straight trailing edge foil in the ENSTA tunnel with different upstream turbulence intensities have shown that increasing the turbulence intensity makes the cavities less lasting.

3.2 Velocity Measurements. In general, the radial variation of swirl velocity has the classical behavior described by a Lamb type vortex. The viscous core, assimilated to the radius at which the maximum swirl velocity occurs, is thinner for the elliptical planform than for the other tested foils. The axial velocities show either over or undershoots in the core region depending on the planform of the foils and the Reynolds num-

bers at which the tests are performed (see for example Fruman et al., 1992 for the modification of the axial velocity profiles as a result of the increase of the Reynolds numbers for elliptical foils).

As an example, Fig. 3 shows, for tests performed in the ENSTA tunnel, the radial distribution of the azimuthal velocities, V_1, normalized with the free-stream velocity, W_1, and, C_L, as in Arndt and Keller (1992), in the vortex generated by the rectangular planform wing operating at three different incidence angles, 6, 8 and 10 deg, three chords downstream of the trailing edge. It is noteworthy that the velocities are nearly proportional to the lift coefficient and this normalization seems appropriate. However, for $r/c < 0$ and for incidence angles, 8 and 10 deg, the velocity profiles are more affected by the wake of the foil, so the 6 deg incidence angle points are off the two other normalized curves. The profiles follow the usual behavior: solid body rotation within the vortex core and potential velocity distribution outside it. The swirl velocity profile is quite well adjusted by a Lamb vortex (Eqs. (2) and (3)), as shown in Fig. 3 for 6 and 10 deg incidence angle. The lines are almost identical, as expected from the normalization procedure.

The nondimensional azimuthal and axial velocities are shown in Figs. 4(a) and (b), respectively, for stations situated at 0.6, 1, 2, and 3 chords downstream the trailing edge of the rectangular foil. On the suction side ($r > 0$), and from 0.6 to one chord, the maximum azimuthal velocity increases substantially while the viscous core dimension decreases. Further downstream the maximum velocity decreases slightly and the viscous core increases indicating the initiation of the diffusion process. On the pressure side, ($r < 0$), there is hardly any difference for the maximum azimuthal velocities except for the 0.6c velocity profile.

As shown in Fig. 4(b), the axial velocity displays an overshoot around the vortex axis whatever the distance to the tip; this is typical of what is known in the vortex-breakdown terminology as a supercritical flow, Escudier (1988). This overshoot could be explained for inviscid flow if the stagnation pressure is uniform. However, since viscous effects in the core dissipate mechanical energy, both the stagnation pressure, and the magnitude of the overshoot, should be smaller than expected from ideal theory. Another argument to explain this overshoot is that, as a consequence of the roll-up of the vorticity shed from the tip of the wing, the vorticity in the core is not purely axial, and has a helical pattern with an azimuthal component, which spirals in the same sense of the circulation, thus inducing, by the Biot-Savart law, the overshoot velocity. The diameter of the overshoot region is slightly larger than the diameter of the viscous core estimated from the position of the maximum swirl velocity.

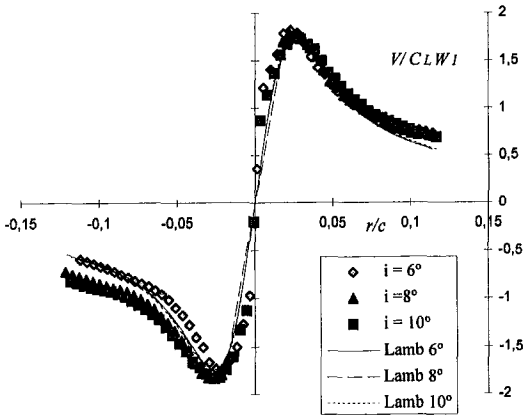

Fig. 3 Radial distributions of azimuthal velocities normalized with W_1 and C_L as a function of distance to the vortex axis, for three different incidence angles. Rectangular planform (RY), 3 chords downstream. Comparison with Lamb vortex for i = 6 and 10 deg. ENSTA tunnel.

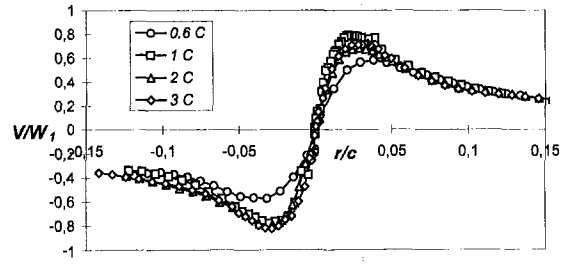

Fig. 4(a) Radial distribution of azimuthal velocities

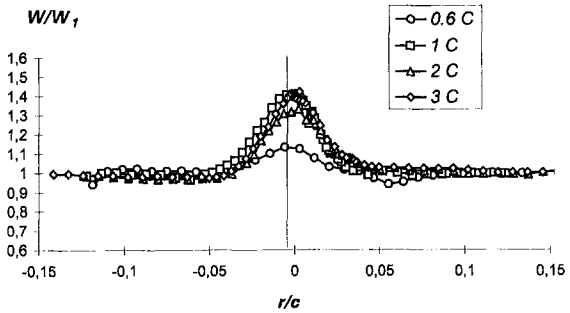

Fig. 4(b) Radial distribution of axial velocities

Fig. 4 Radial distribution of azimuthal and axial velocities made nondimensional with W_1 for different downstream positions: 0.6, 1, 2, and 3 chords. Rectangular planform (RY). W_1 = 5 m/s and i = 10 deg. ENSTA tunnel.

Velocity measurements were also conducted with a ventilated detached cavity in the test section. Measurements were made 0.6 chords downstream from the foil, slightly upstream from the leading bubble. The results near the vortex axis are presented in Fig. 5 and compared to the data obtained in the absence of a cavity. The axial velocities decrease but the tangential velocities are unaffected by the cavity; this indicates that the spatial distribution of circulation has not been altered by the presence of the cavity.

The azimuthal and axial velocity distribution for the straight trailing edge foil, both without and with the air cavity, at approximately one chord downstream the tip, is shown in Fig. 6. The axial velocity profile shows a deficit in the core region and no significant change because of the presence of the cavity; although it should be pointed out that now the bubble is, as compared to Fig. 5, further downstream from the measuring point. For the azimuthal velocities, the slope of the rigid body rotation core and the maximum velocity decrease significantly when the cavity is present. These results are in contrast to those obtained with the rectangular foil, Fig. 5, for reasons which are not as yet elucidated.

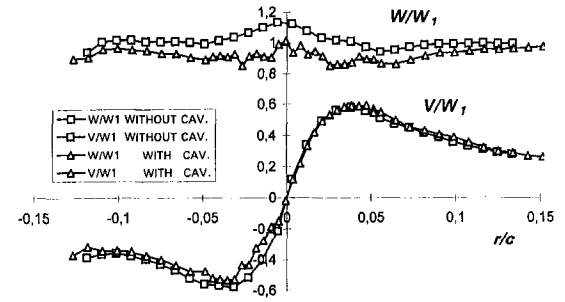

Fig. 5 Radial distribution of the axial velocity and azimuthal velocity for a section upstream of the cavity position, both with and without cavity. The measurements are made 0.6 chords downstream from the wing. Rectangular planform (RY). i = 10 deg. ENSTA tunnel.

Figure 7 shows the swirl velocity profiles for conditions under which the cavity moves toward the foil. These profiles are measured three chords downstream the tip with the rectangular, the elliptical and the straight trailing edge foils; the incidence angle are, respectively 10, 11, and, 12 deg. The swirl velocities have been made non-dimensional with the velocity at the axis, W_o (maximum overshoot or minimum undershoot velocity), because it will be shown later that the parameter,

$$k = \frac{V_{MAX}}{W_o} \tag{1}$$

determines the stability conditions of the cavity, where V_{MAX} is the maximum value of the swirl velocity. The value of k as a function of the downstream distance, for the foils tested in the ENSTA and the ETSII tunnels is displayed in Fig. 8(a). The parameter k shows, in general, a tendency to decrease with the distance to the tip, except for the rectangular planform (RY) foil. The significance of this behavior will be discussed later.

4 Proposed Model

Figure 9 shows schematically the geometry of the axysimmetric flow adopted. The model assumes that in region 1, far enough upstream, the velocity vector has only axial and azimuthal components, W_1 and V_1. The cavity is supposed to be very slender so that far enough downstream, in region 2, the radial component of velocity also vanishes.

In region 1 the azimuthal velocities are supposed to behave as in a Lamb vortex,

$$V = \frac{\Gamma}{2\pi r}\left(1 - e^{-r^2/\delta^2}\right) \tag{2}$$

The values of Γ and δ are calculated so that the maximum azimuthal velocity and the corresponding radial position,

$$V_{MAX} = 0.638\,\frac{\Gamma}{2\pi\delta} \quad \text{at} \quad r = 1.12\delta, \tag{3}$$

are those from experiments; Fig. 3 shows that the experimental values of the swirl velocity are fitted quite well by Eq. (2). By integrating the equation that express the radial balance of momentum,

$$\frac{dp}{dr} = \frac{\rho V^2}{r}, \tag{4}$$

where ρ is the liquid density and using Eq. (2), the following pressure distribution in region 1 is obtained:

$$p_1 = p_o + \frac{\rho\Gamma^2}{4\pi^2\delta^2}\left[\ln 2 - \frac{1}{2X^2} + \frac{e^{-X^2}}{X^2} - \frac{e^{-2X^2}}{2X^2} - E_1(X^2) + E_1(2X^2)\right], \tag{5}$$

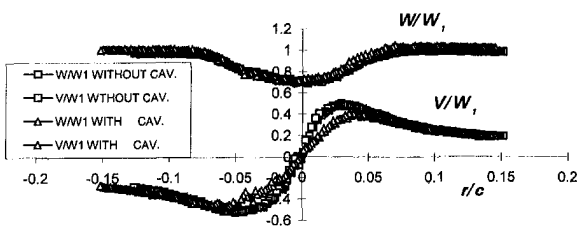

Fig. 6 Radial distribution of the axial velocity and azimuthal velocity for a section upstream of the cavity position, both with and without the cavity. Cavity is one chord downstream from the wing, and the measurements are made 0.6 chords downstream from the wing. Quarter of ellipse planform (STE), i = 12 deg, ENSTA tunnel.

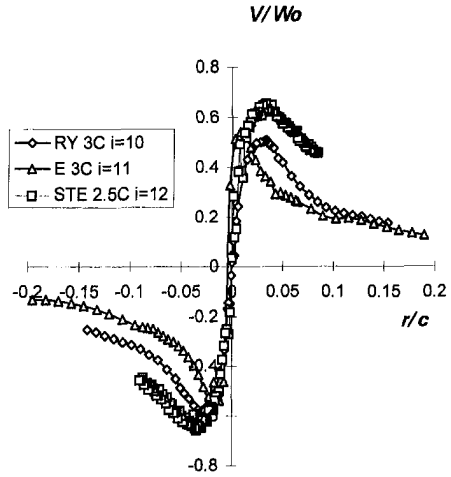

Fig. 7 Comparison of azimuthal velocities for rectangular, elliptical and quarter of ellipse planform wings made nondimensional with W_o, i = 10, 11, and 12 degs, respectively. Three chords downstream, ENSTA tunnel.

where $X = r/\delta$, p_o is the pressure at the axis, and $E_1(X)$ is the exponential integral. For r (or X) going to infinity, a constant value of the pressure is reached,

$$p_{1\infty} = p_o + \frac{\rho\Gamma^2}{4\pi^2\delta^2}\ln 2 = p_o + 1.703\rho V^2_{MAX}, \tag{6}$$

where Eq. (3) has been used. If the radius of the test section is much larger than the size of the vortex core, $R/\delta \gg 1$, it is expected that the pressure will be equal to $p_{1\infty}$ over most of region 1, excluding a cylindrical region around the axis of radius several times δ. The axial velocity is supposed to be uniform over most of the upstream section, except in the vortex core where there is an overshoot or an undershoot, as shown in figures 4(b), 6 and 9; the value of the axial velocity at the axis is denoted by,

$$W_1(0) = W_o. \tag{7}$$

To calculate conditions in Section 2, downstream, it is assumed that the radius of the cavity, R_2, satisfies the following inequalities:

$$\delta \ll R_2 \ll R. \tag{8}$$

For the particular case of Fig. 1(a), typical values are δ = 1 mm, R_2 = 10 mm and R = 100 mm.

To explain the nature of the inviscid transition of vorticity when going from region 1 to 2 we will use an intuitive argument proposed by Batchelor (1967). In region 1 the incoming vorticity is concentrated in a region of radius δ around the axis and is mainly axial (except for that associated to the overshoot); the incoming vortex lines are straight and parallel to the axis. As one end of the vortex line passes into the transition, it moves radially outward, and the azimuthal velocity of a material point will decrease according to the rule V = constant/r, as this material point moves round the axis more slowly than does the vortex-line in the upstream region, the vortex line is deformed into a spiral with an azimuthal component of vorticity that according to the Biot-Savart law will tend to decelerate the axial flow, thus providing an explanation for vortex breakdown (Jumper et al., 1993). Then, in region 2, there is a vorticity layer of thickness δ_2 in which there are both axial and azimuthal components of vorticity. Another way to interpret the azimuthal vorticity component in this layer is as follows. If the flow behaves as inviscid, the stagnation pressure should be constant along the interface, and, since the pressure in the cavity is uniform, the velocity along the interface should also be constant and equal to zero, that is the value at the stagnation point of

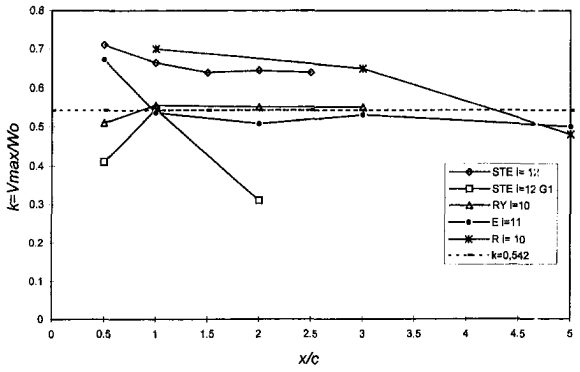

Fig. 8(*a*) Comparison between analytical prediction and measurements for: a quarter of ellipse (with two free turbulence intensities), rectangular and elliptical wings at several downstream distances.

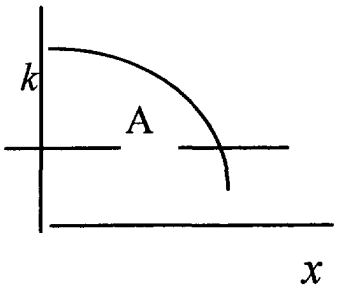

Fig. 8(*b*) *k* decreasing with downstream distance

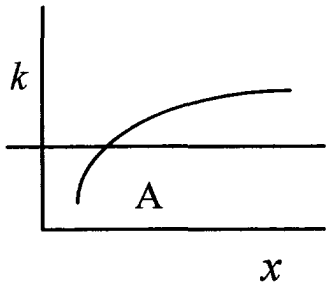

Fig. 8(*c*) *k* increasing with downstream distance

Fig. 8 Variation of *k* with downstream distance

the cavity. The change across δ_2 from zero axial velocity to the finite value outside the rotational layer, corresponds to the azimuthal vorticity component. The structure of this layer has been studied by Keller et al. (1985). Escudier and Keller (1983) suggest that the rotational layer may grow by viscous diffusion or become unstable. Actually, viscous forces drag along the fluid at the interface, that may attain significant velocities if the downstream distance is large enough. This viscous layer is highly unstable, because its velocity profile should have an inflexion point, required to satisfy the zero normal velocity gradient condition at the interface. This may explain the distorted aspect of the interface, and even the existence of the reentrant jet in the back. In any case, the question concerning the right velocity condition to be applied to the interface is subject of much debate, in particular for modeling the cavities in CFD codes.

As the flow is ideal, and there is no viscous diffusion of vorticity, only the fluid particles inside the rotational core of radius δ in region 1 are the ones that can be in the rotational layer of thickness δ_2 in region 2, consequently, the mass fluxes across both rotational regions should be equal, and if the axial velocities are of the same order of magnitude, the areas should also be of the same order. Because of inequality (8) and mass conservation, the axial velocities in regions 1 and 2, outside the rotational regions, are approximately equal. Inside the rotational core there is the overshoot, and on the rotational layer in region 2 the axial velocity changes from zero to the outside value; this means that, although the average axial velocity in the rotational layer in region 2 should be somewhat smaller that in the rotational core in 1, both should be of a similar order of magnitude, and consequently the areas should also be of the same order,

$$\delta_2 \approx O\left(\frac{\delta^2}{R_2}\right) \ll \delta. \tag{9}$$

This means that over most of Section 2 the flow is irrotational and the azimuthal velocity should be given by,

$$V_2 = \frac{\Gamma}{2\pi r}. \tag{10}$$

The value of the pressure in region 2, far from the cavity where $r/R_2 \gg 1$ is given by:

$$P_{2\infty} - p_c \approx O\left(\rho V^2_{\mathrm{MAX}}\left(\frac{\delta}{R_2}\right)^2\right) \tag{11}$$

where p_c is the cavity pressure and Eqs. (3), (4), and (10) have been used.

As the axial velocities, outside the rotational region, in Sections 1 and 2, are approximately equal, applying Bernouilli's equation to a streamline located far from the axis it will be obtained that the corresponding pressures, given by Eqs. (6) and (11), should also be equal. On the other hand, the pressure in the cavity should be the stagnation pressure in the axis:

$$p_c = p_o + \tfrac{1}{2}\rho W^2_o. \tag{12}$$

On using Eqs. (6), (11), and (12), and the relation $p_{1\infty} = p_{2\infty}$, the following equilibrium condition is obtained,

$$k = \frac{V_{\mathrm{MAX}}}{W_o} = 0.542 \tag{13}$$

Equation (13) is very easy to interpret, and states that the head of the axial velocity cancels the pressure minimum of the vortex, given by Eq. (6).

Manuel et al. (1992) performed a similar analysis using a Rankine vortex and obtained for k a value of $1/\sqrt{2} = 0.707$ instead of 0.542. This value is also obtained using the two-stage transition model for breakdown of Escudier and Keller (1983), with a Rankine vortex and without considering overshoot (see also Escudier, 1988; he defines a value of k that differs by a factor 2 from the one used here). Spall et al. (1987) give a criteria for breakdown based on a Rossby number that is related to k by Ro = 0.57/k, without considering overshoot; they find that, for Reynolds numbers based on core radius larger than 100, there is breakdown when $k > k_c$, where $k_c = 0.877$; this result is based on experimental and numerical research both of them and another authors. Spall et al. (1987) also compare with

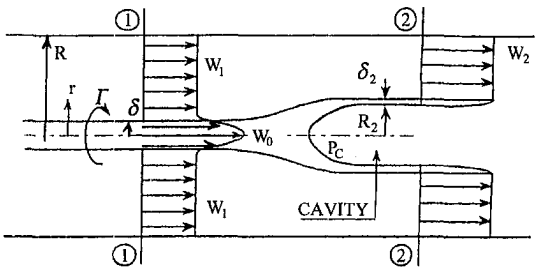

Fig. 9 Schematic showing the geometry of the domain under consideration

the critical value obtained using Squire's (1962) analysis with a Lamb profile, Eq. (2), that yields $k_c = 1.0$. On the other hand, if a Rankine vortex is used the critical value obtained using Squire's analysis is $k_c = 1.202$ that is higher than the value obtained with the two-stage transition model of Escudier and Keller (1983). Except for the two-stage transition model, in which the result is expected to be the same one obtained with the proposed model (if Lamb's vortex instead of Rankine's vortex is used) in all the other cases the value of k_c is larger than the one given by Eq. (13). It looks as though larger values of vortex intensity are needed for the appearance of vortex breakdown than for the formation of the cavity. This is consistent with the fact that, if there is no air injection, no vortex breakdown appears in the single phase for the value of k given by Eq. (13).

Jumper et al.'s model (1992) is based on the estimation of the circulation needed to obtain an average self-induced axial velocity equal to $-W_o$; they also choose some fundamental parameters from the literature and their experiments. Then, they give a criterium based on a critical non-dimensional circulation, $\Gamma/(cW_o)$, being equal to 0.132. When this is compared to the result given by Eqs. (3) and (13), it is found that it is impossible, in general, for both results to hold simultaneously, because it will require that there is a fixed ratio of vortex core radius, δ, to the chord, c, namely: $\delta/c = 0.025$ or $r(V_{\max})/c = 0.028$. Nevertheless, and although it must be just a pure coincidence, it is intriguing that for many of the results presented in Figs. 3 to 7 the above value of the ratio $r(V_{\max})/c$ holds.

Consistent with the fact that there is a reentrant jet in the back of the cavity, Manuel et al. (1992) assumed that the constant value of the velocity in the interface is the jet velocity, thus obtaining a lower value of the pressure in the cavity. However, it is not clear how this assumption can hold at the tip stagnation point. Perhaps, it is more reasonable to assume that, if the cavity is long enough for the viscous forces to be significant, the external flow will drag along the stagnant flow in the interface until it reaches a finite velocity, of the order of that of the reentrant jet.

Equation (13) indicates that the value of k for the cavity to be in equilibrium in the test section is 0.542. In Fig. 8(a), this value is compared with those obtained from the measurements corresponding to the occurrence of a stable cavity for rectangular and straight trailing edge foils, and for an oscillating cavity in elliptical wings. Since inequalities (8), hold for all the experiments, it is expected that k should be close to this value whenever the cavity is stable. This is in agreement with the experimental observation that for the cavity to be stable in the test section the range of variation of the incidence angle is very small. In Fig. 8(a) it can be observed that k does not usually change very much as we move along the test section. For the rectangular wing in the ENSTA tunnel, k is close to 0.542 all along the vortex. For the elliptic wing at a short distance from the wing, k is considerably larger than 0.542, and further downstream is very close to 0.542, but as it was already mentioned the cavity is never stabilized and moves back and forth. For the straight trailing edge foil k is bigger than 0.542 all along the vortex; however, if the flow turbulence intensity is increased, the value of k is under this critical value. For the rectangular wing in the ETSII tunnel k gets close to 0.542 about 4 chords downstream, whereas the experimental observations show that the cavity remains stable about 1 to 2 chords downstream of the wing.

A possible interpretation of the cavity stability can be given by writing Eq. (13) in terms of relative velocity: when the cavity moves downstream with a velocity W_c, the criteria (13) should be written as follows:

$$\frac{V_{\mathrm{MAX}}}{W_o - W_c} = 0.542 \qquad (13b)$$

where W_c is the cavity displacement velocity. The equilibrium position (for the bubble to be at rest) is given by point A of schema 8B; in a point downstream of A, to satisfy the relation (13b), W_c has to be positive and the cavity will move further downstream, away from point A, showing that when k decreases with axial distance x, is an unstable configuration; on the other hand, when k increases with x, (schema 8C) the configuration will be stable.

This stability analysis assumes that the flow conditions along the test section (in particular k) change slowly enough with distance, so that this analysis applies locally. The length of the transition region is estimated to be of the order of magnitude of the cavity radius, that is about $\frac{1}{50}$ of the length of the test section, therefore, in a first approximation, this assumption may be justified.

The phenomena observed are quite complex and irregular and, although the results of Fig. 8(a) show a reasonable agreement of the experimental results and the model predictions. It is difficult to reproduce all the aspects with a model as simple as the one proposed. According to the model proposed here, the only position in which the cavity is in equilibrium is where condition (13) is satisfied. However, the experiments, Fig. 1(b), show that the bubble moves downstream in a quasisteady manner as times increases, indicating that the equilibrium position moves downstream as the cavity becomes smaller. If the small bubble assumption (8) is relaxed and frictionless theory is used (see for example Escudier, 1998) it can be shown that the critical value of k depends only on δ/R, and not on cavity size, so that the behavior of the bubble in Fig. 1(b) can not be explained either. If the effect of the reentrant jet on the cavity stability is taken into account, there will be one supplementary degree of freedom that will allow the cavity to move along the test section. At present, a model taking these effects into account is being developed (Crespo et al., 1996).

5 Conclusions

Ventilated cavities formed in the tip vortex issued from finite span hydrofoils have different behaviors depending on the hydrofoil planform. Experiments show that the cavities are generally formed by a leading bubble with a reentrant jet followed by a satellite cavity with longitudinal waves whose amplitude and length decrease with the distance downstream. Moreover, depending on the wing and the flow conditions, the cavity formed initially in the transition between the test section (of constant area) and the diffuser (of increasing area and adverse pressure gradient) can or cannot move upstream and, sometimes, get in contact with the foil.

By considering the equilibrium of the leading bubble, a model is proposed that gives the value of the ratio of the local maximum tangential velocity to the free stream velocity that has to be maintained to allow for cavity stability. A possible interpretation of the cavity stability has been given by writing the criteria for cavity stability in terms of relative velocity. Comparison of the model prediction and experimental results show a good agreement and can explain some aspects of the observed behavior.

Further experimental and theoretical work should be conducted to investigate the behavior of the tip vortex and its interaction with the ventilated cavity for a greater range of flow conditions. Test should also provide information on the length at which instabilities occur in the interface.

Acknowledgments

The authors wish to express their deep appreciation for the partial support received from the Spanish (grants no. 86-B, A.I., PB 89-0184 and PB93-1234) of the DGICYT) and French (grants no. 92/205 A.I. and DRET 88/1038) governments.

References

Ackerett, J., 1930, "Uber Stationäre Hohlwirbel," *Ing. Archiv.*, pp. 399–402.

Althaus, W., Brucker C. H., and Weimer, M., 1995, "Breakdown of Slender Vortices" *Fluid Vortices,* S. I. Green, ed., Kluwer Academic Publishers.

Arndt, R. E. A., 1981, "Cavitation in Fluid Machinery and Hydraulic Structures," *Annual Review of Fluid Mechanics,* Vol. 13, pp. 273–328.

Arndt, R. E. A., Arakeri, V. H., and Higuchi, H., 1991, "Some Observations of Tip Vortex Cavitation," *Journal of Fluid Mechanics,* Vol. 229, pp. 269–289.

Arndt, R. E. A., and Keller, A. P., 1992, "Water Quality Effects on Cavitation Inception in a Trailing Vortex," ASME JOURNAL OF FLUIDS ENGINEERING, June.

Arndt, R. E. A., 1995, "Vortex Cavitation," *Fluid Vortices,* S. I. Green, ed., Kluwer Academic Publishers.

Batchelor, G. K., 1967 *An Introduction to Fluid Dynamics,* Cambridge University Press.

Castro, F., 1987, "Ondas y Cavidades en la Estela de un Álabe," Ph. D thesis, ETSII Universidad Politécnica de Madrid.

Crespo, A., Manuel, F., Castro, F., and Fruman, D. H., 1996, "Stability of Air Cavities in Tip Vortices," *X VIII IAHR Symposium on Hydraulic Machinery and Cavitation,* Vol. I Edit. Kluwer Academic Publishers, pp. 554–563.

Duguè, C., Daniel, M., and Fruman, D. H., 1989, "Effect of a Pressure Field on Tip Vortex Cavitation," *Cavitation and Multiphase Flow Forum,* San Diego.

Escudier, M. P., 1988, "Vortex Breakdown: Observations and Explanations," *Progress in Aerospace Sciences,* Vol. 25, No. 2, pp. 189–229.

Escudier, M. P., and Keller, J. J., 1983, "Vortex Breakdown: A Two-Stage Transition," AGARD CP No 342, Aerodynamics of Vortical Type Flows in Three Dimensions, paper 25.

Fruman, D. H., Dugué, C., Pauchet, A., Cerruti, P., and Briancon-Marjollet, L., 1992, "Tip Vortex Roll-Up and Cavitation," *Proceedings of the Nineteenth Symposium on Naval Hydrodynamics,* National Academy Press, Washinton, D. C., pp. 633–651.

Jumper, E. J., Nelson, R. C., and Cheung, K., 1993 "A Simple Criterion for Vortex Breakdown," AIAA-93-0866.

Keller, J. J., Egli, W., and Exley, J., 1985, "Force- and Loss-Free Transitions Between Flow States," *Journal of Applied Mathematics and Physics,* Vol. 36(6), pp. 854–889.

Keller, J. J., and Escudier, M. P., 1980, "Theory and Observations on Hollow Core Vortices," *Journal of Fluid Mechanics,* Vol. 99, Part 3, pp. 495–511.

Maines, B. H., and Arndt, R. E. A., 1993, "Bubble Dynamics of Cavitation Inception in a Wing Tip Vortex," *Cavitation and Multiphase Flow,* FED-Vol. 153 ASME, pp. 93–97.

Manuel, F., 1981, "Cavitación en el Torbellino Desprendido del Extremo de un Alabe," Ph.D thesis, ETSII, Universidad Politécnica de Madrid.

Manuel, F., Crespo, A., and Castro, F., 1987, "Wave and Cavity Propagation Along a Tip Vortex Interface," *Physico Chemical Hydrodynamics,* Vol. 9, No. 3/4, pp. 611–621.

Manuel, F., Crespo, A., Castro, F., Fruman, D. H., Beuzelin, F., and Gaudemer, R., 1992, "Ventilated Cavities in Tip Vortices," *Proceedings of the Institution of Mechanical Engineers,* IMechE 1992-11, International Conference on Cavitation, Cambridge, Dec.

Meijer, M. J., 1981, "Swimming Vortex Cavities," Euromech Colloquium 146, Institut de Mécanique de Grenoble.

Okamura, N., Fujino, R., and Tanaka, T., 1994, "An Experimental Investigation of the Mechanism and the Pressure of Counter-Rotating Vortices on a CPP at the Off-Design Condition," *20th Symposium on Naval Hydrodynamics,* Santa Barbara, Ca.

Spall, R. E., Gatski, T. B., and Grosch, C. E., 1987, "A Criterion for Vortex Breakdown," *Physics of Fluids,* Vol. 30, pp. 3434–3440.

Squire, H. B., 1962, "Analysis of the Vortex Breakdown Phenomenon, Part I," M. Schaefer, ed, Miszellanen der angewandten Mechanik, Akademie Berlin, pp. 306–312.

Uberoi, M., 1972, "Stability of a Coaxial Rotating Jet and Vortex of Different Densities," *Physics of Fluids,* Vol. 15.

A. Bhattacharyya[1]
Senior Technical Staff Member,
Able Corporation,
Yorba Linda, CA

A. J. Acosta
Professor Emeritus.

C. E. Brennen
Professor and Head.

T. K. Caughey
Hayman Professor of
Mechanical Engineering.

Department of Mechanical Engineering,
California Institute of Technology,
Pasadena, CA 91125

Rotordynamic Forces in Cavitating Inducers

This paper reports an experimental investigation of rotordynamic forces in a whirling axial flow inducer under the influence of cavitation at various flow coefficients. The results show the occurrence of large destabilizing peaks in the force tangential to the whirl orbit for positive whirl frequency ratios. The magnitude of the destabilizing forces increased with a decrease in cavitation number and flow coefficient. The rotordynamic data obtained do not exhibit quadratic functional behavior normally assumed in many rotordynamic models. Consequently, conventional generalized stiffness, damping, and inertia matrices cannot be determined for the inducer. The results demonstrate the complexity of rotordynamic forces and their consequences on stability of axial flow inducers.

Introduction

The purpose of the research presented in this paper is to obtain an insight into the characteristics of fluid-induced rotordynamic forces acting on an axial flow inducer operating under cavitating conditions. Rotordynamic forces arise when the inducer is displaced off-center and whirls in an orbit. These forces are conventionally decomposed into components normal and tangential to the whirl orbit. These forces can be destabilizing depending on whirl speeds and operating conditions. This paper presents experimental dynamic force data for varying whirl speeds, flow coefficients and cavitation numbers. Experiments have been conducted at the Rotor Force Test Facility (RFTF) at the California Institute of Technology to obtain force data on a whirling inducer, for varying conditions of cavitation, flow rates and whirl. An experimental perturbation technique has been used to obtain force data using an eccentric bearing mechanism and a rotating dynamometer for measuring all force components in a rotating frame. The perturbation is introduced in the form of a circular whirl motion created by an offset of the inducer center with respect to the housing centerline. The radius of this whirl orbit can be set to different eccentricities (ϵ). The hydrodynamic force matrix obtained can be used to study the stability of the inducer.

A survey of the literature shows a lack of dynamic force data on whirling cavitating inducers. Some of the early measurements of hydrodynamic radial forces includes a study by Rosenmann (1965) on a three bladed cavitating inducer. Karyeaclis et al. (1989) conducted previous experiments at the RFTF on a four bladed SEP (Sociéte Européene de Propulsion) inducer. Internal flows in inducers change substantially with flow coefficients and affect fluid-induced forces. One such change is the occurrence of reverse flow. These reverse flows occur both upstream as tip clearance leakage flows and downstream as reentrant flow on the hub. The internal blade passage flows become highly complex and three dimensional (Lakshminarayana, 1972, 1982; Acosta, 1993; Bhattacharyya et al., 1993). It has also been shown that upstream swirling backflow can induce instability in the system through low cycle system oscillations (Kamijo et al., 1977); however the force data reported in this paper were taken at operating conditions at which such oscillations were not observed.

The results of the current experiments show the effect of flow coefficient and cavitation number on the rotordynamic and lateral forces and the range of whirl/shaft speed ratios (or whirl frequency ratios) over which they are destabilizing. The results also show a non-quadratic behavior of these forces with the whirl/shaft speed ratio as a consequence of which the conventional rotordynamic stiffness, damping and inertia coefficients cannot be obtained.

Experimental Procedure

Experiments were conducted in the RFTF to obtain steady (lateral) and unsteady (rotordynamic) force data on a three bladed helical inducer. The inducer has a constant hub/tip ratio and a constant helix pitch of 0.4 and 5.04 cm/revolution respectively. The blade angle is 9° at the tip and the inducer has a swept back leading edge. Further details of the test facility and data acquisition can be found in Jery (1986), Franz (1989) and Franz et al. (1990). A schematic of the inducer installation in the test facility is shown in Fig. 1(*a*).

A brief overview of the data reduction process is presented here; further details can be obtained from Jery (1986). The components of the instantaneous forces on a whirling inducer and the reference frames are shown in Fig. 1(*b*). The instantaneous force $[F]$ can be expressed as the sum of a steady force $[F_o]$ and an unsteady force which is linearized with respect to perturbation, ϵ, represented by $[A]$:

$$\begin{bmatrix} F_x \\ F_y \end{bmatrix} = \begin{bmatrix} F_{ox} \\ F_{oy} \end{bmatrix} + \frac{\epsilon}{R} \begin{bmatrix} A_{xx} & A_{xy} \\ A_{yx} & A_{yy} \end{bmatrix} \begin{bmatrix} \cos \omega t \\ \sin \omega t \end{bmatrix} \quad (1)$$

The components of the rotordynamic matrix $[A]$ for a circular whirl orbit have been experimentally found to be very close to the form $A_{xx} = A_{yy}$ and $A_{xy} = -A_{yx}$. The forces normal to the whirl orbit (F_n) and tangential to the whirl orbit (F_t) can then be expressed as:

$$F_n = \tfrac{1}{2}(A_{xx} + A_{yy}) = A_{xx} = A_{yy} \quad (2)$$

and

$$F_t = \tfrac{1}{2}(A_{yx} - A_{xy}) = -A_{xy} = A_{yx} \quad (3)$$

[1] Currently: Project Engineer, Concepts ETI, Inc., 4 Billings Farm Rd., White River Jct., VT 05001.

Contributed by the Fluids Engineering Division for publication in the JOURNAL OF FLUIDS ENGINEERING. Manuscript received by the Fluids Engineering Division July 20, 1995; revised manuscript received March 19, 1997. Associate Technical Editor: O. C. Jones.

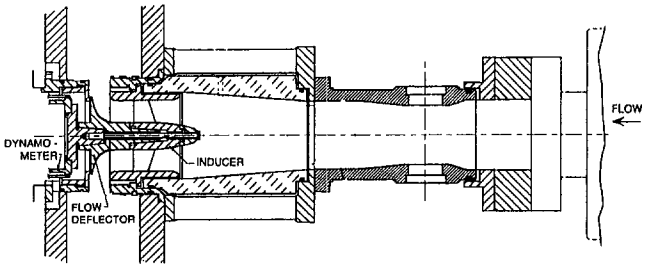

Fig. 1 (*a*) Schematic of inducer installation in the test facility

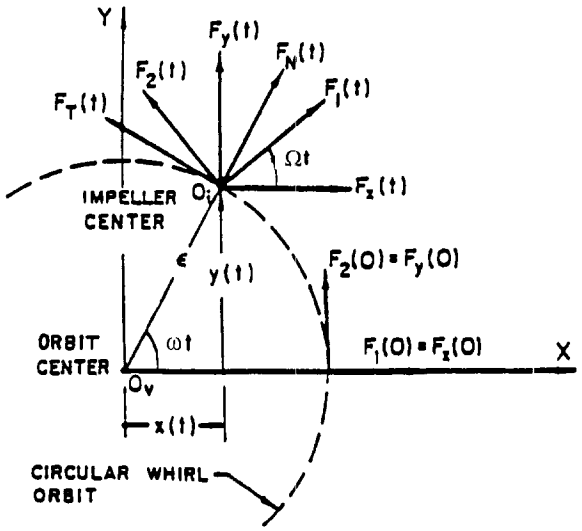

Fig. 1 (*b*) Schematic showing rotordynamic forces in laboratory and rotating reference frames

The sign conventions are such that F_n is positive outward and F_t is positive in the direction of rotation. It follows that a *positive* tangential force is destabilizing when the whirl motion is in the same direction as the shaft rotational motion (i.e. a positive whirl/shaft speed ratio). Conversely, a negative F_t tends to stabilize the whirl motion for a positive whirl/shaft speed ratio. Likewise, a positive F_t would be stabilizing for a *negative* whirl motion. In the case of the normal force, a positive (outward) force could be considered as a destabilizing force in the sense that it tends to increase the radius of the whirl orbit.

Rotordynamicists typically characterize these forces in terms of inertia, stiffness and damping matrices for stability analysis in the following manner:

$$\begin{bmatrix} F_x \\ F_y \end{bmatrix} = \begin{bmatrix} F_{ox} \\ F_{oy} \end{bmatrix} - [K]\begin{bmatrix} x \\ y \end{bmatrix} - [C]\begin{bmatrix} \dot{x} \\ \dot{y} \end{bmatrix} - [M]\begin{bmatrix} \ddot{x} \\ \ddot{y} \end{bmatrix} + \textit{higher order terms} \quad (4)$$

The matrices $[K]$, $[C]$, and $[M]$ are the stiffness, damping and inertia matrices respectively. It can be shown that the components of the rotordynamic force matrix $[A]$ can also be expressed in terms of the components of the stiffness, damping and inertia matrices as:

$$A_{xx} = M_{xx}\left(\frac{\omega}{\Omega}\right)^2 - C_{xy}\left(\frac{\omega}{\Omega}\right) - K_{xx}; \quad (5)$$

$$-A_{xy} = M_{xy}\left(\frac{\omega}{\Omega}\right)^2 + C_{xx}\left(\frac{\omega}{\Omega}\right) - K_{xy}; \quad (6)$$

$$A_{yx} = M_{yx}\left(\frac{\omega}{\Omega}\right)^2 - C_{yy}\left(\frac{\omega}{\Omega}\right) - K_{yx}; \quad (7)$$

$$A_{yy} = M_{yy}\left(\frac{\omega}{\Omega}\right)^2 + C_{yx}\left(\frac{\omega}{\Omega}\right) - K_{yy} \quad (8)$$

where ω is the whirl speed and Ω is the inducer rotational speed.

The above formulation implies that the coefficients of the stiffness, damping and inertia matrices can be obtained from rotordynamic force data if the forces can be expressed as a quadratic function of ω/Ω. Rotordynamic forces in centrifugal

Nomenclature

A_i = inlet cross-sectional area, πr_t^2

$[A] = \begin{bmatrix} A_{xx} & A_{xy} \\ A_{yx} & A_{yy} \end{bmatrix}$ = rotordynamic coefficient matrix, nondimensionalized by $\rho\pi\Omega^2 r_t^2 l$

F_o = steady lateral force on the inducer nondimensionalized by $\rho\pi\Omega^2 r_t^3 l$

F_{ox}, F_{oy} = components of the steady lateral force in the (X, Y) reference frame nondimensionalized by $\rho\pi\Omega^2 r_t^3 l$

F_x, F_y = components of the instantaneous lateral force in the (X, Y) reference frame, nondimensionalized by $\rho\pi\Omega^2 r_t^3 l$

F_n, F_t = components of the time averaged force on the inducer which are normal and tangential to the whirl orbit respectively and are nondimensionalized by $\rho\pi\Omega^2 r_t^2 l\epsilon$

l = axial blading length of the inducer (hub)

p_i = inlet static pressure

p_v = vapor pressure

Δp_t = total pressure rise between inlet and outlet

Q = flow rate

r_t = inducer tip radius

u_t = inducer tip speed, $r_t\Omega$

x, y = instantaneous coordinates of the inducer center in the fixed reference frame, nondimensionalized by r_t

$\dot{x}$, $\dot{y}$ = time derivatives of x and y, nondimensionalized by $r_t\Omega$

$\ddot{x}$, $\ddot{y}$ = acceleration, nondimensionalized by $r_t\Omega^2$

$[K] = \begin{bmatrix} K_{xx} & K_{xy} \\ K_{yx} & K_{yy} \end{bmatrix}$ = generalized stiffness matrix, nondimensionalized by $\rho\pi\Omega^2 r_t^2 l$

$[C] = \begin{bmatrix} C_{xx} & C_{xy} \\ C_{yx} & C_{yy} \end{bmatrix}$ = generalized damping matrix, nondimensionalized by $\rho\pi\Omega r_t^2 l$

$[M] = \begin{bmatrix} M_{xx} & M_{xy} \\ M_{yx} & M_{yy} \end{bmatrix}$ = generalized inertia matrix, nondimensionalized by $\rho\pi r_t^2 l$

Symbols

ϵ = radius of the whirl orbit

ρ = density of the working fluid (water)

σ = cavitation number, $(p_i - p_v)/(\frac{1}{2}\rho u_t^2)$

ω = frequency of whirl motion

Ω = inducer rotational frequency

Ψ = head coefficient, $\Delta p_t/(\rho u_t^2)$

pumps, for example, do indeed show a quadratic variation of the forces with ω/Ω (Jery (1986), Franz (1989)). Recent studies of rotordynamic forces due to leakage flows have also shown such a quadratic relation (Guinzburg, 1992). The research presented in this paper investigates whether the rotordynamic forces on an inducer also show a quadratic behavior with ω/Ω and the manner in which these forces are affected by cavitation.

It should be noted that the data presented in this paper represent purely fluid induced forces in the sense that the effects of tare forces (the dry weight of the inducer and the centrifugal forces arising by running the inducer in air) and buoyancy have been subtracted from the total force. The steady and unsteady forces presented are mean values obtained by integration over many cycles of rotation and whirl. The normal force (F_n) and the tangential force (F_t) are normalized by $\rho\pi\Omega^2 r_t^2 l\epsilon$. The steady forces ($F_o$ with components F_{ox} and F_{oy}) are normalized by $\rho\pi\Omega^2 r_t^3 l$ where ρ is the density of the fluid, r_t is the inducer tip radius (5.06 cm.) and l is the axial blading length (2.413 cm.). The uncertainties in the data are expressed as the standard deviation of the plotted data. The standard deviations associated with each plot are included in the corresponding plot caption. The variances of the derived quantities were obtained from previous data taken in the facility over 256 cycles of a fundamental reference frequency. The fundamental reference frequency is expressed as Ω/J (where $\omega/\Omega = I/J$ and I, J are integers) at which the orientation of the dynamometer and its location on the whirl orbit geometrically repeat (see also Franz et al., 1990). For the data reported in this paper, the standard deviations were typically less than 0.00091 for the lateral force (F_o), and 0.15 and 0.17 for the normal (F_n) and tangential (F_t) forces respectively.

Test Matrix

The effects of cavitation were studied at two flow coefficients, $\phi = 0.074$ and $\phi = 0.049$. The flow coefficient (ϕ) is defined as the ratio of the local axial velocity to tip speed $\phi = Q/(u_t A_i)$ where Q is the flow rate and A_i is the inlet area ($A_i = \pi r_t^2$). These specific flow coefficients were chosen in order to study the effects of flow reversals on the forces ($\phi = 0.049$) and to compare these with the forces at a flow coefficient for which no flow reversals are observed ($\phi = 0.074$). At the flow coefficient of 0.049, upstream tip clearance leakage flow and downstream hub re-entry flows were present. Upstream and downstream flow reversals on this inducer have been studied previously and reported by Bhattacharyya et al. (1993).

For the experiments presented in this paper, the eccentricity was set at $\epsilon = 0.0254$ cm. As a result of this eccentricity the clearance between the inducer blade tip and the housing varied between 0.028 cm. and 0.079 cm. The shaft rotational speed was 3000 rpm and the whirl speed was varied from −0.55 to +0.55 times the shaft speed.

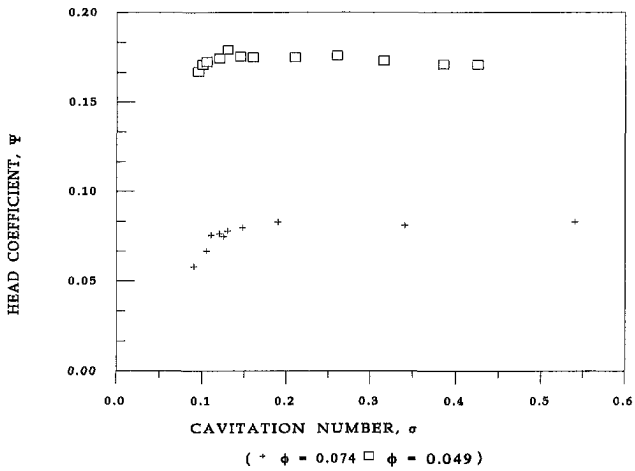

Fig. 2 Cavitation characteristics of the inducer at 3000 RPM. Uncertainty expressed as a standard deviation: $\psi \pm 0.0056$, $\phi \pm 0.00053$ and $\sigma \pm 0.0039$.

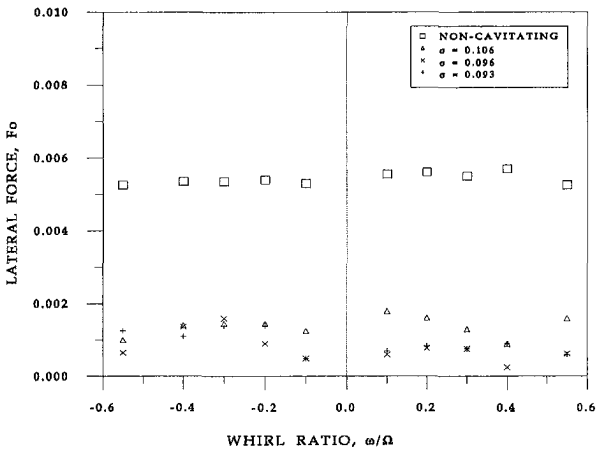

Fig. 3 Lateral force on the inducer at $\phi = 0.074$ for various cavitation numbers. Uncertainty expressed as a standard deviation: $\|F_o\| \pm 0.00091$, $\omega/\Omega \pm 0.001$, $\phi \pm 0.00053$ and $\sigma \pm 0.0039$.

The tests on the inducer were conducted in water, deaerated to an air content of less than 3 ppm. The facility includes a pressure regulation system which allows operation at different suction pressures, p_i. A conventional cavitation number, σ, is used to define the non-dimensional suction conditions:

$$\sigma = \frac{(p_i - p_v)}{\frac{1}{2}\rho u_t^2} \tag{9}$$

where p_v is the vapor pressure (at the water temperature) and the tip speed of the inducer is given by $u_t = \Omega r_t$. The results presented are for various cavitation numbers.

Results

Cavitation Performance. The cavitation characteristics of the inducer used for the current experiments are shown in Fig. 2 at $\phi = 0.074$ and $\phi = 0.049$ (3000 rpm). The head coefficient, ψ, defined as the ratio $\Delta p_t/(\rho u_t^2)$ where Δp_t refers to change in the total pressure, is plotted against various values of the cavitation number. In the case of $\phi = 0.074$, it is seen that as the cavitation number is reduced from noncavitating values, the head coefficient started decreasing at $\sigma = 0.147$. However, there was a slight increase in the head coefficient at $\sigma = 0.113$ followed by a continuous head breakdown below $\sigma = 0.106$. The head coefficient is approximately 0.081 under non-cavitating conditions. At $\sigma = 0.106$ there occurs a 4.9 percent head loss ($\psi = 0.077$). The cavitation characteristics at the lower flow coefficient of $\phi = 0.049$ exhibit a similar behavior.

Steady Forces Due to Cavitation. The results of the steady radial force measurements at $\phi = 0.074$ are presented in Fig. 3 for various whirl/shaft speed ratios (−0.55 to +0.55). The steady forces remain constant for a given cavitation number over the range of whirl/shaft speed ratios, but decrease with cavitation number. It is observed that the noncavitating steady forces are much larger than the steady forces with cavitation; reasons for this are discussed later but it should be pointed out that previous research (Bhattacharyya et al., 1992) has shown that the presence of the downstream asymmetry inherent to the test set up causes large lateral forces.

Figure 4 shows the variation of the steady force for various whirl ratios at the flow coefficient of $\phi = 0.049$. The results differ from those obtained for $\phi = 0.074$ in that the cavitating

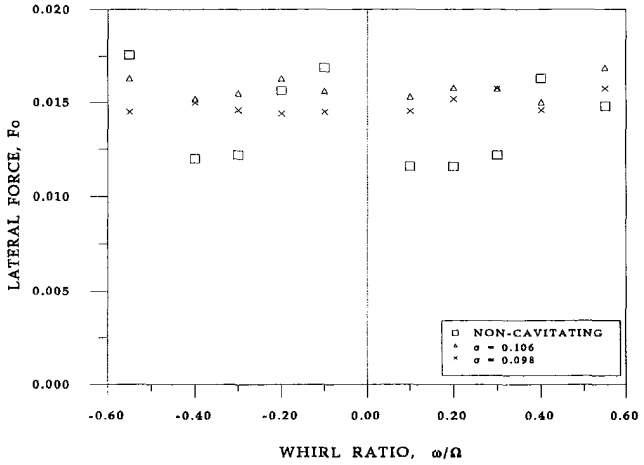

Fig. 4 Lateral force on the inducer at $\phi = 0.049$ for various cavitation numbers. Uncertainty expressed as a standard deviation: $\|F_o\| \pm 0.00091$, $\omega/\Omega \pm 0.001$, $\phi \pm 0.00053$ and $\sigma \pm 0.0039$.

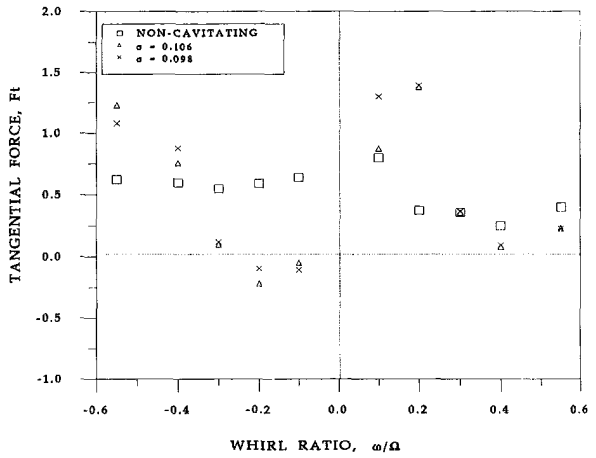

Fig. 6 Tangential force on the inducer at $\phi = 0.049$ for various cavitation numbers. Uncertainty expressed as a standard deviation: $F_t \pm 0.17$, $\omega/\Omega \pm 0.001$, $\phi \pm 0.00053$ and $\sigma \pm 0.0039$.

forces are about the same magnitude as the non-cavitating forces. The large lateral forces at $\phi = 0.049$ are possibly due to the occurrence of reverse flows downstream of the inducer in the presence of a downstream asymmetry inherent to the test set up. Under these conditions, the steady force due to the effect of cavitation cannot be distinguished from the noncavitating steady force.

Rotordynamic Forces Due to Cavitation. The rotordynamic forces on the inducer were also obtained at various flow coefficients and cavitation numbers. The tangential force is plotted against whirl frequency ratio, ω/Ω, for $\phi = 0.074$ in Fig. 5. The significant result obtained is the occurrence of multiple zero crossings. There are some significant differences compared to the non-cavitating force characteristics. One of these is that the tangential force remains negative in a substantial region of negative whirl under cavitating conditions. In fact for $\sigma = 0.106$ and $\phi = 0.074$, the tangential force does not reach a positive value in the negative whirl region (for the range of whirl/shaft speed ratios tested). Another feature of the tangential force is that it exhibits a positive peak in a range of positive whirl frequency ratio around $\omega/\Omega \approx 0.2$. Such a peak is not observed in the noncavitating tangential force at this flow coefficient (with no backflow). In fact, the magnitude of this peak increases as the cavitation number is reduced. The location of the peak also tends to shift to lower whirl/shaft speed ratios. Thus, the extent and manner in which the tangential forces become destabilizing depend on the extent to which the inducer cavitates. At larger positive whirl frequency ratios (especially for $\omega/\Omega > 0.4$), however the tangential force is observed to become increasingly negative (and hence stabilizing) for decreasing cavitation numbers. Thus, for this case, destabilizing tangential forces are generally observed from $\omega/\Omega = 0.0$ to $\omega/\Omega = 0.4$ and in the region $\omega/\Omega < 0.0$.

Figure 6 presents the corresponding results for a flow coefficient $\phi = 0.049$. The variation with whirl frequency ratio are very much similar to those at $\phi = 0.074$, especially in the occurrence of a positive, destabilizing peak around $\omega/\Omega \approx 0.2$. Multiple zero crossings are also evident. However, at this flow coefficient, the tangential force continues to be destabilizing at $\omega/\Omega = 0.55$ for a cavitation number $\sigma = 0.098$ unlike F_t at $\omega/\Omega = 0.55$ for $\phi = 0.074$ (at the same cavitation number).

Figure 7 presents a comparison between the tangential forces at the two flow coefficients for $\sigma = 0.106$. In the region of negative whirl, the forces become more stabilizing for the lower flow coefficient (except for the region between $\omega/\Omega = -0.5$ and $\omega/\Omega \approx -0.3$). The peak force in the region of positive whirl increases in magnitude. The location of this peak also shifts from $\omega/\Omega = 0.3$ at $\phi = 0.074$ to $\omega/\Omega = 0.2$ at $\phi = 0.049$. Another important observation is that for higher positive whirl ratios ($\omega/\Omega > 0.5$), the tangential forces tend to become

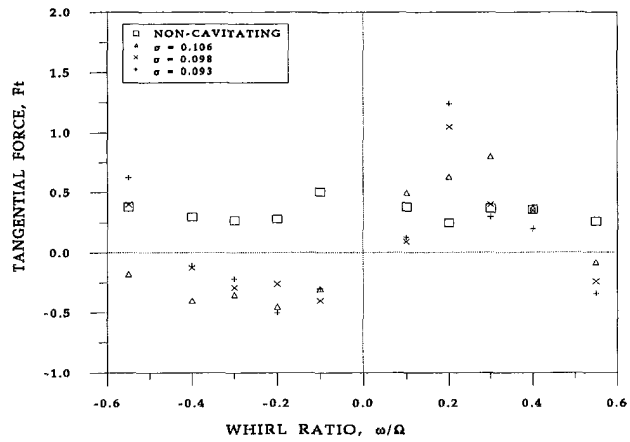

Fig. 5 Tangential force on the inducer at $\phi = 0.074$ for various cavitation numbers. Uncertainty expressed as a standard deviation: $F_t \pm 0.17$, $\omega/\Omega \pm 0.001$, $\phi \pm 0.00053$ and $\sigma \pm 0.0039$.

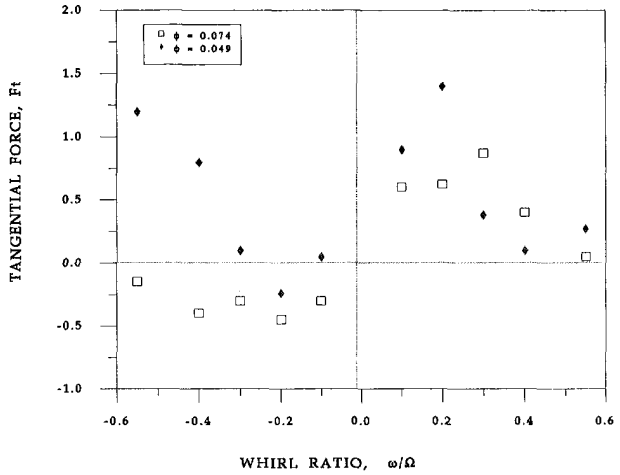

Fig. 7 Comparison of the tangential force on the inducer at a cavitation number $\sigma = 0.106$ for two flow coefficients. Uncertainty expressed as a standard deviation: $F_t \pm 0.17$, $\omega/\Omega \pm 0.001$, $\phi \pm 0.00053$ and $\sigma \pm 0.0039$.

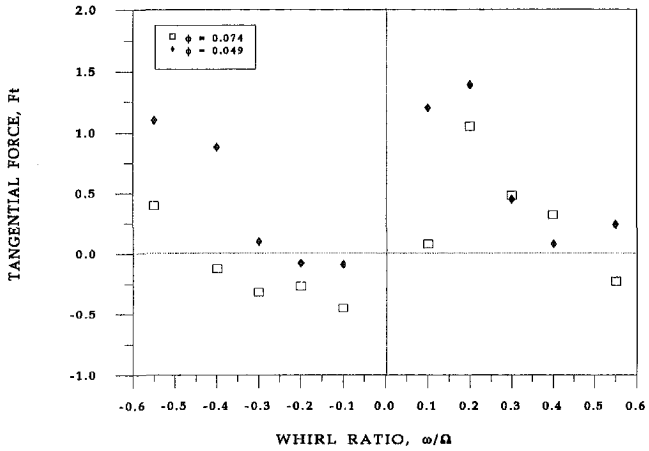

Fig. 8 Comparison of the tangential force on the inducer at a cavitation number $\sigma = 0.098$ for two flow coefficients. Uncertainty expressed as a standard deviation: $F_t \pm 0.17$, $\omega/\Omega \pm 0.001$, $\phi \pm 0.00053$ and $\sigma \pm 0.0039$.

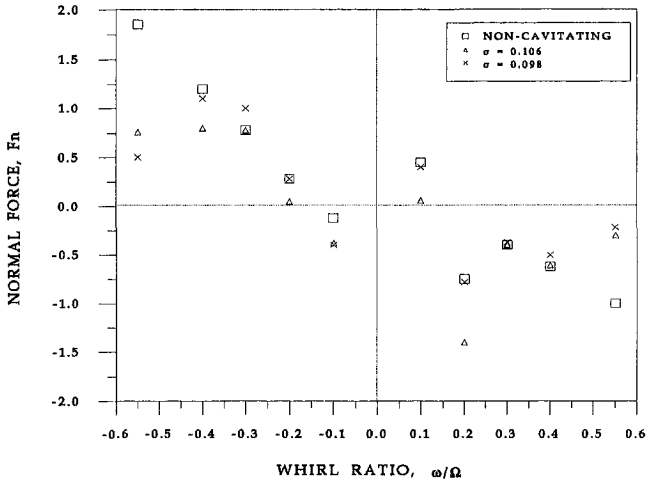

Fig. 10 Normal forces at flow coefficient $\phi = 0.049$ for various cavitation numbers. Uncertainty expressed as a standard deviation: $F_n \pm 0.15$, $\omega/\Omega \pm 0.001$, $\phi \pm 0.00053$ and $\sigma \pm 0.0039$.

increasingly destabilizing for the lower flow coefficient (whereas they become stabilizing for the higher flow coefficient).

Similar data for a cavitation number of $\sigma = 0.098$ is shown in Fig. 8. Again a positive peak of the tangential force occurs at $\omega/\Omega \approx 0.2$. For the lower flow coefficient, the range of destabilizing tangential force decreases for negative whirl (approximately $-0.3 < \omega/\Omega < -0.1$ at $\phi = 0.049$ compared to approximately $-0.4 < \omega/\Omega < 0.1$ at $\phi = 0.074$ for $\sigma = 0.098$).

The forces normal to the whirl orbit on the inducer at the flow coefficient of 0.074 have been plotted for different cavitation numbers in Fig. 9. It is observed that the normal forces do not vary significantly with cavitation number once cavitation has been established. However, compared to the non-cavitating data, we observe large and increasingly positive (destabilizing) normal forces with increasing positive whirl frequency ratios. Furthermore, the normal force in the presence of cavitation tends to be of a larger (negative) magnitude than the non-cavitating normal force for the range of whirl frequency ratios between -0.1 and $+0.1$. The characteristics of the normal force (with cavitation) in the region of negative whirl ($\omega/\Omega < -0.1$) tends to be similar to the noncavitating normal force behavior.

Figure 10 presents similar data for the lower flow coefficient of 0.049. In this case the normal force behavior displays multiple zero crossings. A significant feature is the occurrence of negative peaks at all the cavitation numbers (including the non-cavitating case). It is also noted that the normal force decreases for $\omega/\Omega < -0.4$ and increases for $\omega/\Omega > +0.4$ with decreasing cavitation numbers.

The normal forces at a given cavitation number, $\sigma = 0.106$, and two flow coefficients are compared in Fig. 11. As in the case of the tangential forces, a decrease in the flow coefficient clearly causes changes in the normal force. The number of zero crossings increase with a decrease in the flow coefficient and an additional region of positive (destabilizing) force occurs around $\omega/\Omega = 0.1$. Another significant effect caused by decreasing the flow coefficient is the appearance of a negative peak in the normal force in a region of positive whirl; at $\phi = 0.049$, $\sigma = 0.106$ this peak occurs around $\omega/\Omega \approx 0.2$. It is also observed at lower flow coefficients that the normal force tends to remain negative over a longer range of positive whirl frequencies. A comparison similar to that of Fig. 11 is shown in Fig. 12, but at the lower cavitation number $\sigma = 0.098$. An increase in the number of zero crossings of the force is observed at the lower flow coefficient. A positive (destabilizing) peak appears at $\omega/\Omega \approx 0.1$ for the lower flow coefficient at this cavitation number and along with a negative peak at $\omega/\Omega \approx 0.2$.

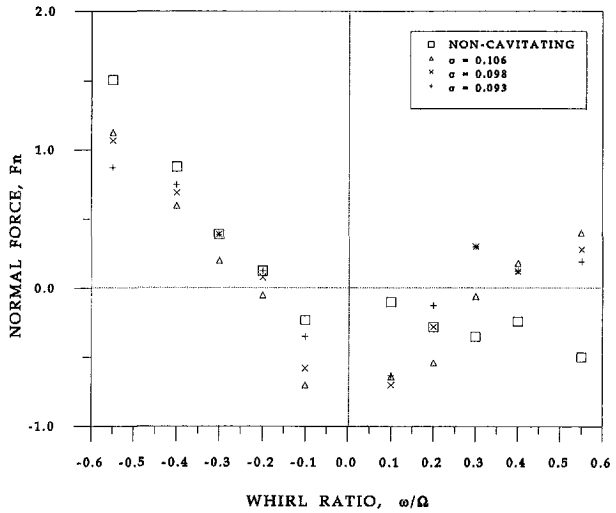

Fig. 9 Normal forces at flow coefficient $\phi = 0.074$ for various cavitation numbers. Uncertainty expressed as a standard deviation: $F_n \pm 0.15$, $\omega/\Omega \pm 0.001$, $\phi \pm 0.00053$ and $\sigma \pm 0.0039$.

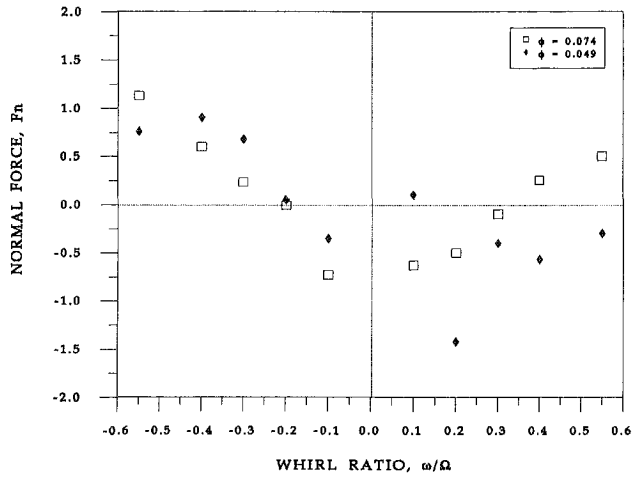

Fig. 11 Comparison of the normal force on the inducer at a cavitation number $\sigma = 0.106$ for two flow coefficients. Uncertainty expressed as a standard deviation: $F_n \pm 0.15$, $\omega/\Omega \pm 0.001$, $\phi \pm 0.00053$ and $\sigma \pm 0.0039$.

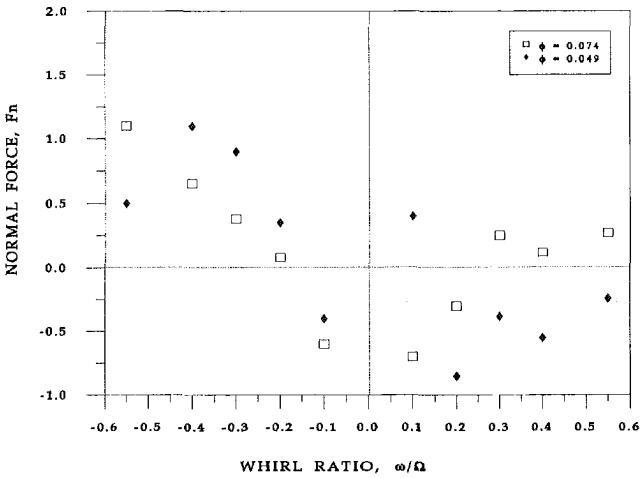

Fig. 12 Comparison of the normal force on the inducer at a cavitation number $\sigma = 0.098$ for two flow coefficients. Uncertainty expressed as a standard deviation: $F_n \pm 0.15$, $\omega/\Omega \pm 0.001$, $\phi \pm 0.00053$ and $\sigma \pm 0.0039$.

Discussion

The results presented in this paper show that cavitation has a significant effect on inducer rotordynamic forces. The destabilizing rotordynamic forces could lead to failure of the device in which the inducer is being used. It is therefore important to gain a fundamental understanding of the nature of these forces, in order to facilitate changes in the design and/or operating conditions of the machine.

A simple helical inducer was chosen for these preliminary tests. The effect of the geometry of inducers of this type on the cavitation performance have been reported previously (Acosta, 1958). The mechanism of head breakdown has also been studied by researchers such as Jakobsen (1964).

The influence of the flow coefficient on non-cavitating steady forces has been reported earlier (Bhattacharyya et al., 1992). It was shown that the presence of a downstream asymmetry causes significantly large steady forces due to the occurrence of a downstream flow reversal. The current experiments with cavitation were conducted with the same downstream asymmetry which is inherent to the system. This is the cause of the large non-cavitating steady force seen in Figs. 3 and 4. However, it may be noted that the downstream flow reversal for $\phi = 0.074$ is probably only incipient since previous flow visualization on the hub did not reveal re-entry flows on the hub (there was no observable upstream swirling backflow either). Furthermore, the occurrence of cavitation at this higher flow rate actually results in a lower net steady force. It may be speculated that this occurs because of the lower pumping work being done on the fluid because of cavitation. In the case of the lower flow coefficient, the steady force always remains high regardless of the extent of cavitation.

The unsteady force data suggest that flow reversals can also have significant consequences for rotordynamic forces. For non-cavitating flow the tangential forces are destabilizing for positive whirl at both flow coefficients. The noncavitating tangential force shows a destabilizing peak for positive whirl at $\omega/\Omega = +0.1$ for the lower flow coefficient. A similar observation was made on noncavitating inducers by Arndt and Franz (1986). A more dramatic effect of the flow coefficient is observed in cavitating flow. In the case of the inducer tested, the effect of lowering the flow coefficient increased the region of destabilization (positive F_t) for positive whirl. Furthermore, the effect of a decreased flow did not change the location of the peak, but rather led to an increase in its magnitude. For negative whirl, the higher flow coefficient was more destabilizing. This is an interesting observation especially when the current results are compared to the data obtained previously by Karyeaclis et al. (1989) on a four bladed inducer (called the SEP inducer) with a hub which increases substantially between inlet and discharge. The inducer installation of the SEP inducer was similar to the current configuration. In the case of the SEP inducer, the tangential forces were less destabilizing for the lower flow coefficient for positive whirl frequencies, unlike the current results. Karyeaclis et al. (1989) argued that for a given cavitation number, larger forces could be expected at the higher flow coefficient because it is closer to the performance breakdown point. The current results do not show the same trend; thus it appears that the *geometry* of the inducer has a significant effect on the rotordynamic forces. Further, the current results show a tangential force peak at $\omega/\Omega = +0.2$ rather than at $\omega/\Omega = +0.5$ observed for the SEP tests. In Karyeaclis et al. (1989) it was argued that the peak at $\omega/\Omega = +0.5$ was a sympathetic resonance with the fluid behind the inducer which rotates at half the shaft speed. In the current tests, however, the peak occurs at much less than half the shaft speed. In the case of the normal forces, the effect of a reduction in the flow coefficient was an increase in the number of positive and negative peaks. These differences in the characteristics of rotordynamic forces with whirl frequencies under cavitating conditions probably stem from the differences in internal flows and reverse flow patterns caused by the geometry differences in inducers.

The effect of cavitation on the tangential forces at a given flow coefficient is significant. It is observed that for decreasing cavitation numbers, the magnitude of the peak in the force at $\omega/\Omega = +0.2$ increases and becomes narrower. Thus the range of destabilizing forces decreases. This is the reverse of the trend to that observed by Karyeaclis et al. (1989) for the SEP inducer where larger forces were accompanied by larger instability regions. Also, in the case of the current inducer the tangential forces with increasing cavitation become increasingly stabilizing for negative whirl.

Another important observation is that the data for F_t and F_n as a function of ω/Ω do not exhibit the kind of quadratic functional behavior which is normally assumed in many rotordynamic models. Rather, as has been reported previously (Karyeaclis et al., 1989) much higher order polynomials would be required to approximate the forces. Thus the representation of the components of the rotordynamic matrix $[A]$ (as given in Eq. (4)) does not hold for the cavitating inducer. Consequently, the generalized stiffness, damping and inertia matrices for the inducer cannot be determined. Instead, rotordynamic analysis of the inducer must include fluid-induced forces which are more general functions of the whirl frequency ratio.

Conclusions

(1) This paper reports an experimental investigation of rotordynamic forces on a simple three bladed, helical, axial flow inducer with a constant hub ratio. The influence of cavitation and off-design flow rates on these forces are presented. Rotordynamic forces are destabilizing at various whirl ratios, when the inducer is whirled in a circular orbit at a fraction of its rotational speed. An understanding of these forces is important to determine dynamic stability of high speed pumping systems such as the high pressure turbopumps used in the space shuttle main engine.

(2) Cavitation has important consequences for fluid-induced rotordynamic forces generated by inducers. These forces can become destabilizing at both positive and negative whirl frequencies. Increasing levels of cavitation could cause an increase in destabilizing forces.

(3) The rotordynamic forces do not exhibit a quadratic functional behavior (typical of centrifugal impellers) and hence the conventional generalized stiffness, damping and inertia matrices cannot be determined.

(4) The internal flow patterns and flow reversals associated with reduced flow coefficients appear to have a significant bear-

ing on these forces. Lower flow coefficients, characterized by upstream backflows and downstream re-entry flows, are also associated with increases in destabilizing peaks of rotordynamic forces. The flow patterns are, in turn, dependent on the inducer geometry and the dependence of the forces on the extent of cavitation must be included in design considerations.

Given that analytical techniques are, as yet, unable to predict unsteady cavitating forces in turbomachinery, the experimental data obtained in the current research provides an appropriate starting point for the understanding of these complex forces in axial flow inducers.

Acknowledgment

The authors would like to thank the NASA George C. Marshall Space Flight Center for sponsoring this project under contract no. NAG8-118, Henry L. Stinson, contract monitor.

References

Acosta A. J., 1958, "An Experimental Study of Cavitating Inducers," *Proceedings 2nd Symposium on Naval Hydrodynamics,* Washington, D.C., pp. 533–557.

Acosta A. J., 1993, "Flow in Inducer Pumps, An Aperçu," *Proceedings 4th International Symposium on Transport Phenomena and Dynamics Of Rotating Machinery,* Honolulu, Vol. A., pp. 1–13.

Arndt N., and Franz R., 1986, "Observations of Hydrodynamic forces on Several Inducers including the SSME LPTOP," Report No. E249.3, Division of Engineering and Applied Sciences, California Institute of Technology, Pasadena, CA.

Bhattacharyya A., Acosta A. J., Brennen C. E., and Caughey T. K., 1992, "The Formation of Backflow and its Consequences on the Lateral Forces in Axial Flow Impellers," *Abstracts of the ASME Fluids Engineering Conference,* Los Angeles, FED-Vol. 133, pp. 237–239.

Bhattacharyya A., Acosta A. J., Brennen C. E., and Caughey T. K., 1993, "Observations on Off-Design Flows in Axial Flow Inducers," *Proceedings Pumping Machinery Symposium,* ASME Fluids Engineering Conference, Washington D.C., FED-Vol. 154, pp. 135–141.

Franz R., 1989, "Experimental Investigation of the Effect of Cavitation on the Rotordynamic Forces on a Whirling Centrifugal Pump Impeller," Ph.D. thesis, Division of Engineering and Applied Sciences, California Institute of Technology, Pasadena, California.

Franz R., Acosta A. J., Brennen C. E., and Caughey T. K., 1990, "The Rotordynamic Forces on a Centrifugal Pump Impeller in the Presence of Cavitation," ASME JOURNAL OF FLUIDS ENGINEERING, Vol. 112, No. 3, pp. 264–271.

Guinzburg A., 1992, "Rotordynamic Forces Generated by Discharge-to-Suction Leakage Flows in Centrifugal Pumps," Ph.D. thesis, Division of Engineering and Applied Sciences, California Institute of Technology, Pasadena, CA.

Jakobsen J. K., 1964, "On the Mechanism of Head Breakdown in Cavitating Inducers," ASME *Journal of Basic Engineering,* pp. 291–305.

Jery B., 1986, "Experimental Study of Unsteady Hydrodynamic Force Matrices on Whirling Centrifugal Pump Impellers," Ph.D. thesis, Division of Engineering and Applied Sciences, California Institute of Technology, Pasadena, California.

Kamijo K., Shimura T., and Watanabe M., 1977, "An Experimental Investigation of Cavitating Inducer Instability," *Proceedings ASME Winter Annual Meeting,* Atlanta.

Karyeaclis M. P., Miskovish R. S., and Brennen C. E., 1989, "Rotordynamic Tests in Cavitation of the SEP Inducer," Report No. E200.27, Division of Engineering and Applied Sciences, California Institute of Technology, Pasadena, CA.

Lakshminarayana B., 1972, "Visualization Study of Flow in an Axial Flow Inducer," ASME *Journal of Basic Engineering,* pp. 777–787.

Lakshminarayana B., 1982, "Fluid Dynamics of Inducers—A Review," ASME JOURNAL OF FLUIDS ENGINEERING, Vol. 104, pp. 777–787.

Rosenmann W., 1965, "Experimental Investigations of Hydrodynamically Induced Shaft Forces with a Three Bladed Helical Inducer," *Proceedings ASME Symposium on Cavitation in Turbomachinery,* pp. 172–195.

Yoshinobu Tsujimoto
Professor.

Yoshiki Yoshida
Assistant Professor.

Yasukazu Maekawa
Graduate Student.

Satoshi Watanabe
Graduate Student.

Osaka University,
Engineering Science,
Toyonaka, Osaka 560,
Japan

Tomoyuki Hashimoto
Researcher,
National Aerospace Laboratory,
Kakuda Reserch Center,
Kakuda, Miyagi,
Japan

Observations of Oscillating Cavitation of an Inducer

Oscillating cavitation of an inducer was observed through unsteady inlet pressure measurements and by use of high speed video picture, covering a wide range of flow coefficient and cavitation number. One of the purposes of the study is to identify a mode of rotating cavitation predicted by a linear analysis, and the other is to obtain a general view of oscillating cavitation. The number of rotating cavitation cells and their propagation velocity were carefully determined from the phase difference of pressure fluctuations at various circumferential locations. Various kinds of oscillating cavitation were observed: rotating cavitation rotating faster/slower than impeller rotation, cavitation in backflow vortices, and surge mode oscillations. Effects of inlet and outlet (effective) pipelength were also studied.

Introduction

During the development stage of LE-7 LOX Turbopump for the H-II rocket, a super-synchronous shaft vibration was observed. This was attributed to rotating cavitation and was successfully suppressed by a minor modification of the inducer housing (Kamijo et al., 1993). Rotating cavitation has also been found in the ARIANE V LH_2 turbopump inducer and the effects of the number of inducer blades have been discussed (Goirand et al., 1992). Thus, rotating cavitation is a problem common to modern high performance pump inducers.

Since the pioneering work by Acosta (1958), observations of rotating cavitation have been made by several authors (Rosenmann, 1965; Kamijo et al., 1977, 1980; Yamamoto, 1980). Major features of rotating cavitation are; (i) cavitated region rotates faster than impeller, (ii) rotating cavitation occurs even with negative slope of the static pressure performance curve. These features are quite different from those of rotating stall (Greitzer, 1981). By constructing a simple theoretical model (Tsujimoto et al., 1993) it was shown that the rotating cavitation is a local 2-D flow instability caused by a positive mass flow gain factor of the cavitation. However, the model predicts a mode which rotates opposite to the impeller rotation, as well as the mode rotating faster than the impeller.

The purposes of the present study are to obtain a general view of oscillating cavitation covering a wide range of flow coefficient and cavitation number, paying attention to the direction of the cavity propagation.

Experimental Apparatus

The pump loop is shown in Fig. 1. The baseline experiments were made with an inlet pipe A with nominal diameter 200 mm and without the outlet accumulator B. The system parameter was changed by using an inlet pipe A with diameter 150 mm or by adding an accumulator B with a volume of air equals to 1.5×10^{-3} m^3 under test condition. The base pressure (and hence cavitation number) was adjusted by using a vacuum pump connected to the pressure control tank with about 0.65 m^3 of gas/vapor.

Figure 2 shows the test section. The impeller is a scale model of LE-7 LOX turbopump inducer, with three blades $Z_i = 3$, outer diameter 149.8 mm; the housing is made of transparent acryllic resin, with inner diameter 150.8 mm (constant tip clearance $s = 0.5$ mm). The inlet pressure fluctuation was measured 27.5 mm upstream of the inducer leading edge, at two circumferential locations with various angular separation angles θ. The number of cells was determined from a plot of the phase difference of those pressure signals. The rotational frequency of the impeller was maintained at $N = 4000 \pm 2$ rpm. The static pressure performance is also shown in Fig. 2. The curve has negative slope throughout the flow range and no conventional surge nor rotating stall is expected to occur. The design point of the inducer is ($\phi = 0.077$, $\psi_s = 0.130$). Since the flow meter was not available at the time of the unsteady pressure measurements, the flow condition is defined by using the value of the static pressure coefficient ψ_s.

Cell Number Identification

Figure 3(a) shows an example of cascade plots of inlet pressure spectrum for various cavitation numbers σ, for a static pressure coefficient $\psi_s = 0.123$ and a rotational frequency $f_N = (4000/60) = (200/3)$ Hz. Hence the blade passing frequency is $Z_i \times f_N = 3 \times f_N = 200$ Hz. We observe frequency components i $\sim$ v and i′ $\sim$ v′. If we represent the frequencies of i and i' components by f_i and f_i', we observe the following relationship

$$f_i + f_i' = 3f_N \quad (1)$$

Contributed by the Fluids Engineering Division for publication in the JOURNAL OF FLUIDS ENGINEERING. Manuscript received by the Fluids Engineering Division April 26, 1996; revised manuscript received May 19, 1997. Associate Technical Editor: J. Katz.

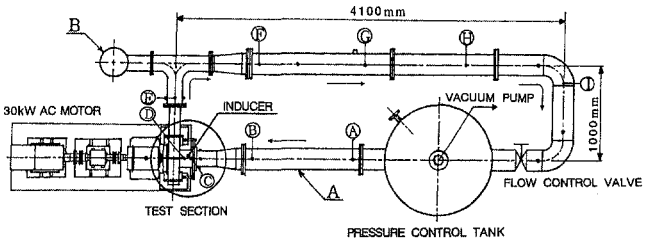

Fig. 1 Pump loop

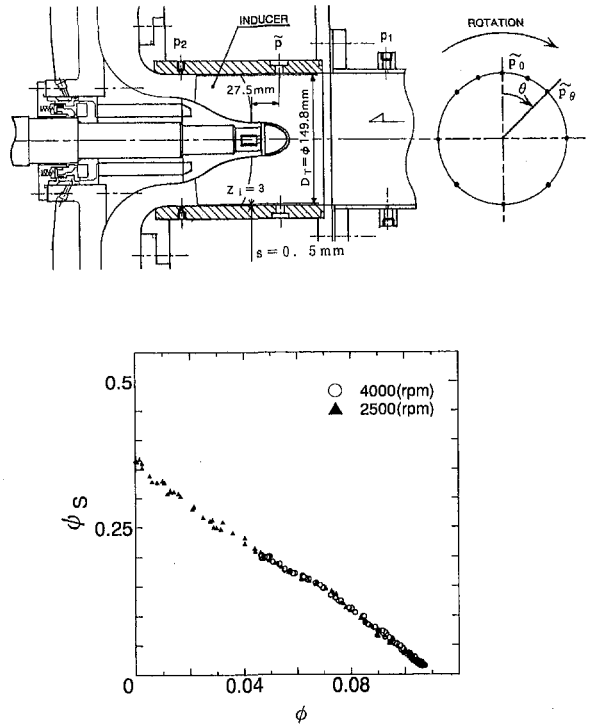

Fig. 2 Inducer crosssection and inlet pressure measurement locations, along with static pressure performance

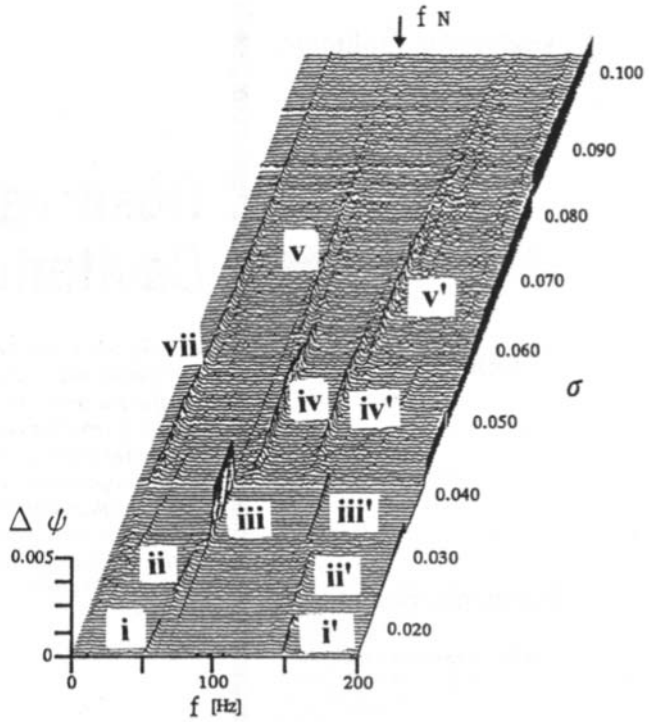

Fig. 3(*a*) Spectral analysis of the inlet pressure fluctuations (for ψ_s = 0.123 ± 0.002, uncertainty in f ± 1.5 Hz, in $\Delta\psi$ ± 0.0001)

within the accuracy of ±1.5 Hz. Hence, it is quite possible that either one of i or i' is substantial and the other is a byproduct of a nonlinear interaction of the substantial component with the blade passing component.

Figure 3(*b*) shows the phase difference Arg $(\tilde{p}_\theta/\tilde{p}_0)$ plotted against the angular separation θ of the pressure taps (see Fig. 2), where the fluctuating pressure is represented by $p_\theta = \tilde{p}_\theta \exp(2\pi j f t)$. By definition, the total amount of the continuous change in Arg $(\tilde{p}_\theta/\tilde{p}_0)$ corresponding to a change in θ of 2π, is 2π times the number of cells n. If Arg $(\tilde{p}_\theta/\tilde{p}_0)$ decreases/increases with increasing θ, it shows that the pressure pattern rotates in the direction of/opposite to the impeller rotation. We represent the direction by adding plus/minus signs to n for co-/counter rotating patterns. From the plots similar to Fig. 3(*b*), the value of n' for i' component is also determined. Then we can obtain the following relationship consistent to the results of nonliner interaction considerations.

$$n + n' = Z_i = 3 \tag{2}$$

The propagation velocity ratio, defined by the ratio of the rotational velocity of pressure pattern to the impeller rotational frequency is given by

$$f/nf_N \tag{3}$$

The number of cells n and the propagation velocity ratio f/nf_N thus determined are shown in Fig. 3(*b*). We cannot distinguish the "substantial" component from the pressure measurements alone. However, from the flow visualization and other studies described later, the components i ~ v appear to be the substantial components. It was suggested by a reviewer that higher order spectral methods, i.e., bispectrum/bicoherence are successfully applied (Jong, Jen-Yi, 1994, Jong, Jen-Yi et al., 1992) by NASA-Marshall Space Flight Center in identifying

Nomenclature

f_i = frequency of the i component of pressure fluctuation [Hz]
f_N = rotational frequency of inducer [Hz]
H = blade spacing at the tip, see Figs. 7 and 8
j = imaginary unit
L = blade length
l_c = cavity length
N = rotational speed of inducer [rpm]
n = number of cavitation cells
p = pressure
p_1, p_2 = inlet, outlet static pressure
p_v = vapor pressure
$\tilde{p}_0$ = pressure fluctuation at $\theta = 0$
$\tilde{p}_\theta$ = pressure fluctuation at $\theta = \theta$
t = time
u_t = inducer tip velocity
Z_i = number of inducer blades
$\Delta\psi$ = coefficient of pressure fluctuation $(= \tilde{p}/\rho u_t^2)$
ψ_s = static pressure coefficient $(= (p_2 - p_1)/\rho u_t^2)$
θ = angular separation of pressure taps
σ = cavitation number $(= (p_1 - p_v)/(\rho u_t^2/2))$
ϕ = flow coefficient $(= \bar{c}_x/u_t$, $\bar{c}_x$: mean axial velocity at inducer inlet)

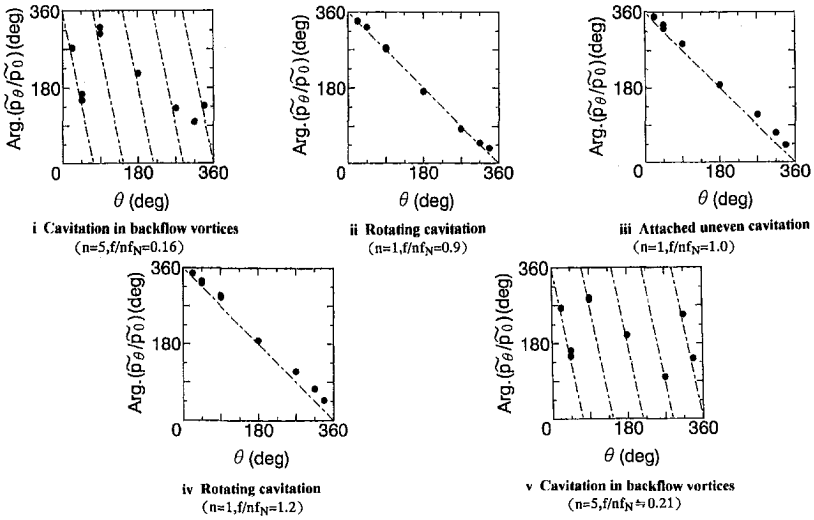

Fig. 3(*b*) The phase difference Arg ($\tilde{p}_\theta/\tilde{p}_0$) plotted against the angular separation θ of the pressure taps (for the components i ~ v in Fig. 3(*a*), uncertainty in Arg ($\tilde{p}_\theta/\tilde{p}_0$) ± 5 deg, in θ ± 1 deg)

such nonlinear oscillations. The authors would like to apply these more sophisticated methods in the future study.

Map of Oscillating Cavitations

Figure 4 presents the cascade plots of inlet pressure power spectra for various static pressure coefficients ψ_s. The design point is ψ_s = 0.130. The number of cells and the propagation velocity ratio for each component is summarized in Table 1. The ranges of occurrence of each component are shown in the suction performance plots of Fig. 5.

Physical Interpretation of Each Component

Cavitation in Backflow Vortices. Figure 6(*a*) presents a picture from high speed video under the condition with the

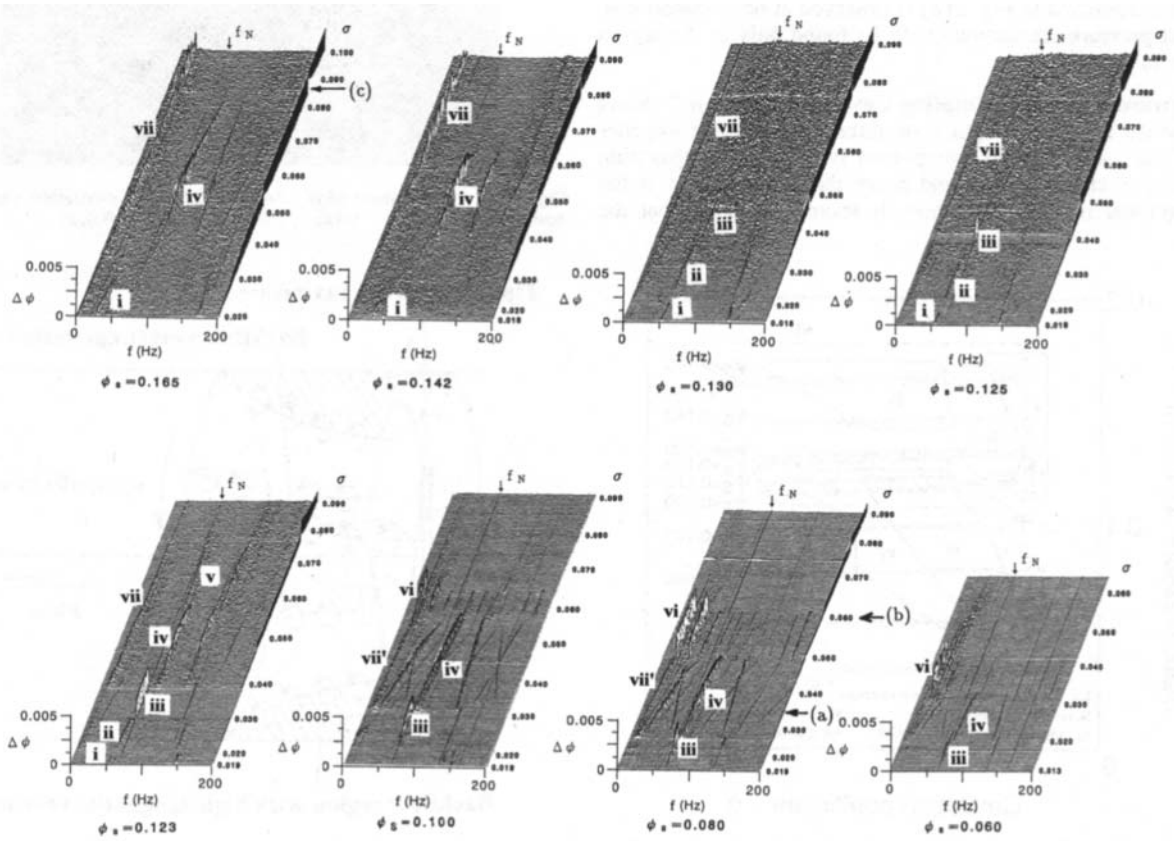

Fig. 4 Spectral analyses of the inlet pressure fluctuations for various static pressure coefficients (uncertainty in ψ_s ± 0.002, f ± 1.5 Hz, in $\Delta\psi$ ± 0.0001)

Table 1 Number of cells and propagation velocity ratio

		Number of cells n	Rotational velocity ratio f/nf_N
i	Cavitation in backflow vortices	5	0.16
ii	Rotating cavitation	1	≒0.9
iii	Attached uneven cavitation	1	1.0
iv	Rotating cavitation	1	1.1～1.3
v	Cavitation in backflow vortices	5	0.21
vi	Surge mode oscillation	0	≒18Hz／(3300～5000 rpm)
vii	Cavitation surge	0	8～19Hz／4000 rpm, proportional to rpm

component i at $\psi_s = 0.130$ and $\sigma = 0.015$. We observe five clouds of cavitation extending upstream from the tip at the inducer inlet. They are supposed to be formed in the backflow vortices as observed by Acosta (1958). The cavitation clouds slowly rotate at an angular velocity close to that corresponding to $f/nf_N = 0.16$. Hence, the component i is considered to be caused by the clouds of cavitation in backflow vortices. Figure 6(b) presents the picture at large cavitation number $\sigma = 0.07$ where the component v is found. We find a system of cavitation composed of that in tip leakage flow, which basically rotates attached to the blades, and that in backflow vortices formed on the boundary of the backflow region, rotating much slower than the impeller, as sketched in Fig. 6(c). As shown in Fig. 6(b), the backflow vortices occur rather irregularly and it was difficult to determine its number and speed definitely from the video picture. However, they were found to be not inconsistent with the values $n = 5$ and $f/nf_N = 0.21$ determined from the pressure measurements. The passage of the backflow vortices is considered to the cause of component v. Although the structure similar to that as sketched in Fig. 6(c) is observed at other conditions, distinct pressure fluctuation could be found only in the region shown in Fig. 5.

Forward Travelling Rotating Cavitation. Figure 7 shows the change in cavity length l_c on three blades of the impeller under the condition with component iv. Forward propagation of cavity is clearly shown and hence the component iv is the conventional rotating cavitation. It should be noted that the

Fig. 6(a) Picture from high speed video under cavitation oscillation component i (for $\psi_s = 0.130 \pm 0.002$, $\sigma = 0.015 \pm 0.002$)

Fig. 6(b) Picture from high speed video under cavitation oscillation component v (for $\psi_s = 0.123 \pm 0.002$, $\sigma = 0.070 \pm 0.002$)

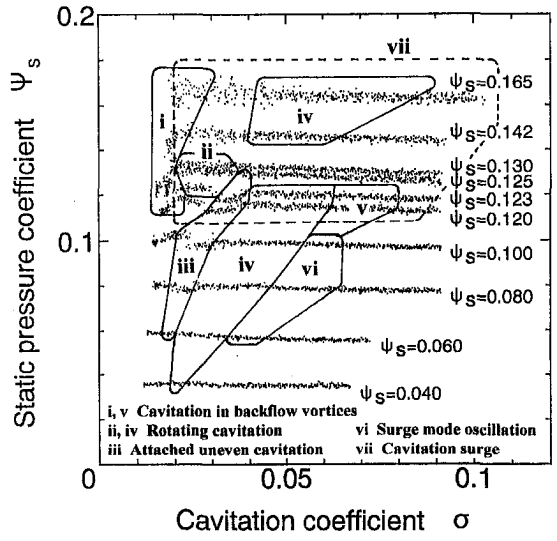

Fig. 5 Suction performance and a map showing the occurrence regions of various oscillating cavitation types (uncertainty in $\psi_s \pm 0.002$, in $\sigma \pm 0.002$)

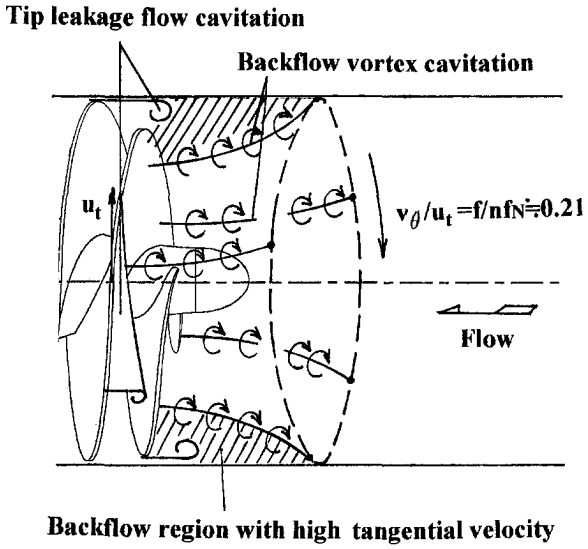

Fig. 6(c) Sketch showing tip leakage flow cavitation and backflow vortex cavitation

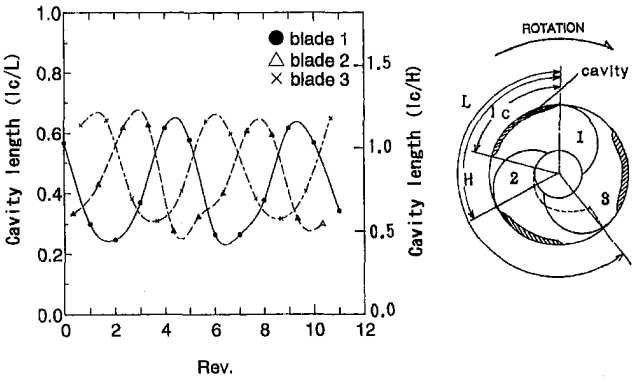

Fig. 7 Oscillation of cavity length with rotating cavitation component iv (for ψ_s = 0.08 ± 0.002, σ = 0.041 ± 0.002, uncertainty in Rev. ± 0.05, in l_c/L ± 0.03, in l_c/H ± 0.055)

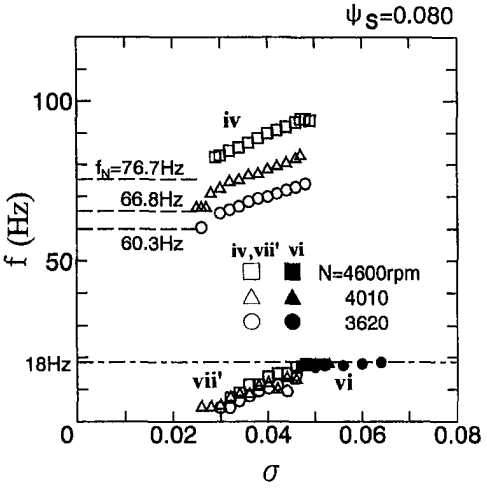

Fig. 9 Effects of the rotational speed N(±2 rpm), on the frequencies of the components iv, vi, and vii′ (uncertainty in f ± 1.5 Hz, in σ ± 0.002, in ψ_s ± 0.002)

maximum cavity length is slightly larger than the circumferential blade spacing H. As shown in Fig. 5, rotating cavitation iv appears in two separate regions with ψ_s larger/smaller than design value. In the region with higher static pressure coefficient, the cavity length is smaller and the cavitated region extends more upstream. With the component iii, we observe one shorter cavity and two longer cavities fixed to three blades of the impeller. Hence, the component iii is caused by uneven cavities attached to the rotor. This might correspond to "alternate blade cavitation" for the case with an even number of blades (Acosta, 1958). With the component ii, the change in the size of the cavities is not so clear as with the components iii and iv. However, the phase plots in Fig. 3(b) for ii is quite similar to that for iii and iv. This resemblance suggests that the component ii with $n = 1$ and $f/nf_N = 0.9$ is substantial. If so, this component could be the "backward travelling mode" predicted by the 2-D flow model (Tsujimoto et al., 1993), since the backward mode becomes a forward mode with $f/nf_N < 1$ if cavitation delay exists (Tsujimoto et al., 1996).

Surge Mode Oscillation. For the components vi, vii, and vii′, the pressure fluctuations are in phase at all circumferential locations. They are called herein "surge mode oscillation" after "surge" in gas handling turbomachines. The major differences between the component vi and the components vii and vii′ are that, for the component vi, the amplitude is larger and the frequency is fairly constant (18 Hz) as shown in Fig. 4. Figure 9 shows the effects of rotational frequency f_N at ψ_s = 0.08. A detailed examination shows that the frequencies of iv and vii′ are proportional to f_N, while that of vi is fixed at 18 Hz. At ψ_s = 0.08, it was also found that $f_{iv} - f_N$ is equal to $f_{vii'}$ within the measurement error (±1.5 Hz). Hence, the component vii′ is caused by a nonlinear interaction of component iv (rotating cavitation) with the rotational frequency component. The difference, $f_{iv} - f_N$, corresponds to the frequency of cavity oscillation observed on a blade. Figure 9 shows that the component vi occurs when this frequency approaches 18 Hz. This suggests that component vi is the result of a resonance of a certain vibration mode with 18 Hz and the cavity oscillation due to rotating cavitation. Various attempts have been made to identify the "vibration mode," but no clear mode could be found.

Although the frequency of vii is also close to $f_{iv} - f_N$, a meaningful difference (larger than ±1.5 Hz, up to ±5 Hz) was observed. In addition, the component vii can appear even without the rotating cavitation component iv. Hence, component vii is considered to be a substantial one and is herein called "cavitation surge" for the purpose of contrasting "cavitation surge" and "rotating cavitation" in pumps with "surge" and "rotating stall" in compressors, although the word "auto-oscillation" is also used in Brennen's textbook (1994). Figure 10 shows the effects of the rotational speed, N, on the frequency of the component vii. The frequency is nearly proportional to N at lower frequencies but the rate of increase decreases at higher frequencies. No "resonance" (or component equivalent to vi) was observed even when f_{vii} approached 18 Hz. This suggests that the component iv is not a simple "resonance."

The modes of pressure fluctuation of iv, vi, and vii in the inlet and outlet pipes are shown in Fig. 11. For the surge mode

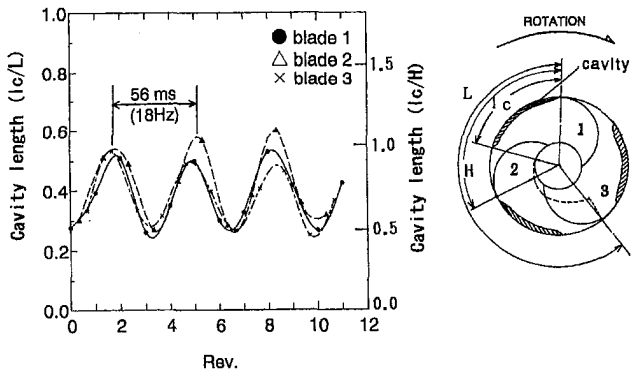

Fig. 8 Oscillation of cavity length with surge mode component vi (for ψ_s = 0.08 ± 0.002, σ = 0.054 ± 0.002, uncertainty in Rev. ± 0.05, in l_c/L ± 0.03, in l_c/H ± 0.055)

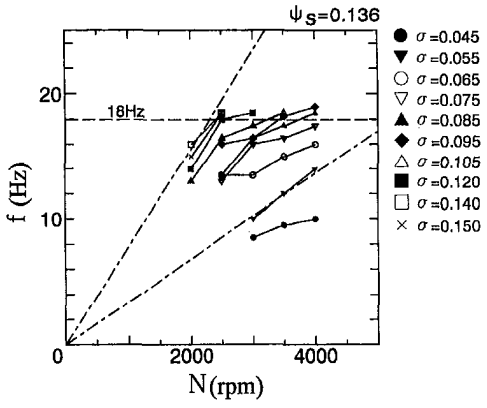

Fig. 10 Effects of the rotational speed N(±2 rpm), on the frequencies of the component vii. The dash dot lines show proportionality relations between N and f. (uncertainty in f ± 1.5 Hz, in σ ± 0.002, in ψ_s ± 0.002)

oscillations vi and vii, the phase is nearly constant throughout the pipes and the amplitudes decrease linearly as the tank is approached from the inducer. The pressure fluctuation amplitude of the rotating cavitation component iv is significantly smaller at the inducer outlet. It is quite surprising that the rotating cavitation component iv can be observed at locations as far downstream as 33 impeller diameters from the impeller.

Effects of Piping System

In order to explore the effects of the piping system, experiments were carried out with the following two configurations (see Fig. 1).

(I) Diameter of the inlet pipe A is reduced from 200 mm to 150 mm.

(II) An added accumulator, B.

No significant change was observed except that the surge mode oscillation vi did not occur for the system (II). Frequencies of each component for these cases are plotted in Fig. 12. We observe no significant change in the frequencies except for the cavitation surge vii. This shows that all of the rotating cavitation types i–v are quite independent of the attached system. This result supports the theoretical result of Tsujimoto et al. (1993) who showed that rotating cavitation is a local flow instability. The frequency of cavitation surge vii is decreased by decrease in the inlet pipe diameter (increase in effective inlet pipe length) and increased by the addition of accumulator tank to the outlet line (decrease in effective outlet pipe length). This agrees with the results of conventional cavitation surge analyses such as by Young et al., (1972). Although the frequency of cavitation surge is system dependent, Brennen (1994) proposes a relation between f_{vii}/f_N and σ to provide a crude estimate of the frequency. This relation is shown by the dashed curve in Fig. 12. The present result agrees qualitatively with the estimation. The frequency of vi is not altered by the change in inlet pipe but the component vi disappeared entirely with the addition of the accumulator to the outlet line. The introduction of small amounts of air to the outlet line also suppressed the surge mode oscillation vi. Irrespective of these observations, the component vi is less well understood.

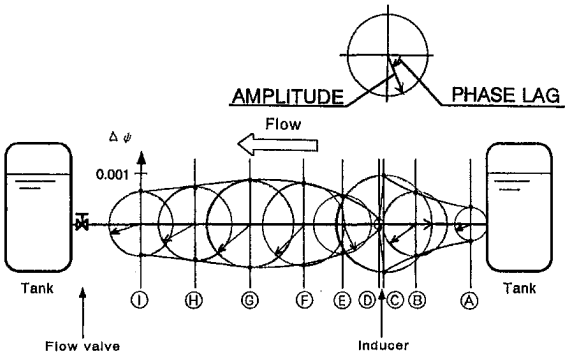

(a) Component **iv**($\psi_s = 0.080, \sigma = 0.035$, point (a) in Fig.4)

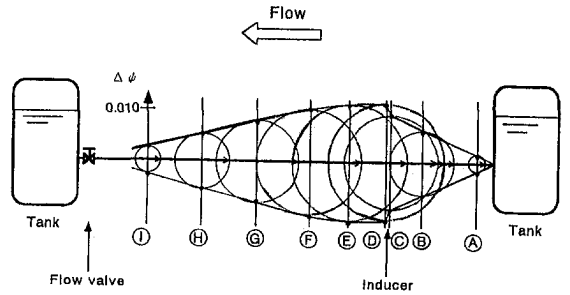

(b) Component **vi** ($\psi_s = 0.080, \sigma = 0.060$, point (b) in Fig.4).

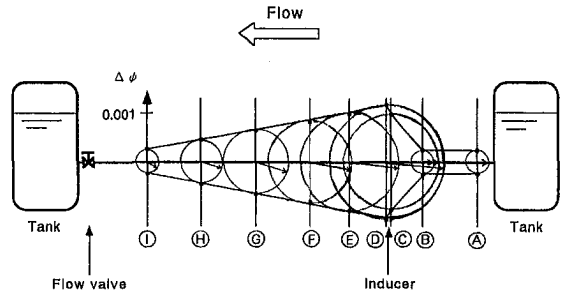

(c) Component **vii**($\psi_s = 0.165, \sigma = 0.087$, point (c) in Fig.4)

Fig. 11 The modes of pressure fluctuations iv, vi, and vii represented by the amplitude and the phase at each of the axial locations shown in Fig. 1 (uncertainty in $\Delta\psi \pm 0.0001$, in phase $\pm$ 5 deg)

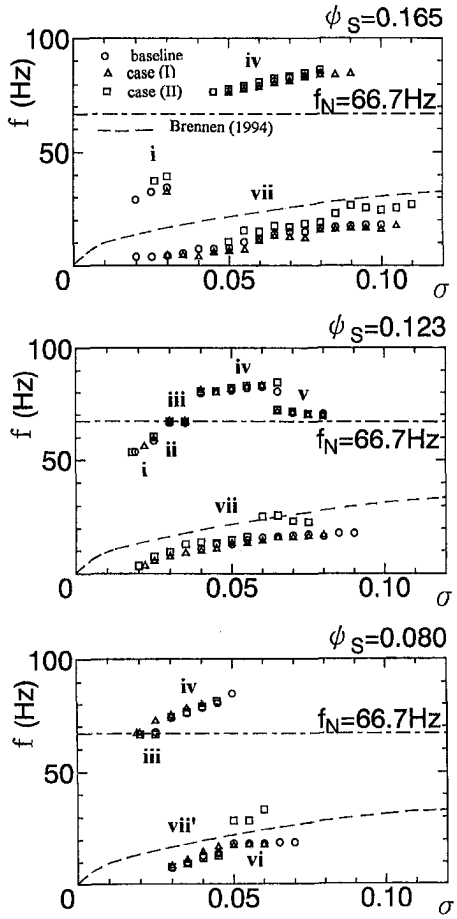

Fig. 12 Comparisons of the frequencies of oscillating cavitation showing the effects of the differences in piping system (uncertainty in $f \pm$ 1.5 Hz, in $\sigma \pm$ 0.002, in $\psi_s \pm$ 0.002)

Conclusion

Various kinds of oscillating cavitation have been observed and a map of their occurrence is given covering a wide range of cavitation numbers and static pressure coefficients. It includes cavitation in backflow vortices which rotates very slowly, rotating cavitation rotating slower than the impeller, attached uneven

cavitation, conventional rotating cavitation rotating faster than the impeller, blade cavitation affected by backflow vortices, large amplitude surge mode oscillations which might be induced by rotating cavitation and conventional cavitation surge. It was shown that the rotating cavitation types are not greatly affected by changes in the inlet and outlet pipes. One of the rotating cavitation types could be the "backward mode" predicted by a theoretical model of Tsujimoto et al. (1993).

Acknowledgments

The authors would like to express their sincere gratitude to Prof. K. Kamijo of Tohoku Univ. and Prof. Allan Acosta of Caltech., who led them to the present interesting problems. The authors would also like to thank Dr. K. Yamamoto and Dr. M. Aoki of Ebara Research Co. LTD for their continued support and interest. Mr. Ming-i Lee's support in conducting experiments is also acknowledged. Prof. Christopher Brennen of Caltech kindly went through the manuscript and made many valuable suggestions and discussions. His contribution are greatly acknowledged. This study is partly supported by the Ministry of Education through the Grant in Aids for Scientific Studies.

References

Acosta, A. J., 1958, "An Experimental Study of Cavitating Inducers," *Proceedings of the Second Symposium on Naval Hydrodynamics,* ONR/ACR-38, pp. 537–557.

Brennen, C. E., 1994, *Hydrodynamics of Pumps,* Concepts ETI and Oxford Science Publications.

Goirand, B., Mertz, A-L, Joussellin, F., and Rebattet, C., 1992, "Experimental Investigations of Radial Loads Induced by Partial Cavitation with a Liquid Hydrogen Inducer," IMechE, C453/056, pp. 263–269.

Greitzer, E. M., 1981, "The Stability of Pumping Systems—The 1980 Freeman Scholar Lecture", ASME JOURNAL OF FLUIDS ENGINEERING, Vol. 103, No. 2, pp. 193–242.

Jong, Jen-Yi, 1994, "Anomaly Identification for Space Shuttle Main Engine Diagnostics," 48th Meeting of the Mechanical Failure Prevention Group (MFPG), Apr.

Jong, Jen-Yi, et al., 1992, "Some Recent Developments in Turbomachinery Diagnostic Monitoring," Advanced Earth-To-Orbit Propulsion Technology Conference, NASA-MSFC, May.

Kamijo, K., Shimura, T., and Watanabe, M., 1977, "An Experimental Investigation of Cavitating Inducer Instability," ASME paper 77-WA/FW-14.

Kamijo, K., Shimura, T., Watanabe, M., and Fujita, T., 1980, "A Visual Observation of Cavitating Inducer Instability", NAL TR-598T.

Kamijo, K., Yoshida, M. and Tsujimoto, Y., 1993, "Hydraulic and Mechanical Performance of LE-7 LOX Pump Inducer," AIAA *Journal of Propulsion and Power,* Vol. 9, No. 6, pp. 819–826.

Rosenmann, W., 1965, "Experimental Investigation of Hydrodynamically Induced Shaft Forces with a Three Bladed Inducer," *Proceedings of the Symposium on Cavitation in Fluid Machinery,* ASME Winter Annual Meeting, pp. 172–195.

Tsujimoto, Y., Kamijo, K., and Yoshida, Y., 1993, "A Theoretical Analysis of Rotating Cavitation in Inducers," ASME JOURNAL OF FLUIDS ENGINEERING, Vol. 115, No. 1, pp. 135–141.

Tsujimoto, Y., Watanabe, S., Kamijo, K., and Yoshida, Y., 1996, "A Nonlinear Calculation of Rotating Cavitation in Inducers," ASME JOURNAL OF FLUIDS ENGINEERING, Vol. 118, No. 3, pp. 589–594.

Yamamoto, K., 1980, "An Experimental Study on Instability in a Cavitating Centrifugal Pump with a Volute Suction Nozzle," *Proceedings of the 10th IAHR Symposium, Tokyo,* pp. 303–312.

Young, W. E., 1972, "Study of Cavitating Inducer Instabilities, Final Report," NASA CR-123939.

Diffusion Induced Bubble Populations Downstream of a Partial Cavity

Po-Wen Yu
Graduate Student.[1]

Steven L. Ceccio
Associate Professor.

Mechanical Engineering
and Applied Mechanics,
University of Michigan,
Ann Arbor, MI 48109-2121

Bubble populations downstream of stable partial cavities were examined using in-line holography, and the bubble number distribution and void fraction of the bubbly clouds were determined. The measured flux of bubbles downstream of the cavity was used to determine the diffusion rate of noncondensable gas into the cavity. Four models of gas diffusion into partial cavities from Parkin and Kermeen (1963), Brennen (1969), and Parkin and Ravindra (1993) are reviewed, and their predictions are compared with the experimentally determined mass diffusion rates. The models, which recognize a turbulent boundary layer over the cavity interface, over-predict the diffusion rate by one order of magnitude for cavities characterized by $L/\delta > 25$.

Introduction

Small bubbles on noncondensable gas are generated downstream of a partial cavity, and this gas originally enters that cavity through diffusion. Thus, a partial cavity represents a source of small bubbles in the flow. Researchers have examined the process of cavity gas diffusion both analytically and experimentally. Parkin and Kermeen (1963) solved the diffusion equation for gas flow into a clear cavity employing the assumption of potential flow, and Gadd and Grant (1965) experimentally examined the partial pressure of noncondensable gas with natural and ventilated cavities behind disks. Brennen (1969) extended the work of Gadd and Grant with measurements of gas entrainment rates and cavity pressures of ventilated and natural cavities behind a sphere, and a model of gas diffusion was formulated which incorporated the presence of a turbulent boundary layer over the cavity interface. Billet and Weir (1975) correlated the rate of air diffusion across the cavity of both ventilated and naturally occurring cavities on a series of ogives, and Parkin and Ravindra (1991) employed these results to extend the model of Parkin and Kermeen (1963) to include the effects of turbulent mixing at the cavity interface. Maeda et al. (1991) experimentally examined the structure and void fraction of cavitation clouds through the use of off-axis holography.

In the present study, the bubble populations downstream of partial cavities are measured, and the gas diffusion rate into the partial cavity is inferred from the bubble measurements. The influence of varying dissolved gas content on the bubble population is examined, and the experimentally determined gas diffusion rates are compared with analytical predictions.

Experimental Setup

The experiments were conducted in the Blow Down Water Tunnel (BDWT) of the Cavitation and Multiphase Flow Laboratory at the University of Michigan. A description of the BDWT is provided by Tassin et al. (1995) and Yu (1995). The test section of the BDWT is 7.62 cm by 7.62 cm square and is 26.0 cm long. The air content of the water in the BDWT can be controlled through deaeration, and the free gas within the water of the BDWT can be removed by allowing the tunnel water to rest prior to a blow down. Partial cavitation was produced on either of two wedges which were fixed to a window of the BDWT test section. The two wedges had angles of 14 and 26.6 degrees leading into a step of height 1.9 cm, and these wedges will be referred to as the "blunt wedge" (26.6 degrees) and the "narrow wedge" (14 degrees). Pressure taps were located at the test section entrance and 15.6 cm downstream of the wedge termination. The surface leading up to the wedge was roughened to stimulate the boundary layer to turbulence. An optically flat window was flush mounted to the wall downstream of the wedge, and the window across from the wedge was fitted with an optical flat to permit passage of the light across the test section. A photograph of the test section setup is shown in Fig. 1.

The bubble populations downstream of the cavity were determined using in-line Fraunhofer holography, and a detailed description of this technique can be found in Vikram (1992). A Spectra Physics GCR130 Nd-YAG laser with an etalon was used to produce coherent light, and images were recorded on photographic glass plates after the collimated light beam was spatially filtered and passed through the sampling volume. The holograms were reconstructed using the spatially filtered light of a Spectra Physics HeNe laser (model 124B). The interrogation beam was passed through the hologram, and the reconstructed image was captured with a Pulnix TM-7AS CCD camera. Manual traverses were used to interrogate a volume of liquid, and the reconstructed image were analyzed manually. The smallest particle resolvable with this setup was 5 μm in diameter. By allowing the water to sit still in the BDWT before a run, freestream nuclei would rise to the free surface of water storage tank. The absence of freestream nuclei with diameter greater than 5 μm in diameter was confirmed with holograms taken across the empty test section.

The freestream velocity and liquid velocity near and behind the partial cavity was determined with planar Particle Imaging Velocimetry (PIV). PIV was also used to determine the thickness and turbulent intensity of the boundary layer just upstream of the cavity separation point. Details of the PIV optical setup and data conditioning are provided in Tassin et al. (1995) and Yu (1995). The freestream velocity was held constant at approximately 8.4 m/s during the tests, and the freestream pressure was varied to maintain similar cavity lengths for all tests. The dissolved air content of the water was varied, and the dissolved oxygen content was measured using a dissolved oxygen meter (Cole Parmer 7946-55). Water samples were taken from the test section and measured at atmospheric pressure. The water temperature was nominally constant at 23°C.

[1] Currently Project Engineer at Optimal CAE Inc.

Contributed by the Fluids Engineering Division for publication in the JOURNAL OF FLUIDS ENGINEERING. Manuscript received by the Fluids Engineering Division September 1, 1996; revised manuscript received May 5, 1997. Associate Technical Editor: J. Katz.

Experimental Results

Cavity Appearance and Flow Field. Figure 2 shows images of two a cavities of similar length on the vertex of the blunt and narrow wedges. The cavity length is 1.2 ± 0.2 cm, and the freestream velocity is 8.4 ± 0.2 m/s. making the freestream Reynolds number, $\mathrm{Re}_c = U_o L/\upsilon$, equal to 1.1×10^5 where U_o is the freestream velocity, L is the cavity length, and υ is the water kinematic viscosity at 23 C. The freestream cavitation number, $\sigma = P_o - P_v/\frac{1}{2}\rho U_o^2$, was 1.6 ± 0.1 for the blunt wedge and 1.5 ± 0.1 for the narrow wedge. Here, P_o is the freestream static pressure, P_v is the water vapor pressure, and ρ is the density of water at 23 C. Because the boundary layer was stimulated to turbulence before the point of cavity separation, the interface of the cavity appears roughened even near the point of cavity inception. The vortical structures in the closure region of the cavity on the blunt wedge are larger than those behind the cavity of the narrow wedge. While changes in air content did not change the visual appearance of the cavities, variation of the freestream dissolved oxygen concentration led to visible differences in the bubble populations downstream of the cavity.

The boundary layer of the flow upstream of the cavity separation point was investigated using PIV, and boundary layer profile and turbulent intensity were measured. For the blunt wedge, the boundary layer thickness, δ, was 800 ± 50 μm, and the average turbulent intensity in the flow and transverse directions were $\sqrt{\overline{u'^2}}/U_c$ = 9.1 percent and $\sqrt{\overline{v'^2}}/U_c$ = 7.7 percent. For the narrow wedge, the boundary layer thickness, δ, was 600 ± 50 μm, and the average turbulent intensity in the flow and transverse directions were $\sqrt{\overline{u'^2}}/U_c$ = 7.9 percent and $\sqrt{\overline{v'^2}}/U_c$ = 5.2 percent. These averages were taken over 1 cm of the boundary layer in the streamwise direction 2 cm upstream of the wedge origin on the test section wall, and the turbulent fluctuations were averaged over the boundary layer thickness. The average velocity downstream of the cavity in the region of the bubble cloud was determined using PIV in order to determine the flux of gas and vapor near the cavity closure region.

Bubble Populations Downstream of the Cavity Closure. A hologram taken across the test section produced a record of the bubbles and particles in a volume of liquid behind the cavity.

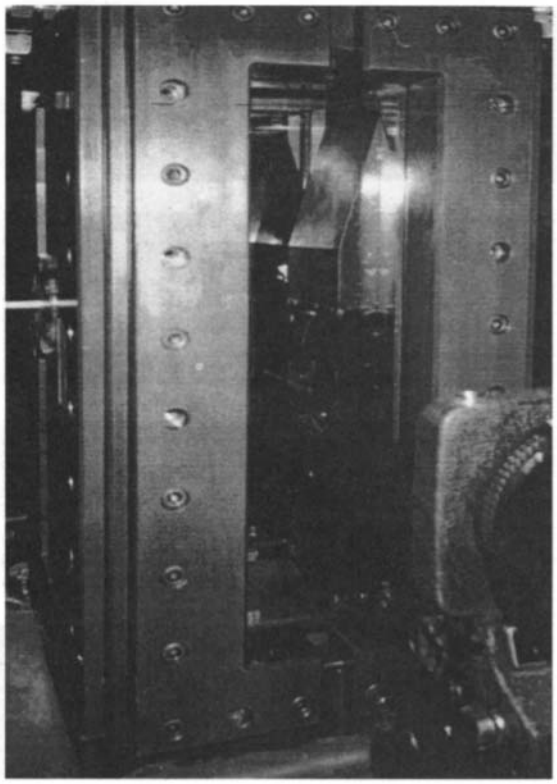

Fig. 1 A wedge mounted in the BDWT

The hologram revealed that almost no freestream nuclei were present in the flow, and the only bubbles observed were in the wake of the partial cavity. Holograms were analyzed for five flow conditions. The Reynolds number was fixed and the freestream pressure was varied to maintain a cavity length of approximately 1.2 cm. Two different oxygen contents were examined for the blunt wedge and three for the narrow wedge. A rectangular volume of the test section liquid was interrogated

Nomenclature

c_s = dissolved gas concentration near the cavity interface
c_o = freestream dissolved gas concentration
D = molecular diffusion coefficient
D_t = turbulent diffusion coefficient
H = Henry's law constant
L = partial cavity length
l_m = mixing length
M_{NG} = gas mean in bubbly cloud
$\hat{M}$ = molecular weight
$\dot{m}_B$ = gas mass flow rate/width, Brennen's model
$\dot{m}_{SF}$ = gas mass flow rate/width, Slug Flow model
$\dot{m}_{PK}$ = gas mass flow rate/width, Parkin and Kermeen's model
$\dot{m}_{PR}$ = gas mass flow rate, Parkin and Ravindra's model
P_{NG} = partial pressure of the noncondensable gas in a bubble
P_o = freestream static pressure
P_s = static pressure at bubble interface
P_v = water vapor pressure
PPM = parts per million
$\mathrm{Re}_c = U_o L/\upsilon$ = Reynolds number
$\mathrm{Sc} = \upsilon/D$ = Schmidt number
$\mathrm{Sc}_t = \upsilon_t/D_t$ = turbulent Schmidt number
R_B = bubble radius
R_{NG} = ideal gas constant
T = gas and liquid temperature
t_D = gas diffusion time scale
$U_c = U_o\sqrt{1+\sigma}$ = liquid velocity near the cavity interface
U_o = freestream velocity
$\sqrt{\overline{u'^2}}/U_c$ = average streamwise velocity fluctuations in the boundary layer upstream of the cavity
$\sqrt{\overline{v'^2}}/U_c$ = average transverse velocity fluctuations in the boundary layer upstream of the cavity
V_B = bubble volume
y = mole fraction of gas in air
γ = surface tension
δ = boundary layer thickness
$\Delta c = c_o - c_s$ = concentration differences
θ = momentum thickness
κ_1 = constant (Brennen's model)
κ_2 = constant (Parkin and Ravindra's model)
υ = liquid kinematic viscosity
υ_t = eddy viscosity of turbulent boundary layer
ρ = liquid density
ρ_{NG} = gas density
$\sigma = P_o - P_v/\frac{1}{2}\rho U_o^2$ = cavitation number

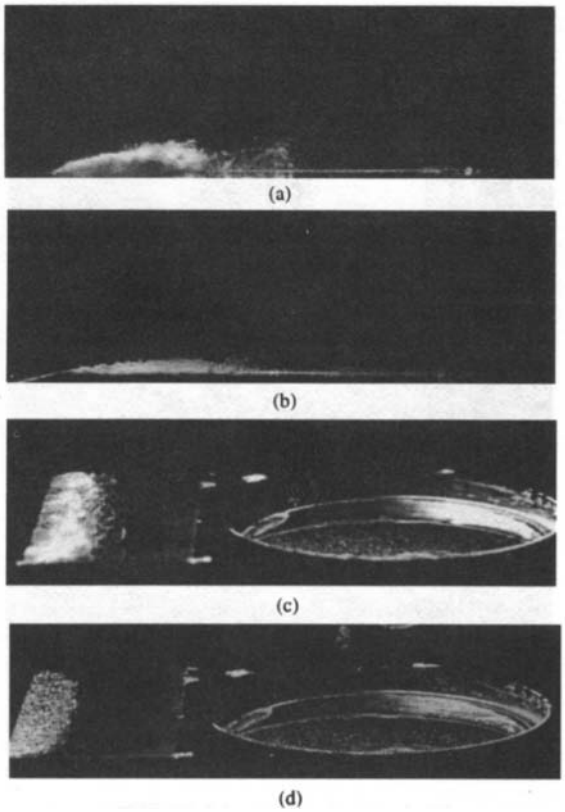

Fig. 2 Side and oblique views of cavities on the blunt wedge (*a*, *c*) and the narrow edge (*b*, *d*). The L = 1.2 cm, U_o = 8.4 m/s, and σ = 1.6 ± 0.1 for the blunt wedge and 1.5 ± 0.1 for the narrow wedge. Flow is from left to right.

which spanned the test section with a cross sectional area of 2.000 ± 0.005 cm^2 making a total volume of 15.24 ± 0.05 cm^3. The leading edge of the measurement volume was 7.0 ± 0.1 cm downstream from the trailing edge of the cavity.

Figure 3 shows a typical spatial distribution of bubbles found in the reconstructed liquid volume, and the bubble location is measured from the downstream surface of the wedge. The cavity maximum thickness was 1.3 ± 0.2 mm, and most of the bubbles are located within 1 cm of the surface. Hence, a rectangular measurement volume which is 1 cm from the surface with base area 2 cm^2 will be defined as the sample volume for bubble size distribution and mixture void fraction. Figure 4 shows the measured bubble distributions behind the partial cavity, and a summary of the data and experimental conditions is presented in Table 1. Also shown in the figure is the bubble distribution reported by Maeda et al. (1991) for the bubbles distribution within a cavitation cloud near the trailing edge of a partial cavity on a hydrofoil. The measured bubble distributions are distinguished by the dissolved oxygen content of the flow. As the dissolved oxygen content is increased, the number and average size of the bubble population increases. The data reported by Maeda et al. (1991) is quite similar to the low oxygen content data of the present study, and those authors reported that the dissolved air content was between 10 to 15 percent of saturation.

Determination of Cavity Gas Flux From the Measured Bubble Populations

Noncondensable gas enters the cavity as a result of gas diffusion across the cavity interface. This gas, together with the cavity water vapor, is entrained by the vortical structures forming in the cavity closure. These cavitating vortices will collapse

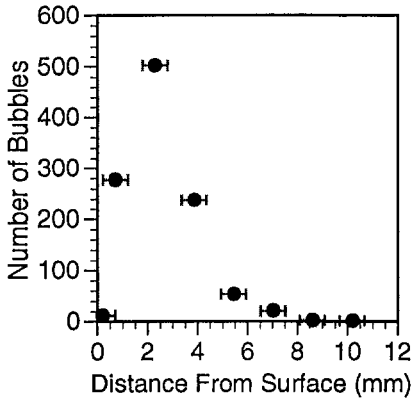

Fig. 3 Spatial distribution of bubbles downstream of a partial cavity. Measurement volume is 2 cm^3.

as they convect downstream, and after condensation of the liquid vapor, only small bubbles on non-condensable gas will remain. Thus, the bubbly flow downstream of the cavity represents a flux of noncondensable gas away from the cavity, and under steady conditions, this will be equal to the flux of gas into the cavity.

First, it will be shown that the bubbles downstream of the cavity are in static equilibrium with the surrounding flow. The static pressure of the flow 3.8 cm downstream of the cloud was measured at a pressure tap in the wall, and we will assume that the pressure drop between the measurement location and bubble cloud is negligible. (Assuming a friction factor of 0.015, the pressure drop would be approximately 0.5 kPa for the flow conditions present, and the measured pressures were approximately 55 kPa.) The Rayleigh collapse time of a 1 mm diameter spherical vapor bubble subject to a pressure difference of 50 kPa (Plesset and Prosperetti, 1977) will collapse in about 60 μs,. Thus the bubbles can collapse and reach an equilibrium diameter during the 5 ms it takes for them to convect to the measurement volume. It will be assumed that the bubbles are moving at the velocity of the surrounding liquid flow.

Next, the mass flux of noncondensable gas is determined. The total of the noncondensable gas present in the bubbly cloud, M_{NG}, can then be calculated as

$$M_{NG} = \sum V_B P_{NG} / R_{NG} T$$

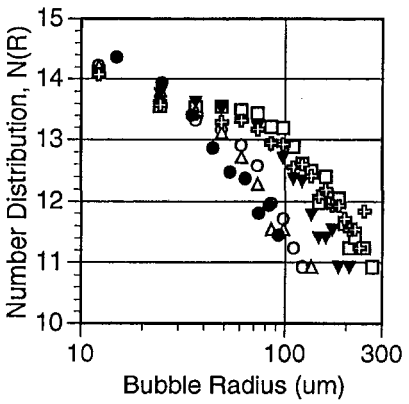

Fig. 4 Bubble number distribution measured downstream of five partial cavities. Dimension of $N(R)$ is m^4. ○ and □ denote the blunt wedge with dissolved oxygen concentration of 27 and 47 percent, respectively. △, ▼, and ✣ denote the narrow wedge with dissolved oxygen concentration of 27, 42, and 72 percent, respectively. Also plotted are data from Maeda et al. (1991) denoted by ●.

where V_B is the bubble volume, P_{NG} is the partial pressure of the noncondensable gas, R_{NG} is the ideal gas constant for the noncondensable gas, and T is the gas temperature (which is taken to be equal to the liquid temperature). The partial pressure of the noncondensable gas is given by

$$P_{NG} = P_s - P_v + 2\gamma/R_B$$

where P_s is the liquid static pressure, P_v is the water vapor pressure, R_B is the bubble radius, and γ is the surface tension. Before the total mass of gas can be calculated, however, the composition of the noncondensable gas must be determined. Because the diffusivities of oxygen in water is greater than that of nitrogen, the relative mole fraction of oxygen and nitrogen in the water will be different from that in air. Thus, the content of the noncondensable gas which will diffuse into the cavity (and end up in the bubbles) will have proportionally more oxygen than that of air. However, it will be assumed here that the noncondensable gas within the bubble can be treated as air, recognizing that the molecular weight ratio of nitrogen to oxygen is near unity (e.g., 88 percent). Thus, the total mass of air within the bubbly cloud and the noncondensable gas flux behind the partial cavity can be determined.

Finally, the gas flux carried by the bubbles will be equivalent to the flux into the cavity if negligible gas is lost when the cavitating vortices collapse near the trailing edge of the cavity. The time scale for dissolution of small gas bubbles, t_D, is approximated by

$$t_D \approx \frac{\rho_{NG} R_B^2}{2D(c_s - c_o)}$$

where R_B is the bubble radius, ρ_{NG} is the density of the gas, D is the molecular diffusion coefficient, and $(c_s - c_o)$ is the difference in gas concentration of liquid at the bubble interface and far from the bubble (Plesset and Prosperetti, 1977). For the bubbles in the closure region t_D is on the order of seconds indicating that the bubbles will not lose a significant amount of gas traveling between the closure region and the measurement region over a period of a few milliseconds. Gas may also be lost when the cavitating vortices collapse and rebound, but this process takes place in microseconds and would result in little diffusion. In the absence of significant rediffusion, the flux of noncondensable gas into the cavity can be inferred from the flux of bubbles downstream of the cavity.

Comparison of Measured Gas Flux With Models of Gas Diffusion

Models of gas diffusion into partial cavities have been proposed by Parkin and Kermeen (1963), Brennen (1969), and Parkin and Ravindra (1991). Figure 5 shows a simplified two dimensional description of the flow where $U_c = U_o\sqrt{1 + \sigma}$ is the liquid velocity near the cavity interface, and L is the cavity length. The momentum boundary layer at the cavity interface has a thickness of δ, and a momentum thickness of θ. The

Table 1 Summary of results for five holographically measured bubble populations for a 2 cm³ sample volume downstream of the cavity closure. Oxygen contents are percent saturation at atmospheric pressure and are accurate to within 10 percent.

	Blunt wedge		Narrow wedge		
Freestream O_2 (%)	27	47	27	42	70
# Bubbles (>5 μm dia)	3048	4105	3218	3168	3709
Void Fraction ($\times 10^5$)	2.6	33.8	2.1	12.7	26.9

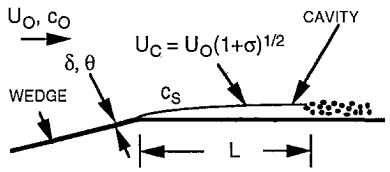

Fig. 5 A schematic drawing of the partial cavity

dissolved gas concentration at the cavity interface is c_s, the freestream concentration is c_o, and $\Delta c = c_o - c_s$.

Parkin and Kermeen (1963) formulated a model based on potential flow outside the cavity and molecular diffusion of gas into the cavity. The mass flow rate of gas per unit cavity width, $\dot{m}_{PK}$, is given by

$$\dot{m}_{PK} = 4\Delta c\sqrt{\frac{DU_o(1 + \sigma)L}{\pi}}$$

where D is the molecular mass diffusion coefficient. This model corresponds to flows with Schmidt number, $Sc = \upsilon/D$, of zero.

Brennen (1969) proposed a model which incorporates the presence of a turbulent boundary layer over the cavity interface. Brennen assumed that the diffusion boundary layer profile is geometrically similar to that of the momentum boundary layer, which corresponds to a turbulent Schmidt number, $Sc_t = \upsilon_t/D_t$, of unity. υ_t and D_t are turbulent momentum and mass diffusivities. The mass flow rate of gas per unit cavity width, $\dot{m}_B$, is given by

$$\dot{m}_B = \kappa_1 \Delta c\, U_o\sqrt{(1 + \sigma)}\sqrt{\theta L}$$

where θ is the momentum thickness of the boundary layer just upstream of the cavity, and κ_1 is a constant which is related to the shape of the diffusion boundary layer profile over the cavity. A value of $\kappa_1 = 0.45$ will be used here, after Brennen (1969).

Parkin and Ravindra (1991) proposed a simplified version of Brennen's model named the "Slug Flow" model. Here, a uniform boundary layer of thickness δ is assumed, and all of the non-condensable gas within the boundary layer fluid is assumed to diffuse into the cavity ($Sc_t \ll 1$). The mass flow rate of gas per unit cavity width, $\dot{m}_{SF}$, is given by

$$\dot{m}_{SF} = \Delta c\, \delta U_o\sqrt{(1 + \sigma)}$$

Note that the mass flow rate is not a function of the cavity length, L.

Parkin and Ravindra (1991) modified the model of Parkin and Kermeen (1963). The molecular mass diffusivity is replaced with a turbulent mass diffusivity, the turbulent Schmidt number is assumed to be unity ($Sc_t \approx 1$), and a mixing length model is used to approximate the turbulent mass diffusivity. The mass flow rate of gas per unit cavity width, $\dot{m}_{PR}$, is given by

$$\dot{m}_{PR} = 4\Delta c\sqrt{\frac{D_t U_o(1 + \sigma)L}{\pi}}$$

Parkin and Ravindra (1991) employed a Launder-Spalding mixing length model to approximate the turbulent mass diffusivity where

$$\upsilon_t \approx D_t \approx l_m\sqrt{\overline{v'^2}} \quad \text{with} \quad l_m \approx 0.07\delta \quad \text{and} \quad \sqrt{\overline{v^2}} \approx 0.09U_o$$

which yields $D_t \approx 0.0063\delta U_o$. The mass flow rate per unit cavity width becomes

$$\dot{m}_{PR} = \kappa_2 \Delta c\, U_o\sqrt{(1 + \sigma)}\sqrt{\delta L}$$

where $\kappa_2 = 0.18$. Since the momentum thickness is approximately $\frac{1}{10}$ of the boundary layer thickness for developed turbu-

Table 2 Measured and predicted rates of gas diffusion into the partial cavity for the five cases presented in Table 1. Percentage in each entry is the ratio of predicted to measured diffusion rates.

Measured (g/s) ($\times 10^3$)	0.101 ± 0.007	1.238 ± 0.061	0.071 ± 0.005	0.398 ± 0.021	0.611 ± 0.031
Parkin and Kermeen (g/s) ($\times 10^3$)	0.028 ± 0.004	0.047 ± 0.006	0.027 ± 0.004	0.042 ± 0.006	0.064 ± 0.009
	27%	4%	37%	11%	10%
Brennen (g/s) ($\times 10^3$)	2.93 ± 0.40	4.96 ± 0.68	2.45 ± 0.34	3.87 ± 0.54	5.85 ± 0.82
	2892%	400%	3471%	972%	956%
Parkin and Ravindra (g/s) ($\times 10^3$)	3.59 ± 0.49	6.08 ± 0.84	3.01 ± 0.42	4.74 ± 0.66	7.17 ± 1.01
	3545%	491%	4255%	1192%	1171%
Slug flow (g/s) ($\times 10^3$)	5.31 ± 0.65	9.00 ± 1.10	3.86 ± 0.52	6.08 ± 0.81	9.19 ± 1.23
	5248%	727%	5456%	1528%	1502%

lent boundary layers, this formulation for the mass flow rate is nearly equivalent to that of Brennen.

Table 2 presents the predicted and measured rates of gas diffusion for the five test conditions shown in Table 1. The measured turbulent boundary layer thickness and cavity characteristics were used to calculate the predicted mass flow rates, and one tenth of the measured boundary layer thickness was used to approximate the momentum thickness. The measured turbulent intensities on the boundary layer upstream of the cavity confirm that it is a developed turbulent boundary layer. The freestream dissolved air content is calculated from the measurement of dissolved oxygen content after assuming that the molar ratio of dissolved oxygen to nitrogen is equal to the ratio at saturation (in parts per million):

$$\frac{\mathrm{PPM}_{N_2}}{\mathrm{PPM}_{O_2}} \approx \frac{\hat{M}_{N_2}}{\hat{M}_{O_2}} \frac{y_{N_2}}{y_{O_2}} \frac{H_{O_2}}{H_{N_2}} \approx 1.80 \pm 0.05$$

where $\hat{M}$ is the molecular weight, y is the mole fraction in air, and H is Henry's law constant for aqueous solutions of oxygen and nitrogen (the uncertainty is due to variation in water temperature). The dissolved gas concentration at the cavity interface is estimated using the experimental results of Brennen (1969) relating the equilibrium partial pressure of the non-condensable cavity contents with the freestream dissolved air content:

$$P_{NG} \approx (0.030 \pm 0.003) \cdot c_o,$$

where the pressure is in kPa and the freestream gas concentration is in part per million. The low partial pressure of noncondensable air in the cavity implies that $\Delta c \approx c_o$ within the uncertainty of c_o.

Discussion and Conclusion

The model of Parkin and Kermeen under-predicts the gas diffusion by about one order of magnitude as this model relies entirely on molecular diffusion. The models which recognize the turbulent boundary layer over the cavity interface (Brennen, Parkin and Ravindra) over predict the gas diffusion rate by an order of magnitude, as does the Slug Flow model.

These results can be compared with the experimental results of Brennen (1969) who examined the gas pressure within natural cavities behind a spherical headform. Brennen inferred the mass flux of gas out of natural cavities based on measurements of the gas entrainment rate in the closure region of geometrically similar ventilated cavities, and his model was shown to over-predict the noncondensable gas flow rate by a factor of approximately 2.5. Billet and Wier (1975) examined the influence of gas diffusion in and out of ventilated cavities. The ventilation rate into geometrically similar cavities was examined when gas diffusion was present and absent, and Brennen's model was shown to adequately predicted the deviation in the cavity ventilation rate due to gas diffusion.

In the four models of gas diffusion employed here, the mass flow rate of dissolved gas is related to the product of three parameters: Δc, $U_o\sqrt{(1+\sigma)}$, and a length scale which is related to the thickness of the diffusion boundary layer over the cavity interface $\sqrt{\theta L}$ (Brennen), $\sqrt{\delta L}$ (Parkin and Ravindra), δ (Slug Flow), or $\sqrt{LD/U_o}$ (Parkin and Kermeen). It is interesting to note that Brennen's model, the model of Parkin and Ravindra, and the Slug Flow model all yield similar results, even though the Slug Flow model does not include the cavity length. Brennen's model and Parkin and Ravindra's model assume a dynamic diffusion boundary layer over the entire cavity interface. In the Slug Flow model, however, all the dissolved gas within the momentum boundary layer is assumed to enter the cavity, at which point the diffusion into the cavity would cease. Thus, an increase in the cavity length will not increase the overall rate of gas diffusion. (In reality, gas diffusion into the cavity would never stop but would continue slowly via molecular diffusion.) If the cavity length is shorter than this "saturation length," diffusion will not be complete, and the Slug Flow model will over-predict the gas diffusion rate. Table 2 indicates that the Slug flow model yields the greatest overprediction of the mass diffusion.

Over-prediction of the gas diffusion rate suggests that the full potential for gas diffusion may not have been not realized, and an increase in cavity length would result in more gas diffusion. The cavities examined in this study were characterized by the parameter $L/\delta \approx 25$, and this resulted in similar predictions from the three turbulent diffusion boundary layer models, thus cavities with $L/\delta > 25$ should be examined to determined if saturation condition can be identified. In addition, the momentum boundary layer based models will over-predict the gas diffusion rate if the diffusion and momentum boundary layers are not truly similar and if the turbulent mixing near the cavity interface is not as strong as assumed. Another important consideration is the true surface area of the cavity. The cavity interface is rough and unsteady, unlike the smooth interface suggested by the models, and the true area will be greater than that employed by the models. With an increase in surface area of less than one order of magnitude, the prediction of the molecular diffusion model of Parkin and Kermeen would approach the measured values, and the predictions of the turbulent diffusion models would tend further to over predict the rates of gas diffusion. Lastly, it is important to recall that the measured bubble populations are a single "snap shot" of the void fraction behind the cavity, and that the natural time variation in the average void fraction is not captured by single holograms. However, the trends are consistent between all five data sets.

Acknowledgments

The authors would like to thank Todd Armstrong, Dan Johnston, Dan Wasserman, and Shimul Bhuva for their considerable effort expended in reconstructing the holograms of the bubble clouds. This work was supported by the Office of Naval Research under contract N00014-93-1-0029, Dr. E. P. Rood, technical monitor.

References

Billet, M. L. and D. S. Weir, 1975, "The Effect of Gas Diffusion on the Flow Coefficient for a Ventilated Cavity," ASME JOURNAL OF FLUIDS ENGINEERING, Vol. 97, pp. 501–506.

Brennen, C. E., 1969, "The Dynamic Balance of Dissolved Air and Heat in Natural Cavity Flow," *Journal of Fluid Mechanics,* Vol. 37, pp. 115–127.

Gadd, G. E. and Grant, S., 1965, "Some Experiments on Cavities Behind Disks," *Journal of Fluid Mechanics,* Vol. 23, p. 4.

Maeda, M., H. Yamaguchi, and H. Kato, 1991, "Laser Holography Measurement of Bubble Population in Cavitation Cloud on a Foil Section," *Proceedings of the ASME Cavitation '91 Symposium,* Vol. 116, pp. 67–75.

Parkin, B. W., and R. W. Kermeen, 1963, "The Roles of Convective Air Diffusion and Liquid Tensile Stresses During Cavitation Inception," *Proceedings I.A.H.R. Symposium on Cavitation and Hydraulic Machinery,* Sendai, Japan, pp. 21–24.

Parkin, B. W., and K. Ravindra, 1991, "Convective Gas Diffusion in Steady Cavity Flows," ASME JOURNAL OF FLUIDS ENGINEERING, Vol. 113, pp. 285–289.

Plesset, M. S., and A. Prosperetti, 1977, "Bubble Dynamics and Cavitation," *Annual Rev.iew of Fluid Mechanics,* Vol. 9, pp. 145–185.

Tassin, A. L., C.-Y. Li, S. L. Ceccio, and L. P. Bernal, 1995, "Velocity Field Measurements of Cavitating Flows," *Experiments in Fluids,* Vol. 20, pp. 125–130.

Vikram, C. S., 1992, *Particle Field Holography,* Cambridge University Press.

Yu, P.-W., 1995, "Experimental and Numerical Examination of Cavitating Flows," Doctoral thesis, University of Michigan.

Y. Kawanami
Graduate Student.

H. Kato
Professor.

H. Yamaguchi
Associate Professor.

M. Tanimura
Graduate Student.

Y. Tagaya
Graduate Student.

Department of Naval Architecture
and Ocean Engineering,
Graduate School of Engineering,
The University of Tokyo,
7-3-1 Hongo, Bunkyo, Tokyo, 113 Japan

Mechanism and Control of Cloud Cavitation

Generation mechanism of cloud cavitation on a hydrofoil section was investigated in a sequence of experiments through observation of cloud cavitation by high-speed video and high-speed photo as well as pressure measurements by pressure pick-ups and a hydrophone. The mechanism was also investigated by controlling cloud cavitation with an obstacle fitted on the foil surface. From the results of these experiments, it was found that the collapse of a sheet cavity is triggered by a re-entrant jet rushing from the trailing edge to the leading edge of the sheet cavity, and consequently, the sheet cavity is shed in the vicinity of its leading edge and thrown downstream as a cluster of bubbles called cloud cavity. In other words, the re-entrant jet gives rise to cloud cavitation. Moreover, cloud cavitation could be controlled effectively by a small obstacle placed on the foil. It resulted in reduction of foil drag and cavitation noise.

1 Introduction

Of the various cavitation phenomena on a hydrofoil section, cloud cavitation is distinctly periodic and accompanying strong vibration, noise and erosion. These effects are not desirable in fluid machinery, such as ship propellers or pumps. Therefore, various investigations have been done in order to develop foil sections to prevent cloud cavitation. On the other hand, some researches have been carried out to investigate the generation mechanism of cloud cavitation. The shedding of cloud cavitation is a periodic phenomenon. Shedding frequency of cloud cavities is several tens of Hertz in usual conditions. Moreover, the flow field contains a sheet type cavity and a cluster of cavitation bubbles which interact with each other in a complicated manner. These features of cloud cavitation make it difficult to investigate the mechanism experimentally and theoretically. As a result, at the present situation only some hypotheses have been proposed in order to explain the generation mechanism of cloud cavitation without any consensus.

Furness and Hutton (1975) mentioned that a re-entrant jet is the principal mechanism of cloud cavitation. Based on detailed observations and pressure measurements, Shen and Peterson (1978) concluded that the cavity instability resulting in cloud cavitation is principally dependent on the conditions of the free shear flow. Lush and Skipp (1986) also considered a re-entrant jet to be the cause of cloud cavitation on a wedge. Avellan et al. (1988) proposed that transition of boundary layer and growth of instability on cavity surface generate cloud cavitation. Kubota et al. (1992) considered that a shear layer separated at the cavity leading edge causes a jet into the cavity surface and then a cloud cavity is generated. Le et al. (1993) described that the re-entrant jet under a thick cavity is the cause of periodic shedding. Lange et al. (1994) have also proposed that a re-entrant jet is responsible for the cloud generation. Larrarte et al. (1995) demonstrated that a re-entrant jet is indeed responsible of the cavity instability.

Considering the present controversies, the authors have carried out a series of detailed experiments in order to make a thorough investigation of cloud cavitation. In addition, based on the knowledge acquired on this mechanism, experiments have been done in order to control cloud cavitation. This paper is a brief report presenting some of the major findings.

2 Experimental Apparatus and Conditions

Experiments were done in two cavitation tunnels, namely, the Marine Propeller Cavitation Tunnel and the TE Type Cavitation Tunnel at the University of Tokyo. The test sections of these tunnels have rectangular cross sections of 600 × 150 mm with 1000 mm in length and 120 × 50 mm with 580 mm in length, respectively.

A two-dimensional hydrofoil called E.N.Foil (Elliptic Nose Foil), a symmetrical hydrofoil with thickness ratio of 8% was selected as the tested body. Two types of E.N.Foil were tested in these experiments. One of them had a 150 mm chord and was tested in the Propeller Tunnel, the other with a 100 mm chord was tested in the TE Tunnel. Thus, the aspect ratios were 1.0 and 0.5, respectively. It should be noted that the foil section tested in the TE Tunnel is made of acrylic resin enabling observation of the behavior of cloud cavitation on the foil surface from the pressure side. Figure 1 shows the shape of the E.N.Foil and the coordinate system of reference.

Experimental conditions are shown in Table 1. Even when the cavitation numbers were set at the same value in either tunnels, the appearance of cloud cavitation in one tunnel differed from that of the other mainly due to the differences in the width of the test sections. In these experiments, the behavior of cloud cavitation at $\sigma = 1.07$ in the Propeller Tunnel was similar to that at $\sigma = 1.72$ in the TE Tunnel. At these cavitation numbers, the maximum cavity length L_{cav} was about 75 mm (50% C) in the 150 mm wide test section of the Propeller Tunnel, while L_{cav} was about 25 mm (25% C) in the 50 mm wide test section of the TE Tunnel. These differences suggest that cloud cavitation has a certain three-dimensional structure dependent upon cavity size. Air content of the circulating water in both tunnels was retained at 20% which is less than that of saturated water at one atmospheric pressure.

Contributed by the Fluids Engineering Division for publication in the JOURNAL OF FLUIDS ENGINEERING. Manuscript received by the Fluids Engineering Division September 19, 1996; revised manuscript received May 6, 1997. Associate Technical Editor: J. Katz.

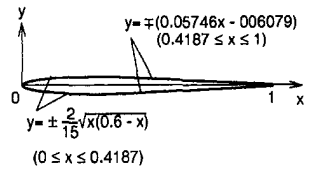

Fig. 1 E.N. Foil and coordinate system

In order to measure the low-frequency pressure fluctuations associated with cloud cavitation, pressure transducers were mounted on the foil surface and a hydrophone was placed in a small basin attached to the acrylic observation window of the test section. The pressure transducer is Kyowa-Dengyo type PS-2KA with a diameter of 6 mm and a capacity of 196.1 Pa. This pressure pick-up can respond linearly up to a frequency of 2.8 kHz in water. The hydrophone used in the experiments is Brüel and Kjer type 8103 with a frequency response 0.1 Hz – 140 kHz ± 2 dB. In order to measure flow velocity near the foil surface, a phase-difference hot wire velocimeter is mounted on the foil tested in Propeller Tunnel. The velocimeter is at 17% C and consists of two hot wires which are arranged perpendicular to the main flow direction at a distance of 1.53 mm (1% C) from each other. The two wires were separated from the foil surface by 1.0 mm whereas the thickness of the fully developed sheet cavity was about 7 mm. Making use of the time lag of the signals of these hot wires, not only the magnitude of velocity but also the direction could be measured.

3 Results and Discussions

3.1 Observation of Cloud Cavitation Figure 2 shows the appearance of cloud cavity in a sequence of sketches. These sketches are based on pictures taken by means of a high-speed camera at 5000 frames per second. In addition, a high-speed video system set at 4500 or 9000 frames per second was used in order to observe the behavior of cloud cavitation in more detail. The camera and the video systems could be synchronized with other measurements by trigger pulses. The shedding frequency of cloud cavity was about 20 Hz in Propeller Tunnel and about 55 Hz in TE Tunnel. The corresponding Strouhal number was 0.29 ± 0.02 in Propeller Tunnel and 0.27 ± 0.04 in TE Tunnel, based on the maximum length of sheet cavity and uniform flow velocity.

The upper sketches of Fig. 2 are for side-angular view, the middle ones for top view on the suction side of the foil section and the lower ones are as viewed from the pressure side. The upper and middle sketches are based on the pictures taken in the Propeller Tunnel, while the lower sketches are based on the pictures taken by the high-speed camera in the TE Tunnel. These pictures were synchronized with the pressure fluctuations on the suction surface of the foil sections. Shen and Peterson (1978) reported that the pressure fluctuations on a fixed-incidence partially cavitating hydrofoil was highly periodic. It is known that the behavior of cloud cavity and the pressure fluctuations on foil surfaces are strongly correlated (Kubota et al., 1989). High peaks periodically appear in pressure fluctuations (see Fig. 8). The pictures taken by the video and the camera systems corresponded well with one another from peak to peak

Table 1 Experimental conditions

	Propeller Tunnel	TE Tunnel
α	6.0 ± 0.2 deg.	
U_∞	5.0±0.1 m/sec (Re=7.2x10^5)	7.5±0.1 m/sec (Re=8.6x10^5)
σ	1.07±0.02	1.72±0.02

in one cycle of cloud cavitation. The sketches corresponding to the three views were drawn from pictures synchronized with one cycle of 2π radians divided into 16 stages. The three views are, however, independent of one another.

The sketches at $\Phi = (\frac{0}{8})\pi$ illustrate the situation immediately after the sheet cavity is cut off in the vicinity of its leading edge. Figure 3 shows a typical top view photograph taken at this instant. It is observed that the old sheet cavity has collapsed into small bubbles and rolled up as a cloud cavity while a new sheet cavity has already grown to nearly 5% C. Subsequently, the cloud cavity moves downstream with a rotating motion in the clockwise direction when the flow is from left to right of the observer. It is noticeable that the sheet cavity starts collapsing into bubbles near the side wall of the tunnel while the sheet cavity is in a growing state as a whole. However, large-scale collapse of the sheet cavity is not observed in these stages. After these stages, the cavity grows to its maximum at $\Phi = (\frac{10}{8})\pi$. At this phase, a re-entrant jet starts rushing towards the upstream direction from the termination line of the fully developed sheet cavity. During $\Phi = (\frac{11}{18})\pi - (\frac{13}{8})\pi$, the front line of the re-entrant jet continues moving from the trailing edge towards the leading edge of the sheet cavity (see the sketch of bottom view at $\Phi = (\frac{12}{8})\pi$ in Fig. 2). Figures 4(a) and (b) show photographs taken simultaneously from the top and the bottom in the TE Tunnel. The front line of the re-entrant jet can be seen clearly in the bottom view while it is not observed so distinctively in the top view. Therefore, the re-entrant jet is not on the cavity surface but on the foil surface. The re-entrant jet reaches the leading edge of the sheet cavity at $\Phi = (\frac{14}{8})\pi$. On the other hand, it can be seen in the sketches of the top view that, during the rushing phase of the re-entrant jet ($\Phi = (\frac{10}{8})\pi - (\frac{14}{8})\pi$), the sheet cavity starts collapsing into bubbles at both side corners downstream. This collapse propagates diagonally from both sides towards the middle of the sheet cavity with remarkable swelling of the cavity surface. This may be due to the condensation shock wave formed in the bubble cluster. The collapse at this stage propagates in a different manner compared with local collapses taking place near both the side walls during the growth of sheet cavity. At $\Phi = (\frac{14}{8})\pi$, frothy bubbles abruptly appear near the leading edge at the span-center, while the downstream end of the cavity still remains transparent (see the sketch of the top view). Figure 5 shows a photograph taken at this instant from the top in the Propeller Tunnel. These bubbles are due to the collision between the re-entrant jet and the cavity surface. During these processes, the swelling of the bubble clusters can also be observed in the sketches of the side view. The swelling propagates from the trailing edge toward

Nomenclature

C = chord length of the hydrofoil
C_D = drag coefficient ($=D/(0.5\rho U_\infty^2 C)$)
C_p = pressure coefficient ($=(p - p_\infty)/(0.5\rho U_\infty^2)$)
D = drag force exerted on the hydrofoil
L_{cav} = maximum streamwise length of sheet cavity
p = local pressure
p_∞ = reference static pressure in cavitation tunnel
U_∞ = uniform flow velocity
α = angle of incidence
ρ = mass density of water
σ = cavitation number ($= (p -$ (vapor pressure))$/(0.5\rho U_\infty^2)$)
Φ = phase in one cycle of cloud cavitation event

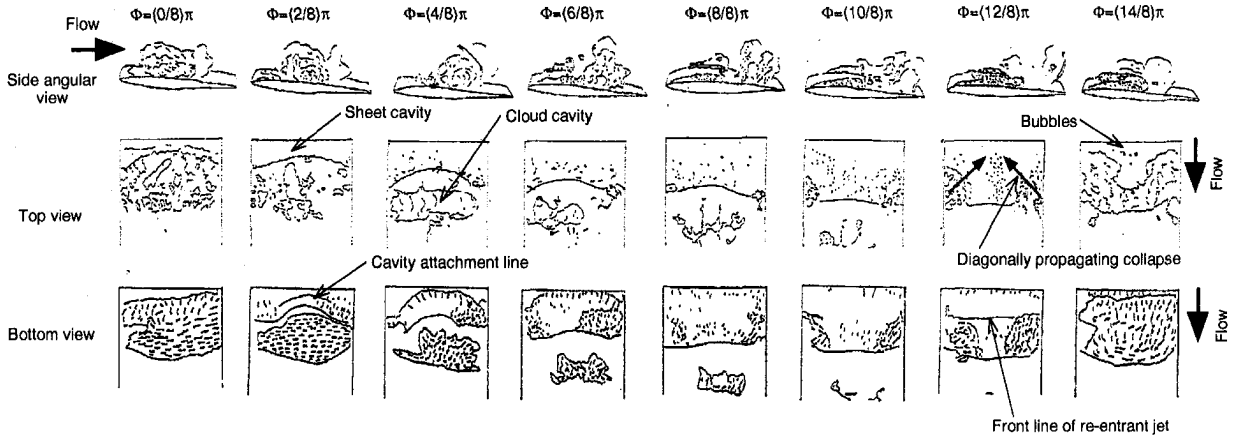

Fig. 2 Sketches of cloud cavitation in one cycle

the leading edge of the sheet cavity as if it were running after the re-entrant jet. Therefore, it can be reasonably said that the re-entrant jet has reached the leading edge of the sheet cavity a little earlier than the arrival of the condensation shock. From the analysis of the pictures taken by the high speed video and the high speed camera, the velocity of the re-entrant jet was estimated to be 2.5–5.0 m/s. In addition to this, direct measurements were made using a phase-difference hot wire velocimeter. Typical outputs from the hot wires are shown in Fig. 6 along with the pressure fluctuations at 10% C. The re-entrant jet is detected periodically before the peak of the pressure fluctuations (indicated by arrows). Lag times were measured for seventy-five cycles of cloud cavitation. The mean velocity of the re-entrant jet was found to be 2.1 ± 1.4 m/s. The present measurements are consistent with those of Le et al. (1993) who found the velocity of the re-entrant jet to be of the same order of magnitude as the main flow velocity. At the final stage ($\Phi = (\frac{15}{8})\pi$), the sheet cavity completely collapses into a cluster of bubbles and is shed in the vicinity of its leading edge followed by the behavior as shown in Fig. 3.

From these results, it is suspected that either the re-entrant jet or the condensation shock is responsible for the large-scale collapse of the sheet cavity or, in other words, for the generation of the cloud cavity. In order to obtain further information on the mechanism, experiments were conducted with dye injection from a hole placed slightly upstream of the termination of the fully developed sheet cavity (point A in Fig. 5). The dye trace was observed near the leading edge of the sheet cavity prone to collapse thoroughly. Such behavior of dye trace was also observed by Le et al. (1993). This suggests that the re-entrant jet reaches the leading edge of the sheet cavity and plays an important role in the generation of cloud cavitation. Moreover, when the re-entrant jet starts impulsively, the trailing edge of the sheet cavity remains transparent (Fig. 4). Thus, the jet is not a mixture of water and bubble, but pure water at the bottom of a pure vapor cavity. In the region occupied by the bubble cluster (labeled as B in Fig. 5), on the other hand, the speed of sound may be sufficiently small, introducing a condensation shock into the cavity. Such a shock in a bubbles-water mixture has been investigated in detail by Noordzij and Wijngaarden (1974). From cavitation erosion point of view, Mørch (1981) has deduced shock formation on the surface of a bubble cluster. Through a study on cavitating induces, Jakobsen (1964) has suggested that condensation shock plays an important role around the cavity termination. The condensation shock wave, however, has no ability to bring the dye from the termination of the fully developed sheet cavity to its leading edge. The condensation around the termination may be stimulated by the

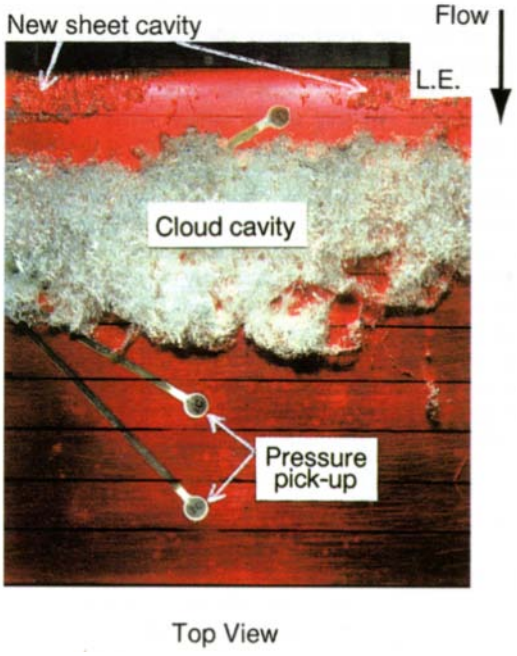

Fig. 3 Photograph of shed cloud cavity; σ = 1.07; $\Phi = (\frac{0}{8})\pi$; in the Propeller tunnel

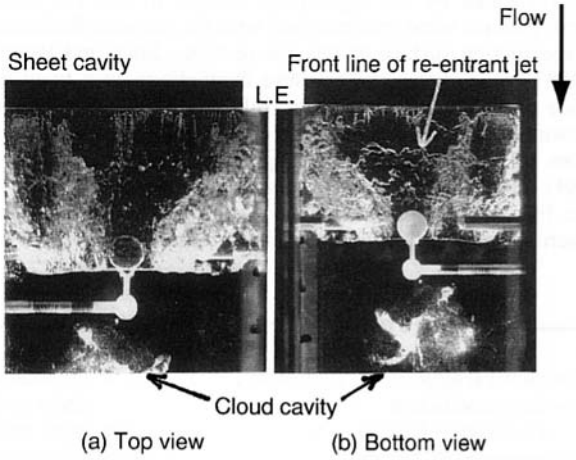

Fig. 4 Appearance of the re-entrant jet under the fully developed sheet cavity; σ = 1.72; $\Phi = (\frac{12}{8})\pi$; in the TE tunnel

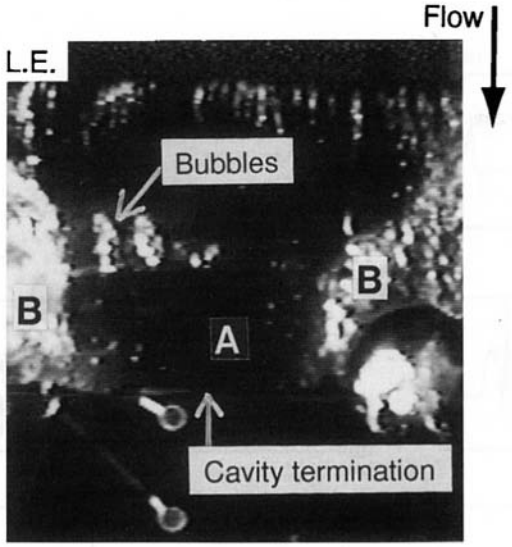

Fig. 5 Photograph of abruptly appearing bubbles on the sheet cavity surface; $\sigma = 1.07$; $\Phi = (\frac{14}{8})\pi$; in the Propeller tunnel

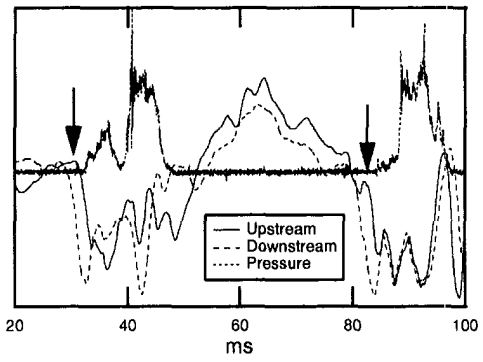

Fig. 6 Typical outputs from the hotwires; in the Propeller tunnel; reverse flows are indicated by arrows. (Uncertainty in estimated velocity = ±1.4 m/s)

re-entrant jet. Le et al. (1993) have suggested that a strong circulation around a shed cloud cavity is consistent with the existence of the re-entrant jet.

From these observations, it is confirmed that, in cloud cavitating conditions, a flow rushes along the foil surface under a fully developed sheet caviyt in the direction opposite to that of the uniform flow. It is known that, along the cavity surface, there is a thin layer of vorticity due to the boundary layer developed near the leading edge of the foil section (Kubota et al., 1992). Therefore, the cavity surface must be unstable. It is anticipated that the sheet cavity collapses into a cluster of bubbles, at least partly, because the re-entrant jet disturbs the cavity surface.

3.2 Control of Cloud Cavitation. From the observations mentioned above, it seems quite reasonable to consider that the re-entrant jet impulsively rushes from the trailing edge to the leading edge of the sheet cavity when the growing motion of the cavity ceases. Moreover, the re-entrant jet plays an important role in the collapse of the sheet cavity and the generation of the cloud cavity. In this section, we discuss whether an obstacle placed on the foil surface can control the re-entrant jet and thereby control the generation of cloud cavity. If the cloud cavity does not appear when the re-entrant jet is held back, we can be convinced that the re-entrant jet gives rise to the generation of cloud cavitation.

Such experiments were carried out on the Propeller Tunnel. A obstacle made of acrylic resin with a square cross section of 2×2 mm was installed on the foil surface in order to hold back the re-entrant jet. Sound pressure was used as a measure of the intensity of cloud cavitation, because it represents the global pressure fluctuations of cavitating flow and is also important from a practical standpoint. The sound pressure was measured by a hydrophone located outside of the acrylic side wall of the Propeller Tunnel and immersed in water with the same air content as the circulating water inside the tunnel.

Figure 7 shows the arrangements of the obstacles and corresponding cavity appearances, pressure fluctuations at 10% C on the suction surface of the hydrofoil and noise intensities up to 1000 Hz. As mentioned in the previous section, when the sheet cavity is in a growing motion, the portion near the side wall has already started collapsing into bubbles. It can also be seen that this phenomenon diagonally propagates from both sides toward the middle of the sheet cavity (see sketch of top view at $\Phi = (\frac{12}{8})\pi$ in Fig. 2). Therefore, there is a possibility that a diagonal secondary flow exists under the sheet cavity giving rise to the large-scale collapse of the sheet cavity. Taking this possibility into account, a pair of obstacles was arranged as shown in Figs. 7(a) and (b). When no obstacle are attached, all the highest peak values in the pressure fluctuations in one cycle exceed the static pressure ($C_p > 0$). This is because the pressure pick-up is exposed to liquid phase downstream of the termination of the sheet cavity at regular cycles. As can be seen in pressure fluctuations, the pressure is nearly constant during a significant portion of the sheding cycle when the pressure transducer is covered with sheet cavity ($C_p \fallingdotseq -\sigma = -1.07$). Both the increase of pressure and the periodicity of pressure fluctuations characterize cloud cavitation. Therefore, one can also judge whether a situation is in cloud cavitation condition or not by observing the wave profile of the pressure fluctuations on the foil surface. Due to the size and frequency response of the pressure pick-up, the peak values are significantly smaller than those observed by many investigators who have measured the cavity collapse pressure related to erosion. The peak values in the present results are nearly 16 kPa, whereas, for example, Avellan and Farhat (1989) detected mean signal levels of 900 MPa during a study on the collapse of vortex cavity. However, the present values are sufficient for investigating the global behaviour of cloud cavitation. The sampling time for the output from the hydrophne was set at 0.5 ms yielding a Nyquist frequency of 1.0 kHz. Therefore, the impulsive pressure with high frequency is not included in these data like the output from the pressure pick-up. Although the peak values of the pressure fluctuations in the configurations (a) and (b) in Fig. 7 are smaller to some extent compared to the smooth condition, the periodicity is fully maintained. Moreover, the appearance of the cavity was completely like a cloud cavity. Further, the mean values of the sound pressure in configurations (a) and (b) were 28.8 Pa and 33.3 Pa, respectively, while that of the smooth condition was 53.6 Pa. Therefore, when the obstacle is attached near the side wall (configurations (a) and (b)), the low-frequency oscillations of the pressure field due to cloud cavitation become somewhat gentle, but is not drastically damped out. It can be suspected that, even if it exists, the secondary flow diagonal to the direction of uniform flow as shown in Fig. 2 ($\Phi = (\frac{12}{8})\pi$) cannot trigger the large-scale collapse of the sheet cavity.

Since the arrangement of the obstacle in configurations (a) and (b) in which the span-center of the sheet cavity remains open has no effect on cloud cavitation, experiments were carried out attaching the obstacle covering the full span. Taking into account a maximum cavity length of about 50% C the obstacles were located at 37% C and 60% C as in Figs. 7(c) and (d). Although the periodicity of the wave profile of the pressure fluctuations is barely retained in configuration (c), the peak values become as small as 40 percent of that of the smooth condition. This result indicates that, in configuration (c), cloud

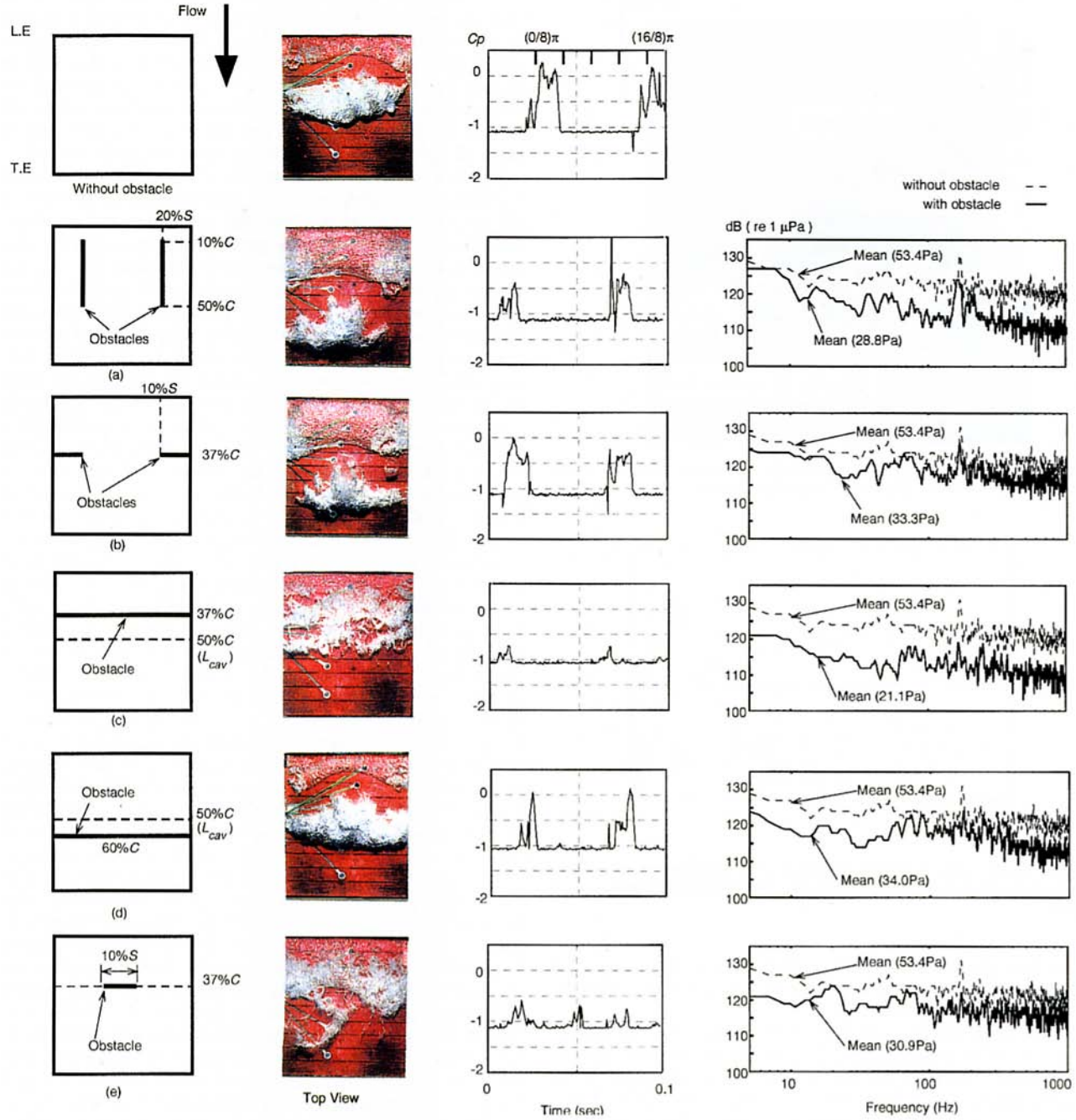

Fig. 7 Arrangements of the obstacles and corresponding cavity appearances, pressure fluctuations at 10 percent C and noise intensities measured by a hydrophone. (Uncertainty in *Cp* = ±0.02)

cavitation is prevented. Instead, many small-scale *U*-shaped vortex cavities are generated from the termination line of the sheet cavity. The mean value of the sound pressure is 21.1 Pa, which is about 40 percent of that of the smooth condition. The sound pressure is reduced by 5–20 dB at almost all frequencies. The reduction in the low frequency range corresponds to the fact that cloud cavitation does not take place and large-scale fluctuations in pressure are damped out. Moreover, as can be seen in Fig. 7, the appearance of the cavity was quite similar to that observed in sheet cavitating conditions without cloud cavity.

On the other hand, in configuration (*d*), the wave profile of the pressure fluctuations is hardly altered compared with that of the smooth condition and the peak values are about 90% of that of the smooth condition. The mean value of the sound pressure is 34.0 Pa, which is higher than those in configurations (*a*) and (*b*) (cloud cavitating conditions). Moreover, appearance of the cavity was similar to that of cloud cavitating conditions. Therefore, it is clear that the obstacle attached downstream of the termination of a fully developed sheet cavity does not affect the behavior of cloud cavitation. However, the sound pressure decreases in both high and low frequency ranges. Since the obstacle is no longer covered by the sheet cavity and the flow stagnates upstream of it, the pressure distribution on the foil surface is changed. Consequently, the pressure fluctuations due to cloud cavitation become different from that of the "smooth" condition.

In order to examine the effect of the length of the obstacle, a short obstacle was attached on the foil surface as indicated in

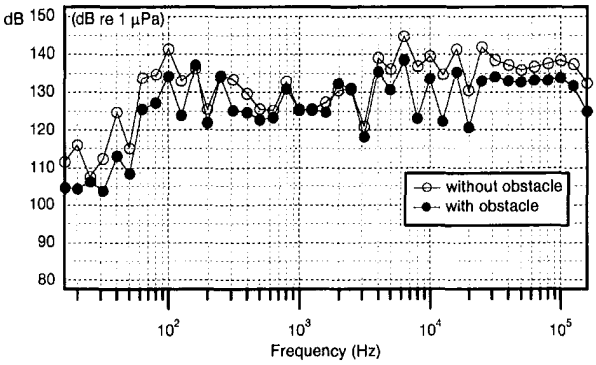

Fig. 8 One-third octave band noise spectrum for the configuration (c) along with that for smooth condition (Uncertainty in noise spectrum = ±1.5 dB)

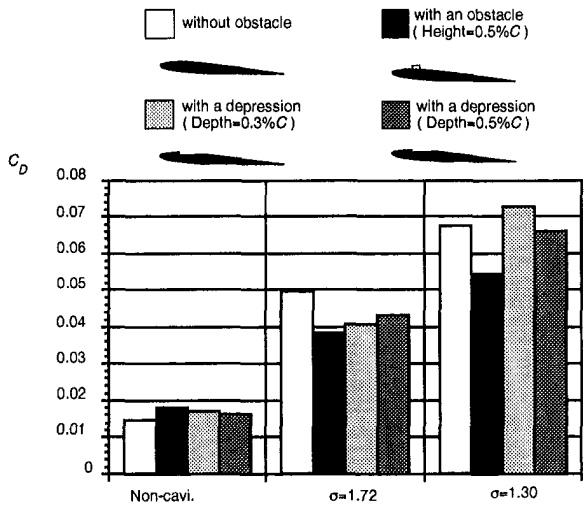

Fig. 9 Drag coefficient of foil section with controlled and uncontrolled cloud cavitation at various cavitation numbers; in the TE Tunnel (Uncertainty in C_D = ±0.002)

Fig. 7(*e*). In this configuration, the mean value of the sound pressure is 30.9 Pa. Although this value is closer to those in configurations (*b*) and (*d*) (cloud cavitating conditions) rather than (*c*), the pressure fluctuations become somewhat irregular and the peak values are as small as 40% of that of the smooth condition. In addition, the appearance of the cavity was similar to that of a sheet cavity without cloud cavitation. The sound pressure is uniformly reduced by 5–10 dB except near 20 Hz and 70 Hz. The influence of the obstacle may not be so remarkable compared with configuration (*c*). It can be safely said that the re-entrant jet loses its momentum due to the existence of the obstacle and, consequently, cloud cavity does not appear. It also turned out that the main flow of the re-entrant jet passes through the middle of a fully developed sheet cavity and that a further reduction of the length of the obstacle in the spanwise direction has no effect on controlling cloud cavitation.

In addition to these measurements, one-third octave band frequency analysis was performed up to 100 kHz. Figure 8 shows the one-third octave band noise spectrum for the configuration (*c*) along with that for the smooth condition. It is seen that noise intensity in the frequency range beyond 4 kHz is uniformly reduced by 5–10 dB. As mentioned above, the noise reduction in low frequency range may result from changes in the type of cavitation. On the other hand, the reduction in high frequency range may be associated with the fact that radiated noise due to the collapse of cavity bubbles decreases. It can be said that the obstacle can suppress not only low frequency periodic vibration but also high frequency cavitation noise caused by the collapse of bubble clusters.

From the experimental results discussed in this section, it may be concluded that cloud cavity is never generated when the re-entrant jet is obstructed, in other words, cloud cavitation is caused by the re-entrant jet.

3.3 Drag Measurements As mentioned in the Introduction, cloud cavitation is harmful to fluid machineries and devices. So, control of cloud cavitation is a practical requirement. The results in the previous sections suggest that an obstacle placed on a foil surface can hold back the re-entrant jet and prevent the formation of cloud cavitation. The drag of a foil section with such an obstacle, however, may become larger, especially in noncavitating conditions. This point is briefly addressed in the following based on measurements in the TE Tunnel.

The drag of the foil section was estimated by the momentum thickness in the wake of the foil section. Four types of E.N. Foil were tested (Fig. 9). A bar or a surface depression was set across the entire span length at 7.5% *C* position. Measured drag coefficients, C_D of these foils are also shown in Fig. 9. In noncavitating conditions, the drag of the foil sections with the bar and the depressions are all larger than that of the smooth foil. However, once cloud cavitation is generated, the results are opposite. The maximum cavity length is 25 percent C at $\sigma = 1.72$ and about 60 percent C at $\sigma = 1.30$. It is remarkable that the differences between 'controlled' and 'uncontrolled' cases in cavitating conditions are larger than those in noncavitating conditions. The surface modifications hold back the re-entrant jet and suppress cloud cavitation. As a result, the drag of the modified foil section becomes smaller than that of the smooth foil. At $\sigma = 1.30$, however, the drag coefficient of the foil section with the depression (depth = 0.3% *C*) is larger than that of the smooth one. When a sheet cavity becomes long, the shallow depression may not be able to hold back the re-entrant jet. From a view point of drag reduction, the bar is superior in cavitating conditions. It should be noted, however, that the drag of the foil section with a depression is smaller than the foil with a bar in non-cavitating conditions.

4 Concluding Remarks

The generation mechanism of cloud cavitation was investigated in a series of experiments involving observation of cloud cavitation by high-speed video and high-speed photography as well as pressure measurements by pressure pick-ups and a hydrophone. The mechanism was also investigated by controlling cloud cavitation with an obstacle fitted on the foil surface. From the results, the relation between the re-entrant jet and the generation process of cloud cavitation was clearly brought out. In addition, methods of controlling of cloud cavitation without drag increase were examined. Following a summary of the principal findings:

1) At appropriately low values of cavitation number, a long sheet cavity cannot steadily attach on a foil section but is broken and shed downstream as a cloud cavity. This is due to a re-entrant jet rushing from the trailing edge to the leading edge of a fully developed sheet cavity triggering the whole collapse of the latter.

2) The velocity of the re-entrant jet is estimated to be of the same order as that of the uniform flow.

3) The re-entrant jet is not the propagation of the collapse of the sheet cavity, but is a substantial flow of water under a fully developed sheet cavity. This is clearly shown by the dye flow from downstream to upstream direction.

4) The re-entrant jet flows from downstream to upstream around the mid-span position of a sheet cavity. A small obstacle attached at the mid-span near the termination of the sheet cavity

is able to hold back the re-entrant jet, thereby preventing the generation of cloud cavitation. When cloud cavitation is controlled by such an obstacle, the drag of a cavitating hydrofoil and the noise intensity around it are both reduced remarkably in comparison with a hydrofoil without control.

Acknowledgment

The authors are extremely grateful to Mr. Masatsugu Maeda and Mr. Masaru Miyanaga for carrying out these difficult experiments skillfully. They are deeply indebted to Photoron Co., Ltd. for lending their high-speed video system. They are also thankful to Dr. Madan Mohan Guin for several discussions and for his assistance during the preparation of this paper.

References

Avellan, F., Dupont, P. and Rhyming, I., 1988, "Generation Mechanism and Dynamics of Cavitation Vortices Downstream of a Fixed Leading Edge Cavity," *17th Symposium on Naval Hydrodynamics,* pp. 317–329.

Avellan, F. and Farhat, M., 1989, "Shock Pressure Generated by Cavitation Vortex Collapse," *ASME International Symposium on Cavitation and Erosion in Fluid Systems,* FED-88, pp. 119–125.

de Lange, D. F., de Bruin, G. J. and van Wijngaarden, L., 1994, "On the Mechanism of Cloud Cavitation—Experiments and Modeling," *2nd International Symposium on Cavitation* (Cav. '94), pp. 45–50.

Furness, R. A. and Hutton, S. P., 1975, "Experimental and Theoretical Studies of Two-Dimensional Fixed-Type Cavities," ASME JOURNAL OF FLUIDS ENGINEERING, Vol. 97, No. 4, pp. 515–522.

Jakobsen, J. K., 1964, "On the Mechanism of Head Breakdown in Cavitating Inducers," ASME *Journal of Basic Engineering,* Vol. 86, pp. 291–305.

Kubota, A., Kato, H., Yamaguchi, H., and Maeda, M., 1989, "Unsteady Structure Measurement of Cloud Cavitation on a Foil Section Using Conditional Sampling Technique," ASME JOURNAL OF FLUIDS ENGINEERING, Vol. 111, No. 2, pp. 204–210.

Kubota, A., Kato, H. and Yamaguchi, H., 1992, "A New Modeling of Cavitating Flows: a Numerical Study of Unsteady Cavitation on a Hydrofoil Section," *Journal of Fluid Mechanics,* Vol. 240, pp. 59–96.

Larrarte, F., Pauchet, A., Bousquet, Ph., and Fruman, D. H., (1995), "On the Morphology of Natural and Ventilated Cavities," ASME *Cavitation and Multiphase Flow,* FED-210, pp. 31–38.

Le, Q., Franc, J. P. and Michel, J. M., 1993, "Partial Cavities: Grobal Behavior and Mean Pressure Distribution," ASME JOURNAL OF FLUIDS ENGINEERING, Vol. 115, pp. 243–248.

Lush, P. A., and Skipp, S. R., 1986, "High Speed Cine Observations of Cavitating Flow in a Duct," *International Journal of Heat Fluid Flow,* Vol. 7, No. 4, pp. 283–290.

Mørch, K. A., 1981, "Cavity Cluster Dynamics and Cavitation Erosion," ASME *Cavitation and Polyphase Flow Forum,* pp. 1–10.

Noordzij, L. and van Wijngaarden, L., 1974, "Relaxation Effects, Caused by Relative Motion, on Shock Waves in Gas-Bubble/Liquid Mixtures," *Journal of Fluid Mechanics,* Vol. 66, pp. 115–143.

Shen, Y. T. and Peterson, F. B., 1978, "Unsteady Cavitation on an Oscillating Hydrofoil," *12th Symposium on Naval Hydrodynamics,* pp. 362–384.

Uncertainties and CFD Code Validation

H. W. Coleman
Eminent Scholar in Propulsion and Professor,
Propulsion Research Center,
Mechanical and Aerospace Engineering Department,
University of Alabama in Huntsville,
Huntsville, AL 35899

F. Stern
Professor,
Iowa Institute of Hydraulic Research,
Department of Mechanical Engineering,
University of Iowa,
Iowa City, IA 52242

A new approach to computational fluid dynamics code validation is developed that gives proper consideration to experimental and simulation uncertainties. The comparison error is defined as the difference between the data and simulation values and represents the combination of all errors. The validation uncertainty is defined as the combination of the uncertainties in the experimental data and the portion of the uncertainties in the CFD prediction that can be estimated. This validation uncertainty sets the level at which validation can be achieved. The criterion for validation is that the magnitude of the comparison error must be less than the validation uncertainty. If validation is not accomplished, the magnitude and sign of the comparison error can be used to improve the mathematical modeling. Consideration is given to validation procedures for a single code, multiple codes and/or models, and predictions of trends. Example results of verification/validation are presented for a single computational fluid dynamics code and for a comparison of multiple turbulence models. The results demonstrate the usefulness of the proposed validation strategy. This new approach for validation should be useful in guiding future developments in computational fluid dynamics through validation studies and in the transition of computational fluid dynamics codes to design.

1 Introduction

Uncertainty considerations involved in using experimental data in validating the predictions of CFD codes (or, more generally, computer simulations) are discussed in this article. The word uncertainty is used in the following sense—the uncertainty U associated with a measured quantity or a predicted quantity defines the $\pm U$ interval about that quantity within which we expect the true (but unknown) value of that quantity to lie 95 times out of 100. It is important to recognize that a validation is restricted to some range, typically the range of conditions of the data used in the (successful) validation effort. This is intended by the authors to be implicit in the discussions in this article.

The comparison process in attempting to validate predictions using experimental data is illustrated schematically in Fig. 1. The hypothetical predictions of result r versus independent variable X from two models (or simulations) are shown along with experimental data points (X_i, r_i). In part (a) of the figure, no uncertainties are considered, and one might well be tempted to argue that Model 1 is superior to Model 2. The predictions from Model 1 seem to "capture the trend of the data" better than the predictions from the (simplistic, linearized, etc.) Model 2. If the uncertainties in the experimentally-determined values of the result r are considered (Fig. 1(b)), the perspective changes completely, and it is obvious that arguing for one method over another based on comparison with the experimental data is wasted effort since the predictions from both methods fall well within the data uncertainty.

Actually, Fig. 1(b) does not show the complete situation. For the data points, uncertainties in both the experimentally-determined r and the experimentally-determined value of the independent variable X should be considered, giving an uncertainty "box" around each experimental data point. Additionally, the prediction from a model should not be viewed as an infinitesimally thin r vs. X line, but rather as a "fuzzy band" that represents the prediction plus and minus the uncertainty that should be associated with the simulation/model/code. This is illustrated in Fig. 2, which also shows that, in general, uncertainties in both the data and the predictions can vary (sometimes dramatically) over the range of X. Figure 2 shows the variables and their uncertainties, but the comparison it shows is deceptive because it is two-dimensional. The independent variable X must be considered a vector ($\mathbf{X}$) of n dimensions—fluid velocity as a function of position and time, $V(x, y, z, t)$, for example—and the "box" around $\mathbf{X}$ will therefore be n-dimensional. The (total) uncertainty in r that should be used in a comparison should include the experimental uncertainty in r and the additional uncertainty in r arising from experimental uncertainties in the measurements of the n independent variables (this is developed in detail in Section 3).

Contributors to the prediction uncertainty $U_r(X)$ can be divided into two broad categories—numerical uncertainty and modeling uncertainty. In fact, insuring that the modeling uncertainty is below some designated value is one purpose of CFD validation through comparisons with benchmark experimental data.

The validation strategy proposed in this article and discussed in detail in Section 3 views the situation from a new perspective, isolating the modeling uncertainty (which the authors do not know how to estimate) from the uncertainties that can be estimated (the data uncertainty and the non-modeling uncertainties in predictions). A direct calculation of the comparison error E (data minus prediction) is made and compared with a validation uncertainty U_V that is composed of the uncertainties in the experimental data and the portion of the uncertainties in the CFD prediction that can be estimated. This validation uncertainty U_V is the best resolution possible in the validation effort (i.e., it sets the "noise level" below which no discrimination is possible). If the absolute value of the calculated comparison error E is less than U_V, then validation is defined as being successful at the U_V level.

From the preceding discussion the authors believe it is evident that *(1) the uncertainties in the data and in the predictions set the scale at which validation is possible, and (2) these uncertainties must be considered in determining if validation has been achieved.* Obviously, these uncertainties should be considered in planning and implementing a computational/experimental research program for validating CFD codes, al-

Contributed by the Fluids Engineering Division for publication in the JOURNAL OF FLUIDS ENGINEERING. Manuscript received by the Fluids Engineering Division March 31, 1997; revised manuscript received August 4, 1997. Associate Technical Editor: D. P. Telionis.

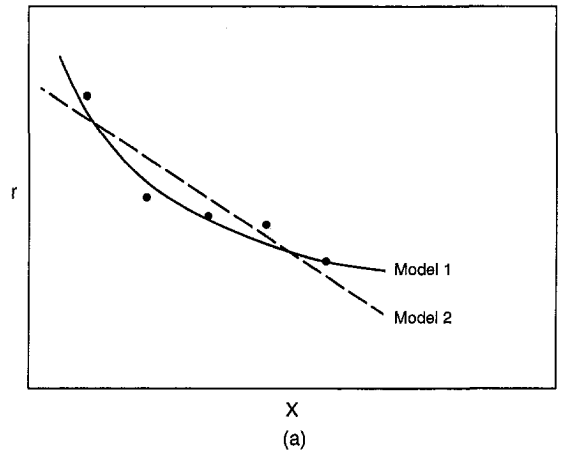

(a)

Fig. 1(*a*) without consideration of experimental uncertainties

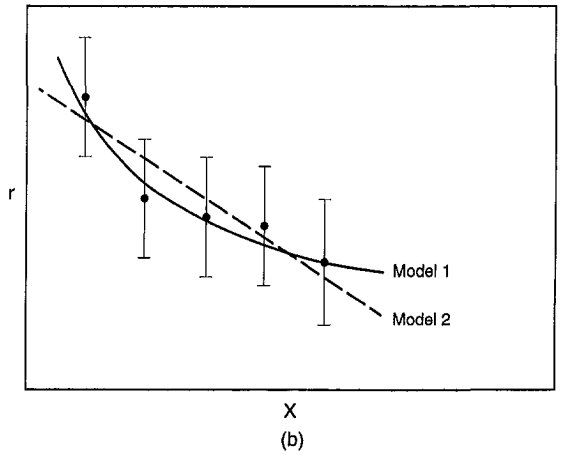

(b)

Fig. 1(*b*) with partial consideration of experimental uncertainties

Fig. 1 Comparisons of experimental data and model predictions

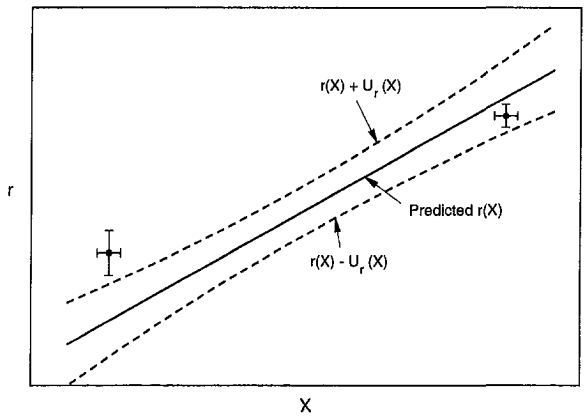

Fig. 2 Uncertainties in data and predictions to be considered in validations

though they typically have not been in the past. Figure 1(*a*) gives a qualitative view of the way most previous validation efforts have proceeded, with Fig. 1(*b*) being typical of the few approaches considering uncertainties at all.

This current work is part of a larger program (Rood, 1996) for developing and implementing a strategy for validation of Reynolds-Averaged Navier-Stokes (RANS) computational ship hydrodynamics codes. The program includes complementary computational ship hydrodynamics and towing tank investigations and considers the uncertainties in both computations and data in assessing the success of validation efforts.

2 Uncertainties in Data and in Simulations

As stated earlier, the uncertainty U associated with a measured quantity or a predicted quantity defines the $\pm U$ interval about that quantity within which we expect the true (but unknown) value of that quantity to lie 95 times out of 100. For detailed discussion of uncertainties associated with experimental data, the reader is referred to Coleman and Steele (1989, 1995). Although the uncertainty in an experimental data point originally comes from both bias (systematic) and precision (random) sources, the uncertainty is "fossilized" into a fixed quantity (a bias) once the value (X_i, r_i) of the data point is recorded and reported. This is logical if one notes that the value of the data point is always the same amount different from the (unknown) true value each time the data point is used.

The uncertainties associated with the predictions of models, simulations, CFD codes, etc. and their role in the validation process have been receiving increasing attention in the last few years, and only a few representative references are cited here. Editorial policies have been set by professional journals (ASME, 1993; AIAA, 1994; Gresho and Taylor, 1994), and standards and guidelines (IAHR, 1994) and recommended practices (ITTC, 1996) have been specified by international organizations. The literature covers a broad range from governmental (Rood, 1996) and industrial (Melnik et al., 1994) perspectives to overall methodology (Coleman, 1996; Marvin, 1995; Mehta, 1996 (also AIAA, 1997); Oberkampf et al., 1995) and detailed application (Blottner, 1990; Roache, 1997; Zingg, 1992). The 1993 ASME Symposium on Quantification of Uncertainty in Computational Fluid Dynamics (Celik et al., 1993) provides a good introduction.

As mentioned in the previous section, uncertainties associated with predictions from simulations can be divided into two broad categories: (1) numerical uncertainties, and (2) modeling uncertainties. The numerical uncertainty category includes uncertainties due to the numerical solution of the mathematical equations (discretization, artificial dissipation, iterative and grid non-convergence, local and global non-conservation of mass, momentum, energy, etc., internal and external boundary non-continuity, computer round-off, etc.) The modeling uncertainty category includes uncertainties due to assumptions and approximations in the mathematical representation of the physical process (geometry, mathematical equation, coordinate transformation approximations, free-surface boundary conditions, turbulence models, etc) and also uncertainties due to the incorporation of previous experimental data into the model (such things as fluid property values and the "constants" in turbulence models). Examples of reported uncertainties associated with property data range from 0.25–0.5 percent for liquid oxygen density (Brown et al., 1994), to 2–5 percent for the thermal conductivity of air at atmospheric pressure (Coleman and Steele, 1989), to huge percentages for properties such as surface tension coefficient that are extremely sensitive to contaminants. A recent study (Beard and Landrum, 1996) utilizing laminar Navier-Stokes computations for hydrogen flow through a solar thermal thruster at temperatures up to 6100 R showed a ±2 percent variation in computed specific impulse due solely to the range of the available reaction rate data reported by different investigators.

The overall process leading to validation and simulation uncertainty estimation can be categorized as documentation, verification, and validation. Documentation involves detailed presentation of the mathematical equations and numerical method. Verification involves estimation of numerical uncertainty through parametric, convergence, and order-of-accuracy studies. Validation involves estimation of the difference (error) between the simulation's prediction and the truth, and this esti-

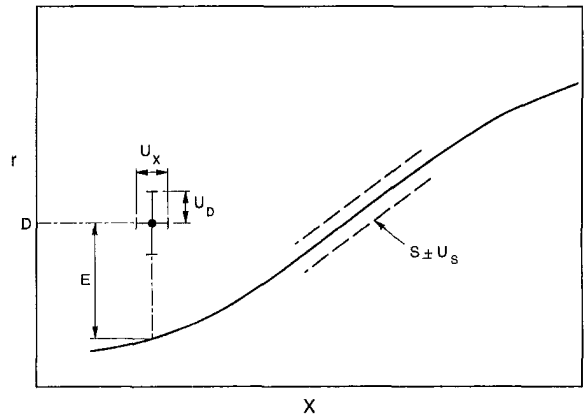

Fig. 3 Definition of comparison error

mate is impossible to make with any confidence without a benchmark. The benchmark can be an analytical solution (with an associated uncertainty) or, more likely and of primary interest here, an experimental value with its associated uncertainty. To paraphrase one reviewer, (verification)/(validation) can be viewed as addressing (equations solved right?)/(right equations solved?).

Although not always available, documentation is relatively straightforward, whereas, in spite of the aforementioned efforts, specific implementation procedures for verification and validation are not yet established. Approaches for verification require procedures for the estimation of the numerical uncertainties. Stern et al. (1996) provided an example approach for their steady RANS CFD method with application to naval surface combatants. In this approach, estimates of uncertainties were provided for both integral and point quantities for iterative and grid nonconvergence and were combined using root sum square. Also, for conditions permitting, order-of-accuracy and Richardson extrapolation studies were conducted.

In the following section, a new approach to CFD validation is developed and discussed with regard to validation of a single CFD code, to validation of a comparison of multiple codes and/or models, and to validation of predictions of trends. Subsequently, in Section 4, example results of validations are presented both for a single CFD code and for a comparison of multiple turbulence models. The CFD code and verification procedures of Stern et al. (1996) are used for two applications for which numerical and experimental uncertainty analyses are available: marine-propulsor flow (Chen, 1996; Jessup, 1994) and two-dimensional turbulent flat-plate boundary-layer flow (Sreedhar and Stern, 1997; Longo, et al., 1998).

3 An Approach to CFD Code Validation

Consider the situation shown in Fig. 3. Using the example mentioned previously, the single-plane representation r versus X might be a mean velocity component V vs. distance (z) normal to a solid surface at a given time and position (x, y, t) on that surface. Define the predicted r-value from the simulation (code) as S, the experimentally determined r-value of the ($\mathbf{X}_i$, r_i) data point as D, and the comparison error, E, as their difference:

$$E = D - S \tag{1}$$

The comparison error E is the resultant of *all* of the errors associated with the experimental data and the errors associated with the simulation. Here it is assumed that a correction has been made for any error whose value is known. Thus, the errors that are the subject of this discussion have unknown sign and magnitude, and the uncertainties are estimates of these errors.

If X_i, r_i, and S share no common error sources, then the uncertainty U_E in the comparison error can be expressed as

$$U_E^2 = \left(\frac{\partial E}{\partial D}\right)^2 U_D^2 + \left(\frac{\partial E}{\partial S}\right)^2 U_S^2 = U_D^2 + U_S^2 \tag{2}$$

where U_D is the uncertainty in the data and U_S the uncertainty in the simulation. The uncertainty U_E should bound the (true) absolute value of the comparison error E 95 times out of 100. The assumptions and approximations made in deriving Eq. (2) are discussed in detail in Coleman and Steele (1995).

Recalling the discussion in Section 2, the simulation uncertainty U_S can be represented as

$$U_S^2 = U_{SN}^2 + U_{SPD}^2 + U_{SMA}^2 \tag{3}$$

where U_{SN} is the simulation numerical solution uncertainty, U_{SPD} is the simulation modeling uncertainty arising from using previous experimental data, and U_{SMA} is the simulation modeling uncertainty arising from modeling assumptions. Substituting Eq. (3) into Eq. (2) gives

$$U_E^2 = U_D^2 + U_{SN}^2 + U_{SPD}^2 + U_{SMA}^2 \tag{4}$$

Ideally, we would like to postulate that if the absolute value of E is less than its uncertainty U_E, then validation is achieved. In reality, the authors know of no approach that gives an estimate of U_{SMA}, so U_E cannot be estimated. That leaves a more stringent validation test as the practical alternative. If we define the validation uncertainty U_V as the combination of all uncertainties that we know how to estimate (i.e., all but U_{SMA}), then

$$U_V^2 = U_E^2 - U_{SMA}^2 = U_D^2 + U_{SN}^2 + U_{SPD}^2 \tag{5}$$

If $|E|$ is less than the validation uncertainty U_V, then the combination of all the errors in D and S is smaller than the estimated validation uncertainty and validation has been achieved at the U_V level. *This quantity U_V is the key metric in the validation process.* U_V is the validation "noise level" imposed by the uncertainties inherent in the data, the numerical solution, and the previous experimental data used in the simulation model—one cannot discriminate once $|E|$ is less than this, i.e., as long as $|E|$ is less than this one cannot evaluate the effectiveness of proposed model "improvements." Choice of the required level of U_V is associated with the degree of risk deemed acceptable in a program.

To estimate U_{SPD} for a case in which the simulation uses previous data d_i in m instances, one would need to evaluate

$$U_{SPD}^2 = \sum_{i=1}^{m} \left(\frac{\partial S}{\partial d_i}\right)^2 (U_{d_i})^2 \tag{6}$$

where the U_{d_i} would be estimated using established uncertainty analysis procedures (Coleman and Steele, 1989, 1995).

As discussed in Section 1, for the data point ($\mathbf{X}_i$, r_i), U_D should include both the experimental uncertainty in r_i and the additional uncertainties in r_i arising from experimental uncertainties in the measurements of the n independent variables $(X_j)_i$ in $\mathbf{X}_i$. The expression for U_D that should be used in the U_V calculation is then

$$U_D^2 = U_{r_i}^2 + \sum_{j=1}^{n} \left(\frac{\partial r}{\partial X_j}\right)_i^2 (U_{X_j})_i^2 \tag{7}$$

In some cases, the terms in the summation in Eq. (7) may be shown to be very small using an order-of-magnitude analysis and then neglected. This would occur in situations in which the U_{X_j}'s are of "reasonable" magnitude and gradients in r are small. In regions of the flow with high gradients (near a surface in a turbulent flow), however, these terms may be very significant.

There is also a very real possibility that measurements of different variables might share identical bias errors. This is easy to imagine for measurements of x, y, and z. Another possibility is D and S sharing an identical error source, for example if r is drag coefficient and the same density table (curvefit) is used both in data reduction in the experiment and in the simulation. In such cases, additional "correlated bias" terms must be included in Eq. (2). Approximation and inclusion of such terms are discussed in Coleman and Steele (1989, 1995), Coleman et al. (1995), and Brown et al. (1996) and will not be covered in further detail in this article.

Validation of a Single CFD Code. The validation uncertainty, U_V, sets the level at which validation can be achieved. If the objectives of a program require that validation be accomplished "within ±2 percent," then $|E|$ must be less than U_V and U_V must be less than (roughly) 0.02 D. If U_V is greater than 0.02 D, the objectives of the program cannot be achieved until the sum of the terms on the right-hand-side of Eq. (5) is reduced to an acceptable level. When $|E|$ is greater than U_V, validation is not accomplished, and the magnitude and sign of E can be valuable in designing strategies to improve the mathematical modeling.

As one reviewer pointed out, consideration of Eq. (5) shows that (a) the more uncertain the data, and/or (b) the more inaccurate the code (greater U_{SN} and U_{SPD}), the easier it is to validate a code. That is true, since the greater the uncertainties in the data and the code predictions, the greater the "noise level" (U_V). If this value of U_V is greater than that designated as necessary in a research/design/development program, however, then the required *level of validation* could not be achieved without improvement in the quality of the data, the code, or both. Likewise, if U_{SN} and U_{SPD} are not estimated but $|E|$ is less than U_D, then validation has been achieved *but at an unknown level.* Obviously, if *no* uncertainties are estimated, no statements about validation can be made within the concept of the validation process as considered in this article.

In general, validation of a code's predictions of a number (N) of different variables is desired, and this means that in a particular validation effort there will be N different E's and U_V's and (perhaps) some successful validations and some unsuccessful. For each variable, a plot of the simulation prediction versus X compared with the (X_i, r_i) data points gives a traditional overview of the validation status, but the interpretation of the comparison is greatly affected by choice of the scale and the size of the symbols. A plot of $\pm U_V$ and E versus X for each variable is particularly useful in drawing conclusions, as demonstrated in Section 4, and the interpretation of the comparison is more insensitive to scale and symbol size choices.

Comparison of Multiple Codes and/or Models in a Validation Effort. When a validation effort involves multiple codes and/or models, the procedure discussed above—comparison of the E's and U_V's for the N variables—should be performed for each code/model.

Since each code/model may have a different U_V, some method to compare the different codes'/models' performance for each variable in the validation is useful. The range within which (95 times out of 100) the true value of E lies is $E \pm U_E$. From Eq. (5), when U_{SMA} is zero then $U_V = U_E$, so for that ideal condition the maximum absolute magnitude of the 95% confidence interval is given by $|E| + U_V$. Comparison of the ($|E| + U_V$)'s for the different codes/models then shows which has the smallest range of likely error assuming all U_{SMA}'s are zero. This allows appropriate comparisons of (low E)/(high U_V) with (high E/low U_V) codes/models.

Validation of Predictions of Trends. In some instances, the ability of a code or model to predict the trend of a variable may be the subject of a validation effort. An example would be the difference in drag for two ship configurations tested at the same Froude number. The procedure discussed above—comparison of $|E|$ and U_V for the drag—should be performed for each configuration. The difference δ in drag for the two configurations should then be considered as the variable that is the subject of the validation. As discussed in detail in Coleman et al. (1995), because of correlated bias uncertainty effects in the experimental data the magnitude of the uncertainty in δ may be significantly less than the uncertainty in either of the two experimentally-determined drag values. This means that the value of U_V for δ may be significantly less than the U_V's for the drag values, allowing for a more stringent validation criterion for the difference than for the absolute magnitudes of the variables.

It is probable that in some instances the U_{SMA} for the difference δ will be less than the U_{SMA}'s for the absolute magnitudes of the variables because of correlated systematic uncertainty effects in the modeling. This is an unexplored area at this time.

4 Results of Verification/Validation for a Single CFD Code and for a Comparison of Multiple Turbulence Models

Example results of verification/validation are presented both for a single CFD code and for a comparison of multiple turbulence models. In both cases, the magnitude of U_{SPD} was assumed negligible relative to the other uncertainties. The CFD code and verification procedures of Stern et al. (1996) are used for two applications for which numerical and experimental uncertainty analyses are available: marine-propulsor flow (Chen, 1996; Jessup, 1994) and two-dimensional turbulent flat-plate boundary-layer flow (Sreedhar and Stern, 1997; Longo et al., 1998). The former represents a practical geometry and is used for the single CFD code validation example, whereas the latter represents an idealized geometry and is used for the comparison of turbulence models example.

For the marine-propulsor geometry, Jessup (1989) provided an extensive data set (including circumferential-average, phase-average, and detailed blade boundary-layer, wake, and tip-vortex velocities) for the relatively simple marine propulsor P4119. This propeller-shaft configuration, shown viewed from upstream in Fig. 4, was tested in a 24 in. water tunnel with measurements made using a three-component laser-Doppler velocimeter (LDV) system. Detailed uncertainty estimates have also been reported (Jessup, 1994). An initial validation effort was

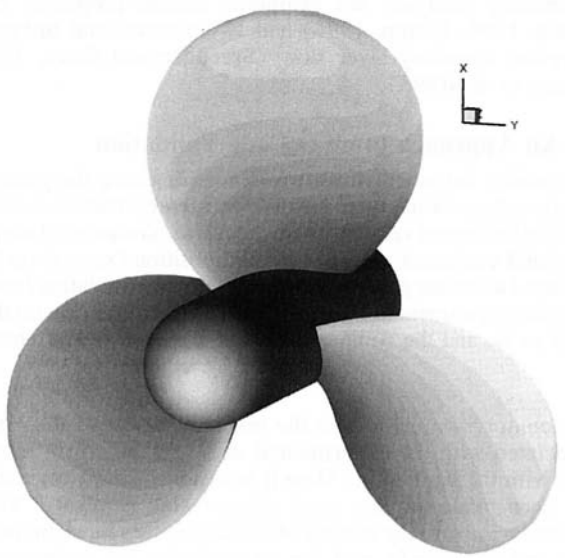

Fig. 4 Marine propulsor P4119

Table 1 Marine-propulsor flow: performance coefficients

	D	S	$E\%$	$U_V\%$	$U_D\%$	$U_r\%$	$U_{SN}\%$	$U_{SI}\%$	$U_{SG}\%$	U_{SN}/U_D
K_T	0.146	0.149	−2.1	3.2	2.0	2.0	2.5	1.0	2.3	1.3
$10K_Q$	0.280	0.276	1.9	3.4	2.0	2.0	2.7	1.0	2.5	1.4

% D.

reported by Stern et al. (1994). Documentation and verification are reported by Chen (1996) in conjunction with studies of design and off-design marine-propulsor performance.

For the two-dimensional turbulent flat-plate boundary-layer flow, Longo et al. (1996) provided data and uncertainty analysis in conjunction with their study of solid/free-surface juncture boundary layer and wake. A 1.2 m surface-piercing flat plate was tested in a 100 × 3 × 3 m towing tank with measurements made using a two-component LDV system configured to obtain three mean velocities and five Reynolds stresses for both boundary layer and wake planes and regions deep and very close to the free surface. Sreedhar and Stern (1997) provided verification for multiple turbulence models for this application in conjunction with the development of nonlinear eddy-viscosity turbulence models, including both wall and free-surface effects.

The CFD method solves the unsteady incompressible RANS and continuity equations using either noninertial cylindrical or inertial cartesian coordinates and the Baldwin-Lomax turbulence model. The RANS equations are solved using finite-analytic spatial and first-order (steady flow) or second-order (unsteady flow) backward difference time discretization. The pressure equation is derived from a discretized form of the continuity equation and solved using second-order-central finite differences. The overall solution procedure is based on the two-step pressure-implicit-split-operator (PISO) algorithm. For steady flow, subiteration convergence is not required and time serves as an iteration parameter.

Verification Procedures. The verification procedures follow the approach of Stern et al. (1996). This approach is based on the editorial policy statement of the ASME (ASME, 1993). The ten issues of the statement are divided as documentation (1, 7, 8), verification (2–6), and validation (9, 10). Verification is comprised of grid-, iterative-, and time-convergence (4, 5, 6), artificial dissipation (3), and order-of-accuracy (2) studies. These studies are implemented using a five-step procedure: (i) grid design and identification of important parameters; (ii) convergence studies; (iii) determination of the effects of explicit artificial dissipation, if used; (iv) estimation of overall uncertainties for integral and point variables; and (v) order of accuracy and Richardson extrapolation.

Step (i) is self-explanatory. For steady flow, step (ii) consists of obtaining estimates for iterative and grid convergence uncertainties (U_{SI} and U_{SG}, respectively) for integral and point variables.

The estimates for grid convergence uncertainty require a minimum of three grids and are based either on (a) the grid convergence metric

$$\epsilon = \frac{(\phi_1 - \phi_2)}{\phi_1} \tag{8}$$

where ϕ represents either an integral or point variable with subscripts 1 and 2 corresponding to the finer and coarser grids, respectively, or (b) the grid convergence index (Roache, 1997)

$$GCI = \frac{3\epsilon}{(r^p - 1)} \tag{9}$$

where r is the grid refinement ratio and p the order of accuracy such that for grid doubling and second-order methods ϵ = GCI. For small grid refinement and/or order, the GCI is recommended since ϵ is arbitrarily small and inappropriate as a metric of grid convergence. Note that for small ϕ (including point variables with regions of small ϕ), ϵ should be normalized by the range of ϕ. Decreasing (increasing) ϵ/GCI indicates grid convergence (divergence) with uncertainty estimates based on ϵ for the finest grids. Oscillatory ϵ/GCI is indeterminate, with uncertainty estimated as roughly one-half the difference between the maximum and minimum values. For simple geometries and flows, negligible grid convergence uncertainty is attainable. For complex geometries and flows, convergence may be limited and oscillatory.

The estimates for iterative convergence uncertainty are based on evaluation of the iteration records for both integral and point variables. The level of iterative convergence is determined by the number of orders of magnitude reduction and magnitude in the residuals

$$\zeta = \phi^n - \phi^{n-1} \tag{10}$$

where n is the iteration number and ϕ can either be the solution variables or equation imbalances obtained by back substitution. Average (L_2 norms) or maximum values are used. For simple geometries and flows, sixteen orders of magnitude reduction of ζ to machine zero is possible such that the iterative convergence uncertainty is negligible. However, for practical geometries and flows, only a few orders of magnitude reduction in ζ to about

Table 2 Marine-propulsor flow: circumferential-average mean-velocity components (radial-magnitude average)

	$\lvert E\rvert\%$	$U_V\%$	$U_D\%$	$U_r\%$	$\left(\frac{\partial r}{\partial x}\right)U_x\%$	$U_{SN}\%$	$U_{SI}\%$	$U_{SG}\%$	U_{SN}/U_D
U_1	1.2	1.3	1.2	1.2	0.02	0.8	0.4	0.7	0.7
V_1	2.6	1.3	1.2	1.2	0.01	0.7	0.2	0.7	0.6
W_1	1.7	1.3	1.2	1.2	0.02	0.6	0.4	0.5	0.5
U_2	2.3	3.2	3.1	3.1	0.02	0.9	0.5	0.8	0.3
V_2	2.1	3.1	3.1	3.1	0.01	0.7	0.3	0.6	0.2
W_2	2.7	3.2	3.1	3.1	0.02	0.9	0.5	0.7	0.3

[1] upstream.
[2] downstream.
% U_0.

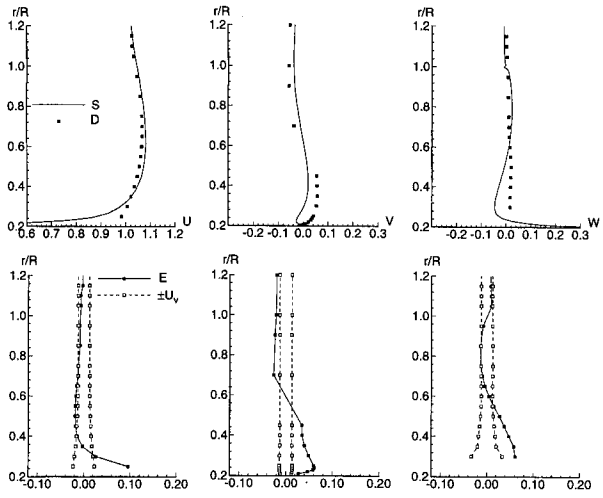

Fig. 5(*a*) Upstream ($x/R = -0.3$)

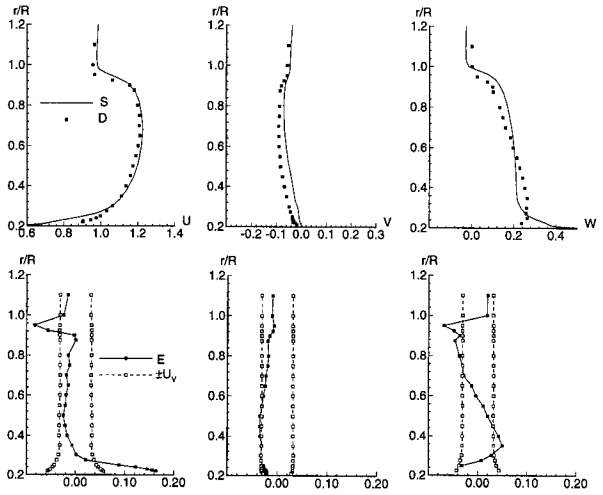

Fig. 5(*b*) Downstream ($x/R = 0.328$)

Fig. 5 Marine-propulsor flow: circumferentially-averaged mean velocity components; simulation prediction and experimental data; comparison error and validation uncertainty

10^{-4} may actually be attainable. In this case, the estimates for iterative convergence uncertainty are based on statistics of the iteration records of integral and point variables and are taken as roughly one-half the difference between the maximum and minimum values.

Step (iii) consists of determination of effects of explicit artificial dissipation through parametric studies with uncertainty estimates U_{SAD} based on a convergence metric similar to Eq. (8). Step (iv) combines the uncertainties (U_{SI}, U_{SG}, U_{SAD}, . . .) using root sum square (in analogy with experimental uncertainty analysis and assumed for the present to be the appropriate form) to obtain overall estimates of the numerical uncertainty U_{SN} for both integral and point variables. Step (v) consists of obtaining solutions on three grids in the asymptotic range (i.e., base, halved, and doubled grids with monotonically decreasing ϵ at rate r^p) and Taylor series expansions to determine the order of accuracy and Richardson extrapolated coarse grid order $3p$ benchmark.

Steps (i)–(iv) are required. Step (v) is useful in providing p and the $3p$ benchmark and desirable for guiding CFD development, but often difficult, especially in obtaining solutions in the asymptotic range for complex geometries. Note that p is required for evaluation of the GCI, that other evaluations (e.g., rate of iterative convergence) are also useful for guiding CFD development, and that additional uncertainty estimates may be required (e.g., local and global non-conservation of mass, momentum, energy, etc.).

Verification/Validation for a Single CFD Code. Variables chosen to illustrate the verification and validation results are the propulsor thrust and torque performance coefficients (K_T and K_Q, respectively); the radial average of the circumferential-average mean-velocity components in a plane upstream (U_1, V_1, W_1) and a plane downstream (U_2, V_2, W_2) of the propeller; and the radial profiles of the circumferential-average mean velocities in the same planes.

The results for the performance coefficients are shown in Table 1, where all percentages given are percentage of D. The verification results show that the uncertainty in grid convergence dominates the iteration convergence uncertainty, resulting in numerical uncertainties in the simulation, U_{SN}, of about 2.4 percent. The uncertainties, U_D, associated with the experimentally determined results are about 2.0 percent, leading to estimates of U_V of about 3.3 percent. This means that, for this flow condition, validation of the CFD code predictions cannot be achieved better than about 3.3 percent for the performance coefficients. Since the calculated comparison error $|E|$ is less than U_V, validation in this case is successful at the 3.3 percent level for both K_T and K_Q.

The results for the average velocities in the upstream and downstream planes are shown in Table 2, where all percentages given are percentage of the uniform inflow velocity U_0. As for the performance coefficients, the uncertainty in grid convergence is always greater than the iteration convergence uncertainty, and the resulting numerical uncertainties in the simulation, U_{SN}, are 0.6–0.9 percent. The uncertainties, U_D, associated with the experimentally determined results are about 1.2 percent (upstream) and 3.2 percent (downstream), leading to estimates of U_V of about 1.3 percent (upstream) and 3.2 percent (downstream). The calculated comparison error $|E|$ is less than U_V for average velocities U_1, U_2, V_2, and W_2, indicating successful validation for those variables. Validation of the simulations of the average velocities V_1 and W_1, however, is not achieved. It should also be noted that since

$$\left(\frac{\partial r}{\partial X_j}\right)_i (U_{X_j})_i << U_{r_i}$$

(where $r_i = (U, V, W)$ and $X_j = r/R$) the influence of the uncertainties in the X_j-locations of the measurement positions are negligible.

Table 3 Two-dimensional turbulent flat-plate boundary-layer flow: streamwise mean velocity (average magnitude across the boundary layer)

Turbulence model	$\|E\|$%	U_V%	U_D%	U_r%	$\left(\frac{\partial r}{\partial x}\right)U_X$%	U_{SN}%	U_{SI}%	U_{SG}%	U_{SN}/U_D	$\|E\| + U_V$%
Baldwin Lomax (1978)	1.30	2.52	1.60	1.60	0.09	1.95	0.00	1.95	1.22	3.82
Chen and Patel (1988)	2.07	2.40	1.60	1.60	0.09	1.79	0.00	1.79	1.12	4.47
Myong and Kassagi (1990)	2.30	2.67	1.60	1.60	0.09	2.14	0.00	2.14	1.34	4.97

% U_e.

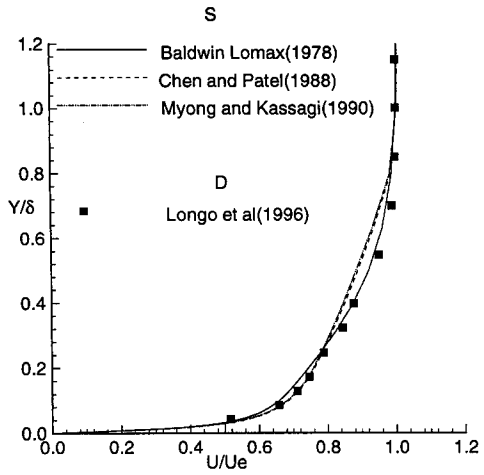

Fig. 6(*a*) Simulation prediction and experimental data

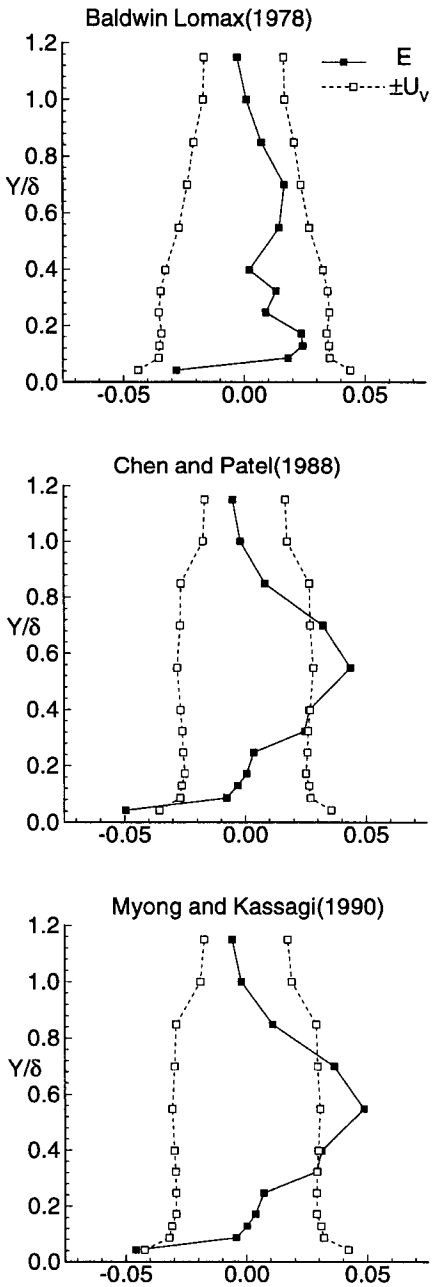

Fig. 6(*b*) Comparison error and validation uncertainty

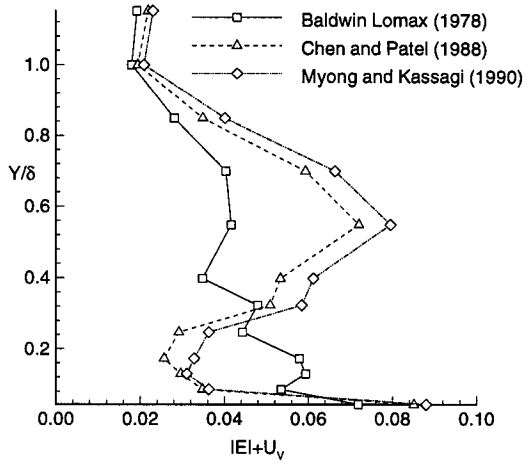

Fig. 6(*c*) $|E| + U_V$

Fig. 6 Two-dimensional turbulent flat plate boundary layer flow-streamwise mean velocity

The validation comparisons for the radial profiles of the circumferential-average velocity components are shown in Fig. 5(*a*) for the upstream plane and Fig. 5(*b*) for the downstream plane. In this presentation, R is the outer radius of the propeller, the outer radius of the shaft is at $r/R = 0.2$, and the three velocity components and E and U_V are normalized by U_0. The plots of U, V, and W versus r/R show the comparisons as they have traditionally been made in past validation efforts. The plots of E and $\pm U_V$ present the new validation view introduced in this article, and it is immediately obvious where validation has been achieved and where it has not. In this specific case presented, validation is achieved for some variables in some regions of the flow but not for all variables in all regions of the flow field. The largest errors are for the regions of the flow corresponding to the shaft/blade juncture and the blade tip regions, which is confirmed by the validation results using the complete data set (Chen and Stern, 1997).

Verification/Validation for Comparison of Multiple Turbulence Models. Variables chosen to illustrate the verification and validation are the average magnitude across the boundary layer of the streamwise mean velocity and the profile of the streamwise mean velocity. The comparisons are for three turbulence models of increasing complexity, i.e., the Baldwin and Lomax (1978) algebraic model (BL), the Chen and Patel (1988) k-ϵ and near-wall model (CP), and the Myong and Kasagi (1990) nonlinear k-ϵ model (MK). In the presentations, the velocity, comparison error, and validation uncertainty are normalized by the edge velocity U_e and the independent variable Y is normalized by the boundary-layer thickness δ.

The results for the average velocity are shown in Table 3. As for the previous example, the uncertainty in grid convergence dominates the iteration convergence uncertainty, resulting in numerical uncertainties U_{SN} for the three models ranging from about 1.8–2.1 percent. The data uncertainty U_D is 1.6 percent leading to validation uncertainties U_V of 2.5–2.7 percent. Here again, the contribution to U_D from uncertainties in the measurement locations (where $r_i = U/U_e$ and $X_j = Y/\delta$) is negligible. All three models are validated at the level $U_V = 2.5$–2.7 percent. The estimates for $|E| + U_V$ range for increasing model complexity from 3.8–5 percent.

The validation comparisons for the streamwise mean velocity are shown in Figs. 6(*a–c*). The simulation prediction and data comparisons U/U_e vs. Y/δ [Fig. 6(*a*)] for the CP and MK models show relatively large underprediction in the mid-region of the boundary-layer, whereas the BL model

shows relatively small underprediction in the near-wall region. The plots of E and $\pm U_V$ show that the BL model is validated across the entire boundary layer, whereas the CP and MK models failure is confined to the mid-region of the boundary layer. The plots of the $|E| + U_V$ comparisons for the three models show that the BL model maximum values are less than 4 percent U_e, except for the near-wall region where the values increase to 7 percent U_e at the wall, whereas the CP and MK models have large values (8 percent U_e) at the wall and in the outer part and relatively small values (3 percent U_e) for the near-wall region.

5 Summary and Conclusions

A new approach to CFD validation is developed that gives proper consideration to both the experimental and simulation uncertainties. The comparison error E is defined as the difference between the data D (benchmark) and simulation prediction value S and thus includes the errors associated with the experimental data and the errors associated with the simulation. The validation uncertainty is defined as the combination of the uncertainties in the experimental data and the portion of the uncertainties in the CFD prediction that can be estimated. Estimates for U_{SN}, the simulation numerical uncertainty, are obtained through verification procedures involving parametric, convergence, and order-of-accuracy studies. The verification procedures are discussed in detail. U_D includes contributions from the independent and dependent variable uncertainties and is obtained using established uncertainty analysis procedures.

The validation uncertainty U_V sets the level at which the validation can be achieved. The criterion for validation is that $|E|$ must be less than U_V. The acceptable level of validation is set by program objectives. If $|E|$ is greater than U_V, than validation is not accomplished and the magnitude and sign of E can be valuable is designing strategies to improve the mathematical modeling. When a validation effort involves multiple codes and/or models, additionally the comparisons should include the quantity $|E| + U_V$. Validation of the prediction of trends involves reduction in uncertainties, at least for the experiments, through inclusion of correlated bias errors.

Example results of verification/validation are presented both for a single CFD code and for a comparison of multiple turbulence models. A RANS CFD code is used for two applications for which numerical and experimental uncertainty analyses are available: marine-propulsor flow and two-dimensional turbulent flat-plate boundary-layer flow. The former represents a practical geometry and is used for the single CFD code validation example, whereas the later represents an idealized geometry and is used for the comparison of turbulence models example. The results demonstrate the usefulness of the proposed validation strategy.

The authors recommend the adoption of this approach for CFD code validation. It will be useful both in guiding future developments in CFD through validation studies and in the transition of CFD codes to design through establishment of credibility and ultimately certification once procedures for the latter are established. Realization of the full potential of the approach requires refinements through applications using various CFD methods and data sets (benchmarks), especially with regard to verification procedures. The authors also recommend that general verification procedures be established similar to those used here, but generalized to encompass broad categories of simulation methods and perhaps additional error sources in those methods.

Acknowledgments

This research was sponsored by the Office of Naval Research under grants N00014-96-1-0018 and N00014-97-1-0014 under the administration of Dr. E. P. Rood. The authors gratefully acknowledge Dr. Rood and other colleagues who made significant contributions through many discussions. In particular, Prof. W. G. Steele's comments on an early draft led to some important modifications. Mr. B. Chen and Dr. M. Sreedhar generously provided the example results. The criticisms and suggestions of the six reviewers were invaluable and resulted in considerable improvements to the initial manuscript. The computations were performed using the NAVO Oceanographic Office supercomputers.

References

American Institute of Aeronautics and Astronautics (AIAA), 1994, "Editorial Policy Statement on Numerical Accuracy and Experimental Uncertainty," *AIAA Journal,* Vol. 32, No. 1.

American Institute of Aeronautics and Astronautics (AIAA), 1997, "Guide to the Assessment of Uncertainty in Computational Fluid Dynamics Simulations," AIAA G-077, Jan. 1997 draft of a recommended practices document.

American Society of Mechanical Engineers (ASME), 1993, "Editorial Policy Statement on the Control of Numerical Accuracy," ASME JOURNAL OF FLUIDS ENGINEERING, Vol. 115, No. 3.

Baldwin, B. S., and Lomax, H., 1978, "Thin Layer Approximation and Algebraic Model for Separated Turbulent Flows," AIAA Paper AIAA 78-257.

Beard, R. M., and Landrum, D. B., 1996, "Effects of Kinetic Rate Uncertainty on the Predicted Performance of Small Hydrogen Thrusters," AIAA Paper AIAA-96-2856.

Blottner, F. G., 1990, "Accurate Navier-Stokes Results for the Hypersonic Flow over a Spherical Nosetip," *Journal of Spacecraft and Rockets,* Vol. 27, No. 2.

Brown, K. K., Coleman, H. W., and Butas, J. P., 1994, "Impact of Uncertainty on Modeling and Testing of the Space Shuttle Main Engine," ASME FED-Vol. 205.

Brown, K. K., Coleman, H. W., Steele, W. G., and Taylor, R. P., 1996, "Evaluation of Correlated Bias Error Effects in Experimental Uncertainty Analysis," *AIAA Journal,* Vol. 34, No. 5.

Celik, I., Chen, C. J., Roache, P. J., and Scheuerer, G., eds., 1993, *Quantification of Uncertainty in Computational Fluid Dynamics,* ASME FED-Vol. 158.

Chen, H. C., and Patel, V. C., 1988, "Near-Wall Turbulence Models for Complex Flows Including Separation," *AIAA Journal,* Vol. 26, No. 6, pp. 641–648.

Chen, B., 1996, "Computational Fluid Dynamics of Four-Quadrant Marine-Propulsor Flow," M.S. thesis, Dept. of Mechanical Engineering, University of Iowa.

Chen, B., and Stern, F., 1997, "Computation of Marine-Propulsor Flow—Part 1: Design Condition," in preparation.

Coleman, H. W., 1996, "Uncertainty Considerations in Validating CFD Codes with Experimental Data," AIAA Paper AIAA-96-2027.

Coleman, H. W., and Steele, W. G., 1989, *Experimentation and Uncertainty Analysis for Engineers,* Wiley, New York.

Coleman, H. W., and Steele, W. G., 1995, "Engineering Application of Uncertainty Analysis," *AIAA Journal,* Vol. 33, No. 10.

Coleman, H. W., Steele, W. G., and Taylor, R. P., 1995, "Implications of Correlated Bias Uncertainties in Single and Comparative Tests," ASME JOURNAL OF FLUIDS ENGINEERING, Vol. 117, No. 4.

Gresho, P. M., and Taylor, C., 1994, "Editorial," *International Journal of Numerical Methods in Fluids,* Vol. 19, No. 12.

International Association of Hydraulic Research (IAHR), 1994, "Guidelines for Documenting the Validity of Computational Modeling Software."

International Towing Tank Conference (ITTC), 1996, 21st ITTC Proceedings, Bergen, Norway.

Jessup, S. D., 1989, "An Experimental Investigation of Viscous Aspects of Propeller Blade Flow," Ph.d. Dissertation, School of Engineering and Architecture, The Catholic University of America.

Jessup, S. D., 1994, "Propeller Blade Flow Measurements Using LDV," ASME Fluids Engineering Division Summer Meeting, Lake Tahoe, NV.

Longo, J., Huang, H. P., and Stern, F., 1998, "Solid-Fluid Juncture Boundary Layer and Wake," to appear in *Experiments in Fluids.*

Marvin, J. G., 1995, "Perspective on Computational Fluid Dynamics Validation," *AIAA Journal,* Vol. 33, No. 10.

Mehta, U. B., 1996, "Guide to Credible Computational Fluid Dynamics Simulations," *Journal of Propulsion and Power,* Vol. 12, No. 5.

Melnik, R. E., Siclari, M. J., Barber, T. J., and Verhoff, A., "A Process for Industry Certification of Physical Simulation Codes," AIAA Paper 94-2235.

Myong, H. K., and Kasagi, N., 1991, "Prediction of Anisotropy of the Near-Wall Turbulence with an Anisotropic Low-Reynolds Number k-ϵ Model," ASME JOURNAL OF FLUIDS ENGINEERING, Vol 112.

Oberkampf, W. L., Blottner, F. G., and Aeschliman, D. P., 1995, "Methodology for Computational Fluid Dynamics Code Verification/Validation," AIAA Paper AIAA-95-2226.

Roache, P. J., 1997, "Quantification of Uncertainty in Computational Fluid Dynamics," *Annual Review of Fluid Mechanics,* Vol. 29, pp. 123--160.

Rood, E. P., 1996, "Validation Strategy for "RANS" Computational Ship Hydrodynamics," Second International Conference on Hydrodynamics, Hong Kong.

Sreedhar, M., and Stern, F., 1997, "Non-Linear Eddy-Viscosity Turbulence Model for Solid/Free-Surface Boundary Layer and Wake," 3rd Forum on Advances in Num. Modeling of Free Surface and Interface Fluid Dynamics, ASME FED Summer Meeting, Vancouver, Canada.

Stern, F., Zhang, D. H., Chen, B., Kim, H. T., and Jessup, S., 1994, "Computation of Viscous Marine Propulsor Blade and Wake Flow," *Proc. 20th ONR Symposium on Naval Hydro.,* Santa Barbara, CA.

Stern, F., Paterson, E. G., and Tahara, Y., 1996, "CFDSHIP-IOWA: Computational Fluid Dynamics Method for Surface-Ship Boundary Layers and Wakes and Wave Fields," Iowa Institute of Hydraulic Research, University of Iowa, IIHR Report No. 381.

Zingg, D. W., 1992, "Grid Studies for Thin-Layer Navier-Stokes Computations of Airfoil Flowfields," *AIAA Journal,* Vol. 30, No. 10.

A Perspective on the Construction of Nonsymmetric Uncertainty Intervals

Paul K. Maciejewski
Visiting Assistant Professor,
University of Connecticut,
Department of Mechanical Engineering,
191 Auditorium Road, J-139,
Storrs, CT 06269-3139

This paper presents a new method for constructing nonsymmetric uncertainty intervals, one that is based on estimates of "expected values" and "variances" associated with deterministic errors that one constructs from estimates of "upper bias limits" and "lower bias limits" for measured variables. On the assumption that upper bias limits and lower bias limits specified by the user correspond to 95 percent confidence intervals for normally distributed deterministic errors, the uncertainty intervals determined by the new method reduce to approximate 95 percent confidence intervals for the true value of the measured variables.

Introduction

The need for the construction of a nonsymmetric uncertainty interval arises in practice when (1) one believes, in one's experience and judgment, that the observed value of a measured variable is expected to be either strictly greater or strictly less than its true value, and (2) one lacks the information that would be required to correct the observed value for a known bias. Under these circumstances, and in the spirit of the ANSI/ASME *Standard for Measurement Uncertainty,* ANSI/ASME PTC 19.1-1985 (1986), one ought to report the observed value of the measured variable without correction and construct a nonsymmetric uncertainty interval to reflect one's belief that the observed value is a biased estimate of the true value.

Given the occasional need for the construction of nonsymmetric uncertainty intervals, what is the most reasonable method for constructing them? The method for constructing nonsymmetric uncertainty intervals that ANSI/ASME PTC 19.1-1985 (1986) presents introduces considerable ambiguity in the interpretation of its end result: What is the meaning of a "total uncertainty" that is determined by means of a root-sum-square combination of a random component of uncertainty, which is always a random variable determined by the data, and a deterministic component of uncertainty, which is often merely a number selected by the user of the instrument? The ISO *Guide to the Expression of Uncertainty in Measurement* (1993), while it does not advocate the construction of nonsymmetric uncertainty intervals, does advocate the inclusion of a "variance" associated with nonsymmetric sources of uncertainty for the purpose of determining a "combined variance" that is employed in the construction of symmetric uncertainty intervals. If it were possible to reduce the estimation of nonsymmetric uncertainty to the estimation of a variance associated with a distribution of deterministic errors, then it would be possible to construct a method for determining a total variance contributing to the uncertainty of a measurement which may be simply interpreted as the combination of a variance associated with deterministic errors and the variance associated with random errors.

The aim of this paper is to present a new method for the construction of non-symmetric uncertainty intervals, one which, in the spirit of the ISO *Guide to the Expression of Uncertainty in Measurement* (1993), reduces the estimation of nonsymmetric uncertainty to the estimation of a variance associated with a distribution of deterministic errors. This work is relevant to the ASME *Journal of Fluids Engineering* through its "Policy on Reporting Uncertainties in Experimental Measurements and Results" (1991).

As a historical note, ANSI/ASME PTC 19.1-1985 (1986) does not attribute its approach to the construction of nonsymmetric uncertainty intervals to any prior publication. Kline and McClintock (1953) do not address the topic of the construction of nonsymmetric uncertainty intervals. Moffat (1982) recognizes the origins of the need for the construction of nonsymmetric uncertainty intervals, but, rather than presenting and defending a method for constructing nonsymmetric uncertainty intervals, introduces the notion of a "zero-centered experiment" and expresses a desire to eliminate the need for nonsymmetric uncertainty intervals through the process of "debugging" an experiment. Abernethy and Ringhiser (1985) presents the method for constructing nonsymmetric uncertainty intervals adopted by ANSI/ASME PTC 19.1-1985 (1986) without further elaboration of its properties.

Summary of ANSI/ASME Method

ANSI/ASME PTC 19.1-1985 (1986) recommends the following procedure for constructing a nonsymmetric uncertainty interval for a measured variable:

Step (i): Estimate an "upper bias limit," B^+, and a "lower bias limit," B^-.

Step (ii): Determine the "upper uncertainty," U^+, and the "lower uncertainty," U^-, as follows:

$$U^+ = [(B^+)^2 + (t_{95}S_X)^2]^{1/2} \quad \text{(PTC-1}a\text{)}$$

$$U^- = [(B^-)^2 + (t_{95}S_X)^2]^{1/2} \quad \text{(PTC-1}b\text{)}$$

Step (iii): Express an uncertainty interval providing 95 percent "coverage" as follows:

$$(X - U^-, X + U^+) \quad \text{(PTC-2)}$$

On the surface, the method for constructing nonsymmetric uncertainty intervals recommended by ANSI/ASME PTC 19.1-1985 (1986) appears relatively clear. However, in Step (i), the user is asked to estimate something called a "bias limit" without being told what is meant by the term bias limit. Is an upper bias limit the largest possible value for the deterministic error, is it some upper limit on probable values of the deterministic error, or is it something else? Given that the definition of bias limit is not precisely given in ANSI/ASME PTC 19.1-1985 (1986), the interpretation of U^+ and U^- is ambiguous.

Contributed by the Fluids Engineering Division for publication in the JOURNAL OF FLUIDS ENGINEERING. Manuscript received by the Fluids Engineering Division March 18, 1994; revised manuscript received July 17, 1997. Associate Technical Editor: D. S. Stock.

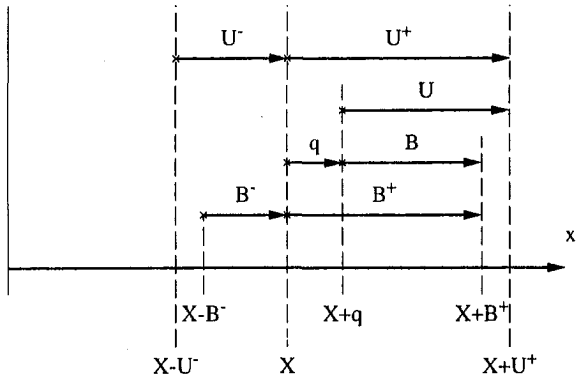

Fig. 1 Relation between parameters used to characterize nonsymmetric uncertainty in a measured variable

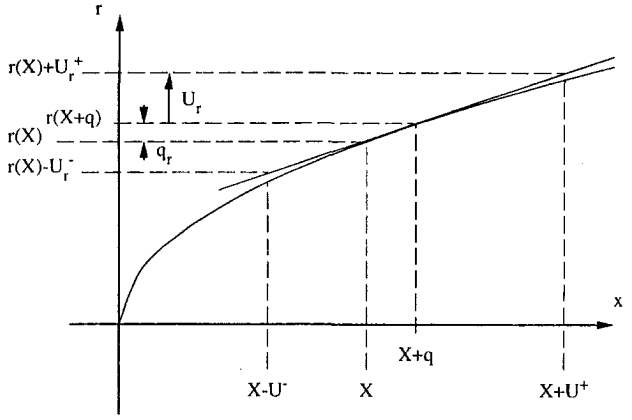

Fig. 2 Relation between parameters used to characterize nonsymmetric uncertainty in a derived result

A New Method for Constructing Nonsymmetric Uncertainty Intervals. The method for constructing a nonsymmetric uncertainty interval given below reduces the estimation of nonsymmetric uncertainty to the estimation of an "expected value" and a "variance" associated with a distribution of deterministic errors. Application of the method is also extended to the case of constructing a nonsymmetric uncertainty interval for a derived result.

Nonsymmetric Systematic Uncertainty Interval for a Measured Variable. The following procedure should be employed for constructing a nonsymmetric uncertainty interval for the measured variable (see Fig. 1):

Step (i): Estimate an upper bias limit, B^+, and a lower bias limit, B^-, such that one may expect the deterministic error to fall on the interval $(-B^-, B^+)$ with 95 percent confidence.

Step (ii): Estimate the "expected value" of the deterministic error, q, as follows:

$$q = (B^+ - B^-)/2 \qquad \text{(M-1)}$$

Step (iii): Estimate twice the "standard deviation" of the deterministic error, B, as follows:

$$B = (B^+ + B^-)/2 \qquad \text{(M-2)}$$

Step (iv): Estimate the total uncertainty for the measured variable as follows:

$$U = t_{95}[(B/2)^2 + (S_X)^2]^{1/2} \qquad \text{(M-3)}$$

Step (v): Determine the upper uncertainty, U^+, and the lower uncertainty, U^-, as follows:

$$U^+ = U + q \qquad \text{(M-4}a\text{)}$$

$$U^- = U - q \qquad \text{(M-4}b\text{)}$$

Step (vi): Express an uncertainty interval providing 95 percent "coverage" as follows:

$$(X - U^-, X + U^+) \qquad \text{(M-5)}$$

In Step (iii), B estimates twice the standard deviation associated with a distribution of deterministic errors assuming that the distribution is approximately normal (since the "observed" value of a random variable that is normally distributed is expected to fall within approximately two standard deviations of its expected value with 95 percent confidence). Consequently, in Step (iv), $(B/2)^2$ estimates a variance associated with the deterministic component of uncertainty, and it is directly combined with the variance associated with the random component of uncertainty, $(S_X)^2$. Indeed, this is the primary difference between the newly proposed method and the method given in ANSI/ASME PTC 19.1-1985 (1986): While the method given in ANSI/ASME PTC 19.1-1985 (1986) combines an "uncertainty" associated with deterministic error, either B^+ or B^-, with an uncertainty associated with random error, $t_{95}S_X$, [see Eq. (PTC-1)], the newly proposed method combines a variance associated with the nonsymmetric deterministic component of uncertainty, $(B/2)^2$, with the variance associated with the random component of uncertainty, $(S_X)^2$, [see Eq. (M-3)].

Nonsymmetric Systematic Uncertainty Interval for a Derived Result. The following procedure should be employed for propagating the non-symmetric uncertainties in a set of measured variables to a derived result (see Fig. 2):

Step (i): Determine X_i, U_i, and q_i for each measured

Nomenclature

B = twice the "standard deviation" of the deterministic error
$(B/2)^2$ = "variance" associated with deterministic component of uncertainty
B^+ = "upper bias limit"
B^- = "lower bias limit"
q = "expected value" of the deterministic error
r = result derived from a set of measured variables
S_X = standard deviation associated with random component of uncertainty
$(S_X)^2$ = variance associated with random component of uncertainty
t_{95} = value from t-distribution corresponding to 95 percent confidence
$t_{95}S_X$ = random component of uncertainty
U = uncertainty
U^+ = "upper uncertainty"
U^- = "lower uncertainty"
X = observed (mean) value of a measured variable
β = deterministic error
δ = total error, $\delta = \beta + \epsilon$
ϵ = random error
μ = true variance
σ^2 = true variance
θ = sensitivity coefficient

variable X_i that contributes to the determination of the derived result, $r(X_1, X_2, \ldots, X_n)$.

Step (ii): Define q_r as follows:

$$q_r = r(X_1 + q_1, X_2 + q_2, \ldots, X_n + q_n) - r(X_1, X_2, \ldots, X_n). \quad \text{(R-1)}$$

Step (iii): Determine the sensitivity coefficient, θ_i, for each measured variable X_i that contributes to the derived result. If a sensitivity coefficient depends on the values of any measured variables, i.e., $\theta_i = \theta_i(X_1, X_2, \ldots, X_n)$, then it should be evaluated at the point $(X_1 + q_1, X_2 + q_2, \ldots, X_n + q_n)$.

Step (iv): Estimate the total uncertainty for the derived result, U_r, as follows:

$$U_r = [(\theta_1 U_1)^2 + (\theta_2 U_2)^2 + \ldots + (\theta_n U_n)^2]^{1/2} \quad \text{(R-2)}$$

Step (v): Determine the "upper uncertainty", U_r^+, and the "lower uncertainty", U_r^-, as follows:

$$U_r^+ = U_r + q_r \quad \text{(R-3}a\text{)}$$

$$U_r^- = U_r - q_r \quad \text{(R-3}b\text{)}$$

Step (vi): Express an uncertainty interval providing 95 percent "coverage" as follows:

$$[r(X_1, X_2, \ldots, X_n) - U_r^-, \; r(X_1, X_2, \ldots, X_n) + U_r^+] \quad \text{(R-4)}$$

An Example

The present section compares, by means of an example, the use of the method for constructing a nonsymmetric uncertainty interval given in ANSI/ASME PTC 19.1-1985 (1986) to the use of the newly proposed method. This example illustrates that the two methods not only result in the construction of two different, i.e., incongruent, intervals expressing the total uncertainty in the measured variable, but that they also offer different interpretations of the deterministic component of uncertainty.

Problem Statement. Suppose a thermocouple is being used to measure the temperature of a gas stream, but the user of the thermocouple believes there may be a tendency for the thermocouple to provide a temperature reading that is lower than the actual gas temperature due to a radiative heat transfer mechanism. The user does not have enough information to properly correct the thermocouple reading for this effect, but wishes to account for it in an uncertainty analysis. From a sample of more than 30 readings using the thermocouple (i.e., $t_{95} \approx 2$), the user finds that $X = 534.7$°C and $S_X = 2.4$°C. Furthermore, there is a known, symmetric, deterministic component of uncertainty of 4°C associated with the quality of the thermocouple wire. If the user believes that the true gas temperature may be as much as 10°C higher than X due to radiation effects, then how should the user specify a nonsymmetric uncertainty interval which accounts for this non-symmetric component of deterministic uncertainty?

Application of the Method Given in ANSI/ASME PTC 19.1-1985 (1986). Before one can apply the method given in ANSI/ASME PTC 19.1-1985 (1986), one must answer the following question: What is the meaning of the term bias limit? More specifically, how does one translate the statement "the user believes that the true gas temperature may be as much as 10°C higher than X" into an assessment of an upper bias limit and a lower bias limit? Once one settles the meaning of the term bias limit, then the application of the method given in ANSI/ASME PTC 19.1-1985 (1986) is as follows:

Step (i): Estimate B^+ and B^-. In this case, the user may choose $B^+ = 10$°C and $B^- = 0$°C for the nonsymmetric component of the deterministic uncertainty, which is then combined with the symmetric component of the deterministic uncertainty as follows: $B^+_{\text{total}} = [(10)^2 + (4)^2]^{1/2} = 10.8$°C and $B^-_{\text{total}} = [(0)^2 + (4)^2]^{1/2} = 4$°C.

Step (ii): Estimate U^+ and U^-. In this case, $U^+ = [(B^+_{\text{total}})^2 + (t_{95}S_X)^2]^{1/2} = [(10.8)^2 + (2 \times 2.4)^2]^{1/2} = 11.8$°C and $U^- = [(B^-_{\text{total}})^2 + (t_{95}S_X)^2]^{1/2} = [(4)^2 + (2 \times 2.4)^2]^{1/2} = 6.2$°C.

Step (iii): Express the uncertainty interval, $(X - U^-, X + U^+)$. In this case, $(X - U^-, X + U^+) = (528.5$°C, 546.5°C).

Application of the New Method. In the application of the newly proposed method for the construction of a nonsymmetric uncertainty interval, the user need only make a judgment as to the interval on which the user expects the deterministic error to fall with 95 percent confidence. The application of the newly proposed method is as follows:

Step (i): Estimate B^+ and B^-. In this case, the user may choose $B^+ = 10$°C and $B^- = 0$°C.

Step (ii): Estimate q. In this case, $q = (10$°C $- 0$°C$)/2 = 5$°C.

Step (iii): Estimate "B" for the nonsymmetric component of uncertainty, then combine it with "B" for the symmetric component of uncertainty. In this case, $B_{\text{non-symmetric}} = (10$°C $+ 0$°C$)/2 = 5$°C and $B_{\text{total}} = [(5)^2 + (4)^2]^{1/2} = 6.4$°C.

Step (iv): Estimate U. In this case, $U = t_{95}\,[(B_{\text{total}}/2)^2 + (S_X)^2]^{1/2} = 2[(\{6.4$°C$\}/2)^2 + (2.4$°C$)^2]^{1/2} = 8$°C.

Step (v): Estimate U^+ and U^-. In this case, $U^+ = U + q = 8$°C $+ 5$°C $= 13$°C, and $U^- = U - q = 8$°C $- 5$°C $= 3$°C.

Step (vi): Express the uncertainty interval, $(X - U^-, X + U^+)$. In this case, $(X - U^-, X + U^+) = (531.7$°C, 547.7°C).

Discussion

The preceding example shows that the two methods for constructing nonsymmetric uncertainty intervals, the one method given in ANSI/ASME PTC 19.1-1985 (1986) and the other method proposed here, can give two different uncertainty intervals for the same problem, i.e., for the same data. Naturally, this raises the following question: Which method gives the correct result? Strictly speaking, neither method gives the "correct result", if by correct result one means an objective assessment of a 95 percent confidence interval for the true value of the measured variable. The fact that each method allows a subjectively based assessment of a deterministic component of uncertainty precludes the possibility that either method can guarantee the correct result.

However, the newly proposed method does have one distinct advantage over the method given in ANSI/ASME PTC 19.1-1985 (1986): On the assumption that the interval $(-B^-, B^+)$ specified by the user corresponds to a central 95 percent confidence interval for a normally distributed deterministic error, the uncertainty interval determined by the method reduces to an approximate 95 percent confidence interval for the true value of the measured variable. This conclusion follows directly from the manner in which one constructs U^+ and U^- in the newly

proposed method (since if the deterministic error, β, is normally distributed with mean μ_β and variance σ_β^2, and if the random error, ϵ, is also normally distributed with mean zero and variance σ_ϵ^2, then the total error, $\delta = \beta + \epsilon$, is normally distributed with mean $\mu_\delta = \mu_\beta$ and variance $\sigma_\delta^2 = \sigma_\beta^2 + \sigma_\epsilon^2$). Furthermore, Steele et al. (1996) demonstrate and confirm, by means of Monte Carlo simulations, that the newly proposed method for constructing nonsymmetric uncertainty intervals leads to the construction of approximate 95 percent confidence intervals when the intervals $(-B^-, B^+)$ correspond to central 95 percent confidence intervals for normally distributed deterministic errors. Although the assumption that the intervals $(-B^-, B^+)$ correspond to central 95 percent confidence intervals for normally distributed deterministic errors cannot be strictly valid, the method given in ANSI/ASME PTC 19.1-1985 (1986) offers no interpretation which reduces its resulting uncertainty interval to an approximate 95 percent confidence interval.

Conclusion

This paper has presented a new method for constructing nonsymmetric uncertainty intervals, one which constructs a subjectively based estimate of a variance associated with the deterministic component of uncertainty and combines it directly with the variance associated with the random component of uncertainty. On the assumption that the interval $(-B^-, B^+)$ specified by the user corresponds to a central 95 percent confidence interval for a normally distributed deterministic error, the uncertainty interval determined by the new method reduces to an approximate 95 percent confidence interval for the true value of the measured variable.

References

Abernethy, R. B., and Ringhiser, B., 1985, "The History and Statistical Development of the New ASME-SAE-AIAA-ISO Measurement Uncertainty Methodology," AIAA-85-1403, American Institute of Aeronautics and Astronautics, New York.

Anon., 1986, *Measurement Uncertainty,* ANSI/ASME PTC 19.1-1985, American Society of Mechanical Engineers, New York.

Anon., 1991, "Journal of Fluids Engineering Policy on Reporting Uncertainties in Experimental Measurements and Results," ASME JOURNAL OF FLUIDS ENGINEERING, Vol. 113, pp. 313–314.

Anon., 1993, *Guide to the Expression of Uncertainty in Measurement,* International Organization for Standardization, Geneva, Switzerland.

Kline, S. J., and McClintock, F. A., 1953, "Describing Uncertainties in Single-Sample Experiments," *Mechanical Engineering,* Vol. 75, pp. 3–8.

Moffat, R. J., 1982, "Contributions to the Theory of Single-Sample Uncertainty Analysis," ASME JOURNAL OF FLUIDS ENGINEERING, Vol. 104, pp. 250–258.

Steele, W. G., Maciejewski, P. K., James, C. J., Taylor, R. P., and Coleman, H. W., 1996, "Asymmetric Systematic Uncertainties in the Determination of Experimental Uncertainty," *AIAA Journal,* Vol. 34, pp. 1458–1463.

Interaction of a Steady Approach Flow and a Circular Cylinder Undergoing Forced Oscillation

Jianfeng Zhang[1]
Research Assistant.
Department of Mechanical Engineering.

Charles Dalton
Associate Dean of Engineering.

University of Houston,
Houston, TX 77204-4814

This paper presents a numerical study on the interaction of a steady approach flow and the forced transverse oscillation of a circular cylinder. The two-dimensional stream-function/vorticity formulation of the Navier-Stokes equations is solved by a semi-implicit finite-difference scheme. Calculations for flows with different amplitude (a) and frequency (f_c) of the oscillation of the cylinder show a strong effect of the oscillation when f_c is close to f_{so}, the vortex shedding frequency, of the stationary cylinder. Lock-on of vortex shedding, distinct flow patterns, and increase in both drag and lift coefficients from those of a stationary cylinder are observed for Reynolds number Re = 200, a/R (R is the radius of the cylinder) from 1.0 to 2.0, f_c/f_{so} from 0.85 to 1.7. For Re = 855, a/R = 0.26, a large eddy simulation model for turbulent flow is used. The results at Re = 855 and a/R = 0.26 show that lock-on has occurred for $f_c/f_{so} \geq 0.85$. The behavior of the drag and lift coefficients is seen to be influenced by the lock-on phenomenon.

Introduction

The unsteady flow past a bluff body has received significant attention because it represents one of the most common problems in fluid/structure interaction. The ability to describe fluid-dynamic loading on a variety of engineering structures, such as marine risers, TLP cables, and subsurface pipelines, is very important in the engineering design of these components of a structure. However, the ability to calculate the steady approach flow past bluff bodies, such as circular cylinders, is limited to numerical solutions at Reynolds numbers low enough for the flow to be viscosity dominated, except for a few higher Reynolds number cases which involved either some form of turbulence modeling or a direct numerical simulation. Even though the existing numerical solutions are somewhat limited, they do serve as a valuable means of studying flow details presently not available through experimental studies.

In the following discussion, we will focus attention on a transversely vibrating circular cylinder in a steady approach flow and on the mechanics of vortex shedding and unsteady separation associated with the viscosity-dominated flow. We will examine the flow past stationary circular cylinders at several Reynolds numbers, producing vortex shedding which occurs at a frequency, f_{so}, consistent with experimental data. The cylinder will then be allowed to oscillate transversely at several frequencies, f_c, (which may be greater or less than the fixed-cylinder vortex-shedding frequency, f_{so}). One of the objectives of this numerical study is to examine the flow patterns which result when f_c and f_{so} are approximately equal. We will investigate the modification of the near wake structure for oscillating cylinders for approximately equal values of f_c and f_{so}. Our approach will be to use the vorticity/stream-function approach in describing the problem, similar to Lecointe and Piquet (1989). Earlier studies have used the velocity/pressure description to represent the solution, e.g., Hurlbut et al. (1982), Chilukuri (1987), and Tamura et al. (1988). A recent study by Hall and Griffin (1993) used a spectral-element direct numerical simulation to represent a viscous flow solution with vortex shedding and lock-on in a perturbed flow. Copeland and Cheng (1995) also did a direct numerical solution of a two-dimensional incompressible laminar flow past a transversely oscillating cylinder up to Re = 200. They found that chaotic solutions, due to mode competition, may occur for frequencies of oscillation just beyond the lock-in region. The critical value of Re, for the onset of vortex shedding, was found to be approximately 50.

In a flow visualization study, Ongoren and Rockwell (1988) examined the flow fields produced for different cylinders subjected to controlled transverse oscillations to an incident flow. The study of Ongoren and Rockwell provides the basis for our comparison to experimental results and these results will be discussed in more detail then.

Analytical Representation

We take the problem to be the two-dimensional flow of an incompressible fluid past a circular cylinder which may or may not be oscillating transverse to the direction of the steady approach flow. The effects of turbulence are included through a large eddy simulation (LES) for the higher Reynolds number case. The dimensional equations to be solved are the vorticity transport equation,

$$\frac{\partial \omega}{\partial t} + u\frac{\partial \omega}{\partial r} + \frac{v}{r}\frac{\partial \omega}{\partial \theta} = (\nu + \nu_t)\left[\frac{\partial^2}{\partial r^2} + \frac{1}{r}\frac{\partial}{\partial r} + \frac{1}{r^2}\frac{\partial^2}{\partial \theta^2}\right]\omega, \quad (1)$$

and the equation relating vorticity ω and stream function ψ,

$$\nabla^2\psi = -\omega, \quad (2)$$

where

$$u = \frac{1}{r}\frac{\partial \psi}{\partial \theta}, \quad v = \frac{-\partial \psi}{\partial r}, \quad \text{and} \quad \omega = \frac{\partial}{\partial r} - \frac{1}{r}\frac{\partial u}{\partial \theta}. \quad (3)$$

In Eqs. (1), (2), and (3), r and θ are the dimensional coordinates in the physical plane, t is the dimensional time, ν is the kinematic viscosity, and ν_t is the turbulent eddy viscosity. The turbulent eddy viscosity is determined using the Smagorinsky model,

[1] Now with Halliburton Energy Services, Houston, TX.

Contributed by the Fluids Engineering Division for publication in the JOURNAL OF FLUIDS ENGINEERING. Manuscript received by the Fluids Engineering Division December 6, 1994; revised manuscript received July 8, 1997. Associate Technical Editor: S. P. Vanka.

$$\nu_t = (C_s\Delta)^2\sqrt{2S_{ij}S_{ij}}\,, \tag{4}$$

where C_s is the Smagorinsky model constant, Δ is the cube root of the product of the mesh sizes, and S_{ij} is the strain rate tensor. The model constant C_s was taken to 0.15 for these calculations; this value was selected after several trials with similar values. For computational purposes, we define a new coordinate system, also used by Justesen (1991), by

$$r = \alpha e^{\xi} + (1 - \alpha), \tag{5}$$

where ξ and η are the transformed variables.

The cylinder radius, R, and the steady approach velocity, U_∞, are the length and velocity scales respectively for nondimensionalization. The cylinder radius is set to a value of unity. We now define $\tau = U_\infty t/R$, $\mathrm{Re} = 2U_\infty R/\nu$, $\mathrm{Re}_t = 2U_\infty R/\nu_t$, $\tilde{\psi} = \psi/U_\infty R$, $\tilde{\omega} = R\omega/U_\infty$, $\tilde{u} = u/U_\infty$, and $\tilde{v} = v/U_\infty$. Equations (1) and (2) become

$$\frac{\partial\tilde{\omega}}{\partial\tau} + \frac{\tilde{u}}{r\xi}\frac{\partial\tilde{\omega}}{\partial\xi} + \frac{\tilde{v}}{\pi}\frac{\partial\tilde{\omega}}{\partial\eta} = \left(\frac{2}{\mathrm{Re}} + \frac{2}{\mathrm{Re}_t}\right)\nabla^2\tilde{\omega} \tag{6}$$

$$\text{and} \quad \nabla^2\psi = -\tilde{\omega}, \tag{7}$$

where

$$\nabla^2 = \frac{1}{r_\xi^2}\frac{\partial^2}{\partial\xi^2} + d(\xi)\frac{\partial}{\partial\xi} + \frac{1}{(r\pi)^2}\frac{\partial^2}{\partial\eta^2},$$

$$\tilde{u} = \frac{1}{\pi r}\frac{\partial\psi}{\partial\eta}, \quad \tilde{v} = \frac{-1}{r_\xi}\frac{\partial\psi}{\partial\xi},$$

$$r_\xi = \frac{dr}{\partial\xi} \quad \text{and} \quad d(\xi) = \frac{1}{r_\xi}\left(\frac{1}{r} - \frac{1}{r_\xi^2}\frac{d^2r}{\partial\xi^2}\right). \tag{8}$$

The boundary conditions can be defined as follows: On the surface of the cylinder, we have both a constant value of $\tilde{\psi}$ and the zero normal velocity condition (relative velocity),

$$\tilde{\psi}(1, \eta, \tau) = 0 \quad \text{and} \quad \frac{\partial\tilde{\psi}}{\partial\eta}(1, \eta, \tau) = 0. \tag{9}$$

The flow field at infinity is satisfied by

$$\tilde{\psi}(\xi_\infty, \eta, \tau) = \left(r(\xi_\infty) - \frac{1}{r(\xi_\infty)}\right)(\sin\pi\eta + U_{\mathrm{cyl}}(\tau)\cos\pi\eta) \tag{10}$$

and

$$\frac{D\tilde{\omega}}{Dt}(\xi_\infty, \eta, \tau) = 0, \tag{11}$$

where $U_{\mathrm{cyl}}(\tau)$ is the nondimensional velocity corresponding to a sinusoidal transverse oscillation with amplitude a and frequency f_c.

The Dirichlet form of the outflow boundary condition, given by Eq. (10), is used in preference to the Neumann form. The Dirichlet condition has been found to represent the steady approach flow solution more accurately while the Neumann condition is more accurate for the unsteady (oscillating) flow case.

Finite-Difference Representation

Equation (5) will be solved using a semi-implicit second-order Adams-Bashforth (AB2) method and the Crank-Nicolson (CN) method for the diffusion terms. We have dropped the symbol $\sim$ which represents a nondimensional variable. Henceforth, all variables are dimensionless. Thus, the finite-difference form of Eq. (6) becomes

$$\frac{\omega_{ij}^{n+1} - \omega_{ij}^n}{\Delta t} = \frac{-1}{2}(3N^n - N^{n-1})_{ij} + \left(\frac{2}{\mathrm{Re}} + \frac{2}{\mathrm{Re}_t}\right)(\nabla^2\omega^{n+1} + \nabla^2\omega^n)_{ij}. \tag{12}$$

In Eq. (12), n represents the time level and ij represents the r_i, θ_j mesh point. Also, the term represented by N is the nonlinear (or convective) term from Eq. (1).

Second-order central differences are used on all spatial terms. No upwinding was used on the convective terms. The transformed version of Eq. (12) is

$$\left[1 - \frac{\Delta\tau}{\mathrm{Re}}\left(\frac{1}{r\xi^2}\frac{\partial^2}{\partial\xi^2} + d(\xi)\frac{\partial}{\partial\xi} + \frac{1}{(r\pi)^2}\frac{\partial^2}{\partial\eta^2}\right)\right](\omega_{ij}^{n+1} - \omega_{ij}^n) = -\frac{\Delta\tau}{2}(3N^n - N^{n-1})_{ij} + 2\Delta\tau\left(\frac{1}{\mathrm{Re}} + \frac{1}{\mathrm{Re}_t}\right)\nabla^2\omega_{ij}^n. \tag{13}$$

Within $0(\Delta\tau^2)$ accuracy, the left-hand side of Eq. (13) can be approximately factored as

$$\left[1 - \frac{\Delta\tau}{(r\pi)^2}\left(\frac{1}{\mathrm{Re}} + \frac{1}{\mathrm{Re}_t}\right)\right] \times \left[\frac{\partial^2}{\partial\eta^2} - \frac{\Delta\tau}{\mathrm{Re}}\left(\frac{1}{r\xi^2}\frac{\partial^2}{\partial\xi} + d(\xi)\frac{\partial}{\partial\xi}\right)\right](\omega_{ij}^{n+1} - \omega_{ij}^n). \tag{14}$$

Hence, Eq. (13) can be solved in the following sequence,

$$\left[1 - \frac{\Delta\tau}{(r\pi)^2}\left(\frac{1}{\mathrm{Re}} + \frac{1}{\mathrm{Re}_t}\right)\frac{\partial^2}{\partial\eta^2}\right]Q_{ij} = R_{ij} \tag{15}$$

and

$$\left[1 - \Delta\tau\left(\frac{1}{\mathrm{Re}} + \frac{1}{\mathrm{Re}_t}\right)\left(\frac{1}{r\xi^2}\frac{\partial^2}{\partial\xi^2} + d(\xi)\frac{\partial}{\partial\xi}\right)\right] \times (\omega_{ij}^{n+1} - \omega_{ij}^n) = Q_{ij}, \tag{16}$$

where R_{ij} is the right-hand side of Eq. (13). When standard central differencing is used, we solve two tridiagonal systems of equations. The boundary conditions on Q_{ij} in Eq. (15) are the periodic conditions in η. The boundary conditions for Eq. (16) are the surface vorticity values, which are unknown.

We now address the problem of the vorticity boundary condition. The usual way to treat the unknown boundary condition for ω^{n+1} (on the cylinder surface) in Eq. (16) is to lag it, i.e., use ω^n,

$$\omega_{\mathrm{wall}}^{n+1} = \omega_{\mathrm{wall}}^n + 0(\Delta\tau), \tag{17}$$

which was used by Justesen (1991). However, lagging introduces a first-order error in time.

Part of the process of the vorticity generation on the solid surface is the diffusion of the existing vorticity into the flow field. This description can be represented by the vorticity transport equation, Eq. (6), evaluated at the wall with the convective terms set to zero which, when put into finite-difference form, yields

$$\omega_{\mathrm{wall}}^{n+1} = \omega_{\mathrm{wall}}^n + 2\Delta\tau\left(\frac{1}{\mathrm{Re}} + \frac{1}{\mathrm{Re}_t}\right)\nabla^2\omega^n|_{\mathrm{wall}} + 0(\Delta\tau)^2. \tag{18}$$

After the stream function and vorticity have been obtained at the inner grid points at time step $n + 1$, we use extrapolation based on the Poisson equation and the no-slip velocity boundary

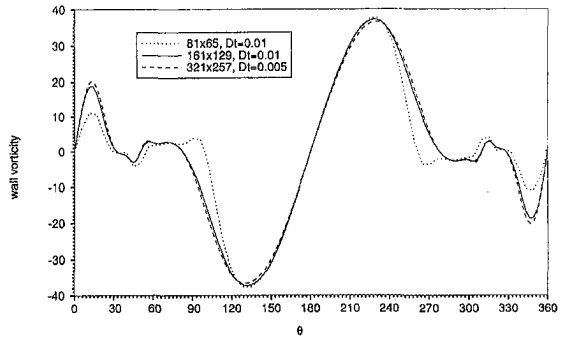

Fig. 1 Wall vorticity distributions at $\tau = 5$ for Re = 855 with three different mesh sizes and time steps, $\alpha = 1.0$, $r \times \theta \times \Delta\tau$, ····· 81 × 65 × 0.01; —— 161 × 129 × 0.01; ----- 321 × 257 × 0.005

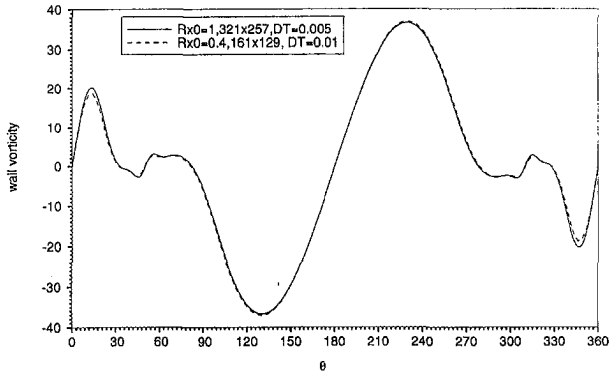

Fig. 2 Wall vorticity distributions at $\tau = 5$ for Re = 855 with two different mesh systems, $r \times \theta \times \Delta\tau$, —— $\alpha = 1$, 321 × 257 × 0.005; ----- $\alpha = 0.4$, 161 × 129 × 0.01

condition to update the wall vorticity. The appropriate expression is

$$\omega_1 = \frac{-r\xi_2^2\omega_2 + 6\psi_2/\Delta\xi^2}{r\xi_1^2(2 - r\xi_1^2 d_1\Delta\xi)}, \qquad (19)$$

with $i = 1$ representing the wall and d_1 is determined from $d(\xi)$ in Eq. (8) for $\xi = 0$. Because Eq. (19) represents the physical situation more accurately, it is expected to produce more accurate solutions than Eq. (17).

Results

We have developed solutions at two different Reynolds numbers, Re = 200 and 855, primarily to compare to the calculated results of Lecointe and Piquet (1989) and the experimental results of Ongoren and Rockwell (1988). First, we examine convergence of the solution. Figure 1 shows the evolution of the surface vorticity at Re = 855 for a progressively finer mesh for a coordinate transformation given by Eq. (4) with $\alpha = 1.0$. The converged solution is obtained for a grid of 321 × 257 (r by θ) and a time step of 0.0025 was necessary for stability. Figure 2 shows the result of applying the transformation with $\alpha = 0.4$. This transformation has the effect of concentrating mesh points near the surface of the cylinder. The net result of using Eq. (4) with $\alpha = 0.4$, as shown in Fig. 2, is a solution for a mesh size and time step of 161 × 129 and 0.01 that is just as accurate as the solution of mesh size and time step of 321 × 257 and 0.0025 with $\alpha = 1.0$. Thus, the transformation with $\alpha = 0.4$ has the capability of producing a solution as accurate as that developed with $\alpha = 1.0$, but with eight times less computational effort. Even though we haven't discussed convergence for the Re = 200 case, it should be clear that the demonstration of convergence for Re = 855 with a grid of 161 × 129 and $\alpha = 0.4$ also infers convergence for the less computationally challenging case of Re = 200. Now that the conditions for convergence have been established, we can proceed to the calculation of the time-dependent flow past both a fixed and a tranversely oscillating cylinder.

We have first done calculations for the case of a stationary circular cylinder in a steady approach flow at values of Re = 200 and 855 at $\alpha = 0.4$. Table 1 summarizes our results for these two Reynolds numbers and also lists the results of Lecointe and Picquet (1989) for the same cases. In Table 1, S is the Strouhal number for the nonoscillating cylinder. The results for the forced-oscillation calculations are at Reynolds numbers of 200 and 855. At Re = 200, the shedding frequency (f_{so}) is 0.098 and at Re = 855, the shedding frequency is 0.119. These values correspond to Strouhal numbers of 0.196 and 0.238, respectively. The LES method was not applied to the case of Re = 200 which means that ν_t in Eq. (1) was set to zero. Table 2 shows the cases which have been calculated to represent the capability of the numerical procedure. In all cases, the cylinder oscillation was sinusoidal (transverse to flow) and began at the onset of the steady approach flow. In Table 2, a is the dimensionless amplitude of oscillation (referenced to the cylinder radius) and f_c is the cylinder oscillatory frequency.

Figure 3 shows the results at Re = 200, $f_{so} = 0.098$, $f_c/f_{so} = 1.7$, $\alpha = 0.4$, and an oscillation amplitude of 1 cylinder radius ($a = 1.0$). The forced oscillation of the cylinder produced an early wake instability and the resulting flow was oscillatory almost from the onset. The lift coefficient oscillated essentially sinusoidally while the drag coefficient oscillated about a consistent mean value but did not exhibit a sinusoidal oscillation because of the nonlinear interaction between vortex shedding and the forced oscillation. The lift coefficient oscillation is quite large (±8.0) and the wake vortex pattern (not shown here), experiences a pronounced oscillatory effect. For $f_c/f_{so} = 0.85$ and an amplitude of 2 radii at Re = 200 (not shown here), the drag coefficient exhibited considerable oscillation (±1.0) about a mean value of about 2.0 while the lift coefficient oscillated between ±3.0. In this case, the wake vortex pattern showed considerable transverse oscillation with an eventual alignment of directly opposed vortices of opposite sign (again, not shown here). The third case at Re = 200, shown in Fig. 4 with $f_c = f_{so} = 0.098$ and an amplitude of 1, has begun to show the effect of a higher harmonic on the drag coefficient while the lift coefficient shows a lesser effect from the higher harmonic. In all three cases at Re = 200, lock-on is observed to have occurred.

The calculation at Re = 855 include the effects of the LES modeling whereas the Re = 200 case did not include the turbulence model. We recognize that the turbulent flow is 3D, but

Table 1 Nonoscillating cylinder values ($r \times \theta \times \Delta\tau = 161 \times 129 \times 0.01$, $\alpha = 0.4$)

Re	C_D (Experimental)	S	C_D	C_L (Present)	S	C_D	C_L (Lecointe and Piquet)	S
200	1.2	0.19	1.25 ± 0.03	±0.54	0.196	1.29 ± 0.04	±0.6	0.195
855	1.1	0.21	1.2 ± 0.2	±0.95	0.238	1.44 ± 0.23	±1.3	0.236

Table 2 Oscillating cylinder values ($\alpha = 0.4$)

Re	f_{so}	f_c/f_{so}	a	Mesh and $\Delta\tau$	C_D	C_L	Lock-on
200	0.098	1.7	1.0	161 × 129 × 0.01	1.9 ± 0.2	±8.0	yes
200	0.098	0.85	2.0	161 × 129 × 0.01	2.0 ± 1.0	±3.0	yes
200	0.098	1	1.0	161 × 129 × 0.01	1.45 ± 0.3	±3.0	yes
855	0.119	0.33	0.26	321 × 257 × 0.0025	no steady average values		no
855	0.119	0.5	0.26	321 × 257 × 0.0025			no
855	0.119	0.7	0.26	321 × 257 × 0.0025			no
855	0.119	0.85	0.26	321 × 257 × 0.0025	1.4 ± 0.7	±1.3	yes
855	0.119	1.0	0.26	321 × 257 × 0.0025	1.3 ± 0.7	±1.06	yes
855	0.119	1.05	0.26	321 × 257 × 0.0025	no steady	average values	yes
855	0.119	1.17	0.26	321 × 257 × 0.0025	1.5 ± 0.8	±1.1	yes

the 2D nature of the flow, driven by the oscillations of the cylinder, essentially make this a 2D problem. This statement is based on the observations of Gu et al. (1994).

We present results at Re = 855 for a dimensionless amplitude of 0.26 and frequency ratios, f_c/f_{so}, of 0.33, 0.5, 0.7, 0.85, 1.0, 1.05, and 1.17. Even though convergence was obtained for a grid of 161 × 129, we have proceeded with these calculations on the finer grid of 321 × 257 with $\Delta\tau = 0.0025$. The LES calculations show that lock-on does not occur for the three lower values of f_c/f_{so} and does occur for the higher four values, as indicated in Table 2. Figure 5 shows the power spectral density (PSD) plots for the seven cases shown in Table 2. Based on the PSD plots, lock-on doesn't occur until a value of $f_c/f_{so} = 0.85$ is reached and lock-on remains through a value of $f_c/f_{so} = 1.17$, the maximum value for which calculations were made. The lock-on phenomenon occurs in a slightly different way than for the nonoscillating cylinder case. At $f_c/f_{so} = 0.85$, lock-on occurs in the conventional manner; the vortex shedding frequency occurs at the cylinder oscillatory frequency. However, at the three higher frequency ratios, lock-on occurs at half the cylinder frequency. This is a consistent pattern and remained so through at least 300 cycles of oscillation.

Figure 6 shows the vorticity fields for two of the cases at Re = 855: $f_c/f_{so} = 0.5$ (no lock-on) and 1.17 (lock-on). The position of the oscillating cylinder for the various positions in both sets of plots is the same: the top (a), middle (c), and bottom (e) frames are at the neutral position, the second frame (b) is at the lowest cylinder position and the fourth frame (d) is at the highest cylinder position in the oscillatory cycle. When lock-on doesn't occur in the $f_c/f_{so} = 0.5$ case, we note that the neutral position vorticity plots are essentially the same which indicates that vortex shedding is occurring virtually unaffected by the oscillation of the cylinder. However, such is not the situation for $f_c/f_{so} = 1.17$ where it is seen that the neutral position vortic-

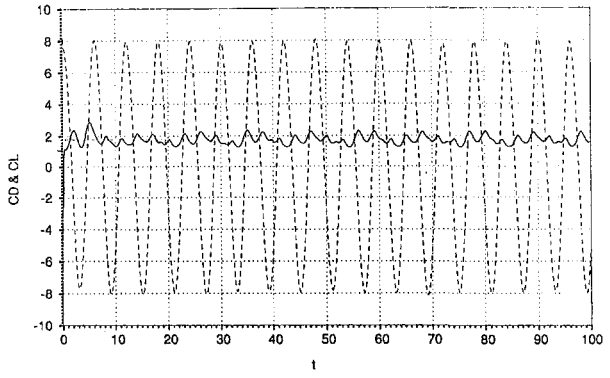

Fig. 3 Drag (solid line) and lift (dashed line) coefficients for an oscillating cylinder at Re = 200, $f_c = 1.7\ f_{so}$, $a = 1.0$, $f_{so} = 0.098$

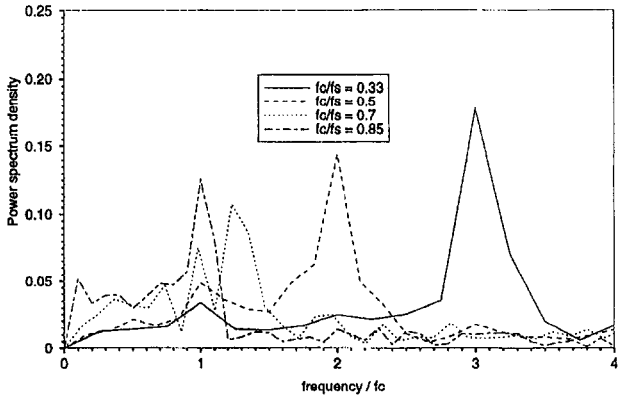

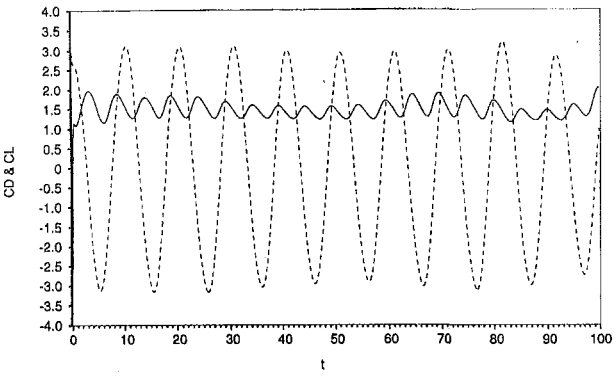

Fig. 4 Drag (solid line) and lift (dashed line) coefficients for an oscillating cylinder at Re = 200, $f_c = f_{so} = 0.098$, $a = 1.0$

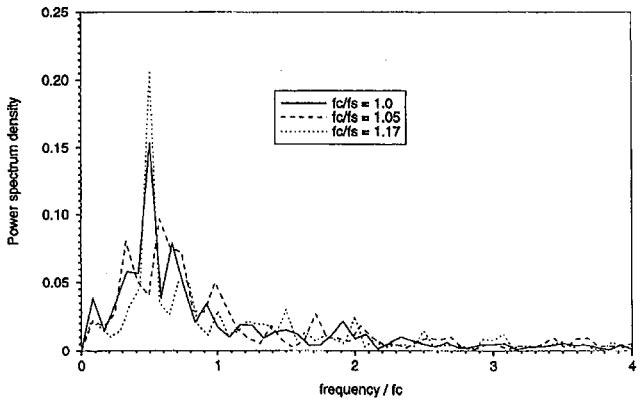

Fig. 5 Power spectral density plots at Re = 855, $a = 0.26$

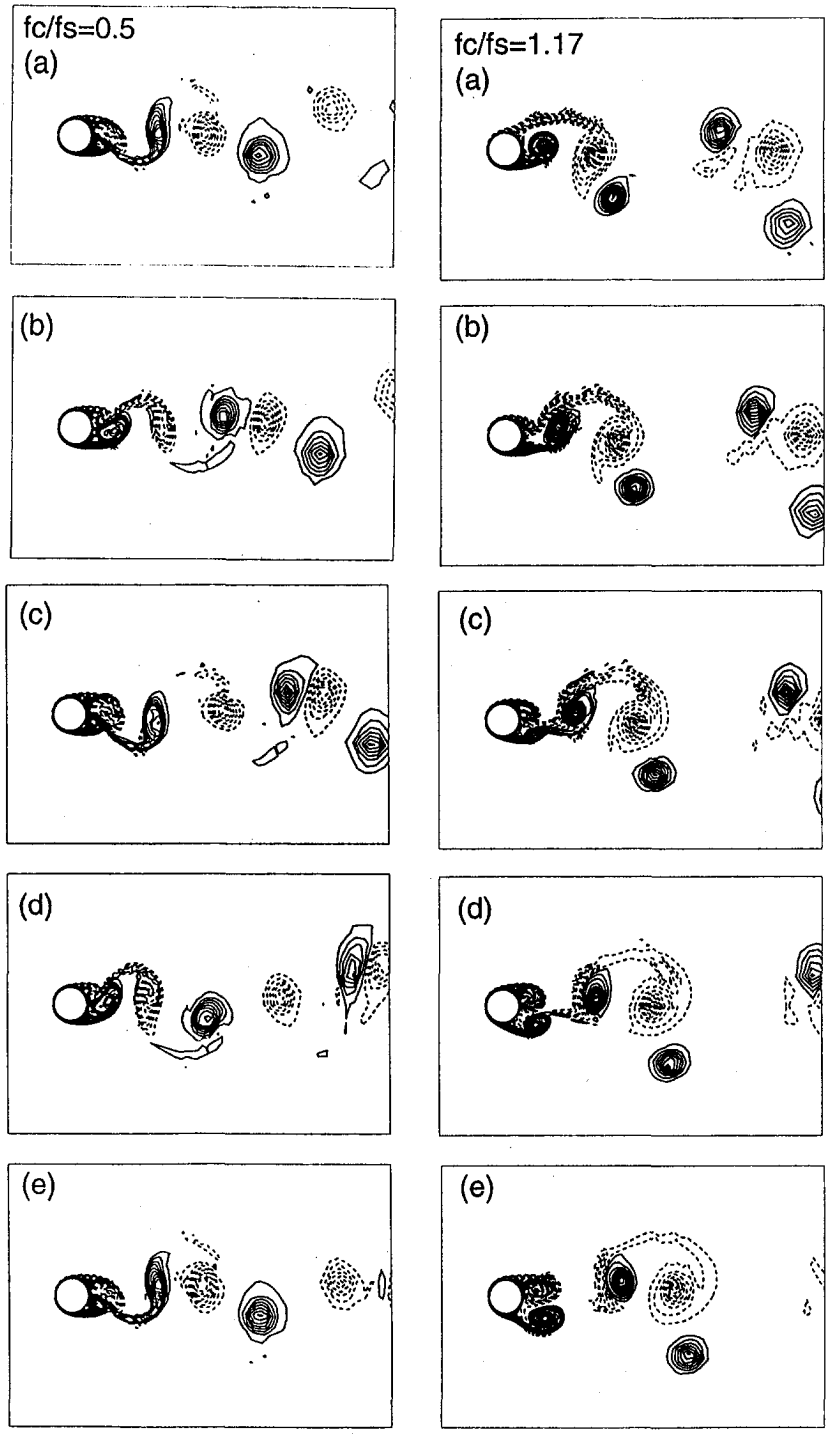

Fig. 6 Vorticity plots at Re = 855 for f_c/f_{so} = 0.5 (no lock-on) and f_c/f_{so} = 1.17 (lock-on)

ity plots are distinctly different. This difference is expected because of lock-on. Frames *a* and *c* appear to be approximately 180° out of phase while frame *e* is not in phase with either. This observation is consistent with the earlier comment regarding vortex shedding (lock-on) occurring at half the cylinder frequency. The same behavior is also noticed at f_e/f_{so} = 1.0 and 1.05 although these results are not shown here.

Figure 7 shows the calculated force coefficients (C_D and C_L) at Re = 855 for f_c/f_{so} = 0.5 and 1.17. The force plots for f_c/f_{so} = 0.5 show the effect of a higher harmonic; this behavior is also present in the PSD plot in Fig. 5 for this frequency where the maximum peak was observed at f/f_c = 2.0 and a lesser peak was observed at f/f_c = 1.0. This same behavior pattern is noted for f_c/f_{so} = 0.7 but these results are not shown here. The force plots at f_c/f_{so} = 1.17 show a fairly regular behavior with a slightly higher harmonic effect which is also borne out in the PSD plot in Figure 5 at this frequency ratio.

Conclusions

We have performed accurate finite-difference calculations for a steady approach flow toward a cylinder which is undergoing sinusoidal transverse oscillations at a prescribed frequency and amplitude. The calculation procedure was validated for a steady

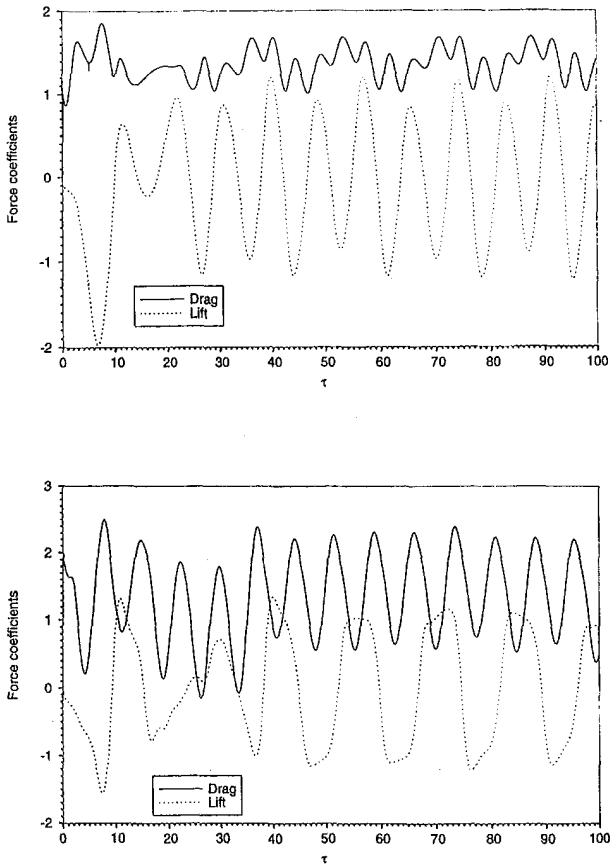

Fig. 7 Drag (solid line) and lift (dashed line) coefficients for an oscillating cylinder at Re = 855 at f_e/f_{so} = 0.5 and 1.17, a = 0.26

flow past a nonoscillating cylinder and these calculated results are found to agree quite well with experimental results.

Results for forced sinusoidal oscillations of the cylinder at approach Reynolds numbers of 200 and 855 have been obtained at oscillation amplitude ratios of 0.26. At Re = 200, the viscous flow calculations show that the drag coefficient and lift coefficient values were enhanced by the cylinder oscillation and that lock-on did occur. At Re = 855, the LES calculations show that lock-on did occur for f_e/f_{so} values of 0.85 and higher.

Acknowledgments

An earlier and shorter version of this paper was presented at the 1994 OMAE/ASME meeting in Houston. We are grateful to the Pittsburgh Supercomputing Center for our time grant. The ERAP grant from the Texas Higher Education Coordinating Board provided some of the support for Jianfeng Zhang.

References

Braza, M. Chassaing, P., and Ha Minh, H. 1986. "Numerical Study and Physical Analysis of the Pressure and Velocity Fields in the Near Wake of a Circular Cylinder," *Journal of Fluid Mechanics,* Vol. 165, pp. 79–130.

Chilukuri, R. 1987. "Incompressible Laminar Flow Past a Transversely Vibrating Cylinder," ASME JOURNAL OF FLUIDS ENGINEERING, Vol. 109, pp. 166–171.

Copeland, G. S. and Cheng, B. H. *1995.* "A Numerical Investigation of Vortex Shedding From a Transversely Oscillating Cylinder," submitted to *Journal of Fluid Mechanics.*

Gu, W., Chyu, C., and Rockwell, D. 1994. "Timing of Vortex Formation From an Oscillating Cylinder," *Physics of Fluids,* Vol. 6, pp. 3677–3682.

Hall, M. S., and Griffin, O. M. 1993. "Vortex Shedding and Lock-on in a Perturbed Flow," ASME JOURNAL OF FLUIDS ENGINEERING, Vol. 115, pp. 283–291.

Hurlbut, S. E., Spaulding, M. I., and White, F. M. 1982. "Numerical Solutions for Laminar Two-dimensional Flow about a Cylinder Oscillating in a Uniform Stream," ASME JOURNAL OF FLUIDS ENGINEERING, Vol. 104, pp. 214–222.

Justesen, P. 1991. "A Numerical Study of Oscillating Flow Around a Circular Cylinder," *Journal of Fluid Mechanics,* Vol. 222, pp. 157–196.

Lecointe, Y., and Piquet, J. 1989. "Flow Structure in the Wake of an Oscillating Cylinder," ASME JOURNAL OF FLUIDS ENGINEERING, Vol. 111, pp. 139–148.

Ongoren, A., and Rockwell, D. 1988. "Flow Structure from an Oscillating Cylinder Part 1. Mechanisms of Phase Shift and Recovery in the Wake," *Journal of Fluid Mechanics,* Vol. 191, pp. 197–223.

Tamura, T., Tsuboi, K., and Kuwahara, K. 1988. "Numerical Solutions of Unsteady Flow Patterns around a Vibrating Cylinder," AIAA Paper No. 88-0128, Aerospace Sciences Meeting, Reno.

Wang, X., and Dalton, C. 1991a, "Oscillating Flow Past a Rigid Circular Cylinder: A Finite-Difference Solution," ASME JOURNAL OF FLUIDS ENGINEERING, Vol. 113, pp. 377–383.

Wang, X., and Dalton, C. 1991b, "Numerical Solutions for Impulsively Started and Decelerated Viscous Flow Past a Circular Cylinder," *International Journal for Numerical Methods in Fluids,* Vol. 12, pp. 383–400.

Zhang, J., and Dalton, C. 1996. "Interactions of Vortex-induced Vibrations of a Circular Cylinder and a Steady Approach Flow," *Computers and Fluids,* Vol. 25, pp. 283–294.

State Estimator of Flow as an Integrated Computational Method With the Feedback of Online Experimental Measurement

Toshiyuki Hayase
Associate Professor.

Satoru Hayashi
Professor.
Mem. ASME

Institute of Fluid Science,
Tohoku University,
Sendai, 980-77, Japan

This paper deals with a state estimator or simply an observer of flow field. The observer, being a fundamental concept in the control system theory, also has a potential in the analysis of flow related problems as an integrated computational method with the aid of experiment. In the framework of the observer, the state of physical flow is estimated from the mathematical model with the feedback of on-line experimental measurement. A SIMPLER based flow simulation algorithm is used as the mathematical model of the real flow and partial experimental measurement of flow is fed back to the boundary condition through the feedback controller. The existence of the feedback-loop essentially distinguishes the observer from ordinary flow simulations. Time variation of the computational result of the observer is expected to converge exactly to that of the physical flow in the whole flow domain even for unstable turbulent flows. A numerical experiment has been performed to confirm the validity of the proposed observer for a turbulent flow through a duct of square cross section. The physical flow to be estimated is modeled by a numerical solution. Appropriate choice for the proportional feedback gain of the observer results in accelerated convergence of the simulation by a factor of 0.012 and reduced error in estimation of the perturbation velocity by a factor of 0.6 in the whole domain or a factor of 0.3 behind the output measurement plane in comparison with the ordinary flow simulation without feedback.

1 Introduction

In the past few decades remarkable progress has been made on capability of numerical analysis as well as advanced experimental techniques in the study of flow phenomena. However, common engineering workstations still do not have enough computational power to properly reproduce velocity fluctuations of turbulent flows, which could easily be obtained in a laboratory experiment, and even the most powerful supercomputers could not fully treat complex flows of practical engineering importance. On the other hand, it is difficult to obtain a complete set of data characterizing a three-dimensional time-dependent flow field, which in turn is relatively easily obtained in numerical analysis. Having their own shortcomings, both of the computational and experimental methods are used in a cooperative way. However, interaction between the methods has usually been one-directional and rather ineffective; e.g., the result of experimental measurement is used to confirm the validity of numerical analysis, while the result of numerical analysis is referred to see the detailed structure of the flow. It is natural to expect an appropriate bidirectional information exchange between numerical and experimental analyses results in more effective method in flow study. Humphrey (1993) proposed the concept of interactive computational and experimental methodology (ICEME), in which the management unit obtains relatively sparse results with allowable efforts through both of the computational and experimental methods to integrate them to produce meaningful information for complex problems. Possible advantages of ICEME, as well as necessary further studies, are discussed in relation to a complex flow related optimization problem seeking the arrangement of electrical heat sources to minimize the temperature in a ventilated box under some constraints. Little is known, however, on how the computational and experimental methods should be integrated in general to obtain useful information of the flow in practical applications. The purpose of this paper is to give one possible answer to this essential problem. In this paper, the concept of *state estimator* or simply *observer* in the control system theory is applied to a numerical method to produce complete information of physical flow including real time velocity fluctuations by supplying the partial on-line experimental measurement of the relevant flow.

In the framework of modern control theory, the control signal is determined as a function of state variables (Skelton, 1988). It is usually difficult to measure the whole states of the large dimensional physical system. The observer is then used to estimate the state variables from the mathematical model of the system and the partial measurement of the system dynamics. For finite dimensional linear systems, the theory of observers is well established and the design of observers is rather straightforward. The state of the mathematical model converges to that of the physical system as a specified exponential function of time. Extension to nonlinear systems has been studied extensively for finite dimensional case (Misawa and Hedrick, 1989). For infinite dimensional systems, on the other hand, the state observer is designed in the same manner as the finite dimensional case and implemented after the finite-dimensional approximation as long as the system is linear (Curtain and Zwart, 1995). However, a general theory of the observer has not been established for infinite dimensional and nonlinear systems such as flow field treated here.

Contributed by the Fluids Engineering Division for publication in the JOURNAL OF FLUIDS ENGINEERING. Manuscript received by the Fluids Engineering Division December 17, 1996; revised manuscript received July 8, 1997. Associate Technical Editor: J. A. C. Humphrey.

Treatment of the observer in this paper, therefore, mainly focuses on physical consideration rather than mathematical formulation. For example, controllability and observability of the system are not explicitly proved below, assuming both of the conditions are naturally satisfied for the system constructed based on proper physical consideration (Luenberger, 1979). Basic structure of the observer consists of the mathematical model of the relevant system and the feedback path from experimental measurement to the model through the control law. A standard numerical simulation scheme is used as the mathematical model and the feedback controller is added to the simulation to modify the boundary condition based on the on-line measurement. Determination of the feedback law is the key of the observer design and properly designed observer distinguishes itself to ordinary numerical simulations in several ways: the state of the observer can converge to the real state after some transient. This means observer produces the actual flow information in a range of its accuracy at all the computational grid points with the aid of limited number of measurements. This is, of course, impossible unless the computation and experiment are conducted simultaneously. Acceleration of convergence and improvement of accuracy are also expected as the result of feedback action. Integration of numerical simulation and experimental measurement in the framework of the observer is expected to provide a powerful tool in analysis of flow related problems.

There is the other goal of the study to provide a fundamental component of control system in the original sense of the observer. Most of existing flow control systems assume that the controlled flow can be modeled as the lumped parameter model of small order and be controlled with a limited number of sensors and actuators. They give satisfactory results for many flow systems including complex aircraft control problem, as long as the system dynamics are properly described by the lumped parameter model (Skelton, 1988). However, there are many other flows which have more complex dynamical structure. In such a case the flow field must be modeled as the nonlinear distributed parameter system and associated control problem becomes extremely difficult. A number of studies have been made to extend the application of the modern control theory to nonlinear distributed parameter systems (Li and Yong, 1995). An example of such control problem of both theoretical and practical importance is the control of turbulent flows. This problem is investigated in a wide variety of aspects from intuitive approach based on experimental observations to the purely theoretical one (Gad-el-Hak, 1994). Typical objective of turbulent flow control is in both directions; enhancement of turbulent transport or reduction of turbulent shear stress. Existing turbulent flow control strategies, such as riblets or other boundary layer control, are classified in *passive control* in which control action is not manipulated based on command nor flow condition. In general, effectiveness and applicability of the passive control are limited under the change of operating condition, since it inherently has fixed structure and, therefore, its control result can be optimized at only one operating condition. More effective control is possible by the *active control* in which the control action is manipulated based on the control law using the command input (*feedforward control*) or the flow condition (*feedback control*). Recently, Choi et al. (1994) performed a numerical experiment for the feedback control of wall velocity of turbulent channel flow showing a significant reduction of wall friction. Necessity of the state observer for the physical implementation is also mentioned in his paper.

This paper deals with development of the observer for flow field. Section 2 of the paper demonstrates the general structure and advantage of the state observer in contrast to ordinary numerical simulations. A SIMPLER-based flow simulation algorithm is modified by adding a feedback path from experimental measurement in order to control the convergence of the computational result to the physical flow. Section 3 verifies the validity of the proposed observer by means of a numerical experiment. Fully developed turbulent flow through a duct of square cross section is considered as a test problem. A numerical solution is first obtained as the model of the physical flow. The observer of special structure is then constructed in the computer program. Computation is performed by supplying velocity data of the model flow solution at a limited number of locations as the model of experimental measurement. Convergence of the state of the observer to that of the model flow solution is discussed in detail. Section 4 summarizes the conclusions of this work.

Nomenclature

A = cross-sectional area of the duct
$\tilde{b}$ = side length of square cross section
$\mathbf{e}$ = estimation error vector
e_a = averaged magnitude of estimation error
$\mathbf{f}$ = body force vector
h_1, h_2, h_3 = computational grid spacing
h_T = computational time increment
K_P = proportional feedback gain of observer
L = periodical length of duct
l_{out} = distance between output measurement plane and upstream boundary
M_d = number of data sampling in power spectrum calculation
N_d = number of data averaging in power spectrum calculation
n_1, n_2, n_3 = number of computational grid points
p = pressure field
$\mathrm{R_e} = \tilde{u}_m\tilde{b}/\tilde{\nu}$ = Reynolds number
S_1 = discretized power spectrum of the u_1-velocity component at the center of cross section
t = time
$\mathbf{u} = (u_1, u_2, u_3)$ = velocity vector field
$\mathbf{u}^*$ = velocity vector field of standard solution
u_c = u_1-component at the center of cross section
$\tilde{u}_m$ = mean axial velocity
$\mathbf{V}$ = arbitrary volume in the flow domain
$\mathbf{x}$ = positional vector
(x_1, x_2, x_3) = Cartesian coordinate system
$\|\cdot\|_{\mathbf{V}}$ = norm in $\mathbf{V}$
$\Delta p'_{jk}$ = modified pressure difference
Δp = constant pressure difference between upstream and downstream boundaries
δp_{jk} = correction of pressure difference due to feedback
$\tilde{\rho}$ = density of fluid
λ = coefficient of resistance
$\tilde{\nu}$ = kinematic viscosity
ω_n = circular frequency of perturbation velocity component

Superscripts

$\tilde{}$ = dimensional value
$\bar{}$ = time averaged value
$*$ = standard solution (model of physical flow)

Subscripts

0 = value corresponding to the exact solution
1, 2, 3 = component in x_1, x_2, x_3 coordinate direction, respectively
c = center of cross section
i, j, k = denotes a computational cell location

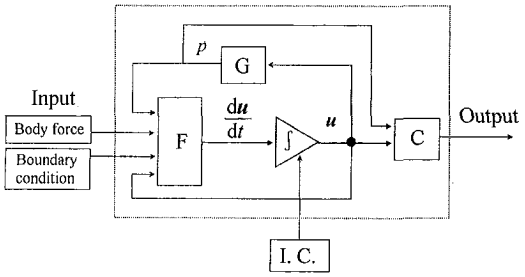

Fig. 1 Block diagram of flow field in view of system dynamics

2 State Observer of Flow Field

This paper deals with incompressible and viscous fluid flow. The dynamic behavior of the flow field is governed by the Navier-Stokes equation:

$$\frac{\partial \mathbf{u}}{\partial t} = -\text{grad}\, p - (\mathbf{u}\cdot\text{grad})\mathbf{u} + \frac{1}{\text{Re}}\nabla^2\mathbf{u} + \mathbf{f}, \qquad (1)$$

and the equation of mass continuity:

$$\text{div}\, \mathbf{u} = 0, \qquad (2)$$

as well as the initial condition and the boundary condition. As a preliminary consideration for construction of the observer, a block diagram representing the flow field dynamics is given in Fig. 1. From the viewpoint of dynamical system theory, the state of the flow system is the infinite dimensional velocity vector field $\mathbf{u}$. It is inherently impossible to know the complete information of the state by experiment. Experimental measurement provides a partial information of the flow field as output variables which are given by an arbitrary finite dimensional vector function of the velocity field $\mathbf{u}$ and the pressure field p, denoted by "C" in the figure. A typical example of the output is the velocity component or the pressure at some designated location, or the drag acting on an obstacle, etc. Evolution of the flow field from the initial state, denoted by "I. C.", is determined by the input to the system, which consists of the boundary condition and the body force.

Basic structure of the observer is explained below in comparison with the ordinary numerical simulation. First, Fig. 2(a) shows a conceptual block diagram of typical numerical analysis of flow field. It is noted that physical flow field, denoted by "physical flow," is always the final concern of study, and the numerical simulation setup, denoted by "model flow," is expected to provide equivalent information of the physical flow. The numerical simulation is performed assuming the same input as the physical flow if possible, but its initial condition is usually different from that of the physical flow which is unknown in many cases. The result of numerical simulation converges to that of the physical flow within an accuracy of numerical scheme for steady flows. However, in more general case of unsteady flows such as turbulent flows, the output of the numerical simulation converges to the physical flow only in time average sense; computational results cannot reproduce the exact time variation of the physical flows. Within the framework of ordinary numerical simulation, information of physical flow does not interact the numerical simulation directly. So it is essentially impossible to obtain the numerical solution which exactly follows the time variation of the physical flow. It is also noted that improvement of the accuracy of numerical solution can be achieved only by refinement of the numerical scheme.

The structure of the observer is shown in Fig. 2(b). It is characterized by a feedback path which has a potential to overcome the drawback of traditional numerical analysis approach mentioned above. In an original usage of the observer in control systems, real time computation is performed parallel to experimental measurement, and the difference between the outputs of the simulation and experiment, or the *estimation error,* is fed back to the input of the numerical scheme through the feedback law. Determination of this feedback law is the key in design of the state observer. Input to the simulation is modified to reduce the estimation error. Convergence of the output implies coincidence over the whole states if the "observability" of the system is satisfied. In finite-dimensional and time-independent linear dynamical systems, the observability of the system is easily examined and the observer of arbitrary exponential convergence property can be designed (Skelton, 1988). However, it is generally quite difficult to confirm the equivalent of observability for nonlinear and distributed parameter systems such as flow field, and general theoretical treatment of the observer has not been established for those systems (Li and Yong, 1995). In the next section, the observer of flow field is constructed from a numerical simulation scheme by adding the feedback path which modify the boundary condition of the simulation using the experimental measurement of the physical system. Turbulent flow through a square duct is treated as an example and a simple feedback law is proposed based on physical consideration of flow dynamics. A SIMPLER-based flow simulation algorithm (Hayase et al., 1990) is used as the flow model and the estimation error in axial velocity component on a cross section of the duct is fed back to the pressure difference boundary condition between the upstream and downstream boundaries. Validity of the proposed observer is confirmed through a numerical experiment.

3 Numerical Experiment

In this section, the flow observer presented above is constructed in a special flow case for a fully developed turbulent flow through a duct of square cross section, and the validity of the proposed observer is examined by numerical experiment. In a former work the authors performed numerical analysis on the relevant flow (Hayase and Suematsu, 1991). In the following the set of time dependent numerical solution, hereafter called "standard solution," is used as the model of the physical flow, the state of which is estimated by the observer. The geometry and the coordinate system are shown in Fig. 3. In computation of the standard solution, periodical velocity condition and constant pressure difference Δp are assumed between the up-

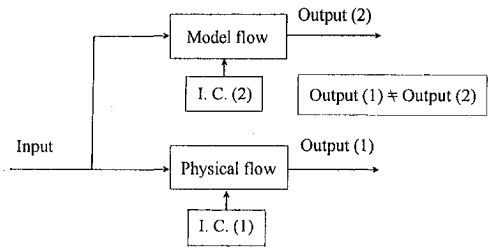

Fig. 2(a) Flow simulation

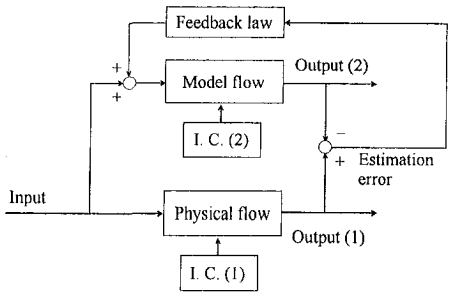

Fig. 2(b) Observer

Fig. 2 Comparison between flow simulation and observer

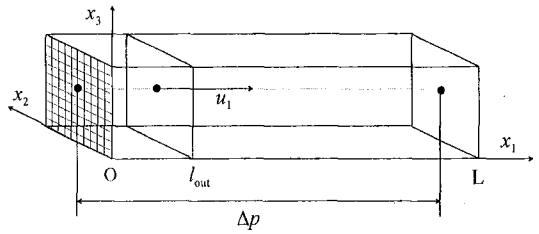

Fig. 3 Domain and coordinate system

stream and downstream boundaries. A set of u_1-velocity components at the grid points on the plane at the distance of l_{out} from the upstream boundary is used as the output variables, or measurement data.

Brief explanation of the numerical scheme is mentioned here. The Navier-Stokes equation (1) and the equation of continuity (2) are discretized through the finite volume method on the three dimensional orthogonal equidistant staggered grid system. Convection terms are discretized by the reformulated QUICK scheme, which assures the continuity of the momentum flux on the control volume boundaries in iteration process (Hayase et al., 1992). Two-time level implicit scheme is used for time dependent terms (Fletcher, 1988). The resultant set of finite difference equations is solved using the SIMPLER-based iterative procedure (Hayase et al., 1990).

Computational conditions are summarized in Table 1. In this paper, all the values are expressed in dimensionless form using the side length of the square cross section $\tilde{b}$, the density of fluid $\tilde{\rho}$, and the mean axial velocity $\tilde{u}_{m0}$ given by

$$\tilde{u}_{m0} = \sqrt{2\Delta\tilde{p}\tilde{b}/(\lambda\tilde{L}\tilde{\rho})}, \tag{3}$$

where the coefficient of resistance λ is evaluated through Blasius' formula (Schlichting, 1979)

$$\lambda = 0.316\mathrm{R}_{e0}^{-1/4}. \tag{4}$$

Constant pressure difference $\Delta p = \Delta\tilde{p}/(\tilde{\rho}\tilde{u}_{m0}^2)$ corresponding to the Reynolds number $\mathrm{R}_{e0} = \tilde{u}_{m0}\tilde{b}/\tilde{\nu}$ of 9000 is assumed between the upstream and downstream boundaries for the duct of the periodical length of 4.

Although the grid system does not have enough grid resolution to simulate the detailed structure of the relevant turbulent flow, the numerical solution qualitatively reproduces the fundamental characteristics of the turbulent flow (Hayase and Suematsu, 1991). In Fig. 4(*a*) profile of the mean axial velocity is plotted for the experimental result (Kawahara, 1990), LES result (Kajishima, 1990) and present calculation with three different computational grids. The present standard solution with the coarsest grid system gives good agreement with the other calculations and experimental result except the region near the wall boundary. Figure 4(*b*) shows the power spectrum of the u_1-velocity perturbation at the center of cross section defined as:

Table 1 Computational conditions

Periodical length L	4
Distance between output measurement plane and upstream boudnary l_{out}	0.3
Pressure difference Δp	0.0649
Reynolds number R_{e0}	9000
Grid points $n_1 \times n_2 \times n_3$	$20 \times 10 \times 10$
Grid spacing $h \times h_2 \times h_3$	$0.2 \times 0.1 \times 0.1$
Time increment h_t	0.05
Total residual at convergence	0.01
CPU time for one time step with Cray C-916 [s]	2

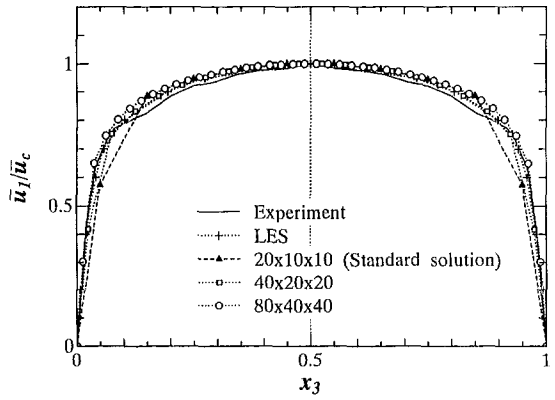

Fig. 4(*a*) Mean axial velocity profile

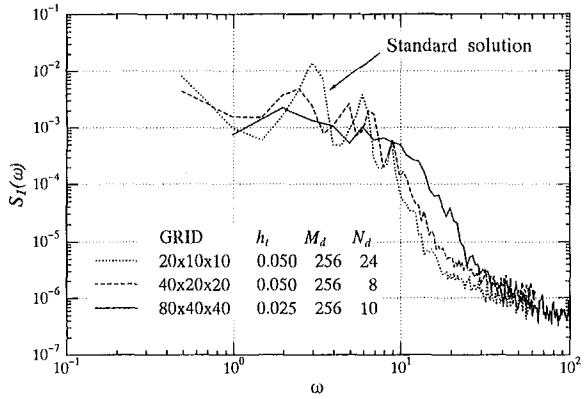

Fig. 4(*b*) Power spectrum of axial velocity component at the center of cross section

Fig. 4 Fully developed turbulent flow through a duct of square cross section. Comparison between the present standard solution and other results

$$S_1(\omega_n) = E\left[\frac{h_T}{M_d}\sum_{m=1}^{M_d}|u_{1c}(mh_T)\exp(-j\omega_n mh_T)|^2\right]_{N_d}$$

$$\left(\omega_n = \frac{2\pi}{M_d h_T}, \frac{4\pi}{M_d h_T}, \ldots, \frac{\pi}{h_T}\right) \tag{5}$$

where $E[*]_{N_d}$ denotes averaging over N_d samples. Comparison of present standard solution with the solutions with 8 times and 64 times finer grid resolution in Fig. 4(*b*) reveals that the present standard solution gives a good result in low frequency domain but its perturbation is rather filtered out in high frequency region. This result implies the present standard solution retaining large amplitude perturbation component of low frequency is assumed to be a filtered version of the physical turbulent flow. Of course, the numerical solution obtained with the finer grid system is a better model for the physical flow than the present standard solution. As will be mentioned below, however, the observer in this paper is constructed and tested on a coarse grid system. Reduced computational load with the coarse grid system is essential for the observer because it assumes the real-time computation parallel to the experimental measurement. An important subject investigated here is whether the feedback action of the observer effectively reduces the numerical error due to insufficient grid resolution. As a basic consideration main part of this paper focuses on the convergence of the observer to the standard solution obtained by the same numerical scheme and the grid resolution as the observer. An example of convergence to the solution on a finer grid system is mentioned in the end of this section.

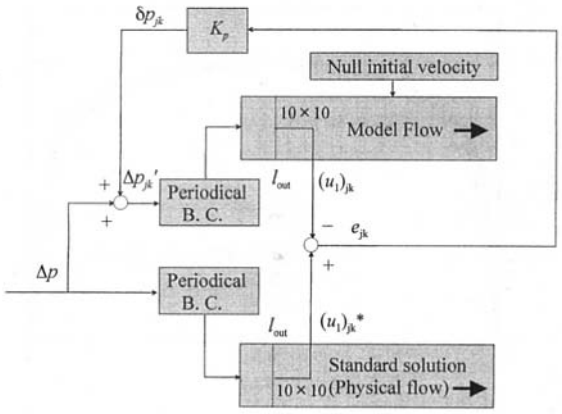

Fig. 5 Structure of the observer for turbulent flow through a square duct

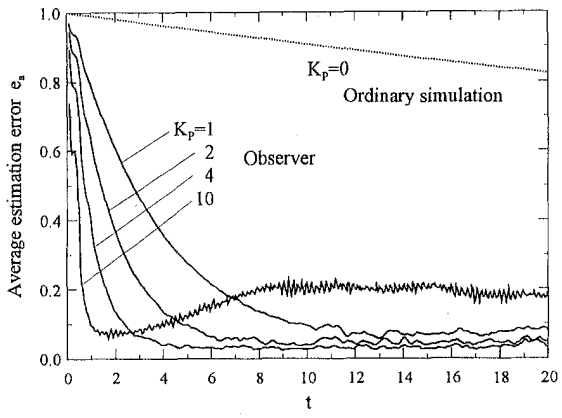

Fig. 7 Variation of average estimation error on the output measurement plane

Block diagram of the state observer considered here is shown in Fig. 5. It is noted that the physical flow is substituted by the standard numerical solution. In this setup, time-dependent flow simulation, denoted by "model flow," is started from the initial condition of null velocity field. The output is defined both for the standard solution and the model flow as the u_1-velocity component at 10×10 grid points on the plane at a distance of $l_{out} = 0.3$ from the upstream boundary. At each time step the estimation error e_{jk} is evaluated on 10×10 grid points as the difference between the output variables of the standard solution and the simulation:

$$e_{jk} = u_{1ijk}^* - u_{1ijk}, \quad (i = \text{fixed}; j, k = 1, \ldots, 10). \quad (6)$$

It is noted that the selection of output variables is critical in designing observers. Observability of the system is closely related to the convergence of the observer in linear systems. The observability physically means that whole system states are reconstructed from the output variables and the system model. The output variables, therefore, should involve sufficient information of the flow but also be compact by considering the physical implementation.

As to the input variables, the pressure boundary condition is modified through the simple proportional feedback law. The pressure difference δp_{jk} proportional to the estimation error e_{jk} is added to the constant pressure difference Δp at the corresponding 10×10 grid points between the upstream and downstream boundaries in order to accelerate or decelerate the fluid to reduce the estimation error

$$\delta p_{jk} = K_P e_{jk},$$

$$\Delta p_{jk}' = \Delta p + \delta p_{jk}, \quad (j, k = 1, \ldots, 10), \quad (7)$$

where K_P is the proportional feedback gain and $\Delta p_{jk}'$ is a modified pressure difference applied to the model flow as the pressure boundary condition. In existing observer theory an appropriately designed function of the estimation error is applied to the state equation as the feedback signal. As a simple possible choice of this function with physical meaning, the additional pressure difference is assumed here as the linear function of the estimation error variables. Further simplification is made that the additional pressure difference at each location depends only on the error just behind the upstream boundary. This assumption is

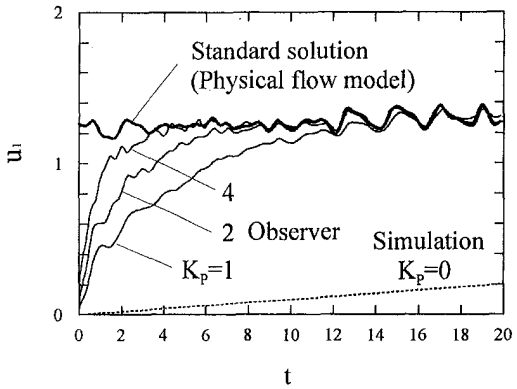

Fig. 6(*a*) Convergent results

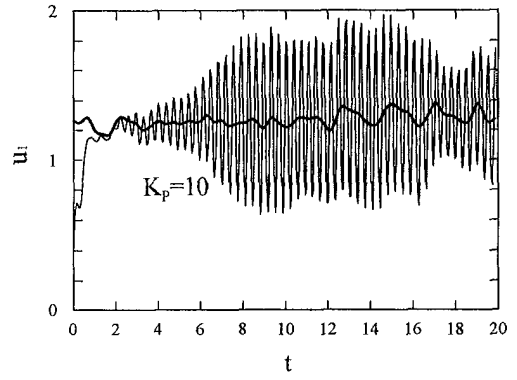

Fig. 6(*b*) Unstable result for large feedback gain

Fig. 6 Variation of the u_1-velocity component at the center of the output measurement plane

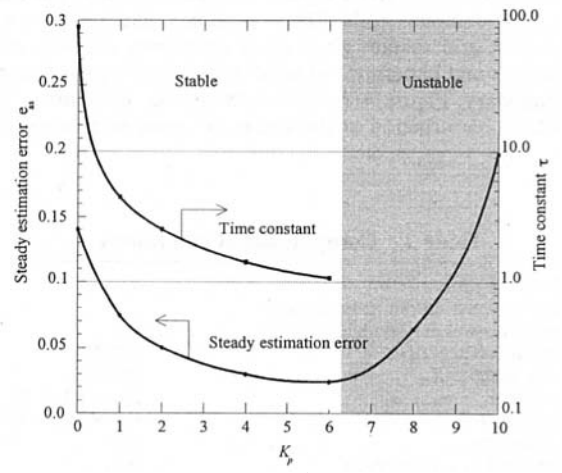

Fig. 8 Steady estimation error and time constant of transient as a function of feedback gain

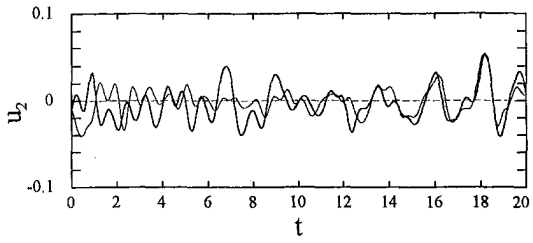

Fig. 9(*a*) u_2-velocity component

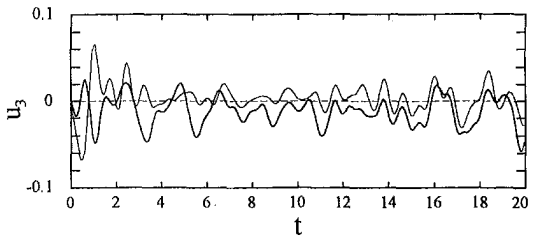

Fig. 9(*b*) u_3-velocity component

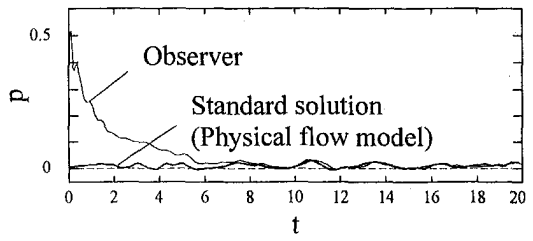

Fig. 9(*c*) Pressure

Fig. 9 Convergence of the observer at the center of output measurement plane (K_P = 2)

validated by the fact that the effect of the pressure decreases with distance, and the most effective terms are retained in Eq. (7). The proportional gain K_P in Eq. (7) expresses the magnitude of the effect of pressure on the u_1-velocity component, and is considered constant over the cross section.

For several values of the feedback gain K_P, variations of the u_1-velocity component at the center of the output measurement plane are plotted in Figs. 6(*a*), (*b*). It is noted that all the velocity components in the following results are normalized by the mean axial velocity $\tilde{u}_m$ of the standard solution, which is 1.6 times larger than $\tilde{u}_{m0}$ in Eq. (3). This discrepancy, apparently due to insufficient grid resolution of the standard solution, does not seriously affect the validity of the following discussion which mainly focuses on the effectiveness of the feedback. The bold line in the figures shows the result of the standard solution, i.e., the model of the physical flow. The others are the results of the observer in which computations are started from the initial condition of null velocity field at $t = 0$. The broken line in Fig. 6(*a*) with feedback gain $K_P = 0$ corresponds to the ordinary flow simulation without feedback loop. In this case, acceleration of the flow due to the originally applied pressure difference Δp is very small, and it takes considerably long time to reach the developed turbulent flow solution. Furthermore, little correlation is expected in this case between perturbation velocities of the simulation and the standard solution. Results of the observer with appropriate values of the feedback gain rapidly converge to the standard solution in Fig. 6(*a*). After short transition the velocity output of the observer properly tracks the standard solution. This result proves the present proportional feedback on the pressure boundary condition effectively reduces the estimation error. In Fig. 6(*a*) increasing the feedback gain improves the convergence and tracking ability of the observer. Further increase of the gain, however, destabilizes the observer as in Fig. 6(*b*). It is common that the feedback system becomes unstable and oscillates as the result of excess correction due to large gain. These results imply appropriate choice of the feedback gain is critical for effective and stable performance of the observer.

The average estimation error e_a is obtained from all the estimation error at 10 × 10 grid points on the output measurement plane as,

$$e_a = \frac{1}{N_{out}} \sum_{j,k} |e_{jk}| \tag{8}$$

where N_{out} is a total number of grid points on the plane. Variation of the average estimation error e_a is plotted in Fig. 7 for several values of the feedback gain. The initial value of e_a is about 1 for all the cases, since the null velocity field is assumed at the beginning of calculation. Estimation error of the observer rapidly reduces and converges to the steady value except for the case of $K_P = 10$ which undergoes instability (see Fig. 6(*b*)). For the ordinary simulation corresponding to $K_P = 0$, on the other hand, estimation error decreases very slowly, since the unmodified boundary condition of the pressure gradient results in only small acceleration of the flow.

The steady value of the estimation error and the time constant for the convergence are obtained from the above plots. The steady estimation error e_{as} is evaluated as the average value of e_a during the interval of $10 \leq t \leq 20$. The time constant τ is estimated as,

$$\tau = \frac{e_{a0} - e_{as}}{de_a/dt|_{t=0}} \tag{9}$$

where e_{a0} is the initial estimation error at $t = 0$. The time derivative in Eq. (9) is evaluated from the best fitted exponential curve to each plot. The result is plotted in Fig. 8. The steady estimation error decreases with increasing feedback gain K_P from the initial value of 0.14 for $K_P = 0$ corresponding to the ordinary simulation to the minimum value of 0.024 at $K_P = 6$ with the reduction of factor of 0.17. With further increase of K_P, however, results in instability of the feedback system and increase in the steady estimation error. At the feedback gain of $K_P = 10$, the result is worse than the case without feedback.

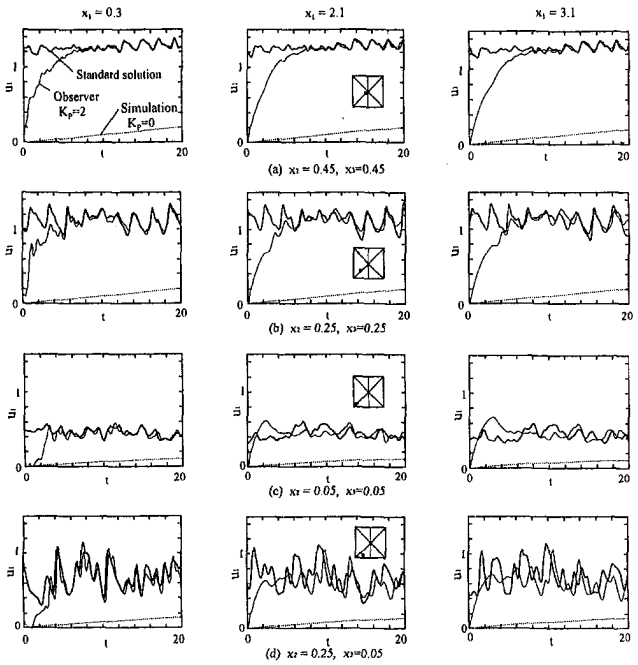

Fig. 10 Variation of the u_1-velocity component at several locations in the flow domain (K_P = 2)

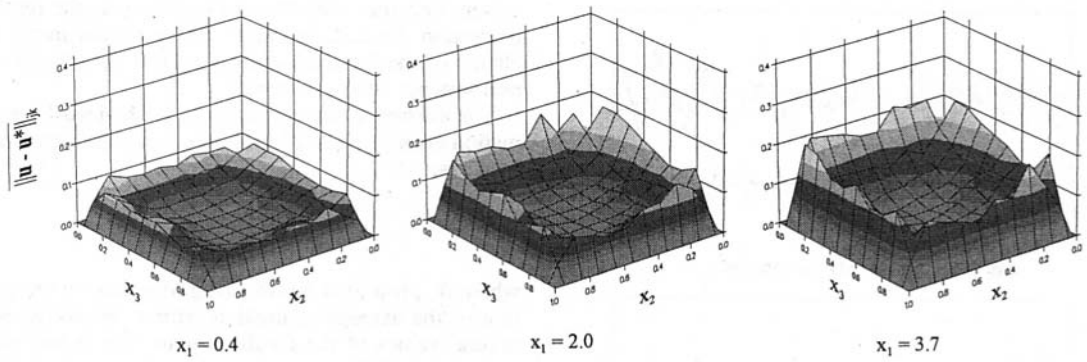

Fig. 11(*a*) $K_P = 2$

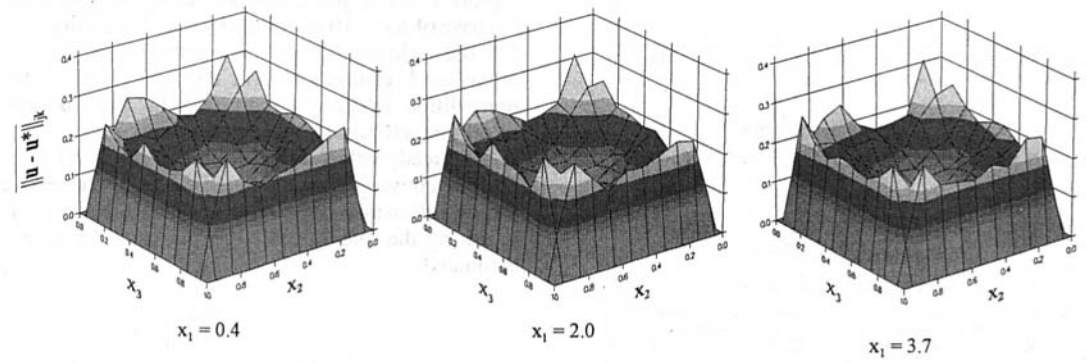

Fig. 11(*b*) $K_P = 0$ (without feedback)

Fig. 11 Distribution of the norm of the error on several x_1-planes averaged in the interval of $10 \le t \le 20$

More drastic improvement due to feedback is seen in convergence speed. Time constant is reduced from $\tau = 89$ at $K_P = 0$ to $\tau = 1.07$ at $K_P = 6$ with a factor of 0.012. These results reveals that larger feedback gain gives better performance as long as the observer remains stable. In the following calculation, however, we use rather small feedback gain of 2 in order to retain sufficient stability margin.

Figures $9(a)-(c)$ show convergence of the u_2- and u_3-velocity components and the pressure p at the center of the output measurement plane. In Figs. $9(a)$ and (b) each velocity component of the observer shown in thin line well tracks the standard solution with bold line for $t > 10$. Substantially large pressure of the observer at the initial stage corresponding to acceleration of the flow in the x_1-direction gradually decreases to converge to that of the standard solution as the convergence of the velocity field. Convergence of the u_2- and u_3-velocity component shows the fundamental feature of the observer to provide the estimation of the complete state variables from the partial measurement of the system dynamics.

In the above discussion the velocity components and the pressure are evaluated at the center of the output measurement plane. In order to confirm the validity of the observer, convergence of the state variables at other locations in the domain should also be examined. Convergence of the u_1-velocity component is plotted in Figs. $10(a)-(d)$ at 12 points which consists of four locations on three x_1-planes at $x_1 = 0.3, 2.1, 3.1$. Figures $10(a)-(c)$ correspond to positions on the diagonal from the center to the corner of the plane, while Fig. $10(d)$ corresponds to the position off the diagonal near the wall (see the sketches in the center column figures). The figures on the left column show that the results of the observer converge closely to the standard solution at all points on the output measurement plane. As shown in the figures on the center and the right columns, tracking performance declines downstream, but degree of degradation near the center of planes (Figs. $10(a)$, (b)) is relatively small in comparison with that near the wall (Figs. $10(c)$, (d)).

Since the measure of convergence of the observer should depend not only on the location in the flow field but also all three velocity components, the norm of the velocity vector field is defined here to evaluate the average magnitude over an arbitrary volume in the flow field.

$$\|\mathbf{u}(t, \mathbf{x})\|_v = \left[\int_V (u_1^2 + u_2^2 + u_3^2) d\mathbf{V}/V\right]^{1/2}. \quad (10)$$

In the above expression $\mathbf{V}$ denotes the control volume over which volumetric integration is performed, and V denotes the volume of $\mathbf{V}$ for normalization. It is noted the norm defined above is a function of time. With this norm the error of the velocity field $u(t, \mathbf{x})$ of the observer with respect to the standard solution $u^*(t, \mathbf{x})$ is evaluated over the control volume as:

$$\|\mathbf{u}(t, \mathbf{x}) - \mathbf{u}^*(t, \mathbf{x})\|_v = \left[\int_V \{(u_1 - u_1^*)^2 + (u_2 - u_2^*)^2 + (u_3 - u_3^*)^2\} d\mathbf{V}/V\right]^{1/2}. \quad (11)$$

First, distribution of steady error is evaluated by averaging the value of Eq. (11) over the period $10 \le t \le 20$ assuming $\mathbf{V}$ as the single computational cell volume on the same plane as in Fig. 10. The result, plotted in Fig. $11(a)$, shows the steady error increases in the downstream direction with relatively large value in near-wall region. The result in Fig. $11(b)$, on the other hand, is the steady error evaluated for the standard solution itself which is shifted in time as,

$$\|\mathbf{u}^*(t + T, \mathbf{x}) - \mathbf{u}^*(t, \mathbf{x})\|_v. \quad (12)$$

With sufficiently large value of T, for which 20 is assumed

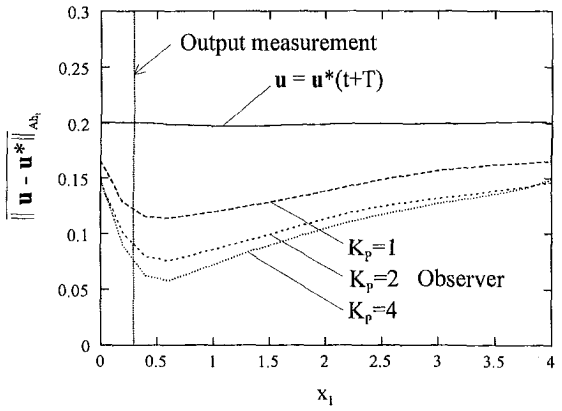

Fig. 12 Norm of the error evaluated on each x_1-plane and averaged in the same time interval as in Fig. 11

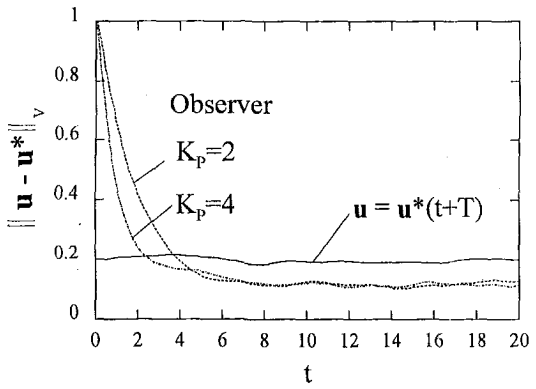

Fig. 13 Variation of the norm of the error evaluated in the whole flow domain

here, the norm of Eq. (12) is regarded as the error between two uncorrelated numerical solutions for the relevant turbulent flow. The result in Fig. 11(*b*) is essentially independent on the x_1-location and provides the steady error distribution by which the effect of the feedback should be evaluated. The strength is about 4 times larger than the feedback case at $x_1 = 0.4$, but the distribution is similar with large magnitude near-wall region where velocity fluctuation itself has large amplitude.

Next the convergence is considered on each cross section normal to the main flow direction. The norm of Eq. (11) was computed over the thin slice of the flow domain $\mathbf{A}(x_1)h_1$. Its steady value was obtained by averaging the result during the period $10 \le t \le 20$. Figure 12 shows the result for the steady error at each axial location for several values of the feedback gain K_P. The solid line in the figure is the result for the equivalence without feedback obtained from the standard solutions $u^*(t + T)$ and $u^*(t)$ in the same manner as in Fig. 11(*b*). The steady error for each feedback gain has its minimum behind the output measurement plane and increases downstream approaching the solid line. It is noted that present calculation assumes the periodical boundary condition and the maximum error at the boundary is still below the result for the uncorrelated case of solid line. The minimum value of the error reduces as increasing the feedback gain. For the case of the feedback gain of 4, the error is reduced by a factor of 0.3 in comparison with the result without feedback.

The control volume **V** in Eq. (11) is assumed as the whole flow domain. Variation of the error is plotted in Fig. 13 for the feedback gain of $K_P = 2$ and 4. Since all the velocity components are assumed to be 0 as the initial condition, errors for both cases are almost 1 at the initial time $t = 0$. They monotonically decreases until $t \approx 10$ reaching almost steady values. Comparison between the results of different feedback gain reveals that the convergence is faster for the case of the larger gain of $K_P = 4$, but little difference is seen in the steady value of the error. The solid line in Fig. 13 shows the norm calculated by Eq. (12) for the standard solution with initial time difference of $T = 20$. The norm for uncorrelated standard solution is about 0.2. The steady error for the present observer has the average value of 0.12, which is reduced by a factor of 0.6 from the result obtained without feedback.

The preceding results confirm the validity of the present observer in estimating the state of flow for the standard solution obtained on the coarse $20 \times 10 \times 10$ grid system. As mentioned earlier, this grid system is not enough to resolve the small scales of turbulence. An example is given here showing the possibility to extend to more realistic flow cases. The convergence of the present observer is tested for the standard solution obtained in the same condition but with 64 times finer $80 \times 40 \times 40$ grid points (see Fig. 4). Figure 14 shows the present observer constructed on the coarse grid system does not approach to the standard solution of the same coarse grid but rapidly converges to the more accurate solution on finer grid as the result of feedback action. This result suggests the present observer could be a prototype of integrated computational and experimental method by which the accuracy of the numerical solution on a coarse grid system is significantly improved by the feedback from experimental measurement. Figure 15 shows the average norm of the error of the present observer is reduced by a factor of 0.1 in comparison with the ordinary numerical simulation.

4 Conclusions

This paper treated the state estimator or the observer of the flow field. The observer, being a fundamental concept in the control system theory, also has a potential in the analysis of flow related problems as an integrated computational method with the aid of experimental measurement. In the framework of the observer, the state of the physical flow is estimated from the mathematical model with the feedback of on-line experimental measurement. A standard finite volume flow simulation algorithm is modified to the observer by adding the feedback controller which compensates the boundary condition of the simulation based on the estimation error between output signals of the experimental measurement and the computational result. In this paper validity of the proposed observer was confirmed by the numerical experiment for the turbulent flow through a duct of square cross section. The physical flow is modeled by a precalculated numerical solution of the developed turbulent flow. The estimation error in the u_1-velocity component at the grid points on the output measurement plane is fed back to the pressure boundary condition based on the simple proportional control law. Appropriate choice of the feedback gain accelerates

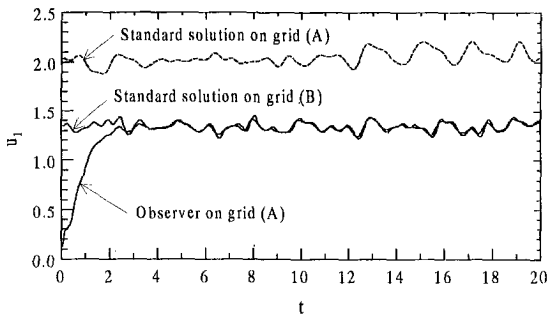

Fig. 14 Convergence of u_1-velocity at the center of output measurement plane. The standard solution is obtained on 64 times finer grid system than the observer. Grid (A): $20 \times 10 \times 10$, Grid (B): $80 \times 40 \times 40$, feedback gain $K_P = 4$, results are normalized using the mean axial velocity $\bar{u}_{m0}$ in Eq. (3).

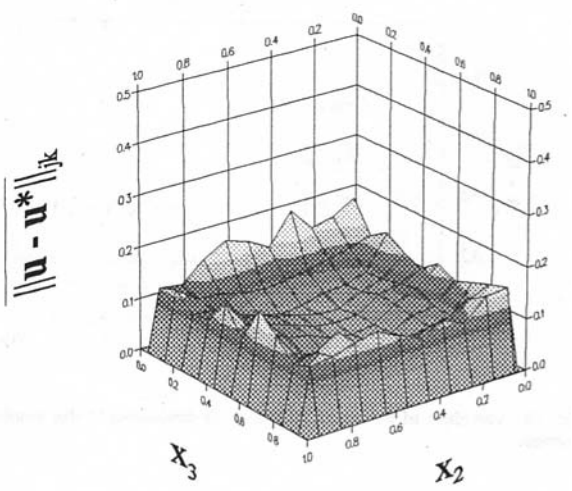

Fig. 15(*a*) $K_p = 4$

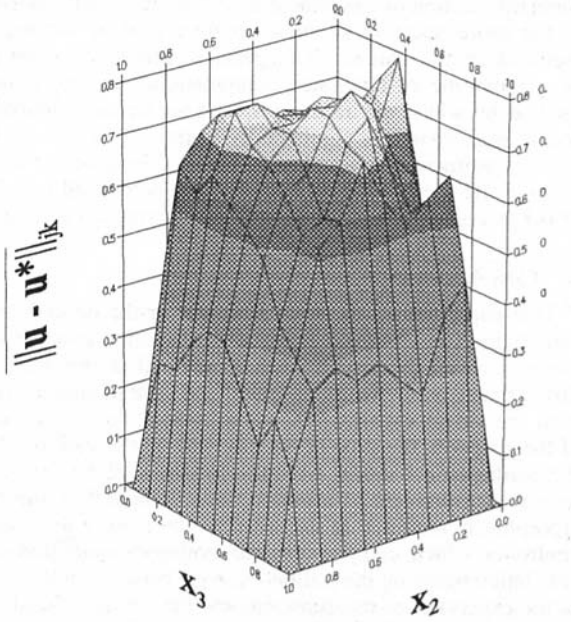

Fig. 15(*b*) $K_p = 0$ (without feedback)

Fig. 15 Distribution of the averaged norm of the error of the observer from the standard solution on the finer grid system (B) ($X_1 = 2.0$). The result for $K_P = 0$ is equivalent to the norm of difference between the standard solutions on coarse grid (A) and fine grid (B) in Fig. 14.

the convergence of the result to the standard solution by a factor of 0.012 and reduces the final estimation error by a factor of 0.6 in the whole domain or a factor of 0.3 behind the output measurement plane. As the first step, present paper focuses on the case the grid system is the same both for the observer and the standard solution. A test calculation using the standard solution of finer grid system suggests that more significant improvement of the numerical accuracy is expected in realistic case where the standard solution is calculated in finer grid or replaced by experimental measurement of real flows.

For the future work, theoretical treatment is necessary for the stability of the observer and the feedback strategy less restrictive than the present study should be considered. Extension to more realistic standard numerical solution or experimental measurement is also essential in the next step.

Acknowledgment

The authors are grateful to Professor J. A. C. Humphrey of Bucknell University for pointing out the importance of Interactive Computational and Experimental Methodology (ICEME) in the study of flow related problems. The computer code used in this study was originally developed at the University of California, Berkeley by T. Hayase, J. A. C. Humphrey, and R. Greif. The calculations were performed on the Cray C-916 in the Institute of Fluid Science, Tohoku University.

References

Choi, H., Moin, P., and Kim, J., 1994, "Active Turbulence Control for Drag Reduction in Wall-Bounded Flows," *Journal of Fluid Mechanics.*, Vol. 262, pp. 75–110.

Curtain, R. F., and Zwart, H. J., 1995, *An Introduction to Infinite-Dimensional Linear Systems Theory,* Springer-Verlag, New York, p. 246.

Fletcher, C. A. J., 1988, *Computational Techniques for Fluid Dynamics,* Vol. 1, Springer-Verlag, p. 302.

Gad-el-Hak, M., 1994, "Interactive Control of Turbulent Boundary Layers: A Futuristic Overview," *AIAA Journal,* Vol. 32, No. 9, pp. 1753–1765.

Hayase, T., Humphrey, J. A. C., and Greif, R., 1990, "Mini Manual for ROTFLO2," *Department of Mechanical Engineering Report,* #FM-90-1, University of California at Berkeley.

Hayase, T., and Suematsu, Y., 1991, "Direct Numerical Simulation of Turbulent Flow in a Square Pipe," *Proceedings of 3rd Triennial International Symposium on Fluid Control, Measurement, and Visualization, FLUCOME '91,* San Francisco, pp. 99–106.

Hayase, T., Humphrey, J. A. C., and Greif, R., 1992, "A Consistently Formulated QUICK Scheme for Fast and Stable Convergence Using Finite-Volume Iterative Calculation Procedures," *Journal of Computational Physics,* Vol. 98, No. 1, pp. 108–118.

Humphrey, J. A. C., Devarakonda, R., and Queipo, N., 1993, "Interactive Computational-Experimental Methodologies (ICEME) for Thermofluids Research: Application to the Optimized Packaging of Heated Electronic Components," *Computers and Computing in Heat Transfer Science and Engineering,* Yang, K. T. and Nakayama, W., eds., CRC Press and Begell House, New York, pp. 293–317.

Kajishima, T., Miyake, Y., and Nishimoto, T., 1990, "Large Eddy Simulation of Turbulent Flow in a Square Duct," *Preprint of the Japan Society of Mechanical Engineers,* No. 900-59(B), pp. 243–245.

Kawahara, G., Ayukawa, K., Kubota, T., and Ochi, J., 1990, "Intensity and Probability Density Distribution of Turbulence in a Pipe with Square Cross-Section," *Preprint of the Japan Society of Mechanical Engineers,* No. 900-59(B), pp. 136–138.

Li, X., and Yong, J., 1995, *Optimal Control Theory for Infinite Dimensional Systems,* Birkhäuser.

Luenberger, D. G., 1979, *Introduction to Dynamic Systems: Theory, Models, and Applications,* Wiley, New York.

Misawa, E. A., and Hedrick, J. K., 1989, "Nonlinear Observers: A State-of-the-art Survey," ASME JOURNAL OF DYNAMIC SYSTEMS, MEASUREMENT, AND CONTROL, Vol. 111, No. 3, pp. 344–352.

Schlichting, H., 1979, *Boundary-Layer Theory,* 7th edition, McGraw-Hill, p. 597.

Skelton, R. E., 1988, *Dynamic Systems Control,* 1988, John Wiley & Sons, New York.

On Oscillatory Instability of Convective Flows at Low Prandtl Number

A. Yu. Gelfgat
Research Associate.
Mem. ASME

P. Z. Bar-Yoseph
Professor.
Mem. ASME

A. L. Yarin
Professor.

Computational Mechanics Laboratory,
Faculty of Mechanical Engineering,
Technion-Israel Institute of Technology,
Haifa 32000, Israel

Numerical investigation of the oscillatory instability of convective flows in laterally heated rectangular cavities is presented. Cavities with no-slip isothermal vertical boundaries, no-slip adiabatic lower boundary, and stress-free adiabatic upper boundary are considered. Dependence of the critical Grashof number and the critical frequency of oscillations on the aspect ratio (A = length/height) of the cavity are investigated. The stability diagrams were obtained for the whole interval of the aspect ratio $1 \le A \le 10$. The study was carried out for two values of the Prandtl number, $Pr = 0$ and 0.015. It was shown that the oscillatory instability sets in as a result of the Hopf bifurcation. It was found that at two different values of the Prandtl number considered the instability is caused by different infinitely small dominant perturbations, which means that the convective heat transfer strongly affects stability of the flow even for cases having small Prandtl number. No asymptotic behavior for large aspect ratios was found up to $A = 10$. Slightly supercritical oscillatory flows were approximated asymptotically by means of the weakly nonlinear analysis of the calculated bifurcation.

Introduction

The present study is devoted to numerical analysis of the transition from steady to oscillatory state of convective flows at low-Prandtl-number in a laterally heated rectangular cavity. This problem attracted a wide scientific interest after experiments of Hurle et al. (1974) showed that convective oscillations cause lattice structure of a growing crystal in the processes of crystal growth from a liquid phase. A particular case of a cavity with aspect ratio (length/height) $A = 4$ has been considered as a benchmark at the GAMM Workshop (Roux, 1989), and since then has been investigated in detail (see for example Winters, 1988; Roux, 1989; Ben Hadid and Roux, 1989; Pulicani et al., 1989; Okada and Ozoe, 1993a, b; Afrid and Zebib, 1990; Gelfgat and Tanasawa, 1994; McClelland, 1995 and references therein). This particular value of the aspect ratio is characteristic for some crystal growth techniques and was used in the experiments of Hurle et al. (1974). However, the dependence of the steady-oscillatory transition on the aspect ratio of the cavity was not examined.

In the present study, the dependence of the critical parameters (critical Grashof number Gr_{cr} and critical frequency ω_{cr} of oscillations) on the aspect ratio is investigated for $1 \le A \le 10$, and for the following boundary conditions: rigid isothermal vertical boundaries, rigid adiabatic lower boundary, and flat stress-free adiabatic upper boundary. This corresponds to the Ra-Fa (**R**igid/**a**diabatic and stress-**F**ree/**a**diabatic horizontal boundaries) case defined at the GAMM workshop. Investigation is carried out for the same values of the Prandtl number $Pr = 0$ and 0.015, which were considered at the GAMM workshop (Roux, 1989). Stability diagrams for the whole interval $1 \le A \le 10$ are obtained here for the first time.

The stress-free upper boundary condition (denoted as R-F case in the GAMM workshop; Roux, 1989) was taken into consideration here because only one branch of steady-state flows is known for this case, at least for fluids with small Prandtl number (we consider here only $Pr = 0$ and 0.015). The case of cavity with four no-slip boundaries (R-R case) is more complicated for numerical study because of the existence of multiple stable steady states. The existence of two different steady states of the flow for $A = 4$ was reported by Crespo del Arco et al. (1989). Recently, Gelfgat, Bar-Yoseph and Yarin (1997) reported the existence of four distinct branches of stable-steady states for $3 \le A \le 10$. Besides this, the central symmetry of the flow in R-R case may cause symmetry-breaking instabilities which makes stability features of the flow in R-R and R-F cases considerably different. The stiff dependence of the critical parameters on the geometry of the cavity shown here allows us to assume that similar stiff dependence on the boundary conditions also exists.

Choice of the stress-free boundary condition on the upper surface is idealization of the practically important model which includes also the thermocapillary force (see for example Ben Hadid and Roux, 1989; Mundrane and Zebib, 1994) and possible deformation of the free surface (McClelland, 1995). However, calculation of the stability maps in the space of several governing parameters has to be started by fixing some of them. It is a natural choice to set the thermocapillary force and the deformation of the free surface to zero for the beginning of such study.

Setting the Prandtl number to zero means that the convective transport of heat is neglected. In this case the temperature can be evaluated analytically from the steady Laplace equation and only the Navier-Stokes equation with the constant buoyancy force has to be solved. This allows one to simplify the problem which may be important for many practical applications. The comparison of the steady-oscillatory transition at zero and small Prandtl numbers is one of the objectives of the present study. Another objective of the study is to check for which values of the aspect ratio it is possible to use the asymptotics of the infinite fluid layer ($A \to \infty$; Laure and Roux, 1989). If such an asymptotics could be applied to a confined flow, the investigation of the instability onset, as well as understanding of the physics of the phenomenon, will be simplified.

Formulation of the Problem

The two-dimensional convective flow in a rectangular cavity $0 \le x \le A$, $0 \le y \le 1$ is described by the dimensionless

Contributed by the Fluids Engineering Division for publication in the JOURNAL OF FLUIDS ENGINEERING. Manuscript received by the Fluids Engineering Division September 5, 1996; revised manuscript received June 23, 1997. Associate Technical Editor: Jong H. Kim.

momentum, energy and continuity equations for a Newtonian Boussinesq fluid

$$\frac{\partial \mathbf{v}}{\partial t} + (\mathbf{v}\cdot\nabla)\mathbf{v} = -\nabla p + \Delta\mathbf{v} + \mathrm{Gr}\theta\mathbf{e}_y, \qquad (1)$$

$$\frac{\partial \theta}{\partial t} + (\mathbf{v}\cdot\nabla)\theta = \frac{1}{\mathrm{Pr}}\Delta\theta, \quad \nabla\cdot\mathbf{v} = 0 \qquad (2, 3)$$

Here $\mathbf{v}$ is the fluid velocity, θ is the temperature, p is the pressure, $\mathrm{Gr} = g\beta(\theta_1 - \theta_2)H^3/\nu^2$ is the Grashof number, $\mathrm{Pr} = \nu/\chi$-is the Prandtl number, $A = L/H$ is the aspect ratio, g is the gravity acceleration, β is the thermal expansion coefficient, $(\theta_1 - \theta_2)$ is the temperature difference between the cold and hot vertical walls, ν is the kinematic viscosity, χ is the thermal diffusivity, L and H are, respectively, the length and the height of the cavity.

The following boundary conditions are imposed:

$$\mathbf{v}(x = 0, 0 \le y \le 1) = \mathbf{0}, \quad \mathbf{v}(x = A, 0 \le y \le 1) = \mathbf{0}$$

(no-slip; vertical walls), (4, 5)

$$\mathbf{v}(0 \le x \le A, y = 0) = \mathbf{0} \quad \text{(no-slip; bottom)}, \qquad (6)$$

$$v_y(0 \le x \le A, y = 1) = 0, \quad \frac{\partial v_x}{\partial y}(0 \le x \le A, y = 1) = 0,$$

(stress-free; flat upper surface) (7, 8)

$$\theta(x = 0, 0 \le y \le 1) = 1, \quad \theta(x = A, 0 \le y \le 1) = 0$$

(isothermal; vertical walls) (9)

$$\frac{\partial \theta}{\partial y}(0 \le x \le A, y = 0) = \frac{\partial \theta}{\partial y}(0 \le x \le A, y = 1) = 0$$

(thermally insulated top and bottom) (10, 11)

Computational Method

Problem (1)–(11) was solved using the spectral Galerkin method with globally defined basis functions which satisfy analytically all the boundary conditions and the continuity equation. The exponential convergence of the global Galerkin method allows us to decrease the number of degrees of freedom (number of scalar modes in the numerical method), and to investigate steady states, their stability and weakly supercritical regimes of the flow in the framework of a single computational model (for computational details and some preliminary test calculations see Gelfgat and Tanasawa (1994)). In particular, it was shown that for $A = 4$ use of 24 basis functions in horizontal and 10 basis functions in vertical directions provides accuracy comparable with the finite element method using 60×20 biquadratic finite elements (Winters, 1988) and the pseudospectral method with Chebyshev polynomial expansions using 50×20 collocation points (Pulicani et al., 1989).

The whole numerical process is as follows. Steady states of the flow are calculated by the Newton method. Then the Navier-Stokes equations are linearized in the vicinity of a stationary solution, and the corresponding spectrum and eigenmodes are calculated. The critical Grashof number is defined as the value at which the real part of the dominant eigenvalue is zero. The corresponding eigenvector describes the most unstable perturbation of the flow (the critical eigenmode). After the critical Grashof number is obtained, the weakly nonlinear analysis of the bifurcation is carried out. The slightly supercritical states of the flow are approximated as

$$\mathrm{Gr} = \mathrm{Gr}_{cr} + \mu\epsilon^2 + O(\epsilon^4),$$

$$T(\mathrm{Gr}) = \frac{2\pi}{\omega_{cr}}[1 + \tau\epsilon^2 + O(\epsilon^4)], \qquad (12, 13)$$

$$\{\mathbf{v}, \theta\}(t, \mathrm{Gr}) = \{\mathbf{v}_0, \theta_0\}(\mathrm{Gr}_{cr}) + \epsilon\,\mathrm{Real}\left[\{\mathbf{v}_E, \theta_E\}\exp\left(\frac{2\pi i}{T}\right)\right] + O(\epsilon^2) \qquad (14)$$

Here ϵ is a small formal parameter, T is the period of oscillations, ω_{cr} is the critical cycle frequency (the imaginary part of the dominant eigenvalue at $\mathrm{Gr} = \mathrm{Gr}_{cr}$). The subscript 0 defines the steady state at $\mathrm{Gr} = \mathrm{Gr}_{cr}$, and the subscript E defines the eigenvector of the linearized Boussinesq equations. The asymptotic approximation (12–14) of the oscillatory state is defined by two parameters μ and τ, which are calculated using the algorithm described in Hassard et al. (1981). Application of this algorithm to the dynamic system corresponding to an incompressible fluid flow is described in Gelfgat et al. (1996a).

The convergence of the critical Grashof number and the critical frequency ($f_{cr} = \omega_{cr}/2\pi$) is shown in the Table 1 for the aspect ratios 1, 4, and 10, respectively. Grashof number in Tables 1–3 is redefined as $\mathrm{Gr}^* = \mathrm{Gr}/A$ in according with the definitions used in the GAMM benchmark problem (Roux, 1989). The critical parameters were calculated using different number of basis functions in the Galerkin series. Numbers of basis functions in x- and y-directions are denoted as N_x and N_y, respectively. It follows from Table 1 that for $A = 1$ and 4 the critical parameters Gr^*_{cr} and f_{cr} converge rapidly with the increase of the number of basis functions. As it is seen from the Table 1 the convergence for $A = 10$ is slower, but two correct digits of Gr_{cr} and f_{cr} can be obtained with the use of 60×20 basis functions.

The numerical code has been validated by comparing its results with other independent solutions (Tables 2 and 3). It is seen (Table 2) that the present results, obtained using the stability analysis, are in a good agreement (to within the second or the third digit) with the results of Ben Hadid and Roux (1989), Pulicani et al. (1990), Le Quere (1989), and Winters (1988). The discrepancy with the results of Okada and Ozoe (1993) is about 10 percent. An additional comparison with the results of the same work for other aspect ratios is shown in Table 3. For $A = 3$, 4 and 5 the discrepancy is also about 10 percent, but at $A = 2.5$ results disagree completely. Since the result of the present work for $A = 4$ is completely validated (see Table 1) and is compared better with the results of other numerical studies, it seems that the results of this reference are not accurate enough.

To ensure convergence, the present calculations were carried out using 40×30 basis functions for $1 \le A \le 5$ and 60×20 basis functions for $4 \le A \le 10$. In the interval $4 \le A \le 5$ the results obtained with the two different truncations coincide to within the third digit.

Results

Numerical investigation of the spectrum of the steady states showed that for the two considered values of the Prandtl number, $\mathrm{Pr} = 0$ and 0.015, and for the whole interval $1 \le A \le 10$ the oscillatory instability sets in due to the Hopf bifurcation.

The dependence of the critical Grashof number Gr_{cr} on the aspect ratio is shown in Figs. 1(a) and 2(a) for $1 \le A \le 3$ and $3 \le A \le 10$, respectively. Steady flows are stable below the curves and unstable above them. The corresponding relations $\omega_{cr}(A)$ are shown in Figs. 1(b) and 2(b). As it is seen from Figs. 1 and 2 the curves $\mathrm{Gr}_{cr}(A)$ and $\omega_{cr}(A)$ consist of several continuous branches corresponding to different dominant perturbations (different eigenmodes of the linearized problem). These eigenmodes become dominant at different values of the aspect ratio and abruptly replace each other at the points where the neutral curves $\mathrm{Gr}_{cr}(A)$ have discontinuities in the slope (Figs. 1(a) and 2(a)). Switches of the dominant eigenmode lead to abrupt changes of the critical frequency (Figs. 1(b) and 2(b)).

Table 1 Convergence study for the critical parameters. $Gr^*_{cr} = Gr/A$, N_x and N_y denote number of basis functions respectively in x- and y- directions

			$A = 1$			
$N_x \times N_y$	16×16	20×20	26×26	30×30	36×36	40×40
$Gr^*_{cr} \times 10^{-6}$	2.6956	2.6776	2.7695	2.7471	2.7467	2.7467
f_{cr}	1474.8	1458.8	1469.4	1466.5	1466.4	1466.4
			$A = 4$			
$N_x \times N_y$	32×18	36×22	40×26	50×20	40×30	60×24
Gr^*_{cr}	19404	19403	19380	19361	19363	19363
f_{cr}	14.916	14.915	14.909	14.901	14.903	14.901
			$A = 10$			
$N_x \times N_y$	40×18	50×20	70×20	60×20	66×24	70×24
Gr^*_{cr}	61917	62314	61942	61663	62330	62515
f_{cr}	51.17	51.30	51.13	50.98	51.34	51.48

Figures 1 and 2 show that the functions $Gr_{cr}(A)$ and $\omega_{cr}(A)$ are non-monotone and very sensitive to a small change of the aspect ratio or the Prandtl number. For example, at Pr = 0.015 the values of the critical Grashof number and the critical frequency for $A = 1.7$ and $A = 1.8$ differ drastically (Fig. 1). The difference between the critical parameters at Pr = 0.015 and Pr = 0 is relatively large almost everywhere except in the interval $3 \leq A \leq 4.95$ (Figs. 2(a) and (b)). Such a big difference in critical parameters for zero and small values of the Prandtl number means that the convective heat transfer plays a significant role in the onset of instability and cannot be neglected when stability features of the flow are considered. This leads to the conclusion that extrapolation of results, obtained for particular values of the Prandtl number or the aspect ratio, to other, even very close, values of the control parameters should be done with an extreme caution.

It is seen from Fig. 2(a) that the function $Gr_{cr}(A)$ has a global minimum very close to $A = 4$. This value of the aspect ratio was chosen for a comparative study with the benchmark of the GAMM workshop (Roux, 1989). Note that this particular value of the aspect ratio may not be a very good choice, since calculations for smaller values of Gr are always more accurate than for larger ones. Moreover, in the interval $3 \leq A \leq 4.95$, the onset of instability for Pr = 0.015 and Pr = 0 is similar (see Fig. 4) and investigation of only a single value of the aspect ratio may lead to a wrong conclusion that the convective heat transfer can be neglected (see Gelfgat and Tanasawa, 1994 for $A = 4$).

There are two hysteresis loops of the critical Grashof number for Pr = 0.015. One is located near $A = 1.6$ (Fig. 1(a)), and another one is located in the interval $4.9 \leq A \leq 5$ (Fig. 2(a)). The hysteresis of Gr_{cr} means that there are three critical values $Gr^1_{cr} < Gr^2_{cr} < Gr^3_{cr}$. The first steady-oscillatory transition occurs at $Gr = Gr^1_{cr}$. With the increase of Gr a backwards transition from an oscillatory to a stable steady state takes place at $Gr = Gr^2_{cr}$, and then, at $Gr = Gr^3_{cr}$, the steady flow finally bifurcates to the oscillatory state. Each of the three transitions is characterized by its critical frequency such that in the hysteresis regions there are 3 critical frequencies corresponding to a single value of the aspect ratio (magnified areas in Figs. 1(b) and 2(b)).

The first hysteresis (Fig. 1(a)) takes place on the branch of the neutral curve which starts at $A \approx 1.59$ (point I in Fig. 1(a)), continues with the decrease of A and Gr_{cr} up to $A \approx 1.57$ (point II), and with the increase of A and Gr_{cr} ends at $A \approx 1.69$ (point III). For example, at $A = 1.59$ the first steady-oscillatory transition takes place at $Gr^1_{cr} = 1.17 \times 10^6$, then the oscillatory-steady transition at $Gr^2_{cr} = 1.63 \times 10^6$, and the final steady-oscillatory transition at $Gr^3_{cr} = 1.77 \times 10^6$ (which belongs to the previous branch of the neutral curve).

The second hysteresis loop (Fig. 2(a)) starts at $A \approx 4.93$ (point IV in Fig. 2(a)) where the neutral curve turns such that the critical Grashof continues to grow with the decrease of the

Table 2 Comparison with the published results ($A = 4$, Pr = 0, $Gr^*_{cr} = Gr/A$)

Reference	Discretization	Gr^*_{cr}	f_{cr}
Okada and Ozoe (1993)	121×35 finite difference non-uniform grid	15050	13.08
Ben Hadid and Roux (1989)	121×41 finite difference non-uniform grid	13500–13750	12.25–12.42
Pulicani et al (1990)	27×15 Chebyshev spectral modes	13100–13500	12.32–12.37
Le Quere (1989)	50×20 Chebyshev pseudospectral modes	13650	12.33
Winters (1988)	60×24 biquadratic finite elements (121×49 non-uniform grid)	13722	12.36
Present work	40×30 spectral modes	13683	12.34

Table 3 Comparison with the results of Okada and Ozoe, 1993a (Pr = 0, $Gr^*_{cr} = Gr/A$)

	Okada and Ozoe (1993)			Present work		
A	Mesh	Gr^*_{cr}	f_{cr}	Number of basis functions	Gr^*_{cr}	f_{cr}
2.5	85×35	90490	60.86	40×30	63916	45.12
3	121×41	30170	22.05	40×30	26703	20.39
4	121×35	15050	13.08	40×30	13683	12.34
5	151×35	13220	12.03	50×20	12136	11.31

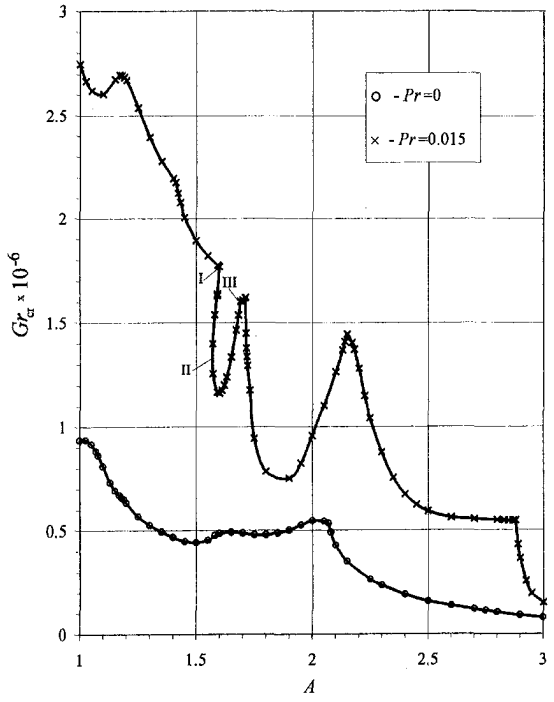

Fig. 1(*a*) Dependence $Gr_{cr}(A)$

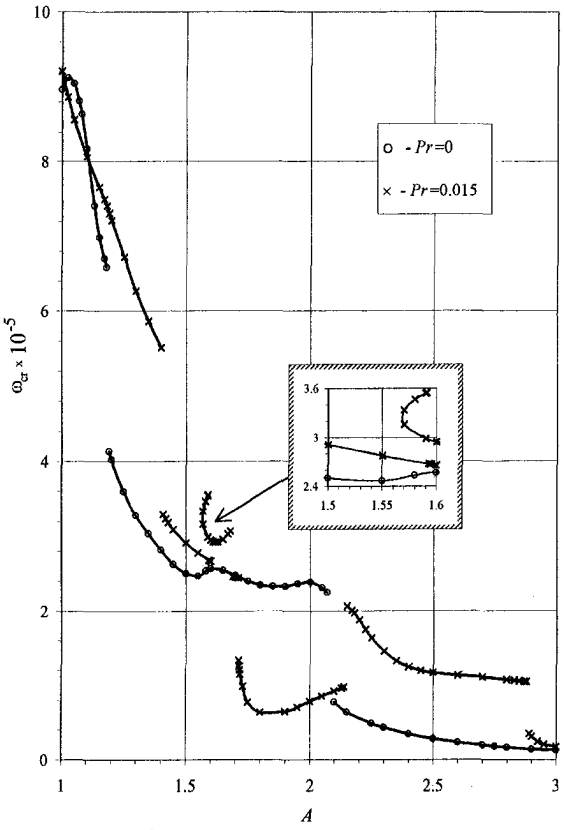

Fig. 1(*b*) Dependence $\omega_{cr}(A)$

Fig. 1 Stability diagram for aspect ratio $1 \leq A \leq 3$.

aspect ratio. When the aspect ratio reaches the value $A \approx 4.85$ (point V) the neutral curve turns once more such that Gr_{cr} increases with the increase of A, e.g. at $A = 4.9$ three critical values of the Grashof number are 1.09×10^5, 1.45×10^5, and 1.88×10^5.

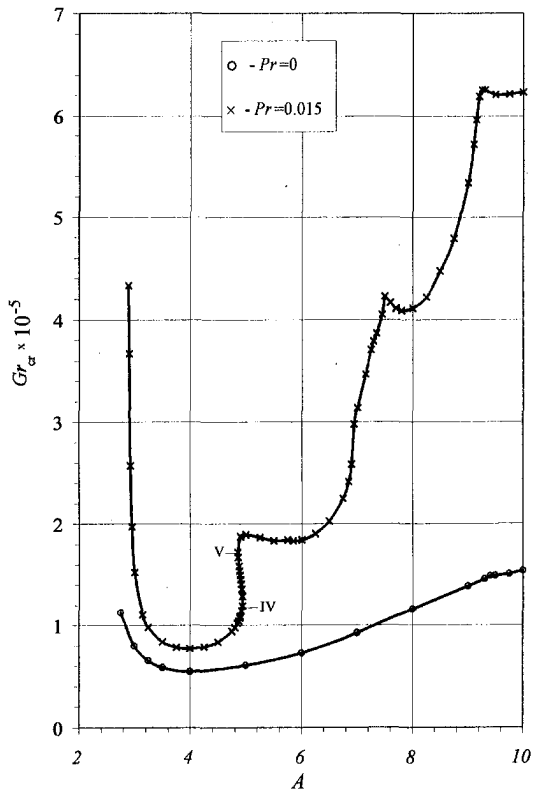

Fig. 2(*a*) Dependence $Gr_{cr}(A)$

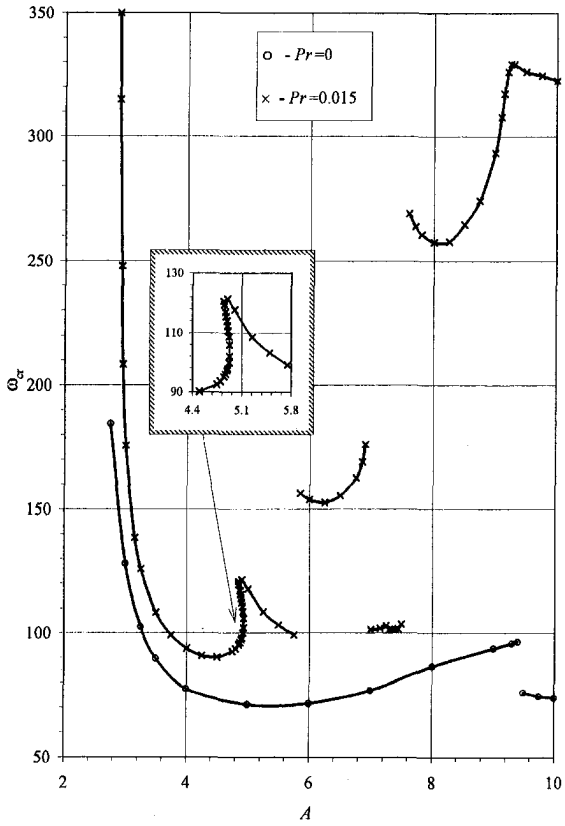

Fig. 2(*b*) Dependence $\omega_{cr}(A)$

Fig. 2 Stability diagram for aspect ratio $3 \leq A \leq 10$.

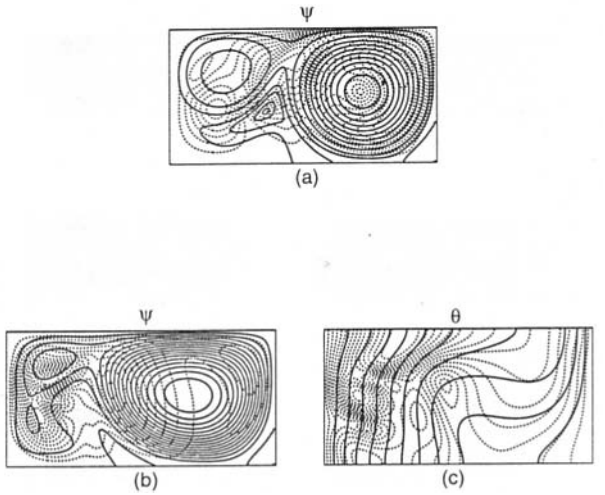

Fig. 3 Isolines of the stream function and the temperature (solid lines), and the corresponding dominant perturbations (dashed lines) for aspect ratio $A = 2$. All isolines, except the stream lines $\psi \leq 0$, are equally spaced. (*a*) Pr = 0, $Gr_{cr} = 5.47 \times 10^5$; $\psi_{max} = 502.9$, $\psi_{min} = -8.957$, (*b*) Pr = 0.015, $Gr_{cr} = 9.59 \times 10^5$; $\psi_{max} = 318.5$, $\psi_{min} = -2.135$.

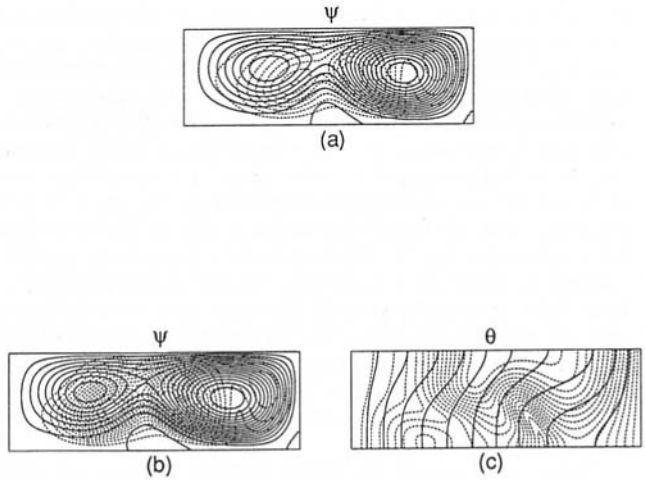

Fig. 4 Isolines of the stream function and the temperature (solid lines), and the corresponding dominant perturbations (dashed lines) for aspect ratio $A = 3$. All isolines, except the stream line $\psi = 0$, are equally spaced. (*a*) Pr = 0, $Gr_{cr} = 8.01 \times 10^4$; $\psi_{max} = 104.8$, $\psi_{min} = -0.5194$, (*b*) Pr = 0.015, $Gr_{cr} = 1.54 \times 10^5$; $\psi_{max} = 141.6$, $\psi_{min} = -0.8440$.

To compare the results with the case of an infinite fluid layer it is necessary to redefine the Grashof number using the average temperature gradient $(\theta_1 - \theta_2)/L$ instead of the characteristic temperature difference $(\theta_1 - \theta_2)$. This yields $Gr^* = g\beta(\theta_1 - \theta_2)H^4/L\nu^2 = Gr/A$. Figure 2 shows that no well defined asymptotic behavior is reached for Gr (neither for Gr*) at aspect ratios close to $A = 10$. Moreover, there is a switch of the dominant perturbation in the interval $9 \leq A \leq 10$ for both values of the Prandtl number Pr = 0 and 0.015 (Fig. 2). Further investigation is necessary to find for which values of A, the infinite layer solution is a valid approximation.

Examples of steady flows at critical values of parameters and the corresponding dominant perturbations are shown in Figs. 3–5 for $A = 2$, 3 and 8. Flows and perturbations for $A = 1$, 4, and 10 are described in Gelfgat and Tanasawa (1994) and Gelfgat et al. (1996b). Since the eigenvector of the linearized problem is a complex vector (see Eq. (14)) which is defined within multiplication by a complex constant, its modulus is used to describe the dominant perturbations. Note that for slightly supercritical oscillatory flows the isolines of the amplitude of oscillations coincide with the isolines of modulus of the perturbation. Each plot in Figs. 3–5 is arranged in the following way: solid curves show isolines of the stream function ψ and the temperature θ. Dashed lines show isolines of the modulus of the most dominant perturbations of functions ψ and θ. For Pr = 0 only the stream function and its perturbation are reported.

In the case Pr = 0 the buoyancy force is constant and the temperature is not perturbed at all. This means that only the fluid flow itself can become unstable, i.e., the instability is caused by the hydrodynamic effect only (heat transfer does not influence the flow stability). This instability is called hydrodynamic instability to distinguish it from the other possible types of instability, which may arise at non-zero Prandtl numbers and may be caused by a thermal-hydrodynamic effect.

Flow patterns and their corresponding dominant perturbations for $A = 2$ are shown in Fig. 3. It is seen that the perturbations of the stream function for Pr = 0 (Fig. 3(*a*)) and Pr = 0.015 (Fig. 3(*b*)) are different: the perturbation of ψ at Pr = 0 has a global maximum in the center of the main convective vortex, while at Pr = 0.015 maximal values of the perturbation of ψ are located near the hot wall. This difference in the patterns means that the onset of the instability at Pr = 0.015 is influenced by the thermal effects and differs from those at Pr = 0. The perturbation of θ (Fig. 3(*c*)) also has a global maximum near the hot wall. This allows us to conclude that the oscillatory instability initiates in the form of oscillations of the velocity and the temperature near the hot wall where convective flow and convective heat transfer are relatively weak (see isolines of ψ and θ in Fig. 3(*b*) and (*c*)).

Figure 4 corresponds to the case $A = 3$ for which the oscillatory instability at Pr = 0 (Fig. 4(*a*)) and Pr = 0.015 (Fig. 4(*b*)) is of the same hydrodynamic type. This conclusion follows from the similarity of the patterns of the perturbations of ψ for two values of the Prandtl number (Fig. 4(*a*) and 4(*b*)). According to the results of this study (Fig. 2), this similarity is preserved only in the interval $3 \leq A \leq 4.95$ (for the case $A = 4$ see Gelfgat and Tanasawa (1994) and Gelfgat et al. (1996b)).

Results for a larger aspect ratio, $A = 8$, are plotted in Fig. 5. Note that at Pr = 0 the critical points for $A = 3$ and $A = 8$ belong to the same branch of the neutral curve, and to different branches at Pr = 0.015 (Fig. 2). Comparison of Figs. 4 and 5 shows that at Pr = 0 the maximum of the perturbation of ψ is located at the outer boundary of the strongest meridional circulation both for $A = 3$ and 8. The same was observed for $A = 4$ (see Gelfgat and Tanasawa, 1994 and Gelfgat et al., 1996b). The pattern of the perturbation at Pr = 0.015 is different

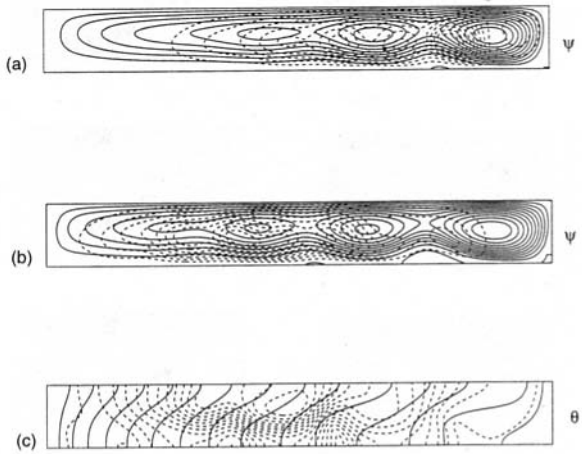

Fig. 5 Isolines of the stream function and the temperature (solid lines), and the corresponding dominant perturbations (dashed lines) for aspect ratio $A = 8$. All isolines, except the stream line $\psi = 0$, are equally spaced. (*a*) Pr = 0, $Gr_{cr} = 1.16 \times 10^5$; $\psi_{max} = 94.79$, $\psi_{min} = -0.009570$, (*b*) Pr = 0.015, $Gr_{cr} = 4.11 \times 10^5$; $\psi_{max} = 209.9$, $\psi_{min} = -2.651$.

(Figs. 5(*b*) and 5(*c*)). Two local maxima of the perturbation of ψ are located near weaker meridional circulations, and the global maximum of the perturbation of θ is located in the same area. As it was previously reported for $A = 10$ (Gelfgat et al., 1996b) and for both cases, Pr = 0 and Pr = 0.015, the flow and their perturbations do not contain any spatially periodic structures. With the increase of the aspect ratio, the global maximum of the stream function remains near the cold vertical boundary, and the whole convective vortex is shifted toward the colder area (Fig. 5). This means that no spatially periodic structure is observed. It is obvious that the dominant perturbation of the nonspatially-periodic flow also does not contain any spatially periodic structures. So, the asymptotic case of an infinite fluid layer ($A \to \infty$) cannot be applied for the considered finite aspect ratio cases ($A \leq 10$). Significantly larger values of the aspect ratio must be considered for investigation of this asymptotic behavior.

Slightly supercritical oscillatory states of the flow are illustrated in Figs. 6–8 for $A = 2$, 3 and 8, respectively. The oscillatory states were approximated asymptotically using weakly nonlinear analysis of the Hopf bifurcation (Hassard et al., 1981) which results in Eqs. (12)–(14). All the supercritical states were approximated for 10 percent supercriticality.

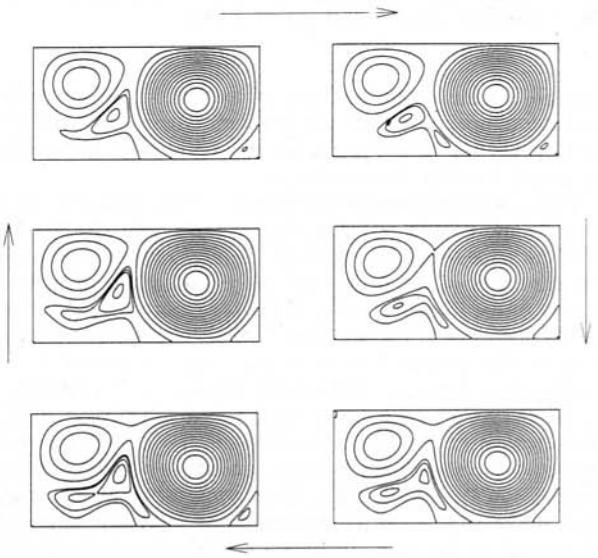

Fig. 6(*a*) Pr = 0, Gr = 5.65×10^5

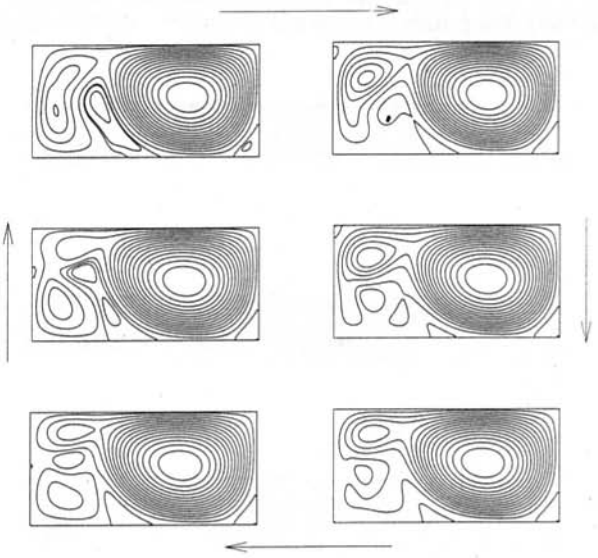

Fig. 6(*b*) Pr = 0.015, Gr = 1.02×10^6

Fig. 6 Instantaneous streamlines of the convective flow plotted for equal time intervals *T*/6 covering the complete period. Aspect ratio *A* = 2.

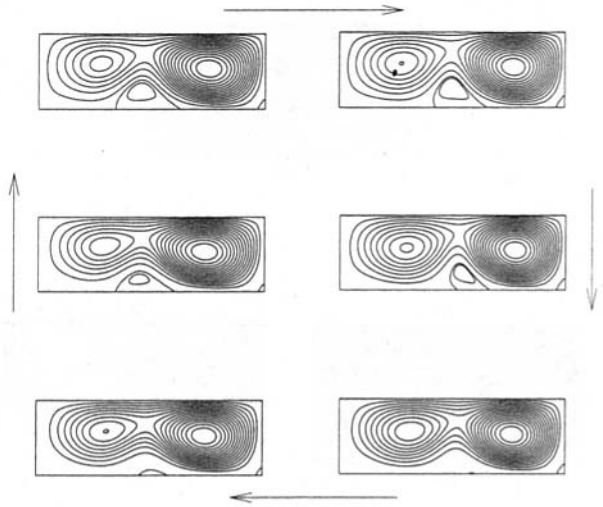

Fig. 7 Instantaneous streamlines of the convective flow plotted for equal time intervals *T*/6 covering the complete period. Aspect ratio *A* = 3. Pr = 0, Gr = 8.8×10^4.

Figure 6 shows the slightly supercritical states for Pr = 0 and 0.015 in a cavity with $A = 2$. One can see that the onset of instability due to different dominant perturbations leads to different oscillations in time. Thus at Pr = 0 perturbation of the stream function has a global maximum inside the main convective circulation (Fig. 3(*a*)). This leads to oscillations of the two clockwise circulations (the stronger and the weaker ones) which merge and split during one period of oscillations (Fig. 6(*a*)). This is followed by oscillations of a weak reverse vortex attached to the lower boundary. Oscillations at Pr = 0.015 are different. Perturbations of the stream function and the temperature in this case are located near the hot wall where the convective motion is relatively weak (Figs. 3(*b*) and 3(*c*)). According to this, oscillations of the stream function, shown in Fig. 6(*b*) have larger amplitude near the hot wall. The main circulation, shifted toward the cold wall, remains almost undeformable during the period of oscillations.

Slightly supercritical oscillatory flow at $A = 3$ and Pr = 0 is shown in Fig. 7. Perturbations for Pr = 0 and 0.015 are similar for this aspect ratio, so the oscillations in slightly supercritical states look similarly. The oscillations appear as weak pulsations of the two local maxima of the stream function followed by oscillations of a weak reverse vortex attached to the lower boundary. This asymptotically approximated oscillatory flow is similar to the flow calculated for $A = 4$ (Gelfgat et al., 1996b), and is in qualitative agreement with the results of the direct numerical solution of the full unsteady problem (Roux, 1989; Pulicani et al., 1989).

Figure 8 illustrates a slightly supercritical oscillatory flows at $A = 8$. At Pr = 0 the critical Grashof numbers for $A = 3$ and 8 belong to the same branch of the neutral curve (Fig. 2). So, the perturbations and the oscillations in both cases are similar (compare Figs. 4(*a*) and 5(*a*) to Figs. 7(*a*) and 8(*a*). At $A = 8$ (Pr = 0, Fig. 8(*a*)) one can see oscillations of the clockwise meridional circulations followed by oscillations of two weak counter clockwise vortices attached to the lower wall. In the case Pr = 0.015 perturbations of ψ and θ are located in the central part of the cavity (Figs. 5(*b*) and 5(*c*)). Accordingly, oscillations of the stream function have larger amplitudes in the central part of the cavity (Fig. 8(*b*)), where one can see oscillations of several clockwise circulations. Oscillations of the weak counter clockwise vortices are much weaker than in the case Pr = 0.

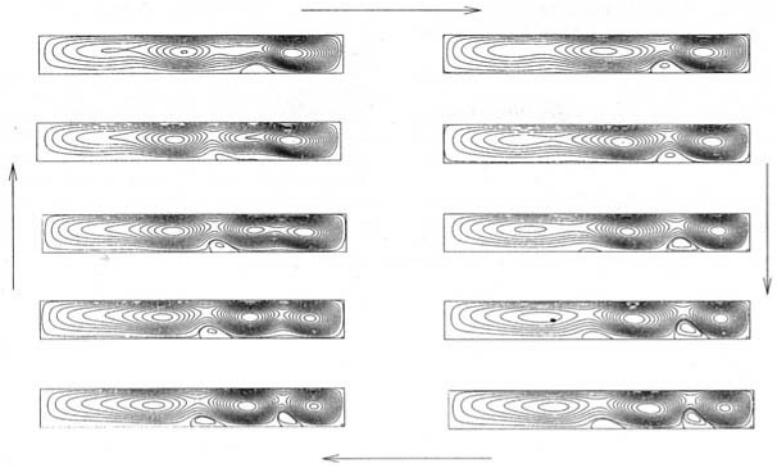

Fig. 8(*a*) Pr = 0, Gr = 1.3×10^5

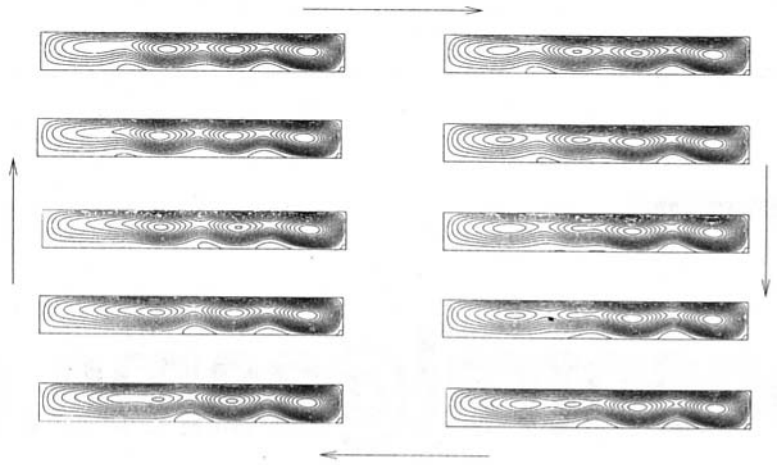

Fig. 8(*b*) Pr = 0.015, Gr = 4.5×10^5

Fig. 8 Instantaneous streamlines of the convective flow plotted for equal time intervals *T*/6 covering the complete period. Aspect ratio *A* = 8.

Conclusions

The oscillatory instability of the considered convective flow sets in due to Hopf bifurcation in the whole interval $1 \leq A \leq 10$ and for the considered values of the Prandtl number (Pr = 0 and 0.015). The dependence of the critical parameters (critical Grashof number and the frequency of oscillations) on the aspect ratio and the Prandtl number is very complicated, and very sensitive to a small change of the control parameter. Stability diagrams show that using the stability features for predicting of other (even close) values of the control parameter is not always possible. In particular, the convective heat transfer is not negligible even at low-Prandtl-number (like Pr = 0.015) flows.

The results for the asymptotic limit of an infinite fluid layer ($A \to \infty$) cannot be used even for long horizontal cavities with the aspect ratio up to $A = 10$. This means that in practically important situations, the finite dimension of the cavity and the corresponding end effects should always be taken into account.

Acknowledgment

This research was supported by the German-Israeli Foundation for Scientific Research and Development, grant No. I-284.046.10/93.

References

Afrid M., and Zebib A. 1990. "Oscillatory Three-Dimensional Convection in Rectangular Cavities and Enclosures," *Physics of Fluids A,* Vol. 2(8), pp. 1318–1327.

Ben Hadid H, and Roux B. 1989a. "Buoyancy and Thermocapillary-Driven Flows in a Shallow Cavity: Unsteady Flow Regimes," *Journal of Crystal Growth,* Vol. 97, pp. 217–225.

Ben Hadid H, and Roux B. 1989b. "Buoyancy-Driven Oscillatory Flows in Shallow cavities Filled with Low-Prandtl Number Fluids," *Proc. GAMM Workshop on Numerical Solution of Oscillatory Convection in Low Prandtl Number Fluids* (ed., B. Roux), Marseille, 1988, Notes on Numerical Fluid Mechanics, Vieweg Braunschweig, Vol. 27, pp. 25–33.

Gelfgat A. Yu., and Tanasawa I., 1994, "Numerical Analysis of Oscillatory Instability of Buoyancy Convection with the Galerkin Spectral Method," *Numerical Heat Transfer,* Part A, Vol. 25, pp. 627–648.

Gelfgat A. Yu., Bar-Yoseph P. Z., and Solan A., 1996a, "Stability of a Confined Swirling Flows with and without Vortex Breakdown," *Journal of Fluid Mechanics,* Vol. 311, pp. 1–36.

Gelfgat A. Yu., Bar-Yoseph P. Z., and Yarin A., 1996b, "Numerical Investigation of Hopf Bifurcation Corresponding to transition from Steady to oscillatory State in a Confined Convective flow," *Proc. 1996 Fluids Engineering Division Conference,* San-Diego, CA, July 7–11, Vol. 2, FED-Vol. 237, pp. 369–374.

Gelfgat A. Yu., Bar-Yoseph P. Z., and Yarin A., 1997. "Patterns of Bifurcating Convective Flows in Long Horizontal Cavities," *Advances in Computational Heat Transfer* (ed. G. de Vahl Davis) to appear.

Hassard B. D., Kazarinoff N. D., and Wan Y.-H., 1981, "Theory and Applications of Hopf Bifurcation," London Mathematical Society Lecture Note Series, Vol. 41.

Hurle D. T. J., Jakeman E., and Johnson C. P., 1974, "Convective Temperature Oscillations in Molten Gallium," *Journal of Fluid Mechanics,* Vol. 64, pp. 565–576.

Laure P., and Roux B., 1989, "Linear and Non-Linear Analysis of the Hadley Circulation," *Journal of Crystal Growth,* Vol. 97, pp. 226–234.

Le Quere P. 1989. "Contribution to GAMM Workshop with a Pseudo-Spectral Algorithm on a Staggered Grid," *Proc. GAMM Workshop on Numerical Solution of Oscillatory Convection in Low Prandtl Number Fluids* (ed. B. Roux). Marseille, 1988, Notes on Numerical Fluid Mechanics, Vieweg Braunschweig, Vol. 27, pp. 227–236.

McClelland M. A. 1995. "Time-Dependent Liquid Metal Flows with Free Convection and a Deformable Free Surface," *International Journal for Numerical Methods in Fluids,* Vol. 20, pp. 603–620.

Mundrane M, and Zebib A. 1994, "Oscillatory Buoyant Thermocapillary Flow," *Physics of Fluids,* Vol. 6(10), pp. 3294–3305.

Okada K., and Ozoe H. 1993a. "The Effect of Aspect Ratio on the Critical Grashof Number for Oscillatory Natural Convection of Zero Prandtl Number Fluid; Numerical Approach," *Journal of Crystal Growth,* Vol. 126, pp. 330–334.

Okada K., and Ozoe H. 1993b. "Various Computational Conditions of Oscillatory Natural Convection of Zero Prandtl Number Fluid in an Open Boat Heated and Cooled From Opposing Vertical Walls," *Numerical Heat Transfer,* Part A, Vol. 23, pp. 171–187.

Pulicani J. P., Crespo del Arco A., Randriampianina A. Bontoux P., and Peyret R., 1990, "Spectral Simulations of Oscillatory Convection at Low Prandtl Number," *International Journal for Numerical Methods in Fluids,* Vol. 10, pp. 481–517.

Roux B. (ed.), 1989, Proc. GAMM Workshop on Numerical Solution of Oscillatory Convection in Low Prandtl Number Fluids. Marseille, 1988," *Notes on Numerical Fluid Mechanics,* Vieweg Braunschweig, Vol. 27.

Winters K. H., 1988, "Oscillatory Convection in Liquid metals in a Horizontal Temperature Gradient," *International Journal of Numerical Methods in Engineering,* Vol. 25, pp. 401–414.

Parametric Studies on a Numerical, Nonlinear Pulse Tube Flow

C. S. Kirkconnell
Cryogenics Engineer,
Hughes Aircraft Company,
El Segundo, CA 90245

G. T. Colwell
Professor Emeritus,
Georgia Institute of Technology,
Atlanta, GA 30332

The need for high reliability, low cost, low vibration cryocoolers, for both military and commercial applications, has spawned and continues to drive the development of pulse tube cryogenic refrigerators. The expander contains no moving parts, yielding the potential for marked improvements in these areas. Though pulse tube refrigeration has been thoroughly studied, more accurate analytic and numerical modeling tools are needed to facilitate the development of thermodynamically efficient pulse tube cryocoolers to meet the needs of the user community. At present, one of the primary areas of modeling uncertainty is in the calculation of the dissipative losses occurring within the pulse tube itself. Toward this end, a numerical model was developed to solve the one-dimensional, nonlinear governing equations for heat and mass flow in a pulse tube. The governing equations are scaled for high-frequency (>60 Hz) pulse tube operation. The resulting system of nonlinear, time-dependent equations was solved directly using the method of lines. The numerical model was verified analytically using a representative set of equations with a known solution. A sensitivity analysis was performed to investigate the influence of different parameters on the solution.

Introduction

Pulse tube refrigeration was first discussed by Gifford and Longsworth (1965) and Longsworth (1967). The Gifford and Longsworth pulse tube refrigerators, today known as basic pulse tube refrigerators (BPTRs), yielded insufficient thermodynamic efficiencies and refrigeration capacities to be of practical use, hence the BPTR did not generate much interest. The innovative addition of a gas distributor and a reservoir volume at the warm end of the pulse tube in the 1980's by Mikulin et al. (1984) led to the development of the orifice pulse tube refrigerator (OPTR), a more efficient device capable of reaching much colder temperatures. Pulse tube refrigeration has received considerable attention since then. Most of today's pulse tube refrigerators are, to various extents, derivations of the OPTR design. Both the BPTR and OPTR configurations are illustrated schematically in Fig. 1.

The history of analytic and numerical pulse tube modeling is relatively short. The first analytic model of an OPTR, commonly called the "SRZ model" for the authors' initials, was developed within the last decade at the National Institute of Standards and Technology (NIST) (Storch and Radebaugh, 1987; Radebaugh, 1987; Storch et al., 1991). The SRZ model is essentially a time-averaged, one-dimensional enthalpy flow model which relies upon the assumption of small pressure fluctuations to simplify the governing equations. This assumption can introduce significant error for real pulse tubes. David et al. (1993) developed a more generally applicable and accurate model than the SRZ model by dropping the assumption of small pressure fluctuations. Their one-dimensional model, which was significantly more accurate than the SRZ model for the pulse tubes they examined, yields a simple integral expression for the heat transfer rate through the pulse tube in terms of the operating frequency, rejection temperature, and the pressure wave amplitude and mean value. In a more recent paper, Lee et al. (1995) describe an analytic solution to the linearized, two-dimensional pulse tube equations which has been used to successfully predict the presence of experimentally observed secondary flows in pulse tubes. Distinct from the pulse tube component models described above, a system-level OPTR numerical model described by Wu and Zhu (1989) uses control volume energy and mass conservation equations for each system component to predict performance. A similar model developed by Kirkconnell (1995), which more accurately accounts for refrigeration losses, has been well correlated to experimental data over a wide range of operating points.

The model developed and discussed in the present paper describes the one-dimensional heat and mass flows in pulse tubes. Unlike the SRZ model, the time dependence of the solution during the operating cycle is considered, and the fundamental difference between this model and those of Lee et al. (1995) and David et al. (1993) is the inclusion of inertial forces in the model. This results in a numerically-challenging, nonlinear set of equations. Lee et al. used a linearized set of equations which would yield to an analytic solution, while David et al. simply argued that the inertial effects were insignificant. For the operational frequencies of interest in their study, in the 2 to 3 Hz range, this is indeed true. Many practical pulse tubes are today operating in the 30 to 40 Hz range, however, allowing the use of a much smaller compressor to yield the same refrigeration capacity as its lower frequency counterpart. As frequencies increase and pulse tube sizes decrease, velocities inside the pulse tube increase and inertial and compressibility effects can no longer be ignored.

Because of this, a model which retains the inertial force in its formulation was developed and solved numerically. A parametric sensitivity analysis was performed to investigate the role of the various model inputs on the solution. The results of that analysis are provided herein.

One-Dimensional, Nonlinear Model

The physical domain of the pulse tube problem is a finite cylinder subjected to time-dependent boundary data, as illustrated in Fig. 2. The walls are assumed to be adiabatic since the thermal time constant governing heat transfer between the gas and the walls is much greater than the operational period for

Contributed by the Fluids Engineering Division for publication in the JOURNAL OF FLUIDS ENGINEERING. Manuscript received by the Fluids Engineering Division September 2, 1996; revised manuscript received May 6, 1997. Associate Technical Editor: S. P. Vanka.

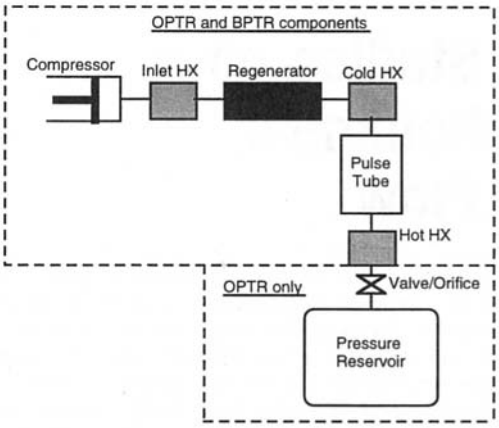

Fig. 1 Schematics of an OPTR and a BPTR

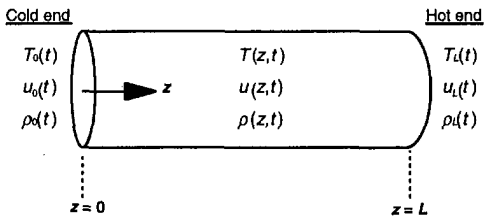

Fig. 2 1-D, time dependent pulse tube model

high frequency flows. (Other gas-to-wall heat transfer scenarios, such as constant heat flux, can be accommodated by adding source/sink terms to the right-hand side of the energy equation.) The radial velocity component and temperature and velocity gradients are identically zero for the one-dimensional model, thus boundary conditions are required only at the ends of the tube.

The governing equations are the mass, momentum, and energy conservation equations for transient, compressible, viscous flows. These equations were nondimensionalized using the scales defined in Table 1. The ideal gas approximation is made, an assumption good to within 10 percent for typical pulse tube flows. Substituting for the dimensional velocity, temperature, and density in terms of their dimensionless counterparts and the scales of the problem and eliminating the pressure from the momentum equation using the ideal gas relationship, the resulting set of dimensionless equations is obtained:

Table 1 Scales for 1-D model

Reference Variable	Definition
z_{ref}	L
t_{ref}	$1/\omega$
u_{ref}	ωL
T_{ref}	$(T_{chx}' + T_{hhx}')/2$
P_{ref}	$\bar{P}$
ρ_{ref}	$\rho(T_{ref}, P_{ref})$
μ_{ref}	$\mu(T_{ref}, P_{ref})$
$k_{th,ref}$	$k_{th}(T_{ref}, P_{ref})$
$c_{p,ref}$	$c_p(T_{ref}, P_{ref})$

$$\frac{\partial \rho}{\partial t} + u\frac{\partial \rho}{\partial z} + \rho\frac{\partial u}{\partial z} = 0 \tag{1}$$

$$\frac{\partial u}{\partial t} + \Lambda\frac{T}{\rho}\frac{\partial \rho}{\partial z} + u\frac{\partial u}{\partial z} + \Lambda\frac{\partial T}{\partial z} - \frac{\epsilon}{\rho}\frac{\partial^2 u}{\partial z^2} = 0 \tag{2}$$

$$\frac{\partial T}{\partial t} + (\gamma - 1)T\frac{\partial u}{\partial z} + u\frac{\partial T}{\partial z} - \frac{\epsilon}{\rho}\frac{\partial^2 T}{\partial z^2} = 0 \tag{3}$$

The dimensionless parameter Λ, termed herein the "compressibility parameter," is defined by the relationship

$$\Lambda = \frac{RT_{\text{ref}}}{u_{\text{ref}}^2} = \frac{1}{\gamma \text{Ma}^2} \tag{4}$$

This parameter represents the ratio of inertial forces to compressibility forces in the pulse tube.

Nomenclature

C = amplitude of cold-end temperature wave
c_p = constant-pressure specific heat
D = amplitude of hot-end temperature wave
F_i = sink and source terms
i = index of solution vector (i = 1. .3)
j = axial position index (j = 1. .JJ)
JJ = number of axial nodes, including end nodes
k = time index (k = 1. .KK)
KK = number of time steps per period
k_{th} = thermal conductivity
L = length of pulse tube
m = dimensionless mass flow rate per unit area
Ma = Mach number
P = thermodynamic pressure
$\bar{P}$ = average pressure
$\bar{P}'$ = dimensionless average pressure
R = gas constant
t = time
T = temperature
T'_{chx} = temperature of cold HX
T'_{hhx} = temperature of rejection HX
T_{chx} = dimensionless temperature of cold HX
T_{hhx} = dimensionless temperature of rejection HX
u = dimensionless velocity
U = solution vector (ρ, u, T)
z = axial coordinate
A = amplitude of cold-end mass flow rate
B = amplitude of hot-end mass flow rate
ϵ = coefficient of numerical dissipation terms
E = amplitude of cold-end pressure wave
Φ = phase angle between hot and cold m
γ = ratio of specific heats
Λ = compressibility parameter (Eq. (4))
μ = dynamic viscosity
ψ = phase angle between cold-end T and m
Θ_{avg} = see Eq. (19)
ρ = density
τ = period (= 1/frequency)
ω = circular frequency
M = mass flow amplitude parameter

Subscripts

c = cold end of pulse tube
ex = exact (analytic) solution
h = hot end of pulse tube
num = numerical solution
ref = reference value

The value of ϵ, the numerical dissipation parameter, governs the magnitude of the second-order terms. It replaces the physical values for the dimensionless viscous diffusion and conduction coefficients in the momentum and energy equations, respectively. Dimensional analysis revealed that the viscous diffusion and thermal conduction terms are negligible with respect to the other terms in the equations. However, trial and error revealed the necessity of including small, but larger than physical, values for these terms in the vicinity of the ends of the tube to enhance the stability of the model. The introduction of the new symbol "ϵ" conveys the fact that the numerical value of the dissipation parameter is distinct from that of the physical coefficients it replaces. This approach was deemed acceptable after it was determined numerically that the accuracy of the solution is negligibly impacted by the presence of the numerical dissipation terms. Typical values for ϵ were $O(10^{-2})$ near the ends of the tube, $O(10^{-5})$ in the core. This and other details of the numerical model are discussed elsewhere (Kirkconnell, 1995).

Numerical Solution

The governing system of equations was solved using a method of lines (MOL) technique, discretizing the spatial coordinate using cubic Hermite polynomials. The particular numerical solver used, called "MOLCH," is a commercially available IMSL subroutine based largely upon the published works of Sincovec and Madsen (1975) and Madsen and Sincovec (1979).

The logic flow is controlled through a FORTRAN driver designed and optimized to solve the 1-D pulse tube equations using MOLCH. Starting from an initial guess constrained only by the requirement that it be consistent with the boundary conditions at the first time step, the solution for two complete periods is computed. The convergence status is evaluated by comparing the 'error' between the two successive solutions to a user-prescribed tolerance value. The "error" is defined by the maximum of the normalized differences for each component of the solution vector at corresponding discrete temporal and spatial nodes in the two successive periods. This procedure is repeated until the solution converges to within a user-prescribed tolerance of 5 percent. Tighter tolerances can be selected, the trade-off being increased computational time. Given the tolerance value used, typical cases take 4 to 6 iterations to converge.

Preliminary runs using a single-step marching technique to advance the solution directly from time level t^* to $t^* + dt$ revealed that the calculations had a strong tendency to diverge. Therefore, a four-step, time-relaxation technique was developed to enhance the stability of the model. Starting at time $t = t^*$, the MOL is used to obtain a preliminary solution at $t = t^* + dt$. A three-point polynomial curve fit is then used to calculate the solution at $t = t^* + dt/2$ using the solution at times $t = t^* - dt/2$, t^* and $t^* + dt$. The MOL is again used, this time to advance the solution from $t = t^* + dt/2$ to $t = t^* + 3dt/2$. Finally, the polynomial curve fit, using the solution at times $t = t^*$, $t^* + dt/2$ and $t^* + 3dt/2$, yields the solution at $t = t^* + dt$.

Boundary Functions

For the purposes of performing these numerical exercises, the functional forms of the boundary equations were specified such that they would lend themselves to parametric evaluation. So that the solutions were representative of real pulse tube flows, the functional forms used were based upon experimental observation. The mass flow rate and pressure waves were assumed to be sinusoidal, representative of the flows produced by a valveless compressor. The heat exchangers at the ends of the pulse tube were assumed to function as perfect isothermalizers, thus the flows into the pulse tube at either end are isothermal. The temperatures of the out flows were assumed, somewhat arbitrarily, to vary sinusoidally, but any waveform can be accommodated by the model. To reduce the set of independent boundary parameters, the additional assumptions were made:

- The mass flow and temperature are in phase with the pressure at the warm end of the pulse tube; this is an approximation of real OPTR operation confirmed by experiment.
- The pressure waves at the ends of the tube are in phase and of the same amplitude; the magnitudes of the pressure drops are within the range of the numerical uncertainty for the pulse tubes considered, thus introducing these small differences into the model through the boundary data offered no additional accuracy.
- The net enthalpy fluxes at the cold and warm ends are equal; since the enthalpy flux is the dominant energy transfer mode, this assumption guarantees that the boundary data represent a relatively steady-state operating point.

Based upon the above discussion, the boundary equations used herein are described by the following set of dimensionless equations:

$$m_c(t) = \mathrm{A}\cos t \tag{5}$$

$$P_c(t) = \bar{P} + \mathrm{E}\cos(t - \Phi) \tag{6}$$

$$T_c(t) = \begin{cases} T_{chx} + C\cos(t - \psi) & m_c < 0 \\ T_{chx} & \text{for } m_c \geq 0 \end{cases} \tag{7}$$

$$m_h(t) = \mathrm{B}\cos(t - \Phi) \tag{8}$$

$$P_h(t) = \bar{P} + \mathrm{E}\cos(t - \Phi) \tag{9}$$

$$T_h(t) = \begin{cases} T_{hhx} & m_h \leq 0 \\ T_{hhx} + D\cos(t - \Phi) & \text{for } m_h > 0. \end{cases} \tag{10}$$

The boundary velocity and density functions required by the 1-D model are calculated from the mass flow rate, pressure, and temperature functions. As determined from a simple enthalpy flow analysis of the pulse tube, the equality of the net enthalpy fluxes at the boundaries is provided by the relationship

$$\psi = \arccos\left(\frac{\mathrm{B}D}{\mathrm{A}C}\right). \tag{11}$$

Model Correlation

In the absence of a pulse tube instrumented with high-speed temperature sensors and anemometers, the numerical model was validated using a test solution with boundary conditions of the form described in the previous section. The governing equations were recast so that the nonzero source and sink terms introduced by the test solution could be accommodated:

$$\frac{\partial \rho}{\partial t} + u\frac{\partial \rho}{\partial z} + \rho\frac{\partial u}{\partial z} = F_1 \tag{12}$$

$$\frac{\partial u}{\partial t} + \Lambda\frac{T}{\rho}\frac{\partial \rho}{\partial z} + u\frac{\partial u}{\partial z} + \Lambda\frac{\partial T}{\partial z} - \frac{\epsilon}{\rho}\frac{\partial^2 u}{\partial z^2} = F_2 \tag{13}$$

$$\frac{\partial T}{\partial t} + (\gamma - 1)T\frac{\partial u}{\partial z} + u\frac{\partial T}{\partial z} - \frac{\epsilon}{\rho}\frac{\partial^2 T}{\partial z^2} = F_3. \tag{14}$$

A test solution was selected which features the important characteristics of the actual pulse tube solutions discussed in the text, i.e., spatial variation in the phase angles and amplitudes as well as oscillatory time dependence. The values for F_i were determined at each time step by substituting the given functions and their derivatives into the left-hand sides of the governing equations (Eqs. (12)–(14)). Starting from an arbitrary initial

Table 2 Model validation—SSE versus discretization space

JJ \ KK	10	20	30
60	unstable	unstable	unstable
90	4.2E-4	5.4E-7	2.1E-8
120	unstable	7.4E-7	2.9E-8
180	1.2E-4	7.0E-7	8.3E-8
360	3.0E-4	6.0E-6	1.9E-7
540	5.1E-4	6.4E-6	4.2E-7

condition, the numerical solution in the interior of the tube was then calculated using the 1-D model. The accuracy of the numerical solution was evaluated by calculating the sum-of-squares error (SSE) between the exact and numerical solutions, defined as

$$\mathrm{SSE} = \sum_{i=1}^{3} \sum_{j=1}^{JJ} \sum_{k=1}^{KK} [U_{i,\mathrm{ex}}(z_j, t^k) - U_{i,\mathrm{num}}(z_j, t^k)]^2 \quad (15)$$

for several different discretization spaces. The results are shown in Table 2. In addition to the information presented in the table, it was discovered that a finer temporal discretization allows stable numerical operation over a wider range of input parameters. The discretization used for the cases described in the next section was selected based upon a balance between accuracy, numerical stability, and run-time.

Sensitivity Analysis

Parametric studies were performed to investigate the influence of five different model inputs on the solution. Three of the parameters investigated, the phase angle Φ, the compressibility parameter Λ, and the ratio of cold-end to hot-end mass flow rates M, can be thought of design parameters in that the designer can largely control these values through component geometry, orifice size, operational setting, etc. The two other model inputs considered, the amplitude of the temperature waves and the phase angle between the mass flow rate and temperature at the cold end, arise from the physics of the problem once the geometry and pressure wave have been specified. From a design standpoint, it is very difficult to tightly control or analytically predict the exact values for these parameters for a given pulse tube cryocooler. Furthermore, the measurement of these parameters requires fast-response, in situ temperature and pressure sensors which represent additional cost and complexity in an experimental setup. Therefore, the intent of the latter two parametric studies was to determine whether the additional effort of obtaining precise values for these parameters is necessary to obtain an accurate solution for a given pulse tube.

A "baseline" set of input parameters, provided in Table 3, was selected as a reference for the parametric tests. For each of the tests, the input parameters were held constant at the baseline values except for the parameter which was the subject of the test. The numerical parameters, including the discretization parameters KK = 360 and JJ = 20, were also held constant. The values provided in Table 3 were obtained primarily by scaling the results obtained from a system-level model for a hypothetical 200 Hz OPTR yielding approximately 4 watts net refrigeration at 50 K.

Though explanations are provided in each discussion regarding the design or operational variables which could influence the parameter of interest, these studies are not intended to mimic physical experiments. In practice, changes to the operating frequency, pulse tube size, and other such variables would typically affect several of the governing parameters, not one. The intent here is to investigate the role of each dimensionless parameter on the numerical solution.

Parametric Study 1: Φ. Φ is most directly influenced by the size of the orifice at the hot end of the pulse tube. For the basic pulse tube design where the orifice is completely closed, the phase angle Φ, neglecting pressure drops in the system, is $\pi/2$. At the other extreme, where there is no flow resistance at the rejection end, the phase angle is zero. The orifice size in an OPTR yields a phase angle between these two limits, a typical value being $\pi/6$. This study investigates the effect of adjusting this phase relationship on the time-dependent solution inside the pulse tube. It is important to note that changing the orifice size causes an amplitude shift in addition to a phase shift (Cai et al., 1994), but for the purposes of investigating the singular influence of this phase angle on the solution, only Φ was varied.

Figure 3 describes the temperature solution for several values of the phase angle Φ. The curves shown are defined by the following expressions:

$$\left.\begin{aligned} T_{\max}(z_j) &= \max_{k=1..KK} \{T(z_j, t^k)\} \\ T_{\min}(z_j) &= \min_{k=1..KK} \{T(z_j, t^k)\} \\ T_{\mathrm{avg}}(z_j) &= \left(\frac{1}{KK}\right) \sum_{k=1}^{KK} T(z_j, t^k) \end{aligned}\right\} \quad \text{for } j = 1, 2, \ldots JJ. \quad (16)$$

(These same definitions apply to all subsequent plots of this type.) The plots clearly reveal the strong influence of Φ on the temperature distribution in the pulse tube. As Φ increases, the curves all shift down toward lower temperatures. The top plot illustrates the case of $\Phi = 0$ where the thermal penetration from both the hot and cold ends is about half of the length of the pulse tube. At the other extreme, the bottom plot illustrates a case analogous to a "hot piston" design, where the passive reservoir has been replaced by a hot piston-cylinder at the rejection end, thus allowing a phase angle greater than $\pi/2$. For this case the cold gas penetrates nearly the entire length of the tube while the hot gas penetrates less than 10 percent, perhaps demonstrating a more favorable temperature distribution for maximum pulse tube refrigeration. The temperature solution for the $\pi/3$ case falls between these two extremes.

In contrast to the temperature solution, the influence of Φ on the velocity and mass flow rate solutions is relatively minor. An interesting result was observed for the $\Phi = 3\pi/4$ mass flow rate versus time curves, however, illustrated in Fig. 4. The interior solution near the middle of the pulse tube, as shown by the $z = 0.63$ curve, exhibits an acceleration-deceleration-acceleration cycle superimposed on the dominant harmonic cycle from $t = 3.1$ to 4.5. The mass flow rate curves for typical OPTR phase angles ($\sim\pi/6$) exhibit no such well-defined sub-

Table 3 Baseline parameters

Parameter	Value
A	1.075
B	0.110
C	0.021
D	0.125
E	0.200
T_{chx}	0.286
$\bar{P}$	1.000
Φ	$\pi/6$
Λ	92

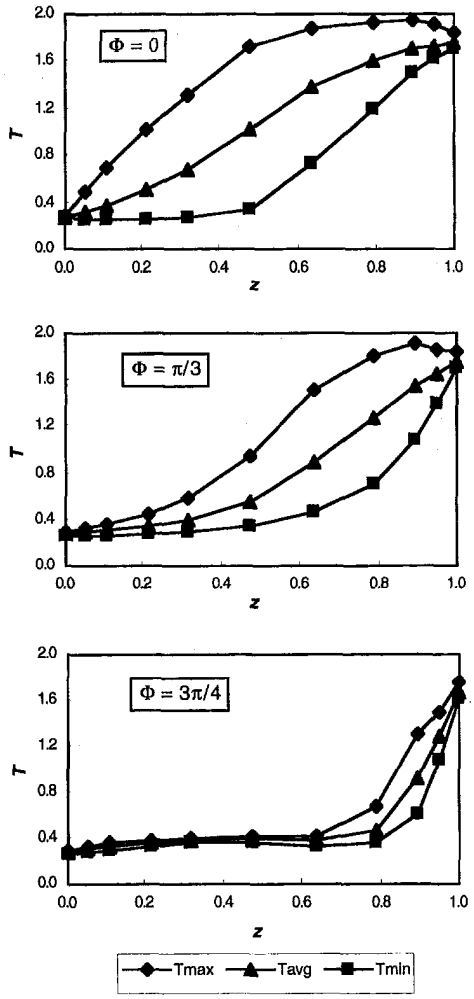

Fig. 3 Temperature solution versus Φ

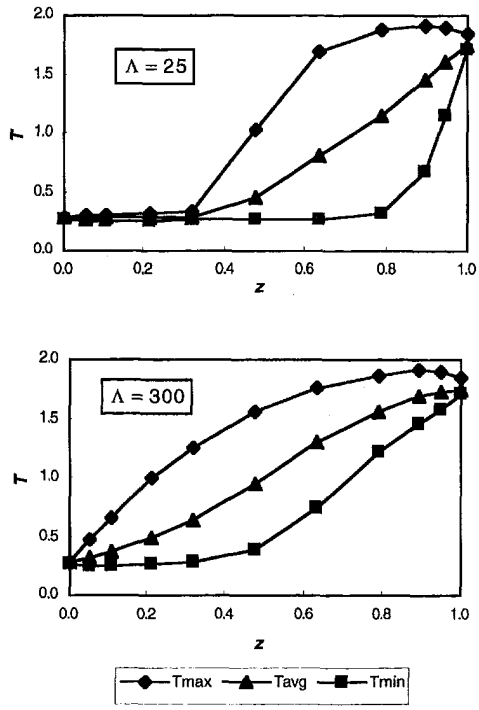

Fig. 5 Temperature solution versus Λ

As shown in Fig. 5 for the extreme values of Λ investigated, the compressibility parameter has a profound influence on the temperature solution, primarily in the depth the cold gas penetrates the tube (see T_{min} curves). In contrast, the velocity solution is virtually independent of Λ. However, due to the variations in the density solution, the mass flow rate solution does change significantly with Λ, as shown in Fig. 6. The increase in Λ clearly results in lower mass flow amplitudes, especially nearer the hot end of the tube ($z = 0.63$). Also note the phase

harmonics. The possible implications of this phenomenon warrant additional investigation.

Parametric Study 2: Λ. The compressibility parameter Λ, which represents the ratio of inertia effects to compressibility effects, is defined above in Eq. (4). Λ is a function of temperature, geometry, the molecular weight of the gas, and the operating frequency. The larger compressibility forces, hence the lower values of Λ, are characteristic of higher frequency, larger aspect ratio (length/diameter) pulse tubes.

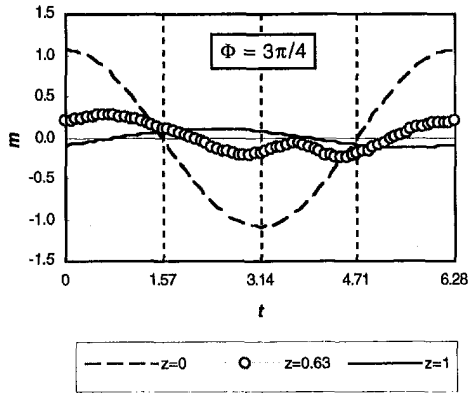

Fig. 4 Mass flow rate subharmonic

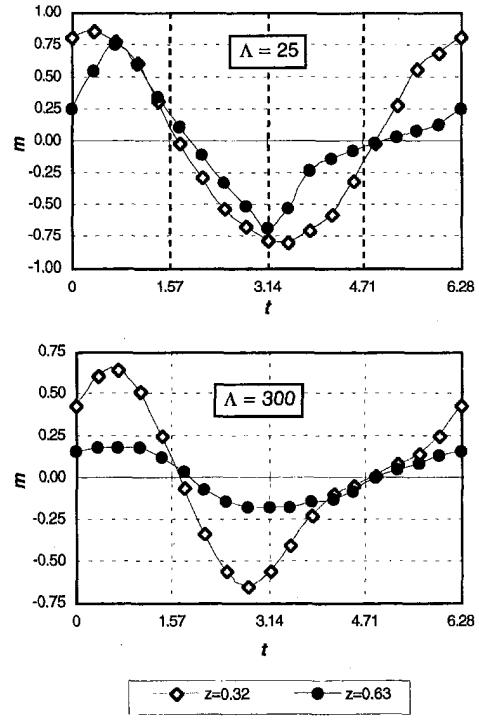

Fig. 6 Mass flow rate solution versus Λ

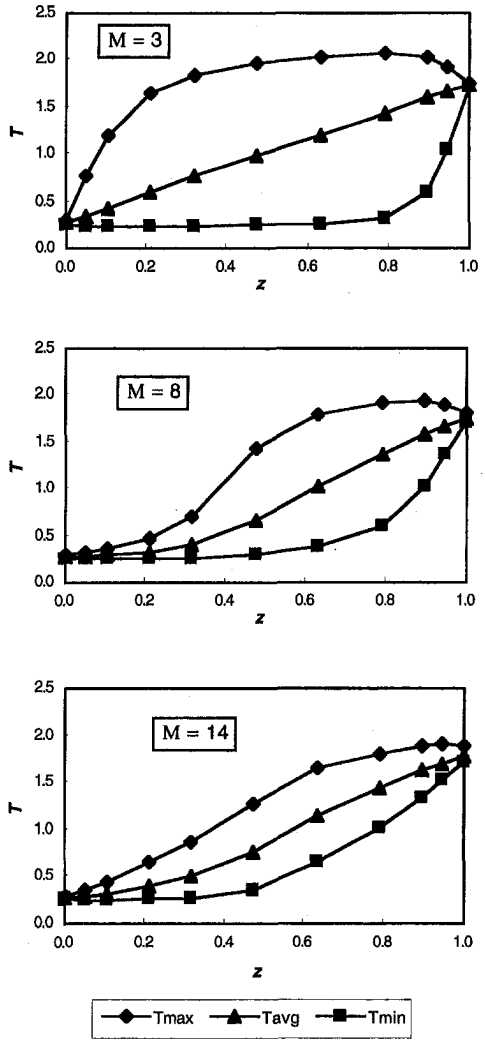

Fig. 7 Temperature solution versus M

shift between the traces. The $z = 0.32$ curve reaches a minimum near $t = 3.3$ for $\Lambda = 25$, but the minimum occurs at about $t = 2.8$ for $\Lambda = 300$. This represents a phase shift of about 29 degrees at that particular axial location, caused solely by changing the value of Λ.

Parametric Study 3: M. Let the mass flow amplitude parameter M be defined by

$$\mathrm{M} = \frac{\mathrm{A}}{\mathrm{B}}, \tag{17}$$

where A and B are the amplitudes of the specific mass flow rates at the cold and hot ends, respectively. M is primarily a function of the geometry of the pulse tube in relation to the swept volume of the compressor, but it is also affected by other physical features of the system, such as the size of the orifice. For the BPT (no orifice) design, the mass flow rate at the hot end is (essentially) zero. As the size of the orifice is increased for a constant compressor swept volume, the amount of mass allowed to flow through the hot end of the tube increases, the amplitude of the mass flow rate at the cold end decreases, hence M decreases. Similar to the parametric study on Φ where A and B were held constant, Φ is held constant for this investigation. The cold-end amplitude is also held constant, so the only model input parameter which varies from case to case is B.

Figure 7 illustrates the strong influence of M on the temperature solution for values ranging from 3 to 14. As the amplitude of the hot mass flow rate increases (i.e., M decreases), the penetration of both the hot and cold gases into the tube increases. The increased mass flow rate at the hot end has the anticipated effect of "pushing" more hot gas toward the cold end and "pulling" more cold gas towards the hot end. Figure 8 reveals that these competing effects on the time-averaged bulk temperature, defined by the relationship

$$\Theta_{\mathrm{avg}} = \frac{\sum_{j=1}^{\mathrm{JJ}} T_{\mathrm{avg}}}{\mathrm{JJ}}, \tag{18}$$

results in a minimum in Θ_{avg} around M = 8. Using a system-level pulse tube cryocooler model to calculate the value of M for well-correlated experimental data, this approximate value has been shown at Hughes to yield maximum net pulse tube refrigeration in 20–40 Hz OPTRs.

Parametric Study 4: *C* and *D*. While the values of Φ and Λ can, to some extent, be actively controlled by changing the setup or operating conditions, the amplitudes of the temperature waves at the ends of the pulse tube are largely passive. The amplitudes C and D are determined by the complex heat transfer interactions between the working gas and the physical components of the system. The motivation for this study is to understand the sensitivity of the solution to the amplitudes of the temperature waves, not to provide design recommendations in this regard.

Five sets of values for the amplitudes of the cold-end temperature wave (C) and the hot-end temperature wave (D) were investigated. For every case the ratio C/D was held constant so that ψ, the phase angle between the mass flow and temperature at the cold end, would remain the same for unchanging values of A and B (see Eq. (11)). The amplitudes, which were selected to cover the scope of perceived physically reasonable values, range from one-fourth to twice the amplitude of the baseline temperature waves. The solution was observed to be highly insensitive to C and D for the values considered with the different solutions being virtually indistinguishable in the interior of the domain, necessitating the use of very high resolution plots to observe any difference between solutions whatsoever.

Parametric Study 5: ψ. ψ was selected for every case such that an essentially steady-state operating point was defined by the boundary parameters (Eq. (11)). Different values of the cold-end temperature phase angle ψ were obtained for this parametric study by varying the amplitude (D) of the hot-end temperature wave while A, B, and C were held constant. As with the other parametric tests, the remaining model parameters were also held constant.

The solution was seen to be very insensitive to variations in ψ. The phase angle ψ was varied from 13 to about 90 deg, where the smaller angles indicate larger enthalpy flow rates. For $\psi > 90$ deg, the net enthalpy flow would actually be into

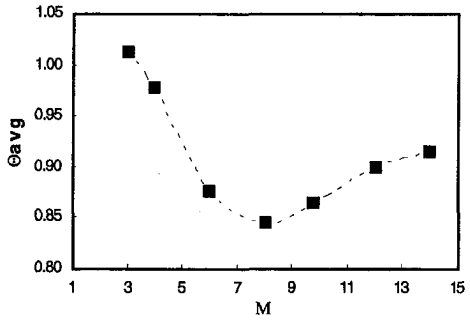

Fig. 8 Time-averaged bulk temperature versus M

the cold exchanger, thus yielding "negative refrigeration." Therefore, almost the entire range of physically reasonable values were investigated, and very little influence on the solution was observed. As with the previous parametric study, the differences between solutions were within the range of the numerical accuracy of the model.

Conclusion

A sensitivity analysis of a one-dimensional, nonlinear pulse tube model was performed. The solution was observed to be very sensitive to the phase angle between the cold and hot mass flow rates, the compressibility parameter, and the amplitude of the mass flow rates. These are all essentially design parameters which can be controlled through component design, selection of operating parameters, etc. Contrarily, the solution was seen to be comparatively insensitive to the amplitude of the temperature waves and the phase angle between the cold temperature and mass flow rate waves. This does not suggest that the performance of a pulse tube cryocooler is insensitive to these parameters, rather the opposite is true. The net enthalpy flow rate through the tube, which dominates the gross refrigeration calculation, is directly related to the boundary temperature wave amplitudes and phase angles. What the results of these parametric studies do indicate, however, is that the solution to the transient temperature, velocity, and density fields is largely unaffected by these boundary parameters. These parameters are difficult to predict or measure with certainty, so it is convenient from a modeling standpoint that an accurate description of the 1-D solution can be obtained using approximate values.

The exercises described herein have provided a good understanding of how the nonlinear model responds to various model inputs. Future work is planned which includes a study to compare the predictions of this model to those of other models for an experimental high frequency pulse tube. Additional analytical work is also planned in which the numerical techniques briefly described herein will be utilized to solve the 2-D, nonlinear governing equations.

References

Cai, J. H., Zhou, Y., Wang, J. J., and Zhu, W. X., 1994, "Experimental Analysis of Double-Inlet Principle in Pulse Tube Refrigerators," *Cryogenics,* Vol. 34, No. 5, pp. 522–525.

David, M., Marechal, J.-C., Simon, Y., and Guilpin, C., 1993, "Theory of Ideal Pulse Tube Refrigerator," *Cryogenics,* Vol. 33, pp. 154–161.

Gifford, W. E., and Longsworth, R. C., 1965, "Pulse Tube Refrigeration Progress," *Advances in Cryogenic Engineering,* Vol. 10, pp. 69–79.

Kirkconnell, C. S., 1995, "Numerical Analysis of the Mass Flow and Thermal Behavior in High-Frequency Pulse Tubes," Ph.D. thesis, Georgia Institute of Technology, Atlanta, GA.

Lee, J. M., Kittel, P., Timmerhaus, K. D., and Radebaugh, R., 1995, "Steady Secondary Momentum and Enthalpy Streaming in the Pulse tube Refrigerator," *Proceedings, 8th International Cryocooler Conference, Cryocoolers 8,* Plenum Press, NY, pp. 359–369.

Longsworth, R. C., 1967, "An Experimental Investigation of Pulse Tube Refrigeration Heat Pumping Rates," *Advances in Cryogenic Engineering,* Vol. 12, pp. 608–618.

Madsen, N. K., and Sincovec, R. F., 1979, "Algorithm 540-PDECOL, General Collocation Software for Partial Differential Equations," *ACM Transactions on Mathematical Software,* Vol. 5, No. 3, pp. 326–351.

Mikulin, E. I., Tarasov, A. A., and Shkrebyonock, M. P., 1984, "Low-Temperature Expansion Pulse Tubes," *Advances in Cryogenic Engineering,* Vol. 29, pp. 629–637.

Radebaugh, R., 1987, "Pulse Tube Refrigeration—A New Type of Cryocooler," *Proceedings, 18th International Conference on Low Temperature Physics—Japanese Journal of Applied Physics,* Vol. 26, Supplement 26-3, pp. 2076–2081.

Sincovec, R. F., and Madsen, N. K., 1975, "Software for Nonlinear Partial Differential Equations," *ACM Transactions on Mathematical Software,* Vol. 1, No. 3, pp. 232–260.

Storch, P. J., and Radebaugh, R., 1987, "Development and Experimental Test of an Analytical Model of the Orifice Pulse Tube Refrigerator," *Advances in Cryogenic Engineering,* Vol. 33, pp. 851–859.

Storch, P. J., Radebaugh, R., and Zimmerman, J. E., 1991, "Analytical Model for the Refrigeration Power of the Orifice Pulse Tube Refrigerator," NIST Technical Note 1343, National Institute of Standards and Technology, Boulder, CO.

Wu, P., and Zhu, S., 1989, "Mechanism and Numerical Analysis of orifice Pulse Tube Refrigerator with a Valveless Compressor," Cryogenics and Refrigeration—*Proceedings of International Conference,* International Academic Publishers, pp. 85–90.

Numerical Simulation of Drag Reducing Turbulent Flow in Annular Conduits

Idir Azouz
Assistant Professor,
Department of Physical Science and Engineering,
Southern Utah University,
Cedar City, Utah
Mem. ASME

Siamack A. Shirazi
Associate Professor,
Department of Mechanical Engineering,
The University of Tulsa,
Tulsa, OK.
Mem. ASME

Inadequate transport of rock cuttings during drilling of oil and gas wells can cause major problems such as excessive torque, difficulty to maintain the desired orientation of the drill string, and stuck or broken pipe. The problem of cuttings transport is aggravated in highly inclined wellbores due to the eccentricity of the annulus which results in nonuniformity of the flowfield within the annulus. While optimum cleaning of the borehole can be achieved when the flow is turbulent, the added cost due to the increased frictional losses in the flow passages may be prohibitive. A way around this problem is to add drag-reducing agents to the drilling fluid. In this way, frictional losses can be reduced to an acceptable level. Unfortunately, no model is available which can be used to predict the flow dynamics of drag-reducing fluids in annular passages. In this paper, a numerical model is presented which can be used to predict the details of the flowfield for turbulent annular flow of Newtonian and non-Newtonian, drag-reducing fluids. A one-layer turbulent eddy-viscosity model is proposed for annular flow. The model is based on the mixing-length approach wherein a damping function is used to account for near wall effects. Drag reduction effects are simulated with a variable damping parameter in the eddy-viscosity expression. A procedure for determining the value of this parameter from pipe flow data is discussed. Numerical results including velocity profiles, turbulent stresses, and friction factors are compared to experimental data for several cases of concentric and eccentric annuli.

Introduction

Cuttings transport during drilling of oil and gas wells can pose a major problem to the petroleum industry. This is particularly true in inclined wellbores, where the annulus is eccentric due to gravity. In this case, the rock fragments loosened from the parent formation by the drill bit have the tendency to form a stationary bed in the narrow region of the annulus, a situation which can result in costly problems. This is due to the nonuniform distribution of velocity and the kinetic energy of the drilling fluid around the annulus. Indeed, in an eccentric annulus most of the flow is diverted to the larger gap of the annulus, and in some cases a no flow zone is created in the narrow gap.

Studies have shown that turbulent flow results in a more uniform annular velocity distribution than in the case of laminar flow (Azouz et al., 1994). This suggests that better cleaning of the borehole can be achieved with a drilling fluid circulated in turbulent rather than laminar flow, since better mixing of the drilled cuttings with the bulk of the flow takes place. Unfortunately, the cost of sustaining turbulent flow is much higher due to the higher frictional losses. However, the high friction factor associated with turbulent flow may be decreased to a great extent through the use of drag reducing agents. Indeed, the addition of a small quantity of a drag reducing agent to a conventional drilling fluid can result in a tremendous decrease of the frictional losses in turbulent flow. Drag reducing fluids may thus in principle provide a solution to the cuttings transport problem which is frequently encountered in drilling of inclined oil and gas wells.

The phenomenon of drag reduction, also known as Toms phenomenon, can be described as the ability of minute quantities of long, flexible, expanded high-molecular weight polymers to drastically reduce the skin friction caused by turbulent flow of an ordinary fluid (solvent). This phenomenon was first observed by Toms in the early 1940's and is described in Toms (1948). It has since received great attention owing to its extensive commercial applications. For instance, a very useful application of drag-reducing fluids could be in the oil and gas industry during drilling operations. In addition to its potential commercial applications, the phenomenon of drag reduction is highly stimulating, especially in the still obscure area of near-wall turbulence. While the phenomenon is by now well known and experimentally reproducible, its mechanism is not yet fully understood.

The phenomenon of drag reduction by polymer additives has been the subject of numerous experimental and theoretical investigations in an effort to elucidate its mechanism. Moreover, several phenomenological models have been proposed for describing the turbulent flow of drag-reducing fluids. Comprehensive reviews of the subject are provided in Hoyt (1972), Lumley, (1973), and Virk (1975). A few of the studies performed by previous researchers and related to the present work are reviewed below.

One of the earliest phenomenological models of drag reduction was formulated by Meyer (1966). He expressed the influence of drag-reducing additives (polymers) through an upward shift of the logarithmic part of the velocity profile and a thickening of the viscous sublayer. An improved model was later proposed by Virk (1971) who suggested that the mechanism responsible for drag reduction must take place somewhere between the viscous sublayer and the logarithmic zone. He named this region "elastic sublayer." He also suggested that the width of this layer is an increasing function of the degree of drag reduction, and at maximum drag reduction the elastic sublayer completely pervades the logarithmic region. Velocity profile expressions were also derived for the three layers, namely viscous sublayer, elastic sublayer, and logarithmic region.

Poreh and Dimant (1972) developed a model based on van Driest's mixing-length with a variable damping parameter to represent the effect of drag-reducing additives on turbulent pipe

Contributed by the Fluids Engineering Division for publication in the JOURNAL OF FLUIDS ENGINEERING. Manuscript received by the Fluids Engineering Division July 15, 1996; revised manuscript received July 8, 1997. Associate Technical Editor: S. P. Vanka.

flow. They concluded from their results that the maximum drag reduction curve might be associated with a maximum value of the damping parameter in the mixing-length expression. Hassid and Poreh (1975), on the other hand, proposed a model based on the turbulent kinetic energy equation and the eddy diffusivity. Although the model is capable of reproducing velocity profiles in drag-reducing flows, it requires an a priori knowledge of the distribution of the turbulent length scale. Aware of this shortcoming, they later proposed an alternative model (Hassid and Poreh, 1978) based on a low-Reynolds number version of the k-ϵ model. They modified the two equations (k and ϵ) to account for the increase in turbulent kinetic energy in drag-reducing flows. However, it should be mentioned that the behavior of the kinetic energy in drag-reducing flows still remains unclear. They also proposed a new eddy-viscosity damping function which, in contrast to the parent function, involves a single adjustable parameter. The value of this parameter must be determined for each polymer-solvent solution from friction factor data.

Tiederman and Reischman (1976) proposed a procedure for predicting mean velocity profiles in drag-reducing pipe flow. This procedure is based on an eddy-viscosity expression originally developed by Cess (1958) for Newtonian fluids. Again, drag reduction is modeled through the adjustment of the damping parameter in the eddy-viscosity expression. The model requires a knowledge of the average velocity, wall shear stress, the density, and kinematic viscosity of the fluid. Although the model cannot predict the velocity profile for maximum drag reduction proposed by Virk (1971), their reported results for pipe flow seem to be in good agreement with experimental data.

Although appreciable progress has been made in the understanding of turbulent flow of drag-reducing fluids, there is still much to be done in this area. The various mechanisms put forward to explain drag reduction are still at the embryo stage. Moreover, the various models proposed in the literature seldom reproduce accurately experimental observation and are much less universal than those proposed for Newtonian turbulent flow.

The purpose of the present study is to contribute, through numerical simulation, to the modeling of the phenomenon of drag reduction. The focus is primarily on turbulent flow of a drag-reducing Power-law fluid in concentric and eccentric annuli, which is of great interest to the drilling industry. A new, one-layer eddy-viscosity/mixing-length turbulent model is proposed for annular flow. This model is applicable to Newtonian fluids as well as non-Newtonian, drag-reducing fluids. For this latter case, the value of the damping parameter in the eddy-viscosity expression is derived from pipe flow results.

Governing Equations

Fully-developed annular flow with negligible cross-flow velocity components can be described by the following time-average axial momentum equation

$$\frac{\partial}{\partial y}\left[\mu\left(1+\frac{\nu_t}{\nu}\right)\frac{\partial \bar{u}}{\partial y}\right]+\frac{\partial}{\partial z}\left[\mu\left(1+\frac{\nu_t}{\nu}\right)\frac{\partial \bar{u}}{\partial z}\right]=\frac{\partial P}{\partial x} \quad (1)$$

where x, y, and z are the Cartesian coordinates with x oriented in the axial direction; $\bar{u}$ is the time-averaged axial velocity component; $\partial P/\partial x$ is the axial pressure gradient; ν_t is the so-called turbulent eddy-viscosity. For a Newtonian fluid μ is the molecular viscosity and ν is the kinematic viscosity, whereas for the Power-law fluid considered in this study μ is an "apparent" viscosity expressed as

$$\mu = K\left[\left(\frac{\partial \bar{u}}{\partial y}\right)^2+\left(\frac{\partial \bar{u}}{\partial z}\right)^2\right]^{(n-1)/2} \quad (2)$$

where K is the fluid consistency factor and n is the flow behavior index. In this case, ν is the kinematic viscosity based on the apparent viscosity and the fluid density. In the derivation of Eq. (2) the nonlinear terms in the second invariant of the rate of deformation tensor have been neglected. These terms have been shown by Krantz and Wasan (1971) to be negligible in the near-wall region.

Eddy-Viscosity Model

Closure of the problem described by Eqs. (1) and (2) requires the modeling of the eddy-viscosity ν_t. Several empirical expressions for ν_t based on the mixing-length approach have been proposed by past investigators (Leung et al., 1962; Michiyoshi and Nakajima, 1968; Quarmby and Arnand, 1970; Usui and Tsuruta, 1980; and Ogino et al., 1987) for turbulent annular flow of Newtonian fluids. These expressions require the subdivision of the annular domain into several regions, and a different expression for ν_t is applied in each region. This in turn requires the specification of the boundaries of each region (see, for instance, Azouz et al., 1993b). While this presents no major difficulty for Newtonian fluids, it is not so for drag-reducing fluids. Indeed, the extent of the elastic sublayer (Virk, 1971) depends on the degree of drag reduction and thus, is not a priori known. Anticipating this problem, a new eddy-viscosity/mixing length model is proposed in this work for turbulent annular flow. This model is similar to that proposed by Tiederman and Reischman (1976) for pipe flow, in the sense that it can be applied across the whole shear layer. However, since two shear layers are present in annular flow (see Fig. 1), two different expressions for ν_t are used: one in the region between the inner cylinder wall and the plane of zero-shear (hereafter, "inner region"), and another in the region between the outer cylinder wall and the plane of zero-shear (hereafter, "outer region"). In the inner region, ν_t is expressed as

Nomenclature

A^+ = damping parameter
C_f = skin-friction factor
K = fluid consistency factor
n = flow behavior index
P = pressure
Re = Reynolds number
r = radial coordinate
r_0 = pipe radius
r_1 = radial distance from outer wall of annulus
u_b = bulk velocity
$\bar{u}$ = time-averaged axial velocity component
u', v' = fluctuating velocity components in x-direction and y-direction, respectively
$\bar{u}^+$ = dimensionless axial velocity component ($\bar{u}/u_\tau$)
u_τ = frictional velocity $\sqrt{\tau_w/\varrho}$
x, y, z = Cartesian coordinates
y^+ = law of the wall coordinate based on apparent viscosity at the wall
δ = shear layer thickness
δ^* = ratio of inner to outer shear layer (δ_i/δ_o)
ζ = dimensionless distance from the wall (y/δ)
μ = molecular viscosity for Newtonian fluid or apparent viscosity for non-Newtonian fluid
ν = kinematic viscosity
ν_t = turbulent eddy-viscosity
ϱ = fluid density
ξ = dimensionless radius (r/r_o)
τ^* = wall shear stress ratio (τ_o/τ_i)
τ_w = wall shear stress

Subscripts

i = inner cylinder region
o = outer cylinder region

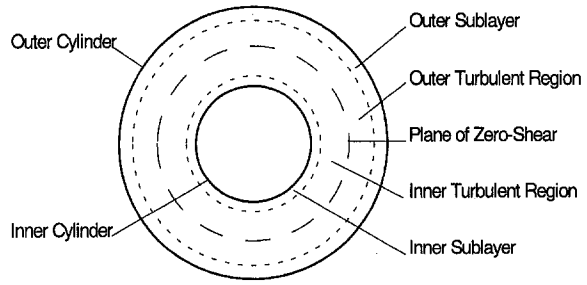

Fig. 1 Subdivision of the flow domain (concentric annulus)

$$\frac{\nu_t}{\nu} = \frac{1}{2}\left\{1 + \left[\frac{\varkappa_i \delta_i u_{\tau i}}{3\nu}(1 - \zeta_i^2)(1 + 2\zeta_i^2)(1 - (1 - \delta^*/\sqrt{\tau^*})\zeta_i)(1 - \exp(-y_i^+/A^+))\right]^2\right\}^{1/2} - \frac{1}{2} \quad (3)$$

and in the outer region, the following expression is used

$$\frac{\nu_t}{\nu} = \frac{1}{2}\left\{1 + \left[\frac{\varkappa_o \delta_o u_{\tau o}}{3\nu}(1 - \zeta_o^2)(1 + 2\zeta_o^2) \times \left(1 - \exp\left(-\frac{y_o^+}{A^+}\right)\right)\right]^2\right\}^{1/2} - \frac{1}{2} \quad (4)$$

In the above expressions y^+ is the dimensionless distance from the wall; δ is the shear layer thickness; $\varkappa$ is the von Karman constant, which assumes a value of 0.4 in the outer region; u_τ is the frictional velocity; $\delta^* = \delta_i/\delta_o$; $\tau^* = \tau_o/\tau_i$; $\zeta = 1 - y/\delta$, where y is the radial distance from the wall. The subscripts i and o refer to the inner (cylinder) region and the outer (cylinder) region, respectively. For the inner region the von Karman constant $\varkappa_i$ is determined by equating, at the plane of zero-shear, the expressions for the eddy-viscosity given by Eqs. (3) and (4). The shear layer thicknesses δ_i and δ_o in the inner and outer regions are determined from a force balance on an annular element of fluid. The extra terms in Eq. (3) are included to reproduce the non-symmetry of the eddy-viscosity profile in the annular gap (see Michiyoshi and Nakajima, 1968). For Newtonian flows, $A^+ = 26$. The use of a value of 0.4 for the Karman constant in the outer region is based on the similarity of the flow in this region with that of pipe flow (see, for instance, Shigechi et al., 1990; Barrow and Roberts, 1965; Brighton and Jones, 1964; Johnson and Sparrow, 1964; and Shigechi et al., 1990.)

While a few models have been developed for turbulent flow of drag-reducing fluids in pipes, no model has yet been proposed for annular passages. The extension of the proposed eddy-viscosity model to turbulent flow of drag-reducing fluids is done through an adjustment of the damping parameter A^+. For Newtonian fluids A^+ is approximately equal to 26 and is somewhat universal for wall bounded shear flows with no separation. By analogy to turbulent flow of Newtonian fluids, and short of experimental evidence, it is assumed in this study that a value of A^+ obtained for a given drag-reducing pipe flow at a particular Reynolds number may also be used for annular flow of the same fluid at the same Reynolds number. Therefore, it is implied that drag reduction behavior is the same in pipe flow and annular flow.

Determination of A^+. The starting point in the determination of A^+ is the pipe flow model developed by Tiederman and Reischman (1976), wherein drag reduction is reproduced through a variable damping parameter in the eddy-viscosity expression. This expression is shown below with minor modifications to make it a function of the friction factor, Reynolds number, and the damping parameter.

Table 1 Power-law fluids parameters

Solution	K (pa.s^n)	n
0.4% CMC	0.447	0.56
0.3% CMC	0.184	0.64
0.2% CMC	0.044	0.75
0.1% CMC	0.0075	0.90

$$\frac{\nu_t}{\nu} = \frac{1}{2}\left\{1 + \frac{C_f}{2}\left[\frac{\varkappa \mathrm{Re}}{12}(1 - \xi^2)(1 + 2\xi^2) \times [1 - \exp\{(1 - \xi)\mathrm{Re}\sqrt{(C_f/2)}/4A^+\}]\right]^2\right\}^{1/2} - \frac{1}{2} \quad (5)$$

where ν is the kinematic viscosity of the fluid; ν_t is the turbulent eddy-viscosity; Re is the Reynolds number based on the diameter of the pipe, the kinematic viscosity and the bulk velocity; ξ is the nondimensional radius ratio r/r_o, where r_o is the pipe radius; $\varkappa = 0.4$ is the von Karman constant; A^+ is a variable damping parameter which assumes a value of 26 for Newtonian fluids; and C_f is the skin friction factor defined as

$$C_f = \frac{2(\Delta P/L)D}{\varrho U_b^2} \quad (6)$$

where $\Delta P/L$ is the pressure gradient; D is the pipe diameter; ϱ is the fluid density; u_b is the bulk velocity.

When friction factor data is available for a given drag-reducing flow situation, the following equation can be used to obtain the corresponding value of A^+:

$$1 = \frac{\mathrm{Re}C_f}{8}\int_0^1 \left(\int_0^1 \frac{\xi}{1 + \nu_t/\nu}\,d\xi - \int_0^\xi \frac{\xi}{1 + \nu_t/\nu}\,d\xi\right)\xi d\xi \quad (7)$$

Eq. (7) is obtained as follows. First, the pipe flow equation of motion is integrated to obtain the mean velocity profile. This latter is then integrated, yielding the bulk velocity. Finally the resulting expression for the bulk velocity is non-dimensionalized to obtain Eq. (7). A trial-and-error procedure is used to solve for A^+ from Eq. (7), where ν_t/ν is given by Eq. (5). Re and C_f are assumed to be given.

To illustrate the application of the above procedure, values of A^+ were determined for the turbulent pipe flow of CMC polymer solutions at four different concentrations. Table 1 lists the fluid parameters as given by Pinho and Whitelaw (1990). Experimental values for the friction factor and corresponding Reynolds numbers used in the calculations were obtained from the same Reference. Table 2 lists values of A^+ obtained for each each polymer-solvent solution at several Reynolds num-

Table 2 Calculated values of A^+ for several values of the Reynolds number

	n	A^+
Re = 9200	0.90	40
	0.75	142
	0.64	160
	0.56	160
Re = 15000	0.90	70
	0.75	160
	0.64	160
Re = 30000	0.90	100
	0.75	160

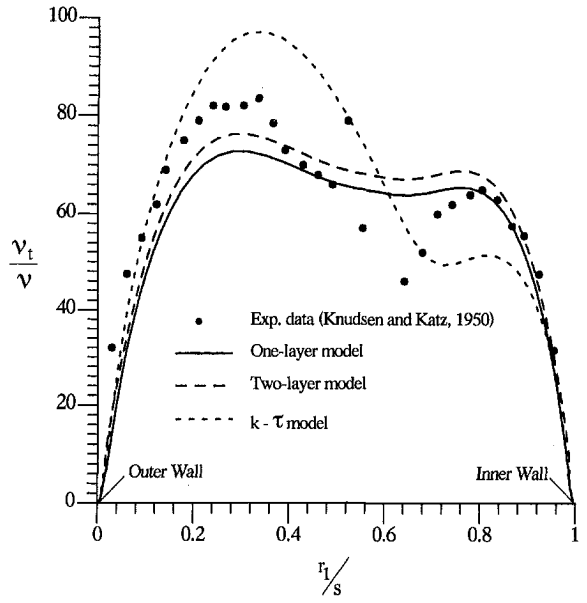

Fig. 2 Calculated eddy-viscosity profiles for the concentric annulus (Re = 69,900)

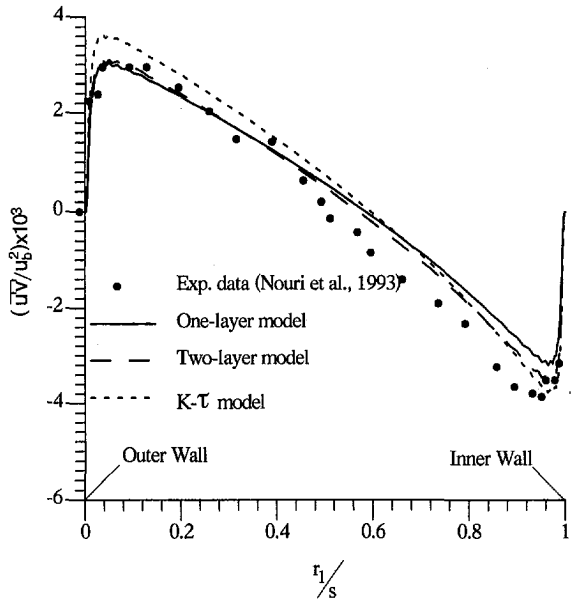

Fig. 4(*a*) $\overline{u'v'}$ cross correlations in wider gap at the plane of symmetry of the eccentric annulus (Re = 26,600)

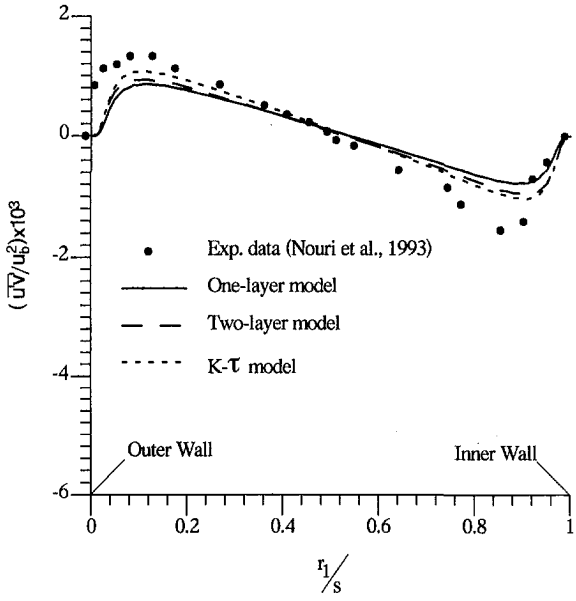

Fig. 4(*b*) $\overline{u'v'}$ cross correlations in narrow gap at the plane of symmetry of the eccentric annulus (RE = 26,600)

bers. The results seem to indicate that for a given Reynolds number value, A^+ is an increasing function of concentration. This is in agreement with experimental observation that drag reduction increases with concentration (Lumley, 1973). Moreover, it can be noticed that as the Reynolds number is increased, A^+ increases and seems to approach an asymptotic value. For instance, A^+ for the 0.2 percent CMC solution has the same value for Re = 15,000 and Re = 30,000. However, this fact cannot be positively ascertained because not enough experimental data is available for Reynolds number values beyond 10,000.

Results and Discussion

The mean flow governing equations were solved numerically using the finite difference technique. A boundary-fitted, curvilinear coordinate system was used for the eccentric annulus to facilitate the implementation of the boundary conditions and the writing of the computer code. The solution procedure is described in detail in Azouz et al. (1993a, 1993b).

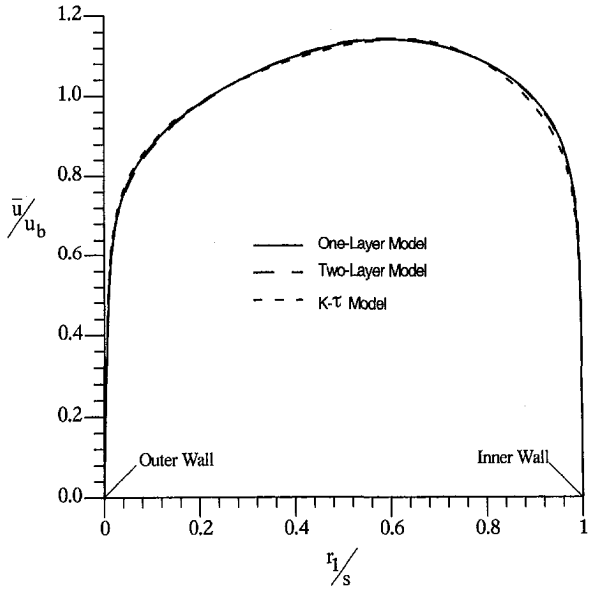

Fig. 3 Velocity profile in the concentric annulus (Re = 69,900)

Newtonian Fluids. Before discussing results for the non-Newtonian fluids, it is important to consider the accuracy of the model to predict turbulent Newtonian fluid in concentric and eccentric annuli. The validity of the proposed eddy-viscosity model was first assessed for the case of Newtonian fluids by comparing the numerical predictions with the experimental data of Nouri et al. (1993) and that due to Knudsen and Katz (1950), obtained for concentric and eccentric annuli. The results are shown in Figs. 2 through 5(*d*). Also shown in these figures are the corresponding results obtained using the two-layer mixing-length model of Michiyoshi and Nakajima (1968) and the low-Reynolds number, two-equation ($\varkappa$ and τ) model of Speziale et al. (1992). Details of these predictions are given in Azouz et al. (1993b). In these figures, as well as in the subsequent ones, u' and v' are fluctuating velocity components; r_1 is the radial dis-

tance measured from the outer cylinder wall; s is the width of the annular gap; and the superscript + refers to the law of the wall coordinates. Notice that although the eddy viscosity profiles seem substantially different (see Fig. 2), the corresponding velocity profiles are almost a perfect match of each other, as seen from Fig. 3. At first this would seem inconsistent. However, a careful study of Fig. 2 reveals that the predictions from the three models agree well with each other and with experimental data in the near-wall region. Furthermore, in the turbulent core, the average eddy-viscosity is approximately the same for the three models. Several tests were performed to study the effect of moderate changes of the value of the eddy-viscosity in the turbulent core. The results suggest that the velocity profile is not very sensitive to these changes. This explains the good agreement of the velocity profiles shown in Fig. 3.

The models were also applied to several eccentric annulus cases. For instance, Figs. 4(a) through 5(d) show the Reynolds stresses and velocity profiles, respectively, along the plane of symmetry of a 50 percent eccentric annulus. It can be observed that the proposed model performs at least as good as the other two models. However, the present model avoids the computational difficulties associated with the two-layer and the two-equation models (Azouz et al., 1993b).

Drag-Reducing Fluids. The proposed model was applied to the turbulent annular flow of a drag-reducing Power-law fluid having a consistency factor $K = 0.044$ Pa.s^n and a flow behavior index $n = 0.75$. This case was studied experimentally by Nouri et al. (1991). The flow geometries consist of a concentric annulus and a 50 percent eccentric annulus, with inner and outer diameters of 20.1 mm and 40.3 mm, respectively. It should be mentioned that a single value for the apparent viscosity at the wall is given in Nouri et al. (1993). This suggests that their experimental data was normalized using this constant apparent viscosity. However, in the present study the local apparent viscosity computed as part of the solution is used. This is more consistent with the physical situation since the value of the apparent viscosity is not the same at the inner and outer walls. In fact, the numerical predictions suggest that it is slightly higher at the outer wall. Moreover, it also varies in the circumferential

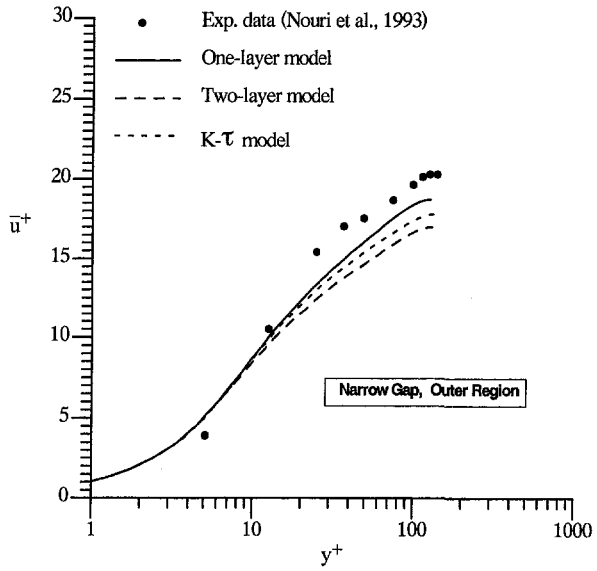

Fig. 5(a) Velocity profiles in the law of the wall coordinates along the plane of symmetry of the eccentric annulus (Re = 26,600)

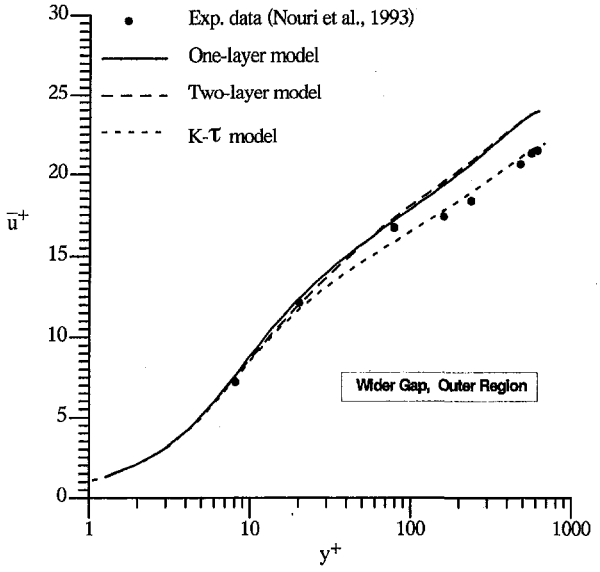

Fig. 5(b) Velocity profiles in the law of the wall coordinates along the plane of symmetry of the eccentric annulus (Re = 26,600)

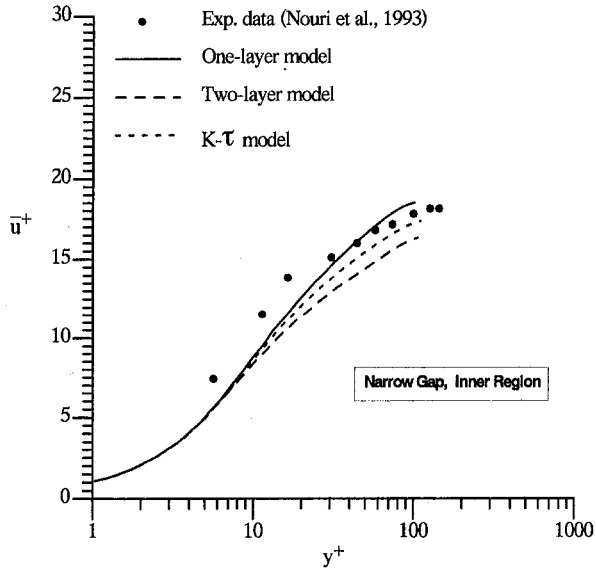

Fig. 5(c) Velocity profiles in the law of the wall coordinates along the plane of symmetry of the eccentric annulus (Re = 26,600)

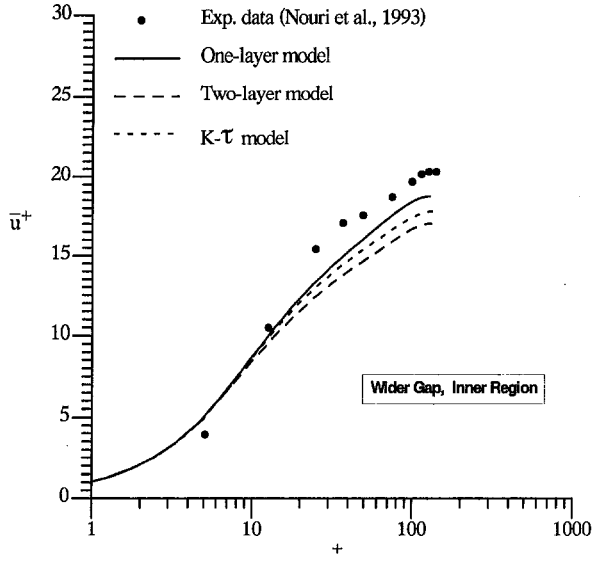

Fig. 5(d) Velocity profiles in the law of the wall coordinates along the plane of symmetry of the eccentric annulus (Re = 26,600)

direction in the case of an eccentric annulus, being higher in the narrow gap than in the wider gap.

Concentric Annulus. The numerical results for the concentric annulus case are shown in Figs. 6 through 9. A value of A^+ of 142 obtained for pipe flow of the same fluid and Reynolds number is used. Predicted velocity profiles normalized with the bulk velocity are plotted, along with experimental data, in Fig. 6 for turbulent Newtonian, turbulent non-Newtonian, and laminar non-Newtonian. A slight disagreement of the predicted turbulent non-Newtonian profile with experimental data is noticeable close to the walls. However, the agreement is good in the core region. Moreover, the profile lies between the laminar non-Newtonian and the turbulent Newtonian profiles. This is consistent with experimental observation. Figure 7(*a*) shows velocity profiles in the inner region in the law of the wall coordinates. Also shown in the figure is Virk's ultimate asymptote given by

$$u^+ = 11.7 \ln y^+ - 17 \qquad (8)$$

which represents the situation obtained at maximum drag reduction. It can be noticed that the numerical predictions agree well with experimental data and are higher than the Newtonian values for values of y^+ higher than approximately 8. Again, this is in agreement with Virk's suggestion (Virk, 1971) that drag reduction behavior does not affect the viscous sublayer. Figure 7(*b*) shows the velocity profile corresponding to the outer region. There is a good agreement away from the wall. Close to the wall, however, the experimental data, in contrast to the numerical predictions, does not seem to follow the relationship $u^+ = y^+$ suggested by theoretical analysis (Virk, 1971). Furthermore, it can be noticed that the experimental values are higher than those given by Virk's asymptote. On the other hand, the numerical predictions follow closely this asymptote, without ever crossing it. The predicted $\overline{u'v'}$ cross correlations (Reynolds stresses) are presented in Fig. 8. No experimental data is available for comparison. However, it can be noticed that the non-Newtonian values are much smaller than the corresponding Newtonian predictions. Again, this is in agreement with Virk's observation (Virk, 1971) that drag reduction effects decouple the axial and radial turbulent flow fields.

The calculated skin friction is illustrated graphically in Fig. 9. A good agreement with experimental data is noticeable in both laminar and turbulent regimes. Notice also that the friction factor is not very sensitive to moderate variations of the damping parameter. For instance, when A^+ is varied from 142 to 160 the predicted friction factor curves nearly match each other.

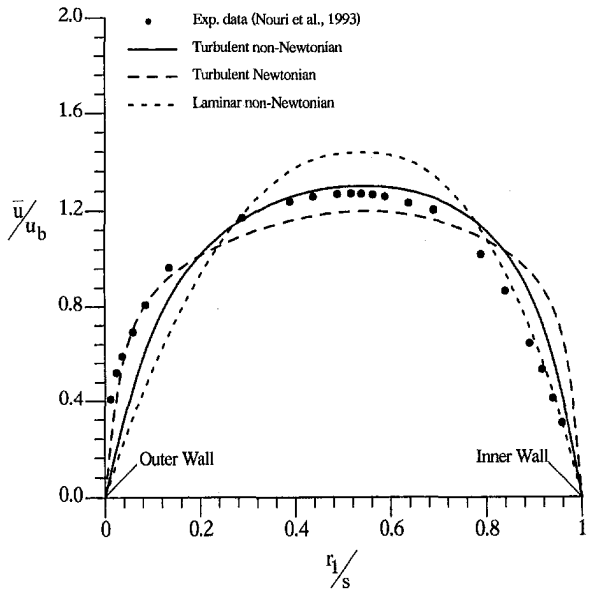

Fig. 6 Velocity profiles in the concentric annulus (Re = 9600)

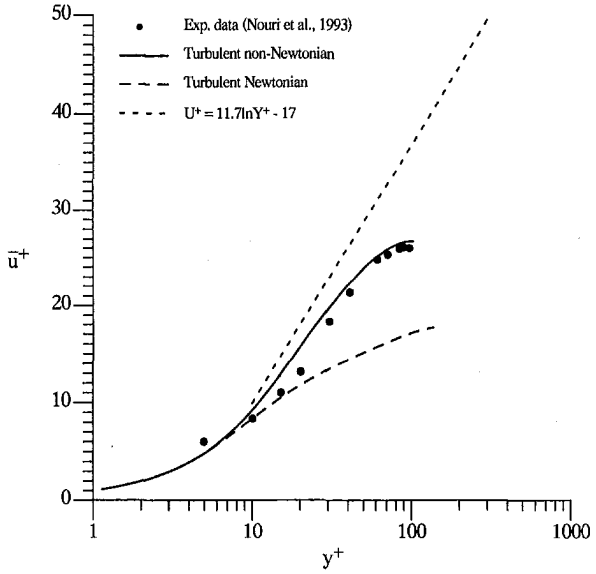

Fig. 7(*a*) Velocity profiles in the law of the wall coordinates in the inner region of the concentric annulus (Re = 9600)

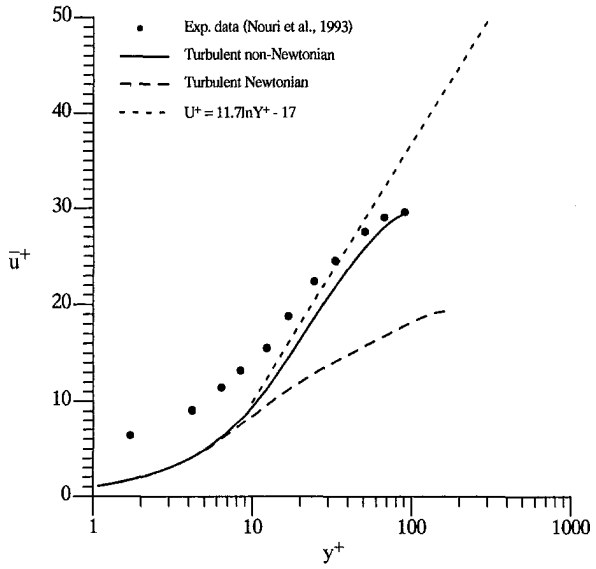

Fig. 7(*b*) Velocity profiles in the law of the wall coordinates in the outer region of the concentric annulus (Re = 9600)

The results obtained for the concentric annulus case are overall in good agreement with experimental data. Moreover, they seem to confirm theoretical analysis of the drag reduction phenomenon proposed by previous researchers. They also seem to confirm, at least for the concentric case, the assumption made earlier in this report that a value of A^+ obtained for pipe flow could be used for turbulent annular flow, under the same conditions of fluid type and Reynolds number.

Eccentric Annulus. As mentioned earlier, turbulent non-Newtonian flow in an eccentric annulus was also investigated. Unlike for Newtonian flow where A^+ is constant and equal to 26, the choice of an appropriate value for the non-Newtonian case under investigation is not obvious. Indeed, the local Reynolds number based on the gap width varies considerably from the narrow gap to the wider gap. Consequently, A^+ which is a function of the Reynolds number should also vary in the circumferential direction. The choice of A^+ is further complicated by the possibility of the flow being laminar in the narrow

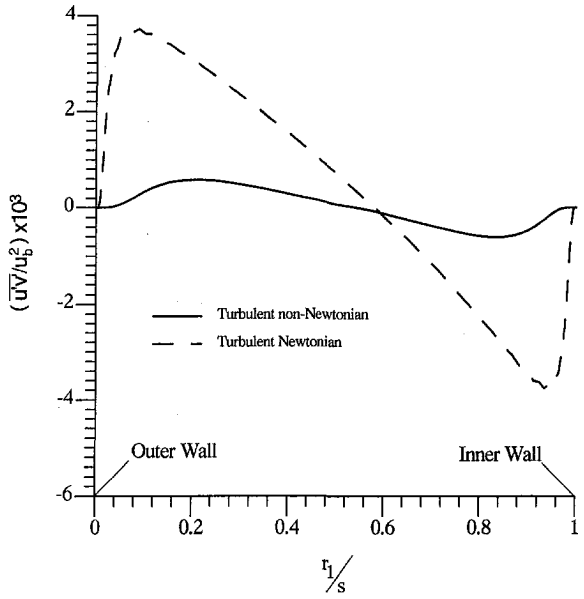

Fig. 8 $\overline{u'v'}$ cross correlations for the concentric annulus (Re = 9600)

gap and turbulent in the wider gap, as pointed out by Nouri et al. (1993). Several values of A^+, including the value $A^+ = 142$ corresponding to the bulk Reynolds number, were tested. It was found that a value of $A^+ = 80$ yielded better results than all the other choices. This value is approximately the average of the Newtonian value and the non-Newtonian value corresponding to the bulk Reynolds number (average of 26 and 142). The numerical predictions based on $A^+ = 80$ are presented in Figs. 10(*a*) through 12. The experimental results of Nouri et al. (1993) are also shown for comparison.

Velocity profiles along the plane of symmetry, in the outer region, are shown in Figs. 10(*a*) and 10(*b*). No experimental data for the inner region is given in Nouri et al. (1993). It can be noticed that a better agreement with experimental data is obtained in the wider gap of the annulus than in the narrow gap, except in the sublayer region where, again, the experimental data deviates from the expected $u^+ = y^+$ relationship. In the narrow gap, on the other hand, the numerical predictions are almost the same as for the Newtonian case. Drag reduction

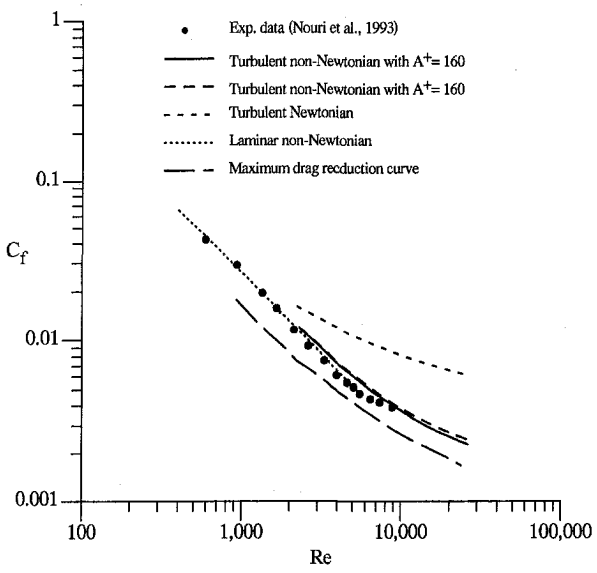

Fig. 9 Skin friction versus Reynolds number for the concentric annulus

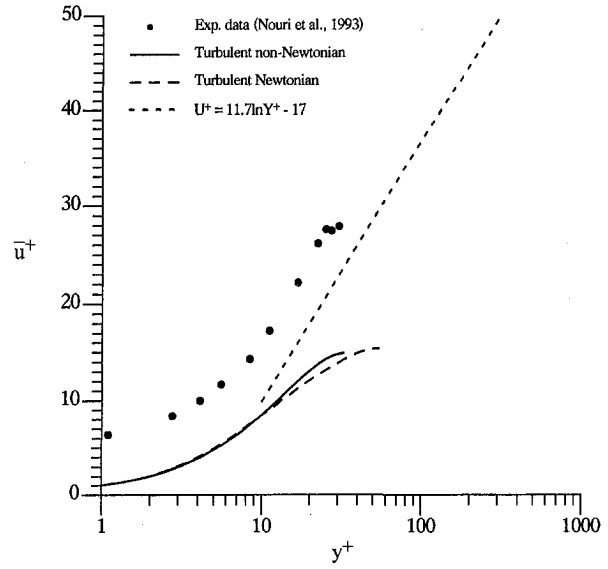

Fig. 10(*a*) Velocity profiles in the law of the wall coordinates in the narrow gap at the plane of symmetry of the eccentric annulus (Re = 9600)

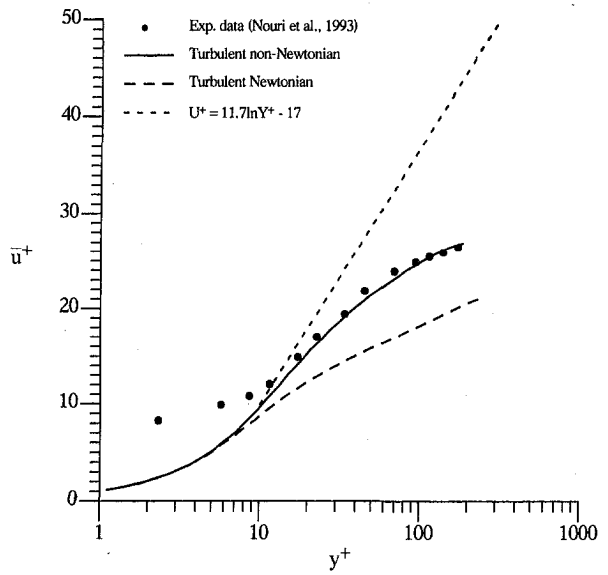

Fig. 10(*b*) Velocity profiles in the law of the wall coordinates in the wider gap at the plane of symmetry of the eccentric annulus (Re = 9600)

effects are barely noticeable in this region. This may be due to the low local Reynolds number value in this region. Again, the experimental results shown in Fig. 10(*a*) for the narrow gap are higher than the present predictions and are everywhere higher than those predicted by Virk's asymptote. This inconsistancy of the experimental data with the maximum drag reduction theory and the law-of-the-wall was also noticed by Nouri et al. (1993), but no explanation was offered for this behavior. The predictions, on the other hand, are in agreement with the drag reduction theory. However, more experimental data are required for further evaluation of the present turbulence model.

The predicted $\overline{u'v'}$ cross correlations in the narrow gap and the wider gap, along the plane of symmetry, are shown in Figs. 10(*a*) and 10(*b*). No experimental data is available for comparison. Again, a decoupling of the axial and radial turbulent flow fields is evidenced by the much lower values of the non-Newtonian predictions compared to the Newtonian values. Moreover, it can be noticed that the Reynolds stresses are much lower in the narrow gap than in the wider gap.

The skin friction factor shown in Fig. 12 presents interesting features. The appreciable deviation of the data from the numerical predictions in the laminar region confirms Nouri's suspicion that the flow may not be fully-developed for Reynolds numbers greater than 500. Since in the present model fully developed flow is assumed, direct comparison of the numerical predictions with the experimental data for Re > 500 may not be appropriate. In the fully turbulent region (Reynolds number larger than approximately 3000), the lower slope of the predicted turbulent non-Newtonian curve (as compared to the data) seems to confirm that A^+ is an increasing function of the Reynolds number in the range considered. Indeed, if lower values of A^+ are used for Re < 10000 and higher values for Re > 10000, then a better agreement with experimental data may be obtained. This in turn implies that the use of a constant value for A^+ in eccentric annuli may not be appropriate since the local Reynolds number varies greatly in the circumferential direction. Of course, the above reasoning is based on the assumption that the flow is fully developed in the range of Reynolds number considered. In either case, more and accurate experimental annular flow data is needed to ascertain the claim.

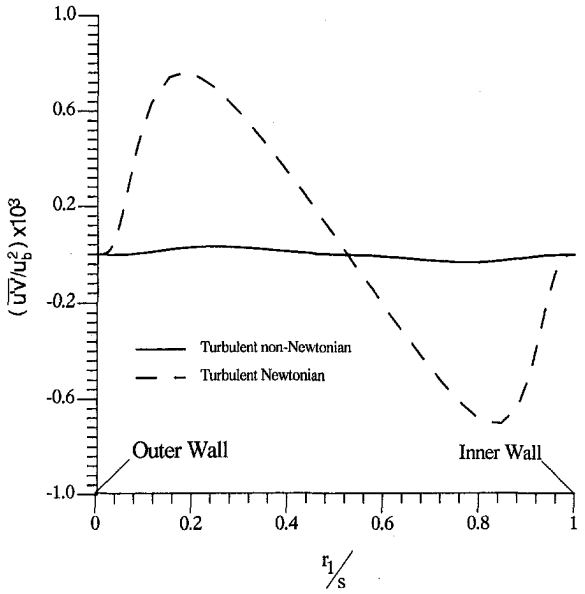

Fig. 11(*a*) $\overline{u'v'}$ cross correlations in the narrow gap at the plane of symmetry of the eccentric annulus (Re = 9600)

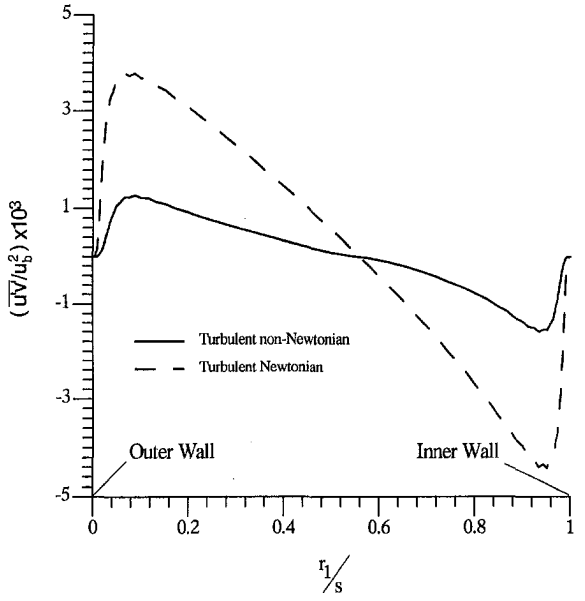

Fig. 11(*b*) $\overline{u'v'}$ cross correlations in the wider gap at the plane of symmetry of the eccentric annulus (Re = 9600)

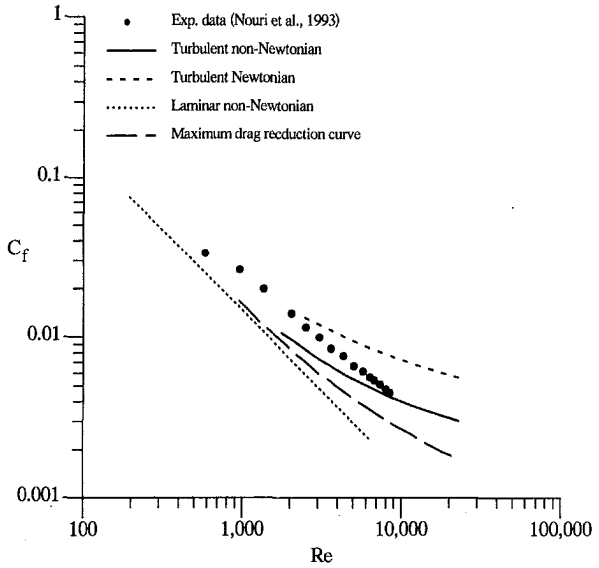

Fig. 12 Skin friction versus Reynolds number for the eccentric annulus

Conclusions

In this study, a model is developed which can be used for the numerical simulation of turbulent annular flow of Newtonian and non-Newtonian, drag-reducing fluids. This model, which is a one-layer eddy-viscosity/mixing-length model, uses a variable damping parameter in the eddy-viscosity expression to simulate drag reduction effects. Numerical predictions for Newtonian flows are in excellent agreement with those obtained with earlier two-layer models, as well as with a higher order, low-Reynolds number, two-equation model. For the drag-reducing fluid flow situation considered in this study numerical predictions are in better agreement with experimental data in the concentric annulus case than in the eccentric case. This is mostly due to the difficulty associated with the choice of an appropriate value for the damping parameter, due to the variation of the local Reynolds number in the circumferential direction. Further improvement of the model requires accurate experimental data for evaluation and verification.

The results presented in this study suggest that the damping parameter is an increasing function of the Reynolds number, probably approaching an asymptotic value. The results also suggest that values of the damping parameter obtained from pipe flow measurements may be used for annular flow calculations under the same conditions of fluid type and Reynolds number. Finally, in all the cases considered in this paper, the numerical predictions are in good agreement with the drag reduction theory.

Acknowledgments

The authors wish to thank Southern Utah University and The University of Tulsa for their support.

References

Azouz, I., Shirazi, S. A., Pilehvari, A., and Azar, J. J., 1993a, "Numerical Simulation of Laminar Flow of Yield-Power-Law Fluids in Conduits of Arbitrary Cross-Section," ASME JOURNAL OF FLUIDS ENGINEERING, Vol. 115, No. 4, pp. 710–716.

Azouz, I., Shirazi, S. A., Pilehvari, A., and Azar, J. J., 1993b, "Numerical Simulation of Turbulent Flow in Concentric and Eccentric Annuli," AIAA Paper No. 93-3106, presented at the AIAA 24th Fluid Dynamics Conference, Orlando, FL.

Barrow, H. L., and Robert, A., 1965, "The similarity Hypothesis Applied to Turbulent Flow in an Annulus," *International Journal of Heat and Mass Transfer,* Vol. 8, pp. 1499–1505.

Brighton, J. A., and Jones, J. B., 1964, "Fully Developed Turbulent Flow in Annuli," ASME *Journal of Basic Engineering,* Vol. 86, pp. 835–844.

Cess, R. D., 1958, "A Survey of the Literature in Heat Transfer in Turbulent Flow," Westinghouse Research Report 80529-R-24.

Hassid, S., and Poreh, M., 1975, "A Turbulent Energy Model For Flows With Drag Reduction," ASME JOURNAL OF FLUIDS ENGINEERING, Vol. 97, No. 2, pp. 234–241.

Hassid, S., and Poreh, M., 1978, "A Turbulent Energy Dissipation Model For Flows With Drag Reduction," ASME JOURNAL OF FLUIDS ENGINEERING, Vol. 100, pp. 107–112.

Hoyt, J. W., 1972, "The Effect of Additives on Fluid Friction," ASME *Journal of Basic Engineering,* Vol. 94, pp. 258–285.

Jonsson, V. K., and Sparrow, A., 1964, "Experiments on Turbulent Flow Phenomena in Eccentric Annular Ducts," *Journal of Fluid Mechanics,* Vol. 25, pp. 65–86.

Knudsen, J. R., and Katz, D. L., 1950, "Velocity Profiles in Annuli," *Proceedings of Midwestern Conference on Fluid Mechanics.*

Krantz, W. B., and Wasan, D. T., 1971, "A Correlation for Velocity and Eddy Diffusivity for the Flow of Power-Law Fluids Close to a Pipe Wall," *Industrial and Engineering Chemistry Fundamentals,* Vol. 10, No. 3, pp. 424–427.

Leung, E. Y., Kays, W. M. and Reynolds, W. C., 1962. "Heat Transfer with Turbulent Flow in Concentric and Eccentric Annuli with Constant and Variable Heat Flux," Stanford Report No. AHT-4, Stanford University, CA.

Lumley, J. L., 1973, "Drag Reduction in Turbulent Flow by Polymer Additives," *Journal of Polymer Science,* Vol. 7, pp. 263–290.

Meyer, W. A., 1966, "A Correlation of Frictional Characteristics for Turbulent Flow of Dilute Non-Newtonian Fluids in Pipes," *AIChE Journal,* Vol. 12, pp. 522–525.

Michiyoshi, I., and Nakajima, T., 1968, "Fully Developed Turbulent Flow in a Concentric Annulus," *Journal of Nuclear Science Technology,* Vol. 5, pp. 354–359.

Nouri, J. M., Umur, H., and Whitelaw, J. H., 1993, "Flow of Newtonian and Non-Newtonian Fluids in Concentric and Eccentric Annuli," *Journal of Fluid Mechanics,* Vol. 253, pp. 617–641.

Ogino, F., Sokano, T. and Mizushina, T., 1987, "Momentum and Heat Transfer from Fully Developed Turbulent Flow in an Eccentric Annulus to Inner and Outer walls," *Warme-und Stoffubertragung,* Vol. 21, pp. 87–93.

Pinho, F. T., and Whitelaw, J. H., 1990, "Flow of Non-Newtonian Fluids in a Pipe," *Journal of Non-Newtonian Fluid Mechanics,* Vol. 34, pp. 129–144.

Poreh, M., and Dimant, Y., 1972, "Velocity Distribution and Friction Factors in Pipe Flows With Drag Reduction," Technion, Israel Institute of Technology, Faculty of Civil Engineering, Publication No. 175.

Quarmby, A. and Arnand, R. K., 1970, "Turbulent Heat Transfer in Concentric Annuli with Constant Wall Temperatures," ASME *Journal of Heat Transfer,* Vol. 92, pp. 33–44.

Shigechi, T., Kawae, N., and Lee, Y., 1990, "A Critical Evaluation of Two-Equation Models for Near Wall Turbulence," *AIAA Journal,* Vol. 30, No. 2, pp. 352–331.

Speziale, C. G., Abid, R., and Anderson, E. C., 1992, "Turbulent Fluid Flow and Heat Transfer in Concentric Annuli with Moving Cores," *International Journal of Heat and Mass Transfer,* Vol. 33, pp. 2029–2037.

Tiederman, W. G., and Reischman, M. M., 1976, "Calculation of Velocity Profiles in Drag-Reducing Flows," ASME JOURNAL OF FLUIDS ENGINEERING, pp. 563–566.

Toms, B. A., 1948, "Some Observations on the Flow of Linear Polymer Solutions Through Straight Tubes at Large Reynolds Numbers," *Proceedings of First International Congress on Rheology,* North Holland, Amsterdam, Vol. 2, pp. 135–141.

Usui, H. and Tsuruta, K., 1980, "Analysis of Fully Developed Turbulent Flow in an Eccentric Annulus," *Journal of Chemical Engineering of Japan,* Vol. 3, p. 445.

Virk, P. S., 1971, "An Elastic Sublayer Model for Drag Reduction by Dilute Solutions of Linear Macromolecules," *Journal of Fluid Mechanics,* Vol. 45, Part 3, pp. 417–440.

Virk, P. S., 1975, "Drag Reduction Fundamentals," *AIChE Journal,* Vol. 21, No. 4, pp. 625–656.

Friction Factor Determination for Flow Through Finite Wire-Mesh Woven-Screen Matrices

J. R. Sodré
Associate Professor,
Pontifícia Universidade Católica
de Minas Gerais,
Department of Mechanical Engineering,
Av. Dom José Gaspar, 500,
30535-610, Belo Horizonte, MG, Brazil

J. A. R. Parise
Associate Professor,
Pontifícia Universidade Católica
do Rio de Janeiro,
Department of Mechanical Engineering,
Rua Marquês de São Vicente, 225,
22453-900 Rio de Janeiro, Brazil

Experiments were carried out to determine the pressure drop through an annular conduit filled with a plain square wire-mesh woven-screen matrix. The tests involved turbulent fully developed flow of air at steady-state conditions, with the modified Reynolds number ($M(1-\bar{\epsilon})/Re$), based on the hydraulic radius of the packed bed, ranging from 5×10^{-4} to 5×10^{-3}. The test section was built according to the geometry of a Stirling engine, simulating an annular regenerator with a radius ratio of 1.369 and a screen of mesh size 10. A corrected Ergun equation was used to correlate the experimental data, considering the wall effects. Comparisons with results obtained by other authors extended the validation of the correlation obtained to a wider range of modified Reynolds numbers ($1 \times 10^{-4} \leq M(1-\bar{\epsilon})/Re \leq 1$) and to different screen mesh sizes. The correlation has been found to work for annular and circular cross-section beds.

Introduction

Wire-mesh woven-screen matrices have been largely applied as packing material for Stirling engine regenerators. Examples of Stirling engine regenerators can be found in the literature (Urieli and Berchowitz, 1984; Reader and Hooper, 1983). Several works have been published about the porosity and pressure drop at steady state flow conditions for this kind of porous medium. Kays and London (1964) presented curves for the friction factor for woven-screen types, specifying porosity values. An equation based on Kays and London's (1964) data is provided by Urieli and Berchowitz (1984). Armour and Cannon (1968) investigated several types of screens through experiments made in a bed with a single screen layer. An expression to calculate the pressure drop was obtained. Correlations to evaluate the porosity, based on the geometry of the screen, were also proposed. Another expression for the porosity was developed by Chang (1990), who demonstrated the importance of the inclusion of the actual thickness of the wire screen for an accurate estimate. Simon and Seume (1988) provide a further review of friction factor correlations for steady-state flow. Two other aspects are addressed by Simon and Seume (1988): compressibility effects and the oscillating characteristics of the flow through Stirling engine regenerators.

In addition to steady-state flow, Thonger and Rice (1986) also investigated the pressure drop for reverse flows in Stirling engine regenerators packed with screen matrices. Individual expressions were proposed for the friction factor, for each screen tested. Oscillating pressures and reverse flows in screen-packed Stirling engine regenerators have also been investigated by Jones (1988), who developed expressions for the friction factor in this sort of environment.

Despite the numerous works done to determine the pressure drop through woven-screen matrices, there is still a need for a universal correlation valid for any screen dimension. For instance, the expressions given by Thonger and Rice (1986) are just valid to the corresponding screen geometries from which they were evaluated. Moreover, none of the above-mentioned work has treated the wall effect problem for a screen-packed bed. The results from Armour and Cannon (1968), who tested a single screen layer, cannot be directly applied if more than one layer is considered, as, in this case, the wall effects would influence the friction factor. These effects are expected to be more important for annular beds, due to the presence of two walls.

Thus, the aim of this work is to present a general correlation for the friction factor in steady state flow through packed beds of plain square wire-mesh woven-screens. The correlation should be valid for annular or circular beds, and will take into account the wall effects.

Ergun's equation (Ergun, 1952), corrected by Mehta and Hawley (1969) to account for wall effects, and with new coefficients, as indicated by MacDonald et al. (1979), has been proposed. The utilization of coefficients different from those used in the original Ergun equation is due to the kind of packing, as the original expression had been developed for sphere-packed beds. The coefficients were obtained based on experiments of turbulent flow of air at steady state conditions through an annular conduit filled with screen layers.

Theory

Ergun (1952) combined existing correlations for laminar and turbulent flows to suggest a general expression for the pressure drop in fixed beds of uniform particles. The pressure losses in this type of packing were attributed to kinetic and viscous effects. The coefficients for the equation were obtained from experiments carried out in a circular bed of spheres with negligible wall effect. Mehta and Hawley (1969) introduced a correction in the original Ergun expression to account for the wall effect, so that it could also be applied to beds with low bed-to-particle diameter ratios. A correction parameter was developed from the definition of hydraulic radius, taking into consideration the contribution of the wall to the wetted perimeter. To adjust Ergun equation so that it is applicable to beds of non-spherical particles, MacDonald et al. (1979) suggested the use of different coefficients.

The matrix of screens can be regarded as a bed of cylinders with diameter d and length l (Fig. 1). Ergun's equation, corrected as in Mehta and Hawley (1969), and with new coefficients, is then applied to calculate the pressure drop in the bed of screens,

$$\Delta P/L = A(1-\bar{\epsilon})^2\mu\bar{v}M^2/[\bar{\epsilon}^3 d^2] + B(1-\bar{\epsilon})\rho\bar{v}^2M/[\bar{\epsilon}^3 d]. \quad (1)$$

Contributed by the Fluids Engineering Division for publication in the JOURNAL OF FLUIDS ENGINEERING. Manuscript received by the Fluids Engineering Division May 28, 1996; revised manuscript received June 10, 1997. Associate Technical Editor: P. W. Bearman.

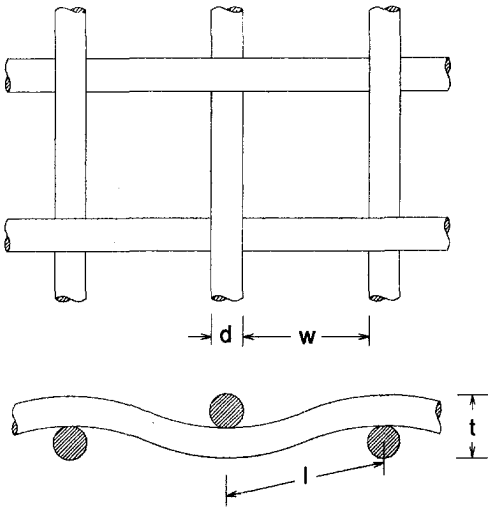

Fig. 1 Screen characteristics

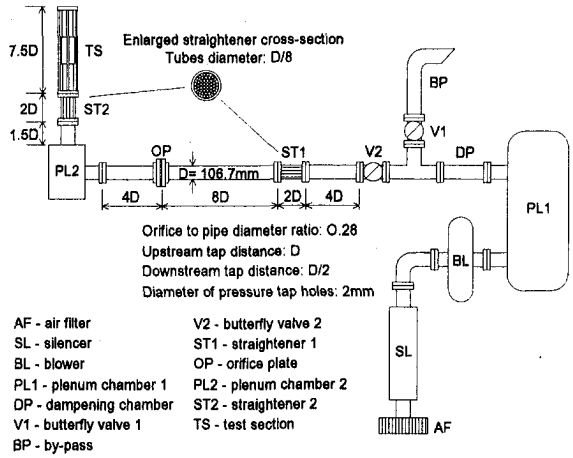

Fig. 2 Schematic of the air circuit

Here, the Mehta and Hawley parameter, M, is redefined for an annular bed of screens. From the concept of hydraulic radius,

$$R_h = (V_v/V_b)/(S_c/V_b + S_w/V_b) \quad (2)$$

$$R_h = \bar{\epsilon}/[4(1 - \bar{\epsilon})/d + 4/D_h] \quad (3)$$

or,

$$R_h = \bar{\epsilon}d/[4(1 - \bar{\epsilon})M] \quad (4)$$

where,

$$M = 1 + d/[D_h(1 - \bar{\epsilon})]. \quad (5)$$

In this analysis the area of the base of the wires has not been taken to contribute to the wetted surface of the cylinders. That means that a perfect adjustment of the screens to the walls of the bed has been assumed.

The friction factor is defined as (Mehta and Hawley, 1969),

$$F_k/M = \Delta P d\bar{\epsilon}^3/[L\rho\bar{v}^2(1 - \bar{\epsilon})M], \quad (6)$$

or, from Eq. (1), it can be expressed in terms of the Reynolds number,

$$F_k/M = A(1 - \bar{\epsilon})M/\mathrm{Re} + B, \quad (7)$$

where the Reynolds number is so defined,

$$\mathrm{Re} = \rho\bar{v}d/\mu. \quad (8)$$

The porosity for the bed of screens can be derived from the geometry of a screen mesh (Fig. 1). From the definition of porosity,

$$\bar{\epsilon} = V_v/V_b \quad (9)$$

$$\bar{\epsilon} = (w + d)^2 t - 2\pi(d/2)^2 l/[(w + d)^2 t] \quad (10)$$

The length of the wire in a mesh can be expressed as,

$$l = [(w + d)^2 + d^2]^{1/2} \quad (11)$$

Taking Eq. (11) into Eq. (10),

$$\bar{\epsilon} = 1 - \pi d^2[(w + d)^2 + d^2]^{1/2}/[2(w + d)^2 t] \quad (12)$$

This expression is similar to that found by Armour and Cannon (1968) for a single screen, which differs from that presented by Chang (1990) by the square root term. However, the screens in a bed can be either compacted or distended. Therefore, the volume occupied by a layer of screen is not necessarily determined by its thickness, t, but rather by the length of the bed, L, divided by the number of layers, n. So, for a bed of screens, the single screen thickness t is replaced by L/n, resulting,

$$\bar{\epsilon} = 1 - \pi d^2[(w + d)^2 + d^2]^{1/2}/[2(w + d)^2(L/n)]. \quad (13)$$

The pressure drop for a steady state flow through a bed of screens can be calculated by Eq. (1). Coefficients A and B are to be determined experimentally. In the absence of an empirical value, the porosity of the bed is estimated by Eq. (13).

Experiments

Experiments were carried out in a test section built to simulate the heat exchangers (cooler and heater) and the regenerator of a Stirling engine. The test section was connected to an air circuit, shown schematically in Fig. 2. The air circuit comprised an air filter, a silencer, a compressor, two valves for flow control, an orifice plate, plenum chambers, dampening chamber and straighteners. Air was blown by a Roots compressor, driven by an electric motor. The flow rate was controlled by two butter-

Nomenclature

A, B = variable coefficients in Eq. (1) (dimensionless)
d = wire diameter (m)
D_h = annular bed hydraulic diameter (m)
F_k = kinetic friction factor (dimensionless)
l = wire length in a mesh (m)
L = bed length (m);
M = Mehta and Hawley parameter (Mehta and Hawley, 1969) (dimensionless)
n = number of screen layers (dimensionless)
R_h = hydraulic radius of the packed bed (m)
S_c = wetted surface of cylinders (m^2)
S_w = wetted surface of bed walls (m^2)
t = screen thickness (m)
$\bar{v}$ = average flow velocity (m/s)
V_b = volume of bed (m)
V_v = volume of voids (m)
w = mesh width (m)
ΔP = pressure drop (Pa)
$\bar{\epsilon}$ = average bed porosity (dimensionless)
μ = viscosity (kg/m s)
ρ = density (kg/m^3)

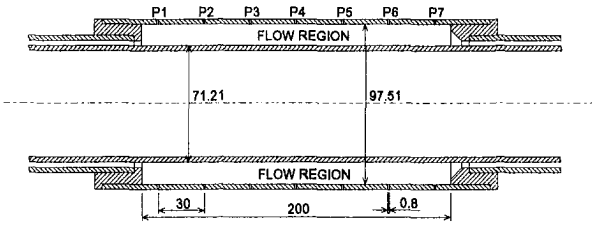

Fig. 3 Longitudinal view of the annular regenerator

fly valves, one of them restricting the flow to by-pass, and the other, to the test section. The mass flow rate to the test section was measured by an orifice plate, installed according to specifications of ASME (1971). The pressure drop in the orifice plate was read by a Dwyer well-type inclined manometer or by a Dwyer U-tube water column manometer, with resolutions of 0.5 mm and 2 mm, respectively. The inclined manometer was used for low flow rates. A silencer was installed between the filter and the compressor, to reduce noise. A plenum chamber and a dampening chamber were located after the compressor, to eliminate pulsation effects. A flow straightener was used after the flow control valve, before the developing length to the orifice plate. Another straightener was used between a second plenum chamber and the test section. The straighteners were tube-bundle types, each of them containing 20 tubes (see detail on Fig. 2).

Copper-constantan ATP/H-TEK T type thermocouples were used to measure the temperature of the air flowing in the orifice plate and in the test section. The readings from the thermocouples were measured by a voltmeter, with resolution of 0.01 mV. Ambient air temperature was read by a mercury-in-glass Incotherm thermometer, with resolution of 0.1°C. Atmospheric pressure was taken by a Fisher Scientific mercury column barometer, with resolution of 0.1 mm Hg. Room air humidity was measured by a Henni-René Graf thermohygrometer, with resolution of 2 percent.

The test section had a single internal pipe and external pipes with different diameters for the cooler, regenerator and heater locations (Fig. 3). That was done to reproduce the radius ratios of the heat exchangers and regenerator of the Stirling engine, as quoted by Bartolini and Naso (1984). The cooler and the heater were located in the extremes of the test section, with the regenerator in the middle, in accordance with the Stirling engine project. To obtain an averaged pressure, each location of reading had four taps, distant 90° from each other along the perimeter (Fig. 4). A multi-point valve was used to select the location of reading.

The pressure drop along the test section was measured with one Dwyer well-type inclined manometer, one Dwyer U-tube water column manometer, and one Dwyer U-tube mercury column manometer. The instruments had resolutions of 0.2 mm, 1 mm, and 1 mm, respectively. The readings from the taps in the extremities (taps P1, P2, P6, and P7 in Fig. 3) were neglected in the evaluation of the pressure drop along the bed, as the flow in these locations was under the influence of entrance and exit effects. These effects happened due to changes in the flowing area, from the tiny, free, annular cooler (heater) to the large, packed, annular regenerator, and then to the tiny, free, annular heater (cooler) (Fig. 3). The entrance and exit flow effects are indicated by Fig. 5, which also shows that the fully developed condition was reached in the intermediate taps (P3, P4 and P5).

The screen used was plain square wire-mesh woven type (see Fig. 1), with mesh size 10 (10 wires per inch) and wire diameter 0.55 mm. One hundred and sixty-five screen layers were fitted in the test section. This screen characteristic was the closest possible to that used in the Stirling engine described by Bartolini and Naso (1984).

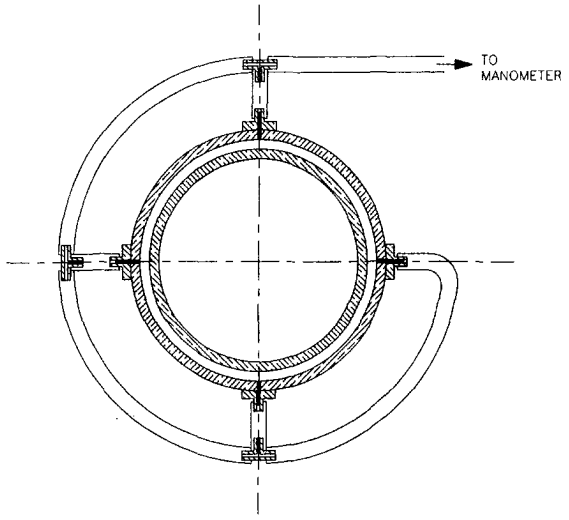

Fig. 4 Pressure taps distribution in a section of reading

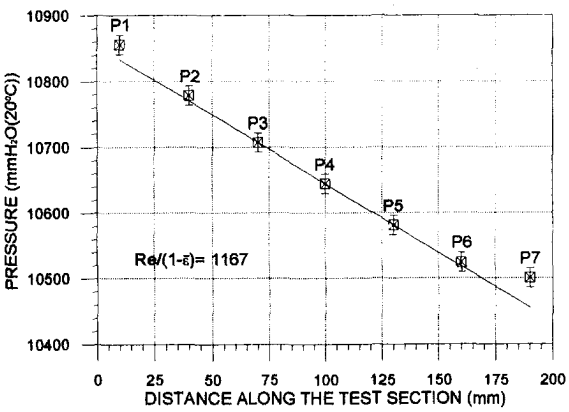

Fig. 5 Typical pressure drop diagram in the annular bed of screens

As the screen had to be cut to fit the annular section, the stability of its structure was affected, making its mounting difficult. Thus, the screen wires had to be welded together, by diving them into a bath of melted tin. As a consequence, the added material to the wire junctions altered the value of the porosity of the bed. The porosity was, thus, measured experimentally, apart from being calculated by Eq. (13). The experimental determination of the porosity was done from the measurement of the volume of voids in the bed. The volume of voids was filled with water, and the weight of the added liquid measured. A precision balance was used to weigh the water amount, with resolution of 0.1 g. The specific weight of water was taken from the tables of Bolz and Tuve (1976), and the total volume of the bed was determined from its measured dimensions. The porosity calculated by Eq. (13) was 0.836, while the measured value was 0.807. This difference was due to the material added to the screen. The experimental value was used for the determination of the friction factor.

The apparatus was constructed in the laboratories of PUC-Rio, where all the experiments were performed. The estimated uncertainties, calculated according to the method proposed by Kline and McClintock (1953), are shown in Table 1.

The procedure adopted in the execution of the experiments involved a regular check of the ambient air condition for each test run. Atmospheric pressure, room air temperature and humidity were always registered. Soon after a new flow was set though the butterfly valves, the steady state condition was obtained. The readings from the instruments were taken manually,

Table 1 Measurement uncertainties

Mass flow rate	±1.4%
Modified Reynolds number	±2.5%
Bed porosity	±0.44%
Friction factor	±4.7%
Calculated pressure drop (Eq. (1))	±6.5%

and each test run took approximately 5 min. Both flow directions in the regenerator were tested.

The measured quantities during the experiments were: atmospheric pressure, ambient air temperature, room air humidity, air temperature at the orifice plate inlet, air temperature at the test section entrance, pressure difference across the orifice plate, pressure difference between the test section exit and the atmosphere, pressure difference through the test section, pressure difference between the orifice plate inlet and the test section entrance, and pressure difference between the compressor outlet and the test section entrance. The preliminary data were converted by a data reduction computer program, written in BASIC language. The output from the program included the corresponding mass flow rate, Reynolds number and friction factor.

Results and Discussion

Figure 6 shows the plot of the experimental data of this work and the corresponding curve fit. The least squares method was applied, leading to the values of 100 and 0.73 for coefficients A and B, respectively. Equation (1), then becomes,

$$\Delta P/L = 100(1-\bar{\varepsilon})^2\mu\bar{v}M^2/[\bar{\varepsilon}^3 d^2] + 0.73(1-\bar{\varepsilon})\rho\bar{v}^2M/[\bar{\varepsilon}^3 d]. \quad (14)$$

Chauvenet's criterion has been applied to eliminate inconsistent data (Holman, 1994). An average standard deviation of ±3.7 percent was found.

In the next figures the results from this work are extrapolated to be compared with the results obtained by other authors. As the work from those authors cover a wider range of Reynolds number and different screen and bed geometries, the extrapolation was necessary to verify if Eq. (14) is also applicable to those conditions.

In Fig. 7 the curve found is compared with the results from Thonger and Rice (1986), obtained from experiments in a circular bed, using different values of porosity and screen mesh sizes. The band of modified Reynolds number ($M(1-\bar{\varepsilon})$/Re) investigated by Thonger and Rice (1986) was in the range 1×10^{-2} to 5×10^{-1}, while the results produced in this work is for Reynolds numbers between 5×10^{-4} to 5×10^{-3}. The circular bed had a large bed to particle diameter ratio, with negligible wall effect. Using a different method of analysis from the one shown here, Thonger and Rice (1986) proposed individual correlations for each different screen size and arrangement investigated. It can be seen that the expression here proposed is in good agreement with the curves produced by Thonger and Rice (1986), validating its use for a wider range of modified Reynolds number (5×10^{-4} to 5×10^{-1}) and for both annular and circular beds.

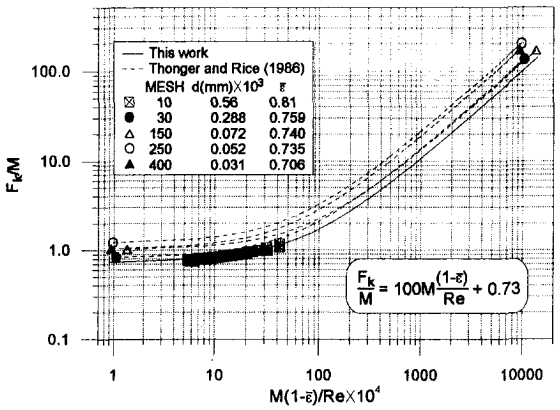

Fig. 7 Comparison of proposed curve with work by Thonger and Rice (1986)

Figure 8 shows the expression here proposed against a curve proposed by Armour and Cannon (1968), obtained from experiments made with a single screen layer. Several screen types were tested (plain square, full twill, semi-twill, plain dutch, and twilled dutch), covering modified Reynolds numbers ($M(1-\bar{\varepsilon})$/Re) between 1×10^{-4} and 1. A reasonable agreement has been found with the curve from Armour and Cannon (1968), which shows a friction factor slightly below the expression here proposed. The trends, however, are the same. The reason for the discrepancy may be due to the fact that the expression from Armour and Cannon (1968) was derived from experiments with different screen types, while just the plain square type has been used in the present work. Another possible reason is that they did not consider the effects of the bed wall on the friction factor. Moreover, a single screen layer has been used by Armour and Cannon (1968).

Finally, Fig. 9 shows the comparison made between the theory proposed in the present work and the data from Kays and London (1964), fitted by Urieli and Berchowitz (1984). The curve by Urieli and Berchowitz (1984) covers modified Reynolds numbers ($M(1-\bar{\varepsilon})$/Re) between 5×10^{-3} and 5×10^{-1}, for a woven-screen matrix with mesh size 60. The proposed correlation gives reasonably close results to the curve by Urieli

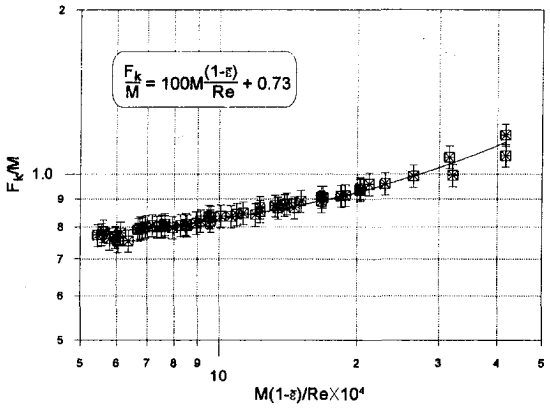

Fig. 6 Ergun equation applied to beds of plain square wire-mesh woven-screens

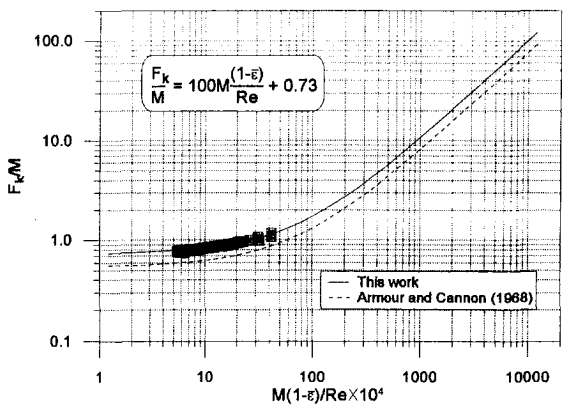

Fig. 8 Comparison of proposed curve with work by Armour and Cannon (1968)

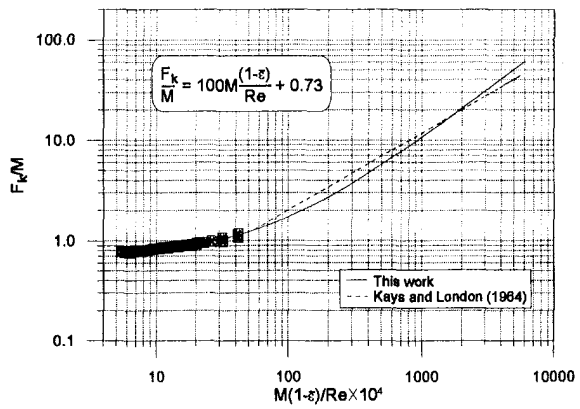

Fig. 9 Comparison of proposed curve with work by Kays and London (1964)

and Berchowitz (1984), though differing in shape. A maximum discrepancy of about 25 percent is found in the range covered.

Conclusion

The Ergun equation, with a corrected hydraulic diameter to consider wall effects, and with new coefficients, has been applied to describe the pressure drop in a finite annular bed of plain square wire-mesh woven-screens. The proposed expression fitted well the experimental data for fully developed turbulent flow of air at steady-state conditions, with modified Reynolds numbers ranging from 5×10^{-4} to 5×10^{-3}. Comparisons of the proposed expression with results by other authors have extended its applicability for modified Reynolds numbers from 1×10^{-4} to 1, for annular and circular beds, with or without wall effects, screen mesh sizes from 10 to 200, and different levels of compactness. Also, an expression has been developed to calculate the porosity of beds of plain square wire-mesh woven-screens, based on the screen dimensions and the number of layers.

Acknowledgments

The authors wish to thank the Brazilian Government's Science and Technology body, CNPq, for the financial support to this project.

References

Armour, J. C., and Cannon, J. N., 1968, "Fluid Flow through Woven Screens," *AIChE Journal,* Vol. 14, No. 3, pp. 415–420.

ASME, 1971, "Fluid Meters, their Theory and Application," Report from the Research Committee on Fluid Meters, The American Society of Mechanical Engineers, 6th ed.

Bartolini, C. M., and Naso, V., 1984, "Theoretical Predictions of the Performance of Stirling Engines Metallic Regenerators," *Proceedings, 2nd International Conference on Stirling Engines,* Shangai, China.

Bolz, R. E., and Tuve, G. L., 1976, *Handbook of Tables for Applied Engineering Science,* CRE Press, 2nd ed.

Chang, W. S., 1990, "Porosity and Effective Thermal Conductivity of Wire Screens," ASME *Journal of Heat Transfer,* Vol. 112, No. 1, pp. 5–9.

Ergun, S., 1952, "Fluid Flow through Packed Columns," *Chemical Engineering Progress,* Vol. 48, No. 2, pp. 89–94.

Holman, J. P., 1994, *Experimental Method for Engineers,* McGraw-Hill, 6th ed., New York.

Jones, J. D., 1988, "Flow Losses in Stirling Engine Heat Exchangers," ASME *Journal of Engineering for Gas Turbines and Power,* Vol. 110, No. 1, pp. 58–62.

Kays, W. M., and London, A. L., 1964, *Compact Heat Exchangers,* McGraw-Hill, New York.

Kline, S. J., and McClintock, F. A., 1953, "Describing Uncertainties in Single Sample Experiments," *Mechanical Engineering,* Vol. 75, pp. 3–8.

Macdonald, I. F., El-Sayed, M. S., Mow, K., and Dullien, F. A. C., 1979, "Flow through Porous Media—the Ergun Equation Revisited," *Industrial and Engineering Chemistry Fundamentals,* Vol. 18, No. 3, pp. 199–208.

Mehta, D., and Hawley, M. C., 1969, "Wall Effect in Packed Columns," *I& EC Process Design and Development,* Vol. 8, No. 2, pp. 280–282.

Reader, G. T., and Hooper, C., 1983, *Stirling Engines,* E. & F. N. Spon, London, Great Britain.

Simon, T. W., and Seume, J. R., 1988, "A Survey of Oscillating Flow in Stirling Engine Heat Exchangers," NASA Contractor Report 182108.

Thonger, J. C. T., and Rice, G., 1986, "Regenerator Effectiveness and Fluid Friction Measurements," *Proceedings, 3rd International Stirling Engine Conference,* Rome, Italy, Vol. I, pp. 335–349.

Urieli, I., and Berchowitz, D. M., 1984, *Stirling Cycle Engine Analysis,* Adam Hilger Ltd., Bristol, Great Britain.

Linear Feedback Control of Boundary Layer Using Electromagnetic Microtiles

S. N. Singh
Professor.
Electrical and Computer Engineering Department,
University of Nevada,
Las Vegas, NV 89154-4026

P. R. Bandyopadhyay
Hydrodynamics Branch,
Naval Undersea Warfare Center,
Newport, RI 02841.
Fellow ASME

This paper presents a system-theory approach to control of a two-dimensional turbulent flow of saltwater on a flat plate using Lorentz forces produced by microtiles of small magnets and electrodes. Beginning with the two-dimensional Navier-Stokes equations of motion, a finite, dimensional, linear state variable, approximate model is obtained using Galerkin's procedure. Based on this model, linear feedback control laws are obtained to achieve stabilization of the perturbed flow to the base flow. It is shown that spatially distributed longitudinal or surface-normal forces stabilize the flow perturbations. However, for lower wave numbers, longitudinal forces are more effective because surface-normal forces require larger electrode voltages for the same response characteristics. Simulation results are presented to show how stabilization is accomplished in the closed-loop system.

1 Introduction

Control of turbulence leads to reduction in the viscous drag and suppression of turbulence-induced noise. Via direct numerical simulation of a low Reynolds number channel flow over a riblet surface, Crawford and Karniadakis (1997) have shown that drag reduction is uniquely related to the suppression of the surface-normal component of turbulence near the wall. Bushnell (1983), Bandyopadhyay (1986), and Gad-el-Hak (1989) describe research carried out in this area. Several experimental and computational studies have also focused on the delay of boundary-layer transition through wave suppression by introducing waves of appropriate amplitudes and phases (Bandyopadhyay, 1986; Lin, 1961; Metcalf et al., 1986). In recent studies, Joshi (1996) has taken system-theory approaches to the channel flow control by suction and injection at the wall. In a system-theory approach, the model is initially represented by a set of first-order differential equations, and then modern system and control theory is applied to the model design and to system analyses.

A Lorentz force field is produced when electric and magnetic fields are applied in an electrically conducting medium. The potential application of Lorentz forces for drag reduction and turbulence control has been investigated by Henoch and Stace (1995) and Nosenchuck and Brown (1991). These approaches to electromagnetic turbulence control, however, do not use feedback algorithms. Nosenchuck and Brown (1991) have pulsed a surface-normal Lorentz force in an attempt to minimize the outward component of the surface-normal perturbations. On the other hand, Meng (1995) has proposed a sensor-based active feedback control scheme and has modeled the turbulence production process as the appearance of a sequence of organized motions given by the probabilistic distributions of their scales. He then proposed a Markov chain control scheme that uses sensors and attempts to control the Lorentz forces over all phases of the turbulence regeneration process. However, he does not present any simulation demonstrating the effectiveness of his proposal.

Bandyopadhyay (1995) has designed two-dimensional thin arrays of electromagnetic tiles with spatial scales on the order of millimeters that are suitable for high Reynolds number turbulence control. The electromagnetic forces produced by these microtiles are confined to within 1 millimeter from the wall and are promising for the boundary-layer turbulence control at high Reynolds numbers (Bandyopadhyay and Castano, 1996). Low Reynolds number laminar flow experiments have indicated that these microtiles produce "pillows" of vorticity that scale with their size. It is believed that the microtiles redistribute the prevailing vorticity in the shear flow but do not introduce vorticity into the flow. The observations of the pillows of vorticity have been later confirmed by direct numerical simulation (Hatay et al., 1997). These microtiles can be described as hairpin vortex-generators that redistribute existing vorticity.

The present study focuses on the control of a two-dimensional turbulent boundary layer on a flat plate and explores the feasibility of a closed-loop control. The system-theory approach taken here is similar to that of Joshi (1995), however, the Lorentz force field produced by microtiles is the control mechanism. Moreover, a flat-plate, boundary-layer flow is, because of the nature of boundary conditions, relatively complicated compared with the channel flow. Although turbulence control for any finite perturbation is the final goal, this study is limited to control of small perturbations in the base flow. The present approach to control via Navier-Stokes equations is rooted in the structural modeling of a turbulent boundary layer as advanced by Perry and Chong (1982) and by Bandyopadhyay and Balasubramanian (1995). Structural modeling of a turbulent boundary layer is better suited for feedback control than is statistical turbulence modeling. In conventional turbulence modeling, a turbulent flow is described by the Reynolds decomposition, where it is said to be composed of a time-mean flow and random perturbations. The time-mean flow is described statistically via closure models. However, in this paper, along the lines of Bandyopadhyay and Balasubramanian (1995 and 1996), a turbulent boundary layer is modeled to be composed of a laminar-like base flow and random perturbations. Because feedback control requires deterministic signals, the perturbations are described via Fourier series and not statistically. To date, there has been no study on feedback control of turbulence via electromagnetic means, which has the potential to achieve a high level of turbulence suppression than what an open-loop control can achieve.

The problem of turbulence control is complex, because the governing equations of motion are nonlinear and infinitely dimensional and control theory for infinite-dimensional systems is not well developed. To simplify, we are influenced by Black's model of the regeneration of turbulence by means of a quasi-

Contributed by the Fluids Engineering Division for publication in the JOURNAL OF FLUIDS ENGINEERING. Manuscript received by the Fluids Engineering Division March 10, 1997; revised manuscript received July 8, 1997. Associate Technical Editor: D. P. Telionis.

periodic breakdown of the viscous sublayer (Black, 1968). Turbulence production is a highly localized intermittent process, which means that, there are long regions and long periods when the sublayer is not participating in the strongly non-linear dynamics. In a cycle, a long region of viscous development is followed by a narrow region of rapid, highly nonlinear instability and breakdown of the mean flow wherein arrays of hairpin vortices are formed which populate the boundary layer. Thus, we assume that, in the former region, turbulence and mean flow are not strongly coupled (second-order terms are negligible) — perturbations merely grow in a quasi-laminar background and modes of instability can be determined. However, if we successfully control this first region, the succeeding strongly non-linear region would have little initial condition available to grow. We believe that a feedback control of linear turbulence has a valid basis. Also usual, linear control theory is applicable to small perturbations only.

In this paper, a finite-dimensional approximate model is derived based on the Galerkin procedure and Chebyshev polynomials (Joshi, 1996; Orszag, 1971; Fletcher, 1984; Fox and Parker, 1968). Based on this model, linear feedback control laws are derived using optimal control techniques and also by using a simple feedback of wall-shear stress for the stabilization of the perturbed flow to the base flow. It is shown that the unstable modes can be controlled by longitudinal as well as surface-normal forces. However, for lower wave numbers, longitudinal forces are more effective and require smaller electrode voltages for control compared with surface-normal forces. It is shown that a judicious choice of spatial distribution of Lorentz forces is important for designing stabilizing controllers, and this requires proper activation of the electrodes. Numerical results are obtained to show that, in the closed-loop system, asymptotic stabilization of the flow is accomplished using moderate input voltage for small perturbations.

This paper is organized as follows. Section 2 presents the mathematical model and addresses the control problem. A linear, finite-dimensional model is obtained in Section 3. Section 4 presents control laws, and simulation results are given in Section 5.

2 Mathematical Model and Control Problem

A two-dimensional flow on a flat plate of length l is considered. The x-axis is in the flow direction, and the y-axis is normal to the plate. The free stream velocity is U_∞. Reference values $h = (\delta_m/2)$, U_∞, and (h/U_∞) are chosen for the normalization of length, velocity, and time, where δ_m is the boundary-layer thickness (location where 99.5 percent of the freestream speed is reached). Suppose that r independent voltages are applied to the microtiles for control. It has been found that Lorentz forces are proportional to the voltages applied to the electrodes because permanent magnets are used.

The nondimensionalized Navier-Stokes equations of motion for the two-dimensional flow are given by

$$\partial u/\partial t + u\partial u/\partial x + v\partial u/\partial y = -\partial p/\partial x + \mathrm{Re}^{-1}\nabla^2 u + k_0 F_1(x, y, E)$$

$$\partial v/\partial t + u\partial v/\partial x + v\partial v/\partial y = -\partial p/\partial y + \mathrm{Re}^{-1}\nabla^2 v + k_0 F_2(x, y, E). \quad (1)$$

and the continuity equation is

$$\partial u/\partial x + \partial v/\partial y = 0,$$

where $k_0 = h/(\rho U_\infty^2)$; u and v are the longitudinal and lateral velocities; p is the pressure field, ρ is the density of the fluid; Re is the Reynolds number; F_1 and F_2 are the longitudinal and lateral Lorentz forces; and $E \in R^r$ is the vector of applied voltages to electrodes. At the wall, y is -1, $y = 0$ is at $\delta_m/2$, and $y = 1$ at the outer edge of the boundary layer at $x = l_1 = l/h$.

For the basic flow, approximate solutions of the boundary layer are given as

$$u = U(y) = U_\infty g(\eta),$$

$$\eta = (y + 1)h/\delta(x),$$

where $g(\eta)$ is assumed to be one of the following forms (Schlichting, 1979):

$$g(\eta) = \sin(\pi\eta/2)$$

or

$$g(\eta) = 2\eta - 2\eta^3 + \eta^4.$$

Although the boundary layer on a flat plate is a function of x and y, to simplify model derivation, a base flow of the form

$$u = U(y), \quad v = 0, \quad p = P(x)$$

is assumed. This is obtained by replacing $\delta(x)$ with δ_m, a constant in the definition of η. For the perturbed motion,

$$u = U(y) + u_1(x, y, t), \quad v = v_1(x, y, t),$$

$$p = P + p_1(x, y, t),$$

where u_1, v_1, and p_1 represent small perturbations in the base flow. It will be seen later that, when the base flow is chosen to also be a function of x for linearization, a model is obtained in which all the modes are coupled—creating complexity in controller design. Restricting the region from the leading edge of the plate causes the base flow to be weakly dependent on x (Schlichting, 1979).

By substituting the expressions of Eq. (2) in Eq. (1), neglecting higher-order terms, eliminating p_1 (by subtracting partial derivative of the second equation with respect to x from the partial derivative of the first equation with respect to y in Eq. (1)), and using the continuity equation, the linear dynamics are obtained by

$$\partial^2 u_1/\partial t\partial y - \partial^2 v_1/\partial t\partial x + U(y)(\partial^2 u_1/\partial x\partial y - \partial^2 v_1/\partial x^2) + U^{(2)}v_1 = \mathrm{Re}^{-1}(\partial^3 u_1/\partial x^2\partial y + \partial^3 u_1/\partial y^3 - \partial^3 v_1/\partial x\partial y^2 - \partial^3 v_1/\partial x^3) + k_0(\partial F_1/\partial y - \partial F_2/\partial x), \quad (3)$$

where $U^{(2)} = d^2U(y)/dy^2$, and the arguments of various functions are suppressed for simplicity. The continuity equation for the perturbations is

$$\partial u_1/\partial x + \partial v_1/\partial y = 0. \quad (4)$$

Theoretically, the boundary conditions are such that u_1 and v_1 tend toward zero as y tends toward infinity. However, the effect of viscosity is negligible beyond the outer edge of the boundary layer. Therefore, in order to obtain a simplified model, the boundary conditions are assumed to be

$$u_1(-1) = v_1(-1) = 0,$$

$$u_1(1) = v_1(1) = 0. \quad (5)$$

The problem is to design a feedback control system so that, in the closed-loop system, perturbations $u_1(x, y, 0)$ and $v_1(x, y, 0)$ at $t = 0$ asymptotically converge to zero as t tends toward infinity. In this case, small but arbitrary perturbations in velocities u and v decay to zero, and the perturbed flow tends toward the base flow asymptotically.

3 A Finite Dimensional Model

In this section, a finite dimensional model is obtained using the Galerkin's method with the Chebyshev polynomials as basis (Joshi, 1996; Orszag, 1971; Fletcher, 1984; Fox and Parker,

1968). The choice of these Chebyshev polynomials has given useful results in the channel flow control problem of Joshi (1996). Some other independent set of functions can be used for derivation. However, the convergence property of the derived model to the actual system depends on the choice of basis.

To this end, a perturbed stream function $\psi_1(x, y, t)$ is chosen for the system (Eq. (3)) such that

$$u_1 = \partial\psi_1/\partial y,$$
$$v_1 = -\partial\psi_1/\partial x \tag{6}$$

satisfy Eq. (4). Substituting the values in Eq. (6) in Eq. (3) provides a single, partial differential equation given by

$$\partial^3\psi_1/\partial t\partial x^2 + \partial^3\psi_1/\partial t\partial y^2 + U(y)(\partial^3\psi_1/\partial x\partial y^2 + \partial^3\psi_1/\partial x^3) - U^{(2)}\partial\psi_1/\partial x = \mathrm{Re}^{-1}\nabla^2(\nabla^2\psi_1) + k_0(\partial F_1/\partial y - \partial F_2/\partial x), \tag{7}$$

Motivated by the choice of periodic function of x in the derivation of the Orr-Sommerfeld equation (Schlichting, 1979) and due to the periodic fluctuations of the velocities in the longitudinal direction, a hypothesis can be formulated for a series solution for the stream function of the form

$$\psi_1(x, y, t) = \sum_{n=0}^{\infty}\sum_{m=0}^{\infty}[a_{nm}(t)\cos(n\alpha_0 x) + b_{nm}(t)\sin(n\alpha_0 x)]L_m(y), \tag{8}$$

where $L_m(y)$, $(m = 0, 1, \ldots, \infty)$ are the set of basis functions formed by a suitable combination of Chebyshev polynomials that satisfy the boundary conditions (Eq. (5)). In view of Eqs. (5), (6), and (8), it easily follows that functions $L_m(y)$ must satisfy

$$L_m(-1) = L_m(1) = 0,$$
$$\partial L_m(-1)/\partial y = \partial L_m(1)/\partial y = 0.$$

Here the fundamental wave number is $\alpha_0 = (2\pi/l_1)$; $n\alpha_0$ is the wave number of the nth harmonic term in the series solution, $b_{0m} = 0$; and a_{nm} and b_{nm} are the time-dependent, generalized coordinates (amplitudes of modes).

Substituting Eq. (8) in Eq. (7) and truncating the series to obtain a finite dimensional model gives

$$\sum_{n=0}^{N}\sum_{m=0}^{M}(\dot{a}_{nm}\cos(n\alpha_0 x) + \dot{b}_{nm}\sin(n\alpha_0 x))[L_m^{(2)}(y) - (n\alpha_0 x)^2 L_m(y)] = \sum_{n=0}^{N}\sum_{m=0}^{M}\{-a_{nm}\sin(n\alpha_0 x) + b_{nm}\cos(n\alpha_0 x)\}n\alpha_0(\{(n\alpha_0)^2U + U^{(2)}\}L_m(y) - UL_m^{(2)}(y)) + \mathrm{Re}^{-1}[a_{nm}\cos(n\alpha_0 x) + b_{nm}\sin(n\alpha_0 x)] \times [(n\alpha_0)^4 L_m(y) + L_m^{(4)} - 2(n\alpha_0 x)^2 L_m^{(2)}(y)] + k_0(\partial F_1/\partial y - \partial F_2/\partial x), \tag{10}$$

where an overdot denotes differentiation with respect to time, and $L_m^{(i)}(y) = d^i L_m(y)/dy^i$. In this derivation, it is assumed that $(M + 1)$ basis functions $L_m(y)$ and N sinusoidal functions give a reasonable approximate model. If the design with chosen values for M and N is unsatisfactory and the residual modes in the closed-loop system are not small, then the controller needs to be redesigned using a model with larger values for M and N.

It has been shown in Bandyopadhyay (1995) that for each volt applied to the electrodes, the Lorentz force can be accurately expressed as $k_1\exp(-q_0 d)$, where d is the lateral distance from the wall and it is negligible for $d > 2$ mm. To this end, spatially distributed Lorentz forces are expressed in a Fourier series of the form $(i = 1, 2)$

$$F_i = k\sum_{n=0}^{N}[F_{ni1}\cos(n\alpha_0 x) + F_{in2}\sin(n\alpha_0 x)]\exp(qy)E, \tag{11}$$

where $y \in [-1, y_m]$, $k = k_0 k_1 \exp(q)$, $q = -q_0 h$, and F_{nik} is an r-row vector. It is assumed that the Lorentz force is negligible for $y \geq y_m$. The values of q_0 and k_1 are obtained from the Lorentz force plot given in Bandyopadhyay (1995).

Because the trigonometric functions form an orthogonal set, substituting Eq. (11) in Eq. (10), multiplying Eq. (10) by $\cos(n\alpha_0 x)$ and $\sin(n\alpha_0 x)$, and integrating over $[0, l_1]$ gives the differential equations for a_{nm} and b_{nm}, respectively,

$$\sum_{m=0}^{M}[\dot{a}_{nm}(L_m^{(2)}(y) - (n\alpha_0)^2 L_m(y))] = \sum_{m=0}^{M} b_{nm}n\alpha_0[((n\alpha_0)^2U + U^{(2)})L_m(y) - UL_m^{(2)}(y)] + \mathrm{Re}^{-1}a_{nm}[(n\alpha_0)^4 L_m(y) + L_m^{(4)}(y) - 2(n\alpha_0)^2 L_m^{(2)}(y)] + k(qF_{n11} - n\alpha_0 F_{n22})\exp(qy)E,$$

$$\sum_{m=0}^{M}[\dot{b}_{nm}(L_m^{(2)}(y) - (n\alpha_0)^2 L_m(y))] = \sum_{m=0}^{M} -a_{nm}n\alpha_0[((n\alpha_0)^2U + U^{(2)})L_m(y) - UL_m^{(2)}(y)] + \mathrm{Re}^{-1}b_{nm}[(n\alpha_0)^4 L_m(y) + L_m^{(4)}(y) - 2(n\alpha_0)^2 L_m^{(2)}(y)] + k(qF_{n12} + n\alpha_0 F_{n21})\exp(qy)E. \tag{12}$$

The inner product of $L_s(y)$ and $L_m(y)$ is defined as (Fox and Parker, 1968)

$$L_{sm} = [L_s(y), L_m(y)] = \int_{-1}^{+1} L_s(y)L_m(y)(1 - y^2)^{-1/2}dy. \tag{13}$$

Define matrices as $(s = 0, 1, \ldots, M; m = 0, 1, \ldots, M)$

$$D_{n0} = [(D_{n0})_{sm}] = [L_s, (L_m^{(2)} - (n\alpha_0)^2 L_m)],$$
$$D_{n1} = [(D_{n1})_{sm}] = [L_s, ((n\alpha_0)^4 L_m + L_m^{(4)} - 2(n_0\alpha_0)^2 L_m^{(2)})],$$
$$D_{n2} = [(D_{n2})_{sm}] = [L_s, (-UL_m^{(2)} + ((n\alpha_0)^2U + U^2)L_m)],$$
$$L_y = ([L_0, \exp(qy)], \ldots, [L_m, \exp(qy)])^T,$$
$$B_{n1} = kL_y(qF_{n11} - n\alpha_0 F_{n22}),$$
$$B_{n2} = kL_y(qF_{n12} + n\alpha_0 F_{n21}), \tag{14}$$

where $(D_{ni})_{sm}$ denotes the s—mth element of matrix D_{ni}, T denotes transposition, and in the computation of L_y integration is performed only over $[-1, y_m]$ where the Lorentz forces are significant.

By using the definitions of matrices in Eq. (14), Eq. (12) is written in a matrix notation as

$$D_{n0}\dot{a}_n = D_{n1}a_n + D_{n2}b_n + B_{n1}E,$$
$$D_{n0}\dot{b}_n = D_{n2}a_n + D_{n1}b_n + B_{n2}E, \tag{15}$$

where $a_n = (a_{n0}, \ldots, a_{nM})^T$ and $b_n = (b_{n0}, \ldots, b_{nM})^T$. The state subvector $x_n = (a_n^T, b_n^T)^T$ is associated with the wave number $n\alpha_0$ and it is described by

$$\dot{x}_n = A_n x_n + B_n E, \quad \text{for} \quad n \neq 0, \tag{16}$$

where

$$A_n = \begin{pmatrix} D_{n0}^{-1}D_{n1} & D_{n0}^{-1}D_{n2} \\ -D_{n0}^{-1}D_{n2} & D_{n0}^{-1}D_{n1} \end{pmatrix},$$

$$B_n = ((D_{n0}^{-1}B_{n1})^T, (D_{n0}^{-1}B_{n2})^T)^T.$$

For $n = 0$,

$$\dot{x}_0 = A_o x_0 + B_0 E, \tag{17}$$

where $x_0 = a_0 = (a_{00}, \ldots, a_{0M})^T$, $A_0 = D_{00}^{-1}D_{01}$, and $B_0 = D_{00}^{-1}B_{01}$. The set of Eqs. (16) and (17) govern the evolution of the state trajectories (x_k, $k = 0, 1, \ldots, N$) associated to various wavenumbers. The vector

$$x_a = (x_0^T \ldots, x_N^T)^T = (a_0^T; a_1^T, b_1^T; \ldots, a_N^T, b_N^T)^T$$

is called the state vector of the system (Eqs. (16) and (17)), because x_a completely describes the perturbed velocity vector in the boundary layer. For a given initial condition $x_a(0)$ and the electrode voltage $E(t)$, Eqs. (16) and (17) can be solved for the state trajectories:

$$x_i(t), \quad i = 0, 1, \ldots, N, \quad t \geq 0.$$

These time-dependent coefficients are substituted in Eq. (8) to obtain the perturbed stream function and the velocity vector field according to Eq. (6). The state vector x_a evolves in the state space of dimension $s = (M + 1)(2N + 1)$.

It is interesting to note that in view of Eq. (16), the dynamics associated with various wave numbers are decoupled for $E = 0$. The decoupling of modes is not possible if x-dependent base flow is taken. It will be seen that decoupling considerably simplifies control system design.

Now the problem of flow control is solved by deriving feedback control laws of the form

$$E = -Kx_c,$$

such that, in the closed-loop system, $x_a(t)$ asymptotically tends toward zero, where x_c is a chosen subvector of the state vector x_a.

4 Control Systems

Using Eqs. (16) and (17), the complete system can be written in a state variable form:

$$\dot{x}_a = A_a x_a + B_a E, \tag{18}$$

where $A_a = \text{diag}\ (A_0, A_1, \ldots, A_N)$ and the input influence matrix is $B_a = (B_0^T, B_1^T, \ldots, B_N^T)^T$. To determine the fluctuations of the wall-shear stress at a point x^*, because it is proportional to du_1/dy, consider an output variable $y_a = du_1/dy(x^*, y = -1, t)$ written as

$$y_a = C_a x_a, \tag{19}$$

where the output matrix C_a is

$$C_a = (c_{a0}, \ldots, c_{aN}),$$

$$L_c = (L_0^{(2)}(-1), \ldots, L_M^{(2)}(-1)),$$

$$c_{a0} = L_c,$$

and for $n \neq 0$,

$$c_{an} = (\cos\ (n\alpha_0 x^*)L_c, \sin\ (n\alpha_0 x^*)L_c).$$

This output can be used for feedback for stabilization or to directly control y_a.

The concept of controllability plays an important role in system theory (Kailath, 1980). The system (Eq. (18)) is said to be controllable if, given any two arbitrary points x_a^1 and x_a^2 in the state space, there exists a control E that can steer the system (Eq. (18)) from x_a^1 to x_a^2 in a finite time. The system is controllable if, and only if, the controllability matrix CO defined as

$$CO = (B_a, A_a B_a, \ldots, A_a^{s-1} B_a),$$

has rank s, which is the dimension of state vector x_a. The spatial distribution of the Lorentz forces must be chosen to satisfy the controllability conditions. For the controllable system, a linear feedback law to stabilize the system can be chosen.

The solution of the unforced system (Eq. (18) with $E = 0$) is $x_a(t) = \exp(A_a t)x_a(0)$, where $x_a(0)$ denotes the state at $t = 0$ and $\exp(A_a t)$ is the transition matrix. The natural modes of the openloop system depend on the eigenvalues of the matrix A_a. Unstable modes have eigenvalues with positive real parts and grow exponentially. For the stabilization of these modes, linear feedback of state variables is used. For a controllable system, one can synthesize a linear feedback control law such that in the closed-loop system eigenvalues associated to all the modes are placed at any desired locations in the complex plane.

For clarity, it is assumed that the electrode voltage $E(t)$ is a scalar function. The design for the multi-input system can be similarly done. It is interesting to note that in the model (equation (18)), not all modes are unstable. For the chosen parameters identified in Section 5, it is found that only matrix A_1 associated with the fundamental wave number α_0 is unstable, the remaining matrices A_i are stable. Because the electrode voltage is limited, it is a good idea to design a control system to stabilize only the dynamics of unstable wave numbers and to leave the responses of other modes unaltered. The dynamics of the unforced system are decoupled, therefore, one way to preserve the dynamics of the stable modes is to choose the spatial distribution of the Lorentz forces such that the control influence matrix B_k of the stable modes are null; that is,

$$B_0 = 0, \quad B_n = 0, \quad n \neq 1. \tag{20}$$

For this choice, when the feedback loop is closed to stabilize the unstable mode using the measured signal y_a, control input will not excite the remaining modes.

The condition in Eq. (20) can be satisfied by choosing F_1 and F_2 of the form

$$F_i = k_1[F_{1i1} \cos \alpha_0 x + F_{1i2} \sin \alpha_0 x] \exp(qy)E,$$

$$(i = 1,2), \tag{21}$$

where $(F_{1i1}^2 + F_{1i2}^2)^{1/2} = 1$. The sinusoidal distribution of Lorentz forces requires appropriate activation of the electrodes. If other harmonic terms are present in Eq. (21), the dynamics of other wave numbers will be excited when the measured signal y_a is fed back.

Because either the longitudinal or the surface-normal force for control can be chosen, a question arises concerning the effectiveness of Lorentz forces for control. In view of the input influence matrices B_{n1} and B_{n2} in Eq. (14), if

$$n\alpha_0 > -q,$$

the input influence matrix B_n is larger when surface-normal force is used. However, for smaller wave numbers not satisfying the above inequality, the longitudinal force is preferable for stabilization because smaller electrode voltage will be needed for control. In Section 5.2 a simple feedback law using wall-shear stress (or $du_1/dy(x^*, y = -1, t)$ for stabilization is simulated.

Several control techniques for linear systems are available for the control system design and can be applied to obtain different response characteristics and to meet design specifications. For the choice of Lorentz force as given in Eq. (21), the

optimal control technique can be used. Consider the dynamics associated with the fundamental wave number

$$\dot{x}_1 = A_{1x1} + B_1 E, \tag{22}$$

which is unstable. Here $x_1 = (a_1^T, b_1^T)^T$ is the state vector associated with the wave number α_0. The optimal control is obtained by minimizing a quadratic performance index of the form

$$J = \int_0^\infty (x_1^T Q x_1 + \lambda E^2) dt, \tag{23}$$

where Q is a positive definite symmetric matrix, and $\lambda > 0$. The matrices Q and λ are selected to weigh the relative importance of performance measures caused by the state vector perturbations x_1 and the electrode voltage $E(t)$. The optimal control law is

$$E = -\lambda^{-1} B_1^T R x_1 = -K x_1, \tag{24}$$

where the positive definite symmetric matrix R is the solution of the Riccati equation (Kailath, 1980)

$$RA_1 + A_1^T R - RB_1 \lambda^{-1} B_1^T R + Q = 0,$$

and K is a row vector of dimension $2(M + 1)$.

Substituting linear control law (Eq. (24)) in Eq. (22) gives the closed-loop system:

$$\dot{x}_1 = (A_1 - B_1 K) x_1,$$

For the controllable system (Eq. (23)), the optimal control law (Eq. (24)) is such that the closedloop system matrix $(A_1 - B_1 K)$ is Hurwitz (i.e., all the eigenvalues of $(A_1 - B_1 K)$ have negative real parts). It is seen that the state variable feedback term $-Kx_1$ in the control law modifies the locations of the eigenvalues of the openloop matrix A_1 in the complex plane. Thus, in the closed-loop system, $x_1(t)$ asymptotically tends toward zero, which implies that the perturbations u_1 and v_1 decay to zero as well. The response characteristics for the state vector x_1 depend on the eigenvalues of the matrix $(A_1 - B_1 K)$ and these eigenvalues depend on the choice of the weighting parameters Q and λ in the performance index J.

Substituting Qy_1^2, $Q > 0$ in place of $x_1^T Q x_1$ in the performance index can be done for minimization, where

$$y_1 = (\cos(\alpha_0 X^*) L_c, \sin(\alpha_0 x^*) L_c) x_1 \Delta c_1 x_1 \tag{25}$$

for directly influencing du_1/dy at $x = x^*$. By a proper selection of the weighting matrix, Q, and the scalar, λ, a tradeoff between the speed of convergence of the perturbed state to the equilibrium state and the magnitude of the electrode voltage, which is required for control, can be obtained. Figure 1 shows the complete closed-loop system, including the optimal controller (solid line) and the simple controller using wall-shear stress feedback (dotted line). In the feedback loop using wall-shear stress feedback, the gain K is scalar.

5 Simulation Results

In this section the results of simulation using MATLAB® and Simulink™ software are presented. To derive the model, it is assumed that the normalized velocity is $U(y) = \sin(\pi(y + 1)/4)$. The parameters chosen for high Reynolds number flow are $U_\infty = 17$ (m/s), $h = (6.77/2)$ mm; kinematic viscosity of water, $\nu = 11.4\ E\text{-}7$ m^2/s, $l_1 = 2\pi$; and density of water, $\rho = 1000$ (kg/m^3). For simulation, the values $k_1 = 45$ (N/m^3) and $q_0 = (1000/1 \cdot 3)$(m^{-1}) are used. These parameters are obtained from Bandyopadhyay (1995). The fundamental wave number is $\alpha_0 = 1$. For a choice of $M = 2$ in the series expansion (equation (10)), a sixth-order state variable model for each wave number is obtained. The three elements of the basis taken from Joshi (1996) are

$$L_0(y) = 3 - 4\,T_2(y) + T_4(y),$$

$$L_1(y) = 2y - 3T_3(y) + T_5(y),$$

$$L_2(y) = 1.5T_3(y) - 2.5T_5(y) + T_7(y),$$

where $T_n(y)$ is the Chebyshev polynomial (Fox and Parker, 1968).

For the chosen parameters, the matrices A_n, B_n, and C_n are computed. It is found that, except for matrix A_1, all other matrices, A_n, are stable. In fact, A_1, which is associated to wave number α_0, has a pair of unstable eigenvalues and the remaining four eigenvalues of A_1 are stable. For any nonzero initial condition the solution of the uncontrolled system diverges. A twelfth-order, open-loop system including the dynamics for wave numbers α_0 and $2\alpha_0$ was simulated with the initial condition $a_1(0) = b_1(0) = 1000(5 \cdot 4,\ 4 \cdot 05,\ 2 \cdot 7)^T$, and $a_2(0) = b_2(0) = a_1(0)/0 \cdot 18$. The divergent and oscillatory responses are shown in Fig. 2. The plots are shown for the velocity perturbations $u_1(x^*, y^*, t)$, $v_1(x^*, y^*, t)$ at the point $(x^*, y^*) = (0.75\ l_1 - 0.409)$, and also for $C_f(x^*, -1, t)$, where $C_f = (\mu/0.5\ U_\infty^2)(\partial u_1/\partial y)$ is evaluated at $(x = x^*, y^* = 0)$. Although a control system can be designed to modify the responses of a set of modes, for simplicity, stabilization of dynamics of only the unstable mode is considered in this paper. The spatial distribution of the Lorentz forces is assumed as given in Eq. (21) for the purpose of control.

Simulation results are obtained using an optimal control system and a simple controller that uses wall-shear stress feedback at one point. For simulation of the optimal controller, it is assumed that complete information on the state variable, x_1, of the subsystem associated with wave number α_0 to be controlled, is available. Unlike the optimal controller, synthesis of the simple controller is relatively easy, because only a measured signal at the wall is required for feedback. For optimal controller synthesis, each component of vector x_1 must be known.

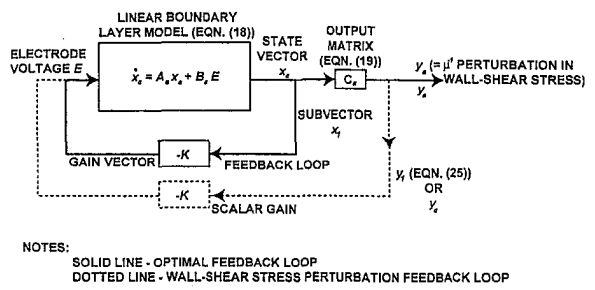

Fig. 1 Closed-loop Lorentz force control system

5.1 Optimal Control. Since the state trajectory $x_1(t)$ has unstable behavior and the remaining modes are stable, regulation of $x_1(t)$ was considered. Using the optimal control technique, a feedback controller was designed for the decoupled system in Eq. (22) describing the dynamics associated with the fundamental wave number. A quadratic term Qy_1^2 was used in the performance index with $Q = 0.01$ and $\lambda = 30$. The weigthing matrix Q and λ were chosen after several trials by observing the simulated responses. Only the component x_1 of the state vector was used for the synthesis of the control law. The complete closed-loop system including the dynamics associated with wave numbers α_0 and $2\alpha_0$ and the feedback control law, $E = -Kx_1$, was simulated. The initial condition of figure 2 was retained. It was assumed that longitudinal control, $F_{111} = 1$; surface-normal control, $F_{121} = 1$; and the remaining parameters F_{1ik} in Eq. (21) were set to zero. Selected responses are shown in Figs. 3 and 4 using longitudinal and surface-normal force control, respectively. The plots are shown for the electrode voltage E, velocity perturbations $u_1(x^*, y^*, t)$, $v_1(x^*, y^*, t)$, and $C_f(x^*, 0, t)$. In the closed-loop system, well-damped responses with moderate input voltage are observed. The corresponding interaction parameter $N^* = h$(Lorentz force/inertial

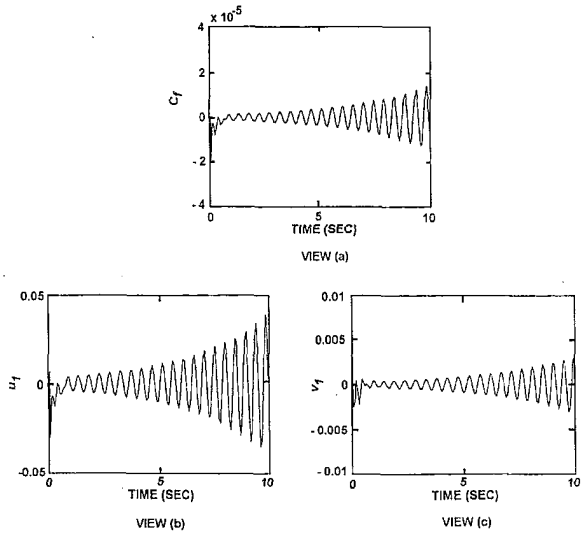

Fig. 2 Uncontrolled system at $x^* = 0.75/l_1$, $y^* = -0.409$ above the plate

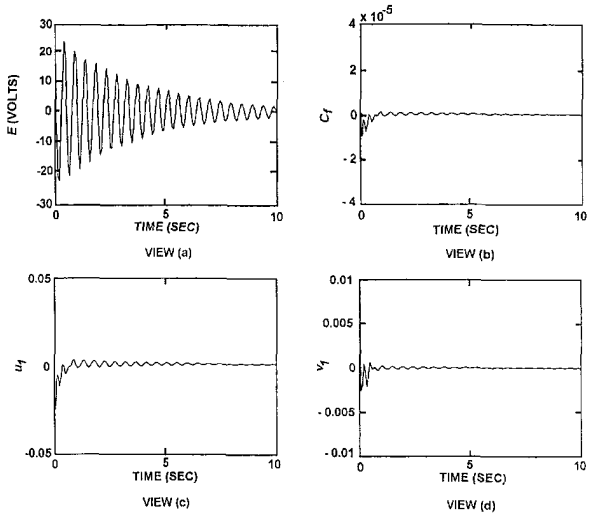

Fig. 4 Optimal surface-normal force control ($x^* = 0.75/l_1$, $y^* = -0.409$)

force) is 0.0678 E, where the Lorentz force at the wall is 45 $E(N)$ and the inertial force is $(\frac{1}{2})\mu(\partial U/\partial y)$ evaluated at the wall. As predicted, the surface-normal force control requires considerably larger electrode voltage compared to the longitudinal force control, since $\alpha_0 < -q$. It is important to note that using this control law, stabilization of all modes is accomplished, even if B_n, $n \neq 1$ are nonzero, since only exponentially decaying signal x_1 of the closed-loop system is superimposed on the stable dynamics for the remaining wave numbers. However, estimation of signal x_1 from measured signals must be made for the synthesis of the optimal controller.

5.2 Stabilization by Wall-Shear Stress Feedback. Because the wall-shear stress is a constant multiple of du_1/dy, a simple feedback of the derivative of $du_1(x^*, y = 0, t)/dy$ is considered by choosing $E = -Kdu_1/dy$. In the derivative du_1/dy, the contribution of only the fundamental component x_1 of the state vector is retained and the higher harmonics are neglected. The gain K is chosen such that, in the closed-loop system $(A_1 - KB_1C_1)$ is Hurwitz. Suitable values for longitudinal force control are $F_{112} = 1$ and $K = 0.05\,(U_\infty/h)$; and suitable values for surface-normal force control are $F_{121} = 0$ and $K = 0.05(U_\infty/h)q$. The feedback gains were selected after several trials so that the peaks in the electrode voltage are not too large during the transient period. The feedback gain K for stabilization is a function of the position x^* where the wall-shear stress is measured. With this choice of gains, the input influence matrix B_1 is the same for both force controls. The remaining parameters F_{1ik} were assumed to be zero. To reduce voltage magnitude, the initial conditions were chosen to be one-ninth the values of $(a_i(0), b_i(0))$ $(i = 1,2)$ assumed in Section 5.1. Selected responses for the longitudinal and surface-normal force control are shown in Figs. 5 and 6.

The responses for u_1, v_1, and C_f are identical for the longitudinal and surface-normal force control. Unlike the optimal controller, responses are poorly damped and, in spite of smaller perturbations in the initial condition, considerably large electrode voltage is required. This result should not be a surprise because the optimal controller design requires complete information on x_1. For this simple control, du_1/dy feedback, which is merely a linear combination of state variables, is used. Larger peaks in the input voltage are observed for lateral control in this case also. For the choice of spatial distribution of Lorentz forces made, stability in the closed-loop system is preserved, even if the complete measured wall-shear stress, including higher harmonics is fed back, because the dynamics associated

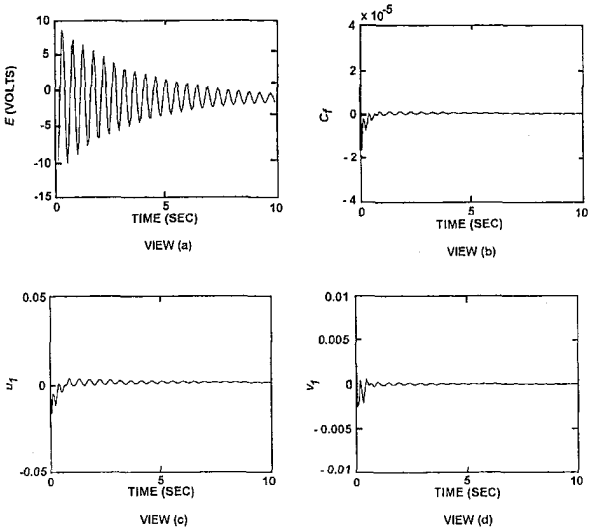

Fig. 3 Optimal longitudinal force control ($x^* = 0.75/l_1$, $y^* = -0.409$)

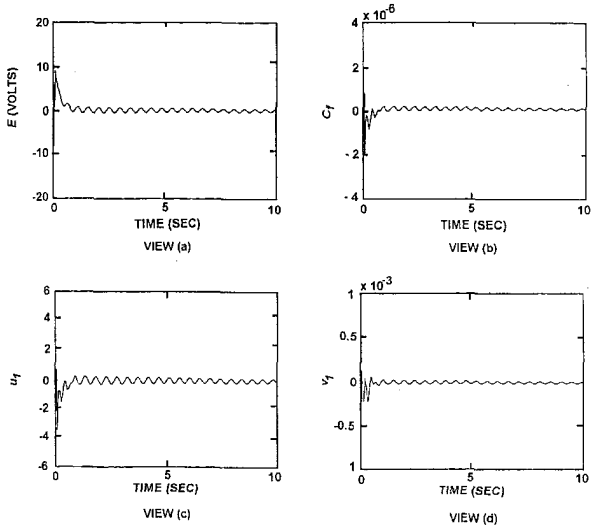

Fig. 5 Longitudinal force control by wall-shear stress feedback ($x^* = 0.75/l_1$, $y^* = -0.409$)

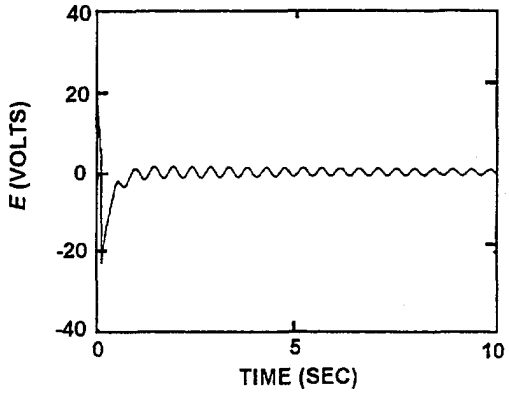

Fig. 6 Surface-normal force control by wall-shear stress feedback ($x^* = 0.75/_1$, $y^* = -0.409$). Note: variables C_f, u_1, and v^1 remain undamped as in Fig. 5.

to all wave numbers except the fundamental one, are stable and the control input influence matrix $B_n = 0$ for $n = 0$ and $n > 1$. These responses can be improved when a feedback controller that uses wall-shear stress signals measured at several locations on the wall is designed.

6 Conclusions

A system-theory approach to the control of high Reynolds number sea water flow over a flat surface using electromagnetic forces produced by microtiles has been examined. Navier-Stokes equations, which include the effect of Lorentz forces, were linearized; and, using the Galerkin procedure, a linear, state variable model of finite dimension was derived. The linear model describes the dynamics of flow for small amplitude velocity perturbations in the boundary layer. For the selected parameters, the modes of the open-loop system associated to the fundamental wavenumber were unstable and divergent oscillations in the velocity responses were observed. Based on this model, linear feedback control laws using optimal control theory and output (wall-shear stress) feedback for system stabilization were obtained. Feedback of state variables essentially allows to shift the unstable eigenvalues of the open-loop system in a stable region in the complex plane. It was shown that by selecting sinusoidal spatially distributed Lorentz forces of frequency coinciding with the wavenumber of unstable modes, divergent oscillations of unstable modes are suppressed and asymptotic stability in the closed-loop system is accomplished using longitudinal and surface-normal force control. It is interesting to note that sinusoidal distribution of Lorentz forces of frequency $k\alpha_0$ generated by the microtiles, where k is any integer, controls only the modes associated to wavenumber $k\alpha_0$ and cannot excite the remaining modes. For lower wave numbers, longitudinal force control is more effective since it requires smaller electrode voltage to suppress velocity perturbations. However, a control system that uses wall surface normal force requires smaller electrode voltage compared with the longitudinal force controller when control of modes associated with higher wave numbers is desired. Although stabilization is possible using simple feedback of measured wall-shear stress signal, an optimal controller gives faster and well-damped responses. However, for the synthesis of the optimal controller, it is necessary to design a state estimator to reconstruct the state for feedback using signals measured by the sensors.

Several problems remain to be solved in this area: questions related to the effect of mode truncation, state estimation, control and observation spillover, digital implementation, and extension of the system-theory approach to nonlinearly perturbed dynamics, which plays a key role in turbulent flow, are all important and require further investigation. Although, linear system theory approach presented here is useful for small velocity perturbations, it is hoped that similar state space approach based on the Lyapunov stability theory and nonlinear geometric control theory will yield fruitful results for non-linear turbulence control.

Acknowledgments

This work was sponsored by the Office of Naval Research (Manager: Dr. L. P. Purtell) and NUWC IR (Manager: Dr. S. Dickinson). The first author served as a Distinguished Faculty Fellow at NUWC while this work was carried out.

References

Bandyopadhyay, P. R., 1986, "Review-Mean Flow in Turbulent Boundary Layers Disturbed to Alter Skin Friction," ASME JOURNAL OF FLUIDS ENGINEERING, Vol. 108, pp. 127–140.

Bandyopadhyay, P. R., 1995, "Microfabricated Silicon Surfaces for Turbulence Diagnostic and Control," *Proceedings of the 1995 International Symposium on Active Control,* Newport Beach, CA, July, pp. 1327–1338.

Bandyopadhyay, P. R., and Castano, J. M., 1996, "Microtiles for Electromagnetic Turbulence Control in Salt Water—Preliminary Investigations," *Proceedings of the ASME Fluids Engineering Division Conference,* San Diego, CA, Nov. FED Vol. 2, pp. 53–60.

Bandyopadhyay, P. R., and Balasubramanian, R., 1995, "Vortex Reynolds Number in Turbulent Boundary Layers," *Theoretical and Computational Fluid Dynamics,* Vol. 7, pp. 101–118.

Bandyopadhyay, P. R., and Balasubramanian, R., 1986, "Structural Modeling of the Wall Effects of Lorentz Force," ASME JOURNAL OF FLUIDS ENGINEERING, Vol. 118, pp. 412–414.

Black, T. J., 1968, "An Analytical Study of the Measured Wall Pressure Field Under Supersonic Turbulent Boundary Layers," NASA CR-888.

Bushnell, D. M., 1983, "Turbulent Drag Reduction for External Flows," AIAA Paper No. 83-0227, 1983.

Crawford, C., and Karniadakis, G. 1997, "Shear Stress Modification and Vorticity Dynamics in Near-Wall Turbulence," *Journal of Fluid Mechanics,* (due to appear).

Fletcher, C. A. J., 1984, *Computational Galerkin Methods,* Springer-Verlag, NY.

Fox, L., and Parker, I. B., 1968, *Chebyshev Polynomials in Numerical Analysis,* Oxford University Press, London.

Gad-el-Hak, M., 1989, "Flow Control," *ASME Applied Mechanics Review,* Vol. 9, pp. 447–468.

Hatay, F. F., O'Sullivan, P. L., Biringen, S., and Bandyopadhyay, P. R. 1997 "Numerical Simulation of Secondary Flows in Channels Driven by Applied Lorentz Forces," *AIAA Journal of Thermophys. & Heat Transf.,* Vol. 11, No. 3, pp. 446–453.

Henoch, C., and Stace, J., 1995, "Experimental Investigation of a Salt Water Turbulent Boundary Layer Modified by an Applied Streamwise Magnetohydrodynamic Body Force," *Physics of Fluids,* Vol. 7, pp. 1371–1383.

Joshi, S. S., 1996, "A Systems Approach to the Control of Transitional Flows," *Ph.D. dissertation,* University of California, Los Angeles, CA.

Kailath, T., 1980, *Linear Systems,* Prentice-Hall, Englewood Cliffs, NJ.

Liepmann, H. W., and Nosenchuck, D. M., 1982, "Control of Laminar Instability Waves Using a New Technique," *Journal of Fluid Mechanics,* Vol. 118, pp. 187–200.

Lin, C. C., 1961, "Some Mathematical Problems in the Theory of the Stability of Parallel Flows," *Journal of Fluid Mechanics,* Vol. 10, pp. 430–438.

Meng, J. C. S., 1995, "Wall-Layer Microturbulence Phenomenology and a Markov Probability Model for Active Electromagnetic Control of Turbulent Boundary Layers in an Electrically Conducting Medium," *NUWC-NPT Technical Report 10,434,* Naval Undersea Warfare Center Division, Newport, RI, June.

Metcalfe, R. W., Rutland, C. J., Duncan, J. H., and Riley, J. J., 1986, "Numerical Simulation of Active Stabilization of Laminar Boundary Layers," *AIAA Journal,* Vol. 9, pp. 1494–1501.

Nosenchuck, D., and Brown, D., 1991, "Direct Control of Wall Shear-Stress in a Turbulent Boundary Layer," Proc. of the NUWC Newport Seminar Series on Turbulence and its Control, *NUWC-NPT TM 922089,* pp. 3-1/3-2, October 1991.

Orszag, S. A., 1971, "Galerkin Approximations to Flows Within Slabs, Spheres, and Cylinders," *Physics Review Letters,* Vol. 26, pp. 1100–1103.

Perry, A. E., and Chong, M. S., 1982, "On the Mechanism of Wall Turbulence," *Journal of Fluid Mechanics,* Vol. 119, pp. 173–217.

Schlichting, H., 1979, *Boundary-Layer Theory,* McGraw-Hill, NY.

K. J. A. Westin
Graduate Student,
Department of Mechanics,
Royal Institute of Technology,
S-100 44 Stockholm,
Sweden

R. A. W. M. Henkes
Senior Research Fellow,
Faculty of Aerospace Engineering,
Delft University of Technology,
Kluyverweg 1,
2629 HS Delft,
The Netherlands

Application of Turbulence Models to Bypass Transition

The present study considers the use of low-Reynolds number, single-point closures for transition prediction at high levels of free-stream turbulence. The work is focused on two differential Reynolds Stress Transport models, which are compared with the $k - \epsilon$ model of Launder and Sharma. Calculations are carried out for attached boundary layer flow on a flat plate equipped with a sharp leading edge at zero-pressure gradient and for various free-stream turbulence levels. Comparisons with results from a large eddy simulation reveal significant shortcomings in the modeling of the dissipation, with a large overprediction in the pretransitional boundary layer. The present results are in some cases in conflict with other results reported in the literature, and it is shown that the discrepancies can be ascribed to the implementation of the free-stream boundary conditions.

Introduction

In many industrial applications laminar-turbulent transition is influenced by large disturbance levels in the incoming flow. For example, in internal flows, such as gas-turbines and internal air systems, the high levels of free-stream turbulence causes a rapid transition (often denoted as bypass transition) which cannot be predicted with traditional methods based on linear stability theory.

One of the major difficulties in the prediction of bypass transition is the lack of understanding of the underlying transition mechanisms. Experimental studies have shown that the free-stream turbulence induces large-amplitude low-frequency fluctuations in the laminar boundary layer (see e.g., Arnal and Juillen, 1978; Kendall, 1985; Westin et al., 1994), and the disturbances seem to be dominated by unsteady longitudinal streaks in the streamwise direction. Although the streamwise fluctuation level (u_{rms}) can be of the order of 10–15%, there is almost no turbulent intermittency in the flow, and the boundary layer exhibits mean velocity profiles close to the undisturbed laminar ones. Consequently, the induced fluctuations have characteristics quite different from what we usually call turbulence, and this highly disturbed (but still laminar) boundary layer is sometimes denoted as pseudo-laminar. The understanding is less clear for the later stages of the transition process. Recent flow-visualizations (Alfredsson and Matsubara, 1996) and numerical simulations (see Henningson, 1995 for a summary), however, indicate that secondary instabilities on the streamwise streaks might be responsible for the breakdown.

During the past years several researchers have investigated the possibility of using turbulence models for the prediction of bypass transition, and since 1990 a large effort is being organized by Dr. A. M. Savill within the framework of a special interest group of ERCOFTAC (the European Research Community On Flow Turbulence And Combustion). An overview of the achievements is reported by Savill (1995b). Most of the studies have focussed on different eddy-viscosity models, with varying success. The picture that emerges from the experiments and the simulations shows flow characteristics quite different from turbulent flow, having an energy spectrum with a lack of higher frequencies, and with distinct structures (streaks) visible in the flow. Consequently, the application of turbulence models is somewhat questionable. However, some of the models predict, at least qualitatively, the correct influence of the free-stream turbulence level on the location of the transition region. A two-equation model that has shown this feature is the $k - \epsilon$ model by Launder and Sharma (1974), and some calculations with this model are also carried out in the present paper. Two major shortcomings with linear eddy-viscosity models are the prediction of nearly isotropic fluctuations inside the boundary layer, and a too short length of the transition region. It should be emphasized that the correct modeling of the behavior inside the transition region is important, since, in for example gas-turbines, a predominant part of the turbine blades can be affected by transitional flow. Different attempts to improve the modeling of the transition region have been suggested in the literature. For instance, Schmidt and Patankar (1991) modified the production term to limit the growth rate of the kinetic energy through the transition region, while a more sophisticated method is to solve a separate transport equation for the intermittency (cf. Steelant and Dick, 1996). The intermittency parameter can be used together with conditionally averaged Navier-Stokes equations to weigh the contributions from laminar and turbulent flow in the transition region. Another approach is to incorporate empirical data into the model, for instance to trigger the start of the transition and to obtain the correct behavior through the transition region. Sieger et al. (1995) make use of a substantial contribution of empirical information in their two-layer model, and the results are very good for free-stream turbulence levels in the range 3–6 percent at various pressure gradients.

The number of studies using differential Reynolds Stress Transport (RST) models is much more limited, and, despite the fact that these models have better prospects to describe the highly anisotropic fluctuations in the pseudo-laminar layer, most of the results have not been very encouraging. However, impressive results with a second-moment closure have been obtained for a wide range of test cases by Savill (1995a), using the so-called SLY-model.[1] The present study is focussed on a low-Reynolds number RST-model by Hanjalić, Jakirlić, and Hadžić (1995), in the following denoted as the HJH-model, and the results are compared with calculations using the Launder and Sharma $k - \epsilon$ model and the SLY-model by Savill. It should be emphasized that, in contrast to many other models which *prescribe* the start of the transition region with an empirical relation, all three models intend to *predict* both the transition onset and the correct behavior through the transition region. Comparisons of individual terms in the modeled equations with data from a Large Eddy Simulation (LES) by Voke and Yang

Contributed by the Fluids Engineering Division for publication in the JOURNAL OF FLUIDS ENGINEERING. Manuscript received by the Fluids Engineering Division October 25, 1996; revised manuscript received March 31, 1997. Associate Technical Editor: P. R. Bandyopadhyay.

[1] The acronym SLY stands for "Savill-Launder-Younis," since the model is a modification of a RST-model by Kebede, Launder and Younis.

(1995) are also carried out. Furthermore, some important aspects concerning the test case specifications and the calculation procedures are highlighted and discussed in connection with the results.

Mathematical Models

The standard form of the Reynolds-averaged momentum and continuity equations are used together with a turbulence model to close the unknown Reynolds stress terms.

Launder and Sharma $k-\epsilon$ Model. The low-Reynolds number $k-\epsilon$ model by Launder and Sharma (1974) is a linear eddy-viscosity model, i.e.,

$$-\overline{u_i u_j} = \nu_t\left(\frac{\partial U_i}{\partial x_j}+\frac{\partial U_j}{\partial x_i}\right)-\frac{2}{3}\delta_{ij}k \tag{1}$$

In the present paper the coordinates $(x_1, x_2, x_3) = (x, y, z)$ denote the streamwise, wall-normal and spanwise directions, respectively, while the corresponding mean and fluctuating velocity components are (U, V, W) and (u, v, w). The eddy viscosity is defined as $\nu_t = c_\mu f_\mu k^2/\tilde{\epsilon}$, in which the kinetic energy (k) and a form of the dissipation $(\tilde{\epsilon})$ are determined from the corresponding transport equations. These are modeled as

$$\frac{\partial k}{\partial t}+U_k\frac{\partial k}{\partial x_k}=\mathcal{P}-\tilde{\epsilon}+\frac{\partial}{\partial x_k}\left[\left(\nu+\frac{\nu_t}{\sigma_k}\right)\frac{\partial k}{\partial x_k}\right]+D \tag{2}$$

$$\frac{\partial \tilde{\epsilon}}{\partial t}+U_k\frac{\partial \tilde{\epsilon}}{\partial x_k}=c_{\epsilon 1}f_{\epsilon 1}\mathcal{P}\frac{\tilde{\epsilon}}{k}-c_{\epsilon 2}f_{\epsilon 2}\frac{\tilde{\epsilon}^2}{k}+\frac{\partial}{\partial x_k}\left[\left(\nu+\frac{\nu_t}{\sigma_\epsilon}\right)\frac{\partial \tilde{\epsilon}}{\partial x_k}\right]+E \tag{3}$$

in which $\mathcal{P}=-\overline{u_iu_j}\partial U_i/\partial x_j$. The model constants and low-Reynolds number functions are defined as $c_\mu = 0.09$, $c_{\epsilon 1} = 1.44$, $c_{\epsilon 2} = 1.92$, $\sigma_k = 1.0$, $\sigma_\epsilon = 1.3$, $f_{\epsilon 1} = 1.0$, $f_{\epsilon 2} = 1-0.3\exp(-\mathrm{Re}_t^2)$, $f_\mu = \exp(-3.4/(1+\mathrm{Re}_t/50)^2)$, $D = -2\nu\times(\partial\sqrt{k}/\partial y)^2$, $E = 2\nu\nu_t(\partial^2U/\partial y^2)^2$. Note that instead of the "true" dissipation ϵ, the variable $\tilde{\epsilon}=\epsilon-2\nu(\partial\sqrt{k}/\partial y)^2$ is introduced to have a quantity that approaches zero at the solid wall. Furthermore, the turbulent Reynolds number is defined as $\mathrm{Re}_t = k^2/(\nu\tilde{\epsilon})$.

Differential Reynolds Stress Models. The HJH-model (Hanjalić et al., 1995; see also Jakirlić et al., 1994) was developed for fully turbulent wall-bounded flows, while the SLY-model (Savill, 1995a) includes modifications to improve the modelling of transitional flows. The modeled versions of the Reynolds stress and dissipation equations read

$$\frac{\partial \overline{u_iu_j}}{\partial t}+U_k\frac{\partial \overline{u_iu_j}}{\partial x_k}=-\left(\overline{u_iu_k}\frac{\partial U_j}{\partial x_k}+\overline{u_ju_k}\frac{\partial U_i}{\partial x_k}\right)+\phi_{ij}-\epsilon_{ij}+\frac{\partial}{\partial x_k}\left[\left(\nu+C_s\frac{k}{\epsilon}\overline{u_ku_l}\right)\frac{\partial \overline{u_iu_j}}{\partial x_l}\right] \tag{4}$$

$$\frac{\partial \epsilon}{\partial t}+U_k\frac{\partial \epsilon}{\partial x_k}=-C_{\epsilon 1}f_{\epsilon 1}\frac{\epsilon}{k}\overline{u_iu_j}\frac{\partial U_i}{\partial x_j}-C_{\epsilon 2}f_{\epsilon 2}\frac{\epsilon\tilde{\epsilon}}{k}+C_{\epsilon 3}f_\mu\nu\frac{k}{\epsilon}\overline{u_ju_k}\frac{\partial^2U_i}{\partial x_j\partial x_l}\frac{\partial^2U_i}{\partial x_k\partial x_l}+\frac{\partial}{\partial x_k}\left[\left(\nu+C_\epsilon\frac{k}{\epsilon}\overline{u_ku_l}\right)\frac{\partial\epsilon}{\partial x_l}\right]+S_{\epsilon 4}+S_l \tag{5}$$

In both Differential Reynolds Stress Models C_s is equal to 0.22. Furthermore, the pressure strain term (ϕ_{ij}) and the dissipation (ϵ_{ij}) are modeled as

$$\phi_{ij}=\phi_{ij,1}+\phi_{ij,2}+\phi^w_{ij,1}+\phi^w_{ij,2}$$

$$\phi_{ij,1}=-C_1\epsilon a_{ij},\quad \phi_{ij,2}=-C_2(P_{ij}-\tfrac{2}{3}\mathcal{P}\delta_{ij})$$

$$\phi^w_{ij,1}=C^w_1 f_w\frac{\epsilon}{k}\left(\overline{u_ku_m}n_kn_m\delta_{ij}-\frac{3}{2}\overline{u_iu_k}n_kn_j-\frac{3}{2}\overline{u_ku_j}n_kn_i\right)$$

$$\phi^w_{ij,2}=C^w_2 f_w(\phi_{km,2}n_kn_m\delta_{ij}-\tfrac{3}{2}\phi_{ik,2}n_kn_j-\tfrac{3}{2}\phi_{kj,2}n_kn_i)$$

$$\epsilon_{ij}=f_s\epsilon^*_{ij}+(1-f_s)\tfrac{2}{3}\delta_{ij}\epsilon$$

although there are differences in the coefficients and low-Reynolds number functions, as well as in some of the terms in Eq. (5). P_{ij} denotes the production term in the right-hand side of Eq. (4), n_i is a unit vector normal to the solid surface and x_n is the wall-normal distance. The characteristics of the HJH-model can be summarized as:

$$f=\min\left\{\left(\frac{\mathrm{Re}_t}{150}\right)^{3/2};1\right\},\quad F=\min\{0.6;A_2\},$$

$$C=2.5AF^{1/4}f\quad C_1=C+\sqrt{A}E^2,$$

$$C_2=0.8\sqrt{A},\quad C^w_1=\max\{1-0.7C;0.3\},$$

$$C^w_2=\min\{A;0.3\},\quad f_w=\min\left\{\frac{k^{3/2}}{2.5\epsilon x_n};1.4\right\}$$

$$\epsilon^*_{ij}=\frac{\epsilon}{k}\frac{[\overline{u_iu_j}+(\overline{u_iu_k}n_jn_k+\overline{u_ju_k}n_in_k+\overline{u_ku_i}n_kn_in_j)f_d]}{1+\frac{3}{2}\frac{\overline{u_pu_q}}{k}n_pn_qf_d}$$

$$f_s=1-\sqrt{A}E^2,\quad f_d=(1+0.1\,\mathrm{Re}_t)^{-1}$$

$$S_{\epsilon 4}=C_{\epsilon 4}(\overline{vv}-\overline{uu})\frac{\partial U}{\partial x}\left(\frac{\epsilon}{k}\right)$$

$$S_l=\max\left\{\left[\left(\frac{1}{C_l}\frac{\partial l_t}{\partial x_n}\right)^2-1\right]\left(\frac{1}{C_l}\frac{\partial l_t}{\partial x_n}\right)^2;0\right\}\frac{\epsilon\tilde{\epsilon}}{k}A$$

$$l_t=\frac{k^{3/2}}{\epsilon},\quad f_{\epsilon 1}=1,\quad f_{\epsilon 2}=1-\frac{C_{\epsilon 2}-1.4}{C_{\epsilon 2}}\exp\left[-\left(\frac{\mathrm{Re}_t}{6}\right)^2\right],$$

$$f_\mu=1,\quad C_\epsilon=0.18,\quad C_{\epsilon 1}=1.44,\quad C_{\epsilon 2}=1.92,$$

$$C_{\epsilon 3}=0.25,\quad C_{\epsilon 4}=1.16,\quad C_l=2.5$$

The term $S_{\epsilon 4}$ is written explicitly for 2D boundary layer flows, and intends to increase the production of ϵ due to normal stresses. The invariants of the stress anisotropy and the dissipation anisotropy tensors are defined as:

$$a_{ij}=\frac{\overline{u_iu_j}}{k}-\frac{2}{3}\delta_{ij},\quad A_2=a_{ij}a_{ji},\quad A_3=a_{ij}a_{jk}a_{ki}$$

$$e_{ij}=\frac{\epsilon_{ij}}{\epsilon}-\frac{2}{3}\delta_{ij},\quad E_2=e_{ij}e_{ji},\quad E_3=e_{ij}e_{jk}e_{ki}$$

$$A=1-\tfrac{9}{8}(A_2-A_3),\quad E=1-\tfrac{9}{8}(E_2-E_3)$$

The SLY-model is given by

$$C_1=1.8,\quad C_2=0.6,\quad C^w_1=0.5,\quad C^w_2=0.3$$

$$f^*=\frac{k^{3/2}}{\epsilon x_n};\quad f^*_{\max}=\max_{x_n} f^*;$$

$$f_w = \begin{cases} 1: & 0 < x_n < (x_n)_{\max} \\ f^*/f^*_{\max}: & x_n > (x_n)_{\max} \end{cases}$$

$$\epsilon^*_{ij} = \frac{\epsilon}{k} \frac{[\overline{u_i u_j} + \overline{u_i u_k} n_j n_k + \overline{u_j u_k} n_i n_k + \delta_{ij} \overline{u_k u_l} n_k n_l]}{1 + \frac{5}{2} \frac{\overline{u_p u_q}}{k} n_p n_q}$$

$$f_s = (1 + 0.1\ \mathrm{Re}_t)^{-1}, \quad R_y = \frac{\sqrt{k} x_n}{\nu}$$

$$f_{\epsilon 1} = \max\left\{ \frac{1}{c_{\epsilon 1}} \left(2.0 - \frac{0.725\ R_y}{65} \right) ; 1 \right\}$$

$$f_{\epsilon 2} = 1 - \frac{0.4}{c_{\epsilon 2}} \exp\left[-\min\left\{ \left(\frac{\mathrm{Re}_t}{6} \right)^2 ; 20 \right\} \right]$$

$$f_\mu = \exp\left(\frac{-3.4}{(1 + \mathrm{Re}_t/50)^2} \right), \quad S_{\epsilon 4} = S_t = 0$$

$$C_\epsilon = 0.15, \quad C_{\epsilon 1} = 1.275, \quad C_{\epsilon 2} = 1.8, \quad C_{\epsilon 3} = 0.25$$

The latter model is sometimes denoted as "basic SLY" by the originator (Savill, 1995a), since later versions of the model have been extended with terms intending to model pressure diffusion and nonlocal effects of the pressure strain. The viscous destruction term in Eq. 5 takes the form $-C_{\epsilon 2} f_{\epsilon 2} \epsilon^2/k$, i.e., no $\tilde{\epsilon}$ is used, and Savill uses $\partial\epsilon/\partial y = 0$ as wall boundary condition. However, the $C_{\epsilon 2}$-term tends to grow toward infinity close to the wall, but this deficiency has been corrected in more recent versions of the model by an additional pressure diffusion term (Savill, private communication).

Since only two-dimensional boundary layers with zero-pressure gradient are considered in the present study, the elliptic terms in the equations are removed, and the remaining parabolic equations can be solved with a marching procedure. Thus, the streamwise diffusion and the allowance of pressure variations across the boundary layer are neglected. However, it should be emphasized that all other terms are maintained, i.e., the complete formulation of the production and pressure strain terms are used, including terms dependent on streamwise derivatives of the mean velocity field. Some tests were also made with the fully elliptic formulation, but the results were only slightly different from the ones obtained with the present approach.

Numerical Method

The equations are solved with a parabolic boundary layer code, which makes use of a rectangular grid with nonequidistant mesh size both in the streamwise (x) and the wall-normal (y) direction. Furthermore, a staggered grid is used in the y-direction. The quantities k, ϵ, and U are evaluated at the staggered grid points, while the V-velocity as well as the Reynolds stresses are calculated at the nonstaggered positions.

The discretization is based on the finite volume method, using a second-order upwind scheme in the x-direction and a central scheme (second-order) in the y-direction. The use of central differences is possible since only flat plates are considered (which have only small wall-normal convection velocities), in combination with relatively fine meshes. Thus the local grid-Reynolds number is small enough to maintain the stability of the code. The previously described discretizations apply to all transport equations that are used, which, in the case of RST-closures, imply equations for U, $\overline{uu}$, $\overline{vv}$, $\overline{uv}$, k, ϵ and the continuity equation.

Due to the nonlinear terms an iterative solution procedure is necessary. The convecting velocities and the additional nonlinear terms are evaluated at the previous iteration level, which means that the equations become decoupled and can be solved sequentially. A line Gauss-Seidel method is used, and the iteration process at a certain streamwise position is continued until all quantities satisfy the convergence criterion, which requires that the maximum difference between the values obtained at two subsequent iterations is at each grid point below a very small value (10^{-7} for the U-equation and 10^{-9} for all other equations). If convergence is obtained the next streamwise position is treated.

Table 1 Influence of grid resolution on the start and end of the transition region, calculated with the SLY-model. $(\mathrm{Re}_x)_{\mathrm{start}}$ and $(\mathrm{Re}_x)_{\mathrm{end}}$ correspond to the local minimum and maximum in each c_f-curve, respectively.

Test case	Grid	$(\mathrm{Re}_x)_{\mathrm{start}}$	$(\mathrm{Re}_x)_{\mathrm{end}}$
T3B	100×50	$8.95 \cdot 10^4$	$2.46 \cdot 10^5$
	200×100	$9.04 \cdot 10^4$	$2.48 \cdot 10^5$
	400×200	$9.07 \cdot 10^4$	$2.49 \cdot 10^5$
T3A	1000×50	$7.20 \cdot 10^5$	$8.02 \cdot 10^6$
($l_{t0} = 9.8$)	1000×100	$8.88 \cdot 10^5$	$9.56 \cdot 10^6$
	2000×200	$9.57 \cdot 10^5$	$10.23 \cdot 10^6$
	4000×400	$9.77 \cdot 10^5$	$10.43 \cdot 10^6$

To check that nearly grid independent solutions are obtained, the number of grid points in both the streamwise and the wall-normal direction were increased until only very small changes in the wall-shear stress or the shape factor could be observed. An example of the typical grids used and the effect of grid refinement on the results are given in Table 1.

Boundary and Initial Conditions. The free-stream boundary conditions for all equations, except for the U-equation, are specified as homogeneous Neumann boundary conditions, i.e.,

$$\frac{\partial \phi}{\partial y} = 0 \quad \text{when} \quad y \to \infty$$

in which ϕ denotes any of the considered quantities. The boundary condition for U is a Dirichlet condition given by the free-stream velocity (U_0), and the boundary conditions at the wall are specified as

$$U = V = \overline{uu} = \overline{vv} = k = \overline{uv} = 0$$

However, the wall boundary condition for the ϵ-equation depends on the model. The HJH-model uses

$$\epsilon|_{y=0} = 2\nu \left(\frac{\partial \sqrt{k}}{\partial y} \right)^2_{y=0} \tag{6}$$

whereas $\tilde{\epsilon}$ is set to zero at the wall in the Launder and Sharma model. Finally, the SLY-model uses a homogeneous Neumann condition as wall boundary condition for ϵ.

The inflow boundary is usually positioned 10 mm downstream of the leading edge of the plate, which means that initial profiles of all variables have to be specified. In most calculations reported in the sequel of this paper the initial conditions are defined as

$$\overline{uu} = \overline{vv} = \overline{ww} = \tfrac{2}{3} k \quad \text{where} \quad k = k_0 \left(\frac{U}{U_0} \right)^2$$

$$\overline{uv} = 0$$

$$\epsilon = \max\left\{ \epsilon_0; 0.3\ k \left| \frac{\partial U}{\partial y} \right| \right\} \quad \text{where} \quad \epsilon_0 = k_0^{3/2}/l_{t0}$$

in which k_0 and l_{t0} are the kinetic energy and the turbulent length scale of the free-stream turbulence, respectively. The previous set of initial conditions is quite different from experi-

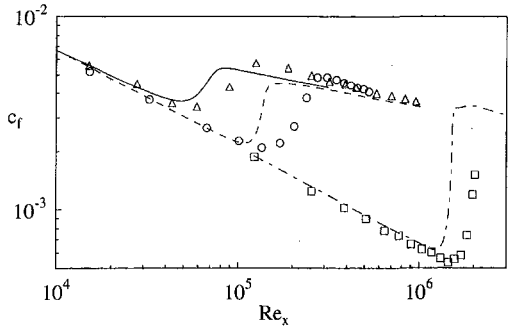

Fig. 1 Wall-shear stress predicted with the Launder and Sharma model for different test cases. Symbols and lines show results from experiments and calculations, respectively. T3B (△, —), T3A (○, - - -), T3A⁻ (□, - · -).

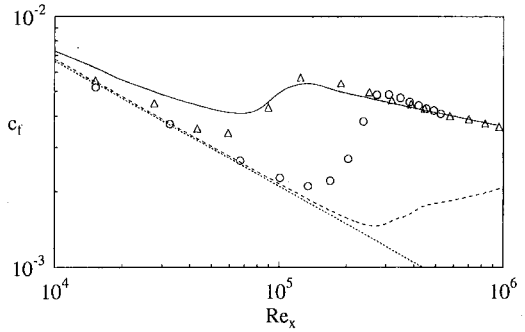

Fig. 2 Prediction of wall-shear stress coefficient with the HJH-model. Symbols and lines show results from experiments and calculations, respectively: T3B (△, —); T3A (○, - - -).

mentally observed profiles, but can be considered as a first choice if one has no specific knowledge about the flow conditions inside the boundary layer. The sensitivity to different initial profiles has been investigated for all models and will be discussed later.

The specification of k_0 and l_{t0} requires a comment. Since homogeneous Neumann boundary conditions are used in the free stream, the decay rate of the free-stream turbulence is dependent on the model constants and the initial values of k_0 and l_{t0}. The kinetic energy is directly given by the free-stream turbulence level at the starting position, while l_{t0} has to be chosen to fit the experimentally determined decay curve of the free-stream turbulence.

Test Cases. Four different transitional test cases are used in the present paper, and all of them consider attached boundary layer flow on a flat plate equipped with a sharp leading edge at zero-pressure gradient. Three experimental test cases at different free-stream turbulence levels (Tu*) are taken from measurements by Rolls-Royce (cf. Roach and Brierley, 1992). The test cases are denoted as T3B (Tu = 6 percent, U_0 = 9.6 m/s), T3A (Tu = 3 percent, U_0 = 5.2 m/s) and T3A⁻ (Tu = 1 percent, U_0 = 19.6 m/s). Furthermore, results obtained with the HJH-model are compared with a Large Eddy Simulation by Voke and Yang (1995), which is denoted as the T3B-LES case (Tu = 6 percent, U_0 = 9.6 m/s). It should be mentioned that the simulations by Voke and Yang were also carried out with the subgrid-scale model switched off (which gives a low-resolution "Direct" Numerical Simulation), showing that the influence of the model is in fact restricted to regions with turbulent flow (i.e., in the free stream and in the turbulent boundary layer), while the pretransitional region, as well as the predicted transition onset, were only slightly affected.

Results

Fully Turbulent Flows. One basic requirement for a turbulence model intending to model bypass transition is the correct description in the fully turbulent region. Calculations of fully turbulent flow at zero-pressure gradient showed that both the HJH-model and the model by Launder and Sharma predict the wall-shear stress coefficient with sufficient accuracy, while the HJH-model clearly exhibits an improvement in the modeling of adverse pressure gradient flows as compared to the two-equation model. The improvements can to a large extent be ascribed to the additional production term in the dissipation equation ($S_{\epsilon 4}$), which enhances the production of ϵ due to normal stresses. However, the calculations with the SLY-model showed an overprediction of the wall-shear stress coefficient with approximately 30 percent in all turbulent test cases. This deviation is caused by the inconsistent near-wall behavior of the dissipation equation, in which the destruction term ($c_{\epsilon 2}$) tends to grow toward infinity close to the wall. This deficiency can be corrected by introducing $\tilde{\epsilon}$ in the $c_{\epsilon 2}$-term, or, as suggested by Savill, by adding an additional pressure diffusion term.

Launder and Sharma Model. In Fig. 1 the predictions obtained with the Launder and Sharma model are shown for three different test cases with Tu in the range from 1 to 6 percent. Although the start of the transition region is consistently predicted too early, the model accounts for the influence of the varying free-stream turbulence level in qualitative agreement with the experiments. However, previous studies have shown that the model does not perform very well in transitional flows with various pressure gradients. It should also be mentioned that the model is rather sensitive to the specified initial conditions, and the transition location can vary significantly with the magnitude and shape of the initial ϵ-profile.

HJH-Model. Similar predictions with the HJH-model are shown in Fig. 2 for the T3B and the T3A cases. Besides a slightly too large value of c_f in the pretransitional region of the flow, the predictions of the start of the transition as well as the variations through the transition region are in good agreement with experiments for the T3B-case. It is also encouraging that the model captures the growth of the $\overline{uu}$-Reynolds stresses in the region upstream of the transition onset (Fig. 3(a)).

However, when the free-stream turbulence level is reduced to 3 percent (T3A), the transition onset is predicted too far downstream, and the transition from laminar to turbulent flow is much too slow. The model does not predict the pretransitional growth of the u-fluctuations, and an increase is only observed just prior to the start of the transition region. It should be emphasized that tests with different initial profiles showed a rather small dependence on the initial shape inside the boundary layer,

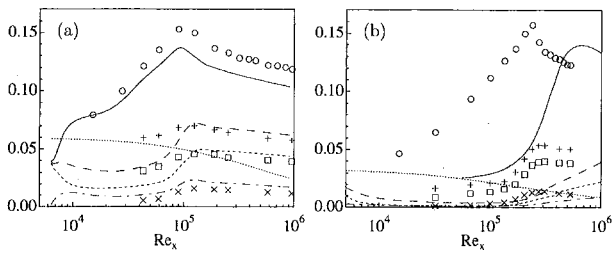

Fig. 3 Downstream development of the maximum level of u_{rms}/U_0(○, —), v_{rms}/U_0 (□, - - -), w_{rms}/U_0 (+, - -) and $-10\,\overline{uv}/U_0^2$ (×, - · -) inside the boundary layer. Dotted line represents the free-stream turbulence level ($u_{rms,0}/U_0$). (*a*) T3B-case, (*b*) T3A-case.

* $Tu = u_{rms,0}/U_0$ measured at the leading edge, in which $u_{rms,0}$ is the streamwise component of the free-stream turbulence.

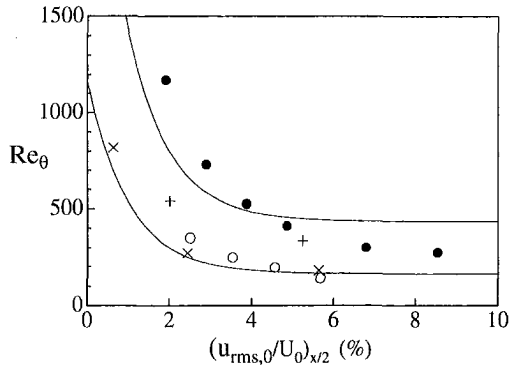

Fig. 4 Start and end of the transition region in terms of Re_θ obtained from experiments by Rolls-Royce (×, +) and calculations with the HJH-model (○, ●), compared with the empirical correlation by Abu-Ghannam and Shaw (1980) (——)

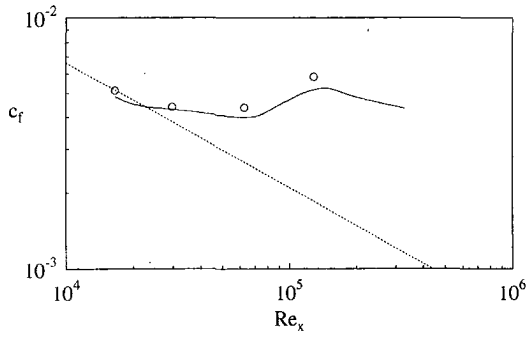

Fig. 5 Wall-shear stress predicted with the HJH-model (——) and compared with LES-data (○) (T3B-LES case). The dotted line represents the laminar solution.

but the transition onset could be slightly delayed if the level of $\overline{vv}$ just outside the boundary layer was initially reduced.

To study the behavior for a wider range of free-stream turbulence levels, the free-stream velocity and the initial turbulent length scale (l_{t0}) were set to 5 m/s and 30 mm, respectively, while Tu was continuously varied. The start and the end of the transition region, defined as the local minimum and maximum in each c_f-curve, were extracted from the calculations in terms of the local Reynolds number based on the momentum loss thickness (Re_θ). These results are plotted in Fig. 4, together with the empirical correlation by Abu-Ghannam and Shaw (1980) and the experimental results by Roach and Brierley (1992). The Abu-Ghannam and Shaw correlation is frequently used for transition prediction in industrial applications, and it relates the start and end of the transition region directly to the free-stream turbulence level (and, in case of nonzero pressure gradient flow, also to a pressure gradient parameter). The present calculations clearly show that the general trend obtained with the HJH-model is not correct. The transition region in terms of the local parameter θ is shifted from being too early at high free-stream turbulence levels, to a delayed transition onset and a prolonged transition region for lower Tu. (Note that the free-stream turbulence level used in the Abu-Ghannam and Shaw correlation is taken midway between the leading edge and the considered x-position, i.e. $(u_{rms,0}/U_0)_{x/2}$.)

Comparison With LES. A detailed comparison between predictions with the HJH-model and the Large Eddy Simulation by Voke and Yang (1995) has been carried out. The intention is to gain further understanding on how the model behaves through the transition region, and to elucidate the terms that are not satisfactorily modeled. Since profiles of all quantities are available at $x = 25$ mm, these are used as initial conditions for the calculations. The predicted wall-shear stress coefficient is displayed in Fig. 5, and profiles extracted from three different x-stations are shown in Fig. 6. The streamwise positions correspond to the pseudo-laminar region, the vicinity of the transition onset and the end of the transition region, respectively. The shape of the u_{rms}-profiles are in reasonably good agreement with the LES-data throughout the boundary layer, although the absolute level is considerably underpredicted at the downstream positions. Also the shear stress profiles ($\overline{uv}$) show fair agreement with the experimental data. However, the dissipation exhibits a severe overprediction in the central part of the pretransitional boundary layer, which consequently counteracts the production of kinetic energy (which is dominated by $\overline{uu}$) in this region.

Further downstream, when the flow has reached the turbulent state, the predicted dissipation is in better agreement with experiments, except close to the wall where the HJH-model fails to predict the large near-wall peak. This peak in the LES, however, is to a large extent balanced by pressure diffusion, which in the $\overline{uu}$-equation is significant close to the wall. In the present RST-model there is no separate term that serves to model the pressure diffusion, and good agreement close to the wall can not be expected.

The large overprediction of ϵ indicates that the present model is not well-suited to describe the behavior in the pseudo-laminar region, despite the fact that the transition location is predicted with good accuracy. This was further corroborated by comparing the different terms in the modeled Reynolds stress equations with the corresponding budgets extracted from the LES (no figures are shown here, see Westin and Henkes, 1996 for more information). The overpredicted dissipation affects all Reynolds stress equations, both directly through the dissipation term, and indirectly through the modeling of the pressure strain terms.

Based on the statistical averages extracted from the LES-data, Voke and Yang (1995) proposed a transition scenario,

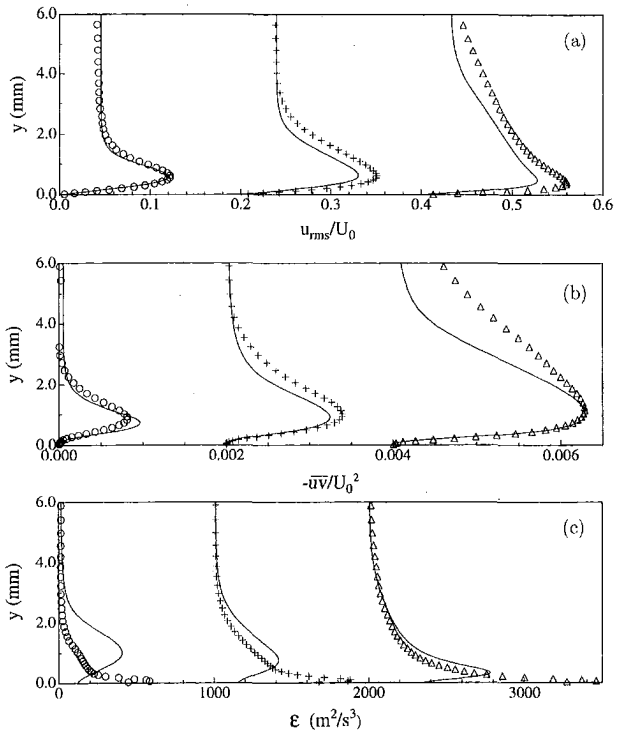

Fig. 6 Different profiles extracted from LES-data (symbols) and calculations with the HJH-model (lines). The x-positions are 45 mm ($Re_x = 3 \times 10^4$) (○), 95 mm ($Re_x = 6.3 \times 10^4$) (+) and 195 mm ($Re_x = 1.3 \times 10^5$) (△). (a) u_{rms}/U_0, (b) $-\overline{uv}/U_0^2$, (c) ϵ.

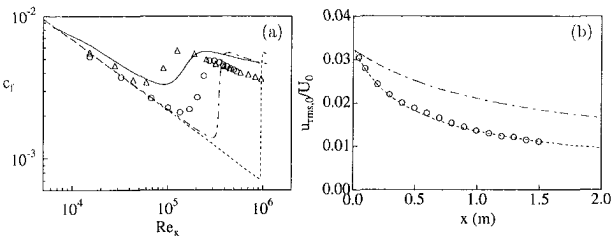

Fig. 7 (*a*) Wall-shear stress coefficient and (*b*) downstream development of the free-stream turbulence level calculated with the SLY-model. Experiments: T3A (○), T3B (△). Calculations: T3B with l_{t0} = 24 mm (——), T3A with l_{t0} = 9.8 mm (– – –) and T3A with l_{t0} = 30.1 mm (– · –).

which is also summarized and discussed by Savill (1996). Although the scenario is somewhat simplified and does not tell anything about the details of the transition mechanisms involved, it elucidates the different roles of the u- and the v-fluctuations during the different stages of the transition process. In the initial stage there is a production of $\overline{uv}$ inside the boundary layer, caused by the overlap between the wall-normal fluctuations in the free stream and the mean shear in the laminar boundary layer. The produced $\overline{uv}$ determines the production of $\overline{uu}$, which results in a growth of u_{rms} in the pseudo-laminar boundary layer. At this stage there is no production or redistribution of energy to the $\overline{vv}$-stresses, and the v-fluctuations observed inside the boundary layer is only dependent on the turbulent free stream.

The second stage of the transition process is more rapid, and, as pointed out by Voke and Yang, less clear. After the initial region with growing $\overline{uu}$-stresses, the redistribution of energy to $\overline{vv}$ and $\overline{ww}$ through the pressure strain terms is suddenly activated. The increase in $\overline{vv}$ will in turn increase the production of $\overline{uv}$, resulting in a feedback, which consequently causes a rapid transition to turbulence. By comparing different terms in the Reynolds stress budgets, it becomes clear that many of these features also are found in the present calculations with the HJH-model (T3B-LES case). The growth of u_{rms} in the pseudo-laminar boundary layer is observed, as well as a sudden increase of both the slow and the rapid pressure strain terms just prior to the start of the transition region. However, the cause of this sudden redistribution of energy is not clear, neither in the LES, nor in the predictions with the RST-model.

Some attempts to modify the HJH-model have been made, with the intention to obtain an upstream movement of the transition onset in the T3A-case. Since transition is preceded by a sudden increase in the pressure strain terms, these were locally increased in the middle of the boundary layer to enhance the redistribution to the lateral components. The effect was a more rapid growth of c_f in the transition region as compared to the curve shown in Fig. 2, while the upstream movement of the transition onset was only very limited. The same effect was found when either the slow or the rapid pressure strain was exaggerated, although a slightly earlier transition could be observed in the latter case. Furthermore, the modifications did not improve the modeling of the pre-transitional u-fluctuations.

Another modification was a reduction of the dissipation by simply setting $C_{\epsilon 3}$ to zero. As expected, this resulted in an increased growth of u_{rms} and an upstream movement of the start of the transition, but with a very slow growth of c_f within the transition region similar to Fig. 2. However, all tested modifications led to a significant deterioration of the good predictions in the T3B-case, indicating that some major changes in the modeling are necessary to achieve any substantial improvement.

The SLY-Model. Figure 7(*a*) shows predictions with the SLY-model, carried out in the same manner as shown in Fig. 2 for the HJH-model. It should be noted that all calculations with the SLY-model are carried out with the equations simplified according to the boundary layer approximation, i.e., all terms that include streamwise derivatives (except for the streamwise convection) are neglected. The motivation for this is to allow direct comparisons with the results reported by Savill (1995a). For both test cases the predicted location of the transition region is considerably late. The start of transition in the T3B-case, estimated from the local minimum in the wall-shear stress curve, occurs at a Reynolds number which is about 50 percent larger than in the experiments. In the T3A-case the calculation fails completely, and the corresponding difference between prediction and experiment is almost 600 percent. Figure 7 also includes a calculation with an initial turbulent length scale of 30.1 mm, which obviously gives a too slow decay rate of the free-stream turbulence (Fig. 7(*b*)). It is interesting to note the large sensitivity of the SLY-model to the free-stream boundary condition, at least for this relatively low free-stream turbulence level. The slow decay of the free-stream turbulence due to the larger length scale results in a considerable upstream movement of the transition region. However, transition still starts at an approximately 100 percent too large Re_x-value. Finally, in the T3A$^-$ case (Tu = one percent), the SLY-model could not predict transition within the considered domain ($Re_x < 6.4 \cdot 10^6$). Concerning the sensitivity to different initial profiles earlier findings by Savill were confirmed in the present study, namely that the model is rather insensitive to the exact shapes of the initial profiles.

The downstream development of the maximum level of the Reynolds stresses inside the boundary layer is shown in Fig. 8. The normal stresses show an almost constant level in the pseudo-laminar region, and an increase is only observable close to transition. The individual profiles also show that the distinct maximum in the $\overline{uu}$-stresses as observed in calculations with the HJH-model (Fig. 6(*a*)), is almost absent in the SLY-model predictions of the pretransitional region. In that respect the model behavior resembles the Launder and Sharma model, i.e., the kinetic energy in the free stream is slowly diffusing toward the wall, followed by a sudden increase in the kinetic energy when transition starts.

Numerical Accuracy. Table 1 gives an example of the successive grid refinement that was carried out for each calculation in the present paper, and its effect on the location of the transition region. Although the grid distribution was not optimized to minimize the number of grid points, it is evident that the requirements on the grid resolution become more severe when the free-stream turbulence level is reduced. This behavior is found for all three models.

Another contribution to the numerical uncertainty is the influence of boundary and initial conditions. The importance of the free-stream boundary condition has already been shown, and will be further discussed in the subsequent section. Regarding the wall boundary condition, the Dirichlet condition (6)

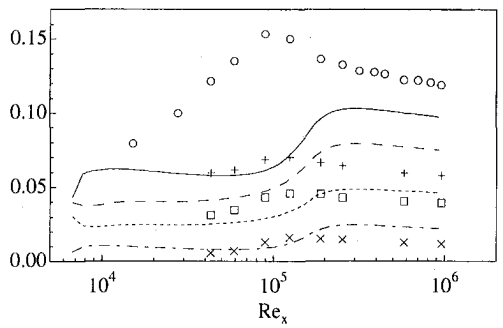

Fig. 8 Downstream development of the maximum level of u_{rms}/U_0 (○, —), v_{rms}/U_0 (□, – – –), w_{rms}/U_0 (+, – –) and $-10\overline{uv}/U_0^2$ (×, – · –) inside the boundary layer, calculated with the SLY-model for test case T3B.

Table 2 Influence of initial condition for ϵ on the start of the transition region ($(Re_x)_{start}$). The different profiles (1, 2, and 3) are described in the text.

Model	Profile 1	Profile 2	Profile 3
Launder and Sharma	$1.07 \cdot 10^5$	$1.24 \cdot 10^5$	$0.69 \cdot 10^5$
HJH	$2.70 \cdot 10^5$	$2.76 \cdot 10^5$	$2.59 \cdot 10^5$
SLY	$9.77 \cdot 10^5$	$9.83 \cdot 10^5$	$9.68 \cdot 10^5$

was also applied to the SLY-model calculations for the T3A and the T3B-case. Although some changes in the wall-shear stress coefficient could be observed in the fully turbulent boundary layer, the predictions of the transition onset were almost identical as the results obtained with a homogeneous Neumann condition.

The response to different initial conditions vary between the models, but some of them show a strong dependence on the initial dissipation profile. Table 2 shows the predicted start of the transition in the T3A-case for three different initial ϵ-profiles. Profiles 1, 2, and 3 are given by $\epsilon = \max\{\epsilon_0; 0.3k|\partial U/\partial y|\}$, $\epsilon = \max\{\epsilon_0; 0.6k|\partial U/\partial y|\}$ and ϵ = constant = ϵ_0, respectively, in which $\epsilon_0 = k_0^{3/2}/l_{t0}$. Even though profiles 2 and 3 are quite extreme choices for the initial conditions, it is clear that the Launder and Sharma model is sensitive to the shape of the ϵ-profile, (giving almost 80 percent difference in $(Re_x)_{start}$ between profiles 2 and 3). The SLY-model and the HJH-model are less influenced, with a maximum difference smaller than 7 percent.

Comparison With Previous Studies. The present calculations with the SLY-model show large discrepancies with the results reported by Savill (1995a), where transition is predicted in almost perfect agreement with experiments for test cases with the free-stream turbulence level in the range 1–10 percent. However, detailed comparisons of the computer code used by Savill with the one used in the present study have clarified some reasons for the differences, which will be discussed in the following.

The code used in the calculations by Savill makes use of an expanding grid, and Dirichlet boundary conditions are implemented at the free-stream boundary. This means that the decay rate of the free-stream turbulence along the plate, as well as all other quantities, are specified as functions of x. One reason for the discrepancies can be ascribed to the specified turbulent length scale. In Savill (1995a) l_{t0} = 30.1 mm is used, which gives a too slow decay rate of the free-stream turbulence as compared with experiments (Fig. 7(b)). Another reason is found when comparing the size of the computational domain. In the code by Savill, the expansion rate of the grid is dependent on the wall-normal extent of non-zero shear stresses ($\overline{uv}$). Since the shear stress contribution drops to zero just outside the boundary layer edge, the grid expands in accordance with the growth of the boundary layer thickness. In Fig. 9(a) calculations using three different sizes of the computational domain are shown: the free-stream boundary positioned just outside the boundary layer edge ($y_{max} \approx 1.15\delta_{995}$), approximately two boundary layer thicknesses ($1.9\delta_{995}$) and finally a large nonexpanding domain similar to the one used by the present authors (δ_{995} is defined as the y-position where $U = 0.995U_0$). It is clearly observed that the transition region moves downstream when the computational domain is increased, and the predictions seem to become independent of the domain size for $y_{max} > 4\delta_{995}$. It should be emphasized that almost identical solutions were obtained when similar nonexpanding grids were used in the two codes.

The major reason for the early transition seems to be a combination of a too small computational domain and the use of Dirichlet boundary conditions. In the v_{rms}-profiles, the fluctuation level is continuously damped from the free stream toward the wall. Since the Dirichlet boundary condition implies a predefined turbulence level at the free-stream boundary, a too small y-domain results in an increased v_{rms}-level at the boundary layer edge (Fig. 9(b)). In other words, the damping of the v-fluctuations due to the modeled wall-reflection is restricted by the boundary. This gives different results compared with a calculation in which the wall-damping is allowed to have an influence over a region solely determined by the model itself. Also in experiments it is observed that the damping of $\overline{vv}$ influences a region which is much larger than δ_{995}, while the nonzero $\overline{uv}$-distribution is more or less restricted to the boundary layer. Consequently, if an expanding grid is used, the $\overline{vv}$-distribution is a more relevant measure to determine a suitable expansion rate than the $\overline{uv}$-distribution.

Summary and Discussion

The main outcome of the present study can be summarized as follows:

(i) The HJH-model shows good predictions for zero-pressure gradient test cases at Tu ≈ 5–6 percent, both regarding the location of the transition region and the prediction of individual stresses upstream and downstream of the transition onset. However, comparisons with other test cases, as well as the empirical correlation by Abu-Ghannam and Shaw (1980), show that the HJH-model predicts too early transition for $Tu > 6$ percent and too late for free-stream turbulence levels below 5–6 percent.

(ii) A major problem seems to be the modeling of the dissipation, and comparisons with LES-data reveal an overestimation of the dissipation in the pretransitional region.

(iii) Calculations with the SLY-model show that also this model predicts transition far too late as compared with experiments when the free-stream turbulence level is not very large. Our results are in conflict with existing other results, but it was shown that the discrepancies can be ascribed to the implementation of the free-stream boundary conditions and the size of the computational domain.

This last point highlights some important aspects concerning the test case specifications and the boundary conditions. Since the models are very sensitive to the decay rate of the free-stream turbulence, any comparison between different calculations can be very misleading if the boundary and initial conditions do not result in a decay of the free-stream turbulence that fits the experiments properly. In the test case specifications for the T3A-case both 30.1 mm and 13.4 mm have been specified as initial turbulent length scale. However, as shown in Fig. 7(b), a value close to 10 mm should be used to obtain a proper decay of the free-stream turbulence with the present model constants.

Another important aspect concerns the implementation of the free-stream boundary conditions. One fundamental demand on numerical studies of boundary layer flow, at least to the present authors' point of view, is that the calculations should not be

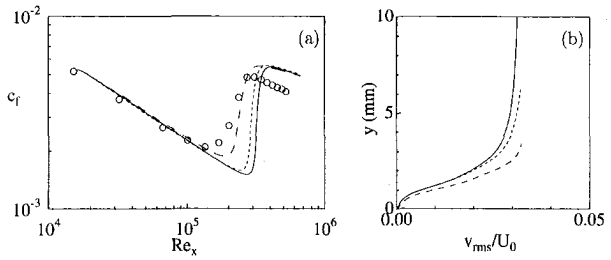

Fig. 9 SLY-model predictions of the T3A-case, using different sizes of the computational domain (Note: l_{t0} = 30.1 mm). (a) Wall-shear stress coefficient and (b) profiles of v_{rms}/U_0 at 95 mm ($Re_x = 3.2 \times 10^4$). Labels: expanding grid with $y_{max} \approx 1.15\ \delta_{995}$ (– –), expanding grid with $y_{max} \approx 1.9\ \delta_{995}$ (– – –), non-expanding grid with y_{max} = 147.5 mm (——).

influenced by the position of the free stream boundary. If that demand is fulfilled, there should only be a minor difference between the use of Dirichlet or homogeneous Neumann free-stream boundary conditions, since the development of the free-stream turbulence at a small distance below the free-stream boundary is determined by the model constants and the specified initial conditions. However, apparently the SLY-model predictions can be very much altered if the size of the computational domain is reduced in y together with Dirichlet conditions for the free-stream turbulence, and Savill (1996) also states that "Best predictions are obtained by using a smaller, δ-sized, expanding grid" (in which δ denotes the boundary layer thickness). This implies that a detailed measure of the free-stream turbulence characteristics must be provided at a specific (and well-defined) wall-normal position in the vicinity of the boundary layer. It is hard to see that a model which requires such strict inputs can be useful for predictions in industrial applications, in which the flow conditions usually are less well known.

The main outcome of the present work is somewhat discouraging, since both tested differential Reynolds Stress Transport models cannot correctly predict the transition location except for a few isolated test cases. In fact, the results are worse than obtained with the Launder and Sharma $k - \epsilon$ model, at least as far as the location of the transition region is concerned. As mentioned in the Introduction, experimental results show very anisotropic fluctuations in the pretransitional region, and with quite different roles of the Reynolds stress components through the transition region. With this in mind one should expect the RST-models to be in favor as compared to linear eddy-viscosity models.[2] The present comparison with the LES indicates that the modeling of the dissipation is a major weakness. Unfortunately, the balance equation for ϵ is not available from the LES, and it is not possible to pinpoint any particular term in the modeled ϵ-equation that should be improved. However, it is not surprising that significant deviations in the predicted dissipation are observed. The modeling of the dissipation equation is in many respects primitive, and the most frequently used version of the equation can be considered as a model of the energy transfer from the larger to the smaller scales in the turbulence. Consequently, it is assumed that the turbulence consists of a spectrum similar to what is found in experiments at high Re_t, and that the dissipation, which mainly takes place in the smaller scales, is determined by the larger energetic scales. This assumption is not valid in the pseudo-laminar boundary layer, which is dominated by large-scale low-frequency motions, and where the small scale structures are almost absent. Modification of the modeling for the dissipation, for instance through the introduction of additional length scales, might be an approach that can improve the predictions of bypass transition.

However, even if the modeling of the dissipation is improved, it is likely that other deficiencies in the present approach will become visible. For instance, just prior to the start of the transition region, the LES-data show a sudden increase in the pressure strain terms which redistribute energy from the streamwise to the lateral and vertical components. This redistribution is most likely caused by a certain instability mechanism, and further understanding of the physics behind the breakdown of a boundary layer subjected to high free-stream turbulence levels is probably necessary to improve the modeling. New experiments, preferably directed toward studies of possible breakdown mechanisms, as well as additional simulations (LES and DNS), are thus of great importance.

[2] Savill (1995a) also reports that the SLY-model can predict effects of free stream anisotropy, which linear $k - \epsilon$ models are unable to capture.

Acknowledgments

The visit of K. J. A. Westin to the Netherlands was supported by the Swedish Institute (SI) and the Swedish National Board for Industrial and Technical Development (NUTEK), and Dr. R. A. W. M. Henkes was supported by the Royal Netherlands Academy of Arts and Sciences (KNAW). Furthermore, Dr. A. M. Savill is acknowledged for generously providing his computer code during the efforts to resolve the discrepancies between our results.

References

Abu-Ghannam, B. J., and Shaw, R., 1980, "Natural Transition of Boundary Layers—The Effects of Turbulence, Pressure Gradient, and Flow History," *Journal of Mechanical Engineering Science,* Vol. 22, No. 5, pp. 213–228.

Alfredsson, P. H., and Matsubara, M., 1996, "Streaky Structures in Transition," *Proc. Transitional Boundary Layers in Aeronautics,* R. A. W. M. Henkes and J. L. van Ingen, eds., pp. 373–386, North-Holland.

Arnal, D., and Juillen, J. C., 1978, "Contribution expérimentale à l'etude de la receptivité d'une couche limite laminaire, à la turbulence de l'écoulement general," ONERA Rapport Technique No 1/5018 AYD.

Hanjalić, K., Jakirlić, S., and Hadžić, I., 1995, "Computation of Oscillating Turbulent Flows at Transitional Re-Numbers," *Turbulent Shear Flows 9,* F. Durst, N. Kasagi, B. E. Launder, F. W. Schmidt, K. Suzuki and J. H. Whitelaw, eds., pp. 323–342. Springer-Verlag.

Henningson, D. S., 1995, "Bypass Transition and Linear Growth Mechanisms," in *Advances in Turbulence V,* R. Benzi, ed., pp. 190–204. Kluwer.

Jakirlić, S., Hadžić, I., and Hanjalić, K., 1994, "Computation of Non-Equilibrium and Separating Flows at Transitional and High Re-Numbers with a New Low-Re-Number Second-Moment Closure Model," in *Proc. Strömungen mit Ablösung,* AGSTAB, DGLR Congress, Erlangen, Germany.

Kendall, J. M., 1985, "Experimental Study of Disturbances Produced in a Pre-Transitional Laminar Boundary Layer by Weak Freestream Turbulence," AIAA Paper 85-1695.

Launder, B. E., and Sharma, B. I., 1974, "Application of Energy-Dissipation Model of Turbulence to the Calculation of Flow Near a Spinning Disc," *Letters in Heat and Mass Transfer,* Vol. 1, pp. 131–137.

Roach, P. E., and Brierley, D. H., 1992, "The Influence of a Turbulent Free-Stream on Zero Pressure Gradient Transitional Boundary Layer Development. Part I: Test Cases T3A and T3B," *Numerical Simulation of Unsteady Flows and Transition to Turbulence,* O. Pironneau, W. Rodi, I. L. Ryhming, A. M. Savill and T. V. Truong, eds., pp. 319–347. Cambridge University Press.

Savill, A. M., 1995a, "The Savill-Launder-Younis (SLY) RST Intermittency Model for Predicting Transition," *ERCOFTAC Bulletin,* Vol. 24, pp. 37–41.

Savill, A. M., 1995b, "A Summary Report on the COST ERCOFTAC Transition SIG Project Evaluating Turbulence Models for Predicting Transition," *ERCOFTAC Bulletin,* Vol. 24, pp. 57–61.

Savill, A. M., 1996, "One Point Closures Applied to Transition," in *Turbulence and Transition Modelling,* M. Hallbäck, D. S. Henningson, A. V. Johansson and P. H. Alfredsson, eds, pp. 233–268. Kluwer.

Schmidt, R. C., and Patankar, S. V., 1991, "Simulating Boundary Layer Transition with Low-Reynolds-Number $k - \epsilon$ Turbulence Models: Part 2—An Approach to Improve the Predictions," ASME *Journal of Turbomachinery,* Vol. 113, pp. 18–26.

Sieger, K., Schiele, R., Kaufman, F., Wittig, S., and Rodi, W., 1995, "A Two-Layer Turbulence Model for the Calculation of Transitional Boundary-Layers," *ERCOFTAC Bulletin,* Vol. 24, pp. 21–25.

Steelant, J., and Dick, E., 1996, "Modelling of Bypass Transition with Conditioned Navier-Stokes Equations Coupled to an Intermittency Transport Equation," *International Journal for Numerical Methods in Fluids,* Vol. 23, pp. 193–220.

Voke, P. R., and Yang, Z., 1995, "Numerical Study of Bypass Transition," *Physics of Fluids,* Vol. 7 No. 9, pp. 2256–2264.

Westin, K. J. A., Boiko, A. V., Klingmann, B. G. B., Kozlov, V. V., and Alfredsson, P. H., 1994, "Experiments in a Boundary Layer Subjected to Free-Stream Turbulence. Part I. Boundary Layer Structure and Receptivity," *Journal of Fluid Mechanics,* Vol. 281, pp. 193–218.

Westin, K. J. A., and Henkes, R. A. W. M., 1996, "Prediction of Bypass Transition with Differential Reynolds Stress Models," Technical Report LR-813, Faculty of Aerospace Engineering, Delft University of Technology.

Shia-Hui Peng
Ph. D. Student,
Department of Thermo and Fluid Dynamics,
Chalmers University of Technology,
S-412 96 Gothenburg, Sweden
Department of Work Organization
and Technology,
National Institute for Working Life,
S-171 84 Solna, Sweden

Lars Davidson
Professor.
Department of Thermo and Fluid Dynamics,
Chalmers University of Technology,
S-412 96 Gothenburg, Sweden

Sture Holmberg
Senior Researcher.
Department of Work Organization
and Technology,
National Institute for Working Life,
S-171 84 Solna, Sweden

A Modified Low-Reynolds-Number k-ω Model for Recirculating Flows

A modified form of Wilcox's low-Reynolds-number k-ω model (Wilcox, 1994) is proposed for predicting recirculating flows. The turbulent diffusion for the specific dissipation rate, ω, is modeled with two parts: a second-order diffusion term and a first-order cross-diffusion term. The model constants are re-established. The damping functions are redevised, which reproduce correct near-wall asymptotic behaviors, and retain the mechanism describing transition as in the original model. The new model is applied to channel flow, backward-facing step flow with a large expansion ratio (H/h = 6), and recirculating flow in a ventilation enclosure. The predictions are considerably improved.

1 Introduction

Turbulence modeling is one of the most important aspects in numerical simulations of fluid flow and heat transfer. In conjunction with empirical wall functions, the conventional k-ϵ model (Launder and Spalding, 1974) has been widely used in engineering practice, and has turned out a success in many applications. Nevertheless, some problems exist when using the wall-function method (Patel et al., 1984). The lack of universality of the wall functions has been frequently criticized. Extensive research has thus been made to develop near-wall low-Reynolds-number (LRN) corrections.

Most of LRN models have been developed based on the k-ϵ model. A major deficiency with the k-ϵ-based LRN models is the uncertainty of specifying ϵ at the wall. There are other deficiencies with some LRN k-ϵ models (Peng et al., 1996a). The damping functions used in LRN models usually rely on wall-proximity-dependent variables (e.g., $y^+ = u_\tau y/\nu$ and $R_y = k^{1/2}y/\nu$ etc.). This gives rise to complications in numerics when solving for internal flows with non-planar wall geometries. Further, Savill (1995) has indicated that LRN models that use damping functions dependent on the turbulent Reynolds number, R_t, are more appropriate for predicting low-Reynolds-number transitions than those that only introduce a dependence on wall proximity. In addition, for some turbulent recirculating flows of engineering interest, e.g., low-velocity displacement ventilation flows, where laminar and transitional phenomena exist locally not only in near-wall regions but also in regions remote from the walls, using an LRN k-ϵ model often turns out unrealistic laminar solutions (Davidson, 1989).

In recent years, some new LRN two-equation models have been proposed as alternatives to the LRN k-ϵ models, e.g., the LRN k-τ model by Speziale et al. (1992). Wilcox has developed a standard two-equation k-ω model (Wilcox, 1988) and its LRN variant (Wilcox, 1994). The standard k-ω model has been validated for predicting boundary layer and free shear flows (Wilcox, 1988). Combining the standard k-ω model with the k-ϵ model, Menter (1994) developed two new models, and obtained predictions improved for adverse pressure gradient flows. Patel and Yoon (1995) used the standard k-ω model to solve separated flows over rough surfaces, and reported good accuracy. Abid et al. (1995) used the k-ω model in combination with an explicit algebraic stress model for recirculating flows, and obtained results in good agreement with experiments. Larsson (1996) applied the k-ω model to predictions of turbine blade heat transfer, and concluded that the k-ω model performs as well as or better than the k-ϵ model. Some other recent applications with the standard k-ω model can also be found, see e.g., Liu and Zheng (1994) and Huang and Bradshaw (1995). With both the wall-function method and the extended-to-wall method (integrating the model directly towards the wall surface), Peng et al. (1996b) recently applied the standard k-ω model to recirculating flows. It was found that this model overpredicted the reattachment length for the flow behind a backward-facing step with a large expansion ratio ($H/h = 6$).

With the LRN k-ω model, satisfactory results have been reported for simulating transitional boundary layer flows by means of the concept of numerical roughness strip (Wilcox, 1994). One of the attractive features of Wilcox's LRN model is that it uses damping functions that depend only on the turbulent Reynolds number, R_t. It is therefore convenient to apply this model to internal flows with complex geometries. Moreover, the k-ω model possesses a nontrivial laminar solution for ω as $k \to 0$. It can thus be expected to be able to capture flow characteristics for e.g. low-velocity displacement ventilation flows of which an LRN k-ϵ model fails to handle. However, the LRN k-ω model, as its standard form, yields significant inaccuracy in predictions for the flow over a large backward-facing step. Furthermore, this model does not reproduce correct asymptotic behavior for $-\overline{u'v'}$, with $-\overline{u'v'} \propto y^4$ as $y \to 0$. It has been argued that the correct wall-limiting condition for $-\overline{u'v'}$, as well as for ϵ, contributes to the improvement of predictions of by-pass transitions (Savill, 1995).

This paper presents an improved form of the LRN k-ω model. A turbulent cross-diffusion term is added to the modeled ω-equation, in analogy to its viscous counterpart in the exact transport equation. The model constants are re-established. New R_t-dependent damping functions are devised to make the model asymptotically consistent as the wall is approached. In addition, the mechanism for simulating boundary layer transitions is pre-

Contributed by the Fluids Engineering Division for publication in the Journal of Fluids Engineering. Manuscript received by the Fluids Engineering Division July 8, 1996; revised manuscript received May 5, 1997. Associate Technical Editor: P. M. Sockol.

served. The modified model is applied to channel flow, a backward-facing step flow with a large expansion ratio, and recirculating flow in a ventilation enclosure. The results are compared with DNS data, experimental data and predictions given by other LRN models. The effects due to the modification are discussed.

2 Development of the Modified k-ω Model

In the k-ω model, it is assumed that the turbulence is characterized by a velocity scale, $k^{1/2}$, and a length scale, $k^{1/2}/\omega$. The eddy viscosity is thus formulated as $\nu_t \sim k/\omega$. Wilcox termed ω as the specific dissipation rate of k, which is actually the reciprocal turbulent time scale, $1/\tau$. The transport equations for k and ω, together with the equations for continuity and momentum, form the mathematical description. In Wilcox's LRN k-ω model (1994), the k- and ω-transport equations are written as

$$\frac{\partial(\rho u_j k)}{\partial x_j} = P_k - c_k f_k \rho \omega k + \frac{\partial}{\partial x_j}\left[\left(\mu + \frac{\mu_t}{\sigma_k}\right)\frac{\partial k}{\partial x_j}\right] \quad (1)$$

$$\frac{\partial(\rho u_j \omega)}{\partial x_j} = c_{\omega 1} f_\omega \frac{\omega}{k} P_k - c_{\omega 2}\rho\omega^2 + \frac{\partial}{\partial x_j}\left[\left(\mu + \frac{\mu_t}{\sigma_\omega}\right)\frac{\partial \omega}{\partial x_j}\right] \quad (2)$$

P_k is the production of turbulence energy, and for incompressible flows takes the form

$$P_k = -\rho\overline{u_i' u_j'}\frac{\partial u_i}{\partial x_j} = \mu_t\left(\frac{\partial u_i}{\partial x_j} + \frac{\partial u_j}{\partial x_i}\right)\frac{\partial u_i}{\partial x_j} \quad (3)$$

With the Kolmogorov-Prandtl relation, the eddy viscosity, μ_t, is defined by

$$\mu_t = c_\mu f_\mu \frac{\rho k}{\omega} \quad (4)$$

In Wilcox's model, the closure constants are determined as $c_\mu = 1.0$, $c_k = 0.09$, $c_{\omega 1} = 0.56$, $c_{\omega 2} = 0.075$, $\sigma_k = \sigma_\omega = 2.0$, and the damping functions are

$$f_\mu = (0.025 + R_t/6)(1 + R_t/6)^{-1} \quad (5)$$

$$f_k = [0.278 + (R_t/8)^4][1 + (R_t/8)^4]^{-1} \quad (6)$$

$$f_\omega = (0.1 + R_t/2.7)[(1 + R_t/2.7)f_\mu]^{-1} \quad (7)$$

where R_t is the turbulent Reynolds number, and $R_t = k/(\omega\nu)$.

2.1 Near-Wall Asymptotic Behavior. In the vicinity of the wall, the fluctuating velocity components can be written with the Taylor series expansion as

$$u' = a_1 y + a_2 y^2 + \ldots \quad (8)$$

$$v' = b_2 y^2 + \ldots \quad (9)$$

$$w' = c_1 y + c_2 y^2 + \ldots \quad (10)$$

where a_i, b_i, and c_i are functions of x, z, t, and the coordinate y is normal to the wall.

With the aid of equations (8–10) and the definitions of k and ϵ, the asymptotic behavior of wall turbulence can be represented by the relations: $k \propto y^2$, $\epsilon \propto y^0$, $\mu_t \propto y^3$, $-\overline{u'v'} \propto y^3$, $P_k \propto y^3$ and $R_t \propto y^4$ as $y \to 0$. Note that $u^+ = y^+$ has been used near the wall and thus $(\partial u/\partial y) \propto y^0$. The specific dissipation rate ω can be expressed in terms of k and ϵ, i.e. $\omega \sim \epsilon/k$. This gives $\omega \propto y^{-2}$. From Eqs. (3) and (4), $f_\mu \propto y^{-1}$ is thus required to make the near-wall shear stress asymptotically consistent.

Close to the wall, the turbulent transport term is negligible in comparison to the dissipation and the viscous diffusion (Speziale et al., 1992). With the aid of DNS data, Mansour et al. (1989) further pointed out that the pressure diffusion term in the turbulent kinetic-energy budget remains negligibly small compared to the other terms. In the immediate wall proximity, Wilcox (1988) showed that the balance between the dissipation term and the molecular diffusion term holds in the equations for both k and ω, from which the asymptotic solutions for k and ω can be derived

$k \to cy^n$ as $y \to 0$, with

$$n = (1 + \sqrt{1 + 24 c_k f_k / c_{\omega 2}})/2 \quad (11)$$

and

$$\omega \to \frac{6\nu}{c_{\omega 2} y^2} \quad \text{as} \quad y \to 0 \quad (12)$$

From Eq. (12), it is apparent that $c_{\omega 2}$ must satisfy $c_{\omega 2} \propto y^0$, so as to keep the correct asymptotic behavior for ω. In equation (11), the damping function for coefficient c_k, i.e. f_k, should then asymptotically behave as $f_k \propto y^0$. Furthermore, the following relation is needed in order to ensure $k \propto y^2$

Nomenclature

c_k, c_ω, $c_{\omega 1}$, $c_{\omega 2}$ = turbulence model constants
f_μ, f_k, f_ω = damping functions of turbulence model
h = height of inlet
H = height of computational domain
k = turbulent kinetic energy
L_t = turbulent length scale
p = pressure
Re = inlet-based Reynolds number, $U_0 h/\nu$
Re_τ = Reynolds number, based on friction velocity, $u_\tau(H/2)/\nu$
R_t = turbulent Reynolds number
T = height of outlet
U_0 = inlet velocity
u_k = Kolmogorov velocity scale
u_m = mean velocity of channel flow
u_i = mean velocity component in direction x_i
u_τ = friction velocity, $(\tau_w/\rho)^{1/2}$
u', v', w' = fluctuating velocities in x, y, z directions, respectively
u^+ = dimensionless velocity, u/u_τ
W = height of backward-facing step
x_i = Cartesian space coordinate
x_r = reattachment length of backward-facing step flow
y^+ = dimensionless distance from wall surface, $u_\tau y/\nu$
ϵ = dissipation rate of k
η_k = Kolmogorov length scale
κ = von Kármán constant
μ = molecular dynamic viscosity
μ_t = turbulent dynamic viscosity
ν = kinematic viscosity, μ/ρ
ν_t = turbulent kinematic viscosity, μ_t/ρ
ρ = density of air
σ_k, σ_ω = model constants
τ = turbulent time scale
τ_w = wall shear stress
ω = specific dissipation rate of k

$$(c_k f_k)/c_{\omega 2} = 1/3 \quad \text{as} \quad y \to 0 \tag{13}$$

Since $D\omega/Dt = (1/k)(D\epsilon/Dt) - (\omega/k)(Dk/Dt)$, the exact ω-equation can readily be obtained from the exact k- and ϵ-equations (Speziale et al., 1992; Peng et al., 1996b)

$$\frac{\partial(\rho u_j \omega)}{\partial x_j} = \left(\frac{P_\epsilon}{k} - \frac{\omega P}{k}\right) + \left(\rho\omega^2 - \frac{\Pi_\epsilon}{k}\right) + \left(\frac{\omega D}{k} - \frac{D_\epsilon}{k}\right) + \left(\mu \frac{\partial^2\omega}{\partial x_j \partial x_j} + \frac{2\mu}{k}\frac{\partial\omega}{\partial x_j}\frac{\partial k}{\partial x_j}\right) \tag{14}$$

where P_ϵ, Π_ϵ and D_ϵ are the production, destruction and diffusive transport terms, respectively, in the exact ϵ-equation, while P and D are the production and diffusive transport terms in the exact k-equation. The exact production term for ω is $P_\omega = (P_\epsilon - \omega P)/k$, and $P_\epsilon \propto y$, $P \propto y^3$ as $y \to 0$. Therefore, $P_\omega \propto y^{-1}$ near the wall. Compared with the modeled production term in the ω-equation, this term will be asymptotically consistent if the damping function $f_\omega \propto y^0$ as $y \to 0$.

2.2 The Modified ω-Equation and Model Constants. In Wilcox's LRN model, the same model equations and constants are adopted as those in the standard k-ω model, but the inconsistent wall-limiting behavior of k is corrected by means of the damping functions. Wilcox's LRN model is capable of satisfactorily yielding the near-wall turbulence level for attached turbulent flows, e.g., channel flows. However, it is found in this study that the reattachment length is significantly overpredicted when this LRN model is applied to a separated flow over a backward-facing step with a large expansion ratio. To improve it, the ω-equation and the model constants need to be modified.

In analogy to its viscous counterpart, the turbulent diffusion term in the exact ω-equation (Eq. (14)) is modeled with two parts: a second-order diffusion term and a first-order cross-diffusion term. In the modeled ω-equation, however, the viscous cross-diffusion term has to be dropped to make the asymptotical solution of ω realizable as the wall is approached (Peng et al., 1996b). Otherwise, a negative ω value arises close to the wall unless $c_{\omega 2}$ is damped. Keeping the viscous cross-diffusion term, Speziale et al. (1992) showed that the near-wall asymptotical solution of ω will behave correctly if $c_{\omega 2}$ takes the form of $c_{\omega 2} = (\text{constant} \cdot f_2 - 1)$, where f_2 is a damping function and $f_2 \propto y^2$ as $y \to 0$. This decomposition, however, will destroy the mechanism preserved in the model for transition simulation according to Wilcox (1994). With the LRN k-ω model, the closure constants have been established to ensure that the production of k is amplified earlier than that of ω. This is an essential condition for the k-ω model to account for transition from laminar to turbulence. This condition consequently requires that a relation, as given by Eq. (17a) in Section 2.3, must be held for the coefficients of the production and dissipation terms in the k- and ω-equation. It is obvious that the above decomposition of $c_{\omega 2}$ does not satisfy this relation. Instead of damping $c_{\omega 2}$, we feel that it is more practical to preserve the mechanism for transition simulation in the modified model as well as in Wilcox's model by dropping the viscous cross-diffusion term. The modified ω-equation then takes the following form

$$\frac{\partial(\rho u_j \omega)}{\partial x_j} = c_{\omega 1} f_\omega \frac{\omega}{k} P_k - c_{\omega 2}\rho\omega^2 + \frac{\partial}{\partial x_j}\left[\left(\mu + \frac{\mu_t}{\sigma_\omega}\right)\frac{\partial\omega}{\partial x_j}\right] + c_\omega \frac{\mu_t}{k}\left(\frac{\partial k}{\partial x_j}\frac{\partial\omega}{\partial x_j}\right) \tag{15}$$

Compared to the original ω-equation in Wilcox's model (Eq. (2)), an additional turbulent cross-diffusion term is included in Eq. (15). Note that the inclusion of this term makes the present model somewhat similar to the k-ϵ model, since a similar turbulent cross-diffusion term can be reproduced by transforming the modeled ϵ-equation into an ω-equation.

In order to eliminate the sensitivity of the k-ω model to the freestream value of ω when solving free shear flows, Menter (1992) has proposed an ω-equation similar to equation (15). A so-called "blending function" is used to determine c_ω. As a result, the turbulent cross-diffusion term disappears close to the wall surface, while being switched on in regions away from the solid boundaries. This approach becomes particularly functional when approaching the shear layer edge of a free shear flow. Wilcox (1993) has also given a simple and straightforward proposal that is nearly identical to Menter's blending function. When applying either Menter's or Wilcox's approach to internal recirculating flows, however, the role played by the cross-diffusion term in the ω-equation is negligibly small, since the gradients for both k and ω often tend to vanish in regions away from walls. These approaches then possess a behavior similar to Wilcox's standard model for internal recirculating flows. In contrast to both Menter's and Wilcox's approaches, the present modification, initiated from the exact ω-equation, makes the cross-diffusion term generalized in both near-wall and far-wall regions. Close to the wall, the gradients of k and ω are often of opposite sign. The turbulent cross-diffusion term as a whole reduces ω and thus raises k near the wall, as desired.

With the ϵ-equation derived from the original k-ω model (i.e., from Eqs. (1) and (2)), Wilcox (1993) has shown that an extra cross-diffusion term appears in the resultant ϵ-equation. This term, similar to the so-called "Yap correction", helps to suppress the rate of increase of the near-wall turbulent length scale, which is often overpredicted by the k-ϵ model for wall-bounded flows in the presence of adverse pressure gradient. When using the modified ω-equation (Eq. (15)), it is easy to show that a similar cross-diffusion term retains in the resultant ϵ-equation, only if $c_\omega < (1/\sigma_k + 1/\sigma_\omega)$. The effect of the turbulent cross-diffusion term on the turbulent length scale will be further discussed in Section 3, by investigating its distribution near the wall and its effects on the turbulent length scale near the reattachment zone for a separated flow.

It is desirable, for an LRN model, to adopt the same model constants as used in its high-Re-number form (the parent model). The closure constants for the high-Re-number form of the present LRN model were evaluated and discussed in a previous work (Peng et al., 1996b). For fully developed turbulence, the model constants were re-established as

$$c_\mu = 1.0, \quad c_k = 0.09, \quad c_{\omega 1} = 0.42, \quad c_{\omega 2} = 0.075, \quad c_\omega = 0.75, \quad \sigma_k = 0.8, \quad \sigma_\omega = 1.35 \tag{16}$$

2.3 Damping Functions. In order not to violate the mechanism for describing transitions contained in the k and ω equations, the following relations are required (Wilcox, 1994)

$$c_{\omega 1} f_\omega c_\mu f_\mu < c_{\omega 2} \quad \text{as} \quad R_t \to 0 \tag{17a}$$

$$(c_k f_k)/(c_\mu f_\mu) \to 1 \quad \text{as} \quad R_t \to 0 \tag{17b}$$

Equations (17a) and (17b), together with Eq. (13), form the lower bound when determining the model constants for viscous modification as the wall is approached ($y \to 0$ or $R_t \to 0$). Equation (16) gives the upper bound of the model constants for fully developed turbulence as $R_t \to \infty$. The coefficient $c_{\omega 1}$, as $R_t \to \infty$, is re-evaluated in the predictions of the reattachment length for backward-facing step flow. For local-equilibrium wall-turbulent flows, this coefficient must also satisfy

$$c_{\omega 1} = \frac{c_{\omega 2}}{c_k} - \frac{\kappa^2}{\sigma_\omega \sqrt{c_k c_\mu}} \tag{18}$$

To make numerical implementation convenient for internal flows with complex geometries, the turbulent Reynolds number,

R_t, is used as the only dependent variable in the damping functions.

In view of the above discussion, the following model functions are proposed

$$f_\mu = 0.025 + \left\{1 - \exp\left[-\left(\frac{R_t}{10}\right)^{3/4}\right]\right\} \times \left\{0.975 + \frac{0.001}{R_t}\exp\left[-\left(\frac{R_t}{200}\right)^2\right]\right\} \quad (19)$$

$$f_k = 1 - 0.722\exp\left[-\left(\frac{R_t}{10}\right)^4\right] \quad (20)$$

$$f_\omega = 1 + 4.3\exp\left[-\left(\frac{R_t}{1.5}\right)^{1/2}\right] \quad (21)$$

As the wall is approached, applying the Taylor series expansion to Eq. (19) gives $f_\mu \sim (1/R_t^{0.25} + \ldots)$, which complies with the correct asymptotic condition $f_\mu \propto y^{-1}$. Furthermore, using Eq. (4) gives

$$\mu_t \sim (k/\omega)R_t^{-1/4} \sim L_t u_k \quad (22)$$

where $L_t \sim k^{1/2}/\omega$ is the turbulent length scale, and u_k is the Kolmogorov velocity scale, $u_k \sim (\nu k\omega)^{1/4}$. Equation (22) thus suggests that the near-wall eddy viscosity is determined by the small-scale eddies. The turbulent length scale, L_t, is proportional to y^3 as the wall is approached, and thus decreases towards the wall surface. As L_t approaches the Kolmogorov length scale, $\eta_k \sim (\nu^3/k\omega)^{1/4}$, the eddy viscosity is reduced to the same order as the molecular viscosity. This is consistent with the analysis of Kolmogorov behavior in near-wall turbulence by Shih and Lumley (1993). With the present proposal, the turbulent effect is therefore suppressed by damping the turbulent velocity scale as the wall is approached.

With the damping functions in Eqs. (19–21), the asymptotic behavior in the modified model is consistently satisfied for near-wall turbulence, and the mechanism of simulating transitions, contained in the k- and ω-equations, is preserved.

3 Application of the Model

In this section, the present model is first applied to a fully developed channel flow, and the results are compared with DNS data. Two internal recirculating flows are then solved: the separated flow over a backward-facing step with a large expansion ratio, and the flow in a confined ventilation enclosure, see Figs. 1(a) and 1(b). The predictions are compared with experimental data. The effects of the modification are discussed.

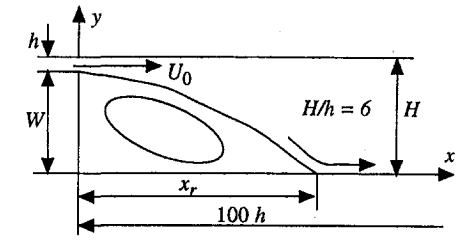

Fig. 1(a) Backward-facing step

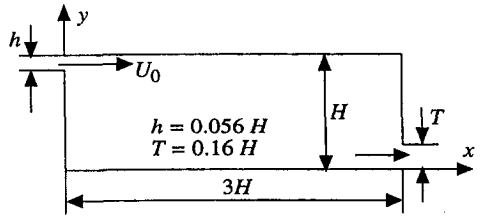

Fig. 1(b) Confined ventilation enclosure

Fig. 1 Configurations for the computed recirculating flows

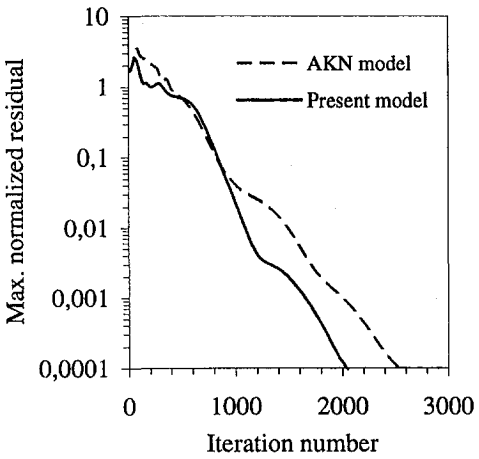

Fig. 2 Typical convergence procedure when solving for the flow in the ventilation enclosure

3.1 Numerical Procedure. The numerical procedure can affect the results of turbulence models. Attention was thus paid to the numerics so as to make the model appraisal meaningful. The calculation was performed with a finite-volume-based computer program (Davidson and Farhanieh, 1992). The third-order QUICK scheme (Leonard, 1979) was used for the convection terms in the momentum equations, and the hybrid upwind/central differencing scheme (Patankar, 1980) was employed in the turbulence-transport equations to ensure a stable solution procedure. The other terms were discretized with the second-order central difference. A collocated grid was used with the aid of Rhie-Chow interpolation (Rhie and Chow, 1983) to avoid non-physical oscillation. The SIMPLEC algorithm was used to handle the pressure-velocity coupling. When solving the discrete algebraic equation for ω, the turbulent cross-diffusion term was added to the right-hand side if it was positive, otherwise to the left-hand side to increase the diagonal dominance for the resulting coefficient matrix.

The iterative solution process was considered to be converged when the sum of absolute cell residuals for each equation, normalized by the respective inlet fluxes, was less than 10^{-4}. When solving the ventilation flow in Fig. 1(b) with the present model and the LRN k-ϵ model by Abe et al. (1994; AKN model), respectively, a typical convergence procedure is shown in Fig. 2, where the normalized residual is plotted versus the iteration number. A faster convergence is shown with the k-ω model. This has also been pointed out earlier by Peng et al. (1996b).

The boundary condition at the inlet was prescribed for all the variables. At the outlet, the streamwise derivatives of the flow variables were assumed to be zero. For the flow in the two-dimensional ventilation enclosure, the velocity component normal to the outlet was specified from global mass conservation. At the wall, $u = v = 0$ and $k = 0$. Equation (12) was used at the near-wall first grid point as the boundary condition of ω.

Adopting the asymptotical solution of ω as the boundary condition requires a very fine grid close to the wall. Extensive tests were made to establish the grid mesh. The grid was nonuniformly distributed, and controlled by the ratio of two successive cells, i.e. $\lambda = \Delta_{i+1}/\Delta_i$. The grid dependence was investigated by varying both λ and the number of mesh points. Various grids were tested for each case considered in this study. The relative difference, R_ϕ, between the solutions yielded with different grids was checked. It is required to be sufficiently small to

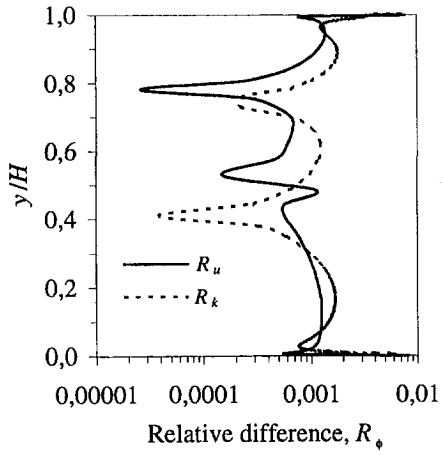

Fig. 3 Evaluation of the relative difference of solutions with two grids (102 × 132 and 204 × 264) for the flow in the ventilation enclosure (at $x = 2H$)

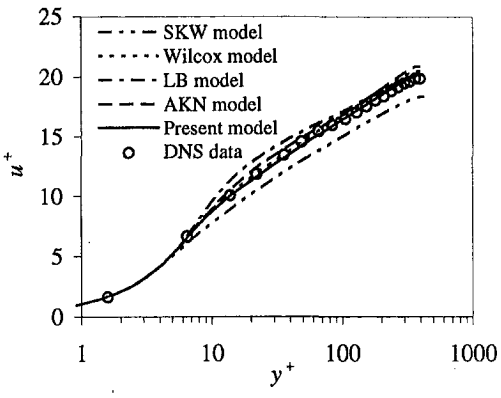

Fig. 4(*a*) Mean velocity

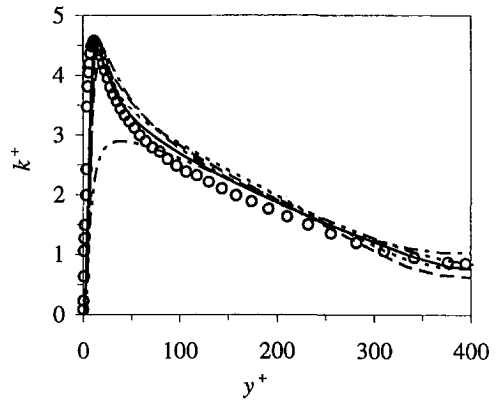

Fig. 4(*b*) Turbulent kinetic energy

Fig. 4 Predictions for turbulent channel flow at $Re_\tau = 395$ (Re = 13750)

minimize the dependence of the solution on the grid used. For the flow in the confined ventilation enclosure, the relative differences for u and k at $x = 2H$, i.e., R_u and R_k, respectively, are shown in Fig. 3 as an example to demonstrate the grid dependence. The solutions used for estimating R_u and R_k in Fig. 3 were obtained with two grids of 102 × 132 and 204 × 264. The solution hardly varies with refining grid when the grid used has already been sufficiently fine. Using $\lambda = 1.05$ for a channel flow, Yang and Shih (1993) showed that the solutions were almost identical as the cross-stream mesh points varied from 30 to 150. For the channel flow considered here, 100 cross-stream grid points were used. It was found that the results became rather insensitive to the number of the mesh points as long as there were two or more points arranged in $y^+ < 1$. This has also been observed by Yang and Shih (1993). A 202 × 86 mesh was used when solving the backward-facing step flow, and 102 × 132 grid points were used to calculate the recirculating flow in the ventilation enclosure. In general, two or more points were located within the range of $y^+ < 1$. For all the flows considered here, numerical tests disclosed that nearly grid-independent solutions were reached.

3.2 Fully Developed Channel Flow. To assess the modified model, the channel flow at $Re_\tau = 395$ was first solved. The results were compared with both the DNS data (Kim, 1990) and the predictions obtained with other LRN models, including the Lam-Bremhorst k-ϵ model (LB model; Lam and Bremhorst, 1981), the Abe-Kondoh-Nagano k-ϵ model (AKN model; Abe et al., 1994) and Wilcox's LRN k-ω model (Wilcox model; Wilcox, 1994). Wilcox's standard k-ω model (SKW model; Wilcox, 1988) was also included in the comparison, since this model can be used by integrating it directly to the wall surface without using the wall function as a bridge (termed here the *extended-to-wall* method).

Figure 4 shows the distributions of mean velocity and turbulent kinetic energy. The near-wall maximum (peak) values for k^+, as well as the friction velocity u_τ, are compared in Table 1. The present model shows reasonable agreement with the DNS data. Both Wilcox's and the present LRN models predict satisfactory profiles for the mean velocity and the turbulent kinetic energy, particularly in the near-wall region. The present model shows acceptable abilities for accommodating the near-wall low-Reynolds-number effect for attached turbulent flows.

When using Wilcox's standard k-ω model (the SKW model) with the extended-to-wall method, the result gives rise to the largest error, compared to the DNS data. This model considerably underpredicts the near-wall peak value of k. The SKW model also overpredicts the wall shear stress (and thus u_τ, see Table 1). The u^+-profile deteriorates in the far-wall region because u_τ is overpredicted, though the non-normalized mean velocity predicted there is actually in reasonable agreement with the DNS data. The dissatisfactory predictions for near-wall turbulence imply that the SKW model cannot satisfactorily account for near-wall viscous effects. It is therefore inappropriate to integrate this model directly towards the wall surface. However, when the extended-to-wall method was applied to internal recirculating flows with the *standard* form of the present model, i.e. with the damping functions set to unity, reasonable predictions were obtained, particularly for the mean flow profiles (Peng et al., 1996b). By using the SKW model with the extended-to-wall method, satisfactory simulations have been reported in other engineering applications, e.g., by Wilcox (1988), Patel and Yoon (1995), Menter (1994), and Liu and Zheng (1994).

The addition of the turbulent cross-diffusion term enhances the diffusion of ω. To make the diffusion of k compatible, it is thus necessary to set $\sigma_k < \sigma_\omega$, see Eq. (16). This also improves the near-centerline predictions, where the dissipations of both k and ω are mainly balanced by their diffusions, with the production terms negligible.

3.3 Backward-Facing Step Flow. The separated flow over a high backward-facing step ($H/h = 6$, see Fig. 1(*a*)) is particularly relevant to ventilation flows (Restivo, 1979), which

Table 1 u_τ and near-wall maximum (peak) k^+-value for channel flow at $Re_\tau = 395$

Model	AKN	LB	Wilcox	SKW	Present	DNS
u_τ/u_m	0.0557	0.0560	0.0562	0.0621	0.0574	0.0571
k^+	4.21	4.51	4.52	2.90	4.48	4.58

Table 2 Comparison of the predicted reattachment length, x_r

Measured data	AKN model	Wilcox model	Present model
6.12W	6.60W	8.24W	6.40W

are usually induced by a wall-jet below the ceiling to create recirculating and mixing air motions. It has therefore been widely used in validations of turbulent models for predicting recirculating ventilation flows (Restivo, 1979; Skovgaard, 1991). With the experimental data available (Restivo, 1979), the flow at Re = 5050 is calculated here.

The reattachment lengths computed with different LRN models are compared in Table 2. Wilcox's LRN model considerably overpredicts the reattachment length by nearly thirty-five percent. By contrast, the modified model is capable of yielding an x_r whose error is less than five percent. By assuming the damping functions to be unity in the modified model, i.e. by using its standard form, a satisfactory result was also predicted with either the wall-function method or the extended-to-wall method (Peng et al., 1996b).

The reattachment length, x_r, is very sensitive to the coefficient $c_{\omega 1}$. It was found that x_r changes by about 1.4 times the step height, with a variation of 0.1 for $c_{\omega 1}$. The turbulent cross-diffusion term alters x_r by about ten percent. This suggests that the modified constant $c_{\omega 1}$, together with the damping function f_ω, plays a main role in raising k by suppressing the production of ω to improve the prediction of x_r.

Figure 5 shows the distributions of the mean streamwise velocity and the turbulent kinetic energy at five positions (x/h = 5, 10, 15, 20, 30). The largest error in the prediction of reattachment length corresponds to the largest inaccuracy in the prediction of velocity with the original model, which unrealistically keeps predicting a too-high velocity peak in the wall-jet along the upper wall. All the models predict reasonable and similar velocity distributions in the far-wall recirculating region. Near the step and close to the lower wall (at x/h = 5 and 10), the AKN model under-estimates the mean velocity. The AKN model also predicts a slightly higher velocity peak in the wall-jet than the present model does. As the flow approaches the reattachment position (near x/h = 30), the Wilcox model fails to capture the mean flow property.

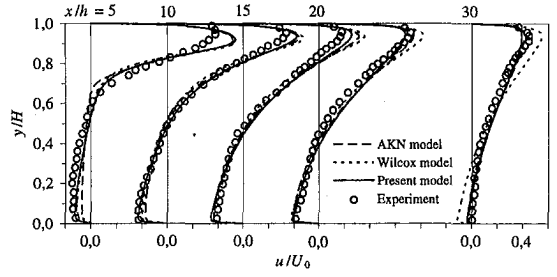

Fig. 5(*a*) Mean streamwise velocity

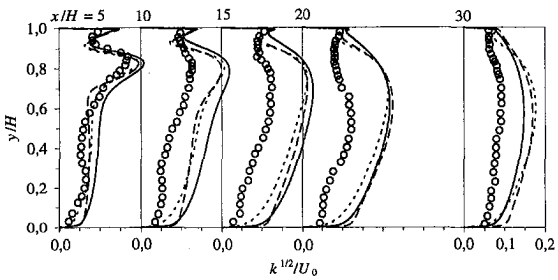

Fig. 5(*b*) Turbulent kinetic energy

Fig. 5 Distributions calculated for the flow over a backward-facing step (the experimental data used in the comparison of k are for $\sqrt{u'^2}/U_0$)

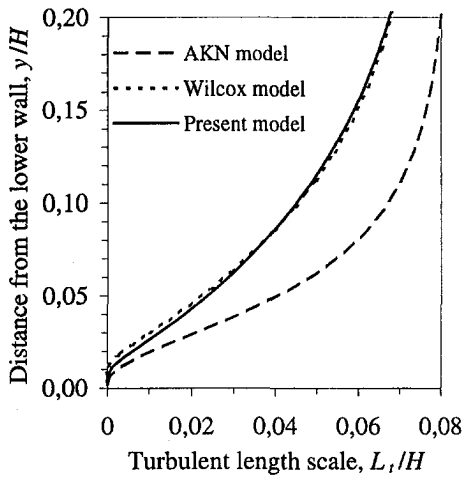

Fig. 6 Predicted turbulent length scales near the lower wall of the backward-facing step at x = 30h

Note that the measured data for $\sqrt{u'^2}$ have been used for comparison of k in Fig. 5. The turbulent kinetic energy computed by all three models is higher than the measured turbulence level. With the Launder-Sharma LRN k-ϵ model, similar predictions have been reported by Skovgaard (1991). For other backward-facing step flows, the predicted maximum value of k has usually been in a range of $(0.02 \sim 0.04)U_0^2$ near the reattachment position, see e.g., Abe et al. (1994). The same can be found in Fig. 5 from the predicted distributions of k near the reattachment zone (x/h = 30). In contrast to other backward-facing step flows, however, the measured $\sqrt{u'^2}$ data for the flow situation considered here are much smaller. In a recent calculation (not included here) the present model was applied to the backward-facing step flow with a lower expansion ratio of H/h = 1.2. In comparison with DNS data (Le et al., 1993), it was found that the present model improved significantly the prediction over Wilcox's original model, particularly for the turbulence kinetic energy.

To further explore the influence of the turbulent cross-diffusion term, the turbulent length scales, L_t, predicted with various models near the reattachment position (x = 30h), are compared in Fig. 6. L_t has been evaluated by means of relations: $L_t = C_\mu f_\mu k^{1/2}/\omega$ for the k-ω model and $L_t = C_\mu f_\mu k^{3/2}/\epsilon$ for the k-ϵ model. The present model yields a turbulent length scale very close to that given by Wilcox's model, and the AKN model predicts the largest L_t in the region near the lower wall. It is known that Wilcox's model performs well for boundary layers with adverse pressure gradient (Wilcox, 1994), because this model possesses the same effect as of the Yap correction used often in the k-ϵ model. The Yap correction was originally invented to suppress the turbulent length scale in the reattachment zone after a sudden pipe expansion (Yap, 1987). The result in Fig. 6 suggests that the addition of the turbulent cross-diffusion term does not change the behavior retaining in Wilcox's model for predicting the turbulent length scale near the reattachment zone for separated flows.

3.4 Recirculating Flow in a Ventilation Enclosure. The flow through a two-dimensional ventilation enclosure (see Fig. 1(*b*)) is similar to the recirculating flow behind a backward-facing step, but with a nearly closed end opposite the inlet. The recirculation in the enclosure depends on the depth reached by the wall-jet, and thus relies on the inlet-based Reynolds number. The present calculations were carried out for the flow at Re = 5000, where experimental data are available.

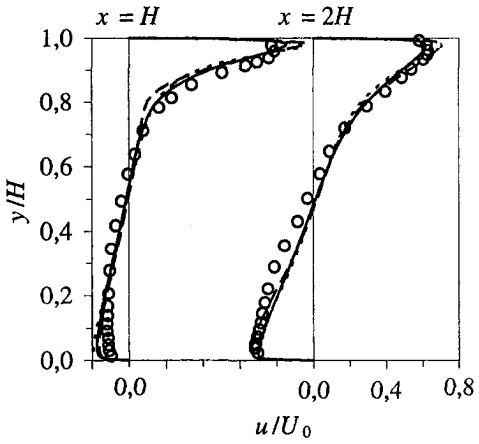

Fig. 7(*a*) Mean streamwise velocity (at $x = H$ and $x = 2H$)

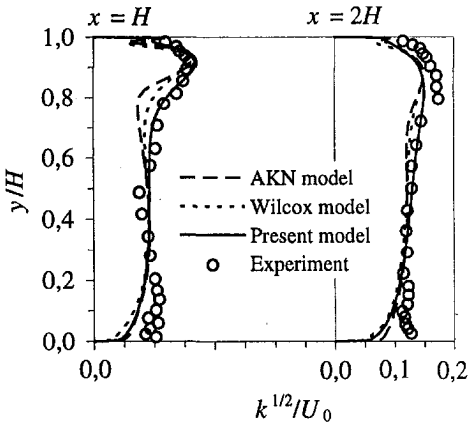

Fig. 7(*b*) Turbulent kinetic energy (at $x = H$ and $x = 2H$)

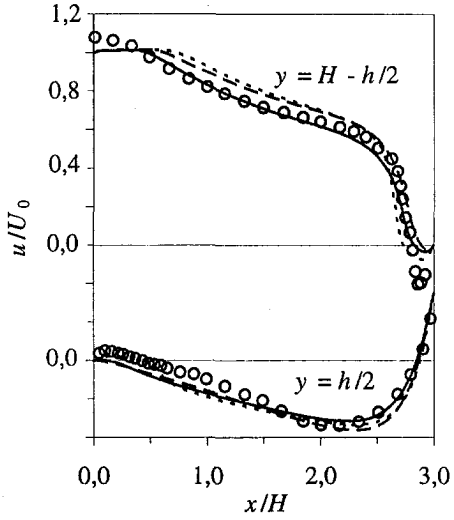

Fig. 7(*c*) Mean streamwise velocity (at $y = h/2$ and $y = H - h/2$)

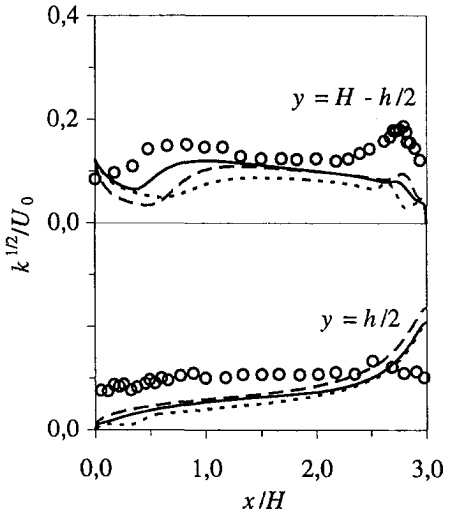

Fig. 7(*d*) Turbulent kinetic energy (at $y = h/2$ and $y = H - h/2$)

Fig. 7 Distributions calculated for the flow in the ventilation enclosure (the experimental data used in the comparison of k are for $\sqrt{u'^2}/U^0$)

In Fig. 7, the calculated distributions are compared with the experimental data of Restivo (1979). In general, the present model gives improved predictions for both the mean streamwise velocity and the turbulent kinetic energy. Wilcox's model and the AKN model overpredict the velocity peak, and under-estimate the near-wall turbulence level in the wall-jet. Near the floor, there is no large variation in the results (see the distributions at $x = H$ and $x = 2H$). At the edge of the wall-jet, however, the turbulent kinetic energy, which is underpredicted by both the AKN model and Wilcox's model, is enhanced by the present model. The enhancement of the turbulent kinetic energy is partly due to the addition of the turbulent cross-diffusion term. This term increases the velocity scale in the near-wall region by reducing the near-wall specific dissipation rate when the gradients of k and ω are of opposite sign, which often holds in regions close to the wall. The constant $c_{\omega 1}$ also makes contributions to the increment of k by reducing the generation of ω, since this constant is decreased comparing to that in Wilcox's model.

On the one hand, it is desired to enhance the near-wall turbulent kinetic energy that is under-estimated by the original LRN model. On the other hand, as the principal aspect for any LRN models, the turbulence level close to the wall needs to be suppressed so as to accommodate viscous effects. This means that an *equilibrium* between the two contrary requirements, damping the turbulent effect and enhancing the turbulent kinetic energy in the near-wall region, must be properly achieved. The present model seems to achieve this equilibrium, and is capable of yielding improved predictions when applied to the recirculating flow considered.

To further investigate the influence of the turbulent cross-diffusion term, we devised an additional group of damping functions and model constants when the turbulent cross-diffusion term was dropped in the ω-equation. These closure functions and constants were capable of yielding reasonable predictions for both channel and backward-facing step flows. However, it was found that the velocities predicted in the wall-jet and near the floor were unsatisfactory (not shown here). Indeed, the model preserves the wall-jet better with the turbulent cross-diffusion term than without it. In the wall-jet, with increasing wall distance, the turbulent kinetic energy k increases in the immediate proximity of the ceiling, then decreases close to the maximum velocity where $\partial u/\partial y \to 0$, before it increases again in the outer shear layer (see Figs. 7(*a*) and 7(*b*)). The gradient of k thus changes sign in the wall-jet. Accordingly, the contribution of turbulent-cross diffusion can be either positive or negative across the wall-jet, depending on the change in ω. The largest contribution, usually, occurs in the immediate proximity of the wall, where the gradients for both k and ω are rather large and of opposite sign. Figure 8 shows that the addition of the cross-diffusion term in the modified model, together with the decreased coefficient $c_{\omega 1}$, in general, reduces ω in the wall-jet. Compared to Wilcox's model, the modified model thus gives a higher eddy viscosity there. This, in turn, enhances the

turbulent diffusion for the momentum, and predicts a lower and wider velocity peak in the wall-jet (Fig. 7(*a*)), as desired.

A more detailed investigation was conducted by analyzing the budget of the ω-equation to clarify the contribution of each term. Figure 9 illustrates the budget of the ω-equation in both Wilcox's and the modified models in the wall-jet at sections $x = 2H$ and $y = H - h/2$, respectively. The modification makes each term redistribution. The near-wall change in the turbulent cross-diffusion term across the wall-jet is consistent with the above analysis. Figure 9(*a*) shows that the contribution of this term is limited mainly in the inner region of the wall-jet where the large gradients exist for both k and ω. Compared with Wilcox's model, all the terms in the modified model have been reduced near the wall surface, particularly the generation and destruction terms.

4 Conclusions

A modified form of Wilcox's two-equation LRN k-ω model is proposed for predicting internal recirculating flows. The modifications include adding a turbulent cross-diffusion term in the ω-equation, and re-establishing the closure constants and damping functions. The modified model reproduces correct near-wall asymptotic behaviors, and leads to improvements in the prediction of recirculating flows.

The turbulent cross-diffusion term in the ω-equation plays a role in the near-wall region. By altering the specific dissipation rate close to the wall, this term affects the prediction of the near-wall turbulence level, and thus of the eddy viscosity and momentum. The role played by this term depends on the sign of the gradients for both k and ω, and is usually limited in the region close to the wall. In general, this term reduces ω and enhances k near the wall, since the gradients there are often of opposite sign. The addition of this term helps to improve the model performance for the wall-jet inducing recirculation in an enclosure, where the original model underpredicts the near-wall turbulent kinetic energy.

In addition, it is well known that the k-ϵ model returns too high turbulent viscosity due to over-estimated turbulent length scale for flows with adverse pressure gradient (Launder, 1992), whereas Wilcox's standard k-ω model performs well (Wilcox, 1988). The present model has shown a reasonable ability to simulate the separated recirculating flows considered. The addition of the turbulent cross-diffusion term shows negligible influences on the turbulent length scale near the reattachment zone. On the other hand, this term is able to reduce the model's sensitivity to the freestream value of ω when solving free shear flows. Nonetheless, it is necessary to further validate this model in predictions of adverse-pressure-gradient boundary layer flows in future work.

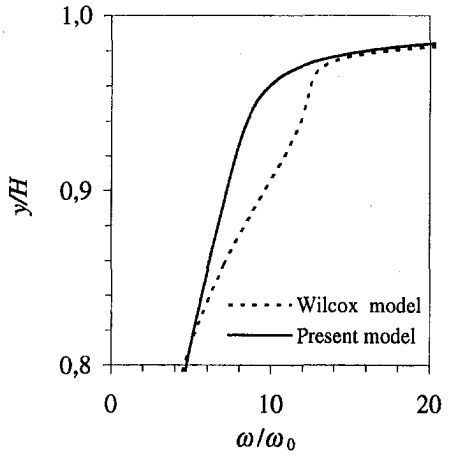

Fig. 8 Comparison of near-wall distributions of ω at $x = 2H$ ($\omega_0 = U_0/H$)

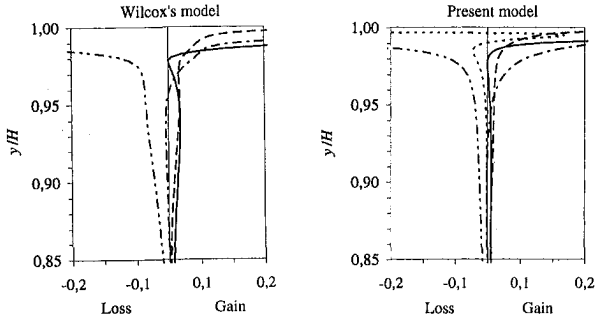

Fig. 9(*a*) Terms in the budget of ω-equation at $x = 2H$

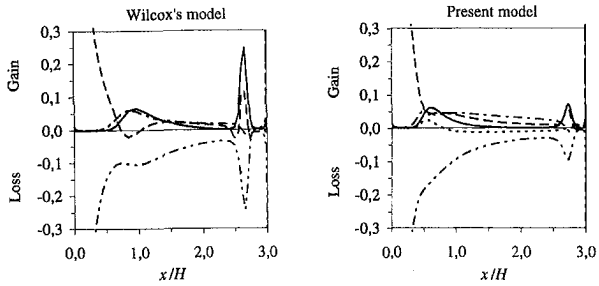

Fig. 9(*b*) Terms in the budget of ω-equation at $y = H - h/2$

Fig. 9 Comparison of the near-wall budget of the ω-equation in Wilcox's model and present model. — — — convection, ——— production, — . . — destruction, — . — . diffusion, ... turbulent cross-diffusion

The calculation of channel flow shows that the new damping functions are able to properly reflect the near-wall low-Reynolds-number effect for attached turbulent flows. For the separated and recirculating flows considered, the damping functions, together with the other modifications, show a satisfactory ability to account for an equilibrium between damping the near-wall turbulence and enhancing the near-wall turbulent kinetic energy underpredicted by Wilcox's original model. The present model appears to be an effective LRN two-equation closure for predicting recirculating flows.

With the new damping functions, moreover, the mechanism describing transitions is preserved in the modified model. It can therefore be used for simulating transitions in boundary layers, as with Wilcox's LRN model.

In future work, this model will be further applied to 3D low-velocity and buoyancy-influenced recirculating flows of engineering interest, such as ventilation flows, where the existing LRN k-ϵ models fail to produce reasonable predictions. The model also needs to be validated for transition simulations of boundary layer flows.

Acknowledgment

The authors are grateful to the referees for their helpful comments.

References

Abe, K., Kondoh, T., and Nagano, Y., 1994, "A New Turbulence Model for Predicting Fluid Flow and Heat Transfer in Separating and Reattaching Flows—I: Flow Field Calculations," *International Journal of Heat and Mass Transfer,* Vol. 37, pp. 139–151.

Abid, R., Rumsey, C., and Gatski, T., 1995, "Prediction of Non-equilibrium Turbulent Flows with Explicit Algebraic Stress Models," *AIAA Journal,* Vol. 33, pp. 2026–2031.

Davidson, L., 1989, "Ventilation by Displacement in a Three-Dimensional Room: A Numerical Study," *Building and Environment,* Vol. 24, pp. 263–272.

Davidson, L., and Farhanieh, B., 1992, "CALC-BFC: A Finite-Volume Code Employing Collocated Variable Arrangement and Cartesian Velocity Components

for Computation of Fluid Flow and Heat Transfer in Complex Three-Dimensional Geometries," Report 92/4, Dept. of Thermo and Fluid Dynamics, Chalmers University of Technology, Gothenburg.

Huang, P. G., and Bradshaw, P., 1995, "Law of the Wall for Turbulent Flows in Pressure Gradients," *AIAA Journal,* Vol. 33, pp. 624–632.

Kim, J., 1990, "The Collaborative Testing of Turbulence Models (Organized by Bradshaw et al.)," Data Disk No. 4.

Lam, C. K. G., and Bremhorst, K., 1981, "A Modified Form of the k-ϵ Model for Predicting Wall Turbulence," ASME JOURNAL OF FLUIDS ENGINEERING, Vol. 103, pp. 456–460.

Larsson, J., 1996, "Numerical Simulation of Turbine Blade Heat Transfer," Lic. Thesis, Report 96/4, Dept. of Thermo and Fluid Dynamics, Chalmers University of Technology, Gothenburg.

Launder, B. E., and Spalding, D. B., 1974, "The Numerical Computation of Turbulent Flows," *Computer Methods in Applied Mechanics and Engineering,* Vol. 3, pp. 269–289.

Launder, B. E., 1992, "On the Modeling of Turbulent Industrial Flows," *Proceedings of Computational Methods in Applied Sciences,* Ch. Hirsch et al., eds., Elsevier, pp. 91–102.

Le, H., Moin, P., and Kim, J., 1993, "Direct Numerical Simulation of Turbulent Flow Over a Backward-Facing Step," *Proceedings of 9th Symposium on Turbulent Shear Flows,* Kyoto, Japan, 13.2.1–13.2.6.

Leonard, B. P., 1979, "A Stable and Accurate Convective Modeling Procedure Based on Quadratic Upstream Interpolation," *Computer Methods in Applied Mechanics and Engineering,* Vol. 19, pp. 59–98.

Liu, F., and Zheng, X., 1994, "Staggered Finite Volume Scheme for Solving Cascade Flow with a k-ω Turbulence Model," *AIAA Journal,* Vol. 32, pp. 1589–1596.

Mansour, N. N., Kim, J., and Moin, P., 1989, "Near-Wall k-ϵ Turbulence Modeling," *AIAA Journal,* Vol. 27, pp. 1068–1073.

Menter, F. R., 1992, "Improved Two-Equation k-ω Turbulence Models for Aerodynamic Flows," NASA TM-103975.

Menter, F. R., 1994, "Two-Equation Eddy Viscosity Turbulence Models for Engineering Applications," *AIAA Journal,* Vol. 32, pp. 1598–1604.

Patankar, S. V., 1980, *Numerical Heat Transfer and Fluid Flow,* McGraw-Hill, Washington.

Patel, V. C., Rodi, W., and Scheuerer, G., 1984, "Turbulence Models for Near-Wall and Low Reynolds Number Flows: A Review," *AIAA Journal,* Vol. 23, pp. 1308–1319.

Patel, V. C., and Yoon, J. Y., 1995, "Application of Turbulence Models to Separated Flow Over Rough Surfaces," ASME JOURNAL OF FLUIDS ENGINEERING, Vol. 117, pp. 234–241.

Peng, S-H., Davidson, L., and Holmberg, S., 1996a, "A Modified Low-Reynolds-Number k-ω Model for Internal Flows in Ventilated Enclosures," Report 96/23, Dept. of Thermo and Fluid Dynamics, Chalmers University of Technology, Gothenburg.

Peng, S-H., Davidson, L., and Holmberg, S., 1996b, "The Two-Equation Turbulence k-ω Model Applied to Recirculating Ventilation Flows," Report 96/13, Dept. of Thermo and Fluid Dynamics, Chalmers University of Technology, Gothenburg.

Restivo, A., 1979, "Turbulent Flow in Ventilation Rooms," Ph.D. Thesis, University of London.

Rhie, C. M., and Chow, W. L., 1983, "Numerical Study of the Turbulent Flow Past an Airfoil With Trailing Edge Separation," *AIAA Journal,* Vol. 21, pp. 1525–1532.

Savill, A. M., 1995, "One-Point Closures Applied to Transition," in ERCOFTAC Series Vol. 2 *Turbulence and Transition Modeling,* pp. 233–268, M. Hallbäck et al., eds., Kluwer Academic Publishers.

Shih, T. H., and Lumley, J. L., 1993, "Kolmogorov Behavior of Near-Wall Turbulence and Its Application in Turbulence Modelling," *International Journal of Computational Fluid Dynamics,* Vol. 1, pp. 43–56.

Skovgaard, M., 1991, "Turbulent Flow in Rooms Ventilated by the Mixing Principle: Comparisons between Computational Fluid Dynamics and Full-Scale Experiments," Ph.D. thesis, Department of Building Technology and Structural Engineering, Aalborg University, Aalborg.

Speziale, C. G., Abid, R., and Anderson, E. C., 1992, "Critical Evaluation of Two-Equation Models for Near-Wall Turbulence," *AIAA Journal,* Vol. 30, pp. 324–331.

Wilcox, D. C., 1988, "Reassessment of the Scale-Determining Equation for Advanced Turbulence Models," *AIAA Journal,* Vol. 26, pp. 1299–1310.

Wilcox, D. C., 1993, Turbulence Modeling for CFD, DCW Industries, Inc. CA.

Wilcox, D. C., 1994, "Simulation of Transition with a Two-Equation Turbulence Model," *AIAA Journal,* Vol. 32, pp. 247–255.

Yang, Z., and Shih, T. H., 1993, "New Time Scale Based k-ϵ Model for Near-Wall Turbulence," *AIAA Journal,* Vol. 31, pp. 1192–1198.

Yap, C., 1987, "Turbulent Heat and Momentum Transfer in Recirculating and Impinging Flows," Ph.D. thesis, Faculty of Technology, University of Manchester.

Eddy Viscosity Transport Equations and Their Relation to the k-ϵ Model

F. R. Menter[1]
Head, Development Department,
AEA Technology GmbH,
Staudenfeldweg, 83624 Otterfing, Germany

A formalism will be presented which allows transforming two-equation eddy viscosity turbulence models into one-equation models. The transformation is based on Bradshaw's assumption that the turbulent shear stress is proportional to the turbulent kinetic energy. This assumption is supported by experimental evidence for a large number of boundary layer flows and has led to improved predictions when incorporated into two-equation models of turbulence. Based on it, a new one-equation turbulence model will be derived from the k-ϵ model. The model will be tested against the one-equation model of Baldwin and Barth, which is also derived from the k-ϵ model (plus additional assumptions) and against its parent two-equation model. It will be shown that the assumptions involved in the derivation of the Baldwin-Barth model cause significant problems at the edge of a turbulent layer.

Introduction

Historically, the turbulence models of choice in aerodynamics have been algebraic models, Baldwin and Lomax (1978), Johnson and King (1985), or, to a lesser extent, two-equation eddy viscosity models, like the k-ϵ (Launder and Sharma, 1974) or the k-ω model (Wilcox, 1993). Recently, the monopoly of these models has been challenged by the re-emergence of one-equation turbulence models. While one-equation models have been used earlier (Wilcox, 1993, Bradshaw et al., 1967), most of these older models solve an equation for the turbulent kinetic energy (or the turbulent shear stress), but, like the algebraic models, depend on the specification of an algebraic length-scale in order to calculate the eddy viscosity (see, however, Nee and Kovasznay, 1969 and Gulyaev et al., 1993). The model introduced by Baldwin and Barth (Baldwin and Barth, 1990) solves one transport equation for the eddy viscosity and is independent of an algebraic length-scale which made it very attractive from a numerical point of view. The Baldwin-Barth model was derived from the k-ϵ model and a number of additional simplifying assumptions. However, in the course of the transformation, several diffusive terms were neglected. The effect of changing these terms could not easily be apprehended, and it turns out that the Baldwin-Barth model does perform very differently from the underlying k-ϵ model even for simple equilibrium flows.

The change in the diffusive terms also changes the behavior of the model near the edge of shear layers and renders the equations ill-conditioned in that region as will be shown later. This is a severe issue, as the model was on its way to becoming the favored choice for aerodynamic applications.

The aim of the present effort is to establish a firm connection between one- and two-equation turbulence models. To achieve this goal, the k-ϵ model will be transformed to a one-equation model based on a set of clearly defined assumptions. Numerical results based on the new model will be compared to those of the underlying k-ϵ model and the Baldwin-Barth model. The computations will show that the new one-equation model performs very similar to the k-ϵ model in situations were the underlying assumptions are acceptable. It will also be shown that the Baldwin-Barth model gives results very different from its parent k-ϵ model.

It should be emphasized that the purpose of the present work is to establish a clear connection between one- and two-equation models of turbulence and not to endorse a new model for general use. Due to the close relation to the standard k-ϵ model, the new model inherits some of that model's deficiencies. Especially for aerodynamic flows, the model does not perform as well as models specifically designed for these applications, as the one-equation model of Spalart and Allmaras (Spalart and Allmaras, 1990; Menter, 1994a) or the author's SST k-ω model (Menter, 1993; Menter, 1994b; Menter and Rumsey, 1994). In Menter (1994a) results are shown for the SST and the Spalart-Allmaras model for the same test cases used in the present work. The interested reader can perform a one-to-one comparison between the models.

Turbulence Models

Transformation of the k-ϵ Model. This section will present a transformation of the high Reynolds number version of the k-ϵ model to a one-equation model. For simplicity the equations will be written in boundary layer coordinates—the general form of the equations will be given later. The k-ϵ model reads in boundary layer coordinates (x-streamwise coordinate, y normal to layer, and $D/Dt = \partial/\partial t + u_j(\partial/\partial x_j)$):

$$\frac{Dk}{Dt} = \tilde{\nu}_t\left(\frac{\partial u}{\partial y}\right)^2 - \epsilon + \frac{\partial}{\partial y}\left(\frac{\tilde{\nu}_t}{\sigma_k}\frac{\partial}{\partial y}(k)\right)$$

$$\frac{D\epsilon}{Dt} = c_{\epsilon 1}\frac{\epsilon}{k}\tilde{\nu}_t\left(\frac{\partial u}{\partial y}\right)^2 - c_{\epsilon 2}\frac{\epsilon^2}{k} + \frac{\partial}{\partial y}\left(\frac{\tilde{\nu}_t}{\sigma_\epsilon}\frac{\partial}{\partial y}(\epsilon)\right) \quad (1)$$

with the following definition of the eddy viscosity:

$$\tilde{\nu}_t = c_\mu\frac{k^2}{\epsilon} \quad (2)$$

In order to arrive at a one-equation model, we follow Baldwin and Barth and express the time derivative of the eddy viscosity by the time derivatives of k and ϵ:

$$\frac{D\tilde{\nu}_t}{Dt} = c_\mu\left(2\frac{k}{\epsilon}\frac{Dk}{Dt} - \frac{k^2}{\epsilon^2}\frac{D\epsilon}{Dt}\right) \quad (3)$$

[1] Formerly NASA Ames Research Center.

Contributed by the Fluids Engineering Division for publication in the JOURNAL OF FLUIDS ENGINEERING. Manuscript received by the Fluids Engineering Division December 18, 1996; revised manuscript received July 8, 1997. Associate Technical Editor: M. M. Sindir.

Replacing the total derivatives of k and ϵ on the right-hand side by the right-hand sides of Eq. (1) gives a single transport equation for the eddy viscosity, which, however, depends on k and ϵ as well as on the eddy viscosity:

$$\frac{D\tilde{\nu}_t}{Dt} = F(\tilde{\nu}_t;\, k;\, \epsilon) \tag{4}$$

This presents a closure problem with one equation for three unknowns. In order to close the equation, two additional relations have to be provided. The first one is the definition of the eddy viscosity, Eq. (2), which allows one to replace ϵ by the eddy viscosity and the turbulent kinetic energy:

$$\epsilon = c_\mu \frac{k^2}{\tilde{\nu}_t} \tag{5}$$

with $c_\mu = 0.09$. Note that this relation does not involve any additional assumptions and the resulting equation is still equivalent to the original k-ϵ model. A second relation is needed to eliminate k from the right-hand side of Eq. (4) and this relation cannot be derived from the k-ϵ model (otherwise the k-ϵ equations would be overspecified). However, there is a relation readily available that relates the turbulent kinetic energy and the eddy viscosity, which has been confirmed for a large number of experimental boundary layer data and was used by Bradshaw et al. (1967) in the derivation of their one-equation model, namely (see also Townsend, 1962):

$$|-\overline{u'v'}| = \tilde{\nu}_t \left|\frac{\partial u}{\partial y}\right| = a_1 k \tag{6}$$

where a_1 is a constant and $|-\overline{u'v'}|$ is the turbulent shear stress. Note that the relation between the turbulent shear stress and the turbulent kinetic energy that results from standard two-equation models is:

$$|-\overline{u'v'}| = \sqrt{\frac{\text{Production}_k}{\text{Dissipation}_k}}\, a_1 k \tag{7}$$

using $a_1 = \sqrt{c_\mu}$. However, Eq. (7) is not confirmed by experimental evidence in strong adverse pressure gradient flows. It is therefore to be expected that the introduction of Eq. (6) will actually lead to improved predictions of non-equilibrium flows.

Since we have a complete set of equations, the one-equation model can be derived by straightforward substitution. The result is:

$$\begin{aligned}\frac{D\tilde{\nu}_t}{Dt} = {} & c_1\tilde{\nu}_t\left|\frac{\partial u}{\partial y}\right| - c_2\tilde{\nu}_t^2\left(\frac{\dfrac{\partial}{\partial y}\left|\dfrac{\partial u}{\partial y}\right|}{\left|\dfrac{\partial u}{\partial y}\right|}\right)^2 + \frac{\partial}{\partial y}\left(\frac{\tilde{\nu}_t}{\sigma_\epsilon}\frac{\partial}{\partial y}(\tilde{\nu}_t)\right) \\ & + 2\,\frac{(\sigma_\epsilon - \sigma_k)}{\sigma_k\sigma_\epsilon}\left[\tilde{\nu}_t\frac{\partial^2\tilde{\nu}_t}{\partial y^2} + \left(\frac{\partial\tilde{\nu}_t}{\partial y}\right)^2\right. \\ & \left. + \tilde{\nu}_t^2\,\frac{1}{\left|\dfrac{\partial u}{\partial y}\right|}\frac{\partial^2}{\partial y^2}\left|\frac{\partial u}{\partial y}\right| + 3\tilde{\nu}_t\frac{\partial\tilde{\nu}_t}{\partial y}\left(\frac{\dfrac{\partial}{\partial y}\left|\dfrac{\partial u}{\partial y}\right|}{\left|\dfrac{\partial u}{\partial y}\right|}\right)\right]\end{aligned} \tag{8}$$

Equation (8) is complicated and difficult to solve numerically. However, the contribution of the terms in the last parenthesis of the equation is proportional to the difference in the diffusive coefficients of the k- and the ϵ-equation. For a number of k-ϵ models these coefficients are equal and the whole term is exactly zero. It was shown in detail in Menter (1994c) that the influence of these terms is small and can be neglected. The second assumption in the derivation of the model is therefore:

$$\sigma_k = \sigma_\epsilon \equiv \sigma \tag{9}$$

The resulting high Reynolds number form of the equation is:

$$\frac{D\tilde{\nu}_t}{Dt} = c_1\tilde{\nu}_t\left|\frac{\partial u}{\partial y}\right| - c_2\frac{\tilde{\nu}_t^2}{L_{VK}^2} + \frac{\partial}{\partial y}\left(\frac{\tilde{\nu}_t}{\sigma}\frac{\partial}{\partial y}(\tilde{\nu}_t)\right) \tag{10}$$

Equation (10) involves the inverse of the von Karman similarity length-scale L_{VK}:

$$\frac{1}{L_{VK}} = \frac{\dfrac{\partial}{\partial y}\left|\dfrac{\partial u}{\partial y}\right|}{\left|\dfrac{\partial u}{\partial y}\right|} \tag{11}$$

The von Karman length-scale was not very successful when used in a mixing length model, mainly because it is singular whenever the denominator goes to zero. In the present one-equation model, the singularity (of the inverse of L_{VK}) is not a problem, because the destruction term that involves L_{VK} can be limited by any other term that has the same dimension, as will be shown later. In the framework of eddy viscosity transport models, the von Karman length scale was also utilized in an unpublished model by Baldwin (1993), and in a model by Durbin et al. (1994), but was never formally derived from the k-ϵ model.

The formalism used in the derivation of Eq. (10) can be applied to transform any two-equation eddy viscosity model to a one-equation model. In the Appendix the transformation for the k-ω model is presented.

The coefficients of the one-equation model follow directly from the k-ϵ model constants:

$$c_1 = (c_{\epsilon 2} - c_{\epsilon 1})\sqrt{c_\mu} = 0.144; \quad \sigma = \sigma_k = 1$$

$$c_2 = \frac{c_1}{\kappa^2} + \frac{1}{\sigma} = 1.86 \tag{12}$$

The standard k-ϵ model constants of $c_{\epsilon 1} = 1.44$, $c_{\epsilon 2} = 1.92$, $c_\mu = 0.09 = a_1^2$ and $\sigma_\kappa = 1.0$ have been used. Note that the transformation leads to $c_2 = 2/\sigma_\epsilon = 1.71$ with $\sigma_\epsilon = 1.17$. Since σ was chosen to be equal to σ_k and not equal to σ_ϵ, the coefficient c_2 had to be slightly recalibrated to match the law of the wall.

The key to the understanding of the one-equation model lies in the comparison of Eqs. (6) and (7). For equilibrium flows the two formulations are equivalent and the one-equation model will be very close in performance to the k-ϵ model. For nonequilibrium adverse pressure gradient flows, Bradshaw's relation, Eq. (6), is better confirmed by experiments than Eq. (7). For these flows the ratio of Production/Dissipation becomes larger than one in the outer region of the boundary layer and the k-ϵ model will give higher shear stresses than the one-equation model. Since the k-ϵ model is well known to overpredict shear stress levels for these flows, it is to be expected that the one-equation model will lead to improved predictions. For flows without shear, Bradshaw's relation, Eq. (6), has no meaning, and the one-equation model cannot be expected to give good results. An example is isotropically decaying turbulence, where one-equation models predict that the eddy viscosity stays constant, whereas the k-ϵ model predicts, more realistically, a decay of the turbulent variables. This deficiency is associated with the lack of a second scale in the model. For shear flows the second scale is provided by the mean shear rate. Regions where the mean shear is locally zero are bridged by the diffusion and the convection terms. Note, however, that the overwhelming

majority of applications of turbulence models is for shear flows, for which one-equation models are well suited.

The main assumption in the derivation of the one-equation model is that the turbulent shear stress is proportional to the turbulent kinetic energy. In standard two equation models this assumption is equivalent to:

$$\text{Production}_k = \text{Dissipation}_k \tag{13}$$

used in the derivation of the Baldwin-Barth model. However, in that model only the production and dissipation terms are transformed based on Eq. (13). The diffusion terms are not transformed exactly. The high Reynolds number form of the Baldwin-Barth (BB) model reads:

$$\frac{D\tilde{\nu}_t}{Dt} = \hat{c}_1\tilde{\nu}_t\left|\frac{\partial u}{\partial y}\right| - \hat{c}_2\frac{\partial\tilde{\nu}_t}{\partial y}\frac{\partial\tilde{\nu}_t}{\partial y} + \frac{\partial}{\partial y}\left(\frac{\tilde{\nu}_t}{\hat{\sigma}}\frac{\partial}{\partial y}(\tilde{\nu}_t)\right) \tag{14}$$

The original Baldwin-Barth model solves an equation for the turbulent Reynolds number. In order to allow a one-to-one comparison of the constants, it has been reformulated here (exactly) as an equation for the eddy viscosity. The transformed constants for this model are:

$$\hat{c}_1 = (c_{\epsilon 2} - c_{\epsilon 1})\sqrt{c_\mu} = 0.24; \quad \hat{\sigma} = \sigma_\epsilon = 0.7$$

$$\hat{c}_2 = \frac{\hat{c}_1}{\kappa^2} + \frac{1}{\hat{\sigma}} = 2.86 \tag{15}$$

They are based on $c_{\epsilon 1} = 1.2$, $c_{\epsilon 2} = 2.0$, $c_\mu = 0.09 = a_1^2$ and $\sigma_\epsilon = 0.7$ for the underlying k-ϵ model. The low Reynolds number form of this model can be found in Baldwin and Barth (1990) and is not repeated here.

In order to distinguish the new model, Eq. (10), from the other models in this study, we call it $(k\text{-}\epsilon)_{1E}$ model where the subscript stands for one-equation. The main difference between the $(k\text{-}\epsilon)_{1E}$ and the BB model is the form of the destruction term (c_2 term). Although the derivation of the BB model starts out from the k-ϵ model, a comparison with Eq. (8) shows that a number of additional assumptions were introduced in order to arrive at Eq. (14). The link between the BB model and the k-ϵ model is thereby broken and it is for this reason that the two models perform very differently, as will be shown later.

Low Reynolds Number Terms. The assumptions leading to the $(k\text{-}\epsilon)_{1E}$ model are obviously not correct in the viscous sublayer, so that the low Reynolds number terms of the k-ϵ model cannot be carried over to the one-equation model. This is not a great loss because the near wall terms of the k-ϵ model are generally complicated and difficult to integrate so that a one-to-one transformation is not desirable.

The purpose of damping functions is to reduce the eddy viscosity in the sublayer. In the present model this is achieved by reducing the production term near the wall and by multiplying the high Reynolds number eddy viscosity, $\tilde{\nu}_t$, by a damping function in order to arrive at the corrected eddy viscosity, ν_t. The damping functions are designed in a pragmatic way that ensures that the resulting model is numerically stable and does not require excessive grid resolution near the surface. Two damping functions are introduced, D_1 in front of the production term and D_2 into the definition of the eddy viscosity:

$$c_1\tilde{\nu}_t\left|\frac{\partial u}{\partial y}\right| \rightarrow D_1 c_1\tilde{\nu}_t\left|\frac{\partial u}{\partial y}\right| \tag{16}$$

$$\nu_t = D_2\tilde{\nu}_t \tag{17}$$

based on the following expressions:

$$D_1 = \frac{\nu_t + \nu}{\tilde{\nu}_t + \nu} \tag{18}$$

$$D_2 = 1 - e^{-(\tilde{\nu}_t/A^+\kappa\nu)^2} \tag{19}$$

and $\kappa = 0.41$. Furthermore, the molecular viscosity is added into the diffusion term in analogy to the k-ϵ model. The coefficient A^+ is equal to $A^+ = 13$.

General Form of the Equations. In order to arrive at an invariant formulation, all occurrences of the strain rate are replaced by the following invariant expression:

$$\left|\frac{\partial u}{\partial y}\right| \rightarrow S = \sqrt{U_{i,j}(U_{i,j} + U_{j,i})} \tag{20}$$

As has been pointed out by Spalart and Allmaras (1994), alternative formulations like the absolute value of the vorticity, or $\sqrt{U_{i,j}U_{i,j}}$ are possible, but for thin shear flows there is little difference among them. In general, applications S has the advantage of being invariant under system rotation and of not producing turbulence under solid body rotation. The term involving the inverse of the von Karman length-scale becomes:

$$E_{k\text{-}\epsilon} \equiv \tilde{\nu}_t^2\left(\frac{1}{L_{VK}}\right)^2 = \tilde{\nu}_t^2\left(\frac{\dfrac{\partial S}{\partial x_j}\dfrac{\partial S}{\partial x_j}}{S^2}\right) \tag{21}$$

An alternative but numerically more expensive (and not yet tested) form would be:

$$E_{k\text{-}\epsilon} = \tilde{\nu}_t^2\left(\frac{1}{L_{VK}}\right)^2 = \tilde{\nu}_t^2\left(\frac{\dfrac{\partial^2 u_i}{\partial x_j\partial x_j}\dfrac{\partial^2 u_i}{\partial x_k\partial x_k}}{\dfrac{\partial u_s}{\partial x_l}\dfrac{\partial u_s}{\partial x_l}}\right) \tag{22}$$

Similarly, all y-derivatives are replaced by their complete invariant forms.

As was pointed out previously, the inverse of the von Karman length-scale can become singular whenever S goes to zero, leading to an infinite destruction term $E_{k\text{-}\epsilon}$. In order to prevent this from happening, the destruction term is limited by a multiple of the Baldwin-Barth destruction term, E_{BB}:

$$E_{1e} = c_3 E_{\text{BB}} \tanh\left(\frac{E_{k\text{-}\epsilon}}{c_3 E_{\text{BB}}}\right) \tag{23}$$

with a constant $c_3 = 7$. E_{BB} is defined as:

$$E_{\text{BB}} = \frac{\partial\tilde{\nu}_t}{\partial x_j}\cdot\frac{\partial\tilde{\nu}_t}{\partial x_j} \tag{24}$$

Equation (23) provides a smooth transition between the two formulations whenever $E_{k\text{-}\epsilon}$ goes to infinity. For most of the flow $E_{k\text{-}\epsilon} \ll c_3 E_{\text{BB}}$ and the original formulation is recovered. A less smooth transition could be achieved by $E_{1e} = \min(E_{k\text{-}\epsilon}; c_3 E_{\text{BB}})$. The numerical results are not sensitive to the constant c_3.

The final form of the $(k\text{-}\epsilon)_{1E}$ model is:

$$\frac{D\tilde{\nu}_t}{Dt} = c_1 D_1\tilde{\nu}_t S - c_2 E_{1e} + \frac{\partial}{\partial x_j}\left(\left(\nu + \frac{\tilde{\nu}_t}{\sigma}\right)\frac{\partial}{\partial x_j}(\tilde{\nu}_t)\right) \tag{25}$$

$$\nu_t = D_2\tilde{\nu}_t \tag{26}$$

Note that the above equations are still strictly local, without dependence on the distance from the surface.

Numerical Results

Free Shear Flows. Self-similar shear layers are very important test cases which provide insight into the performance of turbulence models, without the need for large computer resources. In this section, the models will be tested against the standard free shear cases, namely, a self-similar mixing layer,

Table 1 Definition of variables for free shear flows

Far wake	Mixing layer	Plane/round jet	
U	$u(x, y) = U_\infty - \sqrt{\frac{D}{\rho x}}\, U(\eta)$	$u(x, y) = U_1 U(\eta)$	$u(x, y) = \frac{J}{x^{(j+1)/2}}\, U(\eta)$
N	$v_t(x, y) = \frac{D}{\rho U_\infty} N(\eta)$	$v_t(x, y) = x U_1 N(\eta)$	$v_t(x, y) = \sqrt{J} x^{(1-j)/2} N(\eta)$
η	$\eta = y\sqrt{\frac{\rho U_\infty^2}{Dx}}$	$\eta = \frac{y}{x}$	$\eta = \frac{y}{x}$
Additional definitions	$D = 2\int_0^\infty \rho u(U_\infty - u)dy$	—	$J = \frac{\pi_j}{2}\int_0^\infty u^2 y^j dy$

the plane and round jet and the self similar far wake. The equations are cast into self-similar form following Wilcox (1993), resulting in the following two ordinary differential equations for the nondimensional velocity U and the nondimensional eddy viscosity N:

$$V\frac{dU}{d\eta} - \frac{1}{\eta^j}\frac{d}{d\eta}\left[\eta^j N\frac{dU}{d\eta}\right] = S_U U \tag{27}$$

$$V\frac{dN}{d\eta} - \frac{1}{\eta^j}\frac{d}{d\eta}\left[\frac{1}{\sigma}\eta^j N\frac{dN}{d\eta}\right] = S_N N + c_1\left|\frac{dU}{d\eta}\right| - c_2\left(\frac{N}{L_{VK}}\right)^2 \tag{28}$$

with:

$$\frac{1}{L_{VK}} = \frac{\frac{1}{\eta^j}\frac{d}{d\eta}\left(\eta^j\left|\frac{dU}{d\eta}\right|\right)}{\left|\frac{dU}{d\eta}\right|} \tag{29}$$

where $j = 1$ for the round jet and $j = 0$ for the plane flows. The nondimensional variables are defined as given in Table 2 and Table 3: The coefficients in Table 2 can be obtained from Wilcox (1993) and $S_N = 2S_K - S_\epsilon$. (Note that the coefficient S_K in Wilcox (1993) should be $2U$ for the round jet.)

Asymptotic Solution Near Shear Layer Edge for the (k-ϵ)$_{1E}$ and the Baldwin-Barth Model. The analysis of the asymptotic solution near the edge of turbulent layer is an important part of turbulence model evaluation. It is especially important to determine the sensitivity of the solution to changes in the freestream values specified for the turbulence variables outside the layer. Models with solutions that change significantly with the freestream conditions are not acceptable, because the "correct" freestream conditions are not known in most applications. The problem has been analyzed in detail by Menter (1992a) and Cazalbou et al. (1994) for two-equation eddy viscosity models. It was shown that the k-ω model has a severe dependency on the values specified for ω outside the layer. It was also shown that the k-ϵ model does not suffer from this ambiguity. There is no theory available to decide whether a model has a freestream sensitivity, but the existence of an asymptotic algebraic solution near the boundary layer edge seems to be at least a necessary condition for a model to be well conditioned.

The analysis does not depend on which shear flow is selected for the analysis, since the existence of an algebraic solution implies that the terms involving S_U and S_N decay faster than the other terms near the edge of the layer and can therefore be neglected. The new variable $\tilde{\eta} = \eta - \delta$ is introduced near the shear layer edge, δ, and algebraic solutions of the form:

$$\frac{dU(\eta)}{d\tilde{\eta}} = A\tilde{\eta}^\alpha; \quad N(\tilde{\eta}) = B\tilde{\eta}^\beta \tag{30}$$

are introduced into the equations. Straightforward algebra shows that the exponents for the (k-ϵ)$_{1E}$ model are:

$$\alpha = \frac{\left(-1 + \sqrt{1 - 4c_2\left(1 - \frac{1}{\sigma}\right)}\right)}{2c_2} = 0; \quad \beta = 1 \tag{31}$$

Therefore, the velocity and the eddy viscosity approach the shear layer edge linearly. It is interesting to note that the solution for the k-ϵ model is also linear for $\sigma_k = \sigma_\epsilon = 1$ so that the asymptotic behavior of the k-ϵ model carries over to the present one-equation model.

The Baldwin-Barth model does not have a solution of the form given by Eq. (30). However, as pointed out before, there is no theory available to show that the existence of algebraic solutions is a sufficient, or even a necessary condition to prevent free stream dependency. Numerical test will have to be used to obtain insight into the model characteristics.

Figure 1 shows spreading rates for a far wake, computed with the Baldwin-Barth model as a function of the freestream value, N_f, and the number of grid points, n, across the layer $0 \le \eta \le 0.4$. The gridpoints are evenly distributed and the highest freestream values shown in Fig. 1 are 2 percent of the maximum value of N inside the layer. The Baldwin-Barth model shows a

Table 2 Coefficients for free shear flows

Flow	S_U	S_N	$V(\eta)$
Far wake	1/2	0	$-\frac{1}{2}\eta$
Mixing layer	0	$-U$	$-\int_0^\eta U(\eta')d\eta'$
Plane jet	$1/2U$	$-1/2U$	$-\frac{1}{2}\int_0^\eta U(\eta')d\eta'$
Round jet	U	0	$-\frac{1}{\eta}\int_0^\eta U(\eta')\eta' d\eta'$

Table 3 Spreading rates for free shear flows

Flow	k-ϵ	(k-ϵ)$_{1E}$	Experiment
Far wake	0.256	0.250	0.365
Mixing layer	0.100	0.084	0.115
Plane jet	0.109	0.111	0.100–0.110
Round jet	0.120	0.131	0.086–0.095

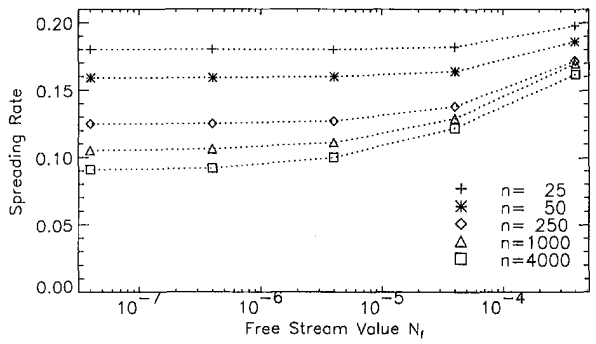

Fig. 1 Spreading rates of the Baldwin-Barth model for far wake, depending on freestream values, N_f, and number of gridpoints, n

strong sensitivity to the values specified for N_f, especially as the grid is refined. Furthermore, none of the solutions is in acceptable agreement with the experimental spreading rate of 0.365 as quoted from Wilcox (1993).

Figure 2 shows the computed velocity profiles on the finest grid (n = 4000) for the highest and the lowest freestream values. It is apparent that the model develops extremely high gradients in the velocity profile for the lower freestream values. The high gradients are the reason why the freestream sensitivity does not show up on the coarse grids, where they cannot be resolved. No grid independent solution could be obtained for the low values of N_f. Even if the number of points is doubled again to n = 8000, the solution develops even higher slopes and lower spreading rates. As with the k-ω model, the influence of the freestream conditions is not restricted to the vicinity of the boundary layer edge, but affects the whole layer. However, the k-ω model becomes more diffusive with decreasing freestream values and no grid sensitivity is observed.

Spalart and Allmaras (1994) have investigated the behavior of a turbulent front and found that for the Baldwin-Barth model the front propagates in the (physically) incorrect direction away from the non-turbulent region. They also report that their results are dependent on the freestream values specified for the eddy viscosity, consistent with the present findings. Spalart (1994) also reports similar problems with the Baldwin-Barth model as shown in Fig. 1 for his computation of a self-similar mixing layer. Like in the present calculations, his results are highly sensitive to grid resolution and free-stream values. On the other hand, Baldwin and Barth (1990) have tested the model for a flat plate zero pressure gradient boundary layer (based on a Navier-Stokes code) and found only a moderate dependency on the freestream values. Note, however, that Navier-Stokes grids are generally coarse near the boundary layer edge (assuming that all points are plotted in Baldwin and Barth (1990), there are about forty points across the boundary layer but only ten of them in the wake region) so that it is apparent that the problem was not resolved in that computation. Note also that the present author has tested the Baldwin-Barth model in Navier-Stokes codes (Menter, 1992b) and did at first not realize the severity of the problem for the same reason. However, Rogers (1994) reported that he could not obtain grid independent solutions for airfoil flows with the Baldwin-Barth model using the INS2D Navier-Stokes code.

Goldberg et al. (1994) and Goldberg (1994) have proposed a number of "pointwise" one-equation models, which are, in their high Reynolds number version, formally identical to the Baldwin-Barth model (note that the present problems are independent of the low Reynolds number treatment). Although Goldberg does not report problems near the edge of turbulent layers, computations by the present author have shown the same deficiencies as with the BB model. Furthermore, the results presented in Goldberg (1994) for self-similar flows could not be reproduced with any reasonable combination of freestream values and grid distributions. These references are therefore not considered in the present discussion.

What are the implications of the results shown in Figs. 1–2 for Navier-Stokes applications? There are two different strategies. The first one is to specify small values for the eddy viscosity in the freestream (inflow). The advantage of low values is that they can be specified unambiguously—values that are a fraction of the molecular viscosity will ensure that they are small compared to those inside the layer. However, due to the large gradients developing in this case, no grid independent solutions can be obtained, a situation not acceptable in a Navier-Stokes code. The second strategy is to specify large freestream values (say x percent of the maximum values inside the layer). Tests have shown that in order to reproduce the experimental spreading rates of free shear flows, freestream values of about 20–30 percent of the maximum inside the layer have to be used. Values that high would severely impact laminar regions in the flowfield and are certainly not acceptable.

The $(k$-$\epsilon)_{1E}$ model was subjected to the same tests as the Baldwin-Barth model. The model did not show any freestream dependency, as long as the freestream values are small (<1 percent) compared to the values inside the layer. Furthermore the solution for the $(k$-$\epsilon)_{1E}$ model did follow the algebraic solution given by Eq. (30) near the boundary layer edge. Even for very small values, grid independent solutions were obtained with only about 15 points inside the half-layer.

Table 3 compares the spreading rates of free shear layers as computed with the standard k-ϵ and the $(k$-$\epsilon)_{1E}$ model. The experimental values are taken from Wilcox (1993). The Baldwin-Barth model is not included because no grid- or freestream independent solutions could be obtained. It is interesting to note that the $(k$-$\epsilon)_{1E}$ model gives very similar spreading rates to the k-ϵ despite the fact that Bradshaw's assumption is not generally true for these flows.

Self-Similar Boundary Layer Flows. Wilcox (1993) has popularized the use of defect layer computations for testing turbulence models under equilibrium pressure gradient conditions. As expected, the Baldwin-Barth model has the same freestream dependency as for the free shear layers. Figure 3 shows computations with this model for the zero pressure gradient boundary layer experiment of Wieghardt (Kline et al., 1981) with two different freestream values on a fine grid of 1000 points. The high freestream value is about 1 percent of the maximum eddy viscosity value inside the boundary layer. Again, the solution develops extreme gradients near the boundary layer edge for the low freestream values. The same computations have shown only a moderate sensitivity on a coarse grid.

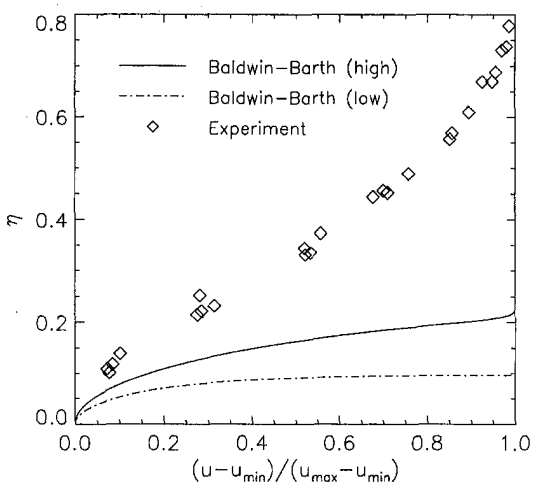

Fig. 2 Velocity profiles for far wake with Baldwin-Barth model for highest and lowest freestream values (number of gridpoints, n = 4000.)

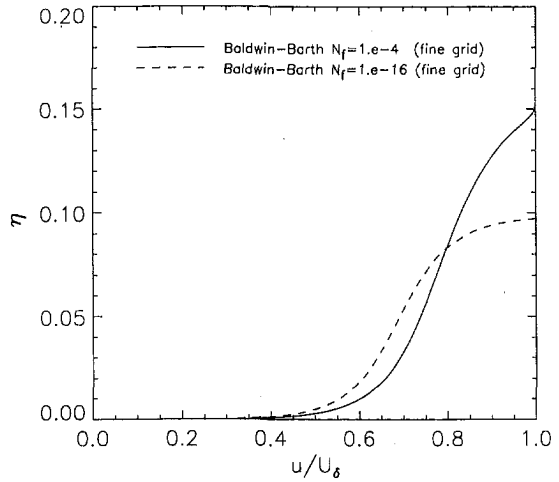

Fig. 3 Velocity profiles for defect layer with Baldwin-Barth model and two different freestream values, N_f, (fine grid with n = 1000)

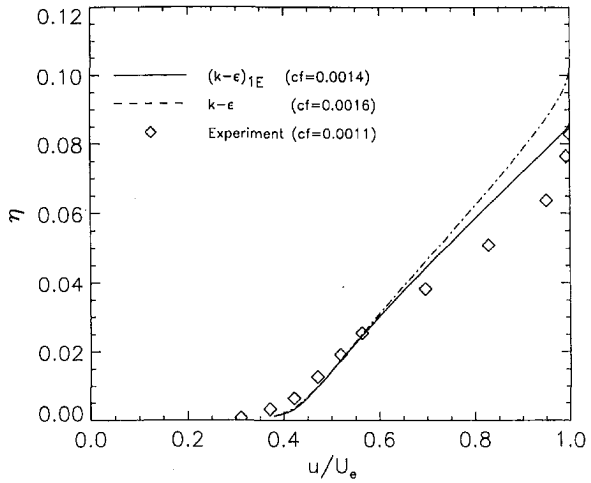

Fig. 5 Velocity profiles for defect layer, β_T = 8.7

It is obvious from these results that the freestream sensitivity could not be resolved in Baldwin and Barth (1990). As in the free shear layer computations, the influence of the freestream values and grid densities is not confined to the vicinity of the boundary layer edge, but affects the whole layer. No grid converged solution could be obtained with the Baldwin-Barth model for the low freestream value. From the present study it is not clear whether an asymptotic solution exists for this model as N_f goes to zero and the number of grid points goes to infinity. Whenever the number of grid-points was increased, the solution changed with an increase in the slope near the edge and a lower eddy viscosity inside the layer.

Figure 4 shows a comparison of results for the zero pressure gradient case of Wieghardt for the k-ϵ and the $(k$-$\epsilon)_{1E}$ models. Both models give very accurate velocity profiles and c_f-predictions.

Figure 5 shows the velocity profiles for the adverse pressure gradient flow of Clauser (Kline et al., 1981) for a nondimensional pressure gradient of β_T = 8.7. It is well known that the standard k-ϵ model overpredicts the skin friction for adverse pressure gradient flows, in this case by about 50 percent. Note that the apparent differences in boundary layer thickness between the computations and the experiment are a result of the definition of η, involving the friction velocity u_τ. The introduction of Bradshaw's relation, Eq. (6), into the $(k$-$\epsilon)_{1E}$ model obviously improves the predictions, but the skin friction is still too high by about 30 percent. Due to the close relationship of the $(k$-$\epsilon)_{1E}$ model to the standard k-ϵ model, it had to be expected that the deficiency in the adverse pressure gradient behavior of the k-ϵ model would not entirely be avoided by the new model.

Navier-Stokes Computations. All of the following test cases have been computed with the NASA Ames INS2D and INS3D codes (Rogers and Kwak, 1988). All flows in this study are part of a test base assembled by the author to evaluate the performance of turbulence models. The flows have been set up in a way to match the experimental boundary conditions as closely as possible. Furthermore, all computations are performed on grids that have been shown to produce grid independent solutions. A number of additional test of the present models can be found in Menter (1994c). All k-ϵ model computations were based on Launder and Sharma (1974).

It was initially intended to compare results of all three models for the following Navier-Stokes applications. However, due to the severe deficiencies discovered in the Baldwin-Barth model for the equilibrium flows, the model was dropped from the study since the results are invariably either grid- or freestream dependent.

Flat Plate Zero Pressure Gradient Boundary Layer. Figure 6 shows a comparison of the computed wall skin friction coefficients, c_f, versus displacement thickness, θ, for a flat plate zero pressure gradient boundary layer. The computations are

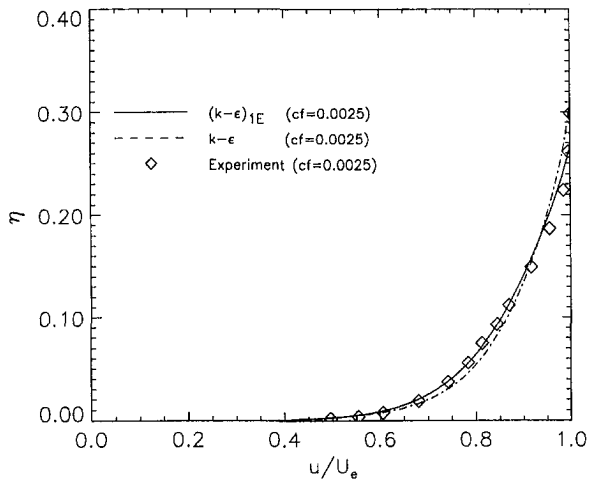

Fig. 4 Velocity profiles for defect layer, β_T = 0

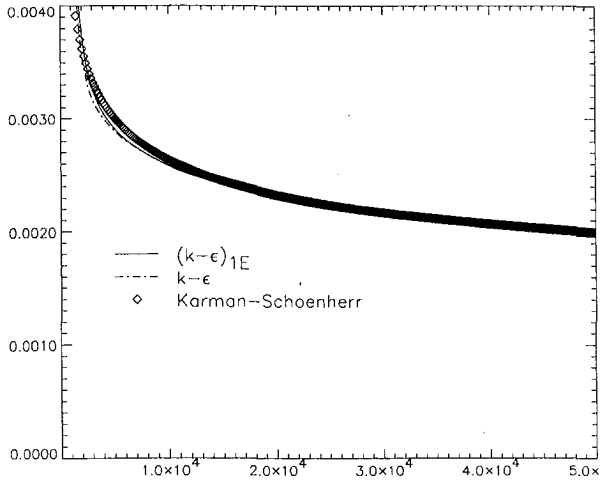

Fig. 6 Skin-friction coefficient for flat plate boundary layer

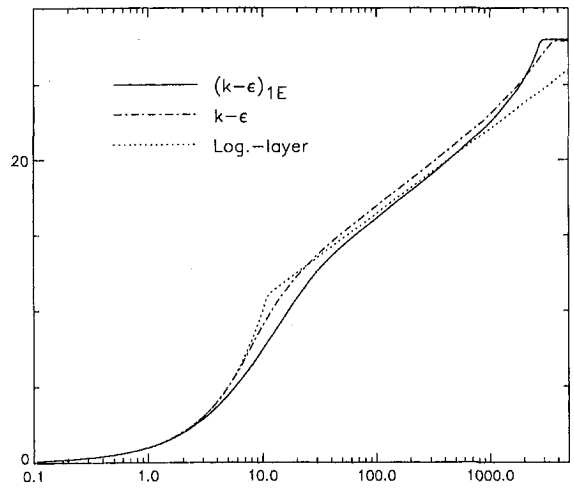

Fig. 7 Velocity profiles for flat plate boundary layer in inner coordinates

compared with the experimental correlation of v. Karman and Schoenherr. The low Reynolds number version of the k-ϵ model is due to Launder and Sharma (1974). Both models are in good agreement with the experimental correlation. The one-equation model gives accurate results, as long as the first grid point satisfies $y_1^+ < \sim 2.0$. The Launder-Sharma model requires a significantly smaller grid-spacing near the wall of $y_1^+ < \sim 0.3$. (Note that a finer grid-spacing is used compared to Menter (1994c), leading to improved results for the Launder-Sharma model.)

The velocity profiles in inner coordinates are depicted in Fig. 7. Again both models are in good agreement with the law of the wall.

Driver Separated Adverse Pressure Gradient Flow. In Driver's flow (Driver, 1991), a turbulent boundary layer develops in the axial direction of a circular cylinder. A strong adverse pressure gradient is imposed on the flow by diverging wind tunnel walls plus suction applied at these walls. The pressure gradient is strong enough to cause the flowfield to separate. The inflow Reynolds number is 2.8×10^5 based on the diameter, D, of the cylinder. The inflow boundary layer thickness is about $0.2D$. The experiments offer independent wall-skin friction measurements and it was found in previous tests (Menter, 1994c) that the data are highly self-consistent and well suited to test models under strong pressure gradient conditions. The computations are performed on a $60 \times 3 \times 60$ (verified on a $90 \times 3 \times 90$) grid.

Figure 8 shows the wall skin friction coefficient for this flow. As in previous comparisons, the standard k-ϵ model predicts

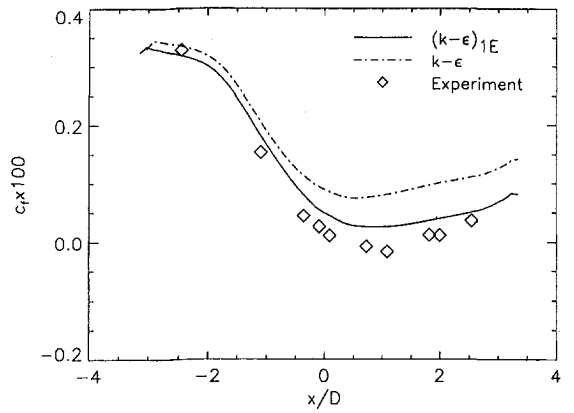

Fig. 8 Skin-friction for Driver's case CS0

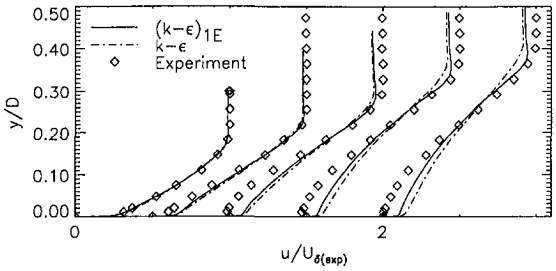

Fig. 9 Velocity profiles for Driver's case CS0 at $x/D = -0.544, -0.091, 0.363, 1.088, 1.633$

significantly higher values than the experiment. The $(k$-$\epsilon)_{1E}$ model is in better agreement with the data, but still somewhat too high, especially in the region where the experiment shows separation.

For the velocity profiles shown in Fig. 9 the one-equation model is a little closer to the data, but both models underpredict the viscous-inviscid interaction. Again, the $(k$-$\epsilon)_{1E}$ model predicts a stronger retardation due to the pressure gradient, but not enough to be in good agreement with the data.

As the flow encounters more severe nonequilibrium conditions, the differences between Bradshaw's relation, Eq. (6), and the relation enforced by the two-equation model, Eq. (7), become more severe and the predictions of the two models start to deviate. Figure 10 shows the ratio of production versus dissipation as predicted by the standard k-ϵ model at the location of the maximum turbulent shear stress. This ratio is an indicator of the nonequilibrium effects and enters into Eq. (7). Since Bradshaw's relation is generally more realistic than Eq. (7), the $(k$-$\epsilon)_{1E}$ model gives better results than the standard k-ϵ model.

Backward Facing Step Flow. The backward facing step is one of the most widely used test cases for turbulence model evaluation. While early results for this flow indicated that the k-ϵ model underpredicts the reattachment length by ~ 30 percent, more recent results have shown that the model is off by only about 5 percent. The earlier computations had not enough resolution to accurately predict the flow. The test case in this study is the flow of Driver and Seegmiller (1985). The Reynolds number, based on the upstream momentum thickness Θ is $\mathrm{Re}_\Theta = 5{,}000$ and the ratio of the boundary layer thickness to step height is about 1.5. The expansion ratio is 1.125. The computations have been performed on a 120×120 grid with substantial grid refinement near the step. The computations are virtually identical to those performed on a 240×240 grid.

Figure 11 shows the computed and the experimental skin friction distributions. The k-ϵ model underpredicts the reattachment location by about 5 percent and is generally not in good agreement with the data in the separated region and

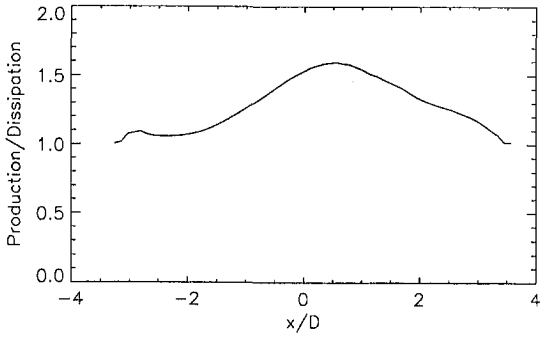

Fig. 10 Ratio of Production/Dissipation for Driver's case CS0 as computed from the k-ϵ model

near reattachment. Different low Reynolds number forms of this model give different skin friction distribution, so that this behavior is certainly a result of the low-Reynolds number terms. The $(k\text{-}\epsilon)_{1E}$ model is in very good agreement with the data. The reattachment location is predicted within experimental uncertainty, and there are no overshoots near reattachment. Especially impressive is the skin friction recovery downstream of reattachment, where other models tend to fall more severely below the experiments (Menter, 1994a; Menter, 1993; Menter, 1994c).

The velocity profiles depicted in Fig. 12 show that the high Reynolds number differences between the models are amazingly small. The velocity profiles are almost identical even inside the separation bubble and it appears again that the two-equation model does not offer an advantage over the one-equation model. Both of the present models fail to predict the recovery of the velocity profiles downstream of reattachment. This is a general problem with existing models and has been observed before (Menter, 1994c).

Conclusions

The connection between one- and two-equation models of turbulence has been reexamined. It was found that the standard k-ϵ model can be transformed into a one-equation model based on only two assumptions. The first assumption is Bradshaw's relation that the turbulent shear stress is proportional to the turbulent kinetic energy. This assumption corresponds to $\text{Production}_k = \text{Dissipation}_k$ in standard two equation models and is therefore closely satisfied for equilibrium flows. For nonequilibrium flows, Bradshaw's relation is actually better confirmed by experiments than the relation enforced by the standard k-ϵ model. The second assumption is that the diffusion coefficients in the k- and the ϵ-equations are identical. By enforcing this condition in the k-ϵ model, it was shown in Menter (1994c) that only minor changes resulted from it. The new model was termed $(k\text{-}\epsilon)_{1E}$ model and tested against the Baldwin-Barth model and the standard k-ϵ model.

Free-shear layer computations have shown that the Baldwin-Barth model is ill-conditioned near the boundary layer edge. The model does not posses an algebraic solution in that region and produces unlimited gradients in the velocity as the grid is refined. Furthermore, results are sensitive to the freestream values specified outside the layer. No grid and freestream independent results could be obtained with this model and it was for this reason not included in the rest of the study. The reason for the failure of the model lies in a destruction term that does not follow from the transformation of the two-equation model.

The findings for the Baldwin-Barth model re-emphasize that the behavior of turbulence models near the turbulent-nonturbulent interface is one of the most important aspects of turbulence modeling. Shortcomings in that area are not confined to the immediate vicinity of the interface, but change the solution through the whole layer, essentially nullifying the calibration process. Unfortunately, not enough attention is paid to this problem in the derivation and calibration of most new models, leaving the door open for potentially devastating failures. This is also true for Reynolds stress models.

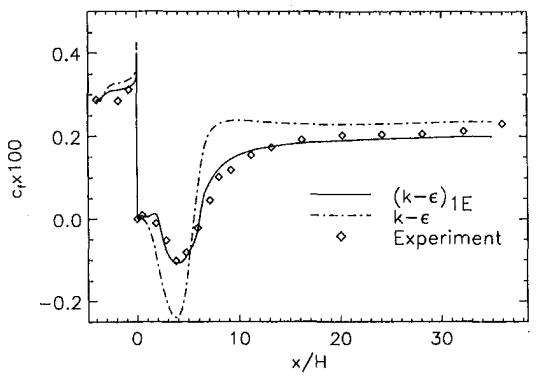

Fig. 11 Skin-friction for backward facing step flow

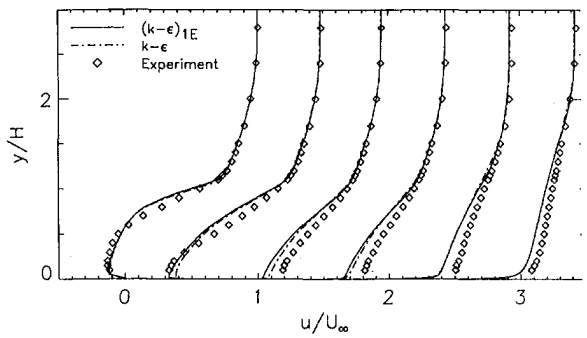

Fig. 12 Velocity profiles for backward facing step flow at x/h = 2, 4, 6.5, 8, 14, 32

The new one-equation model does not suffer from these deficiencies and shows a very close similarity to its parent two-equation model near the boundary layer edge. A comparison of the free shear layer results has shown that the predictions of the one- and two-equation models are fairly close to one another.

The one-equation model gives almost identical results to the k-ϵ model for zero pressure gradient boundary layers. A number of increasingly stronger adverse pressure gradient flows has shown that the results of the one-equation model improve compared to the k-ϵ model predictions as the nonequilibrium effects become more important. The improved results confirm that the main assumption going into the $(k\text{-}\epsilon)_{1E}$ model is more realistic than the relation enforced by the k-ϵ model.

The computations have shown that the new one-equation model produced very similar, and for boundary layer flows improved results when compared to the standard k-ϵ model. Because of its simplicity, the model is also attractive from a computational standpoint. However, a note of caution should be made concerning the use of the second derivative of the velocity field in the von Karman length scale. From the limited tests the model has undergone at this stage, it is not certain whether the von Karman length scale will be general enough for the computation of complex three-dimensional flow fields, especially for cases that are severely out of equilibrium. Further tests will have to be conducted to evaluate the model under these conditions.

Acknowledgment

This paper has greatly benefited from many important comments by Barrett Baldwin, Peter Bradshaw, Tom Coakley, George Huang, and Philippe Spalart. The research was funded by the NASA Ames Research Center.

APPENDIX

Transforming the k-ω Model

The transformation leading to the $(k\text{-}\epsilon)_{1E}$ can be used to transform any two-equation model into a one-equation model. An example is the k-ω model of Wilcox (1993):

$$\frac{Dk}{Dt} = \nu_t\left(\frac{\partial u}{\partial y}\right)^2 - \beta^* k\omega + \frac{\partial}{\partial y}\left(\sigma\nu_t \frac{\partial}{\partial y}(k)\right)$$

$$\frac{D\omega}{Dt} = \alpha\left(\frac{\partial u}{\partial y}\right)^2 - \beta\omega^2 + \frac{\partial}{\partial y}\left(\sigma\nu_t \frac{\partial}{\partial y}(\omega)\right)$$

In the k-ω model the definition of the eddy viscosity is:

$$\nu_t = \frac{k}{\omega}$$

With the help of Eqs. (3) and (6) the following one-equation model can be derived (high Reynolds number form):

$$\frac{D\tilde{\nu}_t}{Dt} = c_1\tilde{\nu}_t\left|\frac{\partial u}{\partial y}\right| + c_2\tilde{\nu}_t\frac{\frac{\partial}{\partial y}\left|\frac{\partial u}{\partial y}\right|}{\left|\frac{\partial u}{\partial y}\right|}\frac{\partial\tilde{\nu}_t}{\partial y} + \frac{\partial}{\partial y}\left(\sigma\tilde{\nu}_t\frac{\partial}{\partial y}(\tilde{\nu}_t)\right)$$

The constants in this model follow directly from the k-ω constants:

$$c_1 = \frac{\beta}{a_1} - a_1\alpha = 0.0833; \quad c_2 = 2\sigma = 1$$

with:

$$\alpha = \tfrac{5}{9}; \quad \beta = 0.075; \quad \sigma = 0.5; \quad \beta^* = a_1^2 = 0.09$$

Note that the diffusion coefficients in the k- and the ω-equation are equal so that no terms proportional to the difference of these two constants appears (see Eq. (8)).

First tests with this model have shown that the solutions develope large gradients in the velocities near the boundary layer edge, similar to the Baldwin-Barth model. This is possibly due to the small diffusion coefficient of $\sigma = 0.5$. Note also that the k-ω model has a strong dependency on freestream values (Menter, 1992a), which seems to carry over to the one-equation model. More analysis and careful testing, as well as a possible recalibration of the coefficients will be required before the model can be applied to engineering flows.

References

Baldwin, B. S., 1993, personal communication.

Baldwin, B. S., and Barth, T. J., 1990, "A One-Equation Turbulence Model for High Reynolds Number Wall Bounded Flows," NASA TM-102847.

Baldwin, B. S., and Lomax, H., 1978, "Thin Layer Approximation and Algebraic Model for Separated Turbulent Flows," AIAA Paper 78-0257, Huntsville, Ala.

Bradshaw, P., Ferriss, D. H., and Atwell, N. P., 1967, "Calculation of Boundary Layer Development Using the Turbulent Energy Equation," *Journal of Fluid Mechanics,* Vol. 23, pp. 31–64.

Cazalbou, J. B., Spalart, P. R., and Bradshaw, P., 1994, "On the Behavior of Two-Equation Models at the Edge of a Turbulent Region," *Physics of Fluids,* Vol. 6(5), May.

Driver, D. M., 1991, "Reynolds Shear Stress Measurements in a Separated Boundary Layer," AIAA Paper 91-1787.

Driver, D. M., and Seegmiller, H. L., 1985, "Features of a Reattaching Turbulent Shear Layer in Divergent Channel Flows," *AIAA Journal,* Vol. 23, No. 2.

Durbin, P. A., Mansour, N. N., and Yang, Z., 1994, "Eddy Viscosity Transport Model for Turbulent Flow," *Physics of Fluids,* Vol. 6, No. 20, Feb.

Goldberg, U. C., and Ramakrishnan, S. V., 1994, "A Pointwise Version of the Baldwin-Barth Turbulence Model," *International Journal of Computational Fluid Dynamics 1,* No. 4, pp. 321–338.

Goldberg, U. C., 1994, "A Pointwise One-Equation Turbulence Model for Wall-Bounded and Free Shear Flows," *International Symposium on Turbulence, Heat and Mass Transfer,* Lisbon, pp. 13.2.1–13.2.6.

Gulyaev, A. N., Kozlov, V. Y., and Secundov, A. N., 1993, "Universal Turbulence Model "$\nu_t - 92$." Ecolen Report, Moscow.

Johnson, D. A., and King, L. S., 1985, "A Mathematically Simple Closure Model for Attached and Separated Turbulent Boundary Layers," *AIAA Journal,* Vol. 23, Nov., pp. 1684–1692.

Kline, S. J., Cantwell, B. J., Lilley, G. M., 1981, eds., "1980–1981 AFOSR-HTTM Stanford Conference on Complex Turbulent Flows," Comparison of Computation and Experiment, Stanford University, Stanford, CA.

Launder, B. E., and Sharma, B. I., 1974, "Application of the Energy Dissipation Model of Turbulence to the Calculation of the Flow Near a Spinning Disc," *Letters in Heat and Mass Transfer,* Vol. 1, No. 2, pp. 131–138.

Menter, F. R., 1992a, "Influence of Freestream Values on k-w Turbulence Model Predictions," *AIAA Journal,* Vol. 30, No. 6.

Menter, F. R., 1992b, "Performance of Popular Turbulence Models for Attached and Separated Adverse Pressure Gradient Flows," *AIAA Journal,* Vol. 30, No. 8, Aug., pp. 2066–2072.

Menter, F. R., 1993, "Zonal Two Equation k-w Turbulence Models for Aerodynamic Flows," AIAA Paper 93-2906, Orlando, FL.

Menter, F. R., 1994a, "A Critical Evaluation of Promising Eddy-Viscosity Turbulence Models," *Proceedings Intern. Symp. on Turbulence, Heat and Mass Transfer,* Portugal, pp. 13.4.1–13.4.6.

Menter, F. R., 1994b, "Two-Equation Eddy-Viscosity Turbulence Models for Engineering Applications," *AIAA Journal,* Vol. 32, No. 8, pp. 1598–1605.

Menter, F. R., 1994c, "Eddy Viscosity Transport Equations and there Relation to the k-ϵ Model," NASA TM 108854.

Menter, F. R., and Rumsey, C. L., 1994, "Assessment of Two-Equation Models for Transonic Flows," AIAA Paper 94-2343, Colorado Springs, CO.

Nee, V. W., and Kovasznay, L. S. G., 1969, "Simple Phenomenological Theory of Turbulent Shear Flows," *The Physics of Fluids,* Vol. 12, No. 3, Mar., pp. 473–484.

Rogers, S. E., 1994, personal communication.

Rogers, S. E., and Kwak, D., 1988, "An Upwind Differencing Scheme for the Time-Accurate Incompressible Navier-Stokes Equations," AIAA Paper 88-2583, Williamsburg, Va.

Samuel, A. E., and Joubert, P. N., 1974, "A Boundary Layer Developing in an Increasingly Adverse Pressure Gradient," *Journal of Fluid Mechanics,* Vol. 66, Part 3, pp. 481–505.

Spalart, P. R., 1994, personal communication.

Spalart, P. R., and Allmaras, S. R., 1994, "A One-Equation Turbulence Model for Aerodynamic Flows," *La Recherche Aerospatiale,* No. 1, pp. 5–21.

Townsend, A. A., 1962, "Equilibrium Layers and Wall Turbulence," *Journal of Fluid Mechanics,* Vol. 11.

Wilcox, D. C., 1993, *Turbulence Modeling for CFD,* DCW Industries, Inc., La Canada, CA.

V. I. Vasiliev
Senior Scientist,
Gas Dynamics Department.

D. V. Volkov
Junior Scientist,
Combustion Chambers Department.

S. A. Zaitsev
Research Scientist,
Gas Dynamics Department.

D. A. Lyubimov
Research Scientist,
Gas Dynamics Department.

Central Institute of Aviation Motors,
2 Ul. Aviamotornaya,
111250, Moscow, Russia

Numerical Simulation of Channel Flows by a One-Equation Turbulence Model

A one-equation model for turbulent viscosity, previously developed and tested for parabolic flows, is implemented in elliptic cases. The incompressible 2-D and axisymmetric flows in channel with back step as well as the incompressible and compressible 2-D flows in turbine blade cascades are calculated. The CFD procedures, developed for both incompressible and compressible turbulent flows simulation, are described. The results of calculations are compared with known experimental and numerical data.

Introduction

CFD is widely distributed in engineering practice now. The effectiveness of CFD modeling strongly depends not only on the numerical scheme, but also on the turbulence model. A satisfactory turbulence model should meet the following requirements: (i) it should provide acceptable accuracy of the turbulent stresses and heat fluxes simulation; (ii) it should be universal, i.e., allow the calculations of different flows without changes of coefficients and source terms; (iii) it should be numerically compatible, i.e. it should not impose additional restrictions on the algorithm which are not required for velocity field simulation, and must allow any reasonable boundary conditions.

The known complex models, like two-equation models, usually satisfy the two former requirements, but do not always satisfy the later one. For example, the well-known k-ϵ model causes instability in some cases. Algebraic models, like the Baldwin-Lomax model, are not universal, but are very compatible, so they are popular in engineering practice. We consider that one-equation models for turbulent viscosity, such as models of Secundov (1971), Spalart and Allmaras (1992), and Secundov (Gulyaev et al., 1993) are a reasonable compromise, which allows to satisfy all three requirements.

Secundov's model (1971) has been used for different parabolic flows simulations. Secundov (1971) calculated plane boundary layers, mixing layers and jets, and showed that, the accuracy of skin friction to be about 8 percent, and mixing layer thickness accuracy to be about 10 percent. Lebedev and Secundov (1976) adopted this model for boundary layer on rough surface. Kozlov et al. (1986) used the model for supersonic jets. Kuznetsov et al. (1976) used the model for diffusion flames. In the latter case, additional set of equations (turbulence energy, mean and variance mixture fraction balance equations) was calculated together with governing system of hydrodynamics equations and equation for turbulent viscosity. Vasiliev (1994) used a one-equation model and semi-inverse method for simulation of boundary layers with small separation bubbles. This model took part in Collaborative Testing of Turbulence Models (Bradshaw et al., 1991), and it showed an accuracy compatible with other tested models for parabolic flows.

Recently Secundov developed a new version of the one-equation model named $\nu_t 92$ (Gulyaev et al., 1993; see also Shur et al., 1995). This version gives results close to the old one in boundary layers, but improves the simulation of jets, i.e., it is more universal. However, the new version is more complex for CFD realization and the simple original ν_t model retains its usefulness for engineering practice.

The aim of the present work was to test the original one-equation model (Secundov, 1971) for elliptic flows. For this purpose the incompressible 2-D and axisymmetric flows in channel with back step, and the incompressible and compressible 2-D flows in turbine blade cascades, were calculated. The paper includes a brief description of numerical procedures, results of computations, and comparisons with known experimental and numerical data.

Mathematical Model

The averaged, steady-state conservation equations for 2-D or axisymmetric turbulent flows were written in curvilinear coordinates (ξ, η) as

$$\frac{\partial}{\partial \xi}\left[\frac{y^m}{J}\left((A - A_v)\xi_x + (B - B_v)\xi_y\right)\right] + \frac{\partial}{\partial \eta}\left[\frac{y^m}{J}\left((A - A_v)\eta_x + (B - B_v)\eta_y\right)\right] = \frac{m}{J} S \quad (1)$$

where: x, y are Cartesian ($m = 0$) or cylindrical ($m = 1$) coordinates; $J = (\partial(\xi, \eta))/(\partial(x, y))$ is Jacobian of mapping; the metrics of transformation ξ_x, ξ_y, η_x, η_y are related to the x, y coordinate system through relationships:

$$\xi_x = J\frac{\partial y}{\partial \eta}; \quad \xi_y = -J\frac{\partial x}{\partial \eta}; \quad \eta_x = -J\frac{\partial y}{\partial \xi}; \quad \eta_y = J\frac{\partial x}{\partial \xi}.$$

For compressible, nonswirling flows the fluxes and source term in (1) were given as:

Contributed by the Fluids Engineering Division for publication in the JOURNAL OF FLUIDS ENGINEERING. Manuscript received by the Fluids Engineering Division July 31, 1996; revised manuscript received July 7, 1997. Associate Technical Editor: P. M. Sockol.

$$A = \begin{pmatrix} \rho u \\ \rho u^2 + p \\ \rho uv \\ (e + p)u \end{pmatrix}, \quad B = \begin{pmatrix} \rho v \\ \rho uv \\ \rho v^2 + p \\ (e + p)v \end{pmatrix}$$

$$A_v = \begin{pmatrix} 0 \\ \tau_{11} \\ \tau_{12} \\ u\tau_{11} + v\tau_{12} + q_x \end{pmatrix},$$

$$B_v = \begin{pmatrix} 0 \\ \tau_{12} \\ \tau_{22} \\ u\tau_{12} + v\tau_{22} + q_y \end{pmatrix}, \quad S = \begin{pmatrix} 0 \\ 0 \\ p - \tau_{33} \\ 0 \end{pmatrix} \qquad (2)$$

where: ρ is density; u, v are components of the velocity vector $\vec{V}$; p is pressure; e is total energy per unit volume; q_x, q_y are heat flux components. The viscous stresses in (2) were written as:

$$\tau_{ij} = (\rho\nu_t + \mu)\left(\frac{\partial u_i}{\partial x_j} + \frac{\partial u_j}{\partial x_i}\right) - \frac{2}{3}\delta_{ij}(\rho\nu_t + \mu)\nabla\mathbf{V}; \quad i, j = 1, 2$$

$$\tau_{33} = 2(\rho\nu_t + \mu)\frac{v}{y} - \frac{2}{3}(\rho\nu_t + \mu)\nabla\mathbf{V} \qquad (3)$$

where subscripts $i = 1, 2$ stands for x and y, respectively; the ν_t is turbulent viscosity and μ is laminar dynamic viscosity; $\nabla\mathbf{V}$ is velocity divergence.

The assumption about perfect gas with constant heat capacities was used in the case of the compressible flows simulations. The total energy e was related with other variables by the conventional relationship $e = p/(\kappa - 1) + \rho(u^2 + v^2)/2$. The specific capacities ratio κ was set to $\kappa = 1.4$ for considered below examples. The heat fluxes were approximated as: $q_i = (\kappa/(\kappa - 1))(\rho\nu_t/\mathrm{Pr}_t + \mu/\mathrm{Pr})(\partial(p/\rho)/\partial x_i)$. Laminar and turbulent Prandtl numbers were equal to $\mathrm{Pr} = 0.7$, $\mathrm{Pr}_t = 0.9$, respectively. The laminar dynamic viscosity was calculated from the Satherland law: $\mu/\mu_0 = (T/T_0)^{3/2}((T_0 + C)/(T + C))$.

In the case of the incompressible flows simulations, the energy conservation equations was dropped out from system (1). The velocity divergence in relations for stress tensor components (3) was equal to zero ($\nabla\vec{V} = 0$). The laminar dynamic viscosity was assumed constant. The density was considered as to be constant except only one test case where CO_2 injection into the air flow was studied. In the latter case, the density was considered as a known function of carbon oxide mass fraction $\rho = \rho(c)$. The CO_2 mass fraction c was calculated from conventional conservation equation.

System (1) was accompanied by the equations for scalar parameters. In curvilinear coordinates, these equations were written as:

$$\frac{\partial}{\partial\xi}\frac{y^m}{J}(\rho(u\xi_x + v\xi_y)f - Q_\xi) + \frac{\partial}{\partial\eta}\frac{y^m}{J}(\rho(u\eta_x + v\eta_y)f - Q_\eta) = \frac{y^m}{J}S \qquad (4)$$

where f is calculated scalar parameter. The duffusive fluxes in (4) were given by the relations:

$$Q_\xi = \left(\rho\frac{\nu_t}{\sigma_t} + \frac{\mu}{\sigma}\right)\left[(\nabla\xi\cdot\nabla\xi)\frac{\partial f}{\partial\xi} + (\nabla\xi\cdot\nabla\eta)\frac{\partial f}{\partial\eta}\right]$$

$$Q_\eta = \left(\rho\frac{\nu_t}{\sigma_t} + \frac{\mu}{\sigma}\right)\left[(\nabla\eta\cdot\nabla\xi)\frac{\partial f}{\partial\xi} + (\nabla\eta\cdot\nabla\eta)\frac{\partial f}{\partial\eta}\right].$$

In present work, two conservation equations for scalar parameters were solved: for turbulent viscosity ($f = \nu_t$) and for passive scalar mass fraction ($f = c$). The latter was integrated only for axisymmetric back step with blowing of contaminant from the blunt side.

For the one-equation turbulence model the source term and coefficients in (4) were taken in the form presented in original work of Secundov (1971) (i.e., terms significant only in supersonic jets and/or in diffusion flames and neglegiable in considered cases were omitted):

$$\text{Source} = \rho\nu_t\left(0.2\alpha\Gamma - \frac{3\nu_t + 50\,\mu/\rho}{S^2}\right)$$

$$\Gamma^2 = 2\left[\left(\frac{\partial u}{\partial x}\right)^2 + \left(\frac{\partial v}{\partial y}\right)^2 + \left(\frac{\partial u}{\partial y}\right)\left(\frac{\partial v}{\partial x}\right)\right] + \left[\left(\frac{\partial u}{\partial y}\right)^2 + \left(\frac{\partial v}{\partial x}\right)^2 + 2m\left(\frac{v}{y}\right)^2\right],$$

$$\alpha = \frac{(\rho\nu_t/8\mu)^2 + 1.4(\rho\nu_t/8\mu) + 0.2}{(\rho\nu_t/8\mu)^2 - 1.4(\rho\nu_t/8\mu) + 1.0},$$

S – minimal distance to the wall, $\sigma_t = 0.5$, $\sigma = 1.0$.

Numerical Procedure

The solution of Eqs. (1), (4) was found as the steady-state solution of the time-dependent problem. For incompressible

Nomenclature

A, B, S, X = vector columns
C_f = skin friction coefficient
c = mass faction (for blowing from back step)/or chord length (for blades)
e = total energy per unit volume
J = Jacobian of mapping/or velocity ratio (for blowing from back step)
h = height of step
n = distance normal to the wall
L_u = turbulence integral length scale
Pr = Prandtl number
p = pressure
Q = diffusion fluxes (in scalar equations)
q = heat fluxes
Re = Reynolds number
S = minimal distance to the wall (in turbulence model equation)
Sc = Schimdt number
s = distance along the wall
T = temperature
t = pitch
U, V = reference velocities
u, v = velocity components
x, y = Cartesian or cylinder coordinates
α, Γ = terms in one-equation model
β = artificial compressibility coefficient
δ = boundary layer thickness
θ = inflow velocity angle
κ = specific heat capacities ratio
Λ, λ = finite-difference operators
μ = laminar viscosity/or molecular weights ratio (for blowing from back step)
ν_t = turbulent viscosity
ξ, η = curvilinear coordinates
ρ = density
σ_t, σ = coefficients in scalar equations
τ = viscous stresses

case the artificial compressibility approach (Chorin, 1967) was used. The artificial compressibility coefficient β was set equal to V_0^2 (Kwak et al., 1986), where V_0 is the reference velocity for each case.

Equations (1), (4) were written in finite-difference form as:

$$\frac{\Delta X}{J\Delta t} + \tilde{\Lambda}(\Delta X) = \Lambda X^n, \quad \frac{\rho^n \Delta f}{J\Delta t} + \tilde{\lambda}(\Delta f) = \lambda f^n,$$

where Λ and λ are the finite-difference operators, which approximate the left-hand sides and $\tilde{\Lambda}$, $\tilde{\lambda}$ are the simplified operators, which control convergence, $X^{n+1} = X^n + \Delta X$, $f^{n+1} = f^n + \Delta f$, n – number of time step, f is scalar parameter.

The approximation of convective fluxes in operator Λ was different for incompressible and compressible cases. For incompressible case the third-order scheme of Rogers and Kwak (1990) was used. For compressible case the Chakravarthy and Szema (1987) third-order TVD scheme was applied.

The diffusion fluxes were approximated by a central-difference scheme of second-order approximation. Only five cross terms were retained in $\tilde{\Lambda}$ and $\tilde{\lambda}$ operators.

The convective fluxes in operators $\tilde{\Lambda}$ and $\tilde{\lambda}$ were approximated by the upwind first-order scheme.

At points adjacent to the boundary, the high-order stencils cannot be maintained, so the central difference scheme with small dissipation was applied there following Rogers and Kwak (1990).

The resulting system of algebraic equations for ΔX was solved by line relaxation block-tridiagonal algorithm. The algebraic equations for scalar parameters were solved by a point Gauss-Seidel method using 2 iterations with alternative directions of scanning at each step.

The numerical procedure for incompressible fluid was checked with the help of analytic solution for round axisymmetric pipe. The numerical procedure for compressible flows was checked by comparisons with analytic solution for oblique shock, self-similar solution for boundary layer, and known numerical solution for laminar flow (shock/boundary layer interaction). The shock/boundary layer interaction was calculated at the same conditions and with the same grid as in the work of Beam and Warming (1978). The comparison with Beam and Warming's data is shown in Fig. 1, where the pressure distribution along the wall and skin friction coefficient are plotted. The agreement is reasonably good.

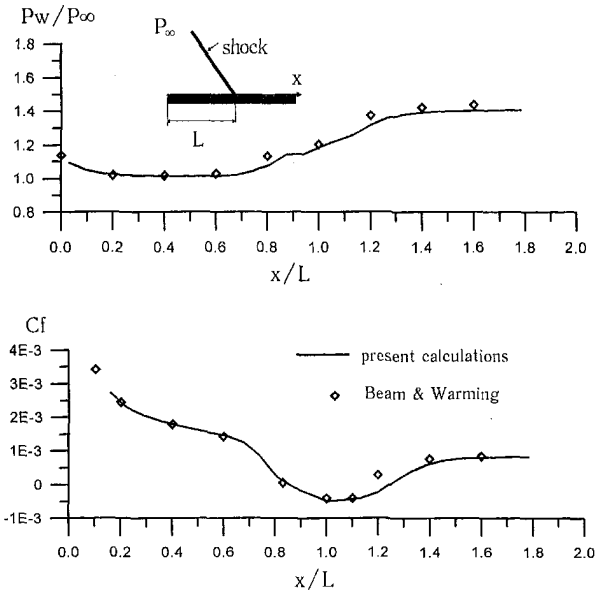

Fig. 1 Shock/boundary layer interaction (laminar case)

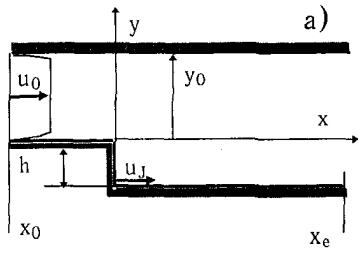

Fig. 2(a) Scheme of flow

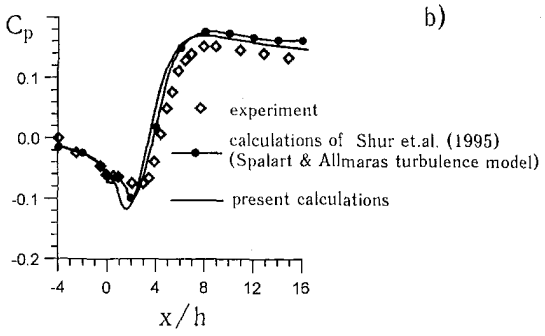

Fig. 2(b) Pressure coefficient on stepped wall

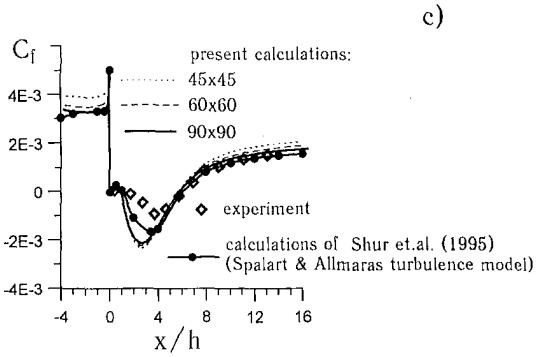

Fig. 2(c) Skin friction coefficient on stepped wall

Fig. 2 The channel with back step

Results of Calculations

Plane Duct With Back Step. The first test for the turbulence model was incompressible flow in a plane duct with sudden expansion. This case was experimentally studied by Driver and Seegmiller (1985) and calculated by Shur et al. (1995), who used Spalart and Allmaras (1992) and $\nu_t 92$ one-equation turbulence models.

The schematic of flow and coordinate system are shown in Fig. 2(*a*). The inlet height of the duct inlet equals $y_o = 8h$, the left boundary of computational domain was located at $x_o = -4h$, and the right one at $x_e = 16h$, where h is the height of step. The H-type computational grid was non-uniform with nodes packed near the wall. The set of grids with 45×45, 60×60, 90×90 cells was used to check the mesh influence (the first figure is the total number of cells in longitudinal direction and the second one is the number of cells in cross direction in outlet part).

The no-slip conditions were prescribed on the walls (i.e., $u = v = \nu_t = 0$, $\partial p/\partial n = 0$, where ∂/∂_n—is a derivative normal to the wall). The incoming flow included homogeneous core and boundary layers near the wall. The velocity and viscosity distributions in boundary layers were assumed the same as in flat plate boundary layer, which thickness was the same as in experiment. These distributions were calculated by the boundary layer code of Vasiliev (1994) which

implemented the same turbulence model. According to experiment the boundary layer thickness at the inlet was equal $\delta/h = 1.5$. The pressure at the entrance satisfied the condition $-\partial^2 p/\partial^2 n = 0$. The velocity and viscosity at the exit satisfied the smooth conditions $\partial^2 f/\partial^2 n = 0$, and the pressure was prescribed there. The calculations were performed for $\mathrm{Re}_h = u_o h/\nu = 3.7 \cdot 10^4$, where u_o is the velocity in potential core of inflow.

The calculated skin friction ($C_f = \tau_w/0.5\rho u_o^2$) and pressure coefficients ($C_p = (p - p_o)/0.5\rho u_o^2$) along the wall with step are presented in Figs. 2(*b*) and 2(*c*), respectively. The data for C_f illustrate the influence of grid and demonstrate that 90 × 90 grid gave adequate resolution. The current results are in reasonable agreement with experimental data, and with calculations of Shur et al. (1995) performed with Spalart and Allmaras model (1992). The interesting feature of this flow is the vortex structure near the corner, shown in Fig. 3, where at least three vortices can be recognized.

Axisymmetric Duct With Back Step. The second example was the flow in an axisymmetric duct with blowing from the blunt side of the step, experimentally studied by Lightman et al. (1980). The primary gas was air and the blowing gas was CO_2. The Mach number was small ($M = 0.14$) so the flow was

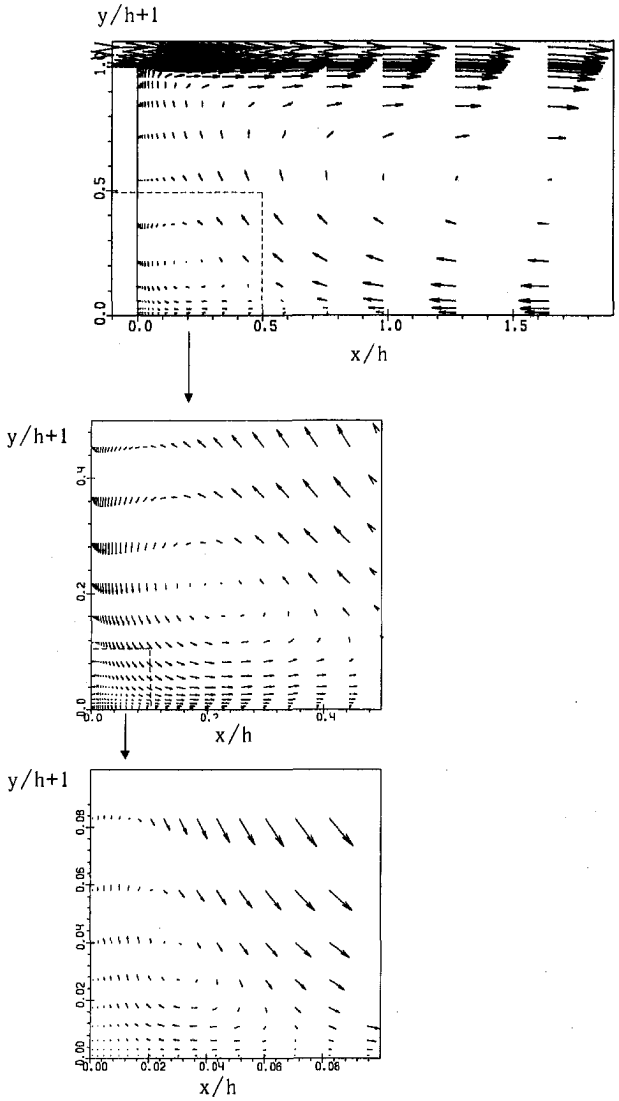

Fig. 3 Vortex structure near the corner

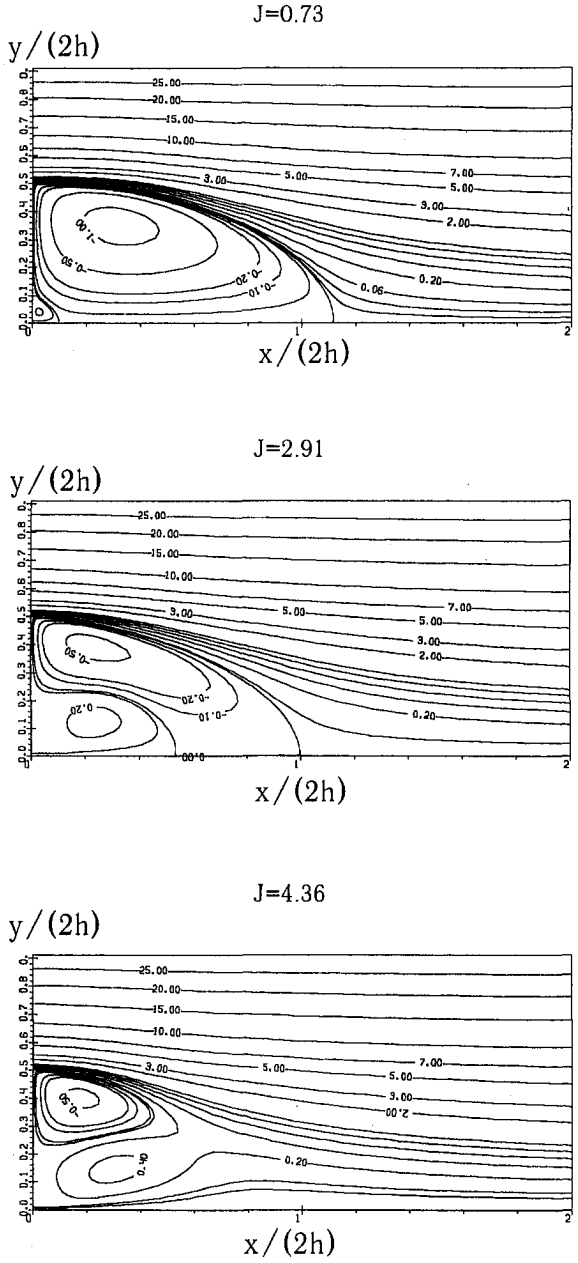

Fig. 4 Streamlines patterns at different intensities of blowing jet

considered as incompressible. The density was related with mass fraction of blowing gas by relationship:

$$\rho/\rho_0 = 1/(1 + (\mu - 1)c)$$

where c is the mass fraction of blowing gas, ρ_o is the density of primary gas, μ is the primary to blowing gases molecular weights ratio.

The schematic of flow and coordinate system were the same as in Fig. 2(*a*), except that now the bottom boundary downstream of the step was the axis of symmetry. The inlet height of the duct was $y_o = 0.814h$, the left boundary of computational domain was located at $x_o = -8h$, and the right one at $x_e = 9h$. The H-type computational grid contained 75 × 120 cells, packed near the walls and axis.

The boundary conditions for velocity, pressure, and viscosity on the walls, at the entrance and at the exit were the same as for the plane case. The mass fraction at the entrance was $c = 0$. The boundary conditions for concentration were: $\partial c/\partial n = 0$

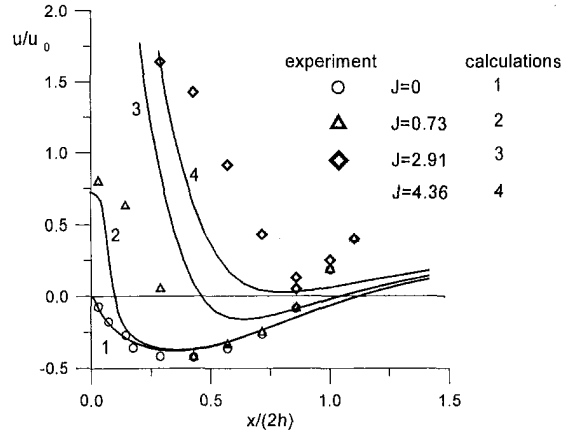

Fig. 5 Velocity distribution along the axis

at the walls and $\partial^2 c/\partial^2 n = 0$ at the exit. The boundary conditions on the axis were prescribed as follows: $\partial u/\partial n = \partial \nu_t/\partial n = \partial p/\partial n = \partial c/\partial n = v = 0$. In order to simulate the blowing from the blunt side of the step, it was assumed, that in region $y/h < 0.034$ velocity and concentration satisfied the requirements: $u/u_o = J$, $c = 1$.

The calculations were performed at $\mathrm{Re}_h = u_o h/\nu = 5.4 \cdot 10^5$, $\mu = 0.659$, and for J varied in the range: $0 < J < 4.36$.

The streamlines patterns at some values of J are shown in Fig. 4. These pictures illustrate the changes of flow structure due to the jet blowing. At low jet momentum, the recirculation zone is disturbed only slightly i.e., the flow structure at $J = 0.73$ was similar to the flow structure at $J = 0$, except small region near injector. At high momentum, the recirculation zone near the axis is destroyed and the separation bubble moves up to the edge of the step. Qualitatively these pictures correspond to experimental observations. The quantitative comparison is presented in Fig. 5, where the velocity distributions along the axis are plotted. In case $J = 0$ the agreement with experiment is good, but the rate of jet dilution is overestimated by the model. One can expect that this is due to the fact that the flow field near injector is close to flow pattern in plume axisymmetric jet. It is known (Pope, 1978) that turbulence models for turbulent viscosity does not provide sufficient accuracy for predictions of such flows without introduction of additional terms which should take into account difference between plane and axisymmetrical cases. Possibly the accuracy of model predictions can be improved by the implementation of more recent $\nu t - 92$ version of the model (Gulyaev et al., 1993), where such additional terms were introduced to describe axisymmetric flows more accurately. However, the question requires additional consideration and this work is in progress now.

Turbine Blades Cascade (Incompressible Flow). The model turbine blades cascade flow was considered as another example. The tests of large scale model (chord $c = 1$ m, pitch to chord ratio $- t/c = 0.64$) was done at CIAM by Kazarin (see Vasiliev et al., 1995) at a very low Mach number ($M = 0.02$).

The incompressible code was used for simulation. The calculations were performed for Reynolds number $\mathrm{Re} = V_0 c/\nu = 3.3\ 10^5$ and for zero value of the inlet flow angle ($\theta = 0$). The free-stream turbulent viscosity (ν_{t0}) was estimated as $\nu_{t0} = 0.12 u' L_u$, where u' is the measured turbulence intensity, and L_u is the measured turbulence length scale. This estimation provided $\nu_{t0}/V_0 c = 1.6 \cdot 10^{-4}$. The boundary conditions on the wall and at the exit were the same as above. The inflow was expected to be uniform i.e., $u = V_0 \cos\theta$, $v = V_0 \sin\theta$, $\nu_t = \nu_{t0}$ and $\partial^2 p/$

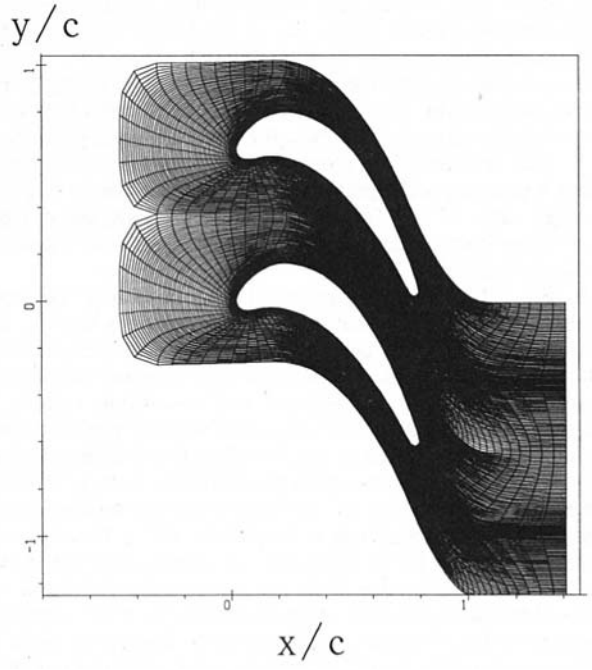

Fig. 6 Computational grid for blade cascade (incompressible case)

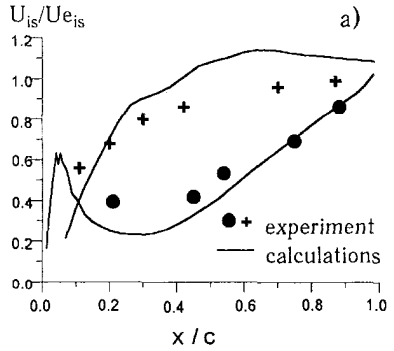

Fig. 7(a) Isentropic velocity distribution along the blade

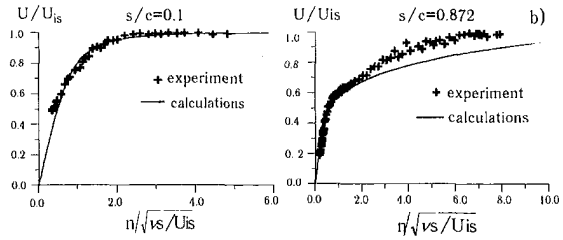

Fig. 7(b) Velocity profiles

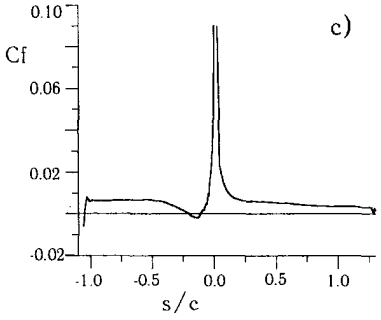

Fig. 7(c) Skin friction coefficient

Fig. 7 Low Mach number flow in blade cascade

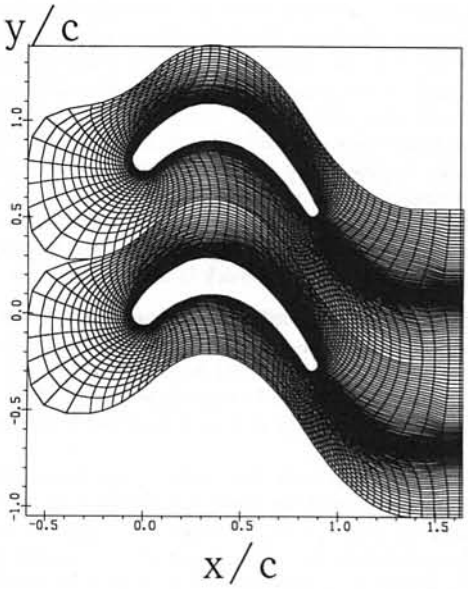

Fig. 8(*a*)

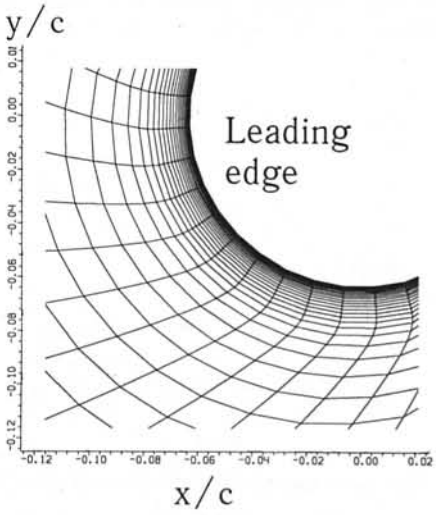

Fig. 8(*b*)

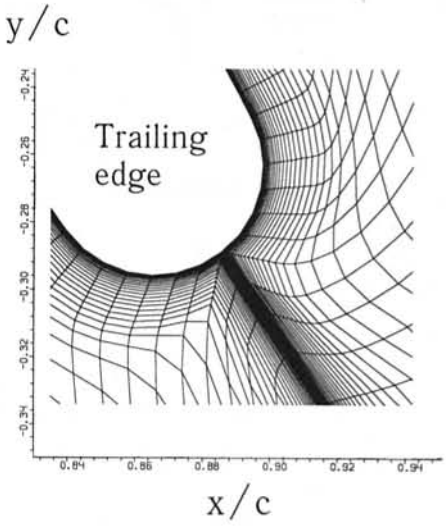

Fig. 8(*c*)

Fig. 8 Computational grid for blade cascade (compressible case)

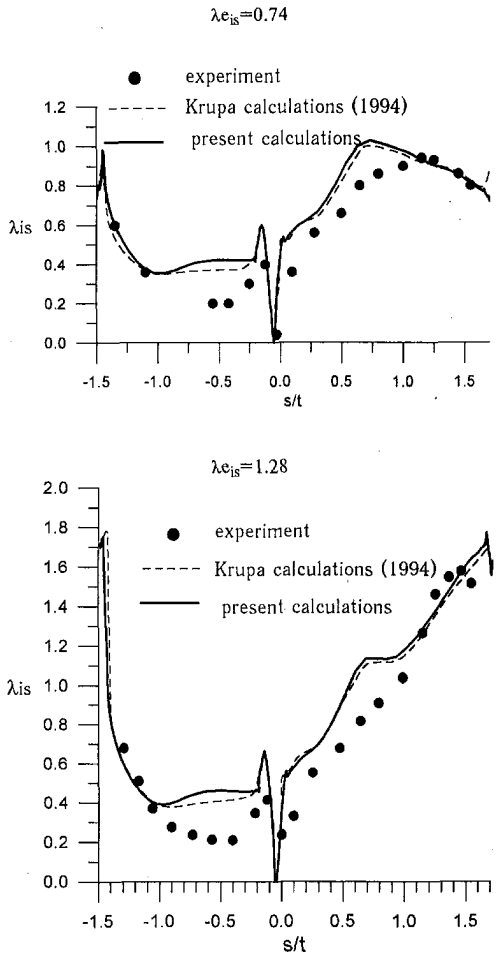

Fig. 9 Isentropic Laval number distribution along the blade

$\partial n^2 = 0$. The upper and lower boundaries of the computational domain were periodic.

The typical computational C-type grid is presented in Fig. 6. The nodes were denser near the wall. The calculations were performed on a set of grids—80 × 20, 120 × 40, 120 × 80, which were characterized by the following values of y^+ in first near-wall cell: about 1 for finest grid, about 3 for midsize, and 10 for coarse grid. The calculated pressure distributions were very close for all grids. However, the boundary layer parameters (e.g., skin friction) were close only for finer grids (difference about 1 percent) and significantly different for coarse grid due to large value of y^+. Thus, the medium grid was the optimal one among considered meshes (i.e., 120 × 40 with 88 points on blade surface).

In Fig. 7(*a*) the comparison of calculated and measured isentropic velocity distributions along the blade is shown. The isentropic velocity was calculated using the Bernoulli equation with total pressure at the entrance and static pressure on the wall. Here U_{is} - local isentropic velocity, Ue_{is} - isentropic velocity at the exit of the cascade. The calculated velocity profiles inside boundary layer are given in Fig. 7(*b*) together with experimental data (U - velocity component parallel to the wall, n - distance normal to the wall, s is the distance from the leading edge). The profile on suction side is laminar at $s/c = 0.1$, but it is turbulent at $s/c = 0.872$. Thus, the turbulence model predicted laminar-turbulent transition in considered case (it should be stressed that we speak here about so-called "bypass" transition mechanism i.e., boundary layer transition due to presence of the external turbulence). The experimental visualizations indicated the existence of a separation bubble on pressure side, and

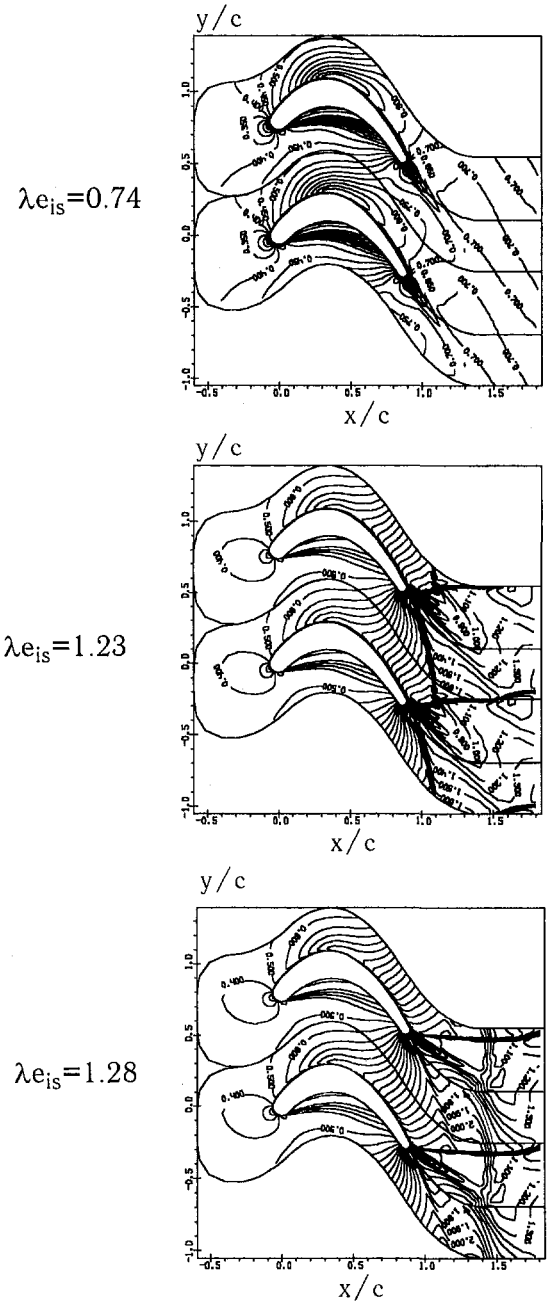

Fig. 10 Mach number contours

this bubble is predicted by calculations, as confirmed by the skin friction distribution, presented in Fig. 7(*c*).

Turbine Blades Cascade (Compressible Flow). As the example of compressible flow in turbine blade cascade the flow previously studied by Krupa (1994) was considered. Krupa performed the calculations using the two-equation Coakley model (Coakley, 1983). Along with calculations, some known experimental data for this cascade were presented in his work (Krupa, 1994).

The parameters of cascade were: chord lenght $c = 62.81$ mm and pitch to chord ratio $t/c = 0.799$. The calculations were performed at $\theta = 38$ deg, the isentropic Laval number at the exit (λe_{is}) is varied in range 0.74–1.28 and Reynolds number ($\mathrm{Re} = \rho e_{is} V e_{is} c/\mu_0$, μ_0-air viscosity at $T = 273$ K) in range $7.76 \cdot 10^5$–$8.43 \cdot 10^5$, where Ve_{is} is the isentropic velocity at the exit of cascade. The free stream turbulent viscosity estimation is based on measured intensity ($Tu = 8$ percent) and evaluated length scale ($L_u/c = 0.05$) and equals $-\nu_{t0}/Ve_{is}c = 2.4 \cdot 10^{-4}$.

The no-slip and adiabatic conditions were prescribed on the walls (i.e., $u = v = \nu_t = 0$, $\partial\rho/\partial n = \partial e/\partial n = 0$). The flow at the entrance was assumed uniform with prescribed flow angle θ, total pressure and temperature; condition for energy was taken in the form: $\partial e/\partial n = 0$. At the exit the pressure was prescribed and other variables were satisfied the conditions $\partial^2 f/\partial^2 n = 0$. Other boundaries were periodic.

The computational C-type grid is presented in Fig. 8(*a*). Details of the grid near the leading and trailing edges are shown in Fig. 8(*b*, *c*). The number of cells for this grid was 120 × 40 with 88 points on the blade surface. The characteristic value of y^+ in the first near-wall cell was about 3.

The distributions of isentropic Laval number along the blade profile for the most distinct cases (subsonic and supersonic) are shown in Fig. 9. The present calculations were compared with calculations and experimental data of Krupa (1994). The Mach number contours are presented in Fig. 10. One can see, that the locations of shocks are well captured by the present scheme. These maps are in good agreement with maps obtained by Krupa. Both CFD modeling indicate separation on the pressure side for the considering geometry and conditions. It should be noted also, that the comparison with known data showed, that the one-equation model ensures at least the same accuracy as the two-equation Coakley model. However, both models reveal some discrepancies with experiment.

Conclusions

1) Two numerical procedures for simulation of incompressible or compressible turbulent flows by one-equation turbulence model were developed. 2) A set of separated flows was calculated and results were compared with known experimental and numerical data. The comparisons showed that the one-equation Secundov model (Secundov, 1971) demonstrated reasonable agreement with experimental data for back step flows, but overpredicted the rate of round jet spreading downstream the axisymmetric back step. The one-equation model demonstrates practically the same accuracy as two-equation Coakley model (Coakley, 1983) for turbine blade cascades, but it is more simple and robust model.

Acknowledgments

The current study was partially supported by the Russian Foundation for Basic Research (Grants No95-01-00251a and No95-01-00642a).

References

Beam, R. M., and Warming, R. F., 1978, "An Implicit Factored Scheme for the Compressible Navier-Stokes Equations," *AIAA Journal,* Vol. 16, No. 4, pp. 393–402.

Bradshaw, P., Launder, B., and Lumley, J., 1991, "Collaborative Testing of Turbulence Models," AIAA paper 91-0215.

Chakravarthy, S. R., and Szema, K. Y., 1987, "Euler Solver for Three-Dimensional Supersonic Flows with Subsonic Pockets," *Journal of Aircraft,* Vol. 24, No. 2, pp. 73–83.

Chorin, A. J., 1967, "A Numerical Method for Solving Incompressible Viscous Flow Problems," *Journal of computational physics,* Vol. 2, pp. 12–26.

Coakley, T. J., 1983, "Turbulence Modelling Methods for the Compressible Navier-Stokes Equations," AIAA paper No. 83–1693.

Driver, D. M., and Seegmiller, H. L., 1985, "Features of a Reattaching Turbulent shear Layer in Divergent Channel Flow," *AIAA Journal,* Vol. 23, No. 2, pp. 163–171.

Gulyaev, A. N., Kozlov, V. Ye., and Secundov, A. N., 1993, "A Universal One-Equation Model for Turbulent Viscosity," *Fluid Dynamics,* No. 4, pp. 485–494.

Kozlov, V. Ye., Secundov, A. N., Smirnova, I. P., 1986, "Models of Turbulence for the Description of a Flow in a Jet of Compressible Gas," *Fluid Dynamics,* No. 6, pp. 875–881.

Krupa, V. G., 1994, "Simulation of Steady and Unsteady Viscous Flows in Turbomachinery," in AGARD lecture series TCP 02/LS198 pp. 7-1–7-39.

Kuznetsov, V. R., Lebedev, A. B., Secundov, A. N., and Smirnova, I. P., 1977, "Calculation of a Turbulent Diffusion Combustion Flame, Taking Account of

Concentration Pulsations and Archimedean Forces," *Fluid Dynamics,* No. 1, pp. 24–33.

Kwak, D., and Chang, J. L. S., Shanks, S. P., Chakravarthy, S. R., 1986, "A Three-Dimensional Incompressible Navier-Stokes Flow Solver Using Primitive Variables," *AIAA Journal,* Vol. 24, No. 3, pp. 390–396.

Lebedev, A. B., and Secundov, A. N., 1976, "Use of Equation of Turbulent Viscosity to Describe the Flow Near a Rough Surface," *Fluid Dynamics,* No. 5, pp. 741–744.

Lightman, A. J., Richmond, R. D., Krishnamurthy, L., and Magill, P. G., Roquemore, W. M., Bradley, R. P., Stutrud, J. S., Reeves, C. M., 1980, "Velocity Measurements in a Bluff-Body Diffusion Flame," AIAA paper 80-1544, 9 p.

Pope, S. B., 1978, "An Explanation of the Turbulent Round Jet/Plane Jet Anomaly," *AIAA Journal,* Vol. 16, p. 279–281.

Rogers, S. E., and Kwak, D., 1990, "Upwind Differencing Scheme for the Time-Accurate Incompressible Navier-Stokes Equations," *AIAA Journal,* Vol. 28, No. 2, pp. 253–262.

Secundov, A. N., 1971, "Application of a Differential Equation for Turbulent Viscosity to the Analysis of Plane Non-Self-similar Flows," *Fluid Dynamics,* No. 5, pp. 828–840.

Shur, M., Strelets, M., Zaikov, L., Gulyaev, A., Kozlov, V., and Secundov, A., 1995, "Comparative numerical testing of one- and two-equation turbulence models for flows with separation and reattachment," AIAA paper 95-0863.

Spalart, P. R., and Allmaras, S. R., 1992, "A One-Equation Turbulence Models for Aerodynamic Flows," AIAA paper No. 92-0439.

Vasilev, V. I., 1994, "Computation of Separated Duct Flows Using the Boundary-Layer Equations," *AIAA Journal,* Vol. 32, No. 6, pp. 1191–1199.

Vasiliev, V. I., Zaitsev, S. A., and Kazarin, F. V., 1995, "The Application of a One-Equation Turbulence Model to and an Experimental Study of Transition Under Typical Turbomachinery Blades Conditions," ERCOFTAC Bulletin, No. 24, Mar., pp. 48–52.

X. Zheng[1]
Research Associate. Mem. ASME

C. Liao
Research Associate.

C. Liu‡
Associate Professor. Mem. ASME

Department of Mathematics and Statistics,
Louisiana Tech University,
Ruston, LA 71272

C. H. Sung
Senior Research Scientist. Mem. ASME

T. T. Huang
Chief Research Scientist. Mem. ASME

David Taylor Model Basin,
Carderock Division, NSWC,
Bethesda, MD 20084

Multigrid Computation of Incompressible Flows Using Two-Equation Turbulence Models: Part I—Numerical Method

A highly efficient numerical approach based on multigrid and preconditioning methods is developed for modeling 3-D incompressible turbulent flows. The incompressible Reynolds-averaged Navier-Stokes equations are written in pseudo-compressibility form, then a preconditioning method is used to reduce the wave speed disparity. The k-ω and k-ϵ turbulence models are used to estimate the effects of turbulence. The model equations are solved together with the N-S equations in a strongly-coupled way, and all the acceleration techniques originally developed for N-S equations are also used for the turbulence model equations. A point-implicit technique is developed to improve the efficiency of the solution of the turbulence model equations.

1 Introduction

The ability to compute the flow over complete under-water vehicles is of great interest in hydrodynamic analysis and design. Theoretically, the physics of flow is described by the incompressible Navier-Stokes equations. However, direct numerical solution of Navier-Stokes equations for engineering applications is not feasible with currently available computer resources since the realistic flow problems are usually of high Reynolds numbers and with multiple length scales. Instead, the Reynolds-averaged Navier-Stokes (RNS) equations are solved supplemented by turbulence model equations. In this way, many fluid dynamic problems can be effectively solved. For incompressible turbulent flows, considerable progress has been made in the simulation of high Reynolds number flows around naval vehicle models (Sung et al., 1991; Alessandrini and Delhommeau, 1994; Sheng et al., 1995; Sung et al., 1995). However, to be really useful to design community, the simulation code must meet several stringent requirements of efficiency, accuracy, robustness and low computer storage. First of all, accuracy is one of the most challenging problems today in CFD. The industry generally requires less than 2 percent error in drag prediction, and 5 percent error in prediction of forces and moments acting on a realistic body at high Reynolds numbers on the order of 10^6 to 10^9. There are many factors that affect accuracy. Among those factors, the performance of turbulence models is commonly blamed for poor predictions. Of course, there are other factors leading to inaccuracy including numerical errors from discretization, artificial dissipation, grid quality and even programming errors. Nevertheless, turbulence modeling remains as one of the major concerns in CFD community.

It is noted that most computations of turbulent flows about underwater vehicles employed an algebraic turbulence model, more specifically, the Baldwin-Lomax model. This model is popular because it is easy to implement for simple geometry and works fairly well in some cases. It is particularly useful in the early stage of development of a code. However, this kind of model has both numerical and physical difficulties. Numerical difficulties include awkward implementation in 3-D case with junctures and multi-wall, slow convergence if length scale jumps between grid points. Physical difficulties include the crude transition model and the neglect of freestream turbulence effects, surface roughness. Most of all, it gives poor prediction of separation.

In the present work, the k-ω model originally developed by Wilcox (1988) is applied. Comparing to other two-equation models such as the k-ϵ models, the k-ω model has the advantage that it does not require damping functions in the viscous sub-layer and no normal distance from the wall needs to be defined. Furthermore, it has been designed to achieve more accurate prediction for adverse pressure gradient flows. Very encouraging results for separated flows have been reported by Menter (1991), Liu and Zheng (1994), and Zheng and Liu (1995).

However, investigators using two-equation models seem to have been more concerned with the solution of the N-S equations. Less attention is paid to the solution method for the turbulence model equations. In most cases, the turbulence model equations are loosely coupled with the N-S equations, multigrid acceleration is only applied to the solution of N-S equations due to perhaps the fact the turbulence model equations are source-term dominant and very stiff in the sub-layer region.

In this paper, a multigrid method is developed to solve the two-equation turbulence models as well as the N-S equations. These two sets of equations are solved by using a strongly-coupled time marching method. Two popular two-equation models, k-ω and k-ϵ, are discussed in this work. A point-implicit technique is developed to improve the efficiency of the solution, and more importantly to alleviate the stiffness of the governing

[1] Current address: Adina R & D, Inc., Watertown, MA 02172.

Contributed by the Fluids Engineering Division for publication in the JOURNAL OF FLUIDS ENGINEERING. Manuscript received by the Fluids Engineering Division May 30, 1996; revised manuscript received July 21, 1997. Associate Technical Editor: P. M. Sockel.

equations exhibited in near wall region. Treatments of the source terms of turbulence model through the multigrid process are tested and analyzed.

2 Governing Equations and Turbulence Model

The incompressible Reynolds-averaged Navier-Stokes equations are:

$$\frac{\partial u_j}{\partial x_j} = 0 \tag{1}$$

$$\frac{\partial u_i}{\partial t} + \frac{\partial u_i u_j}{\partial x_j} + \frac{1}{\rho}\frac{\partial p}{\partial x_j} + \frac{\partial}{\partial x_j}(\overline{u_j' u_j'}) - \frac{\partial}{\partial x_j}\left[\nu\left(\frac{\partial u_i}{\partial x_j} + \frac{\partial u_j}{\partial x_i}\right)\right] = 0 \quad i, j = 1, 2, 3 \tag{2}$$

where u_j is the velocity, p is the pressure, ρ is the constant density, ν is the molecular kinematic viscosity, u_i', u_j' are the fluctuation parts of the velocity u_i and u_j, and $\overline{u_i' u_j'}$ is the Reynolds stress tensor which can be modeled by:

$$\overline{u_i' u_j'} = \tilde{\tau}_{i,j} = \frac{1}{\rho}\hat{\tau}_{i,j} = \frac{2}{3}\delta_{ij}k - \nu_t\left(\frac{\partial u_i}{\partial x_j} + \frac{\partial u_j}{\partial x_i}\right)$$

The turbulent kinetic energy k and eddy viscosity ν_t are to be determined by a turbulence model. In the present work, the k-ω turbulence model by Wilcox (1988) and the k-ϵ model by Launder and Sharma (1974) are used.

The k-ω model consists of two equations:

$$\frac{\partial k}{\partial t} + \frac{\partial}{\partial x_j}(u_j k) = \frac{\partial}{\partial x_j}\left[(\nu + \sigma_k \nu_T)\frac{\partial k}{\partial x_j}\right] + \tilde{\tau}_{i,j}\frac{\partial u_i}{\partial x_j} - \beta_k \omega k \tag{3}$$

$$\frac{\partial \omega}{\partial t} + \frac{\partial}{\partial x_j}(u_j \omega) = \frac{\partial}{\partial x_j}\left[(\nu + \sigma_\omega \nu_T)\frac{\partial \omega}{\partial x_j}\right] + (\gamma_\omega \omega/k)\tilde{\tau}_{i,j}\frac{\partial u_i}{\partial x_j} - \beta_\omega \omega^2 \tag{4}$$

The eddy viscosity is calculated from:

$$\nu_T = \frac{k}{\omega}. \tag{5}$$

The closure coefficients for the standard high-Reynolds number model are: $\beta_k = 9/100$, $\sigma_k = 1/2$, $\beta_\omega = 3/40$, $\gamma_\omega = 5/9$, $\sigma_\omega = 1/2$.

The generic k-ϵ model can be described as:

$$\frac{\partial k}{\partial t} + \frac{\partial}{\partial x_j}(u_j k) = \frac{\partial}{\partial x_j}\left[(\nu + \sigma_k \nu_T)\frac{\partial k}{\partial x_j}\right] + \tilde{\tau}_{i,j}\frac{\partial u_i}{\partial x_j} - \tilde{\epsilon} \tag{6}$$

$$\frac{\partial \epsilon}{\partial t} + \frac{\partial}{\partial x_j}(u_j \epsilon) = \frac{\partial}{\partial x_j}\left[(\nu + \sigma_\epsilon \nu_T)\frac{\partial \epsilon}{\partial x_j}\right] + (\gamma_\epsilon \tilde{\epsilon}/k)\tilde{\tau}_{i,j}\frac{\partial u_i}{\partial x_j} - \beta_\epsilon f_2 \frac{\tilde{\epsilon}\epsilon}{k} + \nu_t E \tag{7}$$

The eddy viscosity is calculated from:

$$\nu_T = C_\mu f_\mu \frac{k^2}{\tilde{\epsilon}}, \quad \tilde{\epsilon} = \epsilon + D \tag{8}$$

The closure coefficients are: $C_\mu = 0.09$, $\sigma_k = 1.$, $\beta_\epsilon = 1.92$, $\gamma_\epsilon = 1.44$, $\sigma_\epsilon = 10/13$.

D, E, f_μ, and f_2 are introduced to better represent the near-wall behavior. For the standard high Reynolds number model, they are simply set to: $D = E = 0$ and $f_\mu = f_2 = 1$. But in the modified low Reynolds number model by Launder and Sharma, those functions are set to: $D = 2\nu(\partial\sqrt{k}/\partial x_i)^2$, $E = 2\nu(\partial^2 u_i/\partial x_j \partial x_k)^2$, $f_\mu = \exp[-3.4/(1 + R_T/50)^2]$, $f_2 = 1 - 0.3 \times \exp(-R_T^2)$ with $R_T = k^2/\nu\tilde{\epsilon}$.

3 Pseudo-Compressibility Methods

The Reynolds-averaged Navier-Stokes (RNS) equations are solved by using the pseudo-compressibility approach first proposed by Chorin (1967) and improved later by Turkel (1987).

The conservative form of the preconditioned incompressible RNS equations can be written as:

$$P^{-1}\frac{\partial q}{\partial t} + \frac{\partial F}{\partial x} + \frac{\partial G}{\partial y} + \frac{\partial H}{\partial z} = 0 \tag{9}$$

where

$$q = \begin{pmatrix} p^* = \frac{p}{\rho} \\ u \\ v \\ w \end{pmatrix} \quad F = \begin{pmatrix} u \\ u^2 + p^* - \tau_{xx} \\ uv - \tau_{xy} \\ uw - \tau_{xz} \end{pmatrix}$$

$$G = \begin{pmatrix} v \\ uv - \tau_{yx} \\ v^2 + p^* - \tau_{yy} \\ vw - \tau_{yx} \end{pmatrix} \quad H = \begin{pmatrix} w \\ uw - \tau_{zx} \\ vw - \tau_{zy} \\ w^2 + p^* - \tau_{zz} \end{pmatrix}$$

$$\tau_{ij} = (\nu + \nu_t)\left(\frac{\partial u_i}{\partial x_j} + \frac{\partial u_j}{\partial x_i}\right)$$

where t is the time, $p^* = p/\rho$, p is the pressure, ρ is the constant density, u, v and w are the three Cartesian velocity components, ν is the molecular viscosity, ν_t is the eddy viscosity, P is a preconditioning matrix. A general form given by Turkel can be expressed as:

$$P^{-1} = \begin{bmatrix} (1+\gamma)\beta^{-2} & \gamma\beta^{-2}u & \gamma\beta^{-2}v & \gamma\beta^{-2}w \\ (1+\alpha+\gamma)\beta^{-2}u & 1+\gamma\beta^{-2}u^2 & \gamma\beta^{-2}uv & \gamma\beta^{-2}uw \\ (1+\alpha+\gamma)\beta^{-2}v & \gamma\beta^{-2}vu & 1+\gamma\beta^{-2}v^2 & \gamma\beta^{-2}vw \\ (1+\alpha+\gamma)\beta^{-2}w & \gamma\beta^{-2}wu & \gamma\beta^{-2}wv & 1+\gamma\beta^{-2}w^2 \end{bmatrix}.$$

For central difference schemes, fourth-order dissipation terms are needed to eliminate odd-and-even decoupling modes for the conservative variables. The final forms of the governing equations for numerical computations can be written as:

$$P^{-1}\frac{\partial q}{\partial t} + \frac{\partial F}{\partial x} + \frac{\partial G}{\partial y} + \frac{\partial H}{\partial z} + C_4\{\delta_\xi(P^{-1}|PA|\delta_{\xi\xi\xi}q) + \delta_\eta(P^{-1}|PB|\delta_{\eta\eta\eta}q) + \delta_\zeta(P^{-1}|PC|\delta_{\zeta\zeta\zeta}q)\} = 0 \tag{10}$$

where C_4 is a parameter to control the amount of dissipation to be added to the system. Usually $C_4 = 0.01 \sim 0.04$. δ is a difference operator. δ_ξ is the first central difference in ξ direction, and $\delta_{\xi\xi\xi}$ is the third central difference in ξ direction. ξ, η, ζ are the three grid coordinate directions. A, B, and C are the Jacobians of the flux vectors in the ξ, η, ζ directions, respectively.

Note that the dissipation term of Eq. (10), for instance in ξ direction, is based on $P^{-1}|PA|$ rather than $|A|$. This makes the evaluation of artificial dissipation terms quite expensive. However, we do have the option of not applying the preconditioner P to the dissipation terms, therefore, the eigenvalues of PA can used to construct the artificial dissipation. Keep in mind that the maximum eigenvalue of $|PA|$ is smaller than that of $|A|$.

Through numerical experiences, the optimal preconditioning parameters are selected as:

$$\alpha = 1, \quad \gamma = 0, \quad \beta^2 = \max(|u|^2, \epsilon_\beta), \quad \epsilon_\beta = 0.7.$$

No preconditioning is needed for the convection terms of the turbulence model equations since the wave speeds are already equal to the convective velocity, which is also one of the eigenvalues of the preconditioned Navier-Stokes equations.

4 Numerical Methods

The flow equations (RNS) and the turbulence model equations are discretized by using different schemes due to the totally different characteristics of their solutions.

In incompressible flows, usually there is no discontinuity phenomenon such as shock waves. High-resolution schemes, like TVD and eigenvalue-based upwind scheme, are not necessary, because those schemes are quite expensive and only make a difference near the shock waves. Therefore, for the flow equations, the regular second-order central difference scheme is used. Only fourth-order artificial dissipation terms are added to the system as shown in Eq. (10). Those terms, in higher order than the numerical scheme, only provide additional dissipation to suppress numerical spurious oscillations. Therefore they will not contaminate the physical solutions as sometimes the second-order dissipation terms might.

Since the fourth-order artificial terms are very small, and there is no significant difference between the eigenvalues after preconditioning, therefore, it is not worthy to use matrix dissipation either. In this work, the maximum spectral radii of the matrices PA, PB, PC are used instead of the matrices A, B, and C.

However, for the turbulence model equations, a high-order upwind-biased MUSCL scheme (Anderson et al., 1986) is used. The reason for that is the steep gradients that exist in the k, ω fields. In a typical profile of ω normal to the wall, the value of ω changes rapidly from about 10^5 (or even higher for fine meshes) near the wall to the order of 1 outside the boundary layer. It is very hard to construct dissipation terms for central difference schemes which will stabilize the computation but will not affect accuracy. On the other hand, the high-resolution scheme is designed to deal with such large gradients. The turbulence model equations have a very simple wave structure. Various orders of upwind schemes can be easily constructed based on the local convective velocities (Liu and Zheng, 1994). In this study, a third-order upwind-biased high-resolution scheme is used.

The diffusive terms of the N-S equation and the turbulence model equations are discretized by a compact central difference scheme with second order accuracy.

After being discretized in space, the governing equations become a set of ordinary differential equations in time. The flow and turbulence equations are solved as one system. As has been shown by Liu and Zheng (1996), the computation can be significantly accelerated by strongly coupling the flow and turbulence equations in the stepping process. In this work, a five-stage Runge-Kutta type scheme is used to advance the solution in time. Since the transient evolution is not of interest, the time stepping scheme can be optimized for faster convergence. Acceleration techniques like local pseudo-time stepping and residual averaging are applied following Jameson et al. (1981, 1983).

5 Point Implicit Techniques

For most two-equation models, the source terms are usually dominant and become stiff near the solid wall. The efficiency of solution then totally depends on the treatment of those source terms.

In this work, a point-implicit technique is developed to improve the efficiency of the solution, and more importantly to alleviate the stiffness of the governing equations exhibited in the near wall region. Treatments of important source terms of turbulence model through the multigrid process is tested and analyzed.

By using the discretization method described in Section 4, the semidiscretized turbulence equation can be expressed as:

$$\frac{\Delta W}{\Delta t} = R(W) + S(W) \tag{11}$$

where $R(W)$ represents the convective and diffusive terms. $S(W)$ represents the source terms. The updating formula with the source terms treated with point-implicit technique can be written as:

$$\left[\frac{1}{\Delta t} I - \frac{\partial S}{\partial W}\right] \Delta W = R(W) + S(W). \tag{12}$$

The implicit coefficient matrix $\partial S/\partial W$ is not unique because the source terms are non-linear and ambiguous in a sense that they can be put in various forms by utilizing other relations defined by the turbulence model itself. Besides, we have the freedom to choose which term should be treated implicitly. From our computational experience, the following criteria should be considered in determining what should be kept in the matrix:

1. Generally, those contributing positively to the diagonal elements of the coefficient matrix can be kept. They do improve the robustness of the algorithm, but sometimes they may slow down convergence, especially with crude initial values.
2. It is very important to keep balance of the growth rate of the turbulent mixing energy (k) and dissipation (ω or ϵ). During the iteration, anyone of them grows or decays too fast will jeopardize the stability and deteriorate convergence. It is true that the growth and diminution of the turbulent mixing energy and dissipation are generally balanced because the turbulence equations are so tailored. However, if acceleration techniques, like residual smoothing and multigrid method, are used, the asymptotic behaviors of the turbulent mixing energy and dissipation are lost. Strong singularity may appear in this case. Therefore, it is very important to construct the coefficient matrix such that it will compensate the deficit and limit over-growth.

For the k-ω model, the first step to better satisfy the above-mentioned criteria is to choose a proper form of the source term. For the k-ω model, we found the following form works quite well:

$$S_k = \nu_t P_d - \beta_k k\omega \tag{13}$$

$$S_\omega = \gamma_\omega P_d - \beta_\omega \omega^2 \tag{14}$$

where

$$P_d = 2(s_{11}^2 + s_{22}^2 + s_{33}^2) + 4(s_{12}^2 + s_{13}^2 + s_{23}^2), \tag{15}$$

$$s_{ij} = \frac{1}{2}\left(\frac{\partial u_i}{\partial x_j} + \frac{\partial u_j}{\partial x_i}\right). \tag{16}$$

The linearized coefficient matrix is then found:

$$-\frac{\partial S}{\partial W} = \begin{bmatrix} \beta_k\omega & \beta_k k \\ 0 & 2\beta_\omega\omega \end{bmatrix}. \tag{17}$$

Based on the criteria described in the above, an optimized coefficient matrix is constructed:

$$-\frac{\partial S}{\partial W}=\begin{bmatrix}\beta_k\omega & 0\\ 0 & \beta_\omega\omega\end{bmatrix}. \tag{18}$$

Some unique features about the k-ω model we observed in computations are that usually k grows faster than ω does if multigrid methods are used, and ω decays faster than it is supposed to be. Numerical difficulty in near-wall region can be relieved if the boundary value of ω is set to a large enough value.

For the k-ϵ model, the source terms are put in the following form:

$$S_k = C_\mu f_\mu \frac{k^2}{\epsilon + D} P_d - \epsilon - D, \tag{19}$$

$$S_\epsilon = \gamma_\epsilon \frac{\epsilon + D}{k} \nu_t P_d - \beta_\epsilon \frac{\epsilon(\epsilon + D)}{k} + C_\mu E \frac{k^2}{\epsilon + D}. \tag{20}$$

The linearized coefficient matrix is obtained from the above equations as:

$$-\frac{\partial S}{\partial W}=\begin{bmatrix}a & b\\ c & d\end{bmatrix} \tag{21}$$

where:

$$a = -2\nu_t P_d/k, \tag{22}$$

$$b = \left(1 + C_1 C_\mu f_\mu P_d \frac{k^2}{(\epsilon + d)^2}\right), \tag{23}$$

$$c = \gamma_\epsilon \frac{\epsilon + D}{k^2} P_d - C_2 \beta_\epsilon f_2 \frac{\epsilon^2}{k^2} - C_\mu f_\mu E \frac{2k}{\epsilon + D}, \tag{24}$$

$$d = -\gamma_\epsilon \nu_t P_d/k + C_3 \beta_\epsilon f_2 \frac{2\epsilon + D}{k} + C_\mu f_\mu E \frac{k^2}{(\epsilon + D)^2}, \tag{25}$$

where $C_1 = (0 - 1)$, the larger, stabler (slower convergence). $C_2 \sim \sqrt{k}$ which is used only when the modification function f_2 satisfies that $f_2 \to 0$ as $k \to 0$. $C_3 \sim (k)$ when the modification function f_2 satisfies that $f_2 \to 0$ as $k \to 0$. For the many versions of k-ϵ models that do not have these properties, C_2 and C_3 should be set to zero.

A sufficient condition for stability of local iteration during the updating step requires:

$$\Delta t \le \frac{1}{\max\left(|b| - a, |c| - d\right)} \tag{26}$$

Δt is also subjected to the limitations from the convection and diffusion terms.

In the early stage of turbulence growth, k develops slower than ϵ. This is in contradistinction to the k-ω model, and it is the keystone for constructing efficient coefficient matrix for k-ϵ model equations.

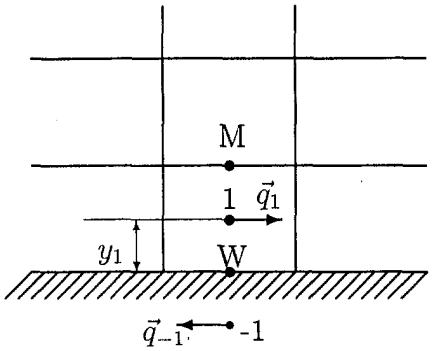

Fig. 1 Wall boundary cell sketch

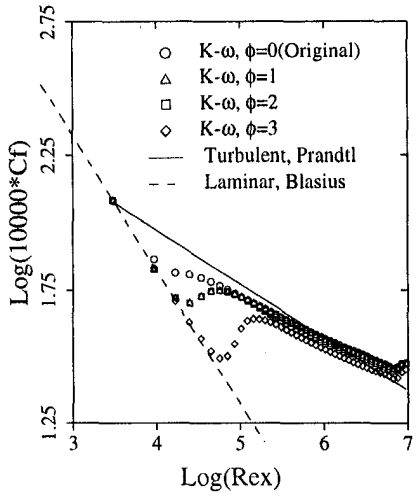

Fig. 2 Skin friction, $R_\theta = 10^7$ modified κ-ω model

6 Improvement to Turbulence Models

In this section, some techniques are presented to improve the performance of the k-ω turbulence models.

6.1 Total Stress Limitation. To alleviate the dependency of the k-ω model on the far field boundary value ω_f, and also to account for the transport effects of the total turbulent shear-stress, a modification is proposed by introducing only one more parameter to the original k-ω model. It was found later it can be also used to control the transition location (Zheng and Liu, 1995).

From the definition of turbulence kinetic energy and Reynolds stresses, we have

$$(2k)^2 = \overline{u'^2}^2 + \overline{v'^2}^2 + \overline{w'^2}^2 + 2(\overline{u'^2}\,\overline{v'^2} + \overline{v'^2}\,\overline{w'^2} + \overline{u'^2}\,\overline{w'^2}) \tag{27}$$

$$\frac{1}{\rho}\Sigma\hat{\tau}_{i,j}^2 = \overline{u'^2}^2 + \overline{v'^2}^2 + \overline{w'^2}^2 + 2(\overline{u'v'}^2 + \overline{v'w'}^2 + \overline{u'w'}^2). \tag{28}$$

Since

$$\overline{u'v'} \le \sqrt{\overline{u'^2}\,\overline{v'^2}}, \tag{29}$$

we therefore have:

$$\sqrt{\Sigma\hat{\tau}_{i,j}^2} \le 2\rho k. \tag{30}$$

By using the Boussinesq constitutive assumption, relation (30) leads to:

$$\sqrt{[2\mu_t s_{i,j} - \tfrac{2}{3}\rho k\delta_{i,j}]^2} \le 2\rho k \tag{31}$$

which can be reduced to:

$$\omega \ge \phi\sqrt{2s_{i,j}\frac{\partial u_i}{\partial x_j}} = \phi\sqrt{P_d} \tag{32}$$

where $\phi = \sqrt{3}/2$, and P_d is the exact velocity strain which contributes to the production of turbulence as defined in Eq. (15).

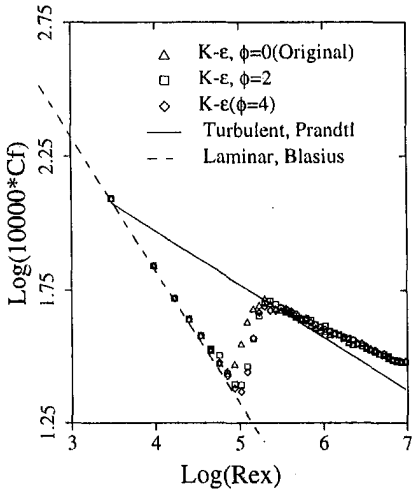

Fig. 3 Skin friction, $R_e = 10^7$ modified low $R_e\kappa$-ϵ model

In our modification,

$$\mu_t = \frac{\rho k}{\omega}, \tag{33}$$

$$\omega = \max\ (\omega_o, \phi\sqrt{P_d}) \tag{34}$$

where ω_o is the solution from Wilcox original k-ω model. Very little additional calculation is needed since P_d is directly available.

Similarly, the modification for k-ϵ model is:

$$\epsilon = \max\ (\epsilon_o, k\phi\sqrt{P_d}), \tag{35}$$

where ϵ_o is the solution from k-ϵ equations.

It has been found that this modification also improves the stability of numerical computations.

6.2 Corrected Formula for ω Values at Solid Wall. When the grid is fine enough to ensure the normalized distance (y^+) from the first grid to the wall is less than 2, the ω values near the wall can be determined from the asymptotic solution:

$$\omega = \frac{6\nu}{y^2} \quad \text{as} \quad y^+ \to 0. \tag{36}$$

which shows ω becomes singular at the wall. Fortunately, both k and ν_t are known to be zero at the wall. The value of ω is not a matter as far as the wall point is concerned. The real boundary condition for ω equation is actually set by applying the above equation to the first point away from the wall (in our scheme, the point is actually at the cell center). The value of ω at the wall is set numerically such that the flux across the interface between the first point and second point is equivalent to the flux evaluated by using Eq. (36). Then the value of ω at wall should be determined from the difference scheme used in the discretization of the ω equation. For example, if the second-order upwind scheme is used, the wall value of ω is only used to determine the flux across surface M as shown in Fig. 1. If the MUSCL-type interpolation without the limiter (Anderson et al., 1986) is used, the ω value at point M can be obtained as:

$$\omega_W = 2\omega_1 - \omega_M = 10.5\,\frac{\nu}{y_1^2}$$

where ω_M is the ω value at point M, ω_1 at the first cell center, and ω_W at the wall.

When y^+ is sufficiently small, the solution is not sensitive to the coefficient 10.5. However, as y^+ increases, so will the sensitivity. In practice, it has been found that

$$\omega_W = 12\,\frac{\nu}{y_1^2} \tag{37}$$

usually gives very good results for y^+ within 1.

If y_1^+ is larger than 2, Eq. (37) and Eq. (37) will give too small values of ω_W. For practical engineering problems, it is very hard to maintain the y^+ of the first grid point within 2 everywhere. Therefore a correction term is needed for reasons of both accuracy and grid-efficiency.

Let Ω be the vorticity near the wall, y^+ can be found from: $y^+ = y_1\sqrt{R_e\Omega}$. The following formula is proposed to correct Eq. (37):

$$\omega_A = 12\,\frac{\nu}{y_1^2}, \quad \omega_\Omega = \text{Min}\ (\omega_A, \Omega)C_e(y^+)^{5/3}, \tag{38}$$

$$\omega_W = \text{Max}\ (\omega_A, \omega_\Omega), \tag{39}$$

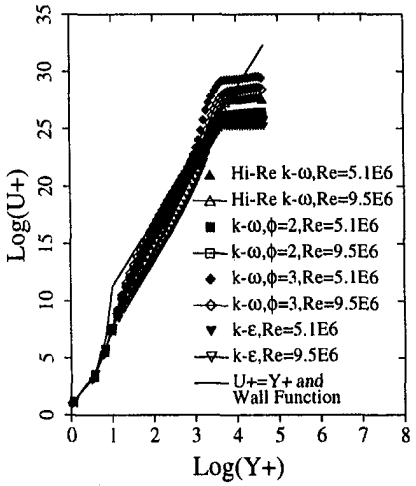

Fig. 4 Velocity profiles, $R_e = 10^7$

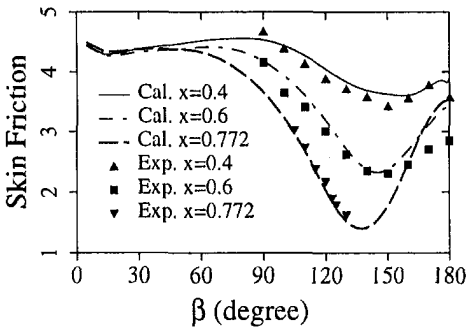

Fig. 5 Skin friction coefficients 6:1 prolate spheroid, Re = 4.2×10^6, $\alpha = 10°$

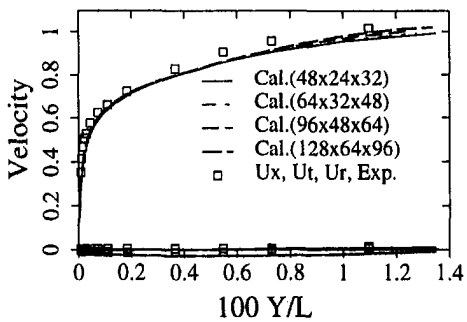

Fig. 6 Velocity pofiles at $x/L = 0.6$, $\phi = 180°$

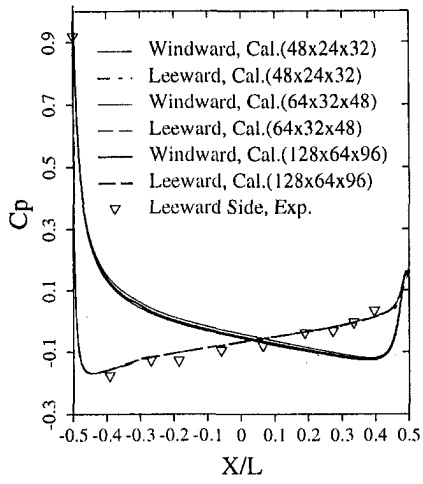

Fig. 7 Pressure coefficients distribution Re = 4.2 × 10⁶, angle of attack α = 10°

where $C_e = 0.46$, tuned for the best results in high Reynolds number region. In the above formula, the correction will take place only for $y^+ > 1.6$. If $y^+ < 1.6$, the ω value at wall is actually determined by Eq. (37). The above formula, has been tested for y^+, which ranges from 3 to 15. This is a range acceptable for engineering computations.

7 Boundary and Initial Conditions

The boundary types encountered in this work are classified as solid wall, symmetrical plane, periodical face, singular line, block interface, and far field. For viscous flow, a nonslip condition is imposed on the solid wall boundary by setting the flow velocity equal to that of the body, and zero pressure gradient normal to the surface is specified to determine the pressure on the wall.

Since ghost cells are introduced to store the variable values and derivatives across the boundary, the boundary conditions for symmetrical, periodical, and block interface are easily accomplished by assigning the ghost cell with the values of corresponding cells. Since there is no flux across singular line, the boundary conditions for singular line are obtained through extrapolation combined with partial averaging.

As has been realized by many researchers, the treatment of far field boundary conditions can have a great impact on the convergence of the solution. In this work, an approximate nonreflecting boundary conditions based on linearized characteristics approach are constructed to improve the convergence rate. The linearized characteristic problem is solved along the direction normal to the outer boundary of the computational domain.

All the computations are started from a uniform initial field with incoming flow quantities.

8 Computational Results

The developed algorithm is first tested by applying it to the flat plate boundary layers at $Re_\infty = 10^7$. A grid of 97 × 65 is used with 16 points before the plate leading edge, 73 on the plate and 8 after. 65 points are placed in the normal direction and stretched out to far field from the plate surface. Figures 2 and 3 show the results obtained with the original k-ω model, k-ϵ model and the modified models as described in Section 6. The original k-ω model gives a rather early transition prediction at about $Re_x = 10^4$. By choosing different values of ϕ in Eq. (34), the transition point can be controlled over a quite wide range. However, for the k-ϵ model, since a low-Reynolds number model is used here and it already predicts a rather late transition, the modification does not improve much.

The calculated skin friction by the k-ω model is very close to the empirical solution of Prandtl's $\frac{1}{7}$th law, that shows the k-ω model is quite good in predicting skin friction of turbulent flows. The calculated boundary layer velocity profiles at different locations (marked by different local Reynolds number Re_x) by different models are plotted against wall-function results in the normalized coordinates in Fig. 4. It can be seen that the modification introduced here does not impair the accuracy of those models in the fully developed turbulent region. It is remarkable that it only postpones the transition and affects the transitional region, without changing the solution in the sublayer region.

After testing the present methods for the flat plate case, we proceed to calculate turbulent flow over a 6:1 prolate spheroid which has been thoroughly investigated experimentally by Ahn (1992) and Chesnakas et al. (1994).

Since the geometrical model is axisymmetric, only half the domain of flow field is actually simulated. Four different sizes of grid, 48 × 24 × 32, 64 × 32 × 48, 96 × 48 × 64, 128 × 64 × 96 along axial, circumferential, radial directions respectively, are used in the study to make sure the grid resolution is high enough for the flow field and for the solution of turbulence model equations. Figures 5–8 show the results for the case of Reynolds number of 4.2×10^6 and angle of attack of 10 degrees. The skin friction distribution along circumferential direction at different axial locations are accurately predicted as shown in

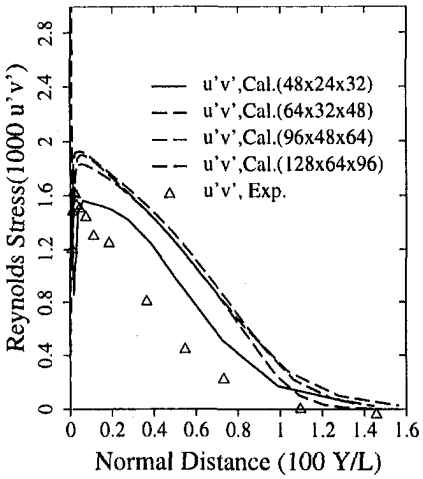

Fig. 8 Reynolds stress distribution at x/L = 0.6, β = 180°

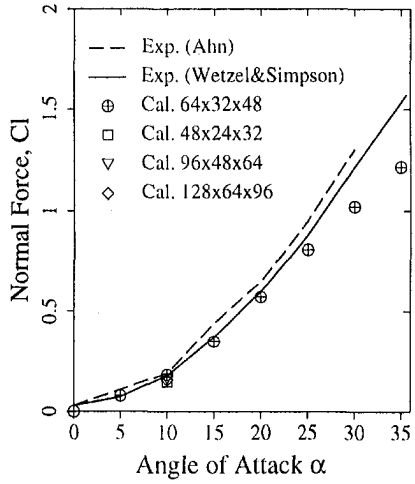

Fig. 9 Normal force versus angle of attack

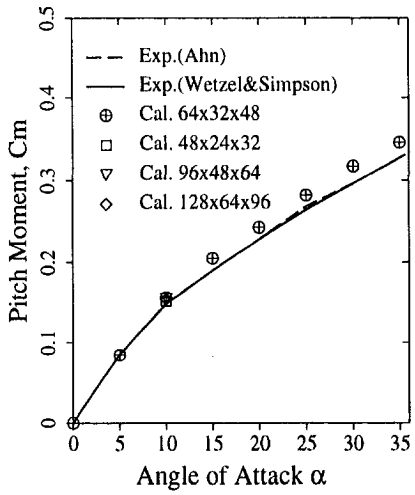

Fig. 10 Pitch moment versus angle of attack

Fig. 5. As observed in experiments, the wall skin friction minimum qualitatively corresponds to the separation location in spheroid cases. Therefore the accurate prediction of skin friction implies the separation locations are also accurately predicted by the k-ω model in this case. It is also found that the axial, circumferential, and radial velocity component profiles at different axial sections (x/L) and different circumferential locations (β) are accurately predicted. A typical plot against experimental data is shown in Fig. 6. It can be found that there is very little difference between the results obtained on the four different grids. The same conclusion can drawn for the surface pressure coefficient distribution as shown in Fig. 7. However, from Fig. 8, it becomes apparent that the spatial resolution of the $48 \times 24 \times 32$ grid is not high enough to predict the Reynolds stresses, even though its result is much closer to the experimental data. The over-prediction of the Reynolds stress in the outer boundary layer region is a known problem for the k-ω model. With the results of the three fine grids collapse onto each other, we can safely conclude that the grid of $64 \times 32 \times 48$ provide sufficient resolution for engineering calculation in this case.

Figures 9 and 10 show the calculated normal force and pitch moment at different angles of attack and experimental results. Computational results match measurements excellently, except in the high angle of attack regime, where the normal force is noticeably underpredicted and the pitch moment is slightly overpredicted. The discrepancy may be caused by the turbulent modeling, or simply due to asymmetrical vortex shedding at high angles of attack.

Most calculations are done in 300 multigrid cycles that reduce the residuals by 5 orders of magnitude. On a single Cray C90 processor, the speed is about 1.29×10^{-5} CPU second per cell per multigrid cycle, or 5.6×10^{-6} multigrid iteration per CPU time per cell.

9 Concluding Remarks

The preconditioning method developed by Turkel has been found very effective in improving efficiency and accuracy because the preconditioned system has better condition numbers and less artificial dissipation is required for stabilizing the numerical algorithm.

Through keeping balance of the growth rates between turbulence energy and dissipation, all the acceleration techniques developed for the N-S equations can be equally applied to the turbulence model equations.

The modification introduced for turbulence dissipation rate not only improves the accuracy of the model, but also significantly improves the robustness of numerical computations.

Acknowledgment

This work was supported by the US Navy under Contract No.: N00024-94NR-01392. Most of the computations were done on the Cray-C90 of Major Shared Resource Center, Naval Oceanographic Office, the Department of Defense. The authors are grateful to Dr. Turkel for his helpful discussions.

References

Ahn, S., 1992, "An Experimental Study of Flow Over a 6 to 1 Prolate Spheroid at Incidence," Ph. D. dissertation, Aerospace and Ocean Engineering Department, Virginia Polytechnic Institute and State University.

Alessandrini, B., and Delhommeau, G., 1994, "Simulation of Three-Dimensional Unsteady Viscous Free Surface Flow Around a Ship Model," *International Journal for Numerical Methods in Fluids,* Vol. 19, pp. 321–342.

Anderson, W. K., Thomas, J. L., and Van Leer, B., 1986, "Comparison of Finite Volume Flux Vector Splittings for the Euler Equations," *AIAA Journal,* Vol. 24, No. 9, pp. 1453–1460.

Chesnakas, C. J., Simpson, R. L., and Madden, M. M., 1994, "Three-Dimensional Velocity Measurements on a 6:1 Prolate Spheroid at 10° Angle of Attack," VPI-AOE-202, Department of Aerospace and Ocean Engineering Department, Virginia Polytechnic Institute and State University.

Chorin, A. J., 1967, "A Numerical Method for Solving Incompressible Viscous Flow Problem," *Journal of Computational Physics,* Vol. 2, pp. 275–312.

Jameson, A., Schmidt, W., and Turkel, E., 1981, "Numerical Solutions of Euler Equations by Finite Volume Methods using Runge-Kutta Time-Stepping Schemes," AIAA Paper 81-1259, June.

Jameson, A., and Baker, T. J., 1983, "Solution of the Euler Equations for Complex Configurations," AIAA Paper 83-1929, July.

Launder, B. E., and Sharma, B. I., 1974, "Application of the Energy Dissipation Model of Turbulence to the Calculation of Flow near a Spinning Disc," *Letters in Heat and Mass Transfer,* Vol. 1, pp. 131–138.

Liu, F., and Zheng, X., 1994, "A Staggered Finite Volume Scheme for Solving Cascade Flow with a Two-Equation Model of Turbulence," *AIAA Journal,* Vol. 32, No. 8, pp. 1589–1597.

Liu, F., and Zheng, X., 1996, "A Strongly Coupled Time-Marching Method for Solving the Navier-Stokes and k-ω Turbulence Model Equations with Multigrid," *Journal of Computational Physics,* Vol. 128, pp. 289–300.

Menter, F. R., 1991, "Performance of Popular Turbulence models for Attached and separated Adverse Pressure Gradient Flows," AIAA Paper 91-1784.

Sheng, C., Taylor, L., and Whitfield, D., 1995, "Multiblock Multigrid Solution of Three-Dimensional Incompressible Turbulent Flows about Appended Submarine Configurations," AIAA Paper 95-0203, 33rd Aerospace Sciences Meeting and Exhibit, Reno, NV, Jan. 9–12.

Sung, C. H., and Griffin, M. J., 1991, "Improvement in Incompressible Turbulent Horseshoe Vortex Juncture Flow Calculations," AIAA Paper 91-0022, AIAA 29th Aerospace Sciences Meeting, Reno, NV, Jan. 7–10.

Sung, C. H., Fu, T. C., Griffin, M. J., and Huang, T. T., 1995, "Validation of Incompressible Flow Computation of Forces and Moments on Axisymmetric Bodies at Incidence," AIAA Paper 95-0528, 33rd Aerospace Sciences Meeting and Exhibit, Reno, NV, Jan. 9–12.

Turkel, E., 1987, "Preconditioned Methods for Solving the Incompressible and Low Speed Compressible Equations," *Journal of Computational Physics,* Vol. 72, pp. 277–298.

Wetzel, T. Z., and Simpson, R. L., 1996, "Unsteady Three-Dimensional Cross-Flow Separation Measurements on a Prolate Spheroid Undergoing Time-Dependent Maneuvers," Paper presented at *21st Symposium on Naval Hydrodynamics,* Trondhein, Norway, June.

Wilcox, D. C., 1988, "Reassessment of the Scale-Determining Equation for Advanced Turbulence Models," *AIAA Journal,* Vol. 26, No. 11, pp. 1299–1310.

Zheng, X., and Liu, F., 1995, "Staggered Upwind Method for Solving Navier-Stokes and k-ω Turbulence Model Equations," *AIAA Journal,* Vol. 33, No. 6, pp. 991–998.

X. Zheng[1]
Research Associate.
Assoc. Mem. ASME

C. Liao
Research Associate.

C. Liu
Associate Professor.
Mem. ASME

Department of Mathematics and Statistics,
Louisiana Tech University,
Ruston, LA 71272

C. H. Sung
Senior Research Scientist.
Mem. ASME

T. T. Huang
Chief Research Scientist.

David Taylor Model Basin,
Carderock Division, NSWC,
Bethesda, MD

Multigrid Computation of Incompressible Flows Using Two-Equation Turbulence Models: Part II—Applications

In this paper, computational results are presented for three-dimensional high-Reynolds number turbulent flows over a simplified submarine model. The simulation is based on the solution of Reynolds-Averaged Navier-Stokes equations and two-equation turbulence models by using a preconditioned time-stepping approach. A multi-block method, in which the block loop is placed in the inner cycle of a multi-grid algorithm, is used to obtain versatility and efficiency. It was found that the calculated body drag, lift, side force coefficients and moments at various angles of attack or angles of drift are in excellent agreement with experimental data. Fast convergence has been achieved for all the cases with large angles of attack and with modest drift angles.

1 Introduction

For practical engineering applications, while the computational accuracy of high-Reynolds number flows computation is largely limited by turbulence model, the computational efficiency has been improved steadily over the years as the result of significant development of advanced numerical algorithms, and is further enhanced by powerful modern computers. Among the numerous methods developed to solve the incompressible Reynolds-averaged Navier-Stokes equations, the pressure-based method and the artificial compressibility method are the most popular approaches. The pressure-based methods represented by the SIMPLE-family codes developed by Patankar et al. (1972) were the dominant approaches in the simulation of incompressible flows and compressible subsonic flows during the 70s and 80s. There are many industrial codes that use this kind of approach. Some of them have evolved to handle transonic and supersonic flows.

The artificial compressibility methods, proposed by Chorin (1967) almost three decades ago, are only getting flourish in recent years, partly because of the success of time-stepping schemes in transonic flow calculation. In this approach, an artificial time derivative of pressure is added to the continuity equation together with a multiplicative variable, β. With this artificial term, the resultant system of equations is symmetric hyperbolic for the inviscid terms. Thus, the system is well posed and efficient numerical methods developed for compressible flows can be used to advance the system in artificial time. Later, Turkel (1987) extended this concept and derived more sophisticated preconditioners than those originally proposed by Chorin, that render the new equation system well-conditioned for numerical computation. When combined with a multigrid acceleration procedure, this approach has been proven to be particularly effective.

Turbulence models are bound to be a major issue whenever accuracy is concerned. For high-Reynolds number flow over under-water vehicles, vortex roll-up and separation are very common even under moderate angles of attack or yaw. Algebraic turbulence models like the Baldwin-Lomax model require too much human interface in determining the length scale in such cases. Two-equation models are favored because they are the next least expensive models who can provide the necessary generality for complicated flows.

In the present work, a numerical method based on the artificial compressibility approach with Turkel-type of preconditioner and multigrid methods is used to calculate high-Reynolds number turbulent flows over a submarine model, SUBOFF. Two popular two-equation models, k-ω and k-ϵ, are used in our study. Calculations were first performed for SUBOFF bare hull model under various angles of attack. The calculated boundary layer velocity profiles, skin friction, turbulent stresses, and pressure coefficients are found in excellent agreement with experimental results. The body drag coefficient, lift coefficient, and moment at different inflow conditions are compared with experimental results. Although only three levels of grids are used in those cases, about 600 multigrid V(1,0) cycles can drive the residuals down by 6 orders of magnitudes.

Two-block grids are used in the calculation of turbulent flows over the SUBOFF with sail. Fast convergence has been achieved for all the cases with modest drift angles. When the drift angle reaches 16 degrees, small magnitude of oscillation was observed in the convergence history after the residual was down by about 4 orders of magnitudes. That might indicate unsteady flow patterns occurring in the flow field, probably caused by vortex shedding from the sail. In this case, a time-dependent solution is required for accurate prediction. The calculated body force coefficients and moments for the drift angle less than 12 degrees

[1] Current address: Adina R & D, Inc., Watertown, MA 02172.

Contributed by the Fluids Engineering Division for publication in the JOURNAL OF FLUIDS ENGINEERING. Manuscript received by the Fluids Engineering Division May 30, 1996; revised manuscript received July 21, 1997. Associate Technical Editor: P. M. Sockol.

are found in excellent agreement with experimental data. We regard this achievement as a key step towards the realization of using computer codes as practical design tools for marine vehicles.

2 Numerical Methods

As described in the first part of this paper, the Reynolds-averaged incompressible Navier-Stokes equations are written in a conservative form with an artificial term of time derivative of pressure added to the continuity equation. The preconditioning method by Turkel (1987) is used to reduce wave-speed disparity of the resultant hyperbolic system. For more details, please refer to Part I.

3 Multigrid Multi-Block Method

The implementation of the multigrid method with a multi-block scheme depends on the depth within the algorithm at which the block loop is placed and how often the communication takes place. Generally, there are two ways that either all blocks are solved on the same grid level before proceeding to the next multigrid level or the multigrid cycles are performed on each block before going to the next block. These two modes are referred to as the "horizontal" and the "vertical" modes by Yadlin and Caughey (1990). In this work, since Jameson's explicit multigrid method is used, the block-loop can be placed as deep as into the the stage-loop of multi-stage Runge-Kutta scheme. If doing so, the multi-block scheme is equivalent to the single block scheme except for minor differences in the residual smoothing step. Therefore, similar convergence rate to the single block computations can be expected. This is the best one can do within the solution procedure frame in terms of convergence rate. So it is called "fully horizontal" mode. The penalty of this mode is the computational overhead in terms of communication and memory by comparing with the vertical mode. A good compromise is that the block loop is placed within multigrid loop but before the Runge-Kutta stage-loop. In our code both modes are implemented.

The multiblock procedure naturally allows parallelization on distributed-memory machines by using PVM or P4 for inter-block communications. This is certainly one of our near future directions.

4 Boundary Conditions

The implementation of different boundary conditions are made extremely easy by introducing ghost cells to store variable values and gradients across the boundary. The treatment of usual types of boundaries and the boundary conditions for turbulence models have been discussed in Part I of the paper, here we only outline the far field boundary conditions of turbulence quantities used in our computations.

The natural transition Reynolds number can be as high as 6 million in submarine flows. In such extreme cases, it is really hard for the two-equation models to predict correct turbulent transition. In our calculations, the nondimensionalized far field dissipation rate is defined as 10 after normalized by the far field velocity and model length scale. The turbulent kinetic energy is calculated by forcing the eddy viscosity to be two-order of magnitude smaller than the molecular viscosity. Even with this really low level of free stream eddy viscosity, the k-ω and k-ϵ turbulence models used in this study still give too early transition predictions. With the modification introduced in the first part of the paper, the transition can be delayed significantly from a local Reynolds number of about a hundred thousand to one million. But it is still not good enough to make accurate prediction. Luckily, most underwater vehicles are mounted with trip strips in the nose area to trigger earlier turbulent transition so that larger loss due possible laminar separations can be avoided. If the transition positions are known and are forced in the calculations, the free-stream values of turbulent quantities do not have much impact on the calculated skin friction and body forces.

The well-known fast decay of dissipation rate ω in free stream does not pose any difficulty in our computations with the k-ω model, since the Total Stress Limitation modification sets a lower limit for dissipation or dissipation rate, avoiding situation of unrealistic huge eddy viscosity in outer boundary layer region.

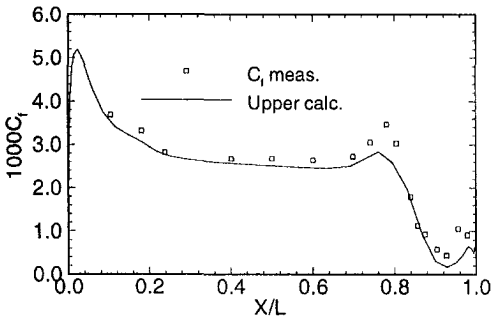

Fig. 2 SUBOFF bare hull skin friction

5 Computational Results

5.1 SUBOFF Bare Hull. The first test case is a turbulent flow about a submarine model, SUBOFF, which was developed by David Taylor Model Basin (Huang et al., 1978, 1992, Roddy, 1990) to establish an experimental database for CFD code validation. First, the computations are carried out for the SUBOFF bare hull. Detailed comparison is made for the working condition of zero degree of incidence. The inflow Reynolds number is 1.2×10^7. Figures 1–3 show the computed pressure coefficients, skin friction coefficients, boundary velocity profiles with

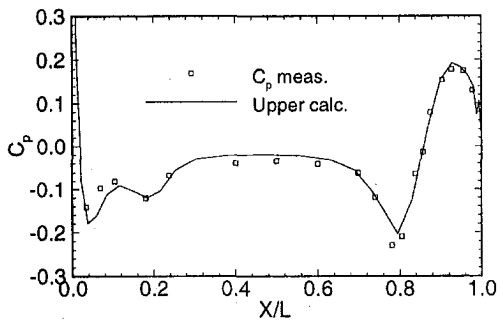

Fig. 1 Bare hull pressure coefficient, $R_e = 1.2 \times 10^7$, $49 \times 25 \times 33$ grid

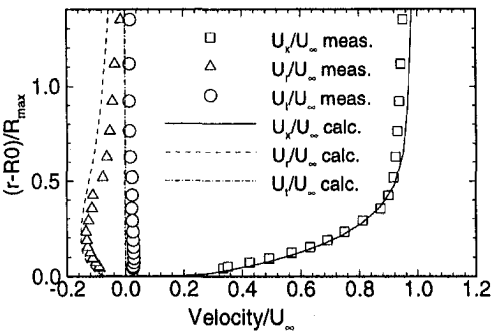

Fig. 3 Velocity profiles at $x = 0.904$, $R_e = 1.2 \times 10^7$, $49 \times 25 \times 33$ grid

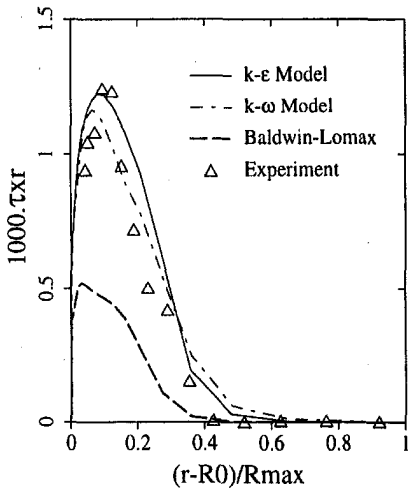

Fig. 4 Reynolds stress at $x = 0.904$

the modified k-ω model. They are found in excellent agreement with the experimental data.

As shown in Fig. 4, the Reynolds stress $\overline{u'v'}$ can be accurately predicted with the k-ω model and the k-ϵ model. Even though the skin friction and the velocity profiles can be predicted correctly by the Baldwin-Lomax model, the Baldwin-Lomax model could not give right prediction of Reynolds stresses. The reason is possibly that the measurement locations are all in the rear part of the SUBOFF, where the upstream effects of turbulent stresses may be significant. However, the algebraic model is unable to account for the historical influence from the upstream, and therefore could not give correct prediction in this area. Both the k-ϵ model and the k-ω model give surprisingly good results even on a relatively coarse grid of 49 $\times$ 24 $\times$ 32 (axial $\times$ circumferential $\times$ radial), in which the normalized distance y^+ from the boundary cell center to the wall ranges from 2 to 9. In this case, the k-ϵ model overpredicts the skin friction a little (not shown here). We believe it can be improved by modifying the boundary value of ϵ as we did for k-ω model.

The convergence history is shown in Fig. 5. The convergence history of single grid computation is also plotted to show the acceleration effects of the multigrid methods. At the beginning, the multigrid is very effective. However, it is noted that the convergence slows down significantly and reaches the rate of single grid computation after the residuals are reduced by four orders of magnitude. That indicates there are still certain long wave of errors that could not be removed by multigrid iterations. One possible reason for the slowing down is that only three

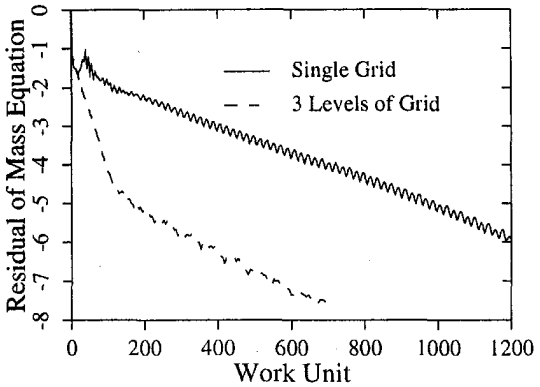

Fig. 5 Convergence history, κ-ω model

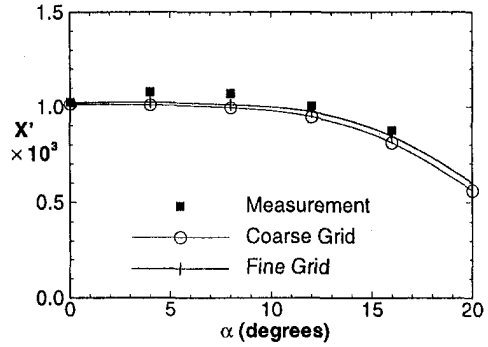

Fig. 6 Drag coefficient versus angle of attack

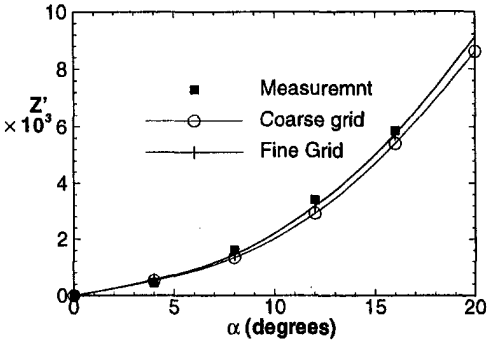

Fig. 7 Life coefficient versus angle of attack

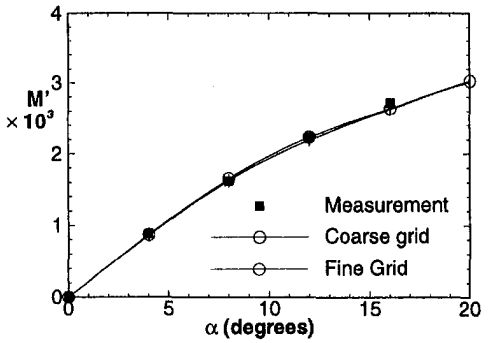

Fig. 8 Pitch-up moment versus angle of attack

levels of grid are used in the computations, in which coarsening in the flow direction is not enough.

In order to show that our code can be really useful for designing engineers, the SUBOFF bare hull at different inflow conditions are calculated on two grids: 49 $\times$ 24 $\times$ 32 and 49 $\times$ 24 $\times$ 48. The body drag force, lift force coefficients, and pitching moment at different angles of attack are plotted with experimental data in Figs. 6, 7, and 8. The difference between the calculated data and the experimental results is within 5 percent. It is worthwhile to mention that in all the calculations of different inflow conditions, we don't need to adjust any turbulence model parameters or boundary values from case to case.

5.2 SUBOFF Bare Hull With Sail. After testing our code for SUBOFF bare hull, we proceed to the calculation of turbulent flows over SUBOFF with sail. The physical model is shown in Fig. 9. The Reynolds number is 1.4×10^7. Two blocks of grids are used in this computation. At zero degree angle of attack and yaw, the computed body skin friction and pressure coefficients are found in excellent agreement with experimental data (Huang et al., 1992) as shown in Figs. 10 and

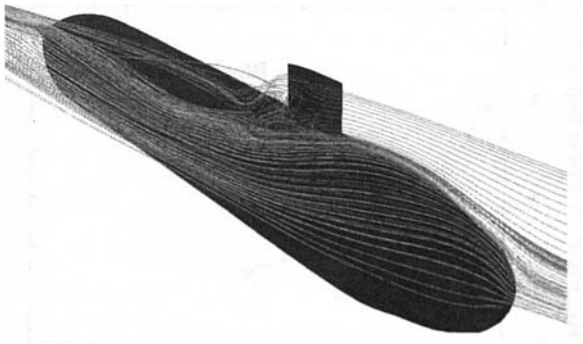

Fig. 9 Particle tracing, 16° yaw

11. It is noted that the skin friction goes to negative in a very small region right in front of the sail, that indicates a small region of separation there. The well-known junction flow pattern was picked up in our computation even though we did not intend to do so at the beginning because of the grid number budget.

The excellent performance of the present algorithm in predicting body force and moment components is demonstrated in the calculation of the SUBOFF with sail under different

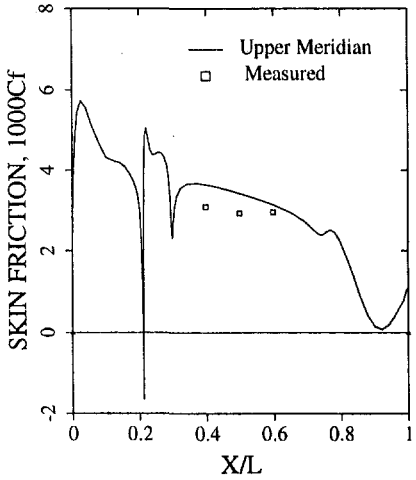

Fig. 10 Skin friction, SUBOFF with sail

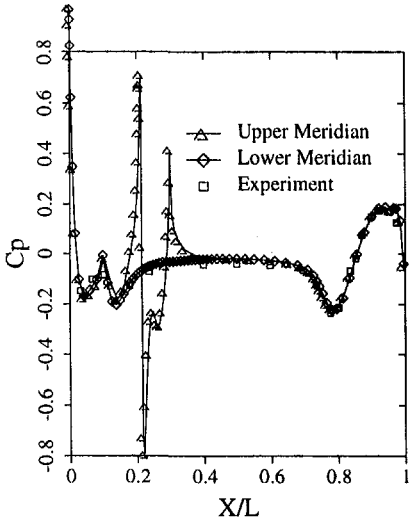

Fig. 11 Pressure coefficients, SUBOFF with sail

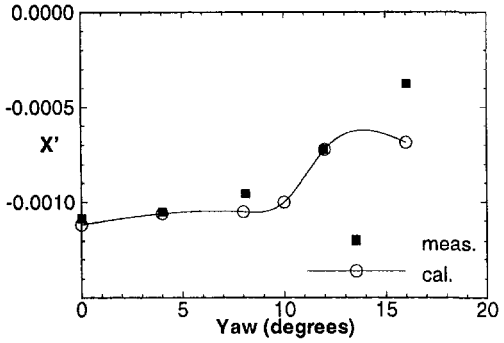

Fig. 12 Axial force versus yaw

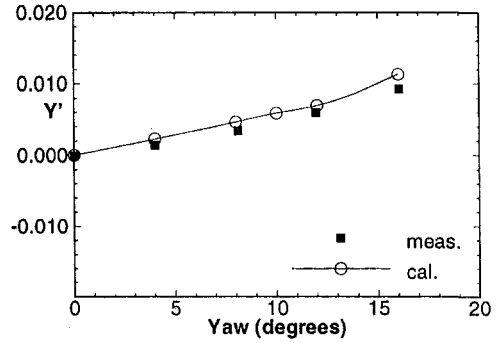

Fig. 13 Side force versus yaw

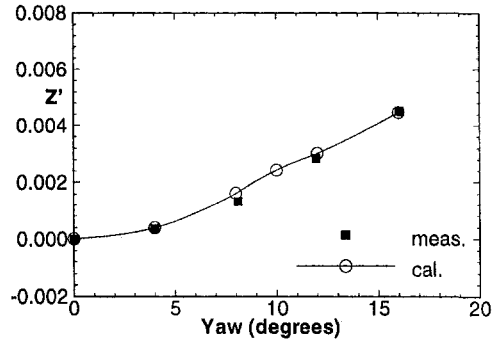

Fig. 14 Lift force versus yaw

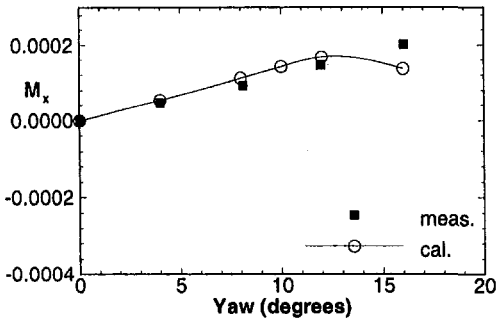

Fig. 15 Rotating moment versus yaw

drift (yaw) angles of attack. Figures 12–17 show the calculated three force components and three moment components variations with different yaw angles of attack. Two different sizes of grids are used in the computation. The finer grid includes two blocks of meshes: 97 × 65 × 65 for hull and sail region and 17 × 17 × 33 for sail tip region. The other

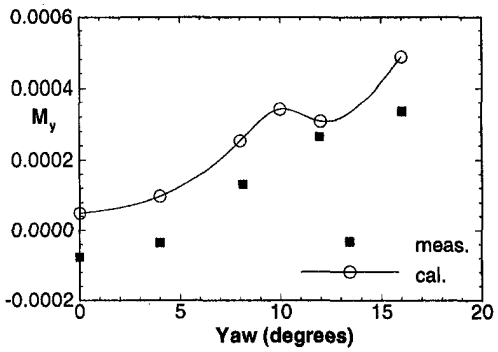

Fig. 16 Upward moment versus yaw

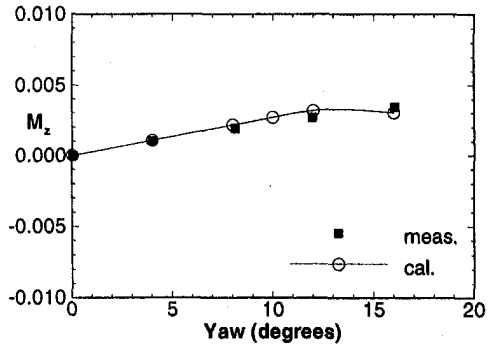

Fig. 17 Turning moment versus yaw

one consists of 97 × 41 × 49 and 17 × 17 × 25. The difference between the results obtained on the two sets of grids are marginal.

The flow patterns under yaw angle of attack can be illustrated by looking at the simulated surface oil flow plots and particle trace lines. Figures 18 and 19 show the surface oil flow patterns on both windward side and leeward side for the case of 16° of yaw. Significant flow separation, and roll-over are found on the leeward side of both hull and sail. From those plots, we can get a clue that periodical vortex shedding from sail might actually occur in this case. Accurate prediction for large angle of yaw requires time-dependent solution.

As expected, the use of two blocks of grids has little adverse effect on the computational efficiency since the block loop is placed within multigrid cycle and communication takes place at each step. Fast convergence has been achieved for all the cases with modest drift angles. A typical convergence history is shown in Fig. 20. When the drift angle reaches 16 degrees, small magnitude of oscillation was observed in the convergence history after the residual was down by about 4 orders of magnitudes. This further confirms there are unsteady flow patterns occurring in the flow field. In this case, time-dependent solution is required to obtain accurate predictions.

Fig. 18 Surface oil flow pattern on windward side for SUBOFF with sail at 16° drift angle, $R_e = 1.4 \times 10^7$ two-block grids of 97 × 41 × 49 and 17 × 17 × 25

Fig. 19 Surface oil flow pattern on leeward side for SUBOFF with sail at 16° drift angle, $R_e = 1.4 \times 10^7$ two-block grids of 97 × 41 × 49 and 17 × 17 × 25

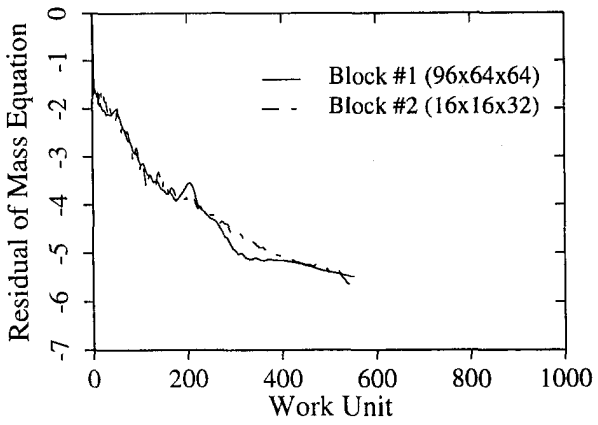

Fig. 20 Convergence history

6 Concluding Remarks

A very efficient and accurate numerical approach based on multiblock, multigrid, and preconditioning methods is used in this work for predicting three-dimensional turbulent flows. The multi-block approach, combined with multigrid schemes, can improve the versatility and efficiency of numerical simulations. By placing the block loop within the multigrid cycle, the accuracy and convergence are virtually not affected by the artificially generated block boundaries.

The test cases carried out so far fully demonstrate the accuracy and efficiency of the present method. The results obtained compare favorably with experimental data, showing the developed code can be a really useful tool for design engineers.

Acknowledgment

This research work was supported by the US Navy under Contract No.: N00024-94NR-01392. Most of the computations were done on the Cray-C90 of Major Shared Resource Center, Naval Oceanographic Office, the Department of Defense. The authors are grateful to Dr. Turkel for his helpful discussions.

References

Sheng, C., Taylor, L., and Whitfield, D., 1995, "Multiblock Multigrid Solution of Three-Dimensional Incompressible Turbulent Flows about Appended Submarine Configurations," AIAA 95-0203, 33rd Aerospace Sciences Meeting and Exhibit, Reno, NV, Jan. 9–12.

Wilcox, D. C., 1988, "Reassessment of the Scale-Determining Equation for Advanced Turbulence Models," *AIAA Journal,* Vol. 26, No. 11, pp. 1299–1310.

Patankar, S. A., and Spalding, D. B., 1972, "A Calculation Procedure for Heat, Mass and Momentum Transfer in Three Dimensional Parabolic Flows," *International Journal of Heat Mass Transfer,* Vol. 15, pp. 1787–1806.

Chorin, A. J., 1967, "A Numerical Method for Solving Incompressible Viscous Flow Problem," *Journal of Computational Physics,* Vol. 2, pp. 275–312.

Turkel, E., 1987, "Preconditioned Methods for Solving the Incompressible and Low Speed Compressible Equations," *Journal Computational Physics,* Vol. 72, pp. 277–298.

Huang, T. T., Santelli, N., Belt, G., 1978, "Stern Boundary-Layer Flow on Axisymmetrical Bodies," Paper presented at the 12th *Symposium on Naval Hydrodynamics,* Washington D.C., June 5–9.

Huang, T. T., Liu, H. L., Groves, N. C., Forlini, T. J., Blanton, J. N., and Gowing, S., 1992, "Measurements of Flows Over an Axisymmetric Body with Various Appendages in a Wind Tunnel: the DARPA Suboff Experimental Program,"

Paper presented at the 19th Symposium on Naval Hydrodynamics, Seoul, Korea, Aug. 24–28.

Roddy, R. F., 1990, "Investigation of the Stability and Control Characteristics of Several Configurations of the DARPA SUBOFF Model (DTRC Model 5470) from Captive-Model Experiments," David Taylor Research Center Report DTRC/SHD-1298-08, Sept.

Launder, B. E., and Sharma, B. I., 1974, "Application of the Energy Dissipation Model of Turbulence to the Calculation of Flow near a Spinning Disc," *Letters in Heat and Mass Transfer,* Vol. 1, pp. 131–138.

Yadlin, Y., and Caughey, D. A., 1990, "Block Multigrid Implicit Solution of the Euler equations of Compressible Fluid Flow," AIAA 90-0106, Jan.

Open Channel Flow Over Submerged Obstructions: An Experimental and Numerical Study

Dani Fadda
Ph.D Candidate.
Assoc. Mem ASME

Peter E. Raad
Associate Professor.
Mem. ASME

Mechanical Engineering Department,
Southern Methodist University,
Dallas, TX 75275-0337

This paper reports on experimental and computational investigations of water flow over two-dimensional obstacles in an open channel. Both triangular and semi-circular obstacles are considered in order to study the effects of obstacle type and size on the flow. The upstream flow is subcritical while the downstream flow is supercritical in all the cases discussed. The results of the experiments indicate that the downstream Reynolds number increases and appears to approach an asymptotic value as the obstacle height is increased. The upstream Reynolds number, on the other hand, decreases linearly as the obstacle height is increased. For the cases involving triangular obstacles, comparisons are presented between the results of the experimental measurements and the computational simulations as well as with available analytical solutions for inviscid flow. The comparisons point to the conclusion that the fluid rotational activity has a negligible effect on the overall flow in the open channel.

Introduction

This work presents an experimental and computational study of water flow over two-dimensional obstacles in an open channel. The obstacle shapes chosen for the comparisons are a semicircular cylinder and an isosceles, right-triangular block whose hypotenuse lies against the bottom of the channel. The objectives of these investigations are (a) to determine experimentally what the influence of the obstacle type and height is on the overall behavior of the flow both upstream and downstream of the chosen obstacles and (b) to perform comparisons between the obtained experimental data and the results of computational and mathematical solutions for flow over triangular obstacles. These comparisons can provide an important basis for assessing the role that viscous effects play in open channel flow, and, consequently, for ascertaining the ability of inviscid (or Euler-based) models to correctly simulate open channel flows for which the free surface undergoes small deformations.

The mathematical model used in this work to investigate flow over a triangular obstacle was developed by Dias and Vanden-Broeck (1989) who considered incompressible, irrotational, open channel flow, and presented a method that computes the height of a triangular obstacle and the upstream Froude number for a given downstream Froude number. Other published models of free surface flows over immersed obstructions have been reported in the literature. Vanden-Broeck and Keller (1986) developed a mathematical model for pouring flow. Dias et al. (1987) studied flows over rectangular weirs. Vanden-Broeck (1987) and Forbes and Schwartz (1980) considered flow over a semicircular obstacle. Cole (1983) studied near-critical flow over a small bump. Cahouet and Lenoir (1983) discussed the horizontal motion of an immersed body.

The current work investigates the dependence of key flow parameters on the nondimensional obstacle height as the volumetric flow rate and the size of the obstacle are varied. The characteristic nondimensional obstacle height (W) is obtained through a convenient combination of the obstacle height, the volumetric flow rate, and the constant gravitational acceleration. For open channel flow, the key characterizing flow parameters are the (nondimensional) Froude (Fr) and Reynolds (Re) numbers. Hence, for each chosen combination of obstacle height and volumetric flow rate, the Fr and Re numbers were determined both upstream and downstream of the obstacle. In all cases considered in this work, the flow was subcritical (i.e., Fr < 1) upstream of the obstacle and supercritical (i.e., Fr > 1) downstream of the obstacle.

The experimental data indicate that the Reynolds number increases toward an asymptotic value downstream of the obstacle and decreases linearly upstream as the nondimensional height of the obstacle is increased. Results for triangular obstacles show that the Froude numbers calculated from the inviscid theory are of the same magnitude as those measured experimentally and those computed numerically by solving the fully viscous Navier-Stokes equations.

Experimental Measurements

The experimental, closed-loop setup shown in Fig. 1 was designed such that tap water flows in an open channel driven by a calibrated, variable-speed pump. A video camera was positioned normal to the flow and at the same elevation as the obstacle. To obtain each data point, the pump was started and water was allowed to flow over the obstacle at the prescribed flow rate. After running the pump long enough for initial transients to die out, the video-taping was started and continued for at least two to three seconds. The videotape was then replayed and studied carefully with the purpose of selecting a single steady-state picture for digitization. The depth of the flow was then measured from the digital picture and recorded. A depth-averaged flow velocity was computed by dividing the flow rate by the measured fluid depth and the known channel width. Finally, once the average velocity and fluid depth had been determined, the Froude and Reynolds numbers were calculated.

Thirty-five combinations of obstacle heights and fluid flow rates were considered for the triangular obstacles, while for the semicircular obstacles, twenty combinations were considered. The results are reported here in terms of the nondimensional Froude and Reynolds numbers which characterize viscous flow in an open channel. An illustrative example of the experimental

Contributed by the Fluids Engineering Division for publication in the JOURNAL OF FLUIDS ENGINEERING. Manuscript received by the Fluids Engineering Division February 17, 1995; revised manuscript received July 14, 1997. Associate Technical Editor: D. Stock.

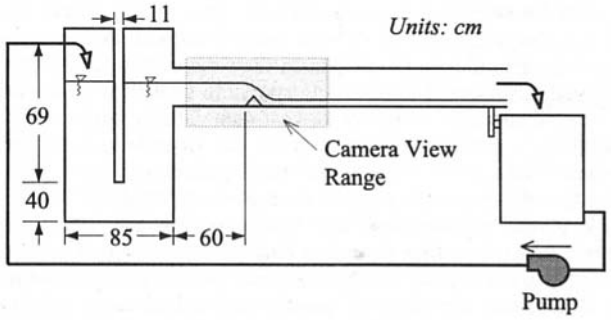

Fig. 1 Schematic of the closed-loop open channel apparatus

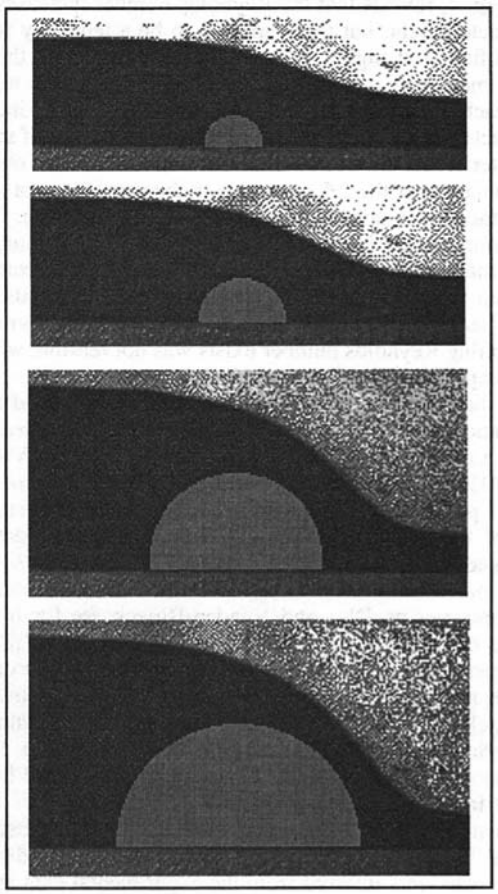

Fig. 2 Digitized pictures of steady-state flows taken by a high-speed video camera (W = 0.55, 0.95, 1.75, and 2.20, top to bottom)

flow captured by the high-speed video camera system is given in Fig. 2 where digitized pictures of water flow over semicircular obstacles are shown. The pictures correspond to flow heights W of 0.55, 0.95, 1.75, and 2.20.

Numerical Methodology

The numerical simulations of flow over triangular obstacles were obtained by the use of the surface marker and micro cell (SMMC) technique which was recently developed specifically for the simulation of incompressible, laminar, free surface fluid flow in two dimensions. In what follows is a brief outline of the technique; further details of the SMMC method can be found in Chen (1991), Chen et al. (1995), Johnson et al. (1994), Raad et al. (1995), and Chen et al. (1997).

The continuity and Navier-Stokes equations presented below (in tensor notation) are solved by a two-step (or projection) method on an Eulerian staggered grid:

$$\frac{\partial u_i}{\partial x_i} = 0, \tag{1}$$

$$\frac{\partial u_i}{\partial t} = -u_j \frac{\partial u_i}{\partial x_j} - \frac{1}{\rho}\frac{\partial p}{\partial x_i} + \nu \frac{\partial^2 u_i}{\partial x_j \partial x_j} + g_i . \tag{2}$$

The projection scheme begins with a calculation of a tentative velocity field ($\tilde{u}_i$) from a subset of the Navier-Stokes equations that excludes the pressure gradient terms; i.e., from

$$\frac{\partial \tilde{u}_i}{\partial t} = -u_j \frac{\partial u_i}{\partial x_j} + \nu \frac{\partial^2 u_i}{\partial x_j \partial x_j} + g_i . \tag{3}$$

The ($\tilde{u}_i$) field represents the correct vorticity for the flow, but, in general, does not satisfy the continuity equation. The deviation from continuity is then calculated and used as the source field on the right hand side of a pressure Poisson equation that appears as follows

$$\frac{\partial^2 p}{\partial x_j \partial x_j} = \frac{\rho}{\Delta t}\frac{\partial \tilde{u}_i}{\partial x_i} . \tag{4}$$

Finally, the resulting pressure field is used to calculate a corrected velocity field (u_i) that satisfies mass continuity without altering the previously determined, correct vorticity field. The correction equation is in fact the definition of the tentative field in terms of the primitive variables:

$$u_i = \tilde{u}_i - \frac{\Delta t}{\rho}\frac{\partial p}{\partial x_i} . \tag{5}$$

In addition to using an Eulerian approach to compute the primitive flow variables, the SMMC method uses surface markers to define and advect the free surface in a Lagrangian manner. The Eulerian domain is subdivided into cells. At each given time level in a flow simulation, the computational cells may or may not contain fluid. The empty and full regions are naturally separated by a layer of cells that are partially filled with fluid; these cells are called surface cells. The surface markers exist only in these surface cells, and make it possible to delineate in the Eulerian domain cells that are filled with fluid from those that are empty. In return, the Lagrangian markers interrogate the Eulerian grid for a velocity field and move subject to that field.

Nomenclature

Fr = Froude number = $U/(gh)^{1/2}$
g = gravitational acceleration constant (m/s^2)
h = fluid depth (m)
L = representative length = $(Q^2/g)^{1/3}$ (m)
p = pressure (N/m^2)
Q = fluid flow rate per unit channel width (m^2/s)
Re = Reynolds number = $(Uh)/\nu$
t = time (s)
U = depth averaged velocity (m/s)
u, v = velocity components (m/s)
W = nondimensional obstacle height = w/L
w = triangular obstacle height (m)
x, y = horizontal and vertical spatial components (m)
ρ = fluid density (Kg/m^3)
ν = kinematic viscosity (m^2/s)

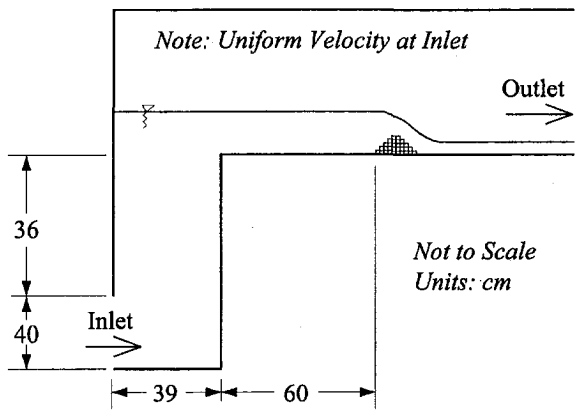

Fig. 3 Computational domain

An additional significant feature of the SMMC method is the subdividing of surface cells and their neighbors into micro-cells which, in concert with surface markers, make it possible to handle severe surface deformations, wave breaking, fluid-solid impact, and flow detachments and reattachments. The cell re-flagging scheme in a marker and cell technique requires that full cells not become empty in a single time step, but rather progress through the normal sequence of full, then surface, then empty. Similarly, empty cells pass through the surface state on their way to becoming full. In order to ensure that this natural sequence is followed, surface markers must not be allowed to travel more than the length of a cell in a single time step. And since, in the SMMC technique, cells on and near the free surface are subdivided into micro cells, the time step must be chosen so that no surface marker can travel more than a micro cell in a single time step. Consequently, in the SMMC method the time step used to march the solution in time is calculated dynamically. At the conclusion of each calculational cycle, the time increment to be used in the next temporal integration is computed based on the maximum allowable travel distance for a marker as well as on several other limiting criteria. Additional restrictions are used on the size of the time increment to ensure, for example, that if impact occurs (either between the fluid front and an obstacle or between two converging fluid fronts), that the physics of the ensuing pressure impulse is resolved accurately. This practice maintains the temporal accuracy of a simulation in a dynamic manner. But, because in marker and cell solutions of free surface flow problems the travel distance of a surface marker is tied to the cell size, the concept of numerical convergence must be adapted accordingly, as will be shown later in the section on Accuracy and Convergence.

The flexibility, accuracy, and efficiency of the method make it possible to simulate a significant portion of the actual closed cycle experimental setup, as shown in Fig. 3. The triangular obstacles were constructed by the use of square computational cells resulting in a stair step representation of the triangles. Each numerical simulation was started with the computational domain filled up to a constant depth such that the obstacle is fully immersed in stationary water. The inlet condition of uniform flow was then activated and the solution was advanced in time until the free surface markers indicated a steady-state fluid depth. The fluid depth was then recorded along with the nondimensional variables. Ten different numerical simulations were considered for triangular obstacles.

Results and Discussion

The raw experimental data for the triangular and semicircular obstacles are presented in Fig. 4 in the form of a plot of the Reynolds number versus the nondimensional obstacle height. The data for the triangles are denoted by solid triangles while the data for semicircles are denoted by open circles. Curve fits are superimposed on Fig. 4, with solid lines and dashed lines denoting triangular and semicircular data, respectively. The data recorded upstream of the obstacle appear to be well represented by a linear curve fit, while the downstream data are better represented by a cubic polynomial curve fit. Examination of the upstream data, which occupy the lower portion of Fig. 4, indicates that the Reynolds number decreases uniformly as the obstacle height is increased. The upstream data also reveals a distinct and interesting repeating pattern. The first two sets of this pattern are highlighted by balloons, but the pattern continues throughout the range of nondimensional obstacle heights (W) considered. Each set in this pattern corresponds to a dimensional obstacle height and five different fluid flow rates.

Examination of the downstream data, which occupy the upper part of Fig. 4, reveals that the Reynolds number increases with the obstacle height, but there appears to be a tendency for the curve to flatten at higher values of W. Extrapolating the data visually may lead one to believe that the Reynolds number could reach an asymptotic value if one continued to increase the obstacle height. However, accurate measurements of steady-state water levels are not possible for nondimensional obstacle heights much over the 2.5 range due to the prevalence of strong free surface fluctuations downstream of the obstacle. These fluctuations appear in flows for values of W near unity, but grow in magnitude as W increases until they finally become too significant to permit accurate steady-state measurements to be taken. Therefore, the determination of whether an asymptotically limiting Reynolds number exists was not feasible with the current experimental setup.

Next, the numerical and experimental results obtained in this investigation for the triangular obstacles are compared with those of a mathematical model developed by Dias and Vanden-Broeck (1989). Figure 5 contains all the different results in the form of a plot of the Froude number versus the nondimensional height of the triangular obstacle. The experimental data are represented by solid circles, the numerical data by open squares, and the mathematical results by solid lines. The mathematical results obtained by Dias and Vanden-Broeck are for inviscid flow and cover the range of W values smaller than 1.2 only. Results pertaining to the flow upstream of the obstacle occupy the upper part of Fig. 5, while those of the flow downstream of the obstacle occupy the lower part of the figure. In addition to the experimental, numerical, and analytical results, Fig. 5 contains a second-order curve fit, represented by a dashed line, of the experimental data downstream of the obstacle.

The results of Fig. 5 show that the Froude number behavior predicted by the inviscid theory is not significantly different from the behaviors inferred from the experimental data and the numerical results for viscous flow. This behavior is not surpris-

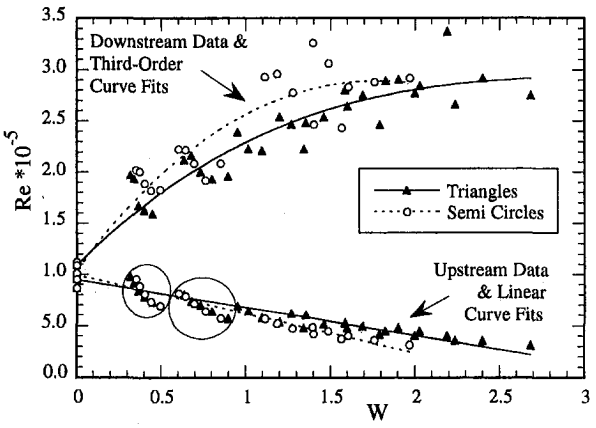

Fig. 4 Experimentally measured data and their curve fits over the considered range of nondimensional obstacle heights

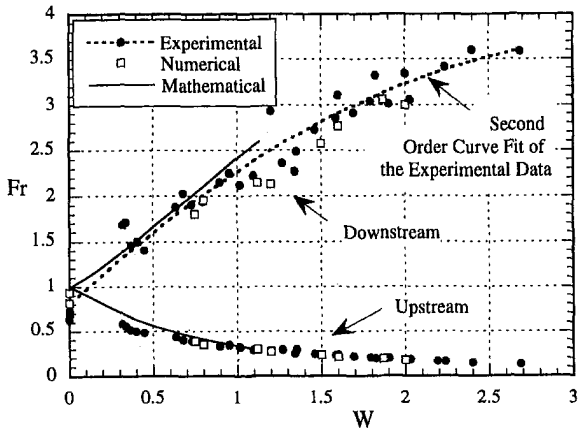

Fig. 5 Comparisons of numerical and analytical results with experimental measurements for the triangular obstacles

ing from an engineering perspective since gravitational forces are expected to dominate viscous forces in open channel flow. For shallow flow, the fluid velocities are high, resulting in a relatively thin boundary layer, while for deeper flows, the boundary layer thickness increases as a result of lower velocities. In either case, the resulting boundary layer thickness is comparatively much smaller than the fluid depth, and consequently, viscous effects have a negligible influence on the shape of the free surface and on the nondimensional parameters that characterize the flow.

The values of the downstream Froude number obtained from the numerical simulations appear in Fig. 5 to be generally slightly lower than those obtained either from the experiments or from the inviscid flow analysis. Meanwhile, all the data and results for the upstream Froude numbers are very close. The discrepancy in the downstream results may be attributed to the fact that, in the numerical simulations, the triangular obstacles are defined by the use of square computational cells rather than by straight surfaces.

Another point of interest relating to Fig. 5 is the fact that the experimentally determined Froude numbers at $W = 0$ are slightly less than unity. As discussed by Potter and Wiggert (1991), the Froude number in an open channel does not reach a value of unity except in the vicinity of rapids, cascades and waterfalls. In the experiments conducted for this investigation, the channel was horizontal and the outlet was a waterfall where, for an infinitesimally small obstacle, a Froude number equal to unity could be expected. However, in order to minimize the effects of the outlet on the test region, the obstacles were located at least twenty obstacle heights upstream of the outlet. Consequently, the experimental Froude number could not reach a value of unity at $W = 0$. These facts account for the slightly lower experimentally obtained values near $W = 0$ as compared to the values obtained from the numerical simulations and analytical predictions.

Accuracy and Convergence

Uncertainty estimates for the experimental results shown in Figs. 4 and 5 are summarized in Table 1 in terms of the minimum and maximum percent precision limit, bias limit, and uncertainty. The maximum and minimum estimates in Table 1 correspond to the cases of minimum and maximum fluid depths, respectively, since the uncertainty in the fluid depth measurement is an estimated constant.

The accuracy of the numerical results presented in Fig. 5 was also assessed by performing spatial and temporal convergence tests for the case of $W = 1.5$. Four incrementally finer grid resolutions were selected for the spatial convergence study by using computational domains with 100 × 33, 150 × 50, 200 × 67, and 250 × 83 grid points. The computed upstream and downstream Froude numbers for the four domains are listed in Table 2. The results of the spatial convergence study indicated that the Froude numbers ceased to change once the grid size was increased beyond 200 × 67. Indeed, the Froude numbers resulting from the computational solutions over the 200 × 67 and 250 × 83 domains are identical to within four significant figures. As a result, the 200 × 67 grid was used to generate all the results discussed in the previous section.

A study of the temporal convergence was conducted on the case with a 200 × 67 grid. At each time level, the time increment calculated dynamically by the SMMC technique was halved (see the Numerical Simulations Section for a discussion of the dynamic calculation of the time increment). Hence, the flow was simulated by marching through time with twice the number of time steps that would have normally been required by the SMMC technique. The upstream and downstream Froude numbers calculated from this simulation were 0.237 and 2.578, respectively, indicating no further dependence on the time step. It is then concluded that the results obtained from the 200 × 67 computational grid size are converged both spatially and temporally.

Table 1 Uncertainty estimates for the experimental data

		Precision limit (%)	Bias limit (%)	Uncertainty (%)
Re	min.	+0.87	+0.09	+0.87
		−0.85	−0.09	−0.86
	max.	+4.35	+0.52	+4.38
		−4.00	−0.52	−4.03
Fr	min.	+1.31	+0.13	+1.31
		−1.28	−0.13	−1.29
	max.	+6.59	+0.79	+6.64
		−5.94	−0.78	−5.99

Conclusions

This work presents the results of an experimental and numerical investigation of open channel flow over two-dimensional, triangular and semi-circular obstacles. Comparisons are made between the numerical and experimental results as well as with the results of an analytical solution of inviscid, irrotational flow. The experimental results for both kinds of obstacles indicate that, as either the obstacle height is increased or the flow rate is decreased, the upstream Reynolds number decreases linearly, while the downstream Reynolds number increases toward an apparent asymptotic value. For the case of a triangular obstacle, the experimental data as well as the numerical and analytical solutions indicate that, as either the height of the obstacle is increased or the flow rate is decreased, the Froude number decreases upstream of the obstacle and increases downstream of it, a behavior similar to that of the Reynolds number. More importantly, however, the close agreement between the experimental data and numerical results, on one hand, and the analytical results, on the other, is a strong indication that the viscous and rotational effects, which are absent from the analytical solution of inviscid irrotational flow, play a minor role in the overall behavior of the open channel flow considered in this work. Even though both theory and experimental observations support the existence of strong rotational activity in a fluid flowing over a

Table 2 Grid accuracy

Grid	Fr Upstream	Fr Downstream
100 × 33	0.240	1.786
150 × 50	0.231	1.827
200 × 67	0.237	2.578
250 × 83	0.237	2.578

stationary blunt body (Lee and Tsai, 1992; Xingkui and Fontijn, 1993), the results of this investigation indicate that this activity has little effect on the shape of the free surface and in turn on the Froude number. Consequently, open channel flows in which the free surface undergoes small deformations may be simulated by the use of inviscid (or Euler-based) models without much apparent loss of realism.

References

Cahouet, J., and Lenoir, M., 1983, "Numerical Solution of the 2-D Non Linear Wave Resistance Problem," *Comptes Rendus de l'Academie des Sciences,* Paris, 297, pp. 819–822.

Chen, S., 1991, "The SMU Method: A Numerical Scheme for Calculating Incompressible Free Surface Fluid Flows by the Surface Marker Utility," Ph.D. Dissertation, Mechanical Engineering Department, Southern Methodist University, Dallas, Texas.

Chen, S., Johnson, D. B., and Raad, P. E., 1995, "Velocity Boundary Conditions For the Simulation of Free Surface Fluid Flow," *Journal of Computational Physics,* Vol. 116, No. 2, pp. 262–276.

Chen, S., Johnson, D. B., Raad, P. E., and Fadda, D., 1997, "The Surface Marker and Micro Cell Method," *International Journal for Numerical Methods in Fluids,* in press.

Cole, S. L., 1983, "Near Critical Free Surface Flow Past an Obstacle," *Quarterly of Applied Mathematics,* Vol. 41, pp. 301–309.

Dias, F., Keller, J. B., and Vanden-Broeck, J. M., 1988, "Flow Over Rectangular Weirs," *Physics of Fluids,* Vol. 31, pp. 2071–2076.

Dias, F., and Vanden-Broeck, J. M., 1989, "Open Channel Flow with Submerged Obstacles," *Journal of Fluid Mechanics,* Vol. 206, pp. 155–170.

Forbes, L. K., and Schwartz, L. W., 1982, "Free-surface Flow Over a Semicircular Obstruction," *Journal of Fluid Mechanics,* Vol. 114, pp. 299–314.

Johnson, D. B., Raad, P. E., and Chen, S., 1994, "Simulation of Impacts of Fluids Free Surfaces with Solid Boundaries," *International Journal for Numerical Methods in Fluids,* Vol. 19, pp. 153–176.

Lee, H. Y., and Tsai, S. Y., 1992, "Experimental Investigation on Flow Passing a Rectangular Pit in an Open Channel Flow," *Journal of the Chinese Institute of Engineers,* Vol. 15, pp. 391–397.

Potter, M. C., and Wiggert, D. C., 1991, *Mechanics of Fluids,* p. 440, Prentice-Hall, New Jersey.

Raad, P. E., Chen, S., and Johnson, D. B., 1995, "The Introduction of Micro Cells to Treat Pressure in Free Surface Fluid Flow Problems," ASME JOURNAL OF FLUIDS ENGINEERING, Vol. 117, pp. 683–690.

Vanden-Broeck, J. M., 1987, "Free-surface Flow Over an Obstacle in a Channel," *Physics of Fluids,* Vol. 30, pp. 2315–2317.

Vanden-Broeck, J. M., and Keller, J. B., 1986, "Pouring Flows," *Physics of Fluids,* Vol. 29, pp. 3958–3961.

Xingkui, W., and Fontijn, H. L., 1993, "Experimental Study of the Hydrodynamic Forces on a Bed Element in an Open Channel With a Backward Facing Step," *Journal of Fluids and Structures,* Vol. 7, pp. 299–318.

C. Crnojević [1]
Assistant Professor,
Laboratoire de Mécanique des Fluides,
Université de Valenciennes, Valenciennes,
France

V. D. Djordjević
Professor,
Faculty of Mechanical Engineering,
University of Belgrade,
27. Marta 80, 11000 Belgrade,
Serbia

Correlated Compressible and Incompressible Channel Flows

Compressible flow in channels of slowly varying cross section at moderately high Reynolds numbers is treated in the paper by employing some Stewartson-type transformations that convert the problem into an incompressible one. Both adiabatic flow and isothermal flow are considered, and a Poiseuille-type incompressible solution is mapped onto compressible plane in order to generate some exact solutions of the compressible governing equations. The results show striking effects that viscosity may have upon the flow characteristics in this case, in comparison with more conventional high Reynolds number flows.

1 Introduction

Viscous compressible channel flows at moderately high Reynolds numbers differ considerably from the more conventional, high Reynolds number flows in that the effect of viscosity is spread over the whole cross session of the channel. Since the velocities in a gas flow are usually very high, especially in supersonic flows, moderately high Reynolds numbers can be obviously maintained in channels of extremely small width only—in so called micro-channels. Such channels find very useful applications in several branches of contemporary techniques, like in externally-pressurized thrust bearings and pressure relief valves (Gross, 1968), in the design of integrated cooling of electronic circuits (Tucherman, 1984), in Joule-Thomson cryo-coolers for infra-red detectors and diode lasers (Wu and Little, 1983), and in small, high-frequency fluidic control elements (Joyce, 1983), to mention just a few.

One of the first papers that deals with viscous compressible flow in channels of slowly varying cross section at moderately high Reynolds numbers is the paper by Williams (1963). In this paper, basic equations governing both incompressible and compressible flow in 2-D and axisymmetric channels are presented, and similarity solutions for an incompressible flow are found and discussed. Since the equations governing compressible flow are amenable to the application of some Stewartson-type transformations, Williams (1963) uses Dorodnitsyn-Howarth transformations (Stewartson, 1964), to convert the equations into a form with is much alike to incompressible flow equations. Similarity solutions of these equations were then mapped onto "compressible plane" and an exact solution of the governing equations for an adiabatic flow was found. The results show dramatic effects that viscosity may have upon the flow characteristics in such a case. There are several other experimental, analytical, and numerical studies concerned with viscous compressible channel flows. Worthwhile mentioning are the papers by Schwartz (1987) and Harley et al. (1995) in which isothermal flow between parallel plates is treated.

This paper is directly related to Williams' (1963) paper. We use slightly modified Stewartson's (1949) transformations in order to reduce the governing equations to fully incompressible form, their modification being caused by the fact that adiabatic flow along the centerline of the channel is not isentropic, which will be precisely shown later. We then map a Poiseuille-type incompressible flow onto compressible plane and obtain an exact solution of the governing equations describing compressible adiabatic flow in a divergent channel. We show that, independently of a reference Mach number, pressure, centerline velocity, and centerline Mach number decrease in the direction of flow, while centerline temperature increases. We also derive a low Mach number approximation and discuss the effect of compressibility on the friction factor. In addition, we also present and discuss an isothermal solution.

2 Problem Statement and Governing Equations

The problem considered is depicted in Fig. 1, where the upper half of a 2-D channel and velocity and temperature profiles in an arbitrarily chosen cross section $x' = 0$ are sketched. All dimensional quantities are denoted by primes. In order to write the governing equations in a suitable nondimensional form, we will introduce the following scales: δ_o for all lengths, u_o for all velocities, p_o for pressure, T_o for temperature, ρ_o for density, and μ_o for viscosity, where p_o, ρ_o, and μ_o (not shown in Fig. 1) are pressure, density, and viscosity at the origin, respectively.

We will assume that the cross section of the channel varies slowly with x', i.e., that $\alpha_{\max} = \epsilon$ is a small parameter. All physical quantities will vary slowly in x' direction in this case, and in order to express their slow variations explicitly we will introduce the slow coordinate $x = \epsilon x'/\delta_o$. Also, transverse velocity component v' will be much smaller then u' everywhere, and we will write: $v'/u_o = \epsilon v$, where $v(x, y)$ is an $O(1)$ transverse velocity. Concerning the magnitude of the Reynolds number $\mathrm{Re} = \rho_o u_o \delta_o/\mu_o$ we will now suppose that it is high and related to ϵ as: $1/\mathrm{Re} = \lambda\epsilon$, where λ is an $O(1)$ parameter. Obviously we have in mind at that moderately high Reynolds numbers, which are in gas flows maintainable in micro-channels only. The theory that follows will be equally applicable to both subsonic and supersonic flows. However, some caution is necessary in its application in supersonic flows. Namely, at only moderately high Reynolds numbers the ration $M_o/\sqrt{\mathrm{Re}}$, where M_o is the reference Mach number, in a supersonic flow may attain values which are not small enough for the continuum hypothesis to hold, and at least slip boundary conditions must be employed, which is beyond the scope of our work. Concerning this question see Harley et al. (1995) for more details.

Continuity equation, Navier-Stokes equations in x and y directions and equation of state, written in nondimensional form, in the limit when $\epsilon \to 0$, read, respectively:

$$\left.\begin{aligned} &(\rho u)_x + (\rho v)_y = 0 \\ &\rho(uu_x + vu_y) = -\frac{1}{\kappa M_o^2} p_x + \lambda(\mu u_y)_y \\ &p_y = 0, \quad p = \rho T \end{aligned}\right\} \tag{1}$$

where $\kappa = c_p/c_v$ is the ratio of specific heats. For brevity we

[1] Present address: Faculty of Mechanical Engineering, University of Belgrade, 27. Marta 80, 11000 Belgrade, Serbia.

Contributed by the Fluids Engineering Division of THE AMERICAN SOCIETY OF MECHANICAL ENGINEERS. Manuscript received by the Fluids Engineering Division October 2, 1996; revised manuscript received April 14, 1997. Associate Technical Editor: M. S. Cramer.

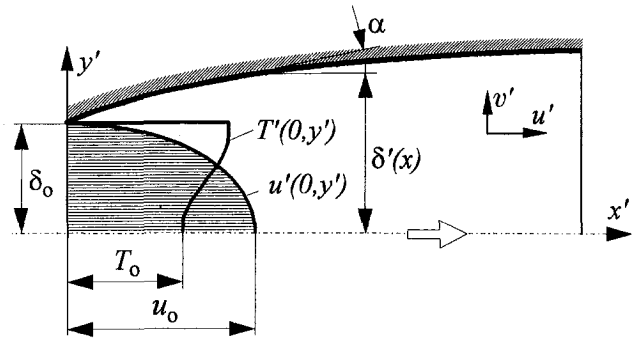

Fig. 1 Viscous compressible flow in a channel of slowly varying cross section

will skip writing the energy equation, because we will consider either adiabatic flow with Prandtl number equal one, or isothermal flow. As is well known, the total enthalpy remains constant throughout in adiabatic flow. Thus:

$$H_o = T + \frac{\kappa - 1}{2} M_o^2 u^2 = \text{const.} = 1 + \frac{\kappa - 1}{2} M_o^2, \quad (2)$$

where H_o is the total enthalpy, made nondimensional by $c_p T_o$. Boundary and symmetry conditions at the channel wall and the centerline are, respectively:

$$\left.\begin{aligned} &y = \delta(x): \quad u = v = 0 \\ &y = 0: \quad u_y = v = 0. \end{aligned}\right\} \quad (3)$$

Equations (1) are typical boundary layer equations. In the Williams' (1963) paper they were intuitively deduced and stated only. We find it useful and necessary to sketch their derivation in more detail, and to reveal precisely geometrical and physical conditions of their validity. In the problem statement, however, there is a considerable difference between classical boundary layer theory and channel flows: the pressure is known in boundary layers and its thickness, together with all other quantities, is required in contrast to the present problem, in which $\delta(x)$, that plays the role of the boundary layer thickness, is given and pressure is required. There is another important difference. The flow on the outer edge of the classical boundary layer is isentropic. Here, the flow along the centerline of the channel, that plays the role of the outer edge of the boundary layer, is not isentropic. We may verify that easily in adiabatic flow case by writing the energy equation in the (dimensional) form:

$$\frac{Ds'}{Dt'} = \frac{\rho' \dot{q} + \Phi}{\rho' T'},$$

where t' and s' are time and entropy, respectively, and Φ and $\rho' \dot{q}$ are, within the performed approximations:

$$\Phi = \mu'(u'_{y'})^2, \quad \rho' \dot{q} = (k' T'_{y'})_{y'},$$

where k' is the conductivity. While the dissipation function Φ vanishes at the centerline, the term $\rho' \dot{q}$ is not zero there because of the nonzero curvature of the temperature profile, and is positive (Fig. 1). Hence, the entropy of individual fluid particles moving along the centerline of the channel increases. This will require some modification of Stewartson's (1949) transformations in converting Eq. (1) into an incompressible form.

3 Transformation of Governing Equations and an Adiabatic Flow Solution

In order to simplify the Eq. (1) by bringing it into a form corresponding to incompressible flow, we will employ the following slightly modified Stewartson's (1949) transformations:

$$\xi = \int_0^x b(x) p^{(3\kappa-1)/2\kappa} dx; \quad (4.1)$$

$$\eta = p^{(\kappa-1)/2\kappa} \int_0^y \rho(x, y) dy, \quad (4.2)$$

$$p = P^{-(\kappa/(\kappa-1))}(\xi), \quad u = p^{(\kappa-1)/2\kappa} U(\xi, \eta), \quad (4.3),(4.4)$$

$$\rho v = b(x) p^{(3\kappa-1)/2\kappa} V(\xi, \eta) - \frac{\partial \eta}{\partial x} U(\xi, \eta), \quad (4.5)$$

where $b(x)$ is the coefficient of proportionality in Chapman-Rubesin (1949) linear dependence of viscosity on temperature: $\mu = b(x)T$. It follows from Sutherland's formula that:

$$b(x) = T_w^{1/2} \frac{1 + T_s/T_o}{T_w + T_s/T_o},$$

where T_s is a constant temperature (T_s = 122 K for air) and $T_w(x)$ is the wall temperature. In our case, however, $T_w = H_o$ = const., which follows from (2), and b will be a constant:

$$b = H_o^{1/2} \frac{1 + T_s/T_o}{H_o + T_s/T_o}. \quad (5)$$

If Eq. (1) and conditions (3) are transformed by means of (4.1) ÷ (4.5) we obtain:

$$\left.\begin{aligned} &U_\xi + V_\eta = 0 \\ &UU_\xi + VU_\eta = \frac{H_o}{(\kappa - 1)M_o^2} \frac{dP}{d\xi} + \lambda U_{\eta\eta} \\ &\eta = \Delta(\xi): \quad U = V = 0 \\ &\eta = 0: \quad U_\eta = V = 0 \end{aligned}\right\} \quad (6)$$

where $\Delta(\xi) = p^{(\kappa-1)/2\kappa} \int_0^{\delta(x)} \rho(x, y) dy$. The form of the system (6) fully corresponds to an incompressible flow in a channel of varying width $\Delta(\xi)$, with the same geometrical and physical conditions as in the considered compressible flow.

At this point we will make a comparison between ours and Stewartson's transformations. For an isentropic flow along the axis of the channel they coincide. However, such a flow is not maintainable, as shown in Section 2. Our transformations are capable of reducing Eq. (1) to the incompressible form (6), while Stewartson's ones are not. For example, Stewartson's transformations applied to (1) lead to an extra term on the right-hand side of the momentum equation in (6), that reads: $-\lambda(T/T_e)U_{\eta\eta}|_{\eta=0}$, where T_e is the centerline temperature, so that the resulting equation is obviously not an "incompressible" one. This extra term is produced by the effect of viscosity (curvature of the velocity profile at the axis) on the pressure gradient in the channel, absent in classical boundary layers, which can be easily deduced from (1) if the momentum equation is written for $y = 0$. Thus, our transformations are equally applicable to both boundary layers and channel flows, while Stewartson's ones can be applied to boundary layers only, and in that sense our transformations are more general.

The obviously present artifact in (6) that the "pressure" P increases/decreases when the velocity profile at the wall is convex/concave is of no practical importance. In principle, any solution to (6) can be mapped onto compressible plane, and in such a way various solutions to (1) can be generated. We will demonstrate this procedure on the example of simplest possible, Poiseuille-type solution, obtainable from (6) for $\Delta(\xi) = \Delta_o$ = const., that reads:

$$U = \frac{K}{2}(\Delta_o^2 - \eta^2), \quad V = 0, \quad (7.1)$$

$$\frac{dP}{d\xi} = \frac{K\lambda(\kappa - 1)M_o^2}{H_o}, \quad (7.2)$$

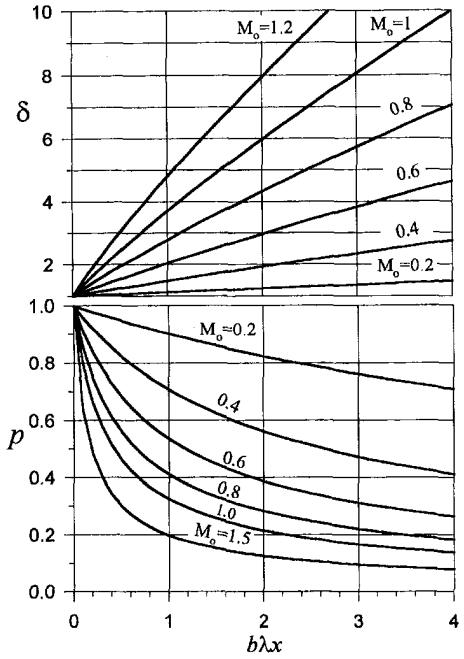

Fig. 2 Form of the channel in compressible plane and pressure drop for different values of the reference Mach number M_o

where K is the separation constant, which can be immediately obtained from (4.4), since $u(0, 0) = 1$ and $p(0) = 1$: $K = 2/\Delta_o^2$. In what follows, we will denote the values of all physical quantities at the centerline of the cannel in compressible plane by index "e". Thus, we will get from (4.4) and (2):

$$\left.\begin{aligned} u &= u_e\left(1 - \frac{\eta^2}{\Delta_o^2}\right), \\ T &= 1 + \frac{\kappa - 1}{2} M_o^2\left[1 - u_e^2\left(1 - \frac{\eta^2}{\Delta_o^2}\right)^2\right] \\ T_e &= 1 + \frac{\kappa - 1}{2} M_o^2(1 - u_e^2) \end{aligned}\right\} \tag{8}$$

where $u_e = p^{(\kappa-1)/2\kappa}$.

Differentiating (4.3), and using (4.1), with b = const., and (7.2), we can easily find the pressure distribution in compressible plane

$$p = \left[1 + \frac{(5\kappa - 3)M_o^2}{H_o\Delta_o^2} b\lambda x\right]^{-(2\kappa/(5\kappa-3))}.$$

In order to find the form of the channel $\delta(x)$, and velocity and temperature profiles in different cross sections, it is necessary to relate y and η coordinates. With the help of the equation of state, (4.2) can be written as:

$$pu_e y = \int_0^\eta T d\eta,$$

yielding:

$$pu_e y = T_e\eta + \frac{\kappa - 1}{3\Delta_o^2} M_o^2 u_e^2 \eta^3\left(1 - \frac{3}{10}\frac{\eta^2}{\Delta_o^2}\right). \tag{9}$$

For $\eta = \Delta_o$, $y = \delta(x)$, so that the form of channel is determined by:

$$pu_e\delta(x) = [T_e + \tfrac{7}{30}(\kappa - 1)M_o^2 u_e^2]\Delta_o.$$

Since p, u_e, T_e and δ are all equal one at $x = 0$, we get:

$$\frac{1}{\Delta_o} = 1 + \frac{7}{30}(\kappa - 1)M_o^2.$$

Thus, single parameter, reference Mach number M_o fully determines the width of the channel in incompressible plane. Final form expressions for the pressure distribution and form of the channel now read:

$$\left.\begin{aligned} p(x) &= \left\{1 + \frac{2(5\kappa - 3)M_o^2}{2 + (\kappa - 1)M_o^2}\left[1 + \frac{7}{30}(\kappa - 1)M_o^2\right]^2 b\lambda x\right\}^{-(2\kappa/(5\kappa-3))} \\ \delta(x) &= \frac{30 + (\kappa - 1)M_o^2(15 - 8u_e^2)}{30 + 7(\kappa - 1)M_o^2} u_e^{-(3\kappa-1)/(\kappa-1)}. \end{aligned}\right\} \tag{10}$$

In Fig. 2 and Fig. 3, p and δ, and u_e and T_e are plotted, respectively, versus $b\lambda x \geq 0$, for various reference Mach numbers. Obviously, the channel in compressible plane is a divergent one. Pressure and centerline velocity decrease in the direction of flow, while centerline temperature increases. In accordance with the classical boundary layer theory, there is no qualitative difference between subsonic and supersonic flow.

Centerline Mach number M_e and entropy s_e can now be easily evaluated by means of the following expressions:

$$\frac{M_e}{M_o} = \frac{u_e}{\sqrt{T_e}}, \quad s_e = 1 + \frac{2c_p}{s_o}\ln\frac{M_o}{M_e},$$

which show that M_e decreases downstream, while s_e increases. Thus, the flow along the centerline of the channel is really not isentropic, as deduced in Sec. 2—fact that made us modify Stewartson's transformations in treating this problem. Finally, the wall shear stress can be evaluated too. If it is made nondimensional by $\mu_o u_o/\delta_o$, we get:

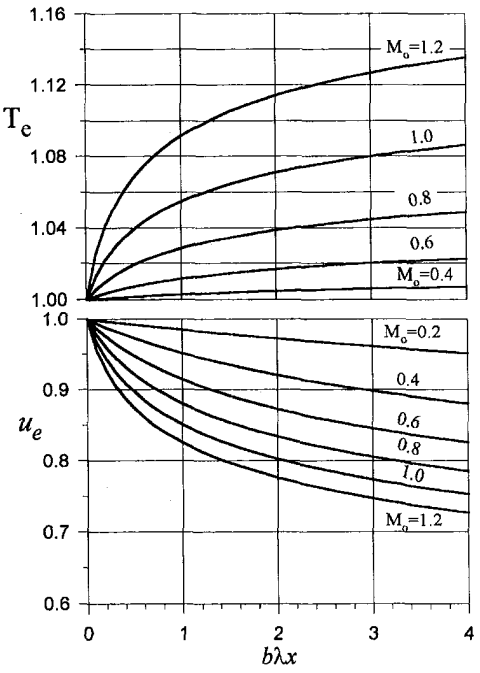

Fig. 3 Centerline temperature and centerline velocity in the channel for different values of the reference Mach number M_o

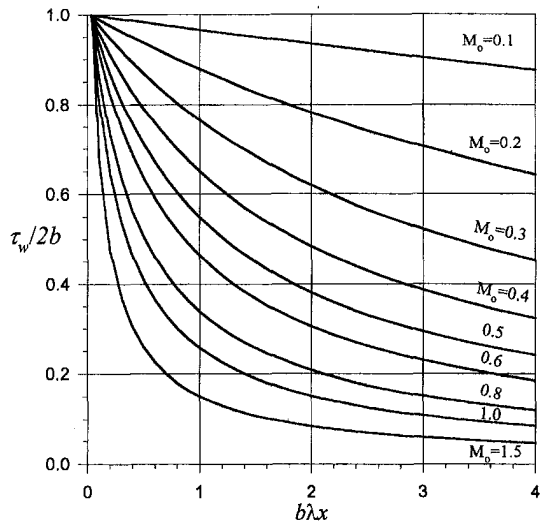

Fig. 4 Wall shear stress in the channel for different values of the reference Mach number M_o

$$\tau_w = 2b[1 + \tfrac{7}{30}(\kappa - 1)\mathrm{M}_o^2]p^{(2\kappa-1)/\kappa}. \tag{11}$$

It is plotted in Fig. 4. It decays with x, but it does not drop to zero for any finite x, which means that such a "boundary layer" does not separate from the wall.

Directly related to the wall shear stress is the friction factor f

$$\tau_w = \mathrm{Re} f \cdot \tfrac{1}{2}\rho_s u_s^2, \tag{12}$$

where ρ_s and u_s are nondimensional average density and velocity in an arbitrary cross section of the channel, respectively. For their evaluation it is necessary to find mass flow rate and volume flow rate. If they are made nondimensional by $2\rho_o u_o \delta_o$ and $2u_o\delta_o$, and denoted by $\dot{\mathrm{M}}$ and $\dot{\mathrm{V}}$, respectively, we get:

$$\dot{\mathrm{M}} = \tfrac{2}{3}\Delta_o, \quad \dot{\mathrm{V}} = \frac{1}{p}\int_0^{\Delta_o} TU d\eta. \tag{13}$$

Then: $u_s = \dot{\mathrm{V}}/\delta(x)$ and $\rho_s = \dot{\mathrm{M}}/\dot{\mathrm{V}}$. The procedure of evaluation of f from (12) is, however, very cumbersome, and we will postpone it for the low Mach number approximation only. Before that, we will plot velocity profiles for different Mach numbers and $b\lambda x = 0$, 2 and 4 in Fig. 5. The temperature profiles can be easily deduced from the expression:

$$\frac{T_w - T}{T_w - T_e} = \left(\frac{u}{u_e}\right)^2.$$

4 Low Mach Number Approximation

For low values of the reference Mach number M_o the expressions (5), (10), (8), (11) and (13) can be expanded into binomial series, which will converge for x not to large. First two terms of these series read, respectively:

$$b = 1 - \frac{\kappa - 1}{4}\frac{T_o - T_s}{T_o + T_s}\mathrm{M}_o^2 + O(\mathrm{M}_o^4),$$

$$p = 1 - 2\kappa\lambda x\mathrm{M}_o^2 + O(\mathrm{M}_o^4),$$

$$\delta = 1 + (3\kappa - 1)\lambda x\mathrm{M}_o^2 + O(\mathrm{M}_o^4),$$

$$u_e = 1 - (\kappa - 1)\lambda x\mathrm{M}_o^2 + O(\mathrm{M}_o^4), \quad T_e = 1 + O(\mathrm{M}_o^4),$$

$$\tau_w = 2\left\{1 + \left[\frac{29T_s - T_o}{60(T_o + T_s)}(\kappa - 1) - 2(2\kappa - 1)\lambda x\right]\mathrm{M}_o^2 + O(\mathrm{M}_o^4)\right\}$$

$$u_s = \frac{2}{3}\left[1 - (\kappa - 1)\left(\frac{8}{105} + \lambda x\right)\mathrm{M}_o^2 + O(\mathrm{M}_o^4)\right],$$

$$\rho_s = 1 - \left[\frac{11}{70}(\kappa - 1) + 2\kappa\lambda x\right]\mathrm{M}_o^2 + O(\mathrm{M}_o^4).$$

From (12) we can now obtain the corresponding series for the friction factor:

$$f = \frac{9}{\mathrm{Re}}\left[1 + \frac{41T_o + 111T_s}{140(T_o + T_s)}(\kappa - 1)\mathrm{M}_o^2 + O(\mathrm{M}_o^4)\right].$$

Surprisingly, f does not depend on x to this order of approximation. It increases with M_o. In the incompressible limit, $\mathrm{M}_o \to 0$, friction factor reduces to the well known Poiseuille formula (note that our Reynolds number is defined via maximum velocity at $x = 0$!).

5 An Isothermal Solution

As well known, isothermal gas flows are not consistent with the governing equations. However, in spite of that, they are treated in literature, like in the papers by Schwartz (1987) and Harley et al. (1995), because gas flows which are nearly isothermal are frequently encountered in applications. Here, we will present an exact solution of (1) for $T = \mu = 1$, obtained essentially in the same manner as the preceding adiabatic flow solution, i.e. by reduction to incompressible flow.

By using the following transformations:

$$\xi = \int_o^x \alpha(x)dx, \quad \eta = p(x)y,$$

Eq. (1) and boundary conditions (3) are reduced to:

$$\left.\begin{aligned} &u_\xi + \tilde{v}_\eta = 0 \\ &uu_\xi + \tilde{v}u_\eta = -\frac{1}{\kappa\mathrm{M}_o^2}\frac{d(\ln p)}{d\xi} + \lambda\frac{p}{\alpha}u_{\eta\eta} \\ &\eta = \Delta(\xi): \quad u = \tilde{v} = 0 \\ &\eta = 0: \quad u_\eta = \tilde{v} = 0, \end{aligned}\right\} \tag{14}$$

where: $\alpha\tilde{v} = uy \cdot dp/dx + pv$, and $\Delta(\xi) = p(x)\delta(x)$. Obviously, for $\alpha = p$ the equations attain a fully incompressible form. If we wish, however, like in adiabatic flow case, to map onto compressible plane the simplest possible solution of (14): $\Delta(\xi) = \Delta_o = \text{const.}$, $u = u(\eta)$, $\tilde{v} = 0$, it turns out that the choice

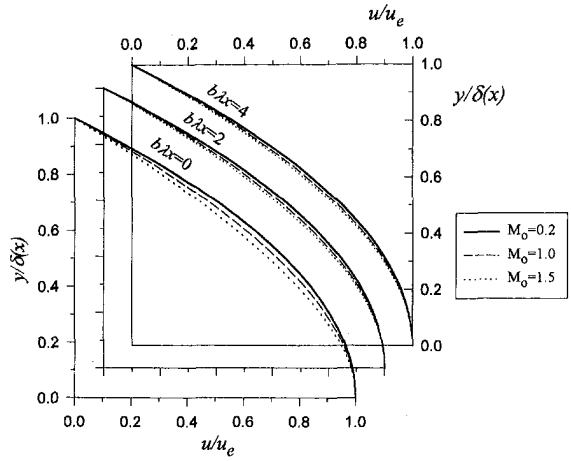

Fig. 5 Velocity profiles at the locations $b\lambda x = 0$, 2 and 4 in the channel for different values of the reference Mach number M_o

of α in this special case is irrelevant, and one can straightforwardly obtain the following exact solution to (1):

$$p = \rho = \frac{1}{1 + 2\lambda\kappa M_o^2 x}, \quad \delta = 1 + 2\lambda\kappa M_o^2 x,$$

$$u = 1 - \frac{y^2}{(1 + 2\lambda\kappa M_o^2 x)^2}, \quad v = -u\frac{d(\ln p)}{dx}y.$$

The solution represents isothermal gas flow in a divergent channel with plane walls in which pressure decreases downstream, while centerline velocity remains constant. Both average density and velocity, and friction factor can now be readily evaluated to be:

$$\rho_s = p, \quad u_s = \frac{2}{3}, \quad f = \frac{9}{\mathrm{Re}}.$$

Interestingly enough, average velocity and friction factor are constants, and even do not depend on the Mach number. If so, they naturally have values pertaining to Poiseuille flow.

6 Conclusions

We demonstrate in this paper that Stewartson-type transformations can be successfully applied in treating compressible flow in channels of slowly varying cross section. At that, reference Reynolds number attains moderately high values for which the effect of viscosity is spread over the entire cross section of the channel, and is maintainable in channels of extremely small width only, in micro-channels. In reducing compressible channel flow to the corresponding incompressible one, Stewartson-type transformations are equally applicable to both adiabatic and isothermal flow. Poiseuille-type incompressible solutions, when mapped onto compressible plane, show striking differences between major characteristics of these flows and high Reynolds number flows in which the effect of viscosity is restricted to relatively thin wall layers only. At this point it must be recognized that an inverse problem, in which the form of the channel in compressible plane is given in advance, would be more important from a practical point of view. Such a problem can be solved in principle, although calculations are much more complex in that the form of the channel in incompressible plane $\Delta(\xi)$ might not be obtainable analytically. Also, a method for solving incompressible flow for an arbitrary $\Delta(\xi)$ should be available for that purpose. We hope to be able to publish some results on that theme before long.

References

Chapman, D. R., and Rubesin, M. N., 1949, "Temperature and Velocity Profiles in the Compressible Laminar Boundary Layer with Arbitrary Distribution of Surface Temperature," *Journal of the Aeronautical Sciences,* Vol. 16, No. 9, pp. 547–565.

Gross, W. A., 1968, *Gas Film Lubrication,* Wiley, New York.

Harley, C. J., Huang, Y., Bau, H. H., and Zemel, N. J., 1995, "Gas Flow in Micros-Channels," *Journal of Fluid Mechanics,* Vol. 284, pp. 257–274.

Joyce, J. W., 1983, "Fluidics: Basic Components and Applications," *US Army Electronics Development Command, Harry Diamond Labs Special Report* HDL-SR-83-9.

Schlichting, H., 1979, *Boundary Layer Theory,* McGraw-Hill.

Schwartz, L. W., 1987, "A Perturbation Solution for Compressible Viscous Channel Flows," *Journal of Engineering Mathematics,* Vol. 21, pp. 69–86.

Stewartson, K., 1949, "Correlated Compressible and Incompressible Boundary Layers," *Proceedings Royal Society,* (London), Series A20, pp. 84–100.

Stewartson, K., 1964, "The Theory of Laminar Boundary Layers in Compressible Fluids," *Oxford University Press.*

Tuckerman, D. B., 1984, "Heat Transfer Microstructures for Integrated Circuits," PhD thesis, Department of Electrical Engineering, Stanford University.

Williams, J. C. III, 1963, "Viscous Compressible and Incompressible Flow in Slender Channels," *AIAA Journal,* Vol. 1, pp. 186–195.

Woo, P., and Little, W. A., 1983, "Measurement of Friction Factors for the Flow of Gases in Very Fine Channels Used for Microminiature Joule-Thomson Refrigerators," *Cryogenics,* May, pp. 273–278.

Interfacial Area Concentration and Void Fraction of Two-Phase Flow in Narrow Rectangular Vertical Channels

T. Wilmarth
Graduate Student.

M. Ishii
Professor of Nuclear Engineering.

School of Nuclear Engineering,
Purdue University,
West Lafayette, IN 47907

Adiabatic concurrent vertical two-phase flow of air and water through narrow rectangular channels, gap widths 1 mm and 2 mm, was investigated. This study involved the observation of flow using a charge coupled device (CCD) camera. These images were then digitized and examined by applying an image processing technique to determine local average void fraction and local average interfacial area concentration. The void fraction data were then plotted using a drift flux plot to determine the distribution parameter and vapor drift velocity for each separate flow regime.

Introduction

The behavior of a gas-liquid mixture confined to the space between flat plates differs from that in a tube due to the increased surface forces and frictional pressure drop. One of these differences is the change of appearance of the narrow channel flow regime map with comparison to the flow regime maps of larger rectangular channels and medium size circular tubes. It is for this reason that continued research concerning narrow channel flow is necessary. There exist many applications for flow through narrow passages. In microelectronics, narrow channels are employed in the cooling systems. In the case of nuclear engineering, this type of flow is encountered in high conversion nuclear reactors, liquid metal cooled reactors and high flux research reactors. Flow in narrow rectangular channels is also an integral part of the design of compact heat exchangers in boiling or condensation in space, aircraft, and other applications.

The main source of difficulties in two-phase modeling is the existence of interfaces between phases and the discontinuities associated with them. Since the flow structures are strongly related to macroscopic geometrical parameters, such as void fraction and interfacial area, it is important to examine these parameters fully. In particular, with the use of the drift flux model under steady state, fully developed conditions, it can be assumed that there exists a unique relation between the void fraction and superficial gas and liquid velocities (Ishii, 1977). Then the traditional approaches of flow regime maps, which are based on the superficial velocities, are suitable for the slow transients.

This study addresses the characterization of two-phase flow in narrow rectangular channels. Two test sections have been examined with gap widths of 1 mm and 2 mm with channel width of 20 mm and 15 mm, respectively. The two test sections were examined in vertical flow. The video data were digitized using an image grabber (480 × 640 pixel image processing board) and then an image processing program was used to determine the local average void fraction and interfacial area concentration. These results were then plotted versus the superficial gas velocity to observe the data trends. Using the drift flux plot, the distribution parameter, C_0, and vapor drift velocity, V_{gj}, were determined for each flow regime. An analysis concerned with the flow regimes and transitions for narrow rectangular channels was presented previously with both vertical and horizontal flow orientations (Wilmarth and Ishii, 1994).

Literature Survey

A method for void fraction measurement was used by Ali and Kawaji (1991), by Ali et al. (1991), and again by Ali et al. (1993) which consisted of a dual system of probes and electrodes. The two pairs of electrodes were mounted flush on the inside surfaces of the back and front plates of the test section. The two electrodes in each pair were mounted facing one another to measure the cross section and average void fraction. The probe was located midway between the upstream and downstream electrode pairs to measure local void fraction. The experiment offered data for both vertical and horizontal flow configurations. The results obtained in this experiment were expressed in the form of flow pattern maps and the authors suggested that there was good agreement with previous results of other authors. Other results, including void fraction data, was correlated in terms of the Martinelli Parameter and the drift flux model. Pressure drop data was correlated using several models for predicting the two-phase frictional pressure drop.

Mishima et al. (1988) used conductance probe to measure void fraction. The five probes were placed at equal intervals across the width of the test section. This point electrode probe would identify the existence of an air bubble at the tip when the change in the electric conductance between the tip and the ground electrode would occur. Then the time-averaged void fraction at the tip was calculated as the probability that the tip touches air bubbles. Mishima used image processing techniques to study flow in narrow rectangular ducts using either optical methods or neutron radiography technique. They obtained data for void fraction, α, and interfacial area concentration, a_i, using image processing and compared the results for void fraction with the conductance probe measurements. The results of both techniques were consistent when compared. The interfacial area concentration data showed a strong correlation to the void fraction data. Flow regime maps were also obtained in this study for slug, churn turbulent and annular regimes. Mishima also used neutron radiography (NRG) to measure void fraction and interfacial area concentration for comparison with the probe measurements. This method made use of differences in attenuation characteristics of radiation in different materials. A neutron television system was developed to observe real-time images of the dynamic behavior of the two-phase flow. The basic concept behind this method was that the neutron beam attenuated by

Contributed by the Fluids Engineering Division for publication in the JOURNAL OF FLUIDS ENGINEERING. Manuscript received by the Fluids Engineering Division June 7, 1995; revised manuscript received May 5, 1997. Associate Technical Editor: Jong H. Kim.

water in the test section made the scintillator emit visible light, producing an image of two-phase flow which was taken by a highly sensitive camera. The video image was then processed and converted into a gray level from which a calibration curve for the relation between the gray level and the water layer thickness was obtained. The original images from this method were found to not be enough to calculate the void fraction, but the overall-mean void fraction was calculated from 255 images. This integral process meant time-averaging and space-averaging the image.

X-ray and gamma-ray methods can also be used in determining void fraction. Jones and Zuber (1975) made an elaborate description of this method and the attenuation involved. They made measurements of a single beam from a continuous X-ray source in a vertical configuration. The time-varying signal was subjected to probability density analysis, and characteristic probability density function (PDF) curves were shown to exist for the different flows excluding churn turbulent. This could also be applied to horizontal flow configurations. Limitations of this type of analysis consisted of high cost and the need for careful installation and safety considerations during operation.

Another method for determining void fraction and interfacial area concentration is to visualize the flow through transparent pipe walls. Photographic methods are useful but they are often limited by the size of the field of view so that only local instantaneous behavior may be observed. In the past, only moving-picture photography was available. This proved to be less successful since the field of view was smaller than necessary to obtain the resolution needed for observation. Recently the advances in technology in the field of microelectronics has made it possible to overcome the difficulties of lost resolution when taking high speed movies. The cameras are capable of recording at a shutter speed of $\frac{1}{10000}$ s and with very high resolution. The only problem is encountered with lighting effects, but with patience and trial and error this is eventually overcome. From the images taken with any of these processes, image processing is then possible for determining local instantaneous void fraction and interfacial area concentration.

Mishima et al. (1991) used the same experimental apparatus as described previously (Mishima et al., 1988) to produce flow regime maps for the three different test sections. Void fraction was measured using the neutron radiography technique and correlated with the drift flux model. The void fraction data was determined to agree well with this correlation. The average slug bubble velocity was correlated using the drift flux model and the distribution parameter was found to be smaller than usual. They also found that the shape and motion of the gas phase in a narrow channel are strongly restricted due to the proximity of the walls. Finally, the pressure data was correlated using the Chisholm-Laird (1958) correlation and agreed well. It was noted that the Chisholm parameter decreased from 20 to zero as the gap decreased from 5 mm to 1 mm.

Sato et al. (1991) examined two-dimensional, two-phase flow in a vertical annulus with a small gap width. Using image processing and by adding a black dye to the liquid, they were able to determine void fraction.

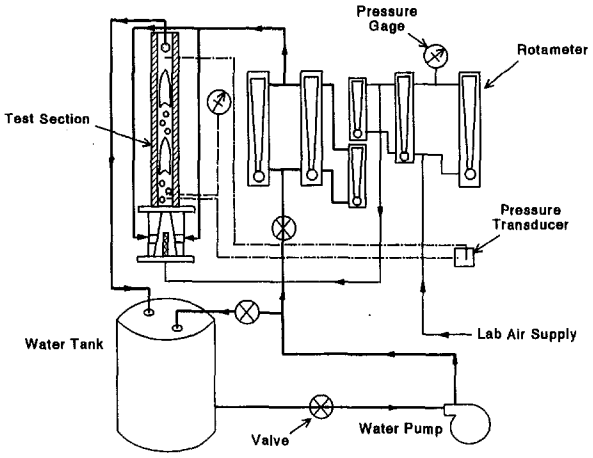

Fig. 1(*a*) Schematic of vertical air-water two-phase flow loop

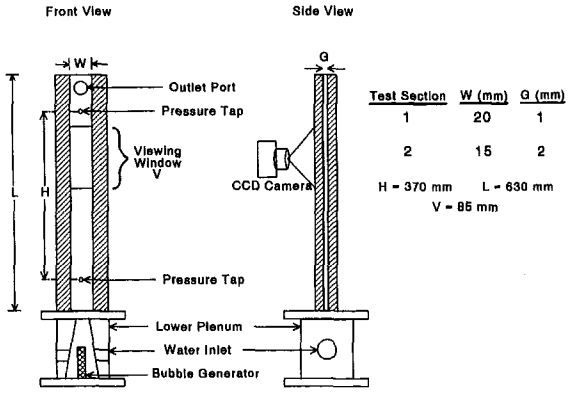

Fig. 1(*b*) Test section schematic in vertical orientation

Experimental Apparatus

The same test loop was used as discussed previously (Wilmarth and Ishii, 1994). This schematic diagram is shown in Fig. 1(*a*). The water was supplied by a pump and was regulated by rotameters. The water flow entered on both sides of the cylindrical lower plenum of the test section and exited into the upper plenum where the two-phase flow was separated. The water was then drained to a collection tank to be recirculated through the system. The air flow was provided by a compressed air supply and was also controlled with rotameters. The air was then injected into the lower plenum by a porous tube with 2.0 micron pores. This bubble generator produced uniformly sized bubbles in the mixing chamber, which then mixed with the water before entering the test section. The test section schematic is shown in Fig. 1(*b*). The two flat plates were made of clear Lucite and connected with bolts. The gap was formed by sealing two stainless steel strips between the plates. The test section was 630 mm in length with two pressure taps 370 mm apart,

Nomenclature

a_i = interfacial area concentration (m^{-1})
C_0 = distribution parameter given by Eq. (2)
D_h = hydraulic diameter (m)
g = gravitational constant (m/s^2)
j_g, j_f = superficial velocity of gas and liquid (m/s)
v_g = weighted mean velocity of gas phase given by Eq. (1) (m/s)
V_{gj} = vapor drift velocity (m/s)
α = void fraction of gas phase
ρ_g, ρ_f = density of gas and liquid (kg/m^3)
σ = surface tension (N/m)
ν_g, ν_f = kinematic viscosity of gas and liquid (m^2/s)

Subscripts

g = gas phase
f = liquid phase
c = centerline position
w = wall position

one located 130 mm past the entrance and one 130 mm before the exit of the test section to yield fully developed, two-phase pressure drop data. The pressure taps were connected to a pressure transducer for pressure drop measurements.

The two test sections used in this experiment were made with slightly differing dimensions: the gaps were 1 mm and 2 mm with channel width 20 mm and 15 mm, respectively. The same overall structure was used for the 1 mm and 2 mm gap widths by simply replacing the highly polished stainless steel strips. Measurements included pressure drop data and local average liquid and gas flow rates. The window length for the visualization part of this experiment was 85 mm and was located 380 mm beyond the entrance to yield fully developed flow. The images acquired by the video camera were then digitized for analysis by an image processing system.

Statistical Analysis

It was determined through experiment that there existed a statistical instability that caused a variance in the data predominantly for the slug flow regime. To methodically decrease this variance, a model was developed to determine the minimum number of images needed in averaging. This model involved constructing a data base for each type of flow. By selecting differently distributed phases, test section dimensions, and window sizes an actual test void fraction was determined geometrically. Next, by stepping the window from the top of the test section to the bottom, a data base was formed. From this data base, void fraction data were randomly chosen using a random number generator, averaged and plotted as void fraction, α, versus sample size, N. This method was repeated for several scenarios until an average sample size was found for each type of flow.

It was found that for bubbly, churn-turbulent and annular flow at least 25 images were needed; and for slug flow, at least 50 images were necessary in averaging to reduce the statistical variance. For a plot with insufficient data, the plot for each parameter against superficial gas velocity with fixed liquid velocity demonstrated that the variance in void fraction and interfacial area concentration was very large when only six images were averaged.

Average Local Void Fraction and Interfacial Area Concentration

An image processing program was written which would take a digitized image and perform several tasks that in the past were typically accomplished by hand. The program first generates the image (from a CCD camera video taken at 30 frames/second) from the digitized images previously obtained by an image grabber (480 × 640 pixel image processing board). An image enhancement was performed using averaging of the background to clarify the interfacial boundaries. Next, the channel boundaries were identified. The program then determined the ratio between the channel width to the number of pixels. This ratio was used to convert the raw pixel data to physical length data. The phase boundaries were then determined and distinguished using two different colors. The program then differentiated between the two phases by determining which pixels belonged to the gas phase. To determine the bubble size, the program traced the perimeter of the bubble and used this 'circumference' of the bubble to find the diameter. If the bubble size was determined to be $D_h \leq 2$ mm for the 2 mm channel and $D_h \leq 1$ mm for the 1 mm channel, then the bubble was assumed to be spherical and the subsequent void fraction and interfacial area concentration were calculated. If the bubble was larger than the channel gap width, the void fraction and interfacial area were calculated by counting the number of pixels contained within the bubble, converting this to a surface area, multiplying this by 2 (for the two faces) and by the gap width to obtain the volume of the gas phase. The liquid film between the bubble and the channel wall is negligibly small

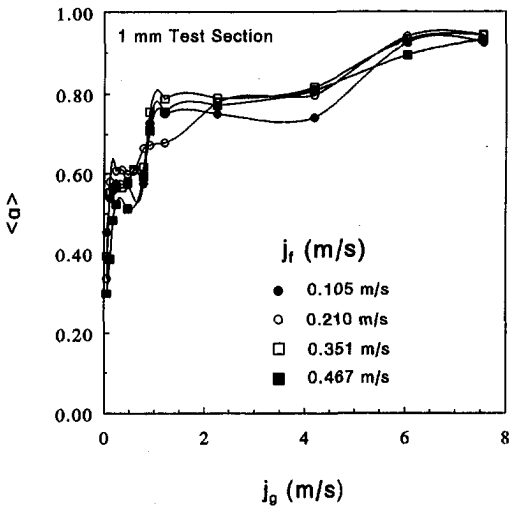

Fig. 2(*a*)

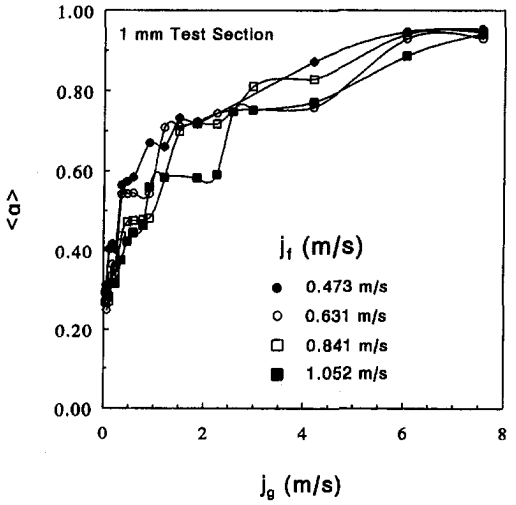

Fig. 2(*b*)

Fig. 2 Comparison of average void fraction data for different superficial liquid velocities versus superficial gas velocity for the 1 mm vertical test section, sets (a) and (b) with experimental uncertainty ~25 percent

according to the measurements of the conductivity film thickness probe and was neglected. Based on geometrical estimations, the assumptions used in this analysis introduce an error of 33 percent for the interfacial area concentration and 25 percent for the void fraction for bubble sizes larger than 1.2 times the gap width but this error decreases notably as the bubbles increase in size. It should be noted that, based on visual observation, the bubble population with diameters between G and $1.2*G$ is a small fraction of the bubble distribution.

These data were plotted on a linear plot and are shown in Figs. 2(*a*) and 2(*b*) for local average void fraction data in the 1 mm vertical test section. Figure 3 shows the local average void fraction data of the 2 mm vertical test section. Figures 4(*a*) and 4(*b*) show the local average interfacial area concentration data for the 1 mm vertical test section. The local average interfacial area concentration data for the 2 mm vertical test section are displayed in Fig. 5. For the observation of the data trends it is customary to plot the data on a linear plot.

The data display a marked increase in void fraction during the transition regions and a flattened curve for each of the individual regimes. For bubbly flow, the void fraction increases linearly with increasing superficial gas velocity. It then flattens out during the slug flow regime, increases during the transition

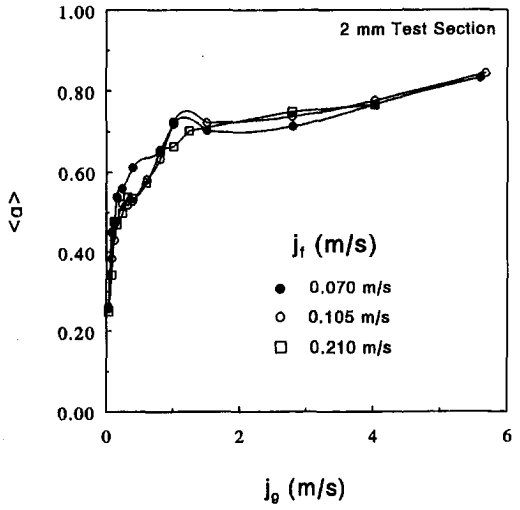

Fig. 3 Comparison of average void fraction data for different superficial liquid velocities versus superficial gas velocity for the 2 mm vertical test section with experimental uncertainty ~25 percent

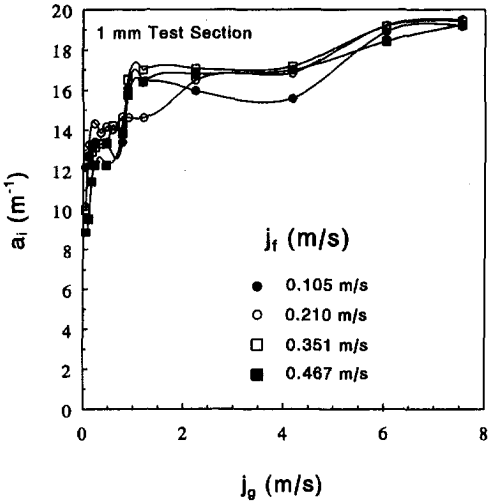

Fig. 4(*a*)

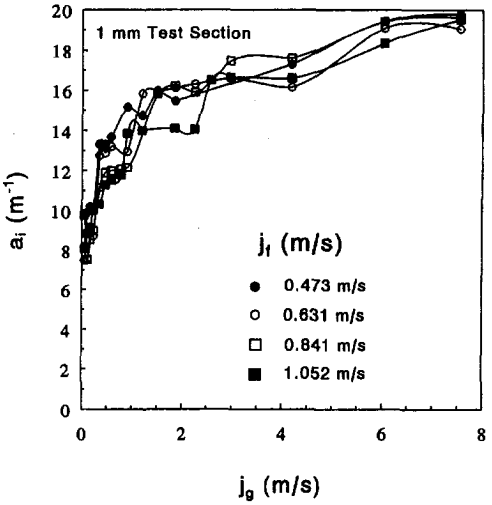

Fig. 4(*b*)

Fig. 4 Comparison of local average interfacial area concentration data for different superficial liquid velocities versus superficial gas velocity for the 1 mm vertical test section, sets (a) and (b) with experimental uncertainty ~33 percent

to churn turbulent flow, again flattens during the churn turbulent regime, and so on. This trend is also observed for the interfacial area concentration data for the 1 mm vertical test section and for the void fraction data of the 2 mm vertical test section. The 2 mm vertical test section demonstrates an interesting effect, which was not noted in the previous channel, caused by the maximum allowed packing of the bubbly flow regime. Considering Fig. 5, the interfacial area concentration decreases suddenly at the transition from bubbly to slug flow. This was easily explained since the interface surface area of the small bubbles combines more to increase the total surface area when compared to the interface of a slug.

Drift Flux Plots

The general method proposed by Zuber and Findlay (1965) was applied in the analysis of the resulting local average void fraction data. It was established by Kroeger and Zuber (1968) that the analysis was also valid for flow through rectangular ducts. This method related the average volumetric flux density of the mixture, $\langle j \rangle$, with the weighted mean velocity of the gas phase, v_g, using the linear relationship:

$$v_g = \langle j_g \rangle / \langle \alpha \rangle = C_0 \langle j \rangle + V_{gj} \tag{1}$$

where C_0 is the distribution parameter and V_{gj} is the vapor drift velocity. Figures 6(*a*) and 6(*b*) show the comparison of all flow regimes when plotted with the drift flux plot. The individual plots for each flow regime are shown in Figs. 7–10.

The line $C_0 = 1.0$ represents homogeneous flow and is displayed on each plot. Also included for each plot is the line formed by the theoretical value of C_0 found from the equation:

$$C_0 = 1.35 - 0.35(\rho_g/\rho_f)^{1/2} \tag{2}$$

with the vapor drift velocity, V_{gj}, found from the following theoretical drift flux model relations (Ishii, 1977). For the distorted bubbly regime this parameter was found based on the bubble rise velocity:

$$V_{gj} = 1.414(\sigma g \Delta\rho/\rho_f^2)^{1/4}(1 - \alpha)^{1.75} \tag{3}$$

For the slug regime the vapor drift velocity equation was found using the falling film velocity:

$$V_{gj} = 0.35(g \Delta\rho D_h/\rho_f)^{1/2} \tag{4}$$

Finally, the churn turbulent regime used the same basis as the distorted bubbly regime:

$$V_{gj} = 1.414(\sigma g \Delta\rho)^{1/4} \tag{5}$$

The experimental value of C_0 for each flow was determined by finding the slope of the resulting line formed by Eq. (1) and the y-intercept gave the experimental value of V_{gj}. For bubbly flow in the 1 mm test section, the distribution parameter was found to be $C_0 \cong 0.8$, which indicated that the gas velocity was smaller than the liquid velocity. This can be explained by incident of the bubble having much resistance being pushed by the liquid. For slug flow, the distribution was found to be $C_0 = 1.0$, which indicated that the void profile was flat in the core region. The churn turbulent regime also exhibited the same distribution as the slug flow regime with $C_0 = 1$. The annular flow, on the other hand, was not easily ascertained due to the limited amount of data available. For this case it is suggested that further data be obtained to better determine the distribution. It was not possible to accomplish this with the present test facility since it would require an increase in the gas flow rate and this would subject the test section to a higher pressure which it may not have been able to withstand. For the 2 mm vertical test section, the only differing distribution parameter was that for the case of bubbly flow. The distribution parameter was again less than

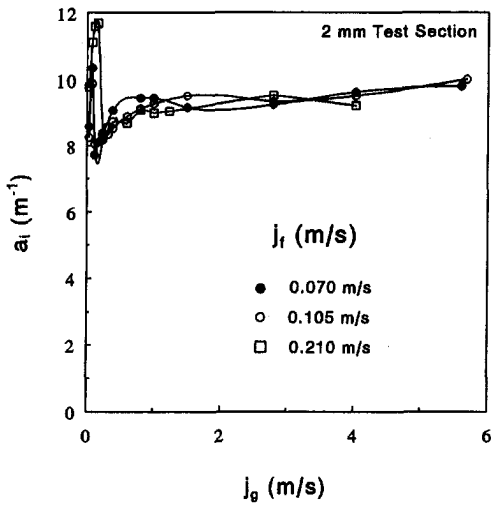

Fig. 5 Comparison of local average interfacial area concentration data for different superficial liquid velocities versus superficial gas velocity for the 2 mm vertical test section with experimental uncertainty ~33 percent

1.0 indicating that the liquid velocity was greater than the gas velocity, and the value for V_{gj} was not below zero. These results are summarized in Table 1. When compared to existing data of Mishima et al. (1991), the results agree well with their findings that the distribution parameter ranged from 1.0 to 1.2 for the slug flow regime, which is smaller than found with the void correlation. Ali et al. (1993) found good agreement with the drift flux correlation with $C_0 = 1.25$. These data did not distinguish the flow regimes and it can be seen that there is also a wide scattering effect for the bubbly flow regime, as pointed out by the authors. Both authors show that the values for V_{gj} are negligibly small, which also agrees with the current experiment for all flows.

Uncertainty Analysis

For each individual experimental data point, an estimate of uncertainty, based on the method outlined by Coleman and Steele (1989), was determined from the precision and bias limits. The following describes the methods used for the various data. Since the information on bias errors is usually inferred from comparison of independent measurements that depend on different physical principles, that have been independently calibrated, or from estimates based on previous experience of the experimenter and of other experimenters, the bias error is difficult to estimate in this case due to a lack of comparison. Thus the calculation of uncertainty is based solely on the precision limits of this experiment.

The precision error for the local average interfacial area concentration and local average void fraction was estimated using the first-order precision limit, $P_\alpha = \pm tS_\alpha$, and $P_{ai} = \pm TS_{ai}$, where t is the t-distribution value corresponding to the number of degrees of freedom, $M - 1$, with a 95 percent confidence level. The precision index, S_α and S_{ai}, of the sample population of the M individual test results was found using,

$$S_\alpha = \left[\frac{1}{M-1}\sum_{k=1}^{M}(\alpha_k - \bar{\alpha})^2\right]^{1/2} \quad (6)$$

for void fraction and

$$S_{a_i} = \left[\frac{1}{M-1}\sum_{k=1}^{M}(a_{ik} - a_i)^2\right]^{1/2} \quad (7)$$

for the interfacial area concentration. The values of P_α and P_{ai}

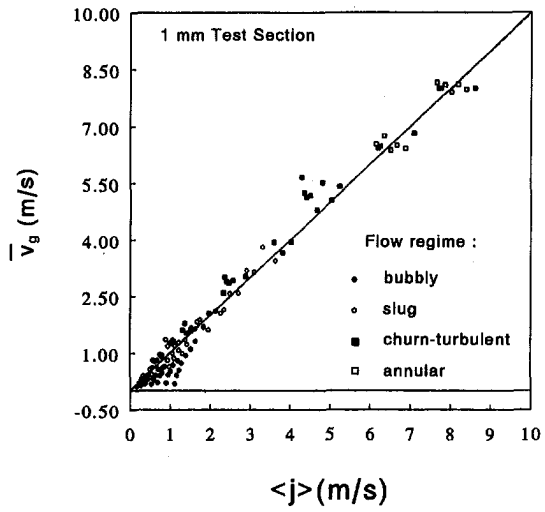

Fig. 6(*a*)

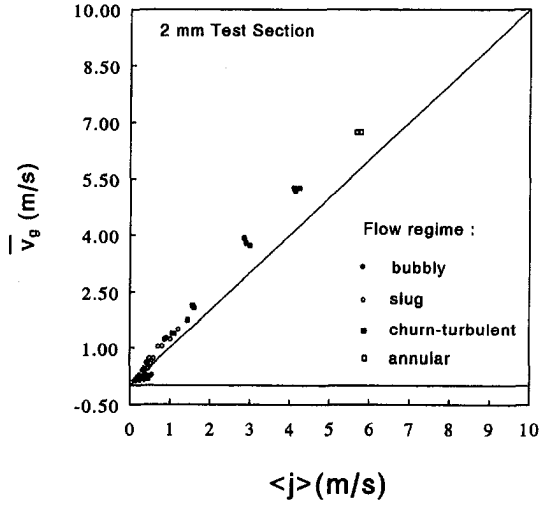

Fig. 6(*b*)

Fig. 6 Comparison of drift flux plots for each flow regime for (a) 1 mm vertical test section and (b) 2 mm vertical test section

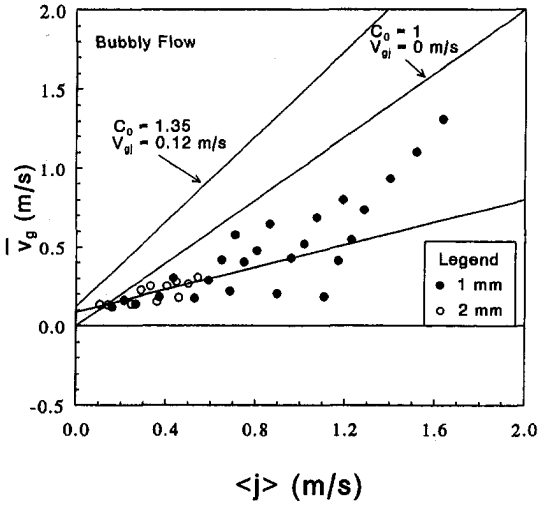

Fig. 7 Drift flux plots for vertical bubbly flow with experimental uncertainty ~0.4 m/s for the 1 mm test section and ~0.1 m/s for the 2 mm test section

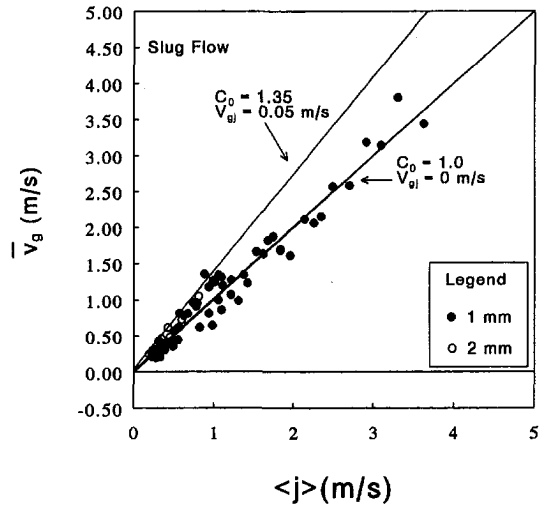

Fig. 8 Drift flux plots for vertical slug flow with experimental uncertainty ~0.4 m/s for the 1 mm test section and ~0.3 m/s for the 2 mm test section

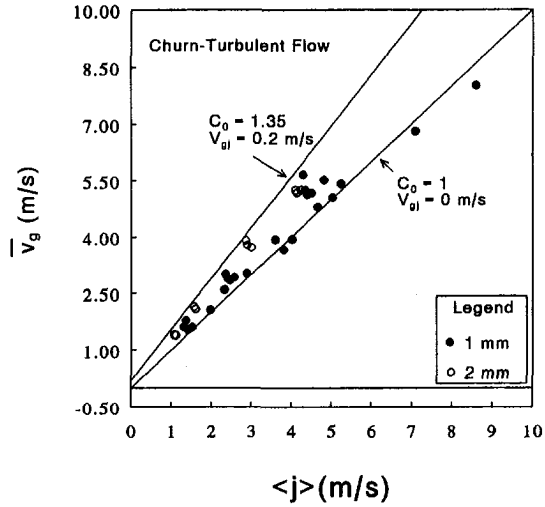

Fig. 9 Drift flux plots for vertical churn turbulent flow with experimental uncertainty ~1.1 m/s for the 1 mm test section and ~0.5 m/s for the 2 mm test section

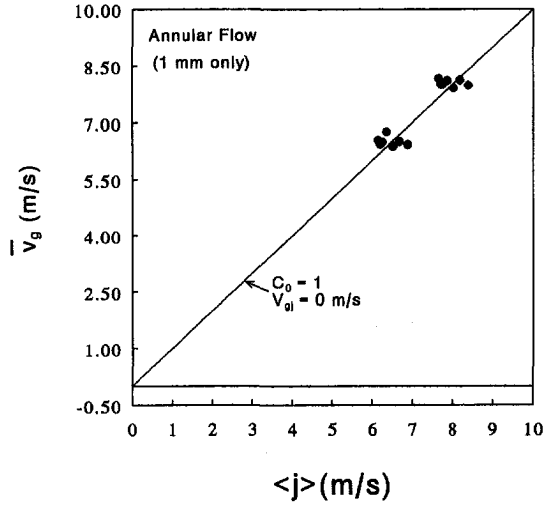

Fig. 10 Drift flux plots for vertical annular flow with experimental uncertainty ~1.1 m/s

Table 1 Results of drift flux plots for vertical test sections

	C_0	V_{gj}
1 mm Test section		
Bubbly	0.8–1.0	-0.07 ± 0.4
Slug	1.0	$\sim 0 \pm 0.4$
Churn turbulent	1.0	$\sim 0 \pm 1.1$
2 mm Test section		
Bubbly	0.4–1.0	0.08 ± 0.1
Slug	1.0	$\sim 0 \pm 0.3$
Churn turbulent	1.2	$\sim 0.01 \pm 0.5$

are the precision limits representing the range around the mean values at which the local average quantities were determined for another measurement would fall within a 95 percent confidence. For this experiment, the precision limit for the local average void fraction was within the range $0.01 \leq P_\alpha \leq 0.31$ and the precision limit for the local average interfacial area concentration was found to be $0.16\ (\mathrm{m}^{-1}) \leq P_{ai} \leq 5.93\ (\mathrm{m}^{-1})$ with a 95 percent confidence level.

The precision limits for the superficial gas velocities, j_g, and superficial liquid velocities, j_f, were found using half the least scale division of the flow meters used in measurements of the volumetric flow rates of each data point. Then the uncertainty of $\langle j \rangle$ was found using the square root of the sum of the squares of the precision limits of each superficial velocity. Since the values reported in Table 1 for C_0 and V_{gj} were found using a linear regression, the standard error of estimate (SEE) was used to measure the scatter of data points about the linear curvefit. Where the SEE is found using:

$$\mathrm{SEE} = \sqrt{\frac{\sum_{i=1}^{M} \left[\left(\frac{\langle j_g \rangle}{\langle \alpha \rangle} \right)_i - (C_0 \langle j \rangle_i + V_{gj}) \right]^2}{M - 2}} \qquad (8)$$

This represents an error band of ± 2 (SEE) around the curvefit that will contain about 95 percent of the data points, the band being a confidence interval on the curvefit. Thus the error reported in Table 1 is the uncertainty calculated using the SEE for each curvefit.

Summary and Conclusions

A study of two-phase flow in narrow rectangular channels has been performed. A new model is needed for the prediction of the distribution parameter for narrow rectangular ducts. The local average void fraction and interfacial area concentration were found using an image processing technique and were plotted against the local average gas superficial velocity. The results showed an increase of void fraction and interfacial area concentration through the transition regions and a uniform section for each individual flow regime. The average mean velocity of the gas phase was correlated using the drift flux model. It was observed that the distribution parameter, C_0, was smaller than the calculated value using the void correlation, Eq. (2) and the drift velocity, V_{gj}, was negligibly small for all flows.

Acknowledgments

This work was performed under the auspices of the U.S. Department of Energy, Office of Basic Energy Science. The authors would like to express their appreciation for the encouragement, support, and technical advice on this work from Dr. O. P. Manley. Appreciation for technical advice is also expressed to Dr. S. T. Revankar and fellow colleagues of the School of Nuclear Engineering Thermalhydraulics and Reactor Safety Lab of Purdue University.

References

Ali, M., and Kawaji, M., 1991, "The Effect of Flow Channel Orientation on Two-Phase Flow in a Narrow Passage Between Flat Plates," *ASME/JSME Thermal Engineering Proceedings,* Vol. 2, pp. 183–190.

Ali, M., Sadatomi, M., Charles, M. E., and Kawaji, M., 1991, "Effects of gap width and orientation on two-phase flow in a narrow passage between two flat plates," *Proceedings of the International Conference on Multiphase Flows,* pp. 15–18.

Chisholm, D., and Laird, A. D. K., 1958, "Two-Phase Flow in Rough Tubes," *Trans. ASME,* Vol. 80, No. 2, pp. 276–286.

Coleman, H. W., and Steele, W. G., 1989, *Experimentation and Uncertainty Analysis for Engineers,* Wiley, New York.

Ishii, M., 1977, "One-Dimensional Drift-Flux Model and Constitutive Equations for Relative Motion Between Phases in Various Two-Phase Flow Regimes," ANL-77-47.

Kroeger, P. G., and Zuber, N., 1968, "Average Volumetric Concentration in Two-Phase Flow Through Rectangular Channels," ASME *Journal of Heat Transfer,* pp. 491–493.

Mishima, K., Fujine, S., Yoneda, K., Yonebayashi, K., Kanda, K., and Nishihara, H., 1988, "A study of air-water flow in a narrow rectangular duct using image processing technique," *Proceedings of the Japan-U.S. Seminar on Two-Phase Flow Dynamics,* C.3-1 to C.3-12.

Mishima, K., Hibiki, T., and Nishihara, H., 1991, "Some Characteristics of Gas-Liquid Flow in Narrow Rectangular Ducts," *Proceedings of the International Conference on Multiphase Flows,* pp. 485–488.

Sato, Y., Sadatomi, M., Kawahara, A., and Asakura, S., 1991, "An Experimental Method of 2-D Two-Phase Flow Measurement of Void Fraction Distribution Using Image Processing," *JSME,* Vol. 57, No. 538, pp. 1979–1984.

Wilmarth, T., and Ishii, M., 1994, "Two-Phase Flow Regimes in Narrow Rectangular Vertical and Horizontal Channels," *International Journal of Heat and Mass Transfer,* Vol. 37, No. 12, pp. 1749–1758.

Zuber, N., and Findlay, J. A., 1965, "Average Volumetric Concentration in Two-Phase Flow Systems," ASME *Journal of Heat Transfer,* Vol. 87, pp. 453–468.

A Study on Converging Thin Annular Jets

D. Sivakumar
Research Student.

B. N. Raghunandan
Professor.

Department of Aerospace Engineering,
Indian Institute of Science,
Bangalore, 560012, India

An interesting feature of jets from liquid-liquid coaxial swirl atomizers used in bipropellant rockets or elsewhere is that the outer jet results in a tulip shaped liquid bulb even at operating pressure levels. In this context, experiments have been performed to study the discharge and tulip characteristics of annular jets through qualitative simulation of outer jet flow conditions at which tulip bulb prevails. It is shown that the discharge coefficient increases steeply with Reynolds number, a trend which is distinct from that of circular orifices. The range of flow conditions at which tulip bulb prevails decreases with the annular gap. If a swirl component is introduced into the annular jet, it alters the discharge characteristics and the tulip range with a tendency to form multiple tulips. Variation of tulip length for different annular gaps shows a common trend when plotted against liquid flow rate. The experimental data of tulip length agree reasonably with the theoretical model reported in literature.

Introduction

Recently, coaxial injectors have been widely studied by many researchers (Sankar et al., 1991; Care and Ledoux, 1991; and Hardalupas and Whitelaw, 1994) for the benefit of getting higher mixing efficiency and, hence, high combustion efficiency in a rocket engine. These injectors are comprised of an outer orifice and an inner orifice to release fuel and oxidizer, respectively, to the combustion chamber. More commonly, these injectors are designed with narrow outer orifice gap relative to the inner orifice to satisfy the mixture ratio requirements. In liquid-liquid coaxial injection systems, the characteristics of spray from the outer orifice could be different from that of the inner orifice because of the difference in the geometrical configuration of the orifices. With a narrow orifice gap, it is observed that a tulip bulb, i.e., a converging annular jet, is formed which may prevail even at operating pressure levels especially with swirling effect.

Over the decades, a number of research articles have been published on annular jet characteristics from the point of view of different practical applications, though not for injectors. The study started from Boussinesq (1869) who formulated the differential equations for water bells and solved them numerically. Many researchers (Binnie and Squire, 1941; Lance and Perry, 1953; and Taylor, 1959) have used Boussinesq's mathematical model to study water bells and modified it by including other physical parameters like air motion inside the cavity, pressure difference across the liquid sheet, surface tension effects and so on. The role of surface tension forces and the air motion inside the cavity formed by the jet were studied by Taylor (1959) and Parlange (1967), respectively. For longer jets (corresponding to Weber number, We $>$ 1), a simple equation was derived by Baird and Davidson (1962) to determine the convergence length, the axial distance between the orifice exit and the convergence point where a nonhollow liquid jet is formed. In the absence of gravity effects, good agreement with the experimental results was reported for different pressure differentials across the liquid sheet. The transition of swirling jet from tulip bulb to divergent shape was predicted by the theoretical model developed by Chuech (1993). The model is validated against the experimental results of Baird and Davidson (1962) for nonswirling annular jets.

A large number of experimental and theoretical analyses on annular jets have been carried out with reference to inertial confinement fusion (ICF) reactor. A detailed experimental study by Hoffman et al. (1980) examined the convergence length of annular jets of liquid lithium and found that the convergence length increases with jet exit velocity. The authors formulated a theory for convergence length based on the earlier theory of waterbells and the results compared favourably with the experimental observations. Esser and Abdel-Khalik (1984) have developed a numerical code which takes into account other physical parameters like nonuniform velocity profile at inlet, viscosity, etc. Their model agrees reasonably with the data of Baird and Davidson (1962). Ramos (1988) extended the work of Hoffman et al. (1980) by incorporating the nozzle exit geometry parameters and derived the governing equations as follows.

$$\rho b \frac{d^2R}{dt^2} = -\cos\theta \left[\frac{2\sigma\cos\theta}{R} + \frac{2\sigma}{r_v} + P_e - P_i\right] \quad (1)$$

$$\rho b \frac{d^2z}{dt^2} = \rho g b + \sin\theta \left[\frac{2\sigma\cos\theta}{R} + \frac{2\sigma}{r_v} + P_e - P_i\right] \quad (2)$$

The two equations are to be solved simultaneously to obtain R as a function of z. The analytical solution obtained by neglecting the curvature in the vertical plane of the jet predicted higher convergence length compared to the numerical predictions. These predictions were further compared with available experimental data (Ramos, 1990). The agreement between the model predictions and experimental results was generally good and the discrepancies between them at certain conditions were attributed to the meniscus and the adverse axial pressure gradient that develop near the convergence point of the jet. In the experimental study by Kihm and Chigier (1990), the major objectives were the visualization of annular jets using photographic techniques and the measurement of convergence length. The experimental results were compared with the theoretical model proposed by Ramos (1988) and the agreement was good at high Froude number, Fr of 8.87.

In a liquid-liquid coaxial injection system, as mentioned earlier, the characteristics of outer and inner jets could be different owing to the exit geometric configuration. The need to study the characteristics of outer liquid jet, both in the absence and presence of swirl, is often emphasized in literature (Amagai and Arai, 1994; Ramamurthi and John Tharakan, 1995; and, Sivakumar and Raghunandan, 1996). Geometrical parameters of the injector, the extent of swirl and the physical properties

Contributed by the Fluids Engineering Division for publication in the JOURNAL OF FLUIDS ENGINEERING. Manuscript received by the Fluids Engineering Division May 14, 1996; revised manuscript received June 24, 1997. Associate Technical Editor: Jong H. Kim.

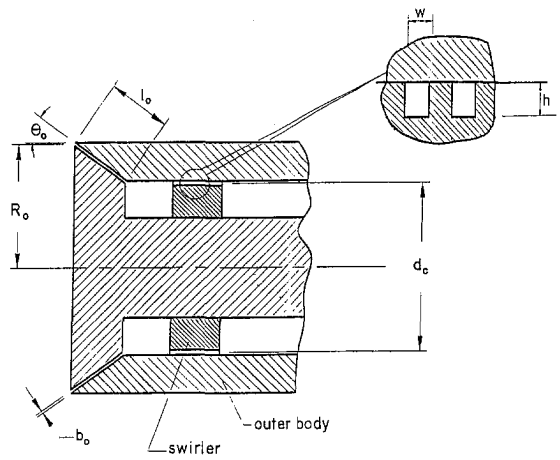

Fig. 1 Sketch of annular injector with swirler element

of the liquid, especially surface tension govern the regime of tulip formation in an annular jet. Also, in a swirl atomizer, there is a critical mass flow rate up to which the tulip bulb prevails and diverges thereafter. There are practical injectors, where the outer jet is in the form of tulip bulb even at operating pressure levels and disintegrates only in the presence of inner jet. Often, this results in poor atomization in a range of flow conditions and, hence, reduces the engine combustion efficiency. Therefore, it is necessary from the point of view of atomizers to study the conditions leading to tulip formation and its characteristics which is the subject matter of the present study.

Experimental Details

The schematic of the annular injector used for the present study is shown in Fig. 1 including key geometric parameters. The annular jet is produced by using a concentric inner body and an outer body. In order to get a diverging liquid sheet, a half divergence angle, $\theta_o = 35$ deg is provided at the exit of the annular orifice. The annular gap, b_o, can be varied to result in liquid films of 50–200 μm thick at the exit of the orifice, which are typical of annular jets from coaxial swirl injectors in liquid propellant rockets. The orifice outer diameter is 49 mm and the length of annular orifice is high enough ($l_o/d_h = 30$–130, where d_h is the equivalent hydraulic diameter of the annular orifice), to get fully developed flow at the exit of the orifice. Calibrated pressure gauges are used to control and monitor the pressure drop across the orifice, $(\Delta P)_{inj}$.

To study the effect of the tangential component of velocity on the annular jet, swirling motion is imparted to the jet by passing the liquid through an annular rectangular single start helical passage as seen in Fig. 1. Swirling intensity developed by the above swirler with flow passage width w and depth h is characterized by the swirl number, S (Beer and Chigier, 1983). For the present case, it takes the form

$$S = \frac{\pi b_o d_c}{wh} \tag{3}$$

where d_c is the mean diameter of the swirler. Values of S used in the present study for different b_o are given in Table 1.

Table 1 Swirl numbers used in the present study

b_o (μm)	55	82	115	140	172
S	2.42	3.61	5.06	6.16	7.57
d_c = 28 mm; w = 2.0 mm; h = 1.0 mm					

Special care was taken to ensure the symmetry and reproducibility of the jet. A centering mechanism for the inner body is provided in the injector assembly to place it concentric with the outer body and to get a symmetrical annular jet at a particular b_o. A practical difficulty arose in measuring the actual value of b_o. Using a 3-D travelling microscope, calibration is obtained between the angular position of the inner body and b_o. During each experiment, both the inner and outer bodies are engaged tightly to ensure zero setting condition for the inner body. An annular jet is then obtained by turning the inner body to the required angular position and hence b_o. If the annular orifice flows full, then the liquid film thickness, t_f, at the exit of the orifice is equal to b_o.

Annular jet profile and other geometric parameters of the jet are determined through a photographic technique. Still photographs at $\frac{1}{15}$ of a second exposure are taken by illuminating the jet with a high power strobe light placed at right-angle to the camera position. Repeated photographs are taken at a particular flow condition to ensure reproducibility and the variation is found to be negligible. Table 2 describes the ranges of experimental conditions used in the present study.

Table 2 Ranges of experimental conditions

Annual gap, b_o	0.055–0.172 mm
Liquid flow rate, $\dot{m}$	34–82 g/s
Liquid exit velocity, V_o	1.5–7.9 m/s
Froude number, Fr	9–257
Reynolds number, Re	500–1250
Weber number, We	3.5–20.5
Convergence number, N_c	$0.4019*10^{-3}$–$21.82*10^{-3}$

Nomenclature

A_o = exit annular orifice area
b = local liquid sheet thickness
b_o = annular gap
C_d = discharge coefficient
d_c = mean diameter of the swirler
d_h = equivalent hydraulic diameter of the annular orifice ($d_h = 2b_o$)
Fr = Froude number (V_o^2/gR_o)
g = acceleration due to gravity
h = depth of the swirler passage
L = jet convergence length
L^* = dimensionless convergence length (L/R_o)
l_o = length of the annular orifice
$\dot{m}$ = liquid flow rate
N_c = convergence number ($\rho g^2 R_o^2 b_o / 2V_o^2 \sigma$)
P_i = pressure inside the jet
P_e = pressure outside the jet
ΔP = pressure difference across the liquid sheet ($P_e - P_i$)
$(\Delta P)_{inj}$ = pressure drop across the annular orifice
Re = Reynolds number ($\rho d_h V_o / \mu$)
R_o = annular jet radius at the exit of the orifice
R = local jet radius
r_v = radius of curvature of the liquid sheet in the vertical plane
S = swirl number
t = time
V_o = velocity of the annular jet at the exit of the orifice
w = width of the swirler passage
We = Weber number ($\rho V_o^2 b_o / 2\sigma$)
z = axial distance
ρ = liquid density
σ = liquid surface tension coefficient
μ = liquid viscosity coefficient
θ_o = exit angle of the jet with respect to jet axis
θ = angle made by the tangent to the liquid sheet with the the jet axis

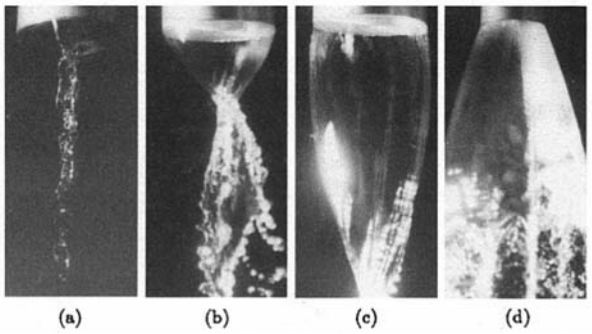

Fig. 2 Effect of liquid flow rate on annular jet without swirling effect ($b_o/R_o = 5.71*10^{-3}$). (*a*) $\dot{m}$ = 18.5 g/s, (*b*) $\dot{m}$ = 50.5 g/s, (*c*) $\dot{m}$ = 76.3 g/s, (*d*) $\dot{m}$ = 211.3 g/s

Typical photographs of the jet showing the effect of $\dot{m}$ are presented in Fig. 2. Figure 2(a) corresponds to the dripping flow of a annular jet occurring at a low $\dot{m}$. Because of surface tension effects, the liquid film is attached to the bottom surface of the inner body and the liquid drips from the center of the inner body. A steady tulip is shown in Fig. 2(b) formed by increasing the $\dot{m}$ slightly. The convergence length, L of the tulip increases with $\dot{m}$ as shown in Fig. 2(c) due to increased inertial forces. A steady oscillation in the jet is observed at flow conditions corresponding to the states between Fig. 2(b) and Fig. 2(c). This behavior has been reported by many authors (Baird and Davidson, 1962; Kihm and Chigier, 1990). This oscillation may be attributed to the dynamic imbalance between the surface tension and inertia forces in the jet. A further increase in $\dot{m}$ produced perforations close to the convergence point which spread to the upstream region of the jet gradually. Finally, a diverged annular jet is developed as shown in Fig. 2(d), where the disruptive inertial and aerodynamic forces dominate over surface tension forces. Figure 3 illustrates the behavior of the jet with swirling effect. It is seen that multiple tulips are generated in the jet in the presence of swirl.

Uncertainty Estimates

Uncertainty estimates for the primary measurables presented here are listed in Table 3. Uncertainty estimates for the derived measurements like, discharge coefficient, C_d, dimensionless convergence length, L^* (L/R_o) etc., can be determined from Table 3. The calculation of net uncertainty of measurements reported here are based on the procedure described by Moffat (1988).

Fig. 3 Multiple tulip formation with swirling effect ($b_o/R_o = 5.71*10^{-3}$)

Table 3 Uncertainty estimates

Quantity	Source of uncertainty	Net uncertainty
$(\Delta P)_{inj}$	Measurement resolution (1.5%) Calibration (3.0%) Repeatability (3.0%)	4.4%
$\dot{m}$	Measurement resolution (0.8%) Repeatability (1.5%–2.0%)	1.7%–2.2%
b_o	Calibration (3.3%–10.4%) Angular rotation measurement of inner body (1.4%–4.5%)	3.6%–11.3%
L	Convergence point identification (<3.1%) Repeatability (2.5%)	<4%
θ_o	Jet exit surface identification (<5.5%) Repeatability (Negligible error)	<5.5%
Other geometrical parameters		<1.0%

Results and Discussion

Discharge Characteristics. Any discussion on tulip characteristics should necessarily be linked to the actual flow rates which are described by C_d. In the present work, C_d given by

$$C_d = \frac{\dot{m}}{A_o\sqrt{2(\Delta P)_{inj}\rho}} \tag{4}$$

is based on the exit area, A_o (product of exit perimeter of inner body and b_o), of the orifice.

The variations of C_d with Re ($= \rho d_h V_o/\mu$) based on hydraulic diameter, in the absence of the swirler for different b_o/R_o are presented in Fig. 4. Flow velocity at the orifice exit, V_o is determined from $\dot{m}$ and A_o. The C_d characteristics in the figure pertain to the range of pressure where tulip formation occurs. It is observed in Fig. 4 that C_d varies almost linearly with Re for all b_o, which is rather distinct from C_d of circular orifices. At higher b_o, the variation is less steep. The variation in C_d may be attributed to the frictional loss along the narrow annular orifice gap. Note that here the wetted area of the orifice is large. Recent measurements of C_d for micro-orifices (orifice diameter < 1.0 mm) made by Hasegawa et al. (1997), show a similar variation against Re. With swirling effect, C_d is almost invariant

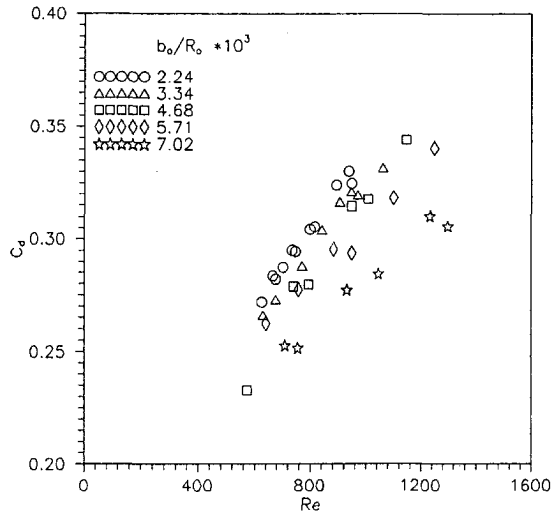

Fig. 4 Influence of Re on the discharge coefficient variation of annular jet with different b_o/R_o (no swirler)

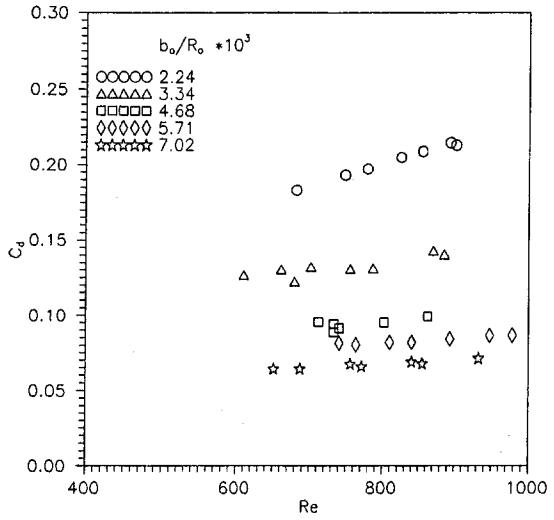

Fig. 5 Influence of Re on the discharge coefficient variation of annular jet with different b_o/R_o (with swirler)

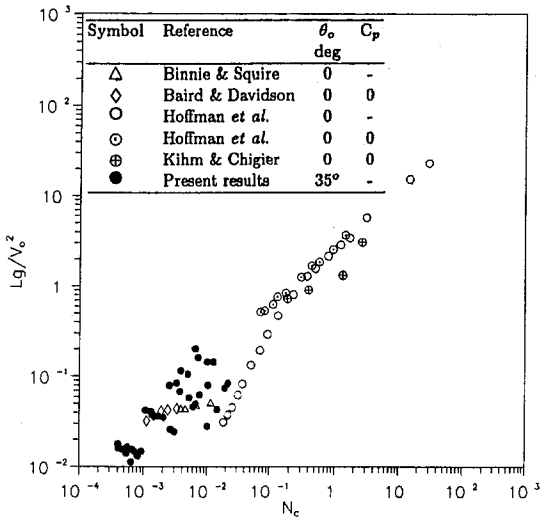

Fig. 7 Convergence length of the jet as a function of convergence number N_c with different b_o/R_o (no swirler)

with Re as shown in Fig. 5 for all b_o except for very low b_o due to the loss of swirling effect in the narrow annular gap. As expected, C_d decreases with increase in b_o/R_o owing to the fact that increase in annular gap provides enough freedom for the propagation of tangential component of velocity generated by the swirler and hence C_d, which depends on axial component of velocity, is lower at higher b_o/R_o.

Tulip Characteristics. A photographic technique has been used to measure the tulip length or convergence length, L. For an oscillating jet, the tulip length is the average value of minimum and maximum convergence lengths. The measured L^* is plotted in Fig. 6 against $\dot{m}$ for different b_o/R_o values. The plot shows that L^* increases with $\dot{m}$ for all b_o/R_o values and the data seem to follow a common curve. Hence for thin liquid sheets as formed in atomizers, the length of the tulip can be represented as a function of $\dot{m}$, independent of b_o/R_o. To compare the present experimental data with the earlier results, the same data of L are plotted in nondimensional form as Lg/V_o^2 in Fig. 7 against convergence number, N_c. Although, Lg/V_o^2 decreases slightly with N_c for constant b_o/R_o, by plotting all the experimental data, it can be seen that the present data follow the basic trend.

As mentioned earlier, in a swirl atomizer, the tulip bulb prevails only in a certain range of flow conditions before changing into fully divergent liquid sheet. Figure 8 shows the extreme values of Fr and We between which tulip bulb exists as a function of b_o/R_o. Both minimum and maximum of Fr and We decrease steeply with b_o and, at higher b_o, the tulip bulb prevails in a narrow range of Fr.

Comparison of Experimental Results With Theoretical Predictions. Analytical and numerical predictions of L have been obtained using Ramos (1988, 1990) mathematical model. Ramos (1988), in his analysis, showed that the exit angle of the annular orifice and pressure difference, $(P_e - P_i)$ across the liquid sheet have a strong influence on the convergence length of the jet. In the present study, though the injector is provided with an exit divergence angle of 35 deg, it is observed from photographic records that the exit angle (θ_o) of the jet is not constant but varies with the flow conditions for the present range of b_o/R_o values. A similar argument was advanced by Ramos (1990) for the validation of his mathematical model with available experimental results. The measured variation of θ_o with $(\Delta P)_{inj}$ is plotted in

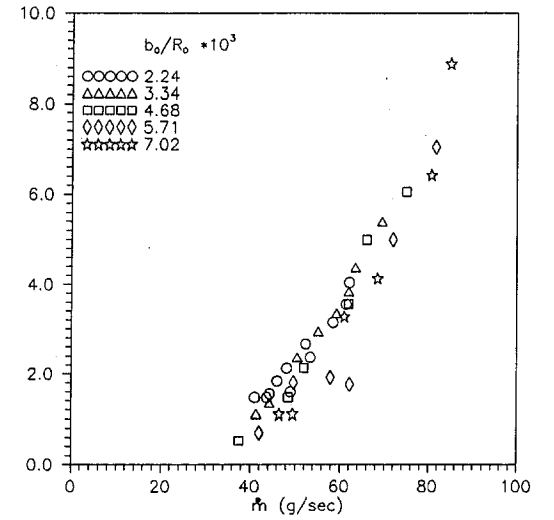

Fig. 6 Effect of liquid flow rate on convergence length of the jet with different b_o/R_o (no swirler)

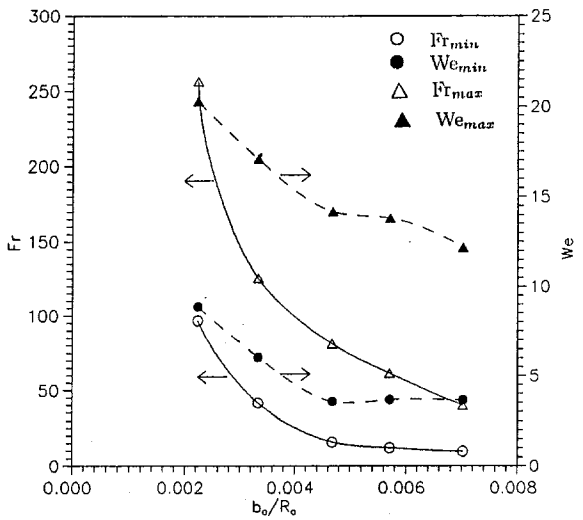

Fig. 8 Flow conditions for the existence of convergent jet with annular gap (no swirler)

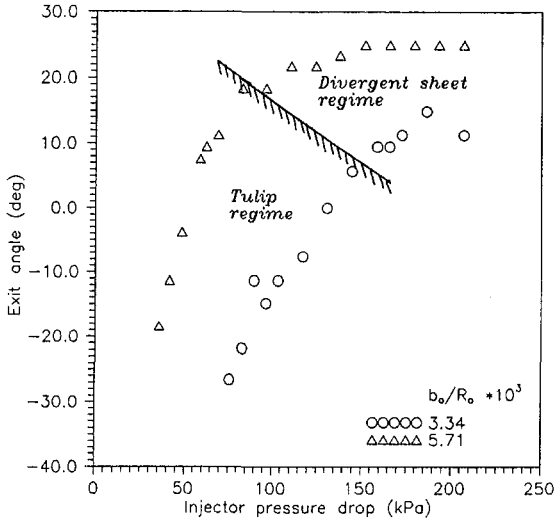

Fig. 9(*a*) With injector pressure drop

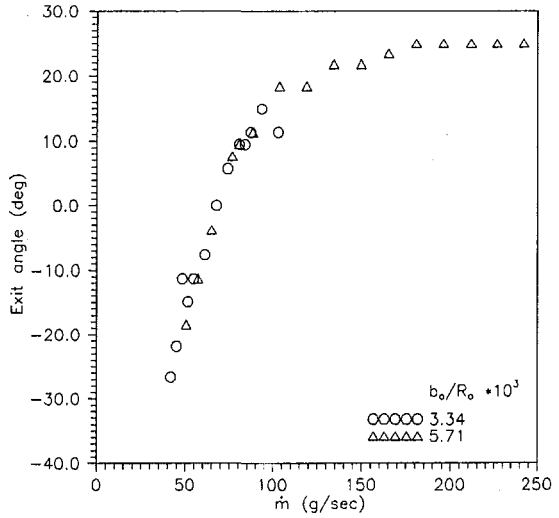

Fig. 9(*b*) With liquid flow rate

Fig. 9 Variation of exit angle of the annular jet with flow conditions for different b_o/R_o (no swirler)

Fig. 9(a) for two different values of b_o/R_o. In the tulip regime, θ_o increases with $(\Delta P)_{inj}$, but increases only slightly in the divergent regime as shown in figure. It is observed from the figure that the maximum value of θ_o attained by the jet increases with b_o/R_o. This is attributed to the stronger contracting effect of surface tension which is more dominant for thinner liquid sheets. The same data plotted against $\dot{m}$ in Fig. 9(b) show that in the tulip regime, the influence of b_o/R_o is felt only through $\dot{m}$. Note that $(\Delta P)_{inj}$ across the annular passage varies with b_o/R_o for the same $\dot{m}$. The analytical and numerical solutions of Ramos model require the value of θ at the exit of the orifice, which is obtained from the experimental data in Fig. 9(b).

The literature reveals (Kihm and Chigier, 1990) that a very small pressure difference across the liquid sheet is sufficient to alter the shape of the jet. At high Fr, inertial force component of the jet is dominant compared to the pressure forces over the jet surface. Hence, the influence of $(P_e - P_i)$ on L^* variation is negligible for high Fr flow conditions. This qualitative argument is supported by the experimental observations of Kihm and Chigier (1990). They studied the influence of $(P_e - P_i)$ on L^* variation for different Fr cases. It is observed through the experimental observations that the influence of $(P_e - P_i)$ on L^* at high Fr (8.87) is less compared to that of low Fr (1.27). The present Fr range also being high (9–257), similar insensitivity of L^* on $(P_e - P_i)$ is not surprising. Practical difficulties restricted the measurement of very small changes in $(P_e - P_i)$ with good accuracy during the experimental study. Based on the above argument, the influence of $(P_e - P_i)$ is ignored for the analytical and numerical predictions of L^* by assuming $P_e - P_i = 0$.

Comparisons of theoretical and experimental results for different b_o/R_o are given in Figs. 10(a)–10(e). The theoretical convergence lengths presented in Fig. 10(a)–10(e) correspond to the axial location at which the jet radius is $b_o/2$ (Ramos, 1988). The analytical solution predicts a higher L^* compared to the numerical predictions. This is attributed to neglecting of radius of curvature variation of the jet in the vertical symmetrical plane. It can be seen from Figs. 10(a)–10(e) that the discrepancies between the analytical and numerical solutions increase with b_o/R_o. For constant $\dot{m}$, the jet inertial component decreases with b_o/R_o owing to the decrease in V_o. The assumption, $\theta = 0$ in deriving the analytical solution may not have much influence on the solution if the inertial force component is more then that due to surface tension. Hence, at high b_o/R_o, neglecting the second term in Eq. (2) would have an influence on the analytical solution. This could be the reason for the above discrepancy between analytical and numerical solutions. In all cases, the analytical and numerical results over-predict L^* compared to the experimental data. During the present study, experimental L^* has been measured where the non-hollow liquid jet is formed just after convergence. But, in case of analytical and numerical predictions, L^* has been calculated where the liquid jet radius is $b_o/2$. This perhaps is a reason for the over-prediction by the mathematical model.

Conclusions

The discharge and tulip characteristics of annular jets have been studied by generating thin liquid sheets typical of those developed by atomizers in the absence and presence of swirling effect using a specially designed annular injector. The major conclusions of the study are as follows.

- Unlike in circular orifices, C_d of the annular orifice without swirler varies steeply with Re; but, with swirling effect, it exhibits a behavior similar to that of circular orifices.
- The range of Fr at which tulip bulb exists decreases with annular gap steeply. The tulip length increases with liquid flow rate and is little influenced by the annular gap width. The presence of swirling effect in the flow leads to the formation of multiple tulips.
- For an annular jet, the exit angle, θ_o of the jet increases linearly with liquid flow rate in the tulip regime, but in the divergent sheet regime, the variation of θ_o is very little. The maximum exit angle attained by the jet increases with the annular gap.
- Experimental data of tulip length agree reasonably with the analytical and numerical predictions of the theoretical model developed by Ramos (1988).

Acknowledgments

This work was supported by a research grant from Advanced Space Technology Laboratory, Indian Institute of Science. The help of T. Kumaresan, post-graduate student, in getting the experimental results is greatly appreciated. The authors wish to thank S. Nagaraj and C. Subramani for their support in conducting the experiments.

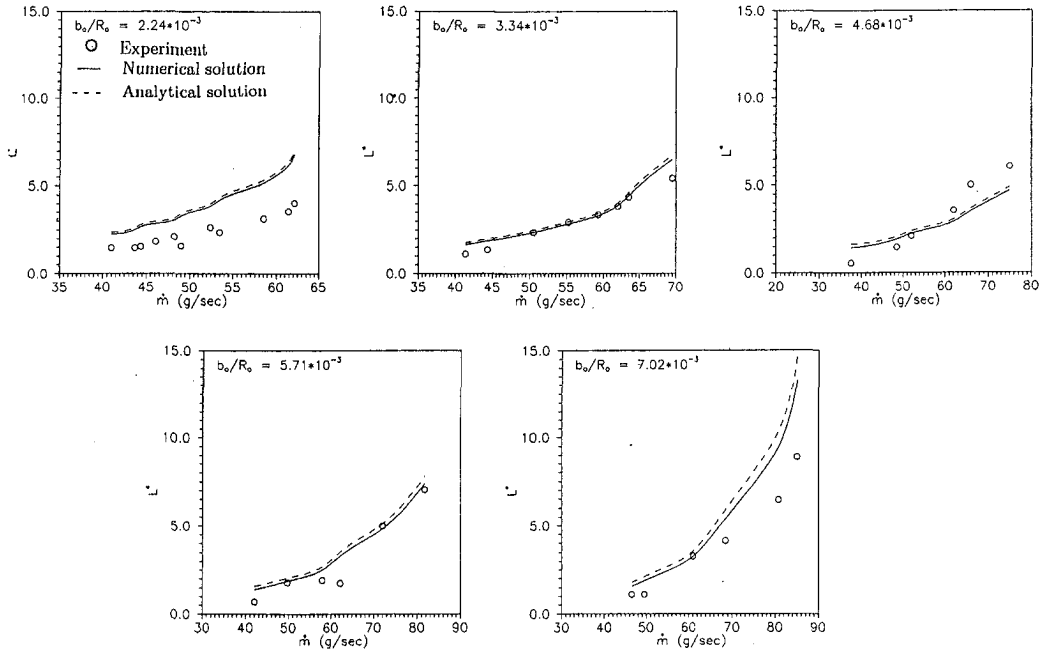

Fig. 10 Comparison of experimental results with analytical and numerical predictions for different b_o/R_o (no swirler)

References

Amagai, K., and Arai, M., 1994, "Disintegration Process of a Liquid Jet Injected from a Coaxial Dual Nozzle," ICLASS-94, July, pp. 71–78.

Baird, M. H. I., and Davidson, J. F., 1962, "Annular Jets-I (Fluid Dynamics)," *Chemical Engineering Science,* Vol. 17, pp. 467–472.

Beer, J. M., and Chigier, N., 1983, *Combustion Aerodynamics,* Robert E. Krieger Publishing Company.

Binnie, A. H., and Squire, H. B., 1941, "Liquid Jets of Annular Cross-Section," *The Engineer,* Vol. 171, London, pp. 236–238.

Boussinesq, J., 1869, "Theorie des experiences de Savart sur la frome que prend une veine liquide apres s'etre choquee contre un plan circulaire," *Comptes Rendus de l'Academie des Sciences,* Vol. 69, pp. 128–131.

Care, I., and Ledoux, M., 1991, "Study of an Airblast Coaxial Atomizer: Experiments and Modelisation," *Proceedings of the 5th International Conference on Liquid Atomization and Spraying Systems (ILASS),* Gaithersburg, MD, pp. 763–770 (Paper 85).

Chuech, S. G., 1993, "Numerical Simulation of Nonswirling and Swirling Annular Liquid Jets," *AIAA Journal,* Vol. 31, June, pp. 1022–1027.

Esser, P. D., and Abdel-Khalik, S. I., 1984, "Dynamics of Vertical Annular Liquid Jets," ASME JOURNAL OF FLUIDS ENGINEERING, Vol. 106, pp. 45–51.

Hardalupas, Y., and Whitelaw, J. H., 1994, "Characteristics of Sprays Produced by Coaxial Airblast Atomizers," *Journal of Propulsion and Power,* Vol. 10, No. 4, July–Aug, pp. 453–460.

Hasegawa, T., Suganuma, M., and Watanabe, H., 1997, "Anomaly of Excess Pressure Drops of the Flow Through Very Small Orifices," *Physics of Fluids,* Vol. 9, Jan., pp. 1–3.

Hoffman, M. A., Takahashi, R. K., and Monson, R. D., 1980, "Annular Liquid Jet Experiments," ASME JOURNAL OF FLUIDS ENGINEERING, Vol. 102, pp. 344–349.

Kihm, K. D., and Chigier, N. A., 1990, "Experimental Investigations of Annular Liquid Curtains," ASME JOURNAL OF FLUIDS ENGINEERING, Vol. 112, Mar., pp. 61–66.

Lance, G. N., and Perry, R. L., 1953, "Water Bells," *Proceedings of the Physical Society,* London, Series B, Vol. 66, pp. 1067–1072.

Moffat, R. J., 1988, "Describing the Uncertainties in Experimental Results," *Experimental Thermal and Fluid Science,* No. 1, pp. 3–17.

Parlange, J. Y., 1967, "A Theory of Water-bells," *Journal of Fluid Mechanics,* Vol. 29, Part 2, pp. 361–372.

Ramamurthi, K., and John Tharakan, T., 1995, "Experimental Study of Liquid Sheets Formed in Coaxial Swirl Injectors," *Journal of Propulsion and Power,* Vol. 11, No. 6, Nov–Dec, pp. 1103–1109.

Ramos, J. I., 1988, "Liquid Curtains: I Fluid Mechanics," *Chemical Engineering Science,* Vol. 43, No. 12, pp. 3174–3184.

Ramos, J. I., 1990, "Analytical, Asymptotic and Numerical Studies of Liquid Curtains and Comparisons with Experimental Data," *Applied Mathematical Modelling,* Vol. 14, Apr., pp. 170–183.

Sankar, S. V., Brena de la Rosa, A., Isakovic, A., and Bachalo, W. D., 1991, "Liquid Atomization by Co-axial Rocket Injectors," AIAA Paper 91-0691, Jan.

Sivakumar, D., and Raghunandan, B. N., 1996, "Jet Interaction in Liquid-Liquid Coaxial Injectors," ASME JOURNAL OF FLUIDS ENGINEERING, Vol. 118, June, pp. 329–334.

Taylor, G. I., 1959, "The Dynamics of Thin Sheets of Fluid. 1. Water Bells," *Proceedings of the Royal Society,* Series A, Vol. 253, pp. 289–295.

Jet-Plate Interaction for Wedge-Shaped Plates of Arbitrary Angles

S. S. Chu
Associate Professor of
Aeronautical Engineering,
Airforce Academy, Kangshan, Taiwan

W. L. Chow
Professor of Mechanical Engineering,
Florida Atlantic University, Boca Raton, FL
Fellow ASME

An investigation has been undertaken to study the problems of jet-plate interaction through the method of hodograph transformation. The physical flow field is first transformed to a hodograph domain. By using properly selected flow parameters, the solution is established through numerical computations with rectangular grid in the hodograph plane. The resulting plate configuration, the free streamlines, and the flow properties in the physical plane are subsequently obtained through direct numerical integration. Jet flows toward wedge-shaped plates of arbitrary angles are solved to demonstrate the ability of the method. To verify the solutions, momentum principle has been employed in the physical plane for all test cases. It is found that the results obtained through this method are satisfactory.

Introduction

The study of jet flows toward a solid wall has been of considerable interest in its simulation of practical flow conditions. When a jet strikes a vertical, infinite flat plate in a two-dimensional configuration, the symmetric free streamline shape can be directly obtained through conformal mapping. A natural question arises if the plate has only a finite length and/or it is not a flat one. When the size of the plate is relatively short in comparison with the width of the approaching jet, the jet flow is usually split into two parts, each will leave the end of the plate and eventually assume an asymptotic flow angle different from that of the plate. The asymptotic flow direction of the jet assumes that of the plate only if the plate is mathematically infinitely long. Most recently, Chow et al. (1995) solved the inviscid interaction flow problems, and the analysis was restricted to a flat plate with symmetric or nonsymmetric flow patterns. For practical flow application as a thrust-reversal device, the symmetric flow past a wedge-shaped plate is considered.

The hodograph transformation was originally devised to solve two-dimensional gasdynamics problems. Application of the method has not been extensively explored for engineering purpose, since the final physical configurations corresponding to the indirect solutions of the hodograph equation are often not of practical interest. However, a few configurations which assume shapes of straight-line profiles do have practical importance, such as the flow discharge through a propulsive system, control valve, and orifice. In recent years a number of studies using the hodograph transformation have been reported (e.g., Chow et al., 1987, 1995; Liu and Chow, 1978, Wu and Chow, 1985; Weng et al., 1987, Chu et al., 1990, 1992) which indicate that the hodograph transformation is particularly efficient for both two-dimensional and axisymmetric flow problems, especially when straight boundaries are involved. With the proposed method, only the asymptotic flow angle and the plate angle need to be specified for the flow. The final flow pattern including the required length of the plate, the stagnation and free streamlines, and other flow properties are found through straight forward numerical integrations.

The present paper demonstrates an effective and economical method of applying hodograph transformation coupled with numerical computation to examine the steady, inviscid, jet flows toward a wedge-shaped plate with an angle which can be less or greater than 90°. Effects of viscosity and gravity are ignored since they often have negligible influence to the flow. The physical flow field is first transformed to the hodograph domain. With properly selected flow parameters, the solution is established through numerical computations on a rectangular grid in the hodograph plane. Finite difference scheme with central differencing is used to treat the hodograph equation. The corresponding plate configuration and the flow field properties in the physical plane are subsequently obtained through direct numerical integrations.

Analysis

Hodograph transformation employs the speed V and the streamline angle θ of the fluid as the independent variables, while all other quantities such as the potential function, the stream function ψ, including also the physical coordinates x and y, are treated as the dependent variables. It is noteworthy that the original motivation of adopting the method of hodograph transformation lies in its reduction of a nonlinear gas dynamic equation to a linear one in the hodograph plane. It can be easily shown that the hodograph equation governing the incompressible potential flow is found to be (Shapiro, 1953):

$$V^2\psi_{VV} + V\psi_V + \psi_{\theta\theta} = 0 \tag{1}$$

and the subscripts V, θ denote their respective partial differentiations with

$$V = \sqrt{u^2 + v^2} \tag{2a}$$

$$\theta = \tan^{-1}\left(\frac{v}{u}\right) \tag{2b}$$

where u, v are the Cartesian components of the velocity vector. The corresponding physical coordinates x, y and the hodograph variables V, θ are related through the following expressions:

$$dx = -\left(\frac{\cos\theta}{V^2}\psi_\theta + \frac{\sin\theta}{V}\psi_v\right)dV + \left(\cos\theta\psi_v - \frac{\sin\theta}{V}\psi_\theta\right)d\theta \tag{3a}$$

Contributed by the Fluids Engineering Division for publication in the JOURNAL OF FLUIDS ENGINEERING. Manuscript received by the Fluids Engineering Division October 1, 1996; revised manuscript received May 5, 1997. Associate Technical Editor: M. S. Cramer.

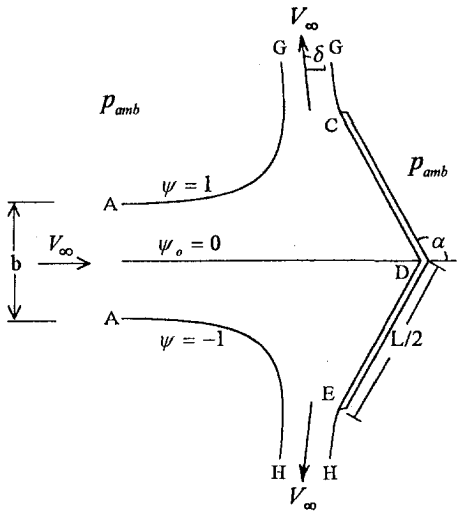

Fig. 1 The symmetric flow configuration of the inviscid interaction of a jet and a wedge

$$dy = \left(-\frac{\sin\theta}{V^2}\psi_\theta + \frac{\cos\theta}{V}\psi_v \right) dV + \left(\sin\theta\psi_v - \frac{\cos\theta}{V}\psi_\theta \right) d\theta \quad (3b)$$

The geometry of a jet flow of width b and velocity V_∞ toward a thrust reverser at an angle α is depicted in Fig. 1, where ψ_0 is the value of the stream function for the stagnation streamline, δ is the asymptotic flow angle after the flow leaves the end of the plate, L is the plate length, and p_{amb} is the ambient pressure. The corresponding hodograph is shown in Fig. 2, where the coordinates are already normalized by the respective reference quantities, V_∞ and α. Upon introducing the dimensionless variables

$$\psi' = \psi/(V_\infty b/2), \quad V' = V/V_\infty,$$
$$\beta = \theta/\alpha, \quad \beta_a = \delta/\alpha,$$
$$x' = x/(b/2), \quad y' = y/(b/2) \quad (4)$$

and after normalization and eliminating the prime $'$ for simplicity, Eqs. (1) and (3) become

$$V^2\psi_{VV} + V\psi_V + \frac{1}{\alpha^2}\psi_{\beta\beta} = 0 \quad (5)$$

and

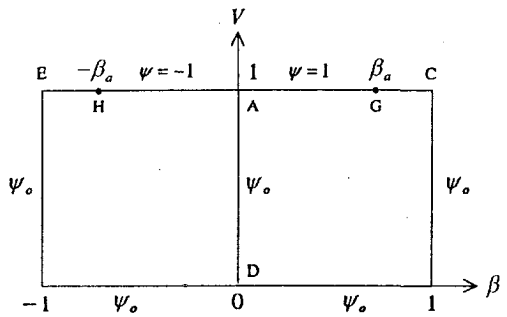

Fig. 2 Computational domain in the hodograph plane for the inviscid interaction flow

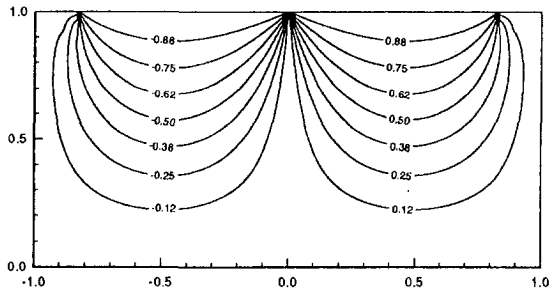

Fig. 3 Solution of a jet flow toward a thrust reversal device with α = 120 deg and δ = 100 deg

$$dx = -\left(\frac{\cos\alpha\beta}{\alpha V^2}\psi_\beta + \frac{\sin\alpha\beta}{V}\psi_v \right) dV + \left(\alpha\psi_v \cos\alpha\beta - \frac{\sin\alpha\beta}{V}\psi_\beta \right) d\beta \quad (6a)$$

$$dy = \left(-\frac{\sin\alpha\beta}{\alpha V^2}\psi_\beta + \frac{\cos\alpha\beta}{V}\psi_v \right) dV + \left(\alpha\psi_v \sin\alpha\beta - \frac{\cos\alpha\beta}{V}\psi_\beta \right) d\beta \quad (6b)$$

For the present flow problem, the dimensionless ψ value of the upper free streamline is set to be 1, while the value of the lower free streamline is -1. It should be noted that the present analysis is based on the premise that the jet is always surrounded by the constant pressure p_{amb} of the approaching jet flow. Since the effect of gravity is ignored, the free jet boundaries are lines of constant velocity according to Bernoulli's principle. They leave at the end of the plate and eventually will assume an asymptotic flow direction. The boundary values of ψ for the rectangular hodograph domain of V and β are completely specified. Once all ψ values throughout the domain are established through numerical computations, the solution can then be interpreted back to the physical plane by direct integration. All free streamlines, AG, CG, AH, and EH are obtained by integrating along the top boundary, while the required plate length is established through integration along the left and right boundaries. With C_p being the pressure coefficient along the plate surface

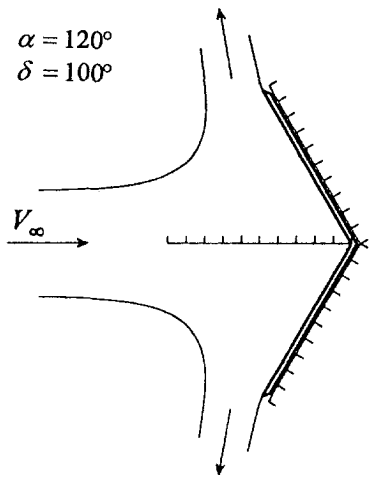

Fig. 4 Solution of a jet flow toward a thrust reversal device with α = 120 deg, δ = 100 deg in physical plane. Tick marks are spaced by $b/6$.

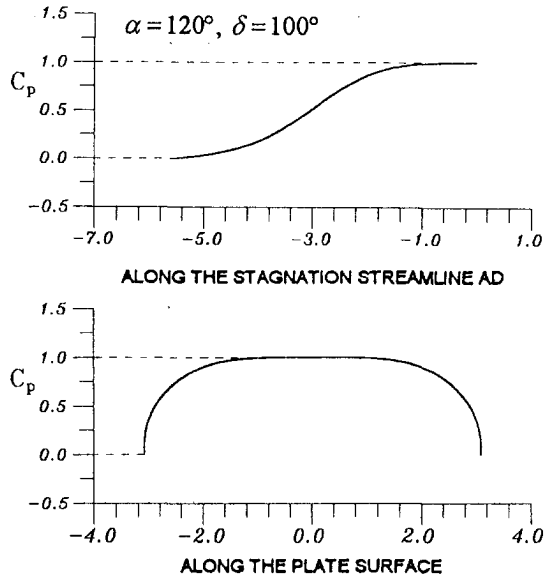

Fig. 5 Pressure coefficient distributions along the stagnation streamline and on the surface of thrust reversal device

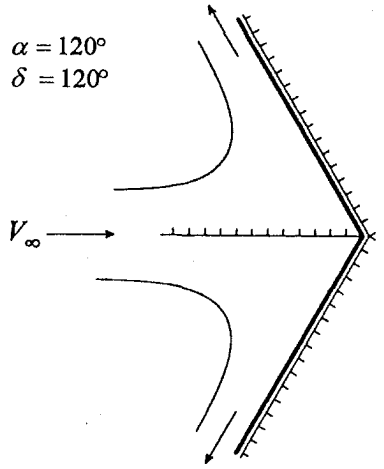

Fig. 7 Solution of a jet flow toward a thrust reversal device with infinitely long plate—established with $L/(b/2) = 10.52$. Tick marks are spaced by $b/6$.

facing the jet, the dimensionless force of the jet on the plate in the x-direction may be defined by

$$C_F = \frac{1}{2}\int C_P dy \tag{7}$$

where $C_p = (p - p_{amb})/[(\rho V_\infty^2)/2]$.

Computations

For solving the hodograph equation, the rectangular hodograph domain is divided into a finite difference mesh of uniform size in both V and β directions. A finite difference scheme with second-order central differencing can be constructed to solve the hodograph equation. Upon writing in the form of a tridiagonal matrix, the finite difference expression of the hodograph equation is given by:

$$\begin{aligned}&\psi_{i,j+1}(2V^2\alpha^2\Delta\beta_{ij}^2 + V\alpha^2\Delta V_{ij}\Delta\beta_{ij}^2)\\ &\quad + \psi_{i,j}(-4V^2\alpha^2\Delta\beta_{ij}^2 - 4\Delta V_{ij}^2)\\ &\quad + \psi_{i,j-1}(2V^2\alpha^2\Delta\beta_{ij}^2 - V\alpha^2\Delta V_{ij}\Delta\beta_{ij}^2)\\ &\qquad = -2\Delta V_{ij}^2(\psi_{i+1,j} + \psi_{i-1,j})\end{aligned} \tag{8}$$

With the boundary values completely specified for the hodograph domain, solutions for the hodograph equation can be established through iterations for selected values of α and δ.

It should be noted that discontinuities of ψ along the boundaries of the hodograph domain are inherent to the method of hodograph transformation. The tridiagonal matrix solver can be found in many commonly used textbooks of CFD. With the given boundary values, ψ is established within the domain through the successive over-relaxation method. Converged solution can be found when the variation of ψ at each grid point is within an arbitrarily small margin. Once all ψ values are established, ψ_V and ψ_β can be formed, and the x and y values can then be obtained by integrating Eqs. (6a) and (6b) numerically. Result of the free streamlines for the jet flow striking a wedge and the configuration of the flow pattern are therefore obtained. The total force of interaction is the integral of the pressure distribution on the plate. It can be evaluated after the velocity distribution over the plate surface is established through the Bernoulli's principle.

Results

Some results are presented to illustrate the application of the method. The mass flow rate of the approaching jet flow is set to be 2 for all test cases. A jet flow toward a thrust reversal device with $\alpha = 120°$ was first considered. When the specified asymptotic flow angle is set to be 100 degrees, the computed

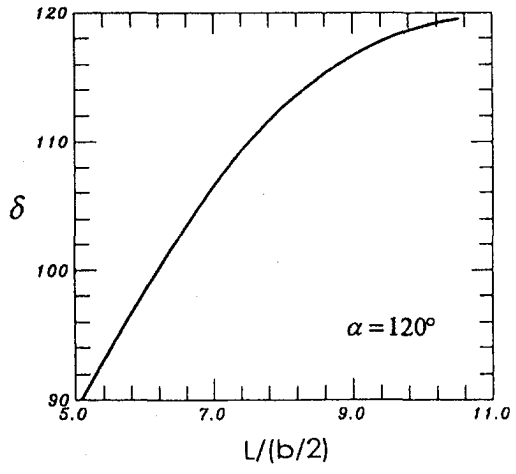

Fig. 6 The deflection angle versus the length of the wedge for a jet flow toward a thrust reversal device

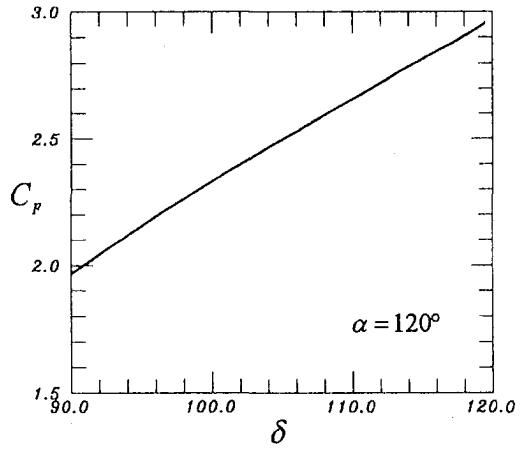

Fig. 8 Variation of C_F with the deflection angle, $\alpha = 120$ deg

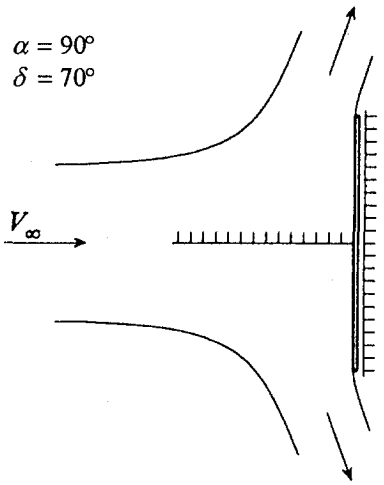

Fig. 9 Solution of a jet flow toward a vertical plate with δ = 70 deg in physical plane. Tick marks are spaced by $b/12$.

solution in the hodograph plane is displayed in Fig. 3. The resulting free streamlines and plate length are shown in Fig. 4. The pressure coefficient distributions along the stagnation streamline and on the plate surface are presented in Fig. 5.

Cases with the specified asymptotic flow angle varies between 90 and 119.5 degrees are also computed for α = 120 deg. The corresponding lengths of the plate are obtained and plotted in Fig. 6. This shows the influence of the size of the plate to the jet flow, and also the corresponding effect on thrust. From this figure we may find the asymptotic angle of 120 degrees is practically reached when the dimensionless length of the plate is about 10.6. It also indicates that the asymptotic flow direction of the jet assumes that of the plate only when the plate is mathematically infinite but practically finite in length. Figure 7 shows a resulting flow pattern of this case. The free streamlines obtained from computations are plotted in the figure. The computed plate length is 10.52, and the asymptotic flow direction assumes nearly that of the wedge. The force of the jet on the plate may be important in consideration of thrust reversal. The value of C_F is clearly a function of the deflection angle (or the length of the plate). Figure 8 shows the case with fixed plate angle (α = 120°), as C_F increases, δ also increases. The jet flow toward a vertical flat plate is a special case when α = 90 deg. With the specified asymptotic flow angle equal to 70°, the computed free streamlines and the plate length required to produce such a flow pattern are plotted in Fig. 9.

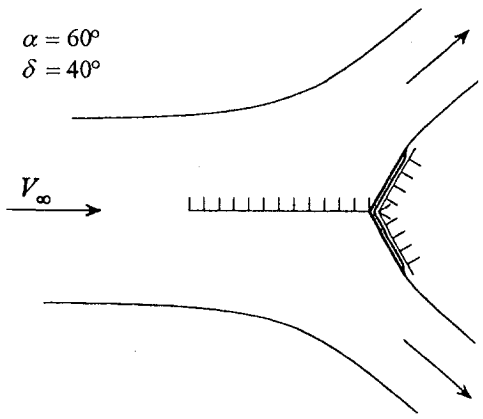

Fig. 11 Solution of a jet flow toward a < plate with α = 60 deg and δ = 40 deg in physical plane. Tick marks are spaced by $b/12$.

For the case of a jet flow toward a ⟨-shaped plate, Fig. 10 displays the resulting flow for α = 60° and δ = 59.5°. It shows the flow pattern of a jet flow toward a ⟨-shaped plate with infinite length for α = 60° is practically reached when the dimensionless length of the plate is about 6. When δ is set to be 40°, the resulting plate configuration and the free streamlines are shown in Fig. 11. The pressure distributions along the stagnation streamline for cases with δ = 50° and 40° are compared in Fig. 12. Cases with other specified asymptotic flow angles between 0 and 59.5 degrees are also computed. The variation of δ with the plate length required to produce such a flow is plotted in Fig. 13. Again, everything else being equal, the asymptotic flow angle is a function of the plate length, which was also displayed through considerations of the flat plates (Chow et al., 1995; Chu and Wei, 1996). Figure 14 shows the variation of C_F with the deflection angle.

It is possible that the differential equation may produce solutions with physically inappropriate boundary conditions (Chow et al., 1995). Thus, a checking of the overall momentum balance must be implemented for each of the test problems. The Euler equations in an integral form was used directly in the physical plane for the present work to verify the conservation of momentum, after the solutions of the hodograph equation have been produced. A comparison between the results obtained through the proposed method and the results obtained through directly using the momentum equation for the x-component force on a vertical flat plate is shown in Fig. 15. Very good agreement is obtained. For typical cases, with a relaxation factor of 1.6 and a 120 × 80 uniform grid, about 1000 iterations were required

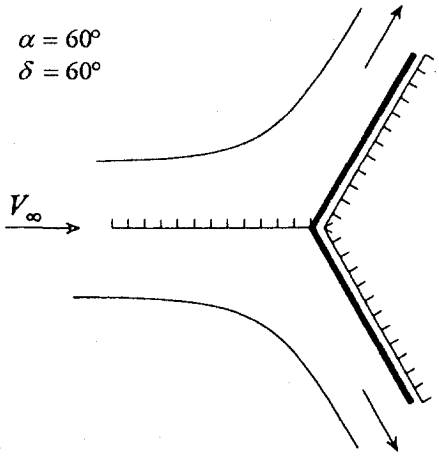

Fig. 10 Solution of a jet flow toward a <-shaped infinitely long plate—established with $L/(b/2)$ = 6. Tick marks are spaced by $b/8$.

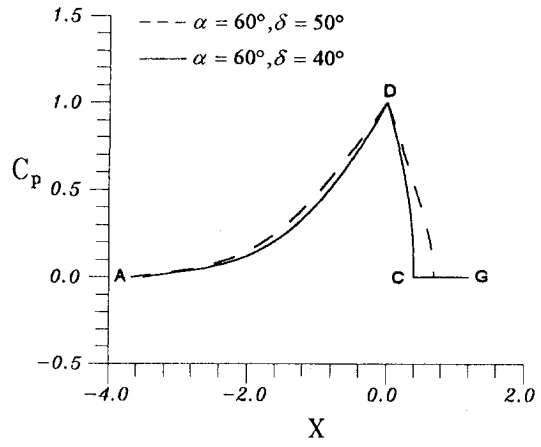

Fig. 12 Pressure coefficient distributions along the stagnation streamline and on the plate surface

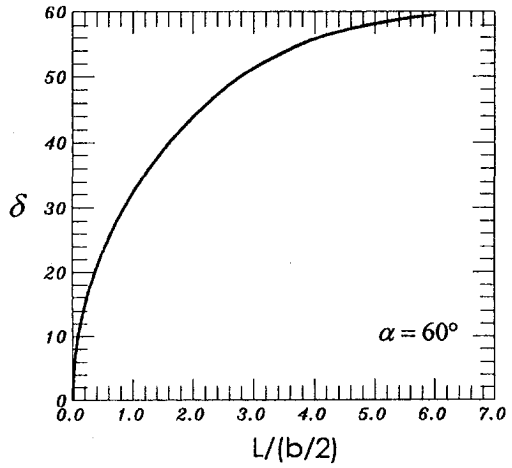

Fig. 13 The deflection angle versus the length of the plate for a jet flow toward a <-shaped plate

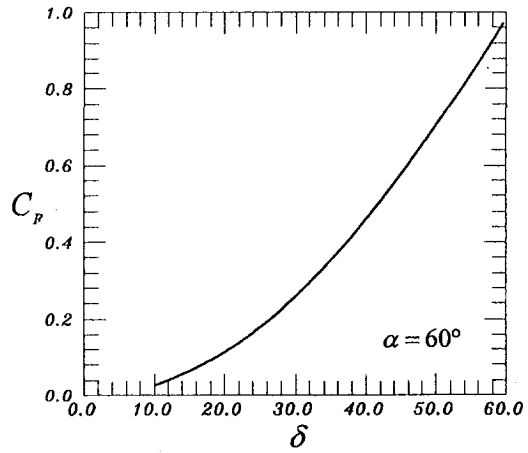

Fig. 14 Variation of C_F with the deflection angle, α = 60 deg

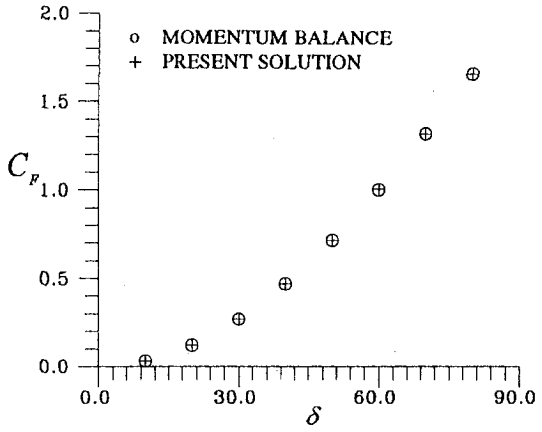

Fig. 15 Comparison between the results from momentum balance and the numerical solution for the force of the jet on the plate in the *x*-direction

to obtain the converged ψ values for the variation of ψ at each grid point less than 10^{-6}. A convergence history is shown in

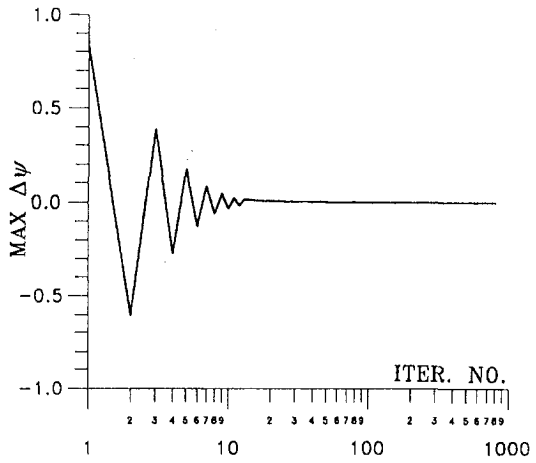

Fig. 16 Maximum correction convergence history for the hodograph solution

Fig. 16. About 75 sec computation time was needed to produce a complete set of results on a SPARC classic workstation.

Conclusions

Problems of steady, inviscid jet flows toward wedge-shaped plates have been solved through the use of hodograph transformation. The present work shows that the hodograph transformation coupled with numerical computations is a fast, effective method for the present problem, although it is recognized as an indirect method. With the proposed method, only the asymptotic and plate angles need to be specified for the whole flow fields calculation. The final flow pattern including the required length of the plate, the stagnation and free streamline shapes, and other flow properties are found through straight forward computations.

The method developed in this paper is not limited to only the flow cases of the present study. It can be extended to many other flow processes, especially when the body has the straight-line profile, whether the flow configuration is two-dimensional or axisymmetric. The simplicity in its specification of the boundary condition of the free boundary problem in the hodograph plane and the ease of finding solution through iterations make the present approach very effective and economical in dealing with many problems of this nature. Also, it is believed that the proposed technology can be extended to compressible flows. Such a capability is under development at present.

References

Chow, W. L., Ke, Z. P., and Lu, J. Q., 1995, "The Interaction Between a Jet and a Flat Plate—An Inviscid Analysis," ASME JOURNAL OF FLUIDS ENGINEERING, Vol. 117, pp. 623–627.

Chow, W. L., Ting, Alice, A. L., and Tsai, P. H., 1987, "Discharge from a Vessel Through an Axisymmetric Control valve," ASME *Journal of Applied Mechanics,* Vol. 54, No. 2, pp. 447–452.

Chu, S. S., and Chow, W. L., 1992, "A Hodograph-Based Method for the Solutions of Axisymmetric Orifice Flows," *Journal of the CSME,* Vol. 13, No. 2, pp. 167–170.

Chu, S. S., Miller, S. K., and Chow, W. L., 1990, "Quasi-Steady Discharge of Fluid from a Vessel Through a Poppet Valve," ASME JOURNAL OF FLUIDS ENGINEERING, Vol. 112, No. 4, pp. 437–440.

Chu, S. S., and Wei, C. Y., 1996, "Study of the Jet-Plate Interaction Using the Method of Hodograph Transformation," *Proceedings of the 38th Conference on Aeronautics and Astronautics,* Taipei, pp. 191–197.

Liu, S. K., and Chow, W. L., 1978, "Numerical Solutions of the Compressible Hodograph Equation," *AIAA Journal,* Vol. 16, pp. 188–189.

Shapiro, A. H., 1953, *The Dynamics and Thermodynamics of Compressible Fluid Flow,* Chapter 11, Vol. 1, The Ronald Press Company, New York.

Weng, Z. M., Ting, Alice, A. L., and Chow, W. L., 1987, "Discharge of a Compressible Fluid Through a Control Valve," ASME *Journal of Applied Mechanics,* Vol. 54, No. 4, pp. 955–960.

Wu, C. C., and Chow, W. L., 1985, "Study of an Asymmetric Flap Nozzle as a Thrust-Vectoring Device," AIAA *Journal of Propulsion and Power,* Vol. 1, No. 4, pp. 286–291.

Nearfield Evolution of a Longitudinal Vortex Generated by an Inclined Jet in a Turbulent Boundary Layer

X. Zhang
Department of Aeronautics and Astronautics, University of Southampton, Southampton, United Kingdom

M. W. Collins
Department of Mechanical Engineering and Aeronautics, City University, London, United Kingdom

The nearfield evolution of a longitudinal vortex embedded in a turbulent boundary layer was examined in a wind-tunnel test. The vortex was produced by an inclined round jet, the diameter of the jet being $0.4\delta_{0.99}$. Flow properties were measured at a freestream velocity of 20 m/s using a laser Doppler anemometer. Control parameters are jet skew and pitch angles, and speed ratio. It was observed that a single vortex is generated at $x = 10D$. The effects of the control parameters on the strength and location of the vortex were examined. For an embedded vortex and favorable velocity distribution, the test results suggested a skew angle of 60 deg, a pitch angle of $\alpha = 30$ deg, and speed ratios of $\gamma = 1.0$. The study provided insight into the flow physics and a database.

Introduction

Longitudinal vortices embedded in a turbulent boundary layer convect and diffuse kinetic and thermal energy in a cross-plane. These capabilities have often been employed in fluid flow and heat transfer applications, e.g., stall control or heat transfer enhancement. The behaviors of the vortices are also of fundamental interest and have been examined by Wallis (1956), Eibeck and Eaton (1987), Compton and Johnston (1991), Shizawa and Eaton (1992), Selby, et al. (1992), and Zhang (1993). It appears that the vortices are able to interact with the large energy-containing eddies in a turbulent boundary layer, and that a properly arranged distribution of longitudinal vortices can regulate a turbulent stress field. It therefore has further potential for many applications including the reduction of skin friction in turbulent flow.

Vortices generated by vanes (see Eibeck and Eaton, 1987) are effective, but the vanes lead to drag penalties and may produce hot spots. Vanes have been used widely, with large variations in geometry, and research into their use continues. An alternative is to employ an inclined jet (see Wallis, 1956 and Johnston and Nishi, 1990). An array of these vortices have the potential to be equally effective in both flow and heat transfer control as those generated by vanes. The jet generated vortices have obvious advantages over those generated by vanes, for example, they can be used in active control and do not suffer from drag penalties.

These devices can only be optimized once the flow physics are better understood. Important parameters include: the ratio of the jet diameter (D) to the thickness of boundary layer; the jet pitch angle (α); the jet skew angle (β); and the velocity ratio γ, defined by V_j/U_∞, where V_j is the jet velocity (area mean value); and U_∞ the oncoming flow velocity. A large body of work focused on a normal jet-in-crossflow (e.g., Margason, 1993), but with an inclined angle the flow structure will be substantially different, particularly in the near-wall region, which calls for suitable measurement techniques for a detailed study. Information on the nearfield process is generally lacking. Attempts have been made to model the flow using numerical models based on solutions of the Reynolds-averaged Navier-Stokes equations (see Zhang and Collins, 1993). This has been performed in the context of a wider ongoing combined measurement/predictive study, and agreement between the numerical predictions and measurement is generally good. The development of the numerical models in turn calls for a solid database for model validation. At this stage, it is believed that the understanding of the flow physics and successful application of the concept could best be served through an experimental investigation into the *nearfield* flow physics. It is in this region that the vortices are formed, a single vortex becomes dominant, the initial secondary vortex is diffused, and turbulent dissipation and diffusion begin to play major roles.

The main objective of this study is therefore to investigate the *nearfield* flow physics of longitudinal vortices generated by inclined jets in a turbulent flow field.

Description of Experiment

Tests were performed in the R. J. Mitchell wind tunnel at the University of Southampton. The tunnel has a low speed closed circuit with a 3.5 m (wide) × 2.6 m (high) test section. A 2.43 m long and 10 mm thick aluminum flat plate with an elliptic leading edge was installed across the span of the test section, at a height of 0.9 m above the tunnel floor. Freestream velocity (U_∞) was set at 20 m/s, and boundary-layer transition was fixed by a 10 mm wide sand band located 100 mm downstream of the leading edge. Measurements indicted that boundary layer at the jet exit ($x = 0$ mm) was two-dimensional with a thickness ($\delta_{0.99}$) of 25 mm, a displacement thickness of 3.02 mm and a momentum thickness of 2.40 mm.

A round jet ($D = 14$ mm) was introduced through the plate at a position 1.219 m downstream of the leading edge of the plate (Fig. 1). The jet nozzle was formed by a straight, round tube, the length of which was 100 mm. The tube was connected to a compressed air supply and pressure controlled by a Fisher valve. Using the LDA system and a pitot-static tube, the jet velocity was found to remain within ±0.2 m/s of the desired value. A list of the test conditions is given in the following tables. A baseline arrangement of $\alpha = 45$ deg, $\beta = 45$ deg and $\gamma = 1$ was selected for the study. Detailed measurements were conducted at $x = 5$, 10, 20, 30, 40, and $50D$.

The mean velocity distributions were obtained using a three-component Dantec LDA system with a 5W Ar-ion Laser (see

Contributed by the Fluids Engineering Division for publication in the JOURNAL OF FLUIDS ENGINEERING. Manuscript received by the Fluids Engineering Division December 20, 1996; revised manuscript received July 8, 1997. Associate Technical Editor: J. K. Eaton.

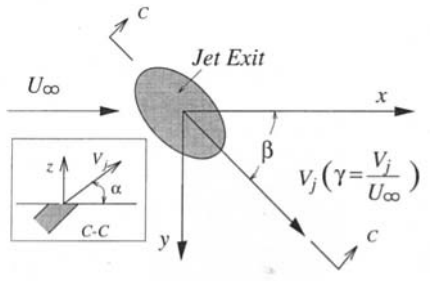

Fig. 1 Schematic of jet exit and test coordinates

Table 1 Pitch angle tests

α	30°	45°	60°
β	45°	45°	45°
γ	1.0	1.0	1.0

Table 2 Skew angle tests

α	45°	45°	45°	45°	45°	45°	45°	45°
β	0°	15°	30°	45°	60°	75°	90°	135°
γ	1.0	1.0	1.0	1.0	1.0	1.0	1.0	1.0

Table 3 Velocity ratio tests

α	45°	45°	45°	45°	45°
β	45°	45°	45°	45°	45°
γ	0.5	1.0	1.5	2.0	2.5

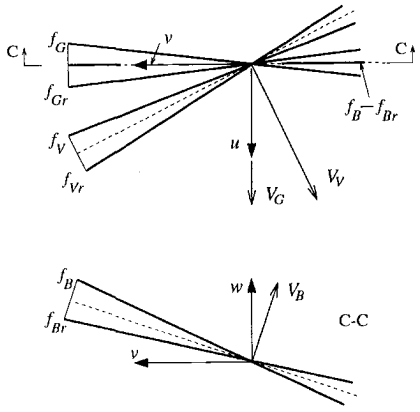

Fig. 2 Schematic of LDA velocity vector (V_G, V_B, V_V) and velocity vector based on test coordinates. u-streamwise velocity.

Zhang and Hurst, 1991). Oil based seedings were released in front of the test rig. Typically, over 2000 samples were collected at each point, and the number of measurement points ranged from 350 to 792. In the transverse direction, the first sampling point was 2 mm away from the plate surface, and the traverse step was then gradually increased from 2 mm to 4 mm. In the spanwise direction the sampling points were separated by 2 mm or 4 mm intervals.

The LDA system was operated in an off-axis backscatter mode. A schematic of the test setup is given in Fig. 2. Calibration was performed through measurement of beam separation and focal length before and after each test. This was done by projecting the beams onto a vertical wall and traversing the system away from the wall by a pre-determined distance. Movement of the beams on the wall then gave the necessary information for beam angle calibration. To obtain the velocities in the tunnel axes system, it is necessary to use three beam-pairs, and

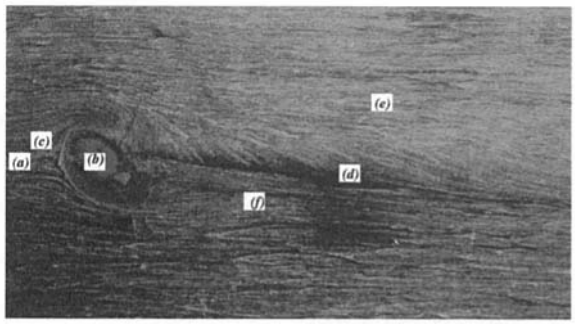

Fig. 3 Surface oil flow at α = 45 deg, β = 45 deg and γ = 1.0; (*a*) oncoming flow; (*b*) jet exit; (*c*) front separation; (*d*) separation; (*e*) reattachment; (*f*) secondary reattachment

Fig. 2 illustrates the arrangement used. The velocities measured in the beam axes (V_G, V_B, V_V) were resolved into the tunnel axes system (u, v, w) using a matrix transformation. The measured data is presented in terms of velocity vectors, contours of velocity, and streamwise vorticity ($\Omega_x = (\partial w/\partial y - \partial v/\partial z)D/U_\infty$), which has been calculated for each data point on the measurement grid. Natural cubic splines were used to obtain the derivatives of w and v with respect to the coordinates y and z.

The LDA beam measurement volume had a cross-section size of 0.326 mm (the length of the volume is 10 cm). It was concluded that the uncertainty in the x, y, z measurements was ±0.16 mm. The uncertainty in the tunnel speed measurement was ±0.25 m/s. The uncertainty in the LDA velocity measurement was influenced by the uncertainties in the beam separation, focal length, wavelength and errors in the tunnel speed which determines the Doppler frequency. Following the procedure of Moffat (1988) the uncertainty in the velocity measurement was estimated at ±0.31 m/s when the freestream value was 20 m/s.

Results and Analysis

Oil flow visualization was conducted for all the test cases to provide qualitative information on the nearfield flow structure. The results suggest that the nearfield is influenced by a number of mechanisms, including jet-in-crossflow, flow separation, reattachment, and entrainment. Figure 3 presents a typical oil flow, with major features as indicated. There exists an area of flow separation just upstream of the jet exit with a visible line of separation. It has been hypothesized (Margason, 1993) that for a normal jet-in-crossflow this line is caused by a horseshoe vortex wrapped around the jet exit. In contrast, the LDA measurements made 1 mm from the surface show no evidence of flow separation. This implies that if there is flow separation upstream of the skewed jet, it must be confined to a region very close to the wall.

Directly downstream of the jet exit, the surface flow is characterized by entrainment, and a spiral point is formed (see Fig. 4). Further downstream, a longitudinal vortex is produced (see later discussion), which induces a line of separation. This line of vortex separation is visible in all the flow visualizations because the vortex is relatively strong compared with those generated in a normal jet-in-crossflow. It was noted that a β variation between 15 and 90 deg will only alter the surface flow pattern quantitatively. When $\beta > 90$ deg, some additional features were observed, but these are not discussed here as this arrangement is unlikely to be effective in flow control and is therefore of less interest. Stronger secondary features were also observed at higher γ values.

The near-wall measurements (Fig. 4) highlight the induced flow in the downwash side of the vortex, which rapidly turns the flow towards the vortex separation line. Immediately down-

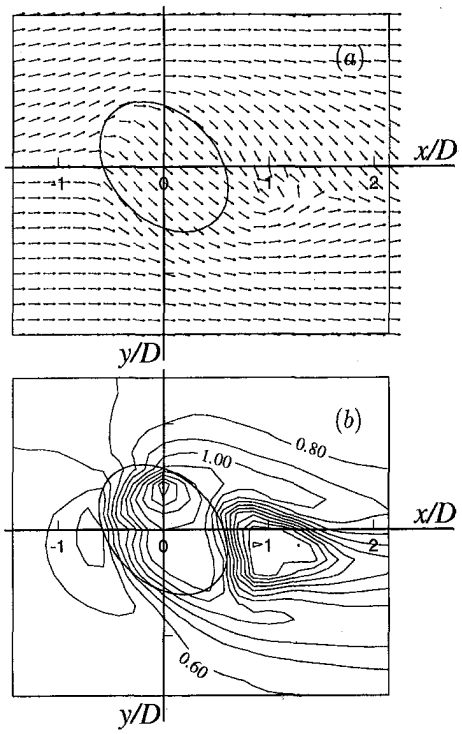

Fig. 4 (*a*) Velocity vectors around the jet exit at z = 2 mm; (*b*) Total velocity ($\sqrt{u^2 + v^2 + w^2}/U_\infty$) contours

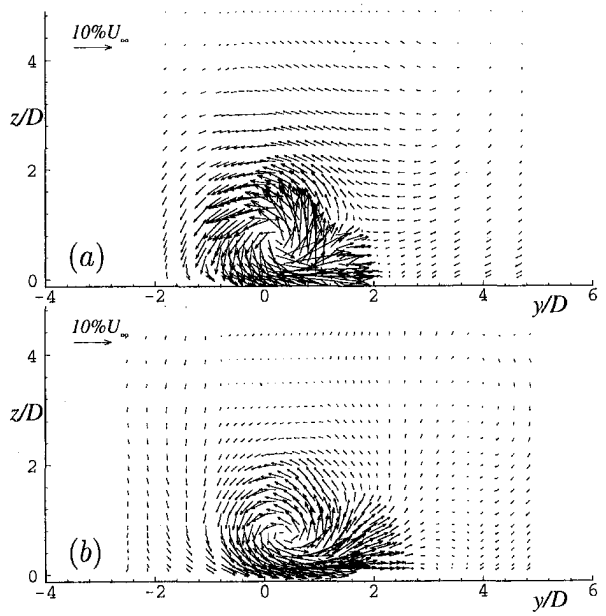

Fig. 5 Velocity vectors at α = 45 deg, β = 45 deg and γ = 1: (*a*) x = 5*D*; (*b*) x = 10*D*

stream of the jet exit, there is a recirculating region in the spanwise direction, which is not fully captured by the LDA measurement due to the coarse sampling grid. The contours of total velocity indicate that the flow at the jet exit plane is not uniform, with a strong distortion caused by the interaction between the nozzle flow and the crossflow. The present measurements point to differences between a skewed jet and a non-skewed jet. Leylek and Zerkie (1994) modeled a 35 deg inclined jet with zero skew in a low speed cross-stream. Their results pointed to two contra-rotating vortices in the jet exit plane, a feature which was not observed in the current study, suggesting strong effects of the skew angle.

In Figs. 5–7, the vortex development for the baseline case is illustrated using the velocity vectors, and contours of Ω_x, and u/U_∞. The results show that the development of the single longitudinal vortex can be divided into two stages. In the first stage, the influence of the jet is still obvious. The contours of Ω_x in Fig. 6(a) show the induced vorticity, and show some similarities with those for a normal jet-in-crossflow. In the latter case, two counter-rotating vortices are produced. Here a strong, dominant vortex is accompanied by a secondary vortex. The secondary features are not clearly visible at $x = 10D$, though the characteristics of the jet flow are still present in the contours of u/U_∞ (Fig. 7(b)). In the second stage, a strong, dominant single vortex begins to appear (near $x = 10D$), and farther downstream, the single vortex prevails.

The presence of the vortex leads to a thinning of the boundary layer on the downwash side, giving rise to a much fuller velocity distribution and a better ability to resist stall and separation. The unfavorable effect on the upwash side can also be seen in Fig. 7. The effects of the vortex are further demonstrated in Fig. 8. At $x \geq 20D$, the velocity profiles across the center of vortex are quite similar, suggesting a diminishing effect of the vortex production physics and that turbulent diffusion and dissipation take over.

The "center of vortex" is used to describe the movement of the vortex, and is defined by the crossflow velocity components (v, w). Instead of circulation, the streamwise vorticity (Ω_c) at this center is used to quantify the strength of the vortex. This method depends on the measurement resolution but not the area. Results are given in Table 4. Comparing Figs. 5(a) and 7(a), it is evident from the velocity contours that there exists a jet center which is located beneath the center of vortex. Existence of this jet center distinguishes the current flow from that of solid vortex generator flow. The center of vortex (y_c, z_c) moves in the spanwise direction, which reflects the presence of the imaginary vortex. In contrast, the distance of the vortex from the wall remains relatively constant, suggesting that the longitudinal vortex is embedded in the turbulent boundary layer within the range of the measured distance. For the base flow discussed here, Ω_c reduces rapidly from $x = 5D$ to $x = 20D$, and then reduces at a smaller rate, indicating a persistent vortex. This

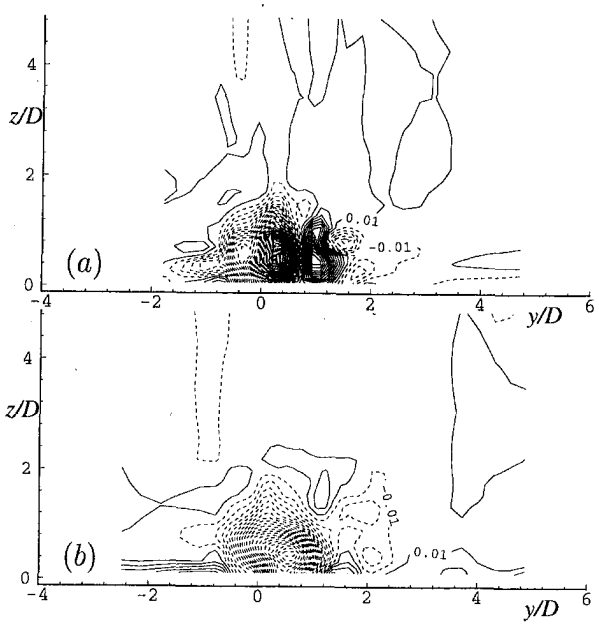

Fig. 6 Ω_x-contours at α = 45 deg, β = 45 deg, and γ = 1: (*a*) x = 5*D*; (*b*) x = 10*D*

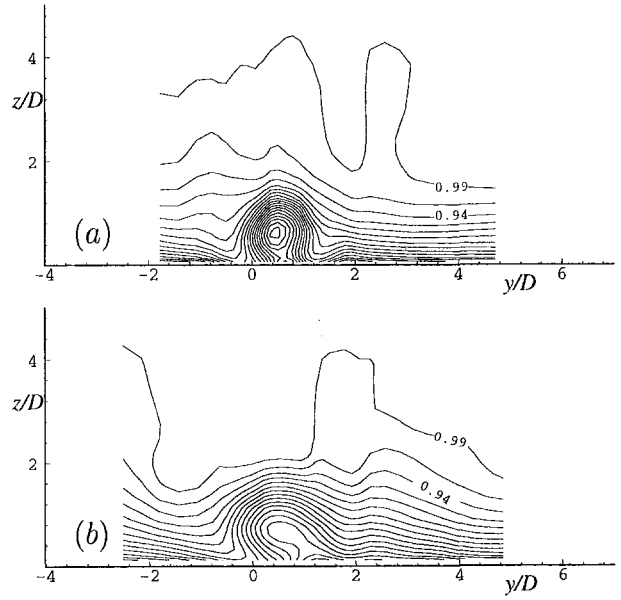

Fig. 7 u/U_∞-contours at α = 45 deg, β = 45 deg, and γ = 1: (*a*) x = 5*D*; (*b*) x = 10*D*. Contour interval is 0.02475.

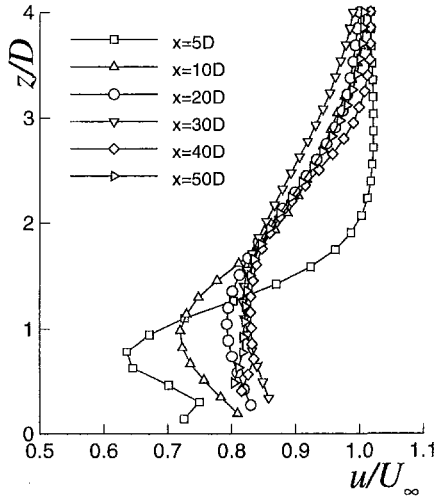

Fig. 8 Streamwise velocity across the center of vortex at α = 45 deg, β = 45 deg, and γ = 1

Table 4 Baseline case

	x = 5*D*	10*D*	20*D*	30*D*	40*D*
Ω_c	−0.769	−0.352	−0.156	−0.115	−0.105
y_c/D	0.24	0.40	0.65	0.83	0.97
z_c/D	0.73	0.71	0.86	0.94	1.08

feature suggests that the vortex has moved away from the wall and the dissipating effect of the boundary layer on the vortex development is reduced.

A normal jet-in-crossflow will produce two longitudinal vortices of equal strength (see Margason, 1993). They will then weaken each other and not be effective in modifying the turbulent stress field for the purpose of flow control. Increasing β from zero alters the flow physics, leading to a strong primary vortex together with a weak secondary vortex. The secondary vortex is dissipated quickly, leaving the dominant vortex (Zhang, 1993), which is then able to maintain its strength and position downstream.

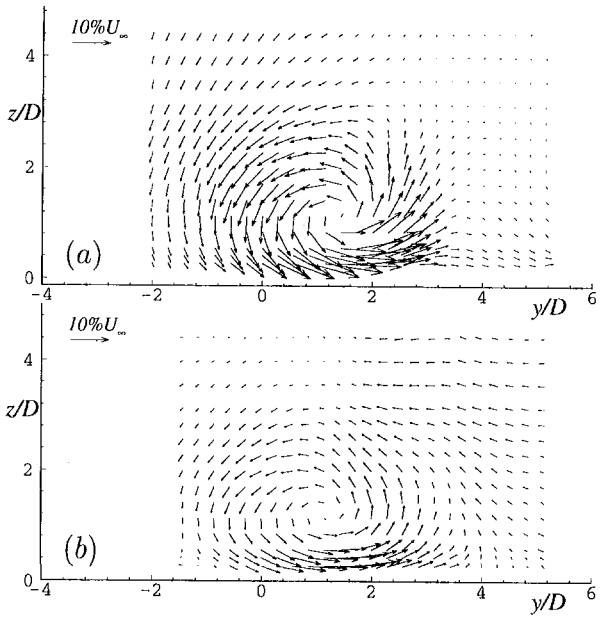

Fig. 9 Velocity vectors at α = 45 deg, γ = 1 and x = 20*D*: (*a*) β = 60 deg; (*b*) β = 90 deg

Measurements suggest that the features of the single vortex appear at β = 30° and remain qualitatively the same until β = 90 deg (see Figs. 9 and 10). Within this skew angle range, the dominant features are all present, such as single, embedded vortex; thinning of boundary layer; and spanwise movement. The evolution of the vortex can be observed more clearly in Fig. 11. Here there are two types of characteristics—one with high streamwise momentum near the wall (β = 30, 45, 60 deg), and the other of relatively low streamwise momentum (β = 75, 90 deg). The 45 and 60 deg skew angles give the highest near wall streamwise momentum, which is a favorable feature for turbulent flow control. The measured values are also listed in Table 5, which shows that Ω_c reaches a maximum at β = 60°. Altering β also moves the center of vortex. The vortex experiences rapid movement between β = 30 and 60 deg, but

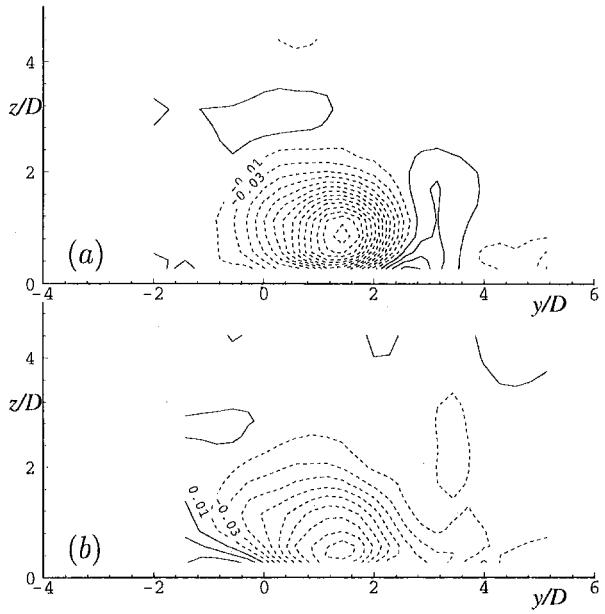

Fig. 10 Ω_x-contours at α = 45 deg, γ = 1 and x = 20*D*: (*a*) β = 60 deg; (*b*) β = 90 deg

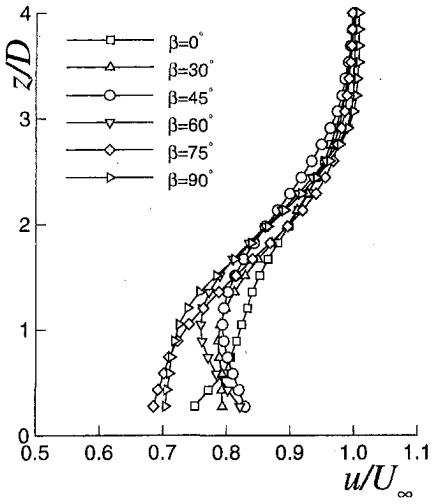

Fig. 11 Streamwise velocity across the center of vortex at α = 45 deg, γ = 1, and x = 20D

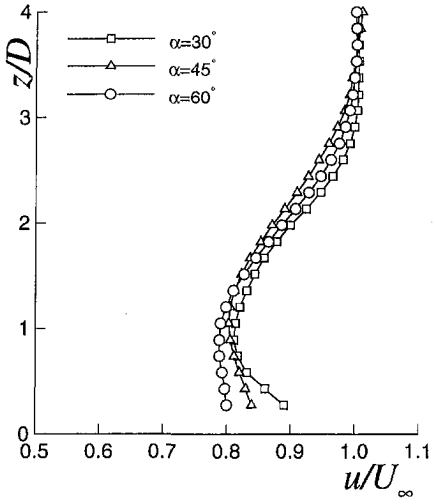

Fig. 13 Streamwise velocity across the center of vortex at β = 45 deg, γ = 1, and x = 20D

Table 5 Effect of skew angle

	β = 0°	30°	45°	60°	75°	90°
Ω_c	±0.067	−0.151	−0.156	−0.258	−0.104	−0.119
y_c/D	−0.67	−0.05	0.65	1.43	1.62	1.13
z_c/D	1.24	0.91	0.86	1.25	1.23	1.21

Table 6 Effect of pitch angle

	α = 30°	45°	60°
Ω_c	−0.331	−0.156	−0.128
y_c/D	1.23	0.65	0.50
z_c/D	1.06	0.86	1.30

Table 7 Effect of velocity ratio

	γ = 0.5	1.0	1.5	2.0	2.5
Ω_c	−0.122	−0.156	−0.314	−0.440	−0.537
y_c/D	0.96	0.65	1.05	0.27	−0.04
z_c/D	0.48	0.86	1.27	1.93	2.85

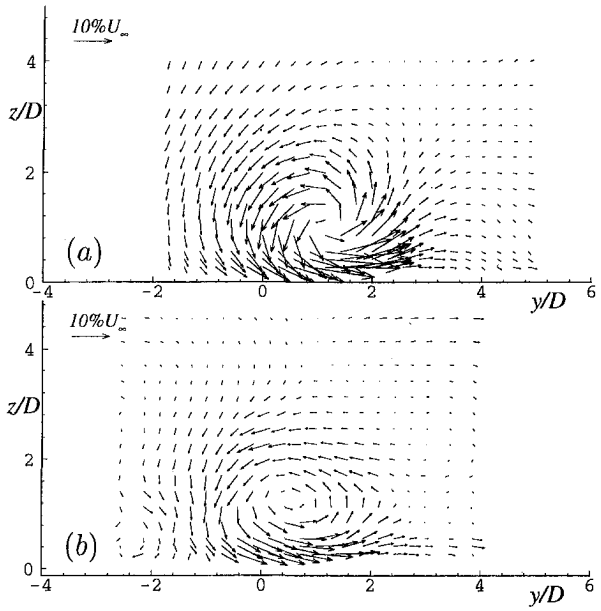

Fig. 12 Velocity vectors at β = 45 deg, γ = 1 and x = 20D: (a) α = 30 deg; (b) α = 60 deg

between β = 60 and 90 deg, the position remains relatively constant. When the center of vortex is considered, the distance from the wall changes only slightly and the vortex remains embedded in the boundary layer. Measurements suggest that the skew angle should be kept between 30 and 60 deg.

In selecting a pitch angle, practical considerations prevail. Three pitch angles have been tested: α = 30, 45, and 60 deg. All of the pitch angles produce a single, dominant vortex consistent with earlier observations (see Fig. 12). However, the streamwise velocity across the center of vortex (Fig. 13) suggests that with α = 30 deg the jet is characterized by high streamwise momentum flow near the wall and thus has favorable velocity stress distribution.

Results from the study suggests that the pitch angle has a significant influence (see Table 6). For α = 30 deg, Ω_c is 2.5 times that found with α = 60 deg. The position of the jet in the boundary layer is important in determining the vortex strength. Here, it is difficult to distinguish the jet from the oncoming flow, as the velocities are of the same order. However, at α = 60 deg, the jet has a tendency to penetrate the boundary layer quickly instead of becoming embedded. This implies that a large amount of momentum is lost through interaction between the jet and freestream. This part of the flow physics will therefore not make a significant contribution to the production of the longitudinal vortex inside the boundary layer. This is reflected in the relatively weak vortex.

Variations in the velocity ratio, γ, will alter the position of the vortex. In this study, five γ values were tested. With the jet at β = 45 deg, a single, dominant vortex is produced for all the jet velocity ratios tested. The main features of the flow are very similar to the baseline case, but the properties of the flow are quite different (see Table 7). Figure 14 shows that varying γ can result in three types of velocity distribution near the wall. At γ = 0.5, the influence of the vortex is marginal. At γ = 1.0 and 1.5, the velocity profile is quite favorable, suggesting an embedded vortex. The γ = 2.0 and 2.5 jets generate vortices further away from the wall, leading to reduced influence in the near-wall region. Ω_c (as well as z_c) is seen to rise rapidly with velocity ratio, especially for $\gamma \geq$ 1.5. If the vortex strength is

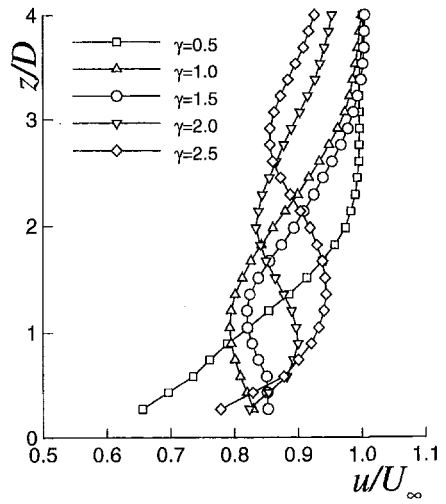

Fig. 14 Streamwise velocity across the center of vortex at α = 45 deg, β = 45 deg, and x = 20D

kept constant, the farther the vortex is from the wall, the lower its effect on the near-wall stress distribution. At γ = 2.0 and 2.5, the jet has penetrated the boundary layer, thus the vortex is located immediately outside the boundary layer. The turbulent dissipation is then low and the vortex is able to maintain its strength for a relatively long distance downstream.

Conclusions

An experimental examination has been conducted of longitudinal vortices generated by an inclined jet in a turbulent flat-plate boundary layer. Velocity measurements were performed for a number of α, β, and γ values. The study has established a database for the mean-velocity field of the flow, and provided insight into the flow physics. In particular, it is observed that:

- At the initial stage, a secondary weak vortex accompanies the main vortex. Around the jet exit, the flow is characterized by an upstream separation bubble, and a spiral point directly downstream of the jet exit, which moves with the skew angle. Downstream the flow structure alters, with a single vortex formed within x = 10D.
- The flow on the jet exit is significantly influenced by the oncoming flow.
- The single vortex moves in both the spanwise and vertical directions downstream. As it develops, turbulent dissipation and diffusion play important roles in defining the vortex. Ω_c decreases rapidly downstream. For the baseline case, this occurs between x = 0 to 20D. A persistent single vortex is produced after x = 20D.
- Between β = 0 and 90 deg the characteristics of the vortex remain qualitatively the same. However, a favorable near-wall velocity distribution is observed between β = 30 and 60 deg. A maximum value of Ω_c occurs at β = 60 deg. Changes in β do not alter z_c significantly.
- Varying α changes Ω_c, but not the location of the vortex. The β = 30 deg jet produces the highest vortex strength.
- The center of vortex undergoes small spanwise movement, but moves away from the wall as γ increases. The favorable near-wall velocity distribution is observed at γ = 1.0 and 1.5.

Acknowledgment

The study is supported by EPSRC under contract number GR/J17722. Part of the LDA data was taken with help from H. L. Zhang and A. Rona.

References

Compton, D. A., and Johnston, J. P., 1991, "Streamwise Vortex Production by Pitched and Skewed Jets in a Turbulent Boundary Layer," AIAA Paper 91-0038.

Eibeck, P. A., and Eaton, J. K., 1987, "Heat Transfer Effects of a Longitudinal Vortex Embedded in a Turbulent Boundary Layer," ASME *Journal of Heat Transfer,* Vol. 109, pp. 16–24.

Johnston, J. P., and Nishi, M., 1990, "Vortex Generator Jets—A Means for Flow Separation Control," *AIAA Journal,* Vol. 28, No. 6, June, pp. 989–994.

Margason, R. J., 1993, "Fifty Years of Jet in Cross Flow Research," *Computational and Experimental Assessment of Jets in Cross Flow, AGARD-CP-534,* Nov., pp. 1.1–1.41.

Selby, G. V., Lin, J. C., and Howard, F. G., 1992, "Control of Low-Speed Turbulent Separated Flow Using Jet Vortex Generators," *Experiments in Fluids,* Vol. 12, No. 6, pp. 394–400.

Shizawa, T., and Eaton, J. K., 1992, "Turbulent Measurements for a Longitudinal Vortex Interacting with a Three-Dimensional Turbulent Boundary Layer," *AIAA Journal,* Vol. 30, No. 1, Jan., pp. 49–55.

Wallis, R. A., 1956, "A Preliminary Note on A Modified Type of Air-Jet for Boundary-Layer Control," ARC, CP-513.

Zhang, X., 1993, "Interaction between A Turbulent Boundary Layer and Elliptic and Rectangular Jets," *Engineering Turbulence Modelling and Experiments 2,* W. Rodi and F. Martell (Ed.), June, pp. 251–260.

Zhang, X., and Collins, M. W., 1993, "Flows and Heat Transfer in A Turbulent Boundary Layer through Skewed and Pitched Jets," *AIAA Journal,* Vol. 31, No. 9, Sept., pp. 1590–1599.

Zhang, X., and Hurst, D. W., 1991, "A Laser Doppler Anemometry Study of A Supersonic Jet in A Low Speed Cross-Flow," *Proceedings of the 4th International Conference on Laser Anemometry, Advance and Applications,* Vol. 2, Aug., Cleveland, OH, pp. 403–411.

Moffat, R. J., 1988, "Describing the Uncertainties in Experimental Results," *Experimental Thermal and Fluid Science,* Vol. 1, pp. 3–17.

Leylek, J. H., and Zerkie, R. D., 1994, "Discrete-Jet Film Cooling: A Comparison of Computational Results with Experiments," *Journal of Turbomachinery,* Vol. 116, July, pp. 358–368.

Chebyshev Collocation Analysis of Axisymmetric Flow and Heat Transfer Between Counter-Rotating Disks

R. W. Hill
Graduate Student.
Assoc. Mem. ASME

K. S. Ball
Associate Professor.
Mem. ASME

Department of Mechanical Engineering,
The University of Texas at Austin,
Austin, TX 78712

Unsteady constant property flow between two counter-rotating finite disks is considered for a range of Reynolds numbers. Both disks are taken to be isothermal with an imposed temperature difference between them. The flow is assumed to be axisymmetric, and buoyancy forces are neglected. The conservation equations for momentum and energy are solved using a spectral Chebyshev collocation technique utilizing a pressure Poisson influence matrix approach to maintain a solenoidal velocity field. Three values of the disk angular velocity ratio, $\Gamma = \omega_2/\omega_1$, are considered: $\Gamma = -1.0$, -0.4, and 0.0. The flow is observed to become more complex, transitioning from steady to periodic to chaotic flow regimes as the Reynolds number is increased. The simulations are found to agree reasonably well with experimental data from the literature for $\Gamma = -1.0$ and 0.0, whereas discrepancies exist for $\Gamma = -0.4$ that are similar to those observed by others in simulations using turbulence models. The heat transfer rates between the disks are shown to increase with Reynolds number due to increasing velocities and to a lesser extent chaotic mixing over the parameter range considered.

Introduction

Numerous engineering applications contain some form of rotating disk geometry. The applications range from the semiconductor/computer industry (wafers and disk drives) to the power industry (turbines). Consequently, the fluid dynamics (and to a lesser extent the heat transfer) have been investigated for various geometries and ranges of conditions. Certain of the numerical/theoretical works have addressed infinite disks (Batchelor, 1951; Stewartson, 1953; Holodniok et al., 1977, 1981) where similarity transformations may be applied to the Navier-Stokes equations. Szeri et al. (1983a, b) assessed the effect of the infinite disk assumption on finite open disk flow and stability characteristics, combining experiments with B-spline approximation Galerkin predictions. Considerable work, both numerical and experimental, has been reported for the co-rotating flow configuration by Humphrey and co-workers (see, for example, Iglesias and Humphrey, 1996; Humphrey et al., 1995; and Humphrey and Gor, 1993). Gan et al. (1994) and Kilic et al. (1994) address counter-rotating disks at various values of Γ and use a steady-state finite volume numerical approach combined with a turbulence model in an attempt to match their experimental data.

The numerical approaches used in the references cited above either incorporated idealized geometric and/or similarity assumptions, low order spatial approximations, steady-state assumptions, or combinations of these. Kilic et al. (1994) report particular difficulty in obtaining agreement between simulation and experiment for counter-rotating disks and intermediate values of Γ. The purpose of the present study is to perform, for what is believed to be the first time, an assessment of the transitional behavior between counter-rotating disks using a high order spatial approximation and unsteady analysis with no simplifying assumptions other than axisymmetry. In addition to exploring the transitional behavior, results will be used to elucidate the potential importance of nonaxisymmetric disturbances on the flow by comparison with select experimental results of Kilic et al. (1994). Nonaxisymmetric flows and the mechanisms for transition to three-dimensional flow will be addressed in a future study.

Model Formulation

The coupled equations describing the time-dependent conservation of mass, momentum, and thermal energy are solved subject to the imposed boundary conditions. The system of interest, shown in Fig. 1, is an annular region formed by a bottom (1) and top (2) disk separated by a spacing of $2h$, with cylindrical shrouds attached to each disk at the inner and outer disk radii. A small axial clearance, δ, separates the shrouds allowing each disk/shroud set to rotate freely from the other. The axial and radial velocities are assumed to be zero across the shroud clearance, thereby creating an enclosed system. This assumption is consistent with Kilic et al. (1994), who could control and thus eliminate net mass efflux through the axial clearance in their experimental apparatus. The azimuthal velocity is arbitrarily assumed to vary linearly between the shrouds; due to the relatively small size of the shroud clearance relative to the disk spacing, this assumption is considered to be reasonable. The bottom disk is held at the minimum system temperature and rotated at the maximum speed, and the top disk is held at the maximum system temperature and rotated in the direction opposite that of the lower disk. For simplicity, the inner and outer shrouds and their separating clearance gaps are assumed to represent adiabatic boundaries. It is emphasized that the presence of the axial clearance between the shrouds and the boundary conditions imposed there are not necessitated by the numerical procedure employed in this study, but rather are included to match the geometry considered by Kilic et al.

The time-dependent momentum and thermal energy conservation equations are considered in a polar-cylindrical coordinate system assuming axisymmetry and constant properties (Bird et al., 1960). An Adams Bashforth/second order backward Euler

Contributed by the Fluids Engineering Division for publication in the JOURNAL OF FLUIDS ENGINEERING. Manuscript received by the Fluids Engineering Division January 8, 1997; revised manuscript received July 8, 1997. Associate Technical Editor: J. A. C. Humphrey.

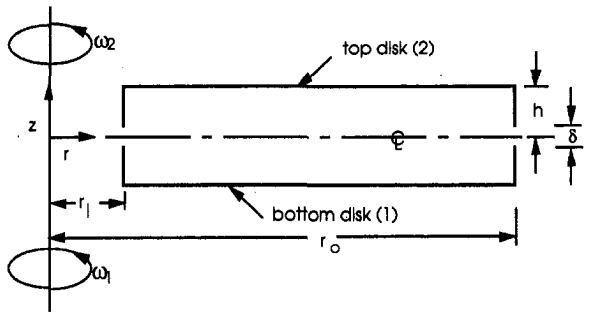

Fig. 1 Schematic of coordinate and physical system

($AB/2BE$) time discretization is applied, giving an implicit treatment of the diffusion terms and an explicit treatment of the advection terms. The following definitions are employed to simplify the nondimensional form of the conservation equations:

$$R = C_1 + \frac{r}{C_2}; \quad Z = -z/h;$$

$$C_1 = \left(\frac{r_o + r_i}{r_o - r_i}\right); \quad C_2 = \left(\frac{r_i - r_o}{2}\right); \quad C_3 = -C_2/h;$$

$$\tau = \omega_1 t; \quad V_r = \frac{v_r}{\omega_1 C_2}; \quad V_\theta = \frac{v_\theta}{\omega_1 C_2};$$

$$V_z = \frac{v_z}{\omega_1 C_2}; \quad P = \mathrm{Re}\left(\frac{C_2}{r_o}\right)^2 \frac{p}{\rho(\omega_1 C_2)^2};$$

$$\mathrm{Re} = \frac{\omega_1 r_o^2}{\nu}; \quad \Theta = \frac{T - T_C}{T_H - T_C}; \quad \mathrm{Pr} = \frac{\nu}{\alpha};$$

$$\mathrm{Pe} = \mathrm{Re}\,\mathrm{Pr}; \quad \mathrm{Nu} = 2\frac{\partial \Theta}{\partial Z} \tag{1}$$

The dimensionless forms of the time discretized conservation equations are then:

mass:

$$\frac{\partial V_r^{n+1}}{\partial R} + \frac{V_r^{n+1}}{R - C_1} + C_3 \frac{\partial V_z^{n+1}}{\partial Z} = 0 \tag{2}$$

R-momentum:

$$\left[\frac{\partial}{\partial R}\left(\frac{1}{R - C_1}\frac{\partial[(R - C_1)V_r]}{\partial R}\right) + (C_3)^2 \frac{\partial^2 V_r}{\partial Z^2}\right]^{n+1} - \left[\mathrm{Re}\left(\frac{C_2}{r_o}\right)^2 \frac{3}{2\Delta\tau}\right] V_r^{n+1} = \frac{\partial P^{n+1}}{\partial R} + S_r^{n,n-1} \tag{3}$$

θ-momentum:

$$\left[\frac{\partial}{\partial R}\left(\frac{1}{R - C_1}\frac{\partial[(R - C_1)V_\theta]}{\partial R}\right) + (C_3)^2 \frac{\partial^2 V_\theta}{\partial Z^2}\right]^{n+1} - \left[\mathrm{Re}\left(\frac{C_2}{r_o}\right)^2 \frac{3}{2\Delta\tau}\right] V_\theta^{n+1} = S_\theta^{n,n-1} \tag{4}$$

Z-momentum:

$$\left[\frac{1}{(R - C_1)}\frac{\partial}{\partial R}\left((R - C_1)\frac{\partial V_z}{\partial R}\right) + (C_3)^2 \frac{\partial^2 V_z}{\partial Z^2}\right]^{n+1} - \left[\mathrm{Re}\left(\frac{C_2}{r_o}\right)^2 \frac{3}{2\Delta\tau}\right] V_z^{n+1} = C_3 \frac{\partial P^{n+1}}{\partial Z} + S_z^{n,n-1} \tag{5}$$

thermal energy:

$$\left[\frac{1}{(R - C_1)}\frac{\partial}{\partial R}\left((R - C_1)\frac{\partial \Theta}{\partial R}\right) + (C_3)^2 \frac{\partial^2 \Theta}{\partial Z^2}\right]^{n+1} - \left[\mathrm{Pe}\left(\frac{C_2}{r_o}\right)^2 \frac{3}{2\Delta\tau}\right] \Theta^{n+1} = S_T^{n,n-1} \tag{6}$$

The source terms in each equation, known from the previous time levels, are (where $x = r$, θ, and z for the radial, azimuthal, and axial directions, respectively):

$$S_x^{n,n-1} = \mathrm{Re}\left(\frac{C_2}{r_o}\right)^2 [(\nabla^* \cdot \vec{V}\vec{V} + \vec{V} \cdot \nabla^* \vec{V})_x^n - 0.5(\nabla^* \cdot \vec{V}\vec{V} + \vec{V} \cdot \nabla^* \vec{V})_x^{n-1}] - \mathrm{Re}\left(\frac{C_2}{r_o}\right)^2 \left(\frac{4V_x^n - V_x^{n-1}}{2\Delta\tau}\right) \tag{7}$$

Nomenclature

C_1, C_2, C_3 = geometric constants
f = frequency
$2h$ = disk spacing
k = thermal conductivity
Nu = Nusselt number
p = dimensional pressure
P = dimensionless pressure
Pe = Peclet number
Pr = Prandtl number
r, z = dimensional radial and axial coordinates, respectively
R, Z = dimensionless radial and axial coordinates, respectively
Re = Reynolds number
S = dimensionless source term
t = time
T = temperature
v = dimensional velocity
V = dimensionless velocity
α = thermal diffusivity
δ = axial clearance between disk shrouds
ν = kinematic viscosity
Γ = disk angular velocity ratio, ω_2/ω_1
θ = azimuthal coordinate
Θ = dimensionless temperature
ρ = density
τ = dimensionless time
ω = angular velocity

Subscripts

1, 2 = bottom and top disks, respectively
a, b = probe points
avg = area average
C, H = cold and hot, respectively
i, o = inner and outer, respectively
$norm$ = normalized by disk 1 azimuthal velocity
r, θ, z, T = radial, azimuthal, axial and thermal energy, respectively
x = arbitrary variable as defined

Superscripts

* = dimensionless quantity
n = time discretization level

$$S_T^{n,n-1} = \mathrm{Pe}\left(\frac{C_2}{r_o}\right)^2 [2(\vec{V}\cdot\nabla^*\Theta)_T^n - (\vec{V}\cdot\nabla^*\Theta)_T^{n-1}]$$

$$- \mathrm{Pe}\left(\frac{C_2}{r_o}\right)^2 \left(\frac{4\Theta^n - \Theta^{n-1}}{2\Delta\tau}\right) \quad (8)$$

When solving the incompressible momentum equations in primitive variable form, a suitable approach must be implemented to determine the pressure. For the present study, a pressure Poisson equation approach is taken. The Poisson equation is generated by taking the divergence of the momentum equations, and since the divergence of the velocity is zero, the following equation is obtained:

$$\frac{1}{R - C_1}\frac{\partial}{\partial R}\left[(R - C_1)\frac{\partial P^{n+1}}{\partial R}\right] + (C_3)^2\frac{\partial^2 P^{n+1}}{\partial Z^2}$$

$$= -\left(\frac{1}{R - C_1}\frac{\partial}{\partial R}[(R - C_1)S_r^{n,n-1}] + C_3\frac{\partial S_z^{n,n-1}}{\partial Z}\right) \quad (9)$$

Using the dimensional boundary conditions and dimensionless parameter definitions of Eq. (1), the dimensionless boundary conditions for the velocities and temperature become:

at $Z = 1$:

$$V_r = V_z = \Theta = 0, \quad V_\theta = R - C_1 \quad (10)$$

at $Z = -1$:

$$V_r = V_z = 0, \quad \Theta = 1, \quad V_\theta = \Gamma(R - C_1) \quad (11)$$

at $R = 1$ and $Z > \delta/2h$:

$$V_r = V_z = \partial\Theta/\partial R = 0, \quad V_\theta = 1 - C_1 \quad (12)$$

at $R = 1$ and $Z < -\delta/2h$:

$$V_r = V_z = \partial\Theta/\partial R = 0, \quad V_\theta = \Gamma(1 - C_1) \quad (13)$$

at $R = -1$ and $Z > \delta/2h$:

$$V_r = V_z = \partial\Theta/\partial R = 0, \quad V_\theta = -(1 + C_1) \quad (14)$$

at $R = -1$ and $Z < -\delta/2h$:

$$V_r = V_z = \partial\Theta/\partial R = 0, \quad V_\theta = -\Gamma(1 + C_1) \quad (15)$$

at $R = 1, -1$, and $|Z| < \delta/2h$:

$$V_r = V_z = \partial\Theta/\partial R = 0,$$

V_θ varies linearly across shroud axial clearance (16)

No natural pressure boundary conditions exist to solve Eq. (9). Additionally, a method must be implemented to satisfy the incompressibility constraint of Eq. (2). Both problems are addressed using an influence matrix approach generally credited to Kleiser and Schuman (1980), the implementation of which (including extensions to two nonperiodic directions) is explained in more detail by others (Canuto et al., 1988; Tuckerman, 1989; Madabhushi et al., 1992). The influence matrix approach provides a direct noniterative method to determine the pressure field that ensures that the incompressibility constraint is satisfied at every interior point and on the boundary.

After obtaining the dimensionless temperature distribution from Eq. (6), local Nu (the dimensionless temperature gradient) are calculated on the surface of each disk. The area averaged Nu is then determined by performing an appropriate integration:

$$\mathrm{Nu}_{avg} = \frac{1}{2C_1}\int_{R_i}^{R_o} \mathrm{Nu}(R - C_1)dR \quad (17)$$

Numerical Approach

To solve the conservation equations at each time step, a Chebyshev collocation spectral method is used with no dealiasing (Canuto et al., 1988). The Chebyshev collocation approach is often preferred over a pseudo-spectral approach due to the simplicity in specifying the boundary conditions, a slight improvement in convergence characteristics, and the elimination of the need to transfer back and forth between physical and wave number space. The physical variables to be determined (velocities, pressure, and temperature) are represented by series expansions of Chebyshev polynomials on a Gauss-Lobatto grid in both the radial and axial directions. This approach enables one to generate matrices of first and second derivative operators for calculating the spatial derivatives in the conservation equations. The equations {Eqs. (4–6, 9)} may then be manipulated to take on the form of a Helmholtz equation, which can be efficiently solved utilizing matrix diagonalization techniques (Haidvogel and Zang, 1979; Yang and Shizgal, 1994).

At each time step, the solution proceeds by first solving for the temperature field. Assuming boundary pressures of zero, a complementary pressure field and accompanying V_r and V_z are calculated. Then employing the predetermined influence matrix, the corrections to the boundary pressures are determined that will ensure a divergence-free velocity field. Using these boundary pressures, an implicitly determined particular pressure field, and finally the new V_r, V_z, and V_θ values are calculated at the new time step (Madabhushi et al., 1992).

Based on a time stepping study that considered agreement in locally probed quantities and the minimum time step required to resolve the highest frequency information, a dimensionless time step of 0.001 was used for all time-dependent results. Time averaged quantities are calculated by sampling the quantity of interest at intervals of 300 time steps and by taking a sufficient number in the sample such that the calculated average is reasonably insensitive to the number of samples or the sampling range.

Finer grid resolutions are required as Re is increased due to increasing flow complexity and thinning Ekman layers, the latter of which is well addressed by the cosine distribution of the Gauss-Lobatto points. Grid independence was determined by comparing velocity profiles, time averaged Nu_{avg}, and power spectra of the velocity time series (at selected probe points) for different grid resolutions. The decay of the Chebyshev expansion coefficients in both the r and z directions was also examined. The profiles of the time averaged velocity in Fig. 2 using four different Gauss-Lobatto grid resolutions (60×20, 80×30, 120×40, and 160×50 $\{R \times Z\}$) and using the parameter combination yielding the most chaotic flow ($\Gamma = -1.0$ and $\mathrm{Re} = 1 \times 10^5$) clearly demonstrate the convergence of the solution with increasing resolution. The power spectra of the velocity time series (not shown) display similar convergence characteristics. For the Chebyshev coefficients, a decay of at least two orders of magnitude was considered to indicate adequate grid resolution, but larger decays were typically achieved. Tests were also performed to confirm that asymmetries observed in the numerical results were not caused by asymmetries in the formulation or the numerical implementation. Though the grid study indicates that less dense grids would be acceptable, for $\mathrm{Re} = 1 \times 10^5$ and $\Gamma = -1.0$, a 160×50 grid was used, whereas less dense grids were used for the other cases of Γ at $\mathrm{Re} = 1 \times 10^5$ due to their less chaotic behavior. For $\mathrm{Re} = 5 \times 10^4$, a grid of 120×40 was used and cases of lower Re used a grid of 70×30 for all values of Γ.

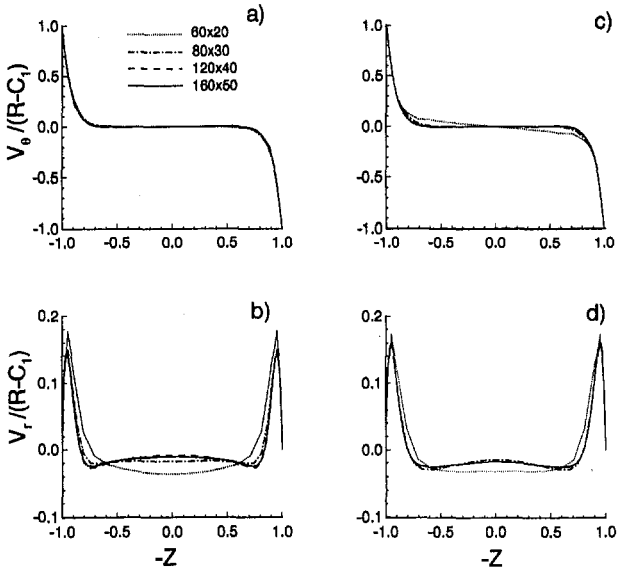

Fig. 2 Time averaged velocity profiles between disks for Re = 1×10^5 and $\Gamma = -1.0$ using different grid resolutions: (*a*) V_θ at $r/r_o = 0.6$, (*b*) V_r at $r/r_o = 0.6$, (*c*) V_θ at $r/r_o = 0.85$, and (*d*) V_r at $r/r_o = 0.85$

Results and Discussion

The domain of interest is taken to be of fixed size and based on the experimental and numerical work of Kilic et al. (1994), with the following values for the geometric parameters (Fig. 1): $r_i/r_o = 0.13$, $h/r_o = 0.06$, and $\delta/r_o = 0.016$. With these values, the axial shroud clearance represents 13.3 percent of the disk spacing. The dimensionless parameters considered are Re varying from 1×10^3 to 1×10^5, Pr fixed at 0.707, and $\Gamma = -1.0$, -0.4, and 0.0.

Disk Rotation Ratio $\Gamma = -1.0$. At low Re, the flow is steady and symmetric about the $Z = 0$ plane. The streamlines of the secondary flow formed by the radial and axial components of the velocity are shown in Fig. 3. The flow is of the Batchelor type (1951) in which radial outflow is present in a boundary layer on each disk, radial inflow is present in a shear layer about the midplane ($Z = 0$), and azimuthally rotating cores of fluid exist on either side of the midplane.

The solution remains symmetric as Re is increased until a pitchfork bifurcation is encountered between Re = 6×10^3 and 7×10^3. This bifurcation point was determined by obtaining steady-state solutions at several Re, from which the magnitude of V_θ was extracted from a point on the midplane. The midplane V_θ magnitude is zero for the symmetric solution, but is nonzero and increases with Re as the degree of asymmetry about $Z = 0$ also increases. Figure 4 shows the secondary flow streamlines for the two asymmetric stable steady-state solutions at Re = 1×10^4. It should be noted that a symmetric solution can also be obtained above the critical Re provided the initial conditions are perfectly symmetric. However, this third solution was found to be unstable, yielding one of the asymmetric solutions when subjected to finite random perturbations. A pitchfork bifurcation was also found for a co-rotating disk system in axisymmetric simulations by Iglesias and Humphrey (1996).

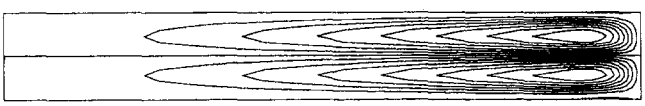

Fig. 3 Secondary streamlines for flow in the *r–z* plane with Re = 1×10^3 and $\Gamma = -1.0$

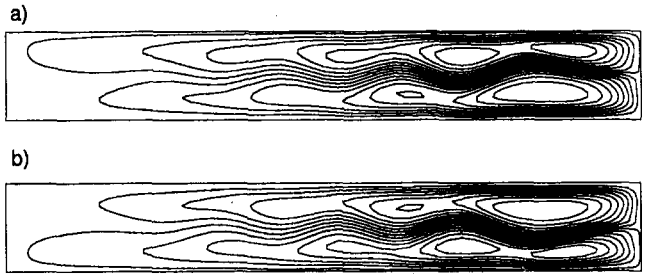

Fig. 4 Secondary streamline solution pair for flow in the *r–z* plane at Re = 1×10^4 and $\Gamma = -1.0$

A subcritical Hopf bifurcation is found between Re = 1.12×10^4 and 1.13×10^4. The subcritical nature of the bifurcation was determined by 1) finding a steady solution branch up to approximately Re = 1.15×10^4 when the solution is approached from below and 2) finding an unsteady oscillatory branch down to 1.13×10^4 when the solution is approached from an oscillatory solution at higher Re. The fundamental frequency of the oscillation is 0.27 Hz.

As Re is increased further, the flow increases in temporal and spatial complexity, first slowly, then in a rather abrupt manner as shown by the Fig. 5 phase plots (velocity at a point versus velocity at another point traced as a function of time). One of the probe points for the phase plots is located slightly off the midplane near the outer shroud, while the other is located near the center of the computational domain. From Re = 1.13×10^4 to 1.5×10^4, oscillations at the fundamental frequency (as determined from power spectra of the time series) increase in amplitude. The fundamental frequency itself decreases slightly from 0.27 to 0.23 Hz. The number of harmonics of the fundamental frequency also increases over this range. Between Re = 1.5×10^4 and 1.6×10^4, a subharmonic frequency emerges and the flow becomes aperiodic, then transitions to chaotic flow between 1.6×10^4 and 1.7×10^4. However,

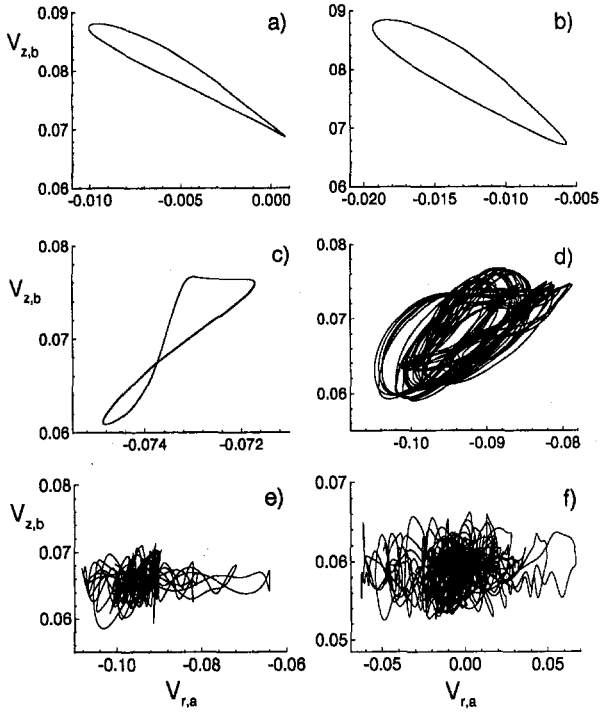

Fig. 5 Phase plots for $\Gamma = -1$ at increasing Re: (*a*) Re = 1.14×10^4, (*b*) Re = 1.18×10^4, (*c*) Re = 1.5×10^4, (*d*) Re = 1.6×10^4, (*e*) Re = 1.7×10^4, and (*f*) Re = 2×10^4

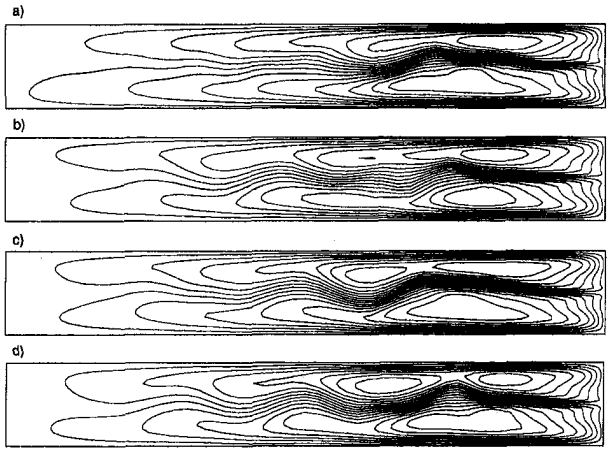

Fig. 6 Secondary streamlines for Re = 2×10^4 at time increments relative to an arbitrary time τ_0: (*a*) $\tau = \tau_0$, (*b*) $\tau = \tau_0 + 10$, (*c*) $\tau = \tau_0 + 20$, (*d*) $\tau = \tau_0 + 30$

even though the flow becomes temporally chaotic, the general character of the flow resembles that of the pitchfork bifurcation shown in Fig. 4(*a*). The secondary flow for Re = 2×10^4, shown in Fig. 6 in a sequence of snapshots spaced 10 dimensionless time units apart (and uncorrelated at this time spacing), appears similar to Fig. 4(*a*), indicating that the Fig. 6 flow is on that particular branch of the solution space. Similarly, the sequence of secondary streamlines at Re = 5×10^4 (spaced 2 dimensionless time units apart) shown in Fig. 7 indicates a stronger radially outward flow on the bottom disk than on the top disk and resembles Fig. 4(*a*) in the area near the outer shroud where the fluid is preferentially thrust toward the top disk.

Disk Rotation Ratio $-1.0 < \Gamma \leq 0.0$. Depending on the system of interest, when symmetry conditions are broken such as in the case of reducing the rotational speed of the top disk (i.e., $|\Gamma| \neq 1.0$), one solution branch (see Fig. 4) remains preferred while the other may move away quickly or slowly. (See Drazin and Reid (1981) or Manneville (1990) for a general discussion of pitchfork and imperfect bifurcations, as encountered here.) To determine how quickly the branches separate, solutions were restarted using each of the two mirror image solutions of Fig. 4 while decreasing the magnitude of Γ at Re = 1×10^4. For $\Gamma = -0.999$, it is possible to obtain a solution

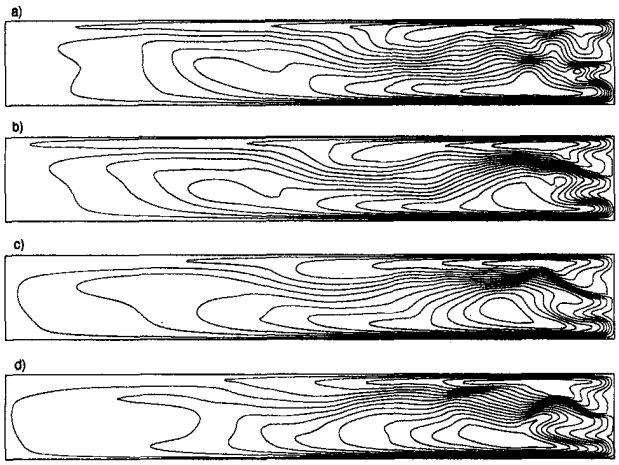

Fig. 7 Secondary streamlines for Re = 5×10^4 at time increments relative to an arbitrary time τ_0: (*a*) $\tau = \tau_0$, (*b*) $\tau = \tau_0 + 2$, (*c*) $\tau = \tau_0 + 4$, (*d*) $\tau = \tau_0 + 6$

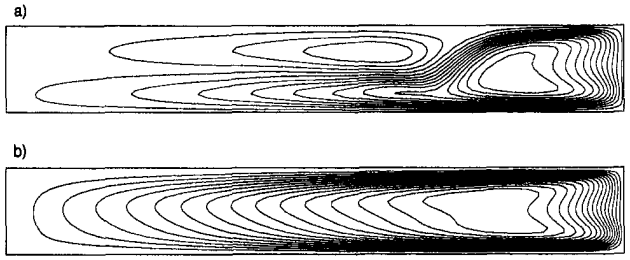

Fig. 8 Secondary streamlines at Re = 1×10^4: (*a*) $\Gamma = -0.4$ and (*b*) $\Gamma = 0.0$

on both the preferred (primary) and nonpreferred (secondary) branches. However, both mirror image initial conditions produced the same steady-state results for $\Gamma = -0.990$, indicating that the nonpreferred branch moves away very quickly and that steady-state and time averaged solutions for the other cases considered ($\Gamma = -0.4$ and 0.0) are not dependent on the initial conditions.

Figure 8 provides an indication of the changes in the flow structure as Γ approaches zero from negative values at fixed Re = 1×10^4 (where the flow is steady). The flow gradually changes from one in which boundary layers of radial outflow are present on both disks and a shear layer of radial in-flow exists about the midplane (Figs. 3 and 4 for $\Gamma = -1.0$) to one in which the radial outflow occurs in a boundary layer on the rotating disk and radial inflow is present in a boundary layer on the stationary disk (Fig. 8(*b*)). At intermediate values of Γ, on the slower (top) disk radial outflow, is present on the inner portion and radial inflow is present on the outer portion of the disk (Fig. 8(*a*)). The location at which this change from radial outflow to inflow occurs is dependent on Re as well as Γ and changes drastically with time for chaotic conditions.

The slowing of the top disk also affects the transitional behavior of the flow with Re. The gradual removal of the shear flow about the midplane as Γ changes from -1.0 to 0.0 is considered the primary contributor to a stabilizing effect. As an indication of the reduced temporal complexity as Γ increases to 0.0, Fig. 9 shows the power spectral density of the V_θ time series at the probed location near the outer shroud for $\Gamma = -1.0$ and -0.4 for Re = 5×10^4. At this Re, the $\Gamma = 0$ case is steady. From Fig. 9, it is clear that at $\Gamma = -1.0$, the flow is fully chaotic with numerous modes contributing to the temporal response whereas at $\Gamma = -0.4$, the flow has just begun to oscillate. At Re = 1×10^5, the $\Gamma = 0.0$ case has also begun to oscillate and the $\Gamma = -0.4$ case has passed through aperiodicity to chaotic flow.

Thermal Response. As with the flow, changing Re and Γ have a profound effect on the heat transfer between the disks. The temperature contours of Fig. 10 provide an indication of the influence of changing Γ at Re = 2×10^4. (Note that at this Re, the flow is steady for $\Gamma = -0.4$ and 0.0 but unsteady for

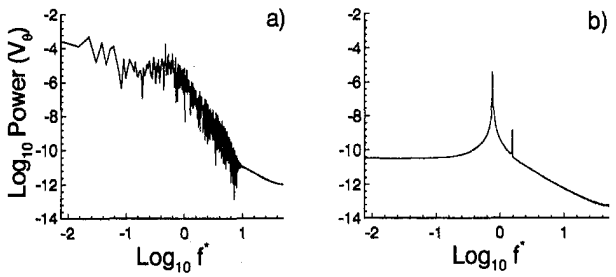

Fig. 9 Power spectral density at Re = 5×10^4: (*a*) $\Gamma = -1.0$ and (*b*) $\Gamma = -0.4$

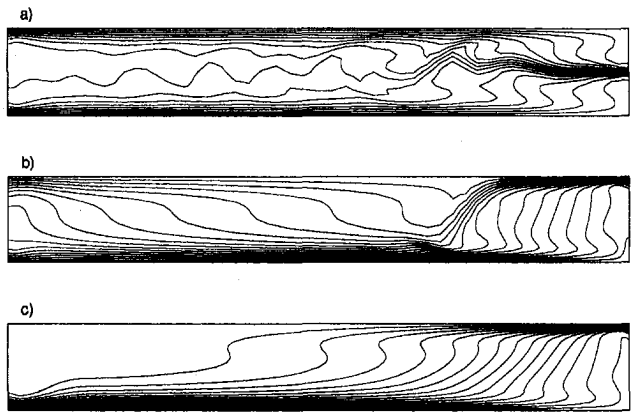

Fig. 10 Dimensionless temperature contours at Re = 2×10^4 (15 equal increments ranging from 0.0 at the bottom to 1.0 at the top): (*a*) $\Gamma = -1.0$, (*b*) $\Gamma = -0.4$, and (*c*) $\Gamma = 0.0$

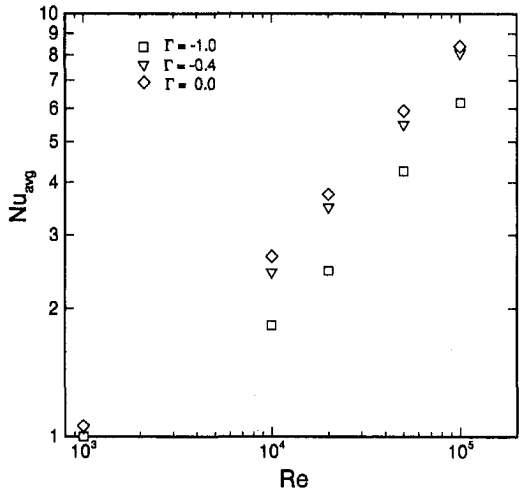

Fig. 12 Time and area averaged Nusselt number variation with Re

$\Gamma = -1.0$.) Figure 11 shows the time averaged Nu for the top and bottom disks corresponding to the same Re as the Fig. 10 temperature contours (note the different scale for Fig. 11(a)). The curves for $\Gamma = -1.0$ alternately cross one another approximately 180 deg out of phase, and the top disk Nu is slightly greater than that of the lower disk near the outer radius and slightly less than the lower disk near the inner radius. This observation is consistent with the flow behavior noted above and shown at various time snapshots in Fig. 6, providing further evidence that even though the flow is temporally varying in a chaotic fashion here, spatially the flow is well organized and in the mean is similar to the steady flow of Fig. 4(a).

The heat transfer behavior for $\Gamma = -0.4$ and 0.0 shown in Fig. 11(b–c) is consistent with the flow observations drawn from Fig. 8 and 10. Unlike the $\Gamma = -1.0$ case, the fluid for $\Gamma = -0.4$ and 0.0 leaves the cold bottom disk and directly strikes the top disk resulting in the relatively high (low) Nu on the top (bottom) disk in the region near the outer radius. The stagnation point, where the flow changes from radially outward to radially inward on the top disk, is evident for the case of $\Gamma = -0.4$ where the temperature gradients of Fig. 10(b) decrease and Nu drops sharply to near zero before rising again as the outer shroud is approached.

Figure 12 provides a plot of the time and area averaged Nu as a function of Re over the range of parameters tested. Area averages were calculated by Eq. (17) using the Clenshaw-Curtis quadrature (Canuto et al., 1988). Note that the averages for the top and bottom disks differed slightly for the nonsteady cases due to the time averaging, but the difference was less than 0.1 percent. Nusselt numbers are seen to increase rapidly as Re increases beyond the conduction regime at Re = 1×10^3. The onset of chaos for the $\Gamma = -1.0$ case appears to have less effect on Nu than the characteristics of the overall flow structure. The cases with fluid from the faster rotating disk contacting the slower disk over a larger portion of the slower disk have the largest Nu for the range of Re considered, i.e., Nu increases as Γ approaches zero.

Comparison With Experimental Data

In Fig. 13, the time averaged axial variation of V_r and V_θ are shown at $r/r_o = 0.6$ and 0.85 for $\Gamma = -1.0$ and Re = 1×10^5.

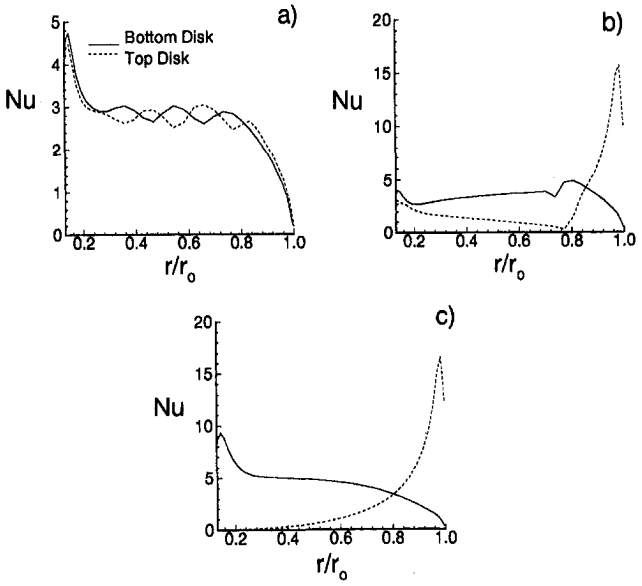

Fig. 11 Time averaged local Nusselt number values along the top and bottom disks at Re = 2×10^4: (*a*) $\Gamma = -1.0$, (*b*) $\Gamma = -0.4$, and (*c*) $\Gamma = 0.0$

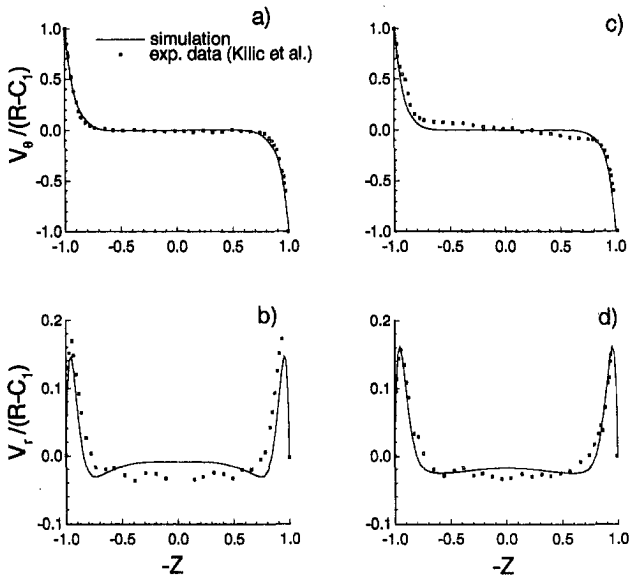

Fig. 13 Time averaged velocity profiles between disks for Re = 1×10^5 and $\Gamma = -1.0$: (*a*) V_θ at $r/r_o = 0.6$, (*b*) V_r at $r/r_o = 0.6$, (*c*) V_θ at $r/r_o = 0.85$, and (*d*) V_r at $r/r_o = 0.85$

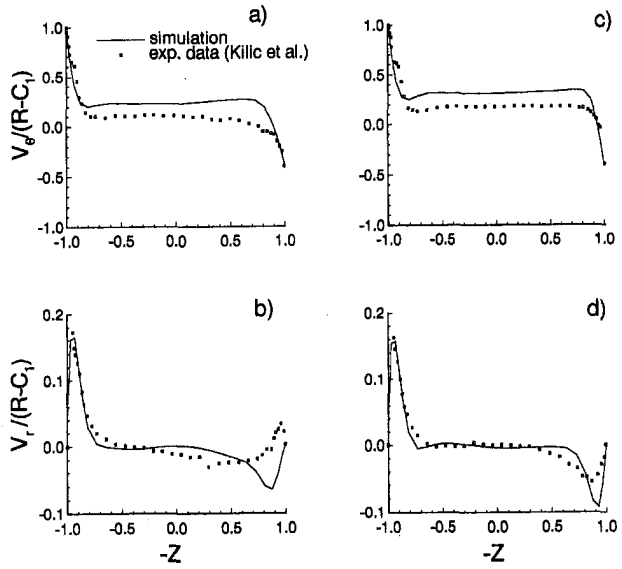

Fig. 14 Time averaged velocity profiles between disks for Re = 1×10^5 and $\Gamma = -0.4$. (*a*) V_θ at $r/r_o = 0.8$, (*b*) V_r at $r/r_o = 0.8$, (*c*) V_θ at $r/r_o = 0.85$, and (*d*) V_r at $r/r_o = 0.85$

Each profile is normalized by $(R - C_1)$, which is the local V_θ for disk 1 (see Eq. (10)). Assuming that the results represent one of a pair of solution branches, the numerical ensemble used in the averaging is doubled by including the mirror image solutions about the $Z = 0$ symmetry line (Sirovich, 1987). Experimental data taken from the literature (Kilic et al., 1994) are also shown in the figure as the discrete points. For the case of $r/r_o = 0.6$, the V_θ solution agrees well with the data, whereas the V_r agreement is less impressive, with the maximum value being low relative to the data and there being an apparent decrease in magnitude about the midplane that is not observed in the data. At $r/r_o = 0.85$, the agreement for V_r is much better. Also at this location, the V_θ data follow a visible nonzero slope about the midplane, but the numerical solution does not. Though not shown here, agreement with experimental data at $\Gamma = 0.0$ is qualitatively similar.

Figure 14 shows profiles of the time averaged V_r and V_θ at $r/r_o = 0.8$ and 0.85 for $\Gamma = -0.4$ and Re = 1×10^5. Unlike the cases of $\Gamma = -1.0$ and 0.0, where the agreement with experiment is reasonable, the agreement between simulation and experiment for $\Gamma = -0.4$ is not very good. The core rotation (V_θ) is substantially overpredicted relative to that observed in the data (Figs. 14(a), 14(c)). Also, the point on the slower disk at which the flow is observed to change from radial outflow to inflow is between $r/r_o = 0.8$ and 0.85 according to the data but occurs below $r/r_o = 0.8$ in the simulation (Figs 14(b) and 14(d)). Although these results appear discouraging, it is noted that the simulation results here are qualitatively very similar to those of Kilic et al. (1994) who used a low order steady-state scheme with a turbulence model. Preliminary results obtained using a three-dimensional extension of the Chebyshev spectral method show much better agreement with the experimental data. The relative agreement of the axisymmetric simulations reported here with those of Kilic et al., combined with the preliminary three-dimensional results, lead to the speculation that the differences between experiment and axisymmetric simulation results are due to three dimensional effects. This assertion is being investigated further and will be reported in a future paper.

Summary and Conclusions

Flow and heat transfer behavior have been presented for two counter-rotating disks at various rotation speed ratios and Re using a fixed and enclosed geometry. For the case of the disks rotating at the same speed ($\Gamma = -1.0$), the flow undergoes first a pitchfork bifurcation, then a subcritical Hopf bifurcation, transitioning eventually to chaotic flow with increasing Re. A similar route to unsteady flow has been observed for a corotating disk system (Iglesias and Humphrey, 1996). Reducing the rotational speed of one disk relative to the other is stabilizing (unsteady flow occurs at higher Re) due to the gradual elimination of a midplane shear layer that flows radially inward for the $\Gamma = -1.0$ case. The numerical results obtained for the $\Gamma = -1.0$ case are apparently from one of the two pitchfork bifurcation paths, since with mirror image data duplication and subsequent averaging, the averaged profiles match turbulent experimental data (Kilic et al., 1994) reasonably well. Simulations for $\Gamma = -0.4$ poorly resemble experimental data but are quite similar to other numerical results (Kilic et al., 1994). Based on agreement with other researchers' numerical results and preliminary three-dimensional extensions of the method used herein, discrepancies between the numerical and experimental results are attributed to the assumption of axisymmetry in the simulations. For increasing heat transfer between the disks, the overall flow structure dictated by Γ and increasing flow velocities with Re are more important than the temporal behavior of the flow for the range of Re considered.

Acknowledgments

The authors are indebted to SEMATECH for providing support and computational resources for this work. In particular, the support of E. H. Bogardus and F. T. Geyling is greatly appreciated. The assistance of D. C. Kuo of the University of Texas at Austin in model formulation and code development is also appreciated. Further support provided by the National Science Foundation under Grant Number CTS-9258006, the Pittsburgh Supercomputing Center under Grant Number CTS-960033P, and the University of Texas High Performance Computing Facility under a High Performance Computer Time Grant Award, is gratefully acknowledged. Any opinions, findings, and conclusions or recommendations expressed in this publication are those of the authors and do not necessarily reflect the views of the sponsors.

References

Batchelor, G. K., 1951, "Note on a Class of Solutions of the Navier-Stokes Equations Representing Steady Rotationally-Symmetric Flow," *Quarterly Journal of Mechanics and Applied Mathematics,* Vol. 4, pp. 29–41.

Bird, R. B., Stewart, W. E., and Lightfoot, E. N., 1960, *Transport Phenomena,* Wiley, New York.

Canuto, C., Hussaini, M. Y., Quateroni, A., and Zang, T. A., 1988, *Spectral Methods in Fluid Dynamics,* Springer, New York.

Drazin, P. G., and Reid, W. H., 1981, *Hydrodynamic Stability,* Cambridge, New York.

Gan, X., Kilic, M., and Owen, J. M., 1994, "Superposed Flow Between Two Discs Contrarotating at Differential Speeds," *International Journal of Heat and Fluid Flow,* Vol. 15, pp. 438–446.

Haidvogel, D. B., and Zang, T. A., 1979, "The Accurate Solution of Poisson's Equation by Expansion in Chebyshev Polynomials," *Journal of Computational Physics,* Vol. 30, pp. 167–180.

Holodniok, M., Kubicek, M., and Hlavacek, V., 1977, "Computation of the Flow Between Two Rotating Coaxial Disks," *Journal of Fluid Mechanics,* Vol. 81, pp. 689–699.

Holodniok, M., Kubicek, M., and Hlavacek, V., 1981, "Computation of the Flow Between Two Rotating Coaxial Disks: Multiplicity of Steady-State Solutions," *Journal of Fluid Mechanics,* Vol. 108, pp. 227–240.

Humphrey, J. A. C. and Gor, D., 1993, "Experimental Observations of an Unsteady Detached Shear Layer in Enclosed Corotating Disk Flow," *Physics of Fluids A,* Vol. 5, pp. 2438–2442.

Humphrey, J. A. C., Schuler, C. A., and Webster, D. R., 1995, "Unsteady Laminar Flow Between a Pair of Disks Corotating in a Fixed Cylindrical Enclosure," *Physics of Fluids A,* Vol. 7, pp. 1225–1240.

Iglesias, I. and Humphrey, J. A. C., 1996, "Two- and Three-Dimensional Laminar Flows Between Disks Corotating in a Fixed Cylindrical Enclosure," *Proceedings of the ASME Fluids Engineering Division,* FED-Vol. 242, O. K. Rediniotis et al., eds., ASME, New York, pp. 291–304.

Kilic, M., Gan, X., and Owen, J. M., 1994, "Transitional Flow Between Contra-Rotating Disks," *Journal of Fluid Mechanics,* Vol. 281, pp. 119–135.

Kleiser, L. and Shumann, U., 1980, *Notes on Numerical Fluid Mechanics,* E. H. Hirschel, ed., Vieweg, Graunschweig, pp. 165–173.

Madabhushi, R. K., Balachandar, S., and Vanka, S. P., 1993, "A Divergence-Free Chebyshev Collocation Procedure for Incompressible Flows With Two Non-Periodic Directions," *Journal of Computational Physics,* Vol. 105, pp. 199–206.

Manneville, P., 1990, *Dissipative Structures and Weak Turbulence,* Academic, New York.

Sirovich, L., 1987, "Turbulence and the Dynamics of Coherent Structures: Part II: Symmetries and Transformations," *Quarterly of Applied Mathematics,* Vol. XLV, No. 3, pp. 573–582.

Stewartson, K., 1953, "On the Flow Between Two Rotating Coaxial Disks," *Proceedings of the Cambridge Philosophical Society,* Vol. 49, pp. 333–341.

Szeri, A. Z., Schneider, S. J., Labbe, F., and Kaufman, H. N., 1983, "Flow Between Rotating Disks. Part 1. Basic Flow," *Journal of Fluid Mechanics,* Vol. 134, pp. 103–131.

Szeri, A. Z., Giron, A., Schneider, S. J., and Kaufman, H. N., 1983, "Flow Between Rotating Disks. Part 2. Stability," *Journal of Fluid Mechanics,* Vol. 134, pp. 133–154.

Tuckerman, L. S., 1989, "Divergence-Free Velocity Fields in Nonperiodic Geometries," *Journal of Computational Physics,* Vol. 80, pp. 403–441.

Yang, H. H., and Shizgal, B., 1994, "Chebyshev Pseudospectral Multi-Domain Technique for Viscous Flow Calculation," *Computer Methods in Applied Mechanics and Engineering,* Vol. 118, pp. 47–61.

Wall Pressure and Effective Wall Shear Stresses in Heat Exchanger Tube Inlets With Application to Erosion-Corrosion

D. G. Elvery
Graduate Student.

K. Bremhorst
Professor.

Department of Mechanical Engineering,
The University of Queensland,
Brisbane, Queensland, 4072
Australia

Inclined flow into tube inlets is studied in order to identify flow characteristics associated with enhanced erosion-corrosion rates at tube inlets. Measured wall pressures and shear stresses are presented for inlet flow with inclination angles up to 60 deg for a tube Reynolds number of 71,000. These show that the areas with most potential for wear are located near the reattachment point of the recirculation bubble as well as in regions at the downstream side of the tube inlet. The latter are located opposite the recirculation region but away from the symmetry plane due to strong swirl of the flow in that region. The results are related to erosion-corrosion patterns observed in practice.

1 Introduction

Erosion-corrosion is a serious problem in the mineral processing industry. The problem plagues many components such as pumps, impellers, valves and tube inlets of shell and tube heat exchangers. Typically, the main mode of metal loss is corrosion, which is an electrochemical phenomenon depending on the chemical properties of the working fluid, but the hydrodynamics of the flow act to greatly accelerate the metal loss rate by preventing the formation of a protective oxide film on the surface under attack thereby allowing further corrosion to take place.

Tubes in shell and tube heat exchangers commonly are subject to high rates of erosion-corrosion in localized areas of banks of tubes as well as in the inlet of individual tubes. In some cases, the corrosion can be so severe that the first few diameters of tubes can be lost within weeks of new tubes being fitted while the remainder of the tube is almost unaffected. There is a direct correlation between the flow angle of impingement and the metal loss observed on the tube (Bremhorst and Lai, 1979). Generally, the higher the angle of impingement, the greater the observed metal loss with angles of impingement of over 40 deg not uncommon in typical shell and tube heat exchangers (Bremhorst and Flint, 1991).

Many possible mechanisms for a lack of formation or destruction of the oxide film have been suggested including cavitation wear, bubble impact erosion, erosion by fluctuating fluid shear forces (Nesic and Postlethwaite, 1990), particulate erosion and film dissolution. Those mechanisms dominated by chemical reactions can have a flow velocity dependence of the mass transfer processes. Since the latter are fundamentally the same as convection controlled heat transfer, hot-film anemometers can be used to measure the heat transfer rate which in turn allows calculation of wall shear stress (Bellhouse and Schultz, 1966) and mass transfer rate.

Few prior studies exist which give quantitative data of the effect of flow at the wall of the inlet when the incoming flow direction and the tube axis are not aligned. Visualization studies by Legkii and Rogachev (1989a and b) show a complex flow structure exists even for the simplest case of coincidence between flow direction and tube axis. Maciejewski and Moffat (1992) highlight the effect of very high turbulence generated just downstream of the leading edge of a plate inclined to approaching flow and the effect on heat transfer. Such work, however, gives no indication of other possible areas of enhanced heat transfer, and hence mass transfer, in the inlet region of tubes inclined to the approaching flow and cannot explain the erosion-corrosion patterns found in practice.

In the present work, experimentally obtained wall pressure distributions, equivalent fully developed flow velocities and wall shear stress measurements are presented for the first 5 diameters of the tube followed by a comparison of metal loss patterns observed in practice.

2 Experimental Facility

The experiments used a simulated heat exchanger tube bank containing tubes of 32 mm internal diameter, Fig. 1. The central tube could be rotated freely about its axis through 360 deg enabling the wall pressure and wall shear stress distributions to be determined around tube as a function of θ. Pressure tappings were located at various intervals down the tube to obtain measurements as a function of downstream distance from the inlet. Wall shear stress distributions were obtained by mounting a hot-film gauge on an insert which could be moved along a slotted tube as shown in Fig. 2. The experimental test rig was hinged so that the whole tube bank could be rotated to experience angles of flow incidence, α, up to 60 deg. The measurement accuracy for α and θ was ± 0.5 deg while that for z was ± 0.25 mm. The working fluid was air with experiments conducted at a Reynolds number of 71000 based on the tube diameter ($\mathrm{Re} = \rho d V/\mu$).

Wall pressures were measured using an Airflow Developments inclined tube manometer with a range of 0 to 2500 Pa. The flow rate in the measuring tube was set by using an Airflow Developments Pitot-static probe inserted into the flow at 13 diameters from the tube inlet. A measure of the wall shear stress was obtained using DANTEC hot-film gauges, type 55R47 which were glued to an acrylic insert to minimise conduction losses (Fig. 2). The gauges were operated as constant temperature anemometers (CTAs) with the mean probe output voltage, E, being obtained by using a 0.2 Hz low pass filter linked to a digital multimeter.

Contributed by the Fluids Engineering Division for publication in the JOURNAL OF FLUIDS ENGINEERING. Manuscript received by the Fluids Engineering Division November 10, 1995; revised manuscript received July 8, 1997. Associate Technical Editor: Jong H. Kim.

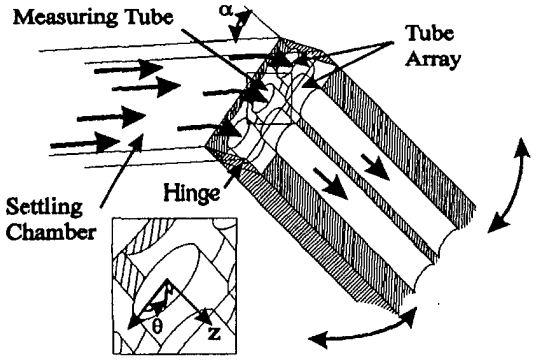

Fig. 1 Schematic of experimental test rig

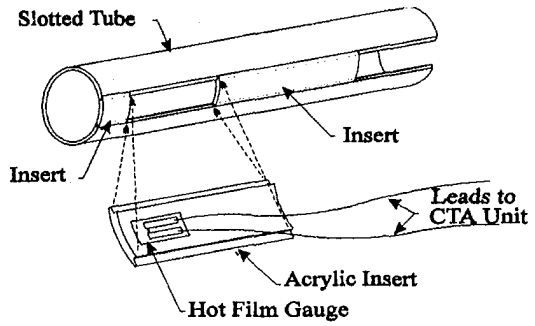

Fig. 2 Hot-film anemometer insert assembly

3 Hot-Film Gauges and Wall Shear Stresses

When operated in the CTA mode, the gauges measure heat transfer from the hot-film to the air flow. The shear stress, τ_w, in a laminar flow has been found to be related to the convected local heat transfer rate, Q_h, (Bellhouse and Schultz, 1966; Liepmann and Skinner, 1954; Menendez and Ramapriam, 1985) according to the relation

$$\tau_w \propto Q_h^3 \tag{1}$$

The above equation can also be used to give the mean wall shear stress in turbulent flows when the thermal boundary-layer generated by the hot-film gauge is completely within the viscous sublayer of the turbulent boundary-layer. The total heat transfer rate, Q_t, is a linear function of the square of the hot-film probe output voltage thus giving

$$Q_t = Q_h + Q_s = A_1 E^2 + B_1 \tag{2}$$

where A_1 is a constant based on the resistance of the hot-film probe and the value of the other resistances in the Wheatstone bridge. Q_s is the heat lost to the substrate of the gauge, which is a constant for CTA operation. Combining (1) and (2), the wall shear stress can be written as

$$\tau_w \propto (A_2 E^2 + B_2)^3$$

$$\text{or} \quad \tau_w = A_3 E^6 + B_3 E^4 + C_3 E^2 + D_3 \tag{3}$$

The four constants were obtained from measurements of anemometer voltage and mean flow velocity at 15 diameters downstream from a bell-mouth entrance where the wall shear stress is already at its fully developed value (Barbin and Jones, 1963). Conversion of mean tube velocity to shear stress required in (3) was by means of the Prandtl friction law (4).

$$\frac{1}{\sqrt{c_f}} = 4 \log_{10} \{ \mathrm{Re} \sqrt{c_f} \} - 0.4 \tag{4}$$

Measured wall shear stresses are reported as effective fully developed velocities. These are the mean tube velocities which for fully developed flow, result in a gauge voltage and hence a shear stress equivalent to that at the measurement location.

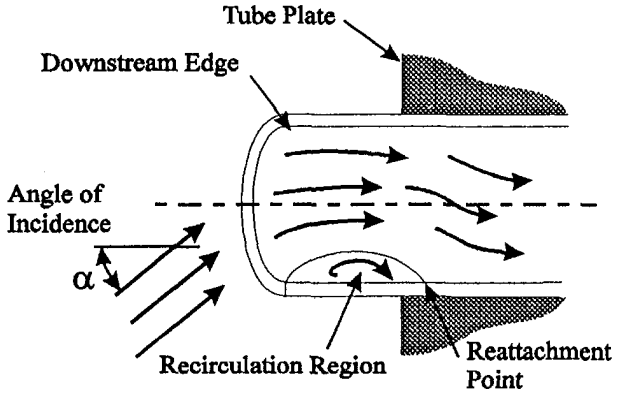

Fig. 3 Reentrant tube inlet flow field

4 General Flow Field

The general flow field of inclined flow into a re-entrant inlet is shown in Fig. 3. On the upstream side of the tube, a recirculation region is generated (Legkii and Rogachev, 1989a and 1989b), while on the downstream side, an accelerated flow results due to a funnelling effect as fluid flows around the edge of the tube and the presence of the recirculation region. These features can be identified from the flow visualization of Fig. 4 which shows the inlet flow for $\alpha = 20$ deg using dye in a water channel.

5 Wall Pressure Measurements

Wall pressures were recorded at circumferential intervals of 30 deg from the upstream flow direction ($\theta = 0$ deg). Corre-

Nomenclature

A, B, C, D = constants
c_f = coefficient of friction $\tau_w / \frac{1}{2}\rho V^2$
c_p = coefficient of pressure $(P - P_{\text{chamber}})/\frac{1}{2}\rho V^2$
E = constant temperature anemometer output voltage
d = inside diameter of tube
P = pressure
P_{chamber} = rig pressure far upstream of the tube
P_{vap} = vapour pressure
Q_h = convective heat transfer rate
Q_s = conductive heat transfer rate
Q_t = total heat transfer rate
Re = Reynolds number
V = mean tube velocity
V_{eff} = effective fully developed velocity corresponding to a given heat transfer rate
z = distance from tube inlet
α = angle of incidence
μ = dynamic viscosity
ρ = density
σ = cavitation number
τ_w = wall shear stress
θ = angle from the upstream direction

Subscripts

1, 2, 3 = identifiers for constants
w = wall

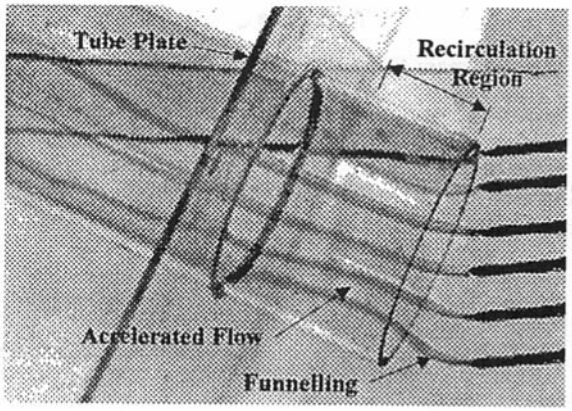

Fig. 4 Flow visualization of inlet flow field

sponding pressure coefficients are shown in Figs. 5–8. At an angle of incidence of $\theta = 0$ deg, the flow is nearly axisymmetric, leading to little variation in the pressures around the tube. For angles of attack not equal to zero, there is significant variation of pressures around the tube. The trends apparent in the first half a diameter of the tube are due to the vena contracta effect at the tube inlet which gives rise to the recirculation region shown in Fig. 3.

The local minima in the pressure profiles—observed at about 0.25 diameter for $\theta \leq 90$ deg—are located in the diametral plane through the centre of the recirculation region. Here the velocity reaches a maximum due to the constricted flow. Reattachment of the flow occurs between 0.5 and 1 diameter after which the flow expands to the full extent of the tube cross-section accompanied by an increase in pressure. The exact position of reattachment cannot be identified from the wall pressures since the flow continues to redistribute downstream of the reattachment point. On the downstream side of the tube inlet, the impinging flow suppresses any separation that might be promoted by funnelling. For $\alpha > 0$ deg, the dynamic pressure component of the impinging flow gives a maximum at $\theta = 180$ deg between $z/d = 0.2$ and 0.5. As the angle of incidence increases, the location of these maximum pressures shifts toward the inlet of the tube.

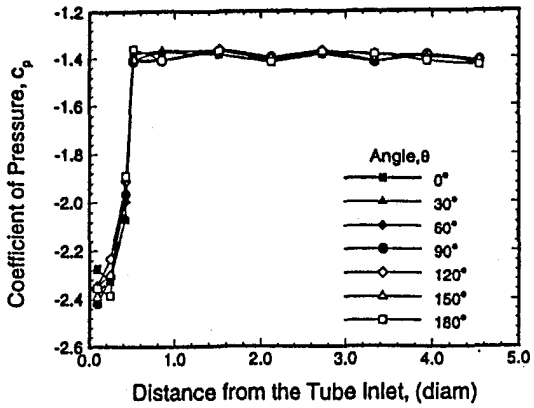

Fig. 5 Wall pressures inside the tube at $\alpha = 0$ deg. Estimated accuracy for c_p is ±1.2 percent.

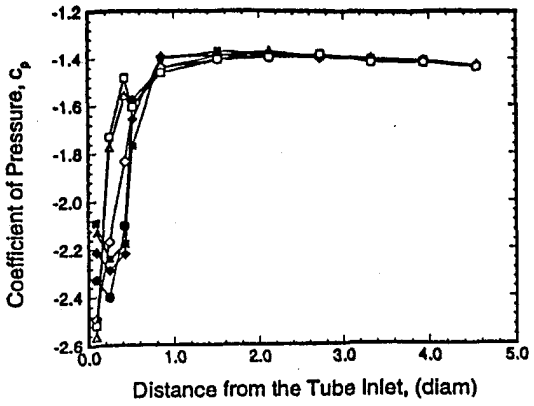

Fig. 6 Wall pressures inside the tube at $\alpha = 20$ deg. Estimated accuracy for c_p is ±1.2 percent.

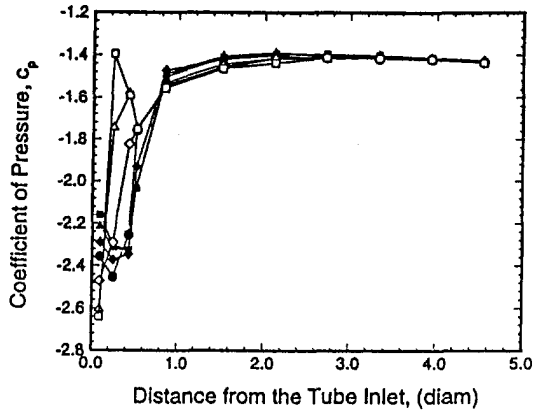

Fig. 7 Wall pressures inside the tube at $\alpha = 40$ deg. Estimated accuracy for c_p is ±1.2 percent.

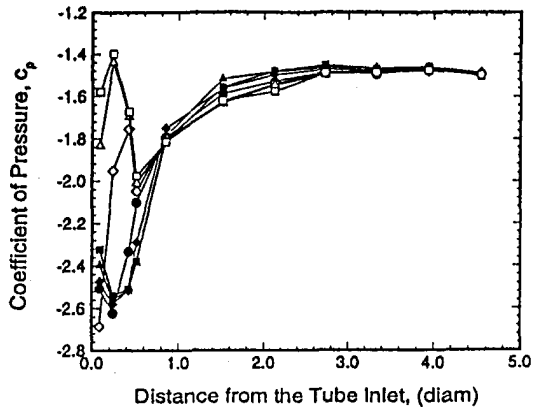

Fig. 8 Wall pressures inside the tube at $\alpha = 60$ deg. Estimated accuracy for c_p is ±1.2 percent.

In the region $z/d > 1.0$, a dynamic pressure exists due to the small radial velocity component toward the wall associated with the expanding flow downstream of the recirculation region giving rise to the difference between the pressures on the upstream ($\theta < 90$ deg) and the downstream ($\theta > 90$ deg) sides of the tube. Following the flow redistribution, wall friction leads to a constant pressure gradient.

For cavitation in a liquid flow to be a feasible wear mechanism, the local pressure must drop to the level of the saturation pressure of the liquid. Cavitation is likely to occur when $\sigma \leq 0$, where σ is the cavitation number defined as

$$\sigma = \frac{P - P_{vap}}{\frac{1}{2}\rho V^2} \tag{5}$$

By assuming dynamic similarity based on the coefficients of pressure, the present experimental data can be applied to conditions in actual heat exchangers. It is seen that except for

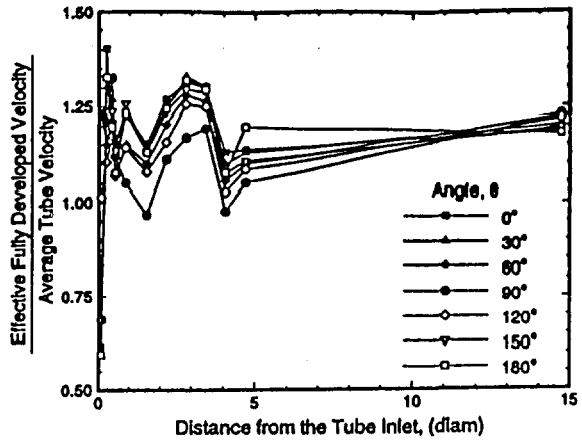

Fig. 9 Effective fully developed velocities for $\alpha = 0$ deg. Estimated accuracy for V_{eff}/V is ±4 percent.

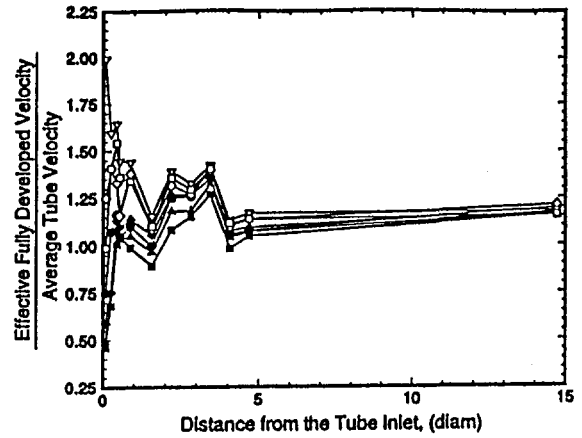

Fig. 10 Effective fully developed velocities for $\alpha = 20$ deg. Estimated accuracy for V_{eff}/V is ±4 percent.

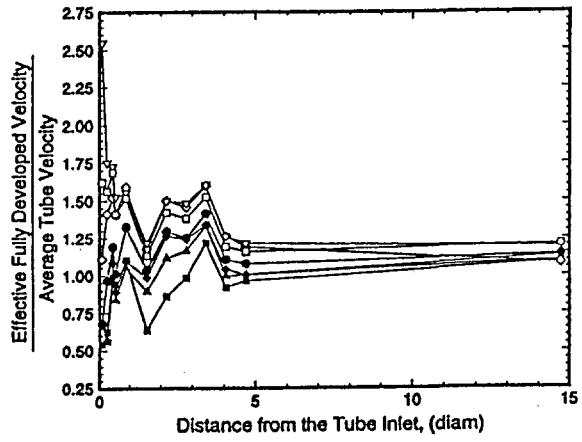

Fig. 11 Effective fully developed velocities for $\alpha = 40$ deg. Estimated accuracy for V_{eff}/V is ±4 percent.

operation below or near the saturation pressure, cavitation is unlikely to occur.

6 Effective Velocity and Shear Stress Measurements

Wall shear stress measurements are shown in Figs. 9–12 in terms of the effective fully developed velocity. The results presented are complex and difficult to interpret as a high heat

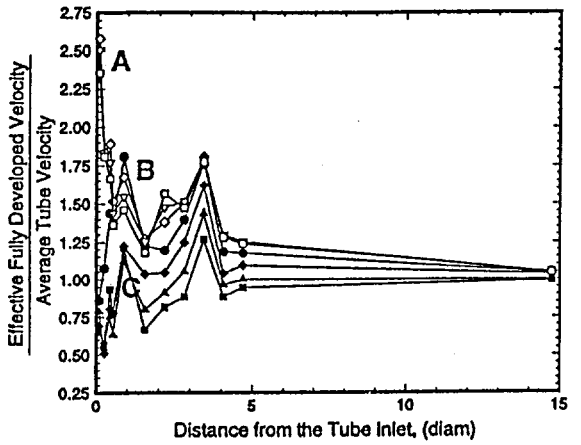

Fig. 12 Effective fully developed velocities for $\alpha = 60$ deg. Estimated accuracy for V_{eff}/V is ±4 percent.

transfer rate could be the result of a high turbulence level such as at the reattachment point or as a result of a high mean velocity gradient near the wall. However, through use of the effective fully developed velocity concept, it is readily seen that in the inlet region for large angles of flow inclination, effective velocities up to 2.5 times that of the mean velocity are experienced. This readily explains why flow at large angles is associated with high erosion-corrosion at tube inlets as high velocities are known to accelerate corrosion.

Within the region $z/d < 0.5$, it is apparent from Figs. 9–12 that the highest effective velocities occur at the downstream side of the tube at $\theta = 150$ deg for $\alpha = 20$ deg and 40 deg and at $\theta = 120$ deg for $\alpha = 60$ deg, not at $\theta = 180$ deg as one would expect. Between 120 and 150 deg is a significant circumferential component of velocity (Elvery, 1995) which does not exist at the axis of symmetry position of 180 deg thus leading to a large velocity at these angles. In contrast, the lowest effective velocities are located at $\theta = 0$ deg within the recirculation region where there is a high turbulence intensity (ratio of root-mean-square of velocity fluctuation to mean velocity) but a very small mean velocity. The location of this minimum moves from a point less than 0.1 diameter from the inlet for $\alpha = 0$ deg to a point close to 0.25 diameters for $\alpha = 60$ deg. The magnitude of the minimum is nearly independent of α. Figure 9 indicates that the flow is not symmetrical. This occurs because the tubes surrounding the measuring tube influence the flow into the central tube.

For $\alpha > 0$ deg, the reattachment point can be identified at about $z/d = 0.5$ where a peak in effective velocities occurs on the upstream side of the tube. The high effective velocity is due to a high turbulence intensity caused by the intrinsic unsteadiness of the impingement. Studies concerning the separation, recirculation and reattachment of flow behind an orifice (Krall and Sparrow, 1966) also show that a maximum in heat transfer occurs at the reattachment point. The position of reattachment did not depend significantly on the radial size of the separation, which is consistent with the present results. The maximum velocity in the main flow is not near the diametral plane through the center of the recirculation bubble, $z/d = 0.25$, where the size of the recirculation bubble is greatest. Instead, it is located downstream of this point, near $z/d = 0.5$ and is due to a large circumferential flow which sweeps fluid downstream (Elvery, 1995).

In the region $z/d > 0.5$, Figs. 9–12 show similarity of effective velocity distributions around the tube downstream of the reattachment point ($z/d \approx 0.5$) with a strong spatially oscillatory effect. The magnitude of the peaks is related to the angle of incidence, though the spacing of the peaks is unaffected by a change in angle of incidence. Even at $\alpha = 0$ deg, Fig. 9, significant oscillations are observed. The oscillations are representative of the distribution of heat transfer coefficients which determine the gauge voltage

from which effective velocities are calculated. The effective velocities at 15 diameters from the tube inlet are above the average tube velocity. The difference is due to the large disturbances introduced by the abrupt inlet condition. These disturbances require a longer tube length to dampen out which is in sharp contrast to a smooth entrance where the wall region becomes fully developed within the first 10–15 diameters.

Equivalent wall shear stresses shown in Fig. 13, were obtained directly from hot-film responses using (3). In regions where the flow is not sufficiently developed to form a boundary layer with a full viscous sublayer, the conversion of gauge voltage to shear stress through (3) yields an equivalent wall shear stress rather than an actual one, thus identifying regions of high transfer rates.

The expected shear stress in a plant situation can be predicted knowing the shear stress in the experimental rig by assuming similarity based on the coefficient of friction. In the case of a flow of caustic liquor at 1 m/s which is of interest in the present investigations, wall shear stresses are only up to 150 Pa. Although a body of data on the mechanical shear strength of oxide layers does not exist in the literature, it is considered that wall shear stresses of this magnitude are too small to mechanically strip the oxide layers from the metal surface. Thus it is doubtful, that mechanical removal by fluid shear forces alone is a credible explanation for the dramatic wear rates observed in a plant situation discussed in the next section.

7 Application to Tube Inlet Erosion-Corrosion

Figure 14 is a photograph of a severe case of erosion at a tube inlet with three main areas of wear identified as **A**, **B**, and **C**. **A** is located on the downstream side of the tube, offset from the axis at $\theta = 150$ deg where the highest equivalent velocities occur, as identified on Fig. 12. The high rate of erosion-corrosion at **A** is due to high velocities generated by the flow area reduction due to the recirculation region. Erosion-corrosion due to high mass transfer associated with the high equivalent effective velocity begins close to the leading edge of the tube (at $z/d < 0.5$) and progresses down the tube due to increased turbulence resulting from surface roughening.

The second critical region of wear, region **B**, is located again on the downstream side of the tube at about $z/d = 1.0$. The initiation point for this region is offset from the symmetry plane by between 30 to 60 deg. Figures 9–12 indicate that the highest transfer rate at $z/d = 1.0$, occurs in the region $\theta = 120$–150 deg and is due to a large velocity and shear stress adjacent to the downstream wall induced by a circumferential flow component.

The third major area of wear, region **C**, is initiated at the flow reattachment point. At reattachment ($z/d = 0.5$), the mean velocity of the flow is small, even though the turbulence is very high and no boundary layer exists thus creating large transfer rates and hence high erosion-corrosion.

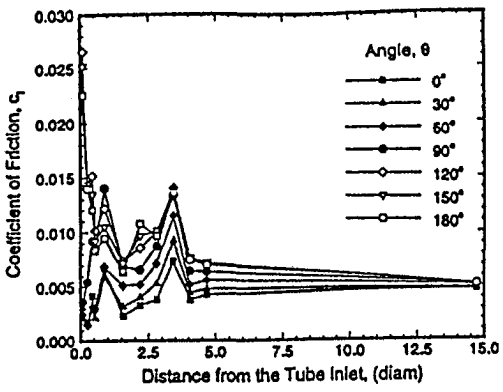

Fig. 13 Equivalent wall shear stress for $\alpha = 60$ deg. Estimated accuracy for c_f is ±0.2 percent.

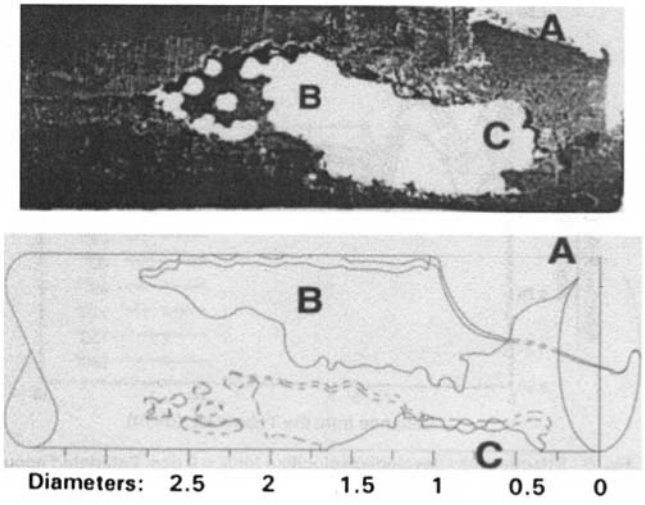

Fig. 14 Severely eroded tube inlet

8 Conclusions

An examination of flow in inlets of tubes representative of those used in shell and tube heat exchangers, has revealed high, localised heat transfer rates which by the analogy between heat and mass transfer are interpreted as high localised mass transfer rates and hence high potential for metal loss. Through the use of an equivalent fully developed velocity concept, it has been possible to express the enhanced transfer rates in terms of an equivalent effect in fully developed pipe flow. Results indicate that for flow inclination relative to the tube axis of 20 deg or more, equivalent velocities of up to 2.5 those of the mean tube velocity exist. Furthermore, these maxima are located away from the plane of symmetry due to swirl components in the flow. Additional flow measurements are given in Elvery (1995) to further define the flow field.

Measurements of wall pressure show variations both axially and circumferentially in the inlet region of up to 1.2 velocity heads. These data can be used for assessment of cavitation potential by means of the cavitation number. For single phase fluids in shell and tube heat exchangers operating at pressures sufficiently far above the saturation pressure, erosion-corrosion damage will be due to the high mass transfer rates found in localised areas identified by the present study.

Acknowledgments

The assistance given by Queensland Alumina Ltd during the course of this research is gratefully acknowledged.

References

Barbin, A. R., and Jones, J. B., 1963, "Turbulent Flow in the Inlet Region of a Smooth Pipe," ASME *Journal of Basic Engineering*, Vol. 85, pp. 29–34.

Bellhouse, B. J., and Schultz, D. L., 1966, "Determination of Mean and Dynamic Skin Friction Separation and Transition in Low-Speed Flow with a, Thin-film Heated Element," *Journal of Fluid Mechanics*, Vol. 24, pp. 379–40.

Bremhorst, K., and Flint, P. J., 1991, "The Effect of Flow Patterns on the Erosion-Corrosion of Shell and Tube Heat Exchangers," *Wear*, Vol. 145, pp. 123–135.

Bremhorst, K., and Lai, J. C. S., 1979, "The Role of Flow Characteristics in Corrosion-Erosion of Tube Inlets in the Inlet Channel of Shell and Tube Heat Exchangers," *Wear*, Vol. 54, pp. 87–100.

Elvery, D. G., 1995, "Erosion-Corrosion in Tube Inlets as a Consequence of Inclined Flow Into Heat Exchangers," PhD thesis, The University of Queensland, Brisbane, Australia.

Krall, K. M., and Sparrow, E. M., 1966, "Turbulent Heat Transfer in the Separated Reattached and Redevelopment Regions of a Circular Tube," ASME *Journal of Heat Transfer*, Vol. 88, pp. 131–136.

Legkii, V. M., and Rogachev, V. A., 1989a, "Flow in the Initial Segment of a Tube with a Sharp Leading Edge. 1. Physical Model of the Flow," *Journal of Engineering Physics,* Vol. 56, pp. 140–143.

Legkii, V. M., and Rogachev, V. A., 1989b, "Flow in the Initial Segment of a Tube with a Sharp Leading Edge. 2. Comparative Analysis," *Journal of Engineering Physics,* Vol. 56, pp. 381–384.

Liepmann, H., and Skinner, G., 1954, "Shearing-Stress Measurements by Use of a Heated Element." NACA TN No. 3268.

Maciejewski, P. K., and Moffat, R. J. 1992, "Heat Transfer with Very High Free-Stream Turbulence: Part I—Experimental Data," ASME *Journal of Heat Transfer,* Vol. 114, pp. 827–833.

Menendez, A. N., and Ramapriam, B. R., 1985, "The Use of Flush-Mounted Hot-Film Gauges to Measure Skin Friction in Unsteady Boundary Layers," *Journal of Fluid Mechanics,* Vol. 161, pp. 139–159.

Nesic, S., and Postlethwaite, J., 1990, "Relationship Between the Structure of Disturbed Flow and Erosion-Corrosion," *Corrosion,* Vol. 46, pp. 874–880.

C. Offtinger
Research Engineer.

C. Henry
Associate Professor.

R. Morel
Professor.

F. Spettel
Associate Professor.

Equipe Hydraulique I.N.S.A. Lyon,
Laboratoire de Mécanique
des Fluides et d'Acoustique,
U.M.R. CNRS 5509 E.C.L., U.C.B. Lyon I,
20, ave A. Einstein,
69621 Villeurbanne,
Cedex, France

Experimental Comparison of Flow Fields at the Inlet and the Outlet of an Inducer With Shrouded and Unshrouded Configurations

The flow field was measured near the inlet and the outlet of an axial flow inducer with shrouded and unshrouded configurations combined with a centrifugal pump. Investigations were conducted using a five-hole probe for several flow rates. The shroud induces a counterrotating flow at the inlet and a blockage effect at the outlet in the region of the tip and for all flow rates. The radial distribution of losses keeps the same shape in both configurations, however, the loss level is higher with the shroud, giving a lower efficiency for the combined inducer-impeller configuration. Effects of shrouded inducer on part load instability are not clear and deserve more research, which is in progress.

Introduction

One of the most attractive ways for improving the suction capability of centrifugal pumps is the use of inducers. These are axial flow pumps designed to withstand problems associated with cavitation. The primary function of an inducer, combined with a centrifugal pump is to pressurize the flow sufficiently to enable the main impeller to perform without appreciable cavitation in the desired capacity range.

Many authors have contributed to better understanding, at least qualitatively, of flow through inducers: Dorey and Provost (1988), Howard and Atif (1993), Janigro and Ferrini (1973), Lakshminarayana (1972), (1973), (1974), and (1982).

Typical inducer characteristics include high solidity and low aspect ratio. The flow in these long and narrow passages is greatly influenced by the effects of turbulence and viscosity, resulting in large friction losses and introducing considerable three-dimensionality in the flow, thus making the prediction of flow behavior extremely difficult. Secondary motions within the inducer are not confined to thin regions at the blade surface, but extend over the entire cross-section of the flow.

A limiting aspect of inducer use is part-load instabilities. In order to avoid tip clearance flow and thus tip clearance cavitation, possibly responsible for instabilities at part-load, a shroud was welded on to the blade tips of a normal inducer by means of a few welding spots to limit blade distortion. The flow at the inlet and at the outlet of this inducer was explored by mean of a five pressure taps conventional cobra probe for shrouded and unshrouded configurations. In order to point out modifications of the flow field induced by the shroud, the results are presented for both configurations for two flow rate coefficients. The first value $\phi_1 = 0.113$ corresponds to the best efficiency flow rate, ϕ_{bep}, of the combination of centrifugal pump + inducer and the second value to $\phi_2 = 0.09$. All measurements were performed under noncavitating conditions with ample $NPSH_a$ above the visible cavitation inception point (at bep $\sigma_{available}/\sigma_{inc} = 1.82$). Furthermore, a study of radial change of mean axial velocity is shown for flow coefficients varying from 0.8 ϕ_{bep} to 1.2 ϕ_{bep}. Finally, local relative pressure losses can be computed from the probe measurements and a comparison of radial progression of these losses for ϕ_1 and ϕ_2 for shrouded and unshrouded configurations is presented in this paper.

Contributed by the Fluids Engineering Division for publication in the JOURNAL OF FLUIDS ENGINEERING. Manuscript received by the Fluids Engineering Division April 8, 1996; revised manuscript received May 19, 1997. Associate Technical Editor: B. Schiavello.

1 Inducer and Test Loop.

The inducer, designed at the INSA Fluid Mechanics Laboratory, Lyon, is placed in front of a centrifugal pump on the same shaft. The geometrical and design characteristics of the inducer tested are given in Table 1.

An assembly diagram of the centrifugal pump and the inducer with the shrouded and unshrouded configurations is given Fig. 1.

Investigations were conducted in a deaerated water test facility arranged in a closed-loop circuit, as shown in Fig. 2. The circuit is mainly composed with a group inducer-centrifugal pump (A) driven by a variable speed d.c. motor (B), two water tanks (C) and (D) with respective capacities of 2.6 m^3 and 2.2 m^3, a vacuum pump (E), valves (F) and interchangeable diaphragms (G).

Upstream and downstream flow rates are measured using Endress Hauser electromagnetic flowmeters. The maximum flow rate through the loop at a rotation speed of 3000 rpm is 0.1 m^3/s. Measurement uncertainty varies with flow velocity, ± 1 percent from 20 to 100 percent of the measurement range and ± 2 percent from 0 to 20 percent of the measurement range.

A Staiger Mohilo dynamic torque meter, with a sampling frequency of 600 Hz, situated on the shaft between the motor and the pump, gives the torque and the rotating speed. The measurement range is 500 Nm with an accuracy (linearity and hysteresis) of ± 0.1 percent for the entire scale.

Two passages in the casing wall allow the investigation of velocity and pressure fields, one at the inlet and the other at the outlet of the inducer, using a directional probe. Measurements were done using a "null balance" method.

The probe is driven in translation and rotation round its main axis by a probe holder.

Treaster and Yocum (1979), Sitaram et al. (1981) list sources of errors in conventional probe measurements of flows in turbomachinery. They also estimate the magnitude of these errors. They agree that wall proximity effects are negligible if

Table 1 Inducer characteristics

Rotation speed		2960 rpm	
Number of blades		3	
Schockless flow coefficient at tip		0.14	
Suction specific speed		456.45	
Hub to tip ratio at inlet		$r_h/r_t = 0.354$	
Hub to tip ratio at outlet		$r_h/r_t = 0.393$	
Best efficiency flow coefficient		0.113	
Radial clearance		$0.0011r_t - 0.0044r_t$	
Sweep angle		7.92°	
		Tip	Hub
Blade thickness/chord		0.0118	0.0412
Solidity		1.6	1.77
Stagger angle	relative	80.35°	61.51°
Inlet blade angle	to axial	81.88°	71.71°
Outlet blade angle	direction	76.71°	50.71°

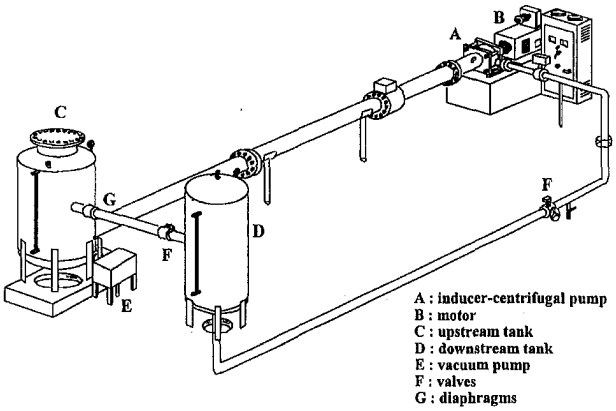

Fig. 2 Test loop

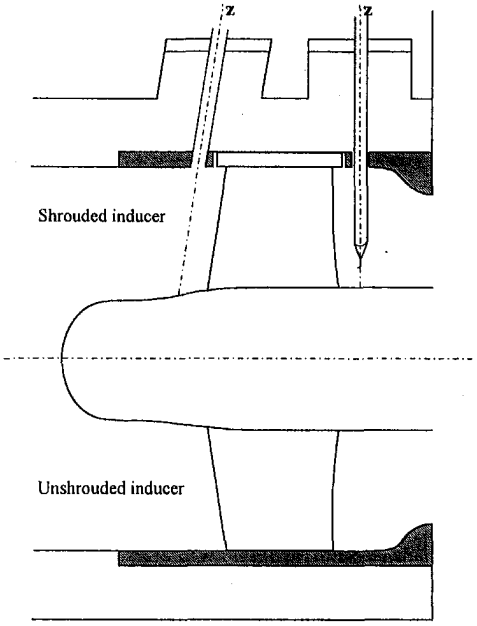

Fig. 1 Assembly diagram

the distance between the measurement position and the wall is more than two times the probe diameter. The first and last of the measurement locations shown here fulfill this condition. The Reynolds number is the same for calibration in air realized at INSA Lyon by the authors and experiments in water, thus the effects of the Reynolds number are almost non-existent. The presence of the probe may perturb the flow but the size of the probe (diameter 2 mm) is more than 10 times smaller than the blade passage, thus the effects of probe blockage are negligible. Effects of turbulence are neglected because they only appear when turbulence intensity is quite high (20 percent). An estimation of the effects of pressure and velocity gradients using formulae provided by the above authors shows that these effects are negligible.

Pressures are measured using two Rosemount 1151 DP differential pressure transducers whose maximum ranges are 7.10^5 Pa and 37.10^3 Pa. These transducers keep their own calibration in memory and the accuracy is from 0.1 to 0.2 percent of the measurements range, this being superior or equal to $\frac{1}{6}$ of the maximum range calibrated.

Estimation of experimental uncertainties are given below: Fig. 3 head coefficient $\psi \pm 0.0003$, efficiency $\eta \pm 0.01$, Fig. 4 undimensional NPSH required at 3 percent head loss $\sigma_{r3\%} \pm 0.0001$, Figs. 5 through 8 undimensional velocity components $C^* \pm 0.01$, undimensional pressures $p^* \pm 0.001$, angles ± 0.5 degrees, Fig. 9 flow coefficient $\Phi_{part} \pm 0.01$, and Fig. 10 pressure loss coefficient $Cp \pm 0.002$.

2 Results and Discussion

2.1 Performance (Head, Efficiency, $NPSH_{r3\%}$). The overall performance curve and the curve of NPSH required at 3 percent head loss of the combination of centrifugal pump and

Nomenclature

C = absolute velocity
W = relative velocity
ω = rotation speed (rad/s)
α = absolute flow angle = $\text{arctg}C_u/C_m$
β = relative flow angle = $\text{arctg}W_u/Wm$
δ = flow deviation angle (outlet) = $\beta - \beta_{geo}$
r = radius
U = peripheral velocity = ωR
p = static pressure
p^o = total pressure
p_r^o = relative total pressure = $p + (1/2)\rho(W^2 - U^2)$
$p1$ = reference static pressure far upstream
ϕ = flow rate coefficient = C_a/U_t
ψ = head coefficient = gH/U_t^2
η = efficiency
C^* = undimensional velocity = C/U_t
p^* = undimensional pressure = $p/0.5\rho U_t^2$
S = suction specific speed = $(N(\text{rpm})\sqrt{Q(\text{m}^3/\text{s})})/(\text{NPSH}(\text{m})^{3/4})$
r^* = undimensional radius = $(r - r_h)/(r_t - r_h)$
Cp = relative total pressure loss coefficient = $(p_{ro}^o - p_n^o)/0.5\rho U_t^2$
$\sigma_{3\%}$ = undimensional NPSH required at 3 percent head drop = $\text{NPSH}/U_t^2/g$

Subscript

c = combination of centrifugal pump + inducer
d = design or schockless at tip (inducer alone)
bep = best efficiency point (inducer + centrifugal pump)
a, r, u, m = axial, radial, tangential and meridional component
h, t = hub and tip (inducer)
geo = geometric
$part$ = partial
i, o = inlet, outlet (inducer)
unsh = unshrouded
sh = shrouded

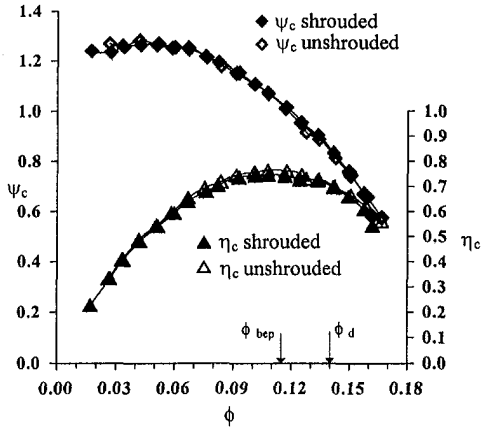

Fig. 3 Overall performance curves of the combination centrifugal pump + inducer in both shrouded and unshrouded configurations

inducer in both shrouded and unshrouded cases are presented Fig. 3 and Fig. 4, respectively. The head curve remains practically unchanged, but the shroud induces an increase of the shaft power (due to additional friction) and consequently a decrease of efficiency by about 3 percent.

2.2 Flow Pattern Measurement. Traverses are made parallel to the meridian projection of either the leading edge or the trailing edge (Fig. 3). These lines are located, respectively, 12 mm and 13 mm away from the inducer.

Experiments are carried out using both shrouded and unshrouded configurations for two flow rates $\phi_1 = 0.113$ and $\phi_2 = 0.09$ under noncavitating conditions.

Due to the size of the probe and the vicinity of the hub, the first measurement is located at $r^* = 0.07$ and the last one at $r^* = 0.963$.

The axial velocity component was integrated using spline smoothing and the result was compared with the measured flow rate; the error was always less than 10 percent.

The flow angles are given relative to the axial direction.

Flow Field for Flow Rate Coefficient $\phi_1 = 0.113$ (ϕ_{bep}). Inlet, see Fig. 5. The inlet flow is almost axial, nevertheless axial velocity decreases slightly and progressively from hub to tip. This fact may be connected to the conical shape of the front side of the inducer and also to the sweep angle.

The hub shape induces a slight outward radial flow.

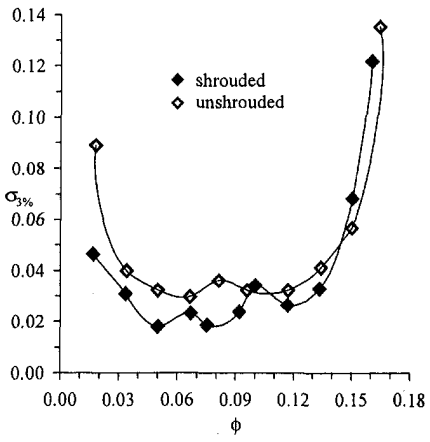

Fig. 4 Curves of NPSH required for 3 percent head loss of the combination centrifugal pump + inducer in both shrouded and unshrouded configurations

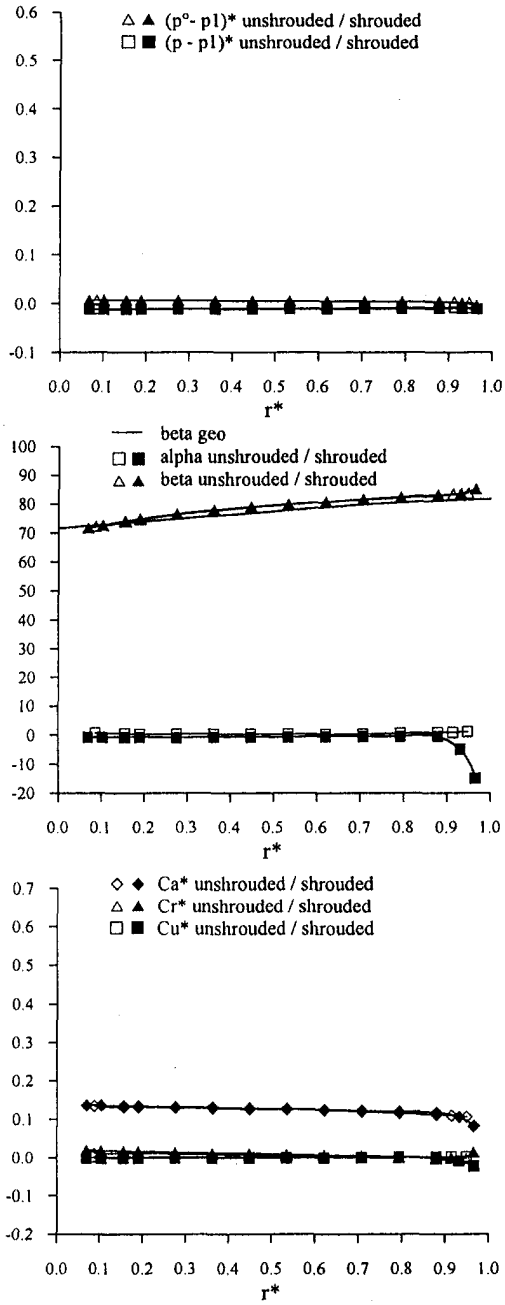

Fig. 5 Hydrodynamic flow field at inlet at various radial locations $\phi_1 = 0.113$

The absolute flow angle α (relative to the axial direction) and the tangential component C_u^* are almost equal to zero, which is the expression of no prerotation.

The tested flow rate is less than the design flow rate and the relative flow angle β is greater than the blade angle β_{geo} (difference of about 2 or 3 deg).

Absolute flow angle α shows a counterrotating flow at tip ($\alpha < 0$) with the shrouded configuration. This is the only disturbance induced on the velocity field by the shroud.

The total and static pressure are constant across the passage.

Outlet, see Fig. 6. The tangential component C_u^* drops in the inner part of the passage and increases on the outer part. This common "V-shape" (Janigro and Ferrini, 1973, Howard and Atif, 1993) is more pronounced for the shrouded case.

The shroud rotating with the inducer creates a blockage effect near the tip, there is a flow deficit in this region (axial compo-

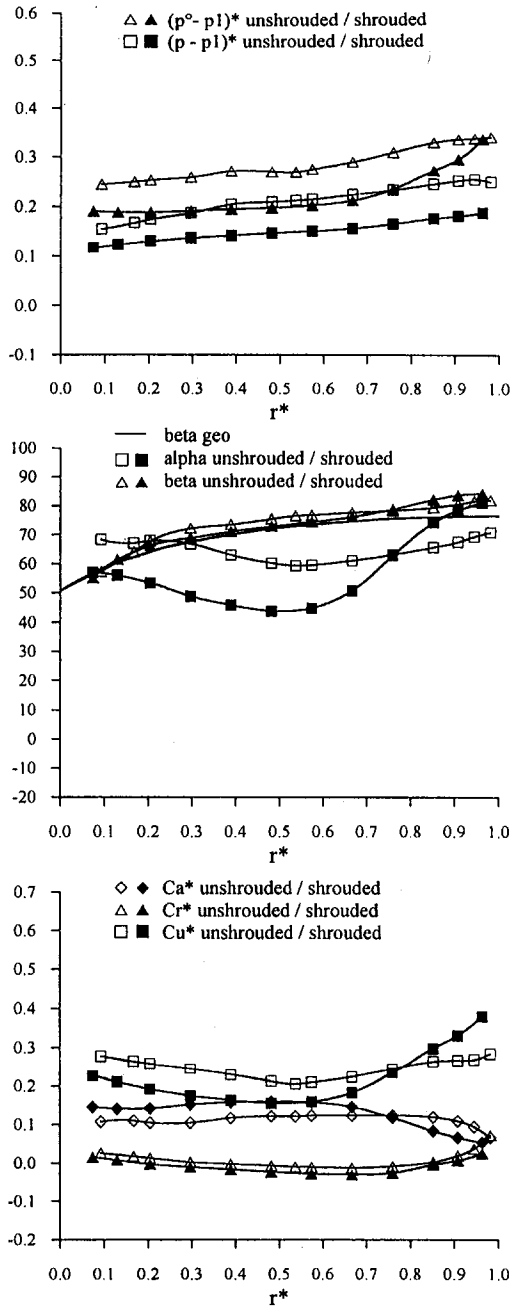

Fig. 6 Hydrodynamic flow field at outlet at various radial locations $\phi_1 = 0.113$

nent C_a^* is light) and centrifugation of the fluid (significant increase of C_u^*).

For the unshrouded inducer, the axial component C_a^* is almost constant across the passage except near the casing where it falls strongly, maybe on account of the leakage.

For both configurations, the radial component C_r^* is low but a small increase can be seen near the tip.

The flow deviation angle δ, equal to zero at the hub, is slight (4 to 5 deg) on the remaining part of the blade height.

Total and static pressures increase linearly from hub to tip. The shroud causes a same constant decrease of these two pressures on all the blade height. However, a significant increase of the total pressure is visible on the tip near the shroud, in this case the centrifugation of the fluid leads to an increase of its kinetic energy and thus of total pressure.

The difference of total pressure between the two configurations induces a ratio $\eta_{sh}/\eta_{unsh} = 0.9$. These efficiencies of the inducer alone are computed by integration of pressure and velocity fields at inlet/outlet of the inducer.

Flow Field for Flow Rate Coefficient $\phi_2 = 0.09$ (0.8 ϕ_{bep}). Inlet, see Fig. 7. When the flow rate is reduced, significant changes occur in the flow field. The new feature is a reverse flow developing on the tip section where axial and radial velocity components become negative. This phenomenon, due to a high incidence angle of the flow in this region, starts at about $\phi = 0.096$. Consequently, an increase of the axial velocity component appears near the hub, where the flow is well adapted.

In connection with the inlet reverse flow, the tangential velocity component rotating in the same direction as the inducer rotation increases strongly near the tip. The same remark is true for the absolute flow angle α.

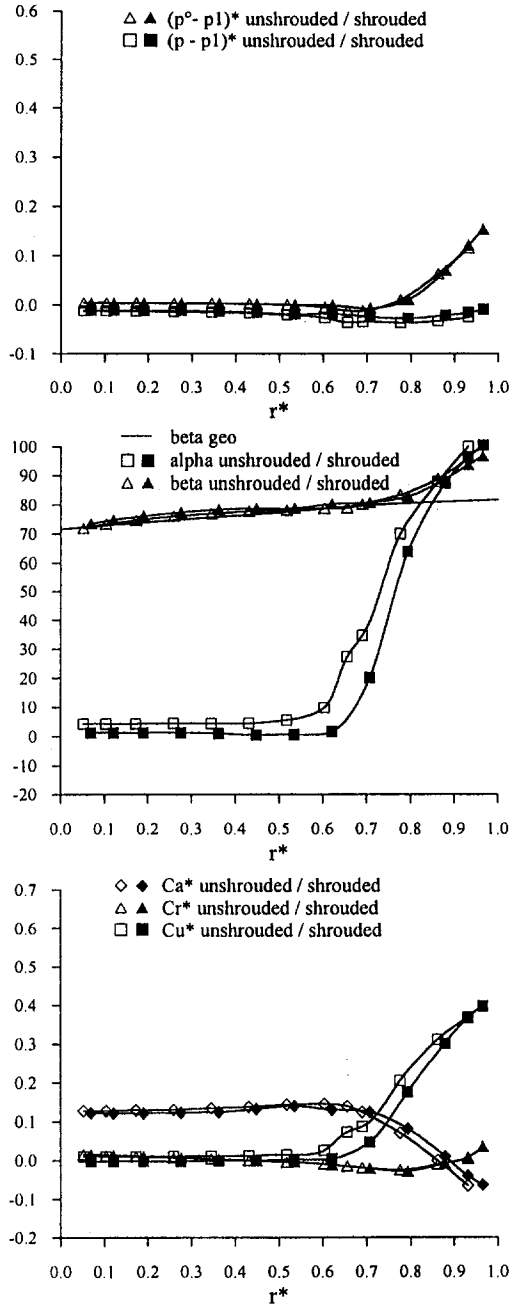

Fig. 7 Hydrodynamic flow field at inlet at various radial locations $\phi_2 = 0.09$

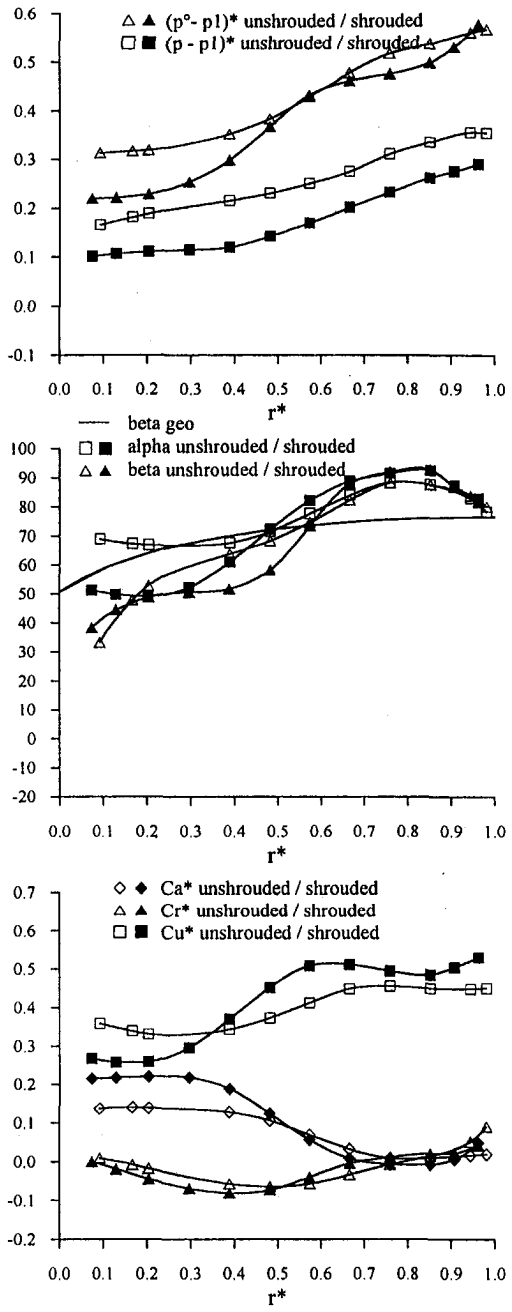

Fig. 8 Hydrodynamic flow field at outlet at various radial locations $\phi_2 = 0.09$

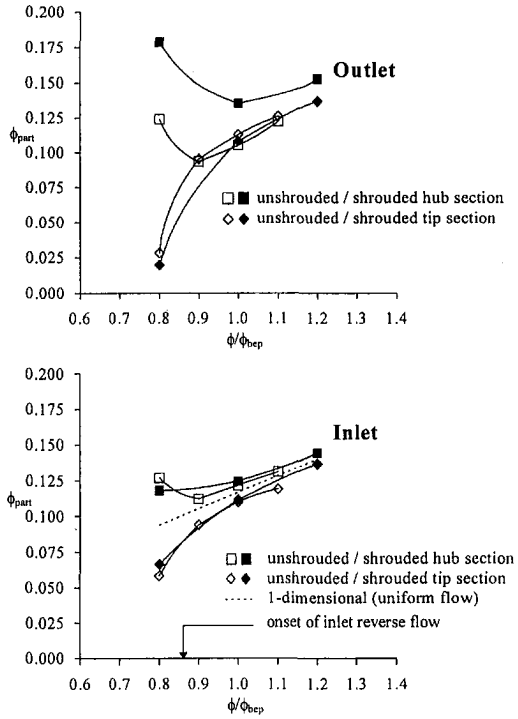

Fig. 9 Mean axial velocity at the inlet and the outlet of the inducer at various flow rates

The rise in the tangential velocity component is related with an increase of total pressure, which is caused by the reverse flow out of the inducer where it received energy from blades. The static pressure remains constant even in the rotating reverse flow region.

The only significant difference between both configurations, which can be observed in Fig. 7, is a more important fluid rotation for the unshrouded case that can be explained by an additional rotation induced by the tip clearance flow.

Outlet, see Fig. 8. The axial velocity component drops strongly in the outer quarter of the blade height, becoming almost equal to zero for the unshrouded configuration and negative with the shroud. This outlet backflow may be the result of the design criterium for head (linear increase from hub to tip). Moreover, it is important to note that the flow at the outlet of the inducer may be influenced by the strongly convergent entrance of the centrifugal pump placed just downstream (Fig. 1). The restriction at outlet forces all flow through hub like a diaphragm, the shroud accentuate this trend.

The tangential velocity component C_u^* increase from hub to mid-radius and remains constant close to 0.5 (half speed of the

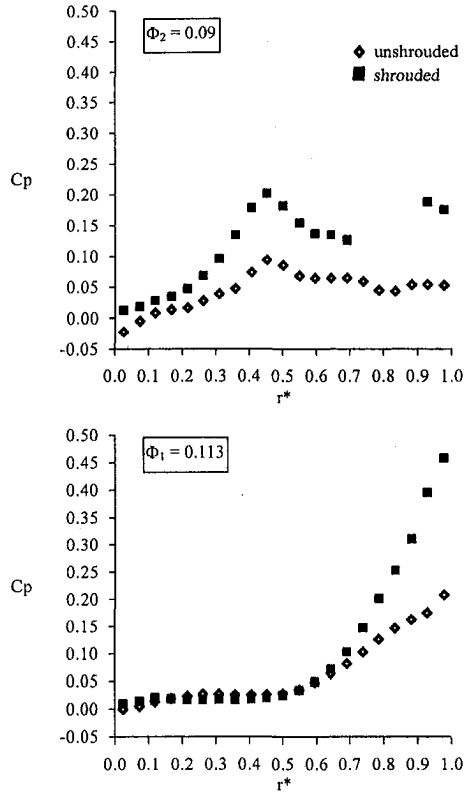

Fig. 10 Radial evolution of local relative total pressure losses

shroud) associated to backflow at tip on the outer part of the passage. The shroud emphasizes the imbalance of C_u^*, increasing it at tip and decreasing it near hub.

Near the hub, flow angles are lower than geometric angles, this can be explained as follows: the blockage created by the imbalance of the axial velocity component at the tip induces an increase of the meridional velocity component at the hub and thus a decrease of the relative flow angle β.

The linear increases of the static and total pressure mentioned for ϕ_1 are stronger for ϕ_2. The difference of static pressure in the two configurations remains constant. On the other hand, the difference of total pressure become very small for $r^* > 0.5$. For this flow rate, the ratio $\eta_{sh}/\eta_{unsh} = 0.86$.

Comparison of Mean Axial Velocity Components Near the Hub and Near the Tip at Various Flow Rate (Fig. 9). In order to point out the imbalance of the axial velocity component with the radius, partial flow rate coefficients are computed in the hub and tip sections (integration of the axial velocity component from hub to mid radius and from mid radius to tip, respectively).

At the inlet, it is noticeable for both configurations that slightly more flow is passing through the hub section. This may be related with the inlet sweep angle. The difference between the partial flow coefficient at the hub and the tip increases when the flow rate is decreased. This is the expression of reverse flow near the tip at a partial flow rate.

At the outlet, a significant difference is clearly evident between unshrouded and shrouded configurations. With the unshrouded configuration, partial flow rate coefficients at the hub and tip sections are the same when approaching the best efficiency flow rate and differ for a partial flow (lower at the tip than at the hub). With the shrouded configuration, the imbalance between the two partial flow coefficients for every flow rate is due to the blockage of the flow at the tip induced by the shroud. Moreover, the shroud influences the secondary flow pattern inside the inducers blades leading to a different three-dimensional flow and so a different axial velocity distribution. The difference between these partial flow coefficients becomes very significant for $\phi_2 = 0.09$ (i.e., 0.8 ϕ_{bep}).

Comparison of Radial Evolution of Relative Total Pressure Losses (Fig. 10). For flow rate coefficient $\phi_1 = \phi_{bep}$, relative total pressure losses are almost equal to zero in the inner half part of blade height and increase from mid radius to tip. The region near the tip is a region of production of important losses where the level of losses is even higher with the shroud. This phenomenon may be correlated with the fact that the inducer has been designed for a linear increase of head from hub to tip.

For flow rate coefficient $\phi_2 = 0.09$, relative total pressure losses increase from hub to mid radius and decrease from mid radius to tip, remaining still high. The form of radial progression of losses is the same with shrouded and unshrouded configurations but the level of losses is more significant with the shrouded one.

In comparison with case $\phi = \phi_1$, an increase of losses near the hub and a decrease near the tip can be seen in Fig. 10. This could be explained by the imbalance of partial flow rate coefficient which according to Fig. 9 shows that for this value of $\phi = \phi_2$, a higher flow is passing through the hub region and less in the tip region.

Maximum losses are noticed at mid-radius, corresponding roughly to maximum velocity. Also, the pattern of secondary flows likely contributes to this distribution of pressure loss.

In the region $0.7 < r^* < 0.9$, it is impossible to compute the losses because of the reverse flow appearing at the outlet with the shrouded configuration.

The greater losses with the shroud may be related to the ratios η_{sh}/η_{unsh} less than one previously mentioned.

Conclusion

Flow in inducers is very complex and greatly influenced by the effects of turbulence and viscosity. The flow field at the inlet and the outlet of a three bladed inducer is presented in this paper with shrouded and unshrouded configurations, in order to emphasize modifications of the flow field induced by the shroud.

The flow field at the inlet of the inducer is always quasi axial for $\phi_1 = 0.113$. The shroud induces a counterrotating flow near the tip. When the flow rate is reduced to $\phi_2 = 0.09$, a rotating reverse flow appears in the tip section at the inducer inlet. This phenomenon is less significant with the shrouded configuration.

The field is three-dimensional at the outlet. The shroud causes a blockage effect in the tip region, this results in a decrease of axial velocity and a centrifugation of fluid in this region. For flow rate $\phi_2 = 0.09$, a reverse flow appears near the tip as mentioned by Dorey and Provost (1988). Other authors (Howard and Atif, 1993; Janigro and Ferrini, 1973; Lakshminarayana (1972, 1973, 1974, 1982) localized this reverse flow near the hub.

The level of losses is increased by the shroud, leading to a drop in the hydraulic efficiency of the inducer, roughly estimated at 10 percent, the decrease of the efficiency of the combination centrifugal pump + inducer being limited to 3 percent.

This study points out that welding a shroud on the blade tips induces certain negative effects on the flow field through the inducer. However, these drawbacks may be tolerable if investigations in progress show an attenuation of part-load instabilities and an improvement of the range of reliable operations.

Acknowledgments

This work was carried out with the support of EDF-DER (Electricité De France-Direction des Etudes et Recherches) and GEC ALSTHOM-BERGERON.

References

Dorey J. M., and Provost, D., 1988, "Hélice de Gavage DER: Compléments d'Essais Hydrauliques," EDF Chatoux France, 13 pp.

Howard J. H. G., and Atif A., 1993, "Near Exit Flow Field Investigation in an Inducer Including Laser Doppler Velocimetry," *Int. J. Heat and Fluid Flow*, Vol. 14, No. 1, Mar., pp. 86–93.

Janigro A., and Ferrini F., 1973, "Recent Progress in Pump Research," Von Karman Institute, Rhode St Genese, Belgium, Lecture Serie 61, Dec. 113 pp.

Lakshminarayana B., 1972, "Visualization Study of Flow in Axial Flow Inducer," ASME *Journal of Basic Engineering*, Dec. pp. 777–787.

Lakshminarayana B., 1973, "Three Dimensional Flow Field in Rocket Pump Inducers. Part 1: Measured Flow Field Inside the Rotating Blade Passage and at the Exit," ASME JOURNAL OF FLUIDS ENGINEERING, Vol. 95, Dec. pp. 567–578.

Lakshminarayana B., 1974, "Experimental and Analytical Investigation of Flow Through Rocket Pump Inducer," Fluid Mechanics, Design and Acoustics of Turbomachinery, NASA SP304, part 2, pp. 690–731.

Lakshminarayana B., 1982, "Fluid Dynamics of Inducers—A Review," ASME JOURNAL OF FLUIDS ENGINEERING, Vol. 104, Dec., pp. 411–427.

Sitaram N., Lakshminarayana B., and Ravindranath A., 1981, "Conventional Probes for the Relative Flow Measurement in a Turbomachinery Rotor Blade Passage," ASME *Journal of Engineering for Power*, Vol. 103, Apr., pp. 406–414.

Treaster A. L., and Yocum A. M., 1979, "The Calibration and Application of Five-hole Probes," *ISA Transactions*, Vol. 18, No. 3, pp. 23–34.

Michel Guilbaud
Professor,
CEAT-LEA (UMR CNRS no. 6609),
Université de Poitiers,
43 rue de l'Aérodrome,
86036 Poitiers Cedex, France

D. R. Rajaona
Professor,
Laboratoire de Mécanique,
Université du Havre, Quai Frissard,
76000 Le Havre, France,
Mem. ASME

Numerical Study of Sail Aerodynamics

A boundary-element method to compute steady flows around a set of sails at close hauled conditions (i.e., the wind is coming from upstream of the boat at a moderate angle of attack for the sails) is presented. It is based on a mixed potential-velocity formulation in order to solve the problem of zero thickness sail conditions. An iterative procedure is proposed to account for the interaction between sails; the shape of the wake of the leading sail is computed as an equilibrium stream surface in such a way that the plane wake assumption is not used. Numerical results are compared with tests conducted on isolated jibs and sets of jib and main sails in wind tunnels.

Introduction

The aerodynamic analysis of sails is a very complex but challenging problem. Up to these last ten to fifteen years, the experience of the skipper, as well as the knowledge of the sail makers, were the only sources of the sail design. Recently, many authors have studied the flow around sails by using numerical methods based upon lifting surface techniques (Register and Irey, 1983) or vortex lattice methods applied to zero thickness airfoil, with or without interacting effects (Thrasher et al., 1979; Sparenberg and Weirsma, 1976; Boudreault, 1985; Smith, 1987). It is well known that under usual conditions, sails are mainly working at small angle of attack. Furthermore, the so-called close hauled conditions play an important role in the performances of the whole sailing boat during a race and also involve aerodynamic conditions suitable for numerical methods applied to flows without separation. Specifically for such a situation, it is well known that the sail shape does not abruptly change if the relative wind direction is roughly constant. As a consequence, the choice of a steady flow condition can be retained. Furthermore, the actual velocities are sufficiently low so that the incompressible flow assumption can be applied. Two computation techniques suitable for incompressible flow have been used: (*i*) the linearized approximation of a lifting surface with a flat plane wake extending downstream the trailing edge, as shown in Milne-Thompson (1958), is suitable for zero thickness case; (*ii*) the vortex lattice technique and some of its extensions (Mook and Nayfeh, 1985). The previous studies have demonstrated the good performance of the vortex lattice method for very low thickness sails. Although theses techniques are available to predict the force coefficients, they do not allow the computation of the pressure field on each side of the sail since only the pressure jump is calculated. Moreover, the knowledge of the pressure field is useful to compute the 3D-shape of the sail, specifically if one needs a complete computation of the properties of the flexible membrane wings aerodynamic (Boudreault, 1985; Schoop, 1990). The discrete vortex methods are quite convenient for the case of unsteady flows, but those methods are very time consuming and need some sophisticated derivations such as cloud in cell technique (Arena and Nelson, 1992). For these reasons, the panel method has been chosen for sake of simplicity. The method is based upon a first-order accuracy because for the comparison with tests on real sails, with shapes not known very accurately, a second-order numerical model seems not to be necessary.

The purpose of this paper is to present a numerical scheme suitable for the computation of the three-dimensional steady flow around sails and the related drag and lift forces. The lift and the induced drag are calculated by using a panel method (Mazzouji et al., 1992), while an attempt is made to estimate the drag due to friction forces upon the basis of a fully developed turbulent boundary layer on each side of the sails.

Despite the apparent simplification inherent to the linearized approximation, a complex problem must be solved due to the following particular conditions: (*i*) complex geometry of sails, masts, booms; (*ii*) some part of geometry has zero thickness, leading to numerical difficulties involved in the discretization of the related integral equations; (*iii*) presence of the boat deck and of the water free surface close to the sail foot; (*iv*) frequent overlapping of a part of the main sail by the jib involving strong interaction between wakes and solid boundaries; (*v*) at last, the knowledge of the sail shape under real conditions is not easy. That is why the retained strategy to validate the numerical scheme was to compare numerical results with experimental ones obtained from experiments conducted in wind tunnel on almost rigid sails, for which the shape is well known. When describing the set of sails and masts, the presence of zero thickness sails makes unsuitable the classical potential based panel method. The velocity formulation is derived from the potential one by applying a normal derivation; the mixed formulation uses a linear combination of both and involves coefficients which are chosen to regularise the related linear system as proposed by Morchoisne et al. (1987). So the condition number of the matrix associated with the linear system for the flow around a rectangular wing with relative thickness 0.1 percent is reduced from 23,917 for the potential based formulation to 64 for the mixed one (Mazzouji et al., 1992).

The presence of the deck and of the free surface is accounted for by the use of a double sail model. As the flow and forces are quite sensitive to the presence of a small gap under the sails, the surface mirror has been located at the upper part of the deck location which must be known with a high accuracy (Charvet and Huberson, 1992). But no attempt was made to model the presence of the boom at the foot of the sail.

For modeling the lifting effects, bodies must be followed by a wake extending downstream to infinity. The choice of a plane wake with direction parallel to the free-stream velocity or the bisector of the trailing edge of a wing gives generally good results for a solitary body (Rajaona, 1978). In case of interacting sails, a strong influence of the direction of the upstream sail wake on the forces on the downstream one has been demonstrated (up to 19 percent on lift, 45 percent on drag for a rotation of 15 deg of the direction of the wake). The shape of the upstream wake has been computed as an equilibrium stream surface using the velocities computed in the wake by the model with the semi-infinite plane wake. Once the wake is known on a length equal to several spans, the entire flow can be computed again, giving more accurate results for sails in close interaction

Contributed by the Fluids Engineering Division for publication in the JOURNAL OF FLUIDS ENGINEERING. Manuscript received by the Fluids Engineering Division October 17, 1996; revised manuscript received July 14, 1997. Associate Technical Editor: D. P. Telionis.

(Register and Irey, 1983). Although several iterations are usually needed to compute the wake (as is also shown in the vortex lattice method, Mook and Nayfeh, 1985), the process has been limited to only one iteration since it has been observed a posteriori that the force coefficients were not significantly sensitive to the iterated shapes of the wake.

Numerical Method

The usual conditions, leading to low effective angle of attack, allow the following assumptions: (*i*) the sails are rigid, the effective incidence is low (less than 22 deg), the Reynolds numbers are sufficiently high ($\mathrm{Re} = 2.10^7$); (*ii*) the boundary layer is assumed to be equivalent to a vortex distribution supported by the boundary of a panel. Several schemes of the vortex distribution are used following the desired degree of accuracy: constant or varying along with the curvilinear abscissa. In the present scheme, the vortex strength is constant along the quadrangular panel limits. Now, using the theorem of equivalence between a closed vortex line of constant strength and a normal dipole distribution, one can discretize the wing surface into panels over which the dipole density is constant. This follows the Sears scheme (Rajaona, 1978); (*iii*) the wake is accounted for by a plane distribution of normal dipole on each panel equivalent to the free vortices in the vortex lattice method.

The momentum conservation law is reduced to the classical Bernoulli relation used to compute the pressure field around the sail. The real fluid is then assumed to be an inviscid one. The continuity equation is reduced to a Laplace equation and the slip condition is applied. As usual, in order to satisfy the Kutta-Joukowski condition, the tangential velocity is continuous on upper and lower sides of the trailing edge. Numerical tests have shown that the lift force applied to the sail is not sensitive to the orientation of this wake plane. The lift force variations are less than 2 percent for a variation of the wake plane orientation in the range of 20 deg (Mazzouji et al., 1992). That is why the wake orientation has been chosen to be in the direction of the incident uniform flow. For the case of interacting sails, the fore sail shape wake has a significant effect onto the pressure field around the aft-sail. As a consequence, the wake has been computed under the physical constraints insuring the wake equilibrium.

(i) Theoretical Justification of the Mixed Formulation. From a mathematical point of view, the problem is the calculation of a velocity potential φ satisfying the Laplace equation in a fluid domain Ω limited by the surface S, the slip condition on the sail, the Kutta condition at the trailing edge, the wake condition on the wake. The usual mathematical method involves the generalized Ostrogradski theorem that leads to the Green identity, in Eq. (1):

$$\int_\Omega \varphi \Delta\Psi d\Omega = \int_S \varphi \frac{\partial \Psi}{\partial n} ds + \int_\Omega \Delta\varphi \Delta\Psi d\Omega, \qquad (1)$$

where φ is the velocity potential and $\Psi = 1/MM'$ is the Green function; $\mathbf{n}$ is the outer normal vector to the surface S surrounding the sail. Vector quantities are shown in boldface type. Alternatively we have:

$$\int_\Omega \Psi \Delta\varphi d\Omega = \int_S \Psi \frac{\partial \varphi}{\partial n} ds + \int_\Omega \Delta\varphi \Delta\Psi d\Omega. \qquad (2)$$

By subtracting these equations and using the Stieltjes integral (Rajaona, 1978) related to the case where the point M is on the surface S, we have:

$$\int_\Omega \Psi \Delta\varphi d\Omega + 2\pi\varphi(M) = \int_S \varphi(M') \frac{\partial \Psi}{\partial n} ds - \int_S \Psi(M') \frac{\partial \varphi}{\partial n} ds. \qquad (3)$$

Accounting for the Laplace equation and the body condition, Eq. (3) becomes:

$$2\pi\varphi(M) = \int_S \varphi(M') \frac{\partial \Psi}{\partial n} ds - \int_S \mathbf{V}\cdot\mathbf{n}_{M'}, \Psi(M') ds. \qquad (4)$$

The surface S includes the body surface S_B and the wake surface Σ. Equation (4) can be rewritten as an integral Eq. (5), keeping in mind that the contribution of the wake does not include any source singularity:

$$2\pi\varphi(M) - \int_{S_B} \varphi(M') \frac{\partial \Psi}{\partial n_{M'}} ds - \int_\Sigma \varphi(M') \frac{\partial \Psi}{\partial n_{M'}} ds = -\int_{S_B} \mathbf{V}\cdot\mathbf{n}_{M'} \Psi(M') ds. \qquad (5)$$

The integral Eq. (5) shows the contribution of source and normal dipole on the body surface and normal dipole on the wake surface. It is a second-kind Fredholm equation that is numerically easy to solve. It should be noticed that the source distribution over the body surface reduces to zero as the body thickness decreases down to a zero value. At the limiting case of zero thickness, numerical instabilities occur since the related linear system is homogeneous. In order to solve numerically this problem, a derivative of Eq. (5) is proposed, and by multiplying both sides of this equation by the operator $\partial/\partial n(M)$, the following expression can be written:

$$2\pi \frac{\partial \varphi(M)}{\partial n_M} - \int_{S_B} \varphi(M') \frac{\partial}{\partial n_M} \frac{\partial \Psi}{\partial n_{M'}} ds - \int_\Sigma \varphi(M') \frac{\partial}{\partial n_M} \frac{\partial \Psi}{\partial n_{M'}} ds = -\int_{S_B} \mathbf{V}\cdot\mathbf{n}_{M'} \frac{\partial}{\partial n_M} \Psi(M') ds.$$

Accounting for the slip condition for the first term and rewriting the previous equation, we have:

$$\int_{S_B} \varphi(M') \frac{\partial}{\partial n_M} \frac{\partial \Psi}{\partial n_{M'}} ds + \int_\Sigma \varphi(M') \frac{\partial}{\partial n_M} \frac{\partial \Psi}{\partial n_{M'}} ds = 2\pi \mathbf{V}\cdot\mathbf{n}_M + \int_{S_B} \mathbf{V}\cdot\mathbf{n}_{M'} \frac{\partial}{\partial n_M} \Psi(M') ds. \qquad (6)$$

This equation shows that for the case of zero thickness body, the previous integral equation is no more homogeneous and then leads to a well-conditioned matrix for the related linear system. The panel method is used to solve either Eq. (5) or Eq. (6). This last equation is a Fredholm integral equation of the first kind; as a consequence, the related linear system leads to numerical difficulties, essentially because it is not a diagonally dominant system, owing to the higher order of singularity of its kernel. That is why this equation was not retained for solving the problem. Instead, we have associated the two linear systems and solved them simultaneously by using a linear combination of Eqs. (5) and (6), Eq. (7):

$$2\pi\alpha\varphi(M) - \int_{S_B \cup \Sigma} \varphi(M') \left[\alpha \frac{\partial \Psi}{\partial n_{M'}} + \beta \frac{\partial}{\partial n_M} \frac{\partial \Psi}{\partial n_{M'}} \right] ds = 2\pi\beta \mathbf{V}\cdot\mathbf{n}_M + \int_{S_B} \mathbf{V}\cdot\mathbf{n}_{M'} \left[\alpha\Psi(M') + \beta \frac{\partial}{\partial n_M} \Psi(M') \right] ds. \qquad (7)$$

Table 1 illustrates the condition numbers related to the system given by Eq. (5) and by Eq. (6). It can be seen that the conditioning of the linear system is improved.

(ii) Numerical Scheme. As recalled in Section (*i*), the panel method was used to solve the linear combination in Eq. (7). As usual, an approximation of both body surface including the upper side S^+ and lower side S^- body surfaces and wake surface Σ is proposed by using a panel juxtaposition over S and Σ. A discretized formulation of the linear combination (7) written on a control point M_i reads in infinite fluid:

$$\alpha_i \sum_{j=1}^{NB+NW} D_{ij}^{(1)}\mu_j + \beta_i \sum_{j=1}^{NB+NW} D_{ij}^{*(1)}\mu_j = \alpha_i \sum_{j=1}^{NB} S_{ij}^{(1)}\sigma_j + \beta_i \sum_{j=1}^{NB} S_{ij}^{*(1)}\sigma_j, \quad (8)$$

where:

$$D_{ij}^{(1)} = \int_{\Sigma_{ej}} \frac{-1}{4\pi}\frac{\partial}{\partial n_{M'}}\frac{1}{|\mathbf{M}_i\mathbf{M}_j'|}\,ds(M') - \frac{1}{2}\delta_{ij};$$

$$D_{ij}^{*(1)} = \int_{\Sigma_{ej}} \frac{-1}{4\pi}\frac{\partial}{\partial n}\frac{\partial}{\partial n_{M'}}\frac{1}{|\mathbf{M}_i\mathbf{M}_j'|}\,ds(M')$$

$$S_{ij}^{(1)} = \int_{\Sigma_{ej}} \frac{-1}{4\pi}\frac{1}{|\mathbf{M}_i\mathbf{M}_j'|}\,ds(M')$$

$$D_{ij}^{*(1)} = \int_{\Sigma_{ej}} \frac{-1}{4\pi}\frac{\partial}{\partial n_{M'}}\frac{1}{|\mathbf{M}_i\mathbf{M}_j'|}\,ds(M') - \frac{1}{2}\delta_{ij}$$

$$\mu_j = -\varphi|_{M_j'} \quad \sigma_j = \mathbf{V}\cdot\mathbf{n}|_{M_j'}. \quad (9)$$

Here NB is the number of panels over the body, NW is the number of strips over the wake and σ_j is the single layer singularity density over panel j and Σ_{ej} is the panel surface. In order to account for the mirror image of the sails, the so-called double model assumption is used by first considering a linear system $2N \times 2N$ where N = NB + NW. Second, because of the symmetry effect, we can write that the unknown variables related to the base panel and the image mirror panel have the same value. We can then reduce the order of the linear system from $2N \times 2N$ to $N \times N$ and then, the final system becomes:

$$\alpha_i \sum_{j=1}^{NB+NW} D_{ij}\mu_j + \beta_i \sum_{j=1}^{NB+NW} D_{ij}^{*}\mu_j = \alpha_i \sum_{j=1}^{NB} S_{ij}\sigma_j + \beta_i \sum_{j=1}^{NB} S_{ij}^{*}\sigma_j, \quad (10)$$

with $T_{ij} = T_{ij}^{(1)} + T_{ij}^{(2)}$, with T being for D, D^*, S and S^* and $T_{ij}^{(2)}$ is the image mirror panel contribution.

Some numerical tests have been performed to match the optimal values of the coefficients α_i and β_i; it has been shown, Mazzouji (1992), that the use of the ratio α_i/β_i should be chosen in order to minimise the number of parameters. It is also shown that the value of this ratio should be of an order of magnitude of the nondimensional characteristic length of the panels lying along the trailing edge.

It should be noted that the previous equations allow only the calculation of NB values of μ_j due to the NB control points, whereas there are NB + NW unknown variables μ_j. The remaining NW required equations are obtained by using the pressure condition at the trailing edge. In the case of steady flow the condition $p^+ = p^-$ is equivalent to Eq. (11):

$$p^+ = p^- \Rightarrow \tfrac{1}{2}\rho(V^{+2} - V^{-2}) = 0$$

$$\mathbf{a}\cdot\nabla(\varphi^+ - \varphi^-) = 0 \quad (11)$$

where p^+ and p^- are, respectively, the pressure values at M^+ and M^- belonging to S^+ and S^- and $\mathbf{a}$ is simply the expression $\mathbf{a} = (\mathbf{V}^+ + \mathbf{V}^-)/2$. Since the velocity field at the trailing edge is not perpendicular to the fluid velocity in the wake, the previous condition is equivalent to:

$$\nabla(\varphi^+ - \varphi^-) = 0 \quad \text{or} \quad \varphi^+ - \varphi^- = K.$$

This is consistent with the Kelvin theorem. The constant K is

Table 1 The condition number for Eq. (5) or (7)

Profile (panel number)	Potential Method	Mixed Formulation
NACA012 (N=168)	182	32
NACA001 (N=168)	23917	64

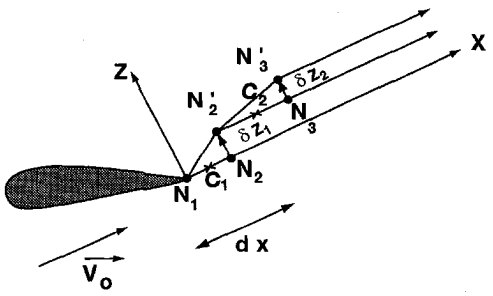

Fig. 1 Scheme of the computation of the shape of the wake

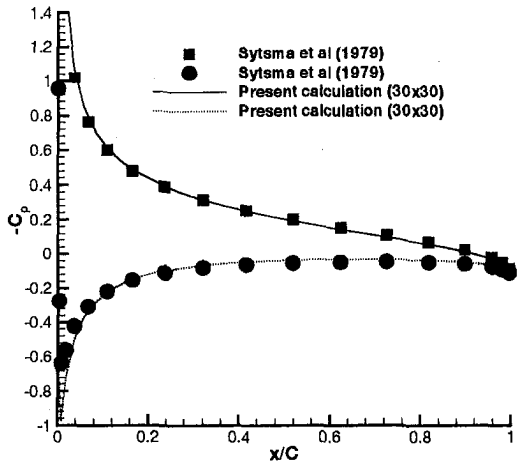

Fig. 2(*a*) Pressure coefficient for RAE wing (y/L = 0.549; T/C = 0.05)

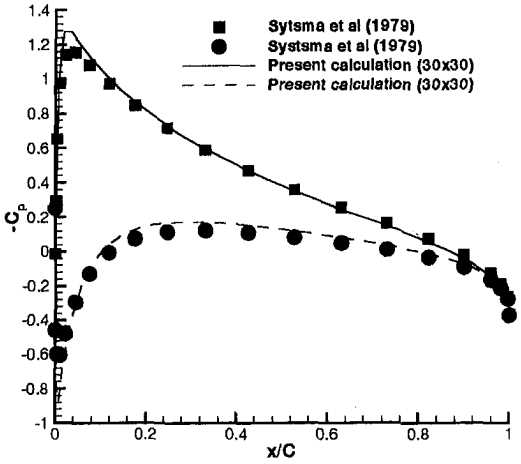

Fig. 2(*b*) Pressure coefficient for RAE wing (y/L = 0.549; T/C = 0.15)

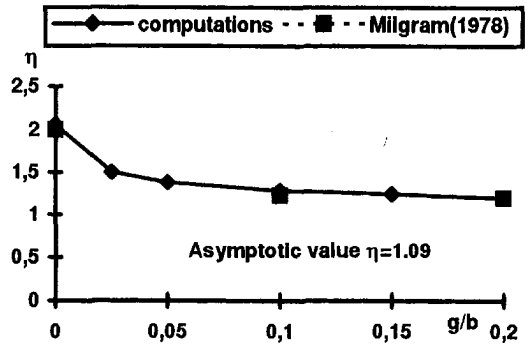

Fig. 3 Influence of gap under wing

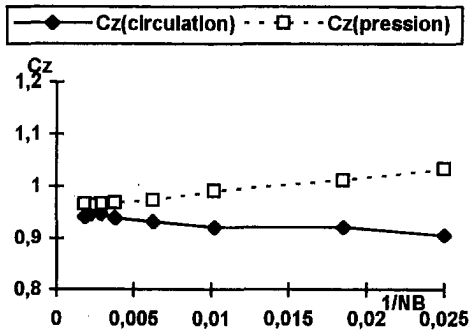

Fig. 5 Convergence on lift rectangular for a single jib (α = 11 deg; NL ≈ 1.5 NW)

equal to the potential jump through the wake. The Kutta-Joukowski condition is then:

$$\varphi^+ - \varphi^- = \|\varphi\|_{TE} \text{ on } \Sigma.$$

The discretized form of this equation is:

$$\mu_{NL*j} - \mu_{NB+NL*j} = \mu_{TEj},$$

for the strip j; NL is the number of panels per strip and TE is for the trailing edge. A linear set of equations is therefore obtained; a part of the unknown vector represents the potential distribution on the body either its thickness is zero or not. After resolution, velocities are computed on the collocation points by using finite difference method and the pressure field is computed by using the Bernoulli theorem. Forces are obtained by integrating the pressure field over the body area, or to improve convergence, particularly for induced drag, by estimating the circulation.

(iii) Wake Shape Computations. In case of two interacting bodies, the upstream wake shape is assumed to be a stream surface in such a way that it will only depend upon the onset flow and its direction is not arbitrary chosen. In steady flow, the wake equilibrium location is given by Eq. (11). Moreover, as the wake is a stream surface, we have:

$$\mathbf{V}^+ \cdot \mathbf{n}^+ = \mathbf{V}^- \cdot \mathbf{n}^- \text{ on } \Sigma.$$

In the case of solitary sail, these equations show that the potential jump is constant along with a vector tangent to **a**. This assumption is no longer correct for interacting sails between two close bodies. The wake shape is computed following a procedure proposed by Butter and Hancock (1971); however, in the present study, the panel method allows a better accounting for the exact geometry of the bodies. The wake is represented by a vortex sheet extending from the trailing edge to infinity downstream. First the flow is computed, assuming a plane wake with an arbitrary direction (here parallel to the free-stream velocity) in order to compute source and dipole intensities satisfying the slip condition on the sail. These values are no longer changed for the remaining computations dealing with the wake shape. It is assumed that the final shape of the wake is not plane. In order to guarantee the spatial conservation of the circulation, the induced velocities are computed between two straight vortex filaments, following an iterative procedure. A longitudinal spatial step dx is chosen, between two points N_i and N_{i+1} of the wake assumed to be locally parallel to axis x (see Fig. 1 assumed in 2D flow for simplicity); the components of velocity (V_{xi} and V_{zi}) are calculated at point C_i, middle of the previous segment, N_{i+1} is then moved to N'_{i+1}, so we have:

$$\mathbf{N}_{i+1}\mathbf{N}'_{i+1} = \frac{V_{yi}}{V_0} dx\mathbf{y} + \frac{V_{zi}}{V_0} dx\mathbf{z}. \quad (12)$$

The computation is carried out from point N_1 located on the trailing edge. Downstream of the point N'_{i+1}, the wake is parallel to the initial direction. This iterative procedure is applied by using a prescribed length l_w. Then the flow can be calculated again with the new shape of the wake and new influence coefficients are thus obtained, leading to a new set of linear equations that must be solved giving new unknown distributions, and then the pressure distribution and the forces acting on the bodies. The convergence of procedures for finding the equilibrium wake is notoriously difficult (Thrasher et al., 1979) and so the full convergence is not obviously obtained after one iteration. How-

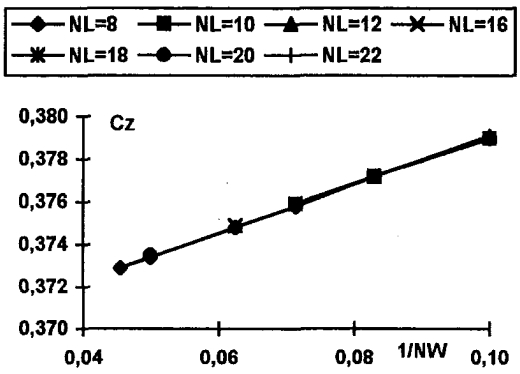

Fig. 4 Convergence on lift for a rectangular flat plate (AR = 3, T/C = 0, α = 5 deg)

Table 2 Geometric parameters of jib no. 1

α=11°

Vertical location	Camber max (% chord)	Location of max.camber (% chord)	Relative Camber at 25% chord	Relative Camber at 50% chord	Relative Camber at 75% chord	Twist angle (°)
0.75b	14.3	42.5	84.8	97.7	66.8	15.1
0.50b	11.8	46.0	79.2	99.5	71.2	9.6
0.25b	6.8	40.0	85.9	97.2	66.0	4.6
0	5.0	45.0	80.3	99.2	70.3	0

α=13°

Vertical location	Camber max (% chord)	Location of max.camber (% chord)	Relative Camber at 25% chord	Relative Camber at 50% chord	Relative Camber at 75% chord	Twist angle (°)
0.75b	13.6	42.5	85.2	97.7	66.8	11.8
0.50b	10.9	35.0	99.6	98.2	71.2	7.4
0.25b	8.2	40.0	85.9	97.2	66.0	3.5
0	5.0	45.0	80.3	99.2	70.3	0

α=15°

Vertical location	Camber max (% chord)	Location of max.camber (% chord)	Relative Camber at 25% chord	Relative Camber at 50% chord	Relative Camber at 75% chord	Twist angle (°)
0.75b	12.7	42.5	85.2	97.7	66.8	9.3
0.50b	10.1	35.0	99.6	98.2	71.2	5.9
0.25b	7.8	40.0	85.9	97.2	66.0	2.8
0	5.0	45.0	80.3	99.2	70.3	0

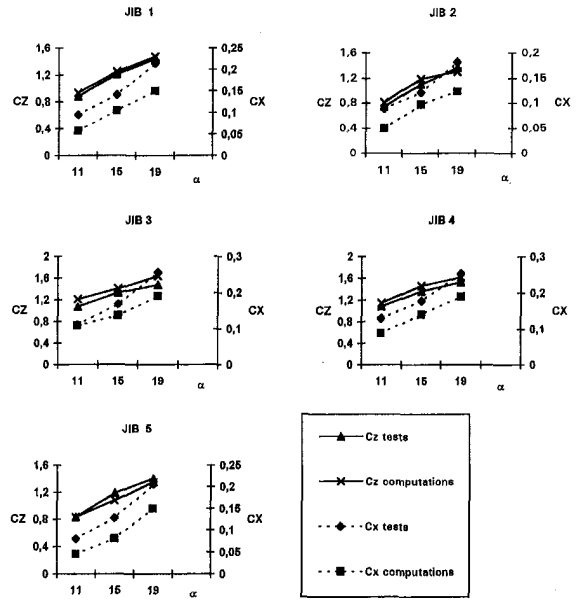

Fig. 6 Force coefficients on jibs

ever, some numerical experiments have shown that the wake shape computed after one iteration is sufficient to account for the interaction in terms of force coefficients. This is probably due to the fact that the local direction of the vortex filaments is the same as the local velocity field one, even if the actual wake shape is not reached. This procedure is used only for the wake of the forebody, a plane wake model is retained for the aft-body. In the following sections this solution will be called the "iterated" solution and the one with two plane wakes, the "linear" solution.

(iv) Boundary Layer Correction. The inviscid flow assumption has been useful to derive the boundary element technique. However, a boundary layer correction has been added. The underlying physical idea is that the sail is a material stream surface, having two sides. So, in order to approximately estimate the viscous effects, an attempt has been made to compute the friction force over each side. A turbulent boundary layer behavior based upon the local velocity is then assumed. For such a situation, Cousteix (1989) proposes the following formula to compute the friction coefficient:

$$C_f = \frac{0.0594}{\mathrm{Re}_x^{0.2}}, \quad \text{where} \quad \mathrm{Re} = \frac{U(x)x}{\nu};$$

$U(x)$ is the local velocity computed by the previous panel method and ν is the kinematic viscosity. These effects are summed up over each side of the sail and added to the inviscid fluid forces.

Numerical Results

(i) Solitary Bodies. Figures 2(*a*) and 2(*b*) show the validation of the results for the RAE wing in infinite fluid (aspect ratio AR = 3, taper ratio $\epsilon = \frac{1}{3}$, mid-chord sweep angle $\Lambda_{1/2}$ = 30 deg and two values of the relative thickness, T/C = .05 and .15), with respect to the results (Roberts ones) given by Sytsma et al. (1979). The pressure coefficient distribution ($-C_p$) along the local chord C is plotted at approximately mid-span (y/b = 0.549, b being the total span) showing good agreement with the previous results, except some differences in the peak region. Initial results on simple shape wings have shown a great influence of the gap between the wing lower part and the free-surface location, the symmetry plane of the double model. For example, in Fig. 3, we present the influence of this gap. It must be kept in mind that no vortex sheets leave the wing at its lower part if there is a gap. The induced drag coefficient $\eta = C_z^2/(\pi ARC_x)$ is plotted versus the relative gap g/b (g is the gap) for a rectangular aspect ratio, AR = 3, and NACA0005 profile wing. η decreases very quickly first when g is increased, then more slowly to reach the value for a solitary wing in infinite medium, showing the need of an accurate knowledge of the location of a sail above the free-surface. The results are in close agreement with those of Milgram (1978).

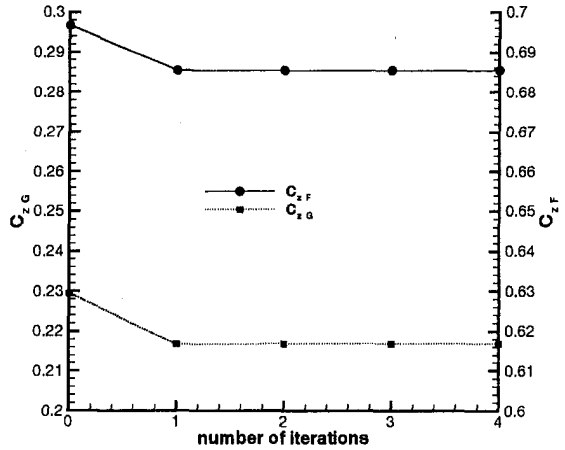

Fig. 8 Influence of the number of iterations in case of moderate interaction (NB = 400) (θ_F = 2 deg; θ_G = 0 deg; α = 8 deg; d/C = 1.25)

An interface has been developed between our numerical code and the computer aided design and manufacture code, FABRIC developed by the Centre de Recherches Appliquées aux Industries Nautiques (Pallu, 1990a). This interface has been first used to perform computations on solitary jibs or for various sets of jib and mainsail. As it was not easy to modify the number of strips and the number of panels per strips on a real jib due to constraints implied by the use of the software FABRIC, the convergence has been first studied on a zero thickness rectangular flat plate AR = 3. The lift coefficient C_z is presented in Fig. 4 versus the parameter 1/NW. It can be observed on this plot that for a given value of NW, the lift is quite independent of NL, except for too low values of NL (for example NL less than

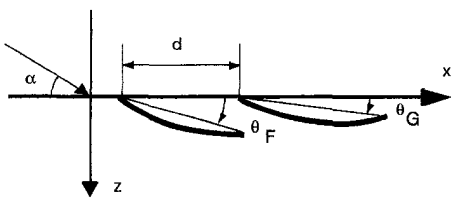

Fig. 7 Locations of a set jib-mainsail

Table 3 Parameters for studied cases of interaction jib-mainsail

Configuration	variable	n°1	n°2	n°3	n°4	n°5
Apparent wind incidence	α	18°	17°	20.1°	17°	13.9°
Jib sheeting angle	θ_F	8.6°	8°	8°	8°	7°
Mainsail sheeting angle	θ_G	2.2°	-2°	-2.5°	-2°	-2°
Mast raking angle	ϕ	3°	3°	3°	3°	3°
Heel angle	φ	0°	0°	0°	0°	0°
Distance between the tack points (scale 1/15)	d	0.507m	0.507m	0.507m	0.507m	0.507m
Hull height	h_c	0.084m	0.088m	0.088m	0.088m	0.088m
Height of the main sail above deck	h_g	0.133m	0.133m	0.133m	0.133m	0.133m
Area mainsail+jib	S	1.524m^2	1.524m^2	1.524m^2	1.185m^2	1.185m^2
Reference length for moments	L_{ref}	2.170m	2.170m	2.170m	2.170m	2.170m

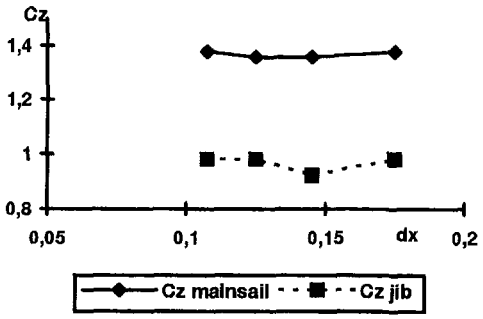

Fig. 9 Influence of the wake streamwise step

NW/2). Extrapolation to NW → ∞ shows an error of about 1.3 percent with respect to the value obtained for NW = 22 (NB = 484). Figure 5 shows same study of convergence on a jib model (type JI 12m, America Cup rule) but versus 1/NB at the incidence α = 11 deg. The shape of the jib is known from photographs taken during the tests on five sections and for each section, the profile is defined in Table 2, by the maximum camber and its location on the local chord, relative camber at 25, 50, and 75 percent of the local chord and twist angle. These previous parameters have been determined by projecting the slides on a large screen. In order to have panels of aspect ratio close to 1, we have chosen a relation NL ≈ 1.5NW. The results show a slight increase of C_z (from 3.7 percent between NB = 40 to NB = 556) for lift calculations from the circulation and a slight increase for pressure integration. The difference between both values decreases as the number of panels increases. For further computations, values of NB close to 378 have been chosen, corresponding to a CPU time of 10 mn on a DEC3000-800S work-station, keeping in mind that the true sail shape is not known with great precision. Lift coefficients have been computed for the same jib but with five various tensions applied to it, at incidence α = 11, 15, and 19 deg to compare with measurements conducted on jib models in wind tunnel, Pallu (1990b). Table 2 shows the slight variation of the jib shapes with the incidence. Similar data for the four other tensions are not given here by lack of space. Results of lift and induced drag coefficients are plotted versus the incidence angle on Fig. 6. For the lift coefficient, the agreement is quite good in spite of the high values of the incidence angle and the uncertainties owing to the exact shape of the jibs. For the drag coefficient, it was not possible to determine from tests the friction coefficient by extrapolation due to the few values of incidence studied; so the comparison is only possible between the total drag (defined as the sum of induced drag and friction drag) and the induced drag computed. Except for two discrepancies for jib 2 and 3, measurements and computations are located on two parallel curves. It should be noticed that no gap between the jibs and the free-surface has been assumed.

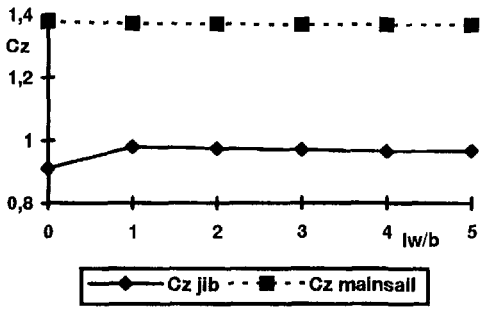

Fig. 10 Influence of the length of the wake

Table 4 Effect of the number of panels for configuration no. 2

Config. n°2	NB	320	320	448	448	1176	1176
	C_z based on	regular	sinusoid.	regular	sinusoid.	regular	sinusoid.
linear	circulation	1.079	1.050	1.087	1.110	1.144	1.151
linear	pressure	1.066	1.133	1.110	1.155	1.148	1.178
iterated	circulation	1.125	1.054	1.053	1.104	1.151	1.158
iterated	pressure	1.205	1.175	1.144	1.185	1.178	1.213

(ii) Interacting Bodies. To study the influence of the number of iterations on the solutions of the numerical calculations, tests have been performed on two rectangular aspect ratio AR = 3 wings (T/C = 0.12). The definition of the relative locations are given in Fig. 7. For a configuration corresponding to a realistic location of a jib and a main sail, with the wake of the upstream body close to the downstream one (θ_F = 2 deg, θ_G = 0 deg, α = 8 deg, and d/C = 1.25), Figure 8 shows that for both bodies, the lift force coefficients of fore and aft bodies, respectively C_{zF} and C_{zG}, are nearly constant after the second iteration; iteration zero corresponds to the "linear" calculation. For stronger interactions, for example two bodies with reference chords on the x-axis, the aft body located just behind the fore one, ($\theta_F = \theta_G$ = 0 deg; α = 8 deg and d/C = 1.25), oscillations have been observed after two iterations, so results are no more valid. It must be noticed that in reducing strongly d/C, results become incoherent even for the linear calculation. Computations have been also carried out on five sets of jib-main sails for America cup class F1 at $\frac{1}{15}$th scale. The shapes of the sails in wind tunnels have been determined from photographs as previously discussed. Definitions of sail parameters are also given in Fig. 7 and the values of these parameters are presented in Table 3. To obtain correct results, the location of sails above the deck must be known very accurately. Computed results show variation of about 20 percent of lift for small changes of geometry as already observed by Charvet and Huberson (1992).

For a set of jib and mainsail, a test of convergence has also been achieved for configuration no. 1. Figures 9 and 10 show the variations of the lift coefficients on jib and mainsail versus the streamwise step dx used for the computation of the wake and versus the length of the computed wake l_w/b, using a regular grid 8 × 10 for each side of each sail, leading to 320 panels. In Fig. 9, results are for dx ranging from $b/16$ to $b/10$ with l_w/b = 4. In Fig. 10, the step is dx = 0.175 (l_w = 0 corresponds to the "linear calculation"). No influence can be seen on the lift of the jib. For the mainsail, the variation is weak with the step and the length of the computed wake has been chosen of about 3 times the span of the jib. Table 4 shows the variation of the global lift coefficient computed by integration of the circulation or by pressure integration on configuration no. 2 for various numbers of panels, with or without iteration. It can be observed that by multiplying the number of panels by 3.68 (from NB = 320 to 1176), the variation of the value is less than 6 percent but the computational time is increased by a factor of about 10. The difference of results obtained with a regular panel step in chord or with a sinusoidal distribution is low and decreases as the number of panels increases; the same

Table 5 Comparison between test measurements and computations for sets jib-mainsail

Configuration	n°1	n°2	n°3	n°4	n°5
C_Z measured	0.739	1.13	1.349	1.21	1.056
C_Z"corrected"	0.724	1.108	1.321	1.181	1.033
C_Z linear	0.703	1.087	1.263	1.308	1.204
C_Z iterated		1.053	1.264	1.304	1.171
$10C_X$ measured	1.15	1.55	2.03	1.61	1.34
$10C_X$ "corrected"	0.55	1.14	1.57	1.06	0.83
$10C_X$ linear	0.359	0.756	0.966	0.843	0.672
$10\ C_x$ iterated		0.743	0.977	0.843	0.654

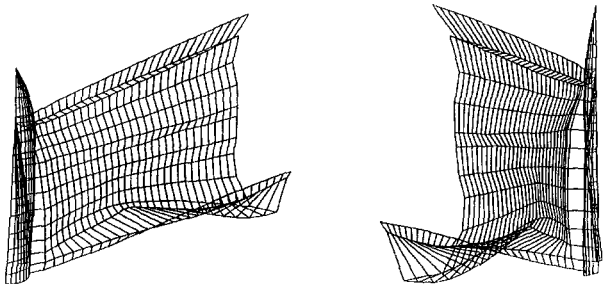

a) side view b) back view

Fig. 11 Computed shape for the wake of configuration no. 2

observation can be done for the two different methods of integration for lift. Furthermore, instabilities appear for computations of velocities in the wake with a grid with sinusoidally streamwise variation.

Force coefficients have been computed by integration of the circulation using a regular 8 × 14 grid on each side of the sail (corresponding to 448 panels); the results are presented in Table 5. In order to know experimental forces on sails only (Pallu, 1990b), two separate experiments have been conducted: the first series were devoted to measure the forces applied to the set "mast + main sail + jib + boat hull above the free-surface"; the measured forces have been corrected by subtracting from these values, related to the so-called total forces (including that of hull, mast and sails) the forces applied to the hull and masts without sails. Agreement for lift is quite good for case 1 to 3 corresponding to quite similar configurations. For cases 4 and 5, also quite similar, but with a different aspect ratio from the value of the three previous cases, the computations overestimate the lift. Nevertheless, the difference is less than 15 percent. For the drag force coefficient, only the induced drag is given; computed drags are about one half of total measured values. Keeping in mind the uncertainties on the shapes of sails, these results can be considered as satisfactory.

Moreover, not only forces but also local information, as pressure, velocities, and shape of streamlines around sails, useful for designing a set of sails, can be obtained. Figure 11 shows

Table 6 Drag coefficients on jib number 1 (see Table 2)

Incidence (°)	11	13	15
C_x (measurements)	0.095	0.141	0.215
C_x (inviscid)	0.058	0.105	0.150
C_x (friction)	0.037	0.041	0.044
C_x (total)	0.095	0.146	0.194

the shape of the computed wake behind the jib from a set of jib + main sail using a 8 × 13 grid (8 × 15 for the mainsail) on each side. Rolling up of the flow due to tip vortices can be seen at both tips. Instabilities appear in the velocity calculations, probably induced by a too long first longitudinal step in the wake and strongly influencing the shape of the wake. Nevertheless, it is not the true shape of the wake which is useful to know, but its influence onto the downstream sail; so only an approximated shape is needed.

Figure 12 shows the distribution of local pressure jump for sails of case no. 1 using a regular 8 × 14 grid, first around a set of interacting jib and mainsail (Fig. 12(a)) and then around a jib and a mainsail considered as solitary bodies with same locations with respect to incoming wind (Figs. 12(b) and 12(c)). Alone, the jib gives very low values of forces compared to the single mainsail. As shown in the case of thin two-dimensional bodies (Marchaj, 1978), or in the case of thick three-dimensional bodies by Gentry (1979), the effect of interaction is quite visible on these graphs. Interaction increases forces acting on the two lower thirds of the jib but decreases forces on the mainsail. It must be recalled that the present computations are based on ideal flow assumption, so the effect of the jib on the mainsail is only due to decrease of the effective angle of attack of the mainsail. Thus the risk of separation is prevented and the loss of forces should not be as high as predicted by computations.

The results of the boundary layer correction are presented in Table 6 for jib number 1 of Fig. 6 and compared with measurements. It can be seen that the viscous effects estimation is reasonably accurate as far as the Blasius formula related to turbulent flow is used and the velocity computed by the boundary element technique on each panel is used instead of the onset one.

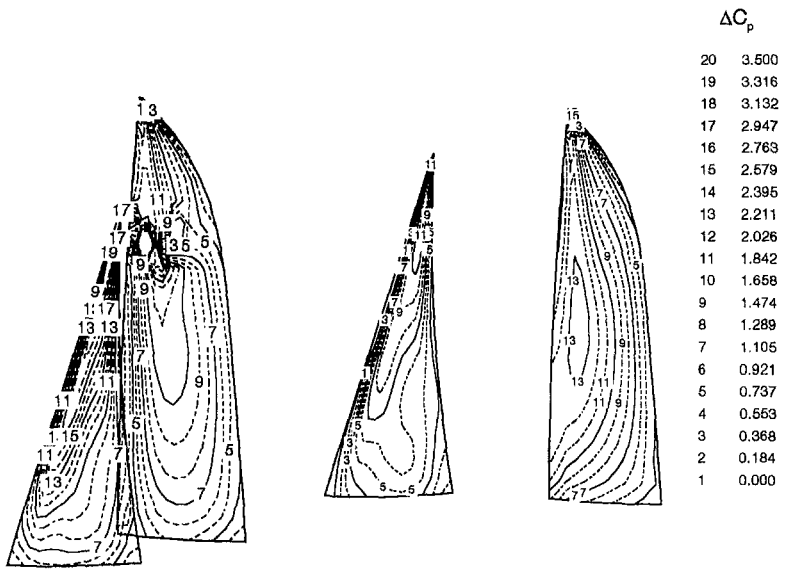

a)set jib mainsail b)jib alone c)mainsail alone

Fig. 12 Pressure coefficients distributions

Conclusion

A boundary-element method applied to the computation of the incompressible inviscid flow around a solitary sail or a set of jib and mainsail has been developed. A model using a linear combination of the potential and velocity formulations has been used. This method is suitable for the computation of the flow around a mixing of thick and/or thin bodies. The main advantage of this approach is its ability to solve the numerical problem related to the zero thickness. It appears to be a complement to the vortex lattice method particularly by its ability to compute the pressure field on each side of a zero thickness body and not only the pressure jump. Such a computation is useful for the flow characteristics around sails and profiled masts. Furthermore, in the case of interacting bodies, an iterative calculation of the wake shape has been developed. However, only one iteration have been achieved since it seems to be sufficient to account for the interaction in terms of force coefficients if the interaction remains moderate. Numerical tests have shown that for realistic configurations, forces are nearly constant for the further iterations. Computations of lift have been compared with measurements led in wind tunnel on jibs or sets of jib and mainsail with relatively good agreement, in spite of the relatively weak precision on the true sail shape. A coupling of the ideal fluid method presented here with a boundary layer method has been achieved to obtain a better description of the flow around the sails and realistic values of the drag coefficients have been obtained, even if it must be considered as an estimation. So, an efficient method of computations is available. Nevertheless some difficulties are still present: specifically for curved leeches and sails with high curvature, the Kutta-Joukowski condition cannot be fully satisfied leading to nonzero pressure jumps at the trailing edge, which must also affect the accuracy of the computations. In spite of this fact, global forces seem to be little affected and are in correct agreement with the measurements; unfortunately, those are the only quantities that may be compared. Some problems appear also at the top of the sails when the leading edge and the trailing edge are very close one to the other, probably due to the high values of surface curvature between close panels.

Acknowledgments

The authors are indebted to the Centre de Recherches pour l'Architecture et les Industries Nautiques and more particularly to the Director, P. Pallu de la Barrière, and M. Kermarec for the communication of measurements on sails in wind tunnels and their friendly encouragement for the pursuit of the work.

The authors are indebted to the reviewers for their suggestions and additional references concerning the sails performances.

References

Arena A. S., and Nelson R. C., 1992, "A Discrete Vortex Model for Predicting Wing Rock of Slender Wings," AIAA paper no. AIAA-92-4497-CP, Hilton Head.

Boudreault R., 1985, "3-D Program Predicting the Flexible Membrane Wings Aerodynamic Properties," *Journal of Wind Engineering and Industrial Aerodynamics,* Vol. 19, pp. 277–283, Amsterdam Elsevier Science.

Butter D. J., and Hancock G. J., 1971, "A Numerical Method for Calculating the Trailing Vortex System Behind a Swept Wing at Low Speed," *Aeronautical Journal,* Vol. 75, pp. 564–568.

Charvet T., and Huberson S., 1992, "Numerical Calculation of the Flow Around Sails," *European Journal of Mechanics, B/Fluids,* Vol. 11, No. 5, pp. 599–610.

Cousteix J., 1989, "Turbulence et couche limite," CEPADUES Editions, Toulouse.

Gentry A. E., 1979, "The Aerodynamics of Sail Interaction," *Proc. of the AIAA 3rd Symposium on Aero/Hydrodynamics of Sailing,* Los Angeles.

Marchaj C. A., 1979, *Aero-Hydrodynamics of Sailing,* Granada Publishing in Asdlard Coles Limited.

Mazzouji F., 1992, "Contribution à l'étude des écoulements stationnaires et instationnaires autour de voiles de navire," Thèse de doctorat, Université de Poitiers.

Mazzouji F., Guilbaud M., and Rajaona R. D., 1992, "A Boundary Element Method Applied to the Computation of Sail Loading," *Proc. 14th Boundary Element Int. Conf.,* pp. 41–58, Sevilla.

Milgram J. H., 1978, "The Analytical Design of Yacht Sails," *Transactions SNAME,* Vol. 76, pp. 118–160.

Milne-Thompson L. M., 1958, *Theoretical Aerodynamics,* MacMillan, London.

Mook D. T., and Nayfeh A. H., "Application of the Vortex-Lattice Method to High Angle of Attack Subsonic Aerodynamics," SAE Technical Paper Series, no. 851817.

Morchoisne Y., Lê T. H., and Ryan J., 1987, "Condition de Fourier dans les méthodes intégrales: application aux corps minces," *La Recherche Aérospatiale,* No. 4, pp. 71–74.

Pallu de la Barrière P., 1990a, Notice du logiciel F.A.B.R.I.C., Centre de Recherches pour l'Architecture et les Industries Nautiques, La Rochelle.

Pallu de la Barrière P., 1990b, "Mesures des forces appliquées à une voile ou à des ensembles foc-grand voile en soufflerie," Private Communication, Centre de Recherches pour l'Architecture et les Industries Nautiques, La Rochelle.

Rajaona D. R., 1978, "Etude théorique et expérimentale d'une quille de voilier en mouvement stationnaire et harmonique," Thèse de Docteur-Ingénieur, Université de Nantes.

Register D., and Irey R. K., 1983, "Analysis of Steady Flow over Interacting Sails," *Transactions SNAME* (Ed.), 6th Chesapeake Symposium, pp. 1–12.

Schoop H., 1990, "Structural and Aerodynamics Theory for Sails," *European Journal of Mechanics A/Solids,* Vol. 9, No. 1, pp. 37–52.

Smith R. W., 1987, "An Inviscid Analysis of the Flow About Wind Surfing Sails," 17th AIAA, pp. 55–64.

Sparenberg J. A., and Weirsma A. K., 1976, "On the Maximum Thrust of Sails by Sailing Close to Wind," *Journal of Ship Research,* Vol. 20, No. 2, pp. 98–106.

Sytsma H. S., Hewitt B. L. and Rubbert P. E., 1979, "A Comparison of Panel Methods for Subsonic Flow Computation," AGARDograph, No. 241.

Thrasher D. F., Mook D. T., and Nayfeh A. H., 1979, "A Computer-Based Method for Analysing the Flow over Sails," *SNAME Chesapeake Symposium,* pp. 119–127.

Flow Analysis in a Pump Diffuser—Part 1: LDA and PTV Measurements of the Unsteady Flow

K. Eisele

Z. Zhang

M. V. Casey

Fluid Dynamics Laboratory,
Sulzer Innotec,
Winterthur,
Switzerland

J. Gülich

A. Schachenmann

Sulzer Pumps,
Winterthur,
Switzerland

This paper describes experimental research aimed at improving our understanding of the complex unsteady three-dimensional flow field associated with the interaction between a pump impeller and its vaned diffuser. The paper provides the results of experiments carried out using Laser Particle Tracking Velocimetry (LPTV) and Laser Doppler Anemometry (LDA), in which time-resolved details of the unsteady flow field in a vaned diffuser of a medium specific speed pump have been obtained as a function of the local position of the pump impeller blades. Detailed flow field measurements have been carried out at several measurement positions in the diffuser and at a number of operating points along the pump characteristic. The measurement results have been analyzed to elucidate some interesting flow features observed in this typical pump diffuser. These include three-dimensional flow at the impeller outlet, flow separation in the diffuser channel, unsteady recirculation of the flow from the diffuser into the impeller, the passage of vorticity in the impeller blade wakes through the diffuser, and periodic unsteadiness and turbulence in the diffuser flow channel. The relevance of these flow features to the stability of the pump characteristic is discussed.

Introduction

It is well known that the close proximity of the impeller and diffuser of a centrifugal pump causes a strong interaction between the flow in both components, see, for example, Cumpsty (1989). This interaction has a large influence on the stability of the pump operating characteristics and on the structural vibrations and pressure pulsations in the impeller caused by flow separation at partload operating points, Gülich and Bolleter (1993).

Detailed analysis of the unsteady and turbulent interaction is at the limit of the simulation capability of CFD methods, although some first attempts at the numerical simulation of this phenomenon are now appearing in the technical literature, Dawes (1994), Muggli et al. (1996). Our experimental knowledge of the rotor-stator interaction is mainly based on hot-wire experiments in low speed compressors, see for example, Inoue and Cumpsty (1984) and Ubaldi et al. (1994), on wall static pressure measurements in pumps, see Arndt et al. (1989) and on PIV mesurements in a simplified model, Akin et al. (1994). Because of the limitations of our theoretical methods and our lack of detailed experimental knowledge, impellers and diffusers are usually considered separately in the design process for industrial pumps and the strong unsteady interaction between the two components is not taken into account in design calculations, Casey (1994).

This paper presents some results of recent detailed optical measurements of the unsteady flow field in a highly loaded vaned diffuser of a medium specific speed pump. The optical flow measurements have been obtained with a two-dimensional Laser Doppler Anemometry (LDA) system and a triggered two-dimensional Particle Tracking Velocimetry (PTV) system. The LDA system has been used from two separate viewing angles to obtain three-dimensional information on the flow field. Both the LDA and the PTV methods allow the local flow patterns in the diffuser to be determined as a function of the position of the impeller blades relative to the diffuser vanes. In this way it is possible to identify the periodic unsteady flows in the diffuser that are caused by the strong potential interaction with the impeller vanes and by the passage of the impeller blade wakes. Detailed measurements of the flow field have been carried out at a large number of positions in the diffuser, both at the design point and at various off-design operating points of the pump including extreme part-load conditions.

The objective of the work is to help advance our understanding of the complex unsteady flow field and the nature of the interaction between the pump impeller and its vaned diffuser. Particular emphasis is given in the paper to the following items:

- Understanding the nature of the flow field at the inlet to the pump diffuser related to the complex three-dimensional and periodically unsteady flow field at outlet of the impeller.
- Examination of the flow field in the diffuser, especially features of the flow caused by the periodic unsteadiness relating to the blade passing frequency, and those caused by turbulence and flow separation in the diffuser.
- Correlation of the observed flow patterns with the onset of instability in the pumping characteristics.
- Understanding the nature of flow recirculation from the diffuser into the impeller at part-load conditions, especially with regard to the elucidation of the requirements of suitable CFD models for predicting these effects.

A second part of this paper, Muggli et al. (1997), describes progress with current CFD simulation methods to model the mean steady-state flow field in this diffuser at its normal operating point.

Experimental Apparatus and Measurements

Test Rig. A dedicated closed-loop test rig for optical measurements in a single stage medium specific speed pump has

Contributed by the Fluids Engineering Division for publication in the JOURNAL OF FLUIDS ENGINEERING. Manuscript received by the Fluids Engineering Division October 12, 1995; revised manuscript received July 21, 1997. Associate Technical Editor: L. Nelak.

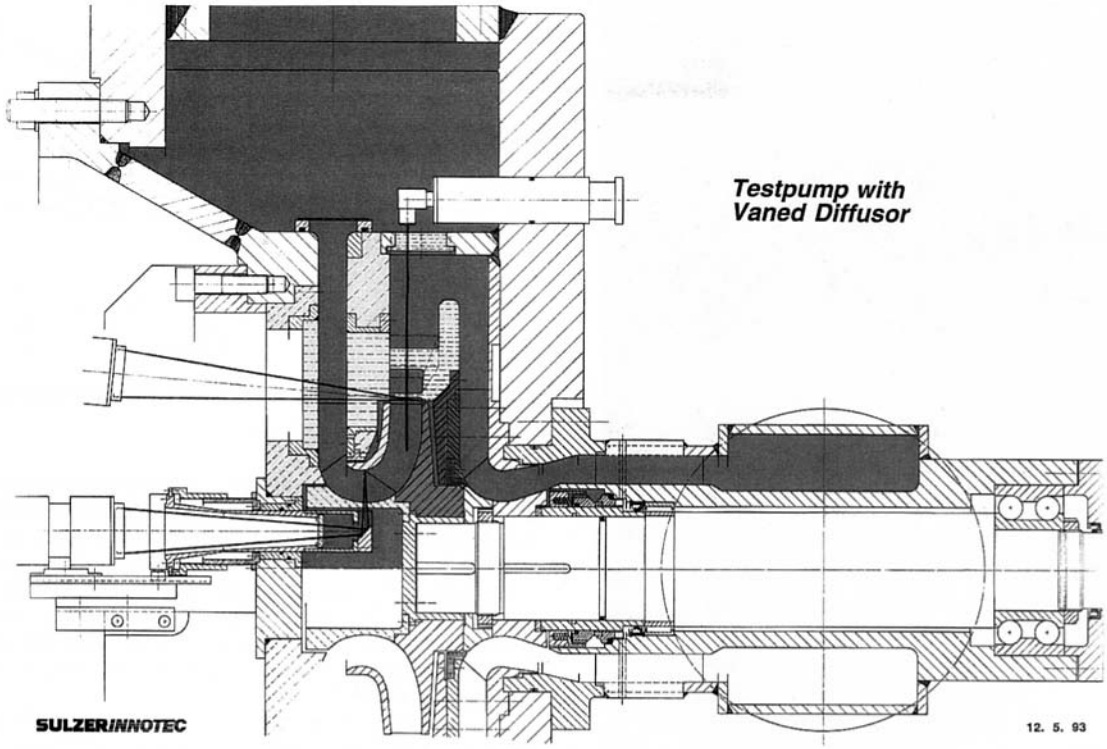

Fig. 1 Test pump with vaned diffuser

been designed, as shown in Fig. 1. Particular attention was given in the design of the rig to the provision of optical windows to enable LDA and PTV measurements to be made, both in the impeller and in the diffuser. The test loop was also made of stainless materials and filled with demineralised water to ensure clean optical access. For the optical measurements seeding of the water was necessary and glass particles of 4μm were used for LDA measurements and polystyrene particles of 60μm for PTV measurements.

The geometry of the pump used for these tests represents a middle stage of a medium specific speed multi-stage pump. The pump inlet geometry in the rig was designed to provide a clean uniform flow at pump inlet. The diffuser geometry in the rig has been modified slightly compared to the standard geometry for normal applications to provide good optical access and to improve the specification of the boundary conditions for numerical simulations. In particular, the return channel was lengthened compared with a normal middle stage diffuser so that a clearly defined outlet boundary condition was available for the diffuser simulations. Further details of the design of test rig can be found in Eisele et al. (1992).

Two diffusers of similar geometry were used in this work. For the flow visualization and LPTV measurements a perspex model was used and for the LDA measurements an aluminum diffuser of similar geometry was manufactured. The perspex model was also equipped with pressure transducers for static and dynamic measurements of the wall pressures (Fig. 2).

The main dimensions of the impeller and the diffuser are listed in Table 1. It is of interest to note that relative to the impeller outlet radius, the diffuser vane inlet radius is very close to the impeller, at $D_3/D_2 = 1.04$ giving a very short (four percent) vaneless radial gap between the impeller and the diffuser. The diffuser vanes are also relatively short with a vane outlet radius at $D_4/D_3 = 1.36$. The diffuser is not of constant axial width and within the diffuser channels the diffuser area increases both between the vanes and between the endwalls by the use of a sloping endwall on the hub side of the diffuser, see Fig. 1. The sloping endwall gives rise to a nonaxisymmetric hub wall and also leads to a very highly loaded diffuser design with a channel length to inlet width ratio of 4.8, an equivalent 2D diffuser opening angle of $2\theta = 14$ deg, and an area ratio of 2.55. In the typical diffuser design charts of Reneau et al. (1967) the diffuser is just below the transition from attached flow to transitory stall. Further details of the three-dimensional aspects of the diffuser geometry can be found in part two of this paper where the steady-state simulations are given, Muggli (1997).

Laser Doppler Anemometry (LDA). A two color Dantec fiber LDA with a PDA processor was used for the measurements in the pump diffuser. A summary of the optical characteristics of the velocimeter is provided in Table 2.

Nomenclature

$B2$ = impeller exit width
$B3$ = diffuser inlet width
C_x, C_y, C_z = velocity components
D_0 = impeller hub diameter
D_1 = impeller shroud diameter
D_2 = impeller exit diameter
D_3 = diffuser vane inlet diameter
D_4 = diffuser vane exit diameter
D_5 = diameter of return channel
n = impeller speed
Δp = pressure difference
u_2 = circumferential velocity of impeller exit
x, y, z = coordinates (Z-axial direction)
ρ = density
$\psi = \Delta p/((\rho/2) \times u_2^2)$ = pressure coefficient
$\varphi = Q/u_2\pi D_2 B_2$ = flow coefficient
$\varphi_0 = \varphi$ = at best efficiency point

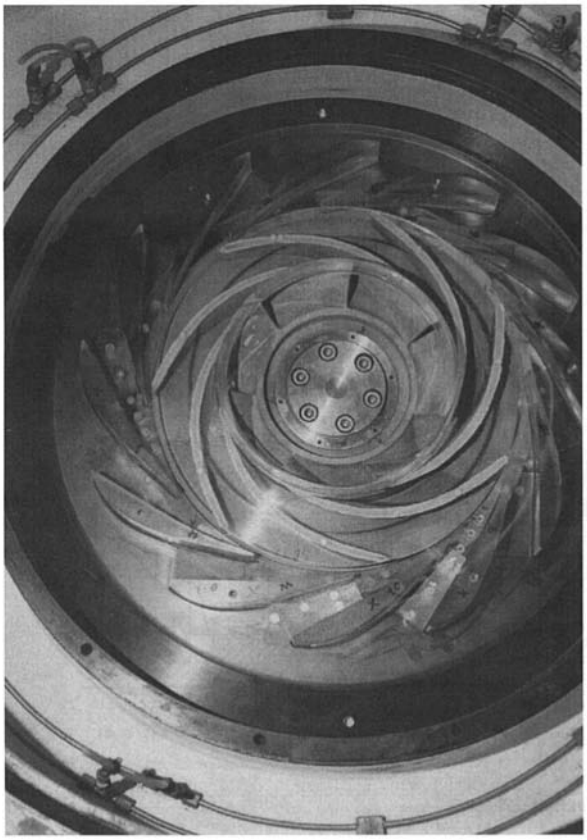

Fig. 2 Photograph of the perspex diffuser and impeller with perspex shroud

With this two color LDA system, two components of the three dimensional velocity vector can be measured from a single viewing angle. The third component of the three-dimensional flow can be measured with the help of an additional measurement from a second LDA viewing angle. For this approach to be satisfactory when taking measurements in water flows, special care needs to be taken with regard to the accuracy of the traverse system and the geometry of the optical setup, see Zhang and Eisele (1995). In particular, the optical system must ensure that the velocity measurements from two different viewing angles are taken at exactly the same point in the flow.

The final accuracy of the measurement position is determined not only by the accuracy of the traversing system but also by

Table 1 Main dimension of the pump

Impeller	Diffuser
D_0 = 140 mm	D_3 = 364 mm
D_1 = 208 mm	D_4 = 496 mm
D_2 = 350 mm	D_5 = 570 mm
B_2 = 32.9 mm	B_3 = 34.5 mm
n = 1000 rpm	
Vanes: 7	Vanes: 12

Table 2 Characteristics of the LDA system

Laser type	Innova 90
Laser wave length	488.0/514.5 nm
Probe diameter	60 mm
Beam spacing	38 mm
Focal length	400 mm
Fringe spacing	5.14/5.42 μm

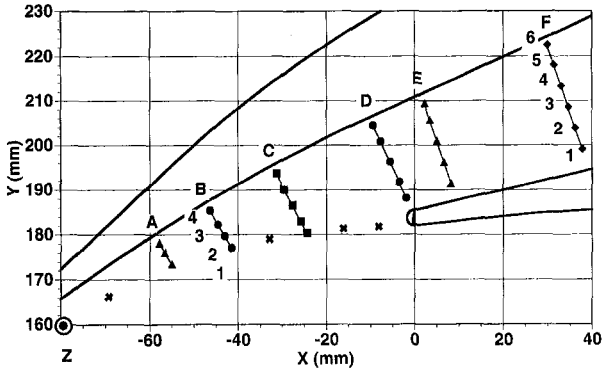

Fig. 3 Location of LDA coordinate system and LDA measurement points

the accuracy of the location of the LDA measurement volume in the diffuser. The location of the LDA measurement volume was calibrated by using a small gold sphere fixed at a defined position in the diffuser. When the LDA measurement volume is focused on the surface of the sphere, such that the reflected beams follow the reverse path of the incoming beams, this provides an exact calibration of position. With this system the accuracy of the positioning system was found to be very high ($\leq \pm 0.05$ mm).

The best measurement results would be obtained if the second LDA viewing angle were perpendicular to the first, in such a manner that the third component of velocity could be measured directly. This was not possible in the existing test pump as the LDA probe had to be mounted directly in front of the pump for both viewing angles (see Fig. 1). The second viewing angle was selected on the basis of the LDA data rate and the accuracy of the measurements, for details see Zhang and Eisele (1995), to be 26 degrees away from the perpendicular to the window in the horizontal plane. The selection of a nonperpendicular view angle effects the LDA characteristics of the two beams differently. The green and blue laser beams no longer cross at the same position and, as a consequence, only one-dimensional measurements are possible from the second viewing position with either the blue or green beams. The fringe spacing in the measurement volume is also influenced by the off-axis viewing angle because of the refraction of the two beams. In addition, the displacement of the measurement volume is also changed by the nonperpendicular view angle of the probe such that during traversing the measurement volume describes a two-dimensional trajectory, even though the LDA probe is merely moving in one direction (see Zhang and Eisele, 1995).

The 3-D flow field in the diffuser was measured at 5 different flow rates from the BEP (best efficiency point) to deep partload with the LDA, see below. The main interest of the LDA measurements was to examine the flow in the semi-vaneless region of the diffuser, so most of the LDA measurement points were localized in this region, as shown in Fig. 3. LPTV measurements and flow visualization with a video camera were used to complement the LDA measurements to gain a better idea of the unsteady flow field in the whole diffuser.

Laser Particle Tracking Velocimetry (LPTV). To obtain two-dimensional steady and unsteady flow field information a particle tracking velocimetry technique was applied. The illumination source was a continuous wave argon ion laser with a glass fiber light sheet probe. This fiber probe was mounted in the pump (Fig. 1). The measurement zone was illuminated through a window and a perspex diffuser vane. Multiple exposures were realized through a video camera with a high speed shutter and with an integrated light amplifier (Fig. 4) (see also Eisele, 1996). The shutter of this camera is computer controlled and the selection of various parameters for PTV could be rapidly

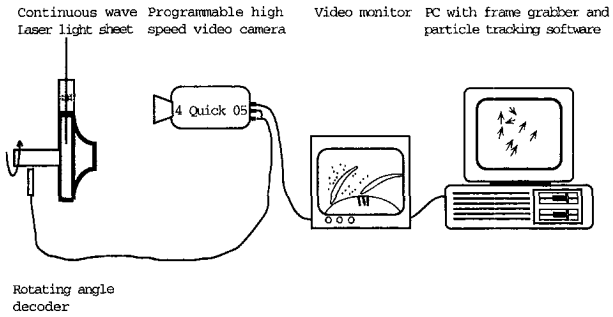

Fig. 4 Laser particle tracking system

optimized. The shutter of the camera and the frame grabber were synchronized with the rotational position of the pump impeller. The one per revolution signal from an incremental angle decoder was used for the synchronization of the PTV system. With a delay box between the one per revolution signal and the camera, a phase-averaged velocity field at different impeller positions could be measured. The direction of the velocity vector was determined by tagged particle traces with long and short exposures. The velocity vectors were determined by a particle tracking software following the procedures outlined by Grant (1990).

Flow Visualization. In addition to the quantitative LDA and PTV measurements, it was found useful to perform qualitative flow visualization of the flow field in the diffuser. First a normal free running video camera with a frame frequency off 25 Hz was used. This showed unsteady flow behavior but was not able to capture flow structures occurring at the blade passing frequency. A second camera synchronized with the impeller rotational speed of 900 rpm (15 Hz) was used to identify the blade passing variations. Also a high speed film with about 500 frames per second (equal to 5 frames per blade passing) was made.

Measurement Results

Stage Characteristics. Prior to carrying out the laser anemometry measurements, the different wall pressures were measured at different operating points along the pump characteristic. With these measurements and additional measurements of the flow rate and torque, the global characteristics of the entire pump, and separate characteristics for the impeller and the diffuser were computed, as shown in Fig. 5. The static pressure

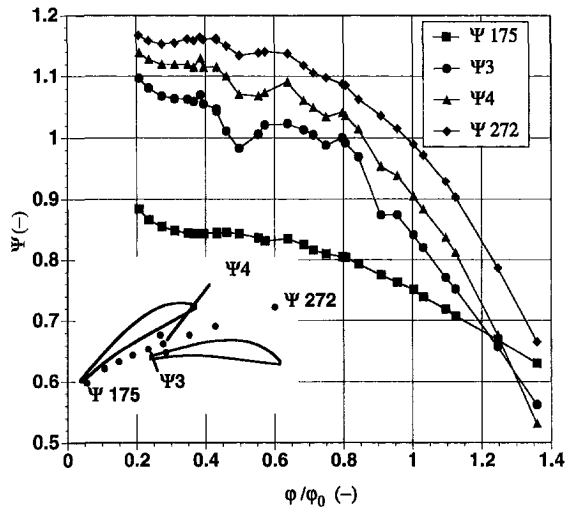

Fig. 5 Pressure rise versus flow rate characteristic of the pump

Table 3 Overview of measurements

Flow rate (φ/φ_0)	Measurement system		
1.00	LDA	PTV	Flow visualization
0.68	LDA	PTV	Flow visualization
0.50	LDA		Flow visualization
0.40	LDA		
0.30	LDA		Flow visualization

rise characteristic of the impeller becomes slightly unstable between $\varphi/\varphi_0 = 0.55$ to 0.65 and $\psi 175$ $\varphi/\varphi_0 = 0.35$ to 0.45. Below $\varphi/\varphi_0 = 0.30$ it rises steeply due to the well-documented effect of fully developed inlet recirculation. The waviness of the impeller pressure rise curve reflects the changing flow patterns at the impeller outlet, as outlined later in the paper. Due to the varying flow conditions at the impeller outlet, the first section of the diffuser contributes most to the instability of the overall pressure-flow rate characteristic, see Gülich (1988) and Hunziker (1993).

With the aid of the head capacity characteristic and the knowledge of the local regions of flow instability, the flow rates for the laser anemometry measurements were determined as shown in Table 3.

This paper presents only a small sample of the total measurement data that has been obtained at these operating points, selected to provide the most interesting insights into the diffuser flow field.

Periodic Unsteadiness and Turbulence. The unsteady turbulent flow in the diffuser can be expressed as a sum of a time averaged steady mean velocity, a phase-averaged periodic component, and a fluctuating component representing the turbulent variations, as follows:

$$\vec{C}(x, y, z, t) = \vec{C}_{\text{Steady}}(x, y, z) + \vec{C}_{\text{Periodic}}(x, y, z, t) + \vec{C}_{\text{Turbulence}}(x, y, z, t) \quad (1)$$

whereby, the periodic component is the difference between the phase averaged and the time averaged velocity, as follows:

$$\vec{C}_{\text{Periodic}}(x, y, z, \Delta\varphi) = \frac{1}{(\Delta\varphi)} \int_{\varphi}^{\varphi+\Delta\varphi} \vec{C}(x, y, z, \varphi) d\varphi - \vec{C}_{\text{Steady}}(x, y, z) \quad (2)$$

These quantities have been individually determined from the LDA measurements in the following way. For each LDA measurement point 20,000 to 30,000 single velocity readings were sampled with a data rate of 600 to 2000 s^{-1}. The analysis of this raw LDA measurement data was first carried out with software from the LDA manufacturer. This software averaged and arranged the data for one complete revolution with an averaging window of 3 degrees, giving 120 values for one impeller revolution. The averaging window of 3 degrees were determined by a detailed analysis of the influence of this window size on the results (Zhang, 1997). The 3-D velocity vectors were then calculated from these data and were then reduced to a single impeller blade pitch by ensemble-averaging, giving 17 values per impeller blade pitch. Each of these 17 phase averaged values represent an average of between 1000 and 1800 samples.

Figure 6 shows the scatter diagrams for a single component of velocity over several revolutions of the impeller for two flow rates at two points in the diffuser. The velocity component shown is the *Cx* component, which is approximately aligned along the main flow direction of the diffuser, see Fig. 3. At the diffuser inlet (measurement point B2), the blade passing frequency is clearly dominant for both flow rates. In the diffuser channel downstream of the throat (measurement point F3), the strength of the blade passing influence clearly decreases and a

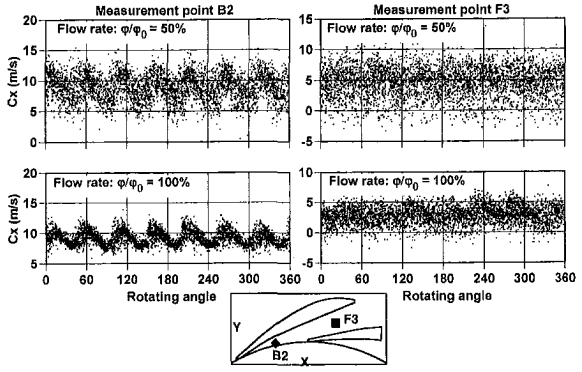

Fig. 6 Scatter diagrams of velocities at two LDA measurement points in the diffuser at two different flow rates

large random fluctuation can also be observed. At partload, other unsteady flow phenomena become important and the turbulence intensity increases. The mean values show that the effect of blade passing frequency decreases along the diffuser. The RMS values show the increasing turbulence along the diffuser (Fig. 7).

The RMS values in the x and y directions at these two points and at the two flow rates are nearly the same, so that an isotropic turbulence can be assumed. The RMS values for the third component of velocity in the axial direction were not analyzed. It can be seen that the axial component of velocity is also dependent on the blade passing frequency. The time lag between passage of the wave maxima between the two measurement points (B2 and F3 in Fig. 7) corresponds with the time which is calculated from the distance between these two measurement points and the mean velocity between them.

The turbulence intensity of the flow has been determined from the following equation, under the assumption that it is isotropic:

$$Tu = \sqrt{(C_x'^2 + C_y'^2)/2(C_x^2 + C_y^2 + C_z^2)} \qquad (3)$$

At the nominal flow rate the turbulence intensity at the diffuser inlet varies between 5 and 13 percent (Fig. 8). The regions of high turbulence intensity correspond to the passage of the impeller blade wakes, which appear to occupy roughly half of the blade flow channels. The turbulence level of 5 percent in the regions of lower turbulence intensity are very similar to those measured by Camp and Shin (1994) in a highly loaded axial compressor operating near its design point. The turbulence intensity increases along the diffuser channel, and this is partly a consequence of the mean velocity level falling through the diffuser but mainly due to the presence of unsteady flow separations in the diffuser channel.

At partload (50 percent of the flowrate at the best efficiency point) the turbulence intensity at the diffuser inlet increases to 20% and there is less evidence of a clean region of flow from the impeller blades. The lowest turbulence level at part load is 14% and extends across roughly 20 percent of the impeller blade channel, and is again in agreement with the turbulence values measured by Camp and Shin (1994) at an off-design operating point of an axial compressor. Further downstream in the diffuser channel, the turbulence intensity at partload increases to about 40%, which is a strong indication of unsteady flow separations.

Meridional Velocity Field at Diffuser Inlet. The LDA measurements at the impeller outlet for all of the measured operating points shown in Table 3 have been analyzed to highlight the nature of the unsteady recirculation of flow from the diffuser into the impeller. Figure 9 highlights the results from this analysis. It shows the meridional velocity vectors (i.e. axial and radial components of the velocity) at the diffuser inlet plotted across the span of the diffuser, as measured at measuring point C1. This measurement point is approximately at the three-quarter pitch position between two blades, see Fig. 3. Each row of figure 9 represents the results at a different operating point, φ/φ_0 = 100, 68, 50, 40, and 31%.

The first four columns in this figure show the instantaneous spanwise velocities at a different position of the impeller vanes and the fifth column shows the time-averaged velocity vectors. These figures show a number of interesting features related to the recirculation of the flow from the diffuser into the impeller at partload operating conditions. At the normal operating point, all of the measured velocity vectors are directed from the impeller into the diffuser and there is no evidence of back flow. At $\varphi/\varphi_0 = 68$ percent, it can be seen that some small flow recirculation of the mean flow from the diffuser to the impeller has just started to occur near to the shroud. It can be seen, however, that the back flow at the shroud is already locally quite strong for some circumferential positions of the impeller vanes. With decreasing flow rate the recirculation zone changes from the shroud side of the diffuser channel to the hub side. At flow rates lower than φ/φ_0 = 50 percent two recirculation zones

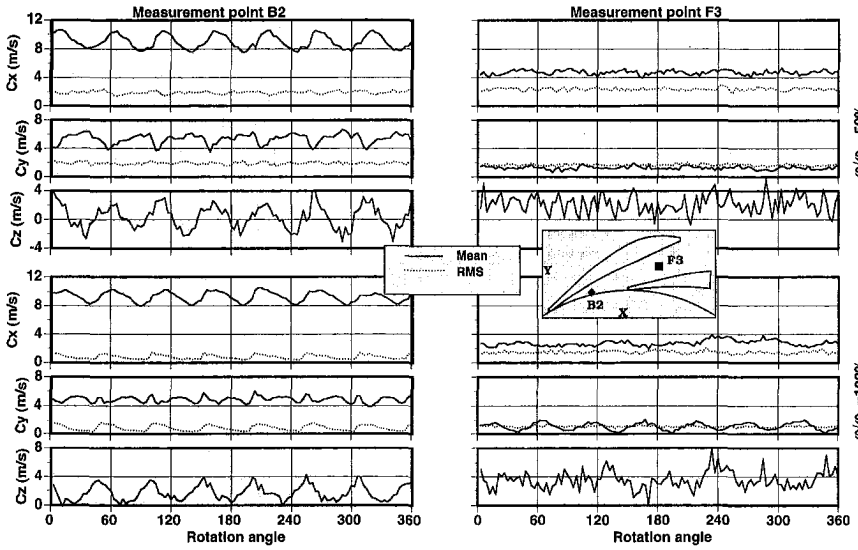

Fig. 7 Phase averaged LDA velocity measurements at two points in the diffuser and two flow rates

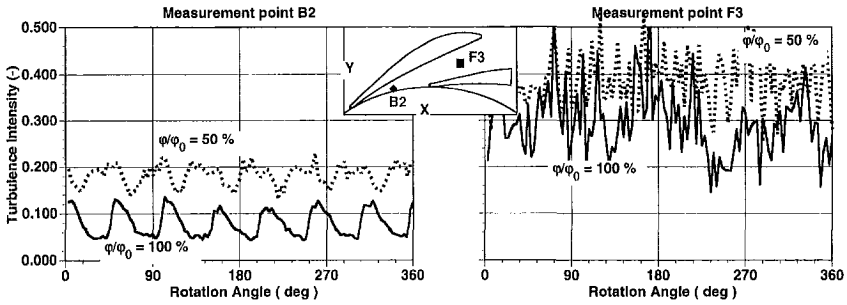

Fig. 8 Turbulence intensities at two points in the diffuser and two flow rates

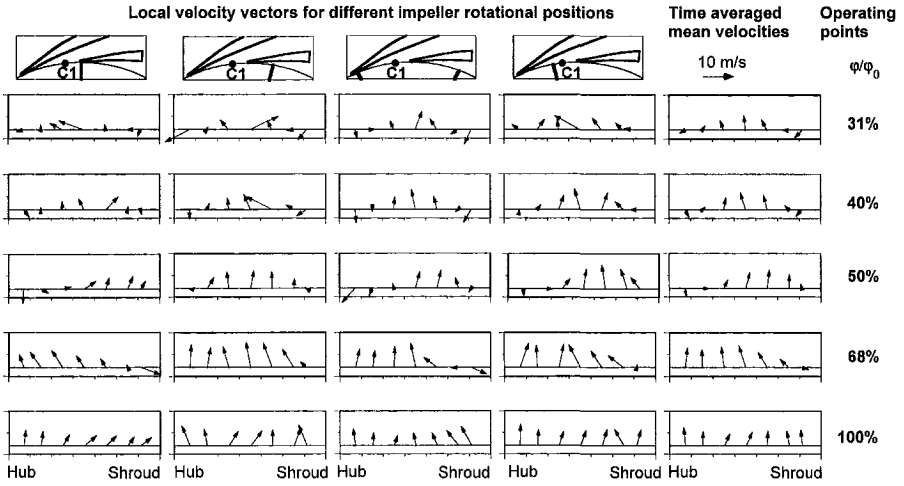

Fig. 9 Meridional velocity vectors for different flow rates near the impeller exit

occur at the impeller outlet. The change of the recirculation zone from the shroud to the hub is considered to be very important for the stability of the head capacity characteristic at partload, as discussed below. Time averaged flow conditions at the diffuser inlet vary very strongly over the diffuser pitch. The information in Fig. 9 for point C1 has also been obtained for other points across the pitch at the diffuser inlet, the strongest recirculation of flow from the diffuser into the impeller is observed close to the leading edge of the vane, as can be seen in Fig. 10.

Visualization of the 3D Unsteady Flow Field. With the large quantity of LDA measurement data that has been taken in this project it is important to find a suitable method to analyze the results of the measurements. The best method that we have found to improve our understanding of the unsteady 3D flow field is to animate the LDA results using modern CFD post processing software. This animation was realized with the graphic software package developed for the visualization of CFD results by AVS (Advanced Visualisation Systems Inc., Waltham, USA). The velocity vectors measured at 224 different measurement points were animated at 17 different impeller positions to produce a video showing the variation of the velocity vectors in space and in time as the impeller blades rotate by the diffuser. The shape of the diffuser vanes and the position of the impeller vane have also been animated to provide better understanding of the flow. One of the images from this animation can be seen in Fig. 10. This shows the impeller vane trailing edges at a certain position viewed from the hub side and the diffuser vanes, whereby the slightly different illumination of the diffuser vane surface along its length arises because of the slope of the diffuser channel wall (Fig. 1).

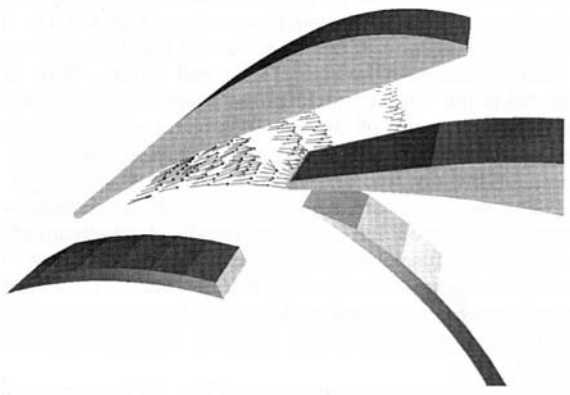

Fig. 10 Snapshot from a computer animation of the 3D velocity field at partload (φ/φ_0 = 50 percent)

The velocity vectors are shown for the operating point at 50% of the normal flow rate with the impeller in the position shown. The full animation shows very clearly that both the magnitude and the direction of the velocity vector change as the impeller rotates. Two interesting flow phenomena can be observed in the instantaneous snapshot of the flow field shown in Fig. 10. First, the onset of recirculation into the impeller from the diffuser can be detected near the leading edge of the diffuser. It is also clear that the recirculation into the impeller is circumferentially nonuniform, with regions of forward flow and reverse flow occurring at different positions around the circumference. Second, the onset of a separation in the diffuser channel can be observed from the spanwise variation of the velocity vectors in the region downstream of the diffuser throat. The lowest velocities are measured on the hub side just downstream of the change in the slope of the diffuser channel wall.

Periodic Unsteady Velocity Components. The periodic component of the flow at mid-span of the diffuser, measured with the LDA is shown in Fig. 11. The velocity vectors shown in this figure are the difference between the phase averaged values and the time-average values at each point, see equation in Section 3.2. The periodic vectors represent that part of the flow that changes periodically with the blade passing frequency. The periodic vectors are shown for different times, whereby the local position of the impeller blade trailing edge at each point in time can also be seen. This type of visualization of the periodic component of the flow was used by Dawes (1994) to identify vortex structures in an unsteady CFD simulation of a diffuser.

In the semi-vaneless region the periodic variations are very strong, as can be recognized from the long vectors. The periodic variations decrease very rapidly in the diffuser channel and are very much smaller downstream of the diffuser throat. This behavior was also observed by Inoue and Cumpsty (1985) and Dawes (1994).

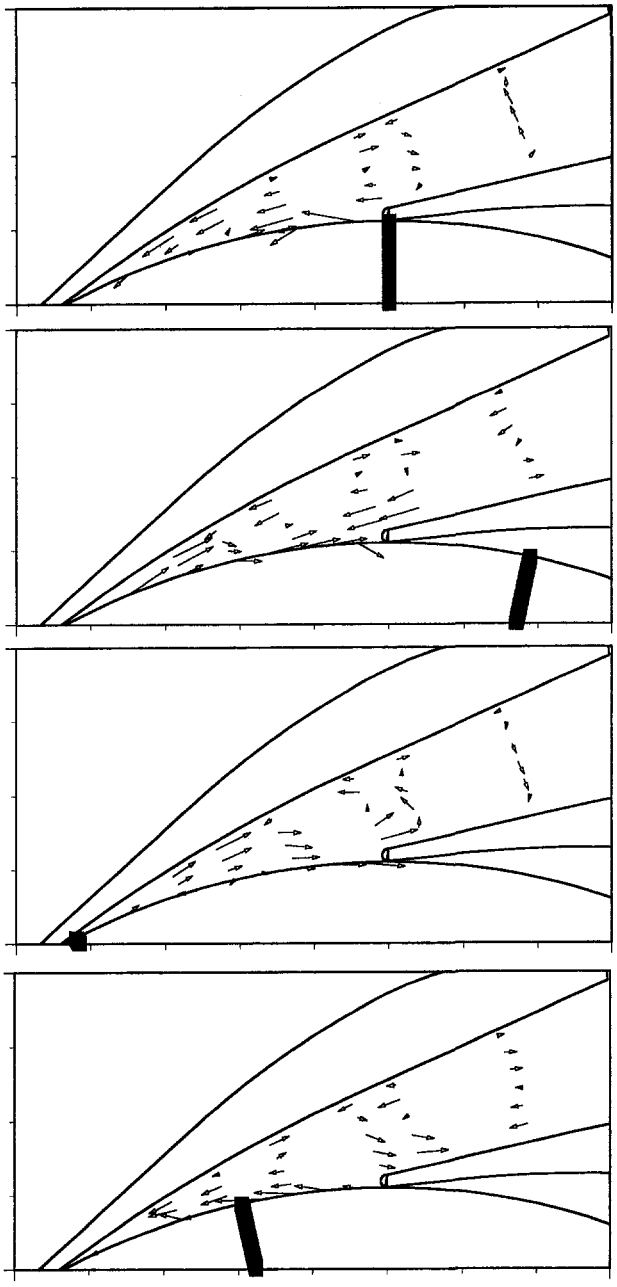

Fig. 11 Periodic component of velocity vectors at the nominal flow rate calculated with the LDA results (midspan of diffuser)

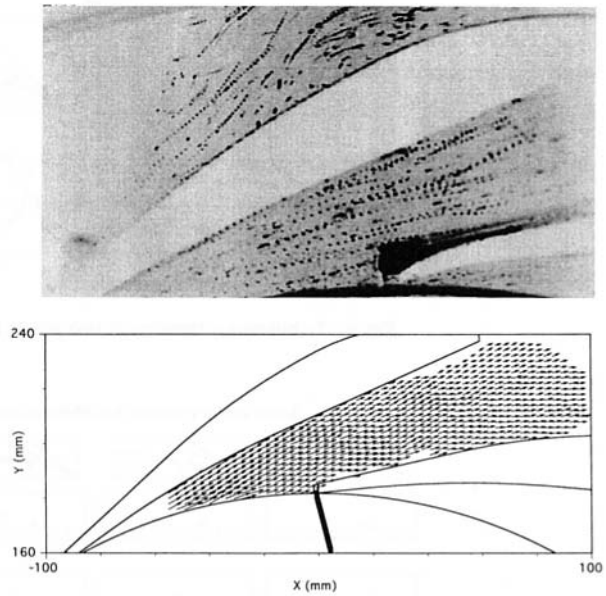

Fig. 12 Particle tracking velocimetry image with the vector field at mid span (φ/φ_0 = 100 percent)

The velocity components were also measured with PTV. A typical image of the velocity vectors determined by the PTV technique is shown in Fig. 12. The top part of Fig. 12 shows an instantaneous image of the PTV particle traces, and the lower part shows the phase averaged velocity vectors calculated from multiple images. The differences between the particles traces and the vectors in these two pictures indicates that the recirculation on the pressure side of the vane is unsteady.

Each of the phase averaged vectors was determined by averaging the vectors from 100 images. The spatial resolution of the PTV System was 0.2 mm/pixel and the accuracy of a single velocity vector lays in the range between 1 to 3 percent in the center of the image.

The periodic component of velocity was also determined from the PTV results, see Fig. 13. The PTV measured velocity field has a high spatial resolution, so that more detail of the vortex structure in the periodic component can be observed.

With the help of Fig. 13, and similar pictures obtained at other impeller vane positions, it is possible to observe the passage of a blade wake through the diffuser channel. The flow entering the diffuser immediately behind the impeller blade is slower than the mean component, and appears in Fig. 13(a) as an apparent reverse flow. This flow is forced by the subsequent jet-flow from the center of the impeller blade passage to be directed toward the diffuser suction surface (Fig. 13(b)). The subsequent convection of this flow through the diffuser channel can then be followed in Figs. 13(c) and 13(d). With these vector fields the vorticity field in the xy-plane was calculated (Fig. 14). The wake of the impeller blade produces regions with high positive and high negative vorticities, whereby the strength of the positive and negative vorticity regions is the same. The vorticities are convected through the diffuser with the mean flow speed and disappear rapidly downstream of the throat of the diffuser because of the high turbulent flow. The vortex pattern resembles classical Karman vortex street, unlike the vortex pattern presented by Akin (1994), where large differences between the positive and negative vorticity values were measured.

If the PTV velocity components (Fig. 13) are compared with the unsteady LDA results (Fig. 11), it can be recognized that the LDA results are a part of the same complex

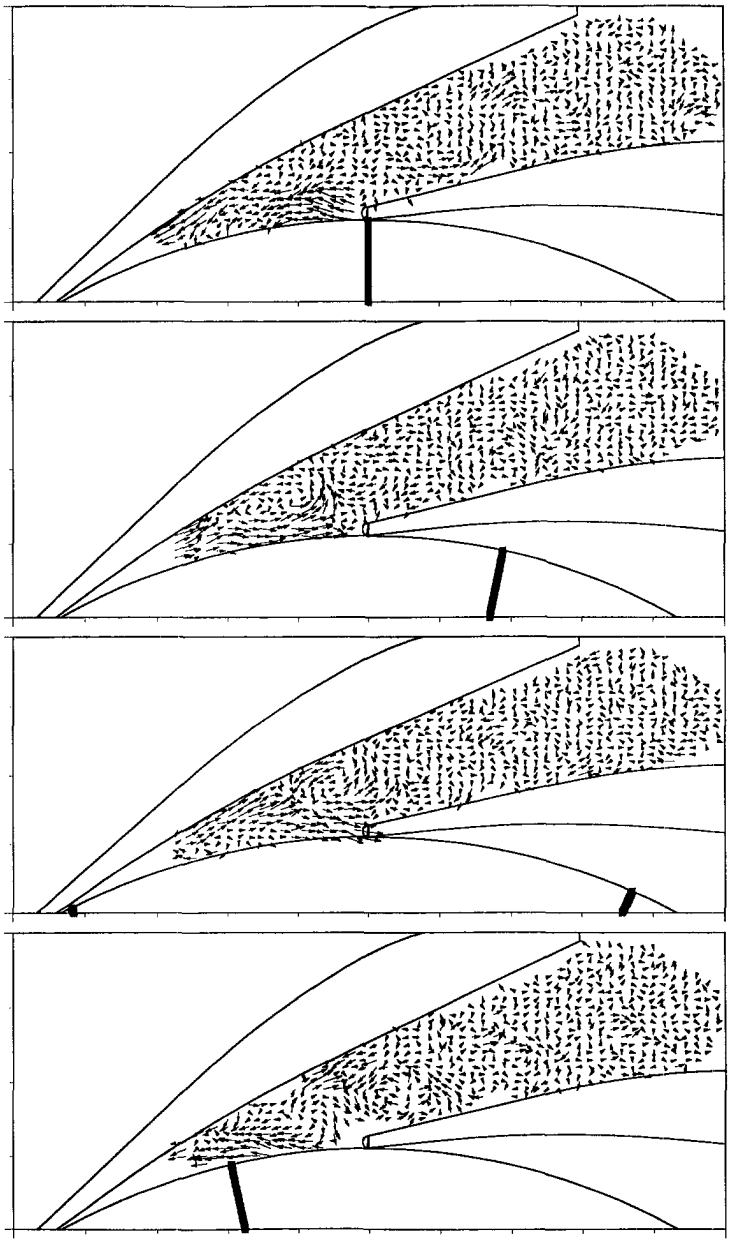

Fig. 13 Periodic component of velocity vectors at the nominal flow rate calculated from the PTV results (midspan of diffuser)

flow field. This indicates very good agreement between the two different measurement systems. A direct quantitative comparison of the LDA and PTV velocity components at three different impeller positions gives excellent agreement (Fig. 15).

Discussion

The optical measurements presented here show the first use of LDA for the determination of the periodic velocity components in a pump diffuser. In order to perform such high quality measurements detailed optical calculations of the laser beams are necessary, Zhang and Eisele (1995). The effort required to perform such three-dimensional velocity measurements with LDA is extremely large, taking two months to complete the traverses described in this paper.

The measurements of the unsteady velocity field using a triggered camera with the PTV technique are also an important development of this technique for industrial research. This is the first example of the use of this technique in unsteady flows at industrially relevant velocity levels found in hydraulic machines. At the design point a full PTV image of the flow field provides a rapid method of determining the two-dimensional velocity vectors with good spatial resolution. This procedure is considerably faster than the LDA method, requiring only a few days for the measurements. At deep partload, however, the three-dimensional nature of the flow field is difficult to capture with the PTV technique.

The measurements presented are the first attempts at using these techniques for the understanding of the complex flow field in the vaned diffusers of a centrifugal pump. This shows that such techniques have now attained a level of reliability that they can be successfully used in the most difficult industrial applications. The measured results show some interesting flow features that could not have been determined with such clarity by any other method.

These optical measurement techniques have identified some of the interesting flow structures that occur in the vaned diffuser, such as three-dimensional nature of the inlet flow from the impeller, the presence of unsteady flow separations, the level of turbulence in the flow, and the unsteady passage of periodic disturbances from the impeller through the diffuser. It is particularly interesting to note that extent of the flow separations in the diffuser were not observed from static wall pressure measurements.

These results are very relevant to the development of improved methods of calculation for diffuser design. First, it is clear that because of the complex nature of the impeller outlet flow, very detailed information of the impeller outflow is necessary in order to calculate the diffuser flow field. Second, in this highly loaded diffuser, the unsteady flow separations in the diffuser flow channel downstream of the throat dominate the flow structure to such an extent that steady calculations may be irrelevant. Third, the observation that the recirculating back flow from the diffuser into the impeller is circumferentially nonuniform suggests that attempts to calculate this feature of the flow using a "mixing-plane" approach for the impeller diffuser interaction are likely to be inaccurate. Some of these issues are discussed in companion papers to this paper. In the first one steady flow simulations of the diffuser flow are compared with the time-average of the measurement data presented here (Muggli et al., 1997)). In the second one, unsteady flow simulations are compared with the same measurement data (Muggli et al., 1996).

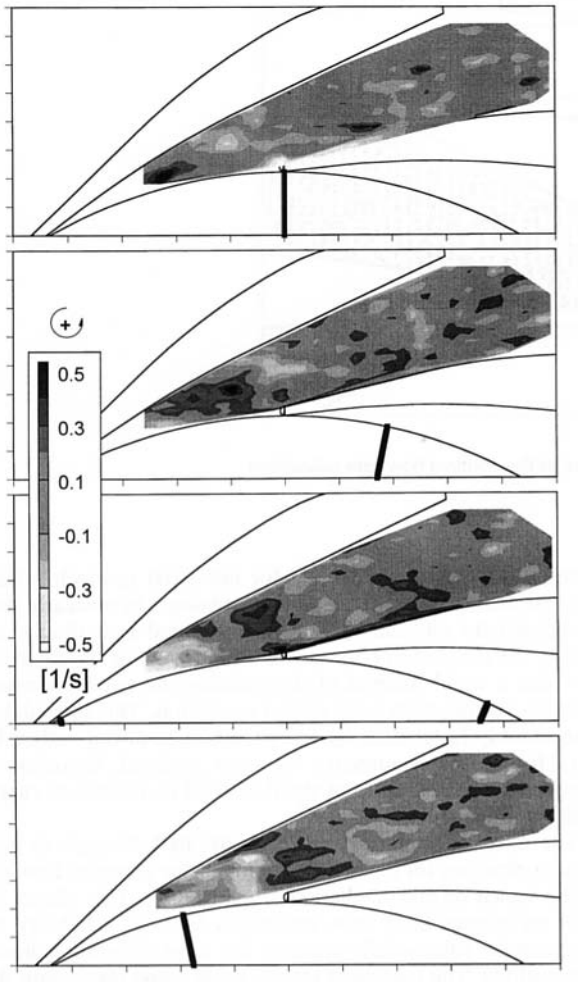

Fig. 14 Vorticity at the nominal flow rate calculated with the PTV results (midspan of diffuser)

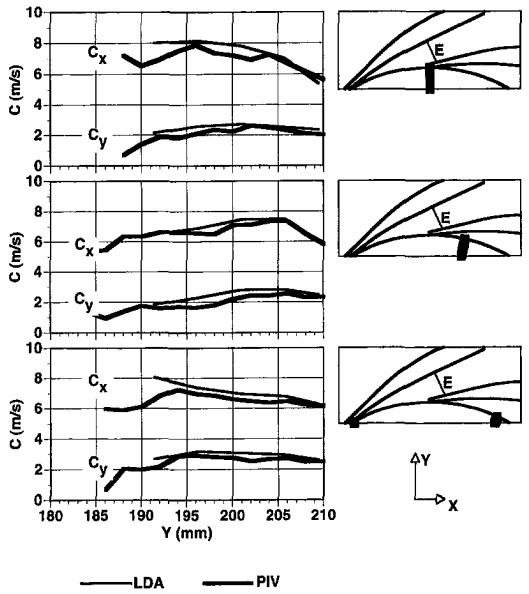

Fig. 15 Comparison of PTV and LDA measured velocity profiles in the diffuser mid-span (φ/φ_0 = 100 percent)

The measurement of the pump head characteristic shows evidence of a so-called saddle type of instability at a partload operating point of 50 percent of the normal flow, see Gülich (1995). The detailed flow measurements at impeller outlet, see Fig. 9, show that the back flow into the impeller from the diffuser changes its structure with the operating point. At 100 percent flow there is no evidence of back flow, at 68 percent flow there is evidence of a recirculation into the impeller on the shroud side. Despite the strongly asymmetric diffuser inlet flow, the overall diffuser performance is little impaired. Between φ/φ_0 = 68 and 50 percent the recirculation shifts to the hub side of the impeller. At lower flowrates there is evidence of a recirculation region on both hub and shroud sides of the impeller. This supports the hypothesis of Gülich (1995), which suggests that the change in the recirculation flow pattern with flow rate is a contributory factor to the presence of a saddle type of instability. It is, of course, very difficult to interpret cause and effect in such a complex three-dimensional flow field. Further work in this project is aimed at examining the flow field in this diffuser with an impeller having a different flow structure at the outlet.

Conclusions

Detailed optical measurements of the time-resolved flow field in a highly loaded diffuser of a centrifugal pump have been carried out with LDA and LPTV systems for the first time. These measurement techniques have identified some of the interesting flow structures that occur in the diffuser, such as the presence of unsteady flow separations and the unsteady passage of periodic disturbances from the impeller through the diffuser.

The main conclusions of the work are:

- The flow field in this typical pump diffuser is strongly three dimensional and unsteady. The three-dimensionality of the flow occurs partly because of the three-dimensional nature of the impeller outlet flow, and partly because of the highly loaded diffuser design with a sloping hub wall leading to a three-dimensional flow separation.
- The magnitude of the periodic unsteadiness in the diffuser vane is strongest at impeller outlet and diminishes rapidly downstream of the diffuser throat. The magnitude of the nonperiodic unsteadiness (turbulence) increases through the diffuser passage and is strongest at partload operating points.

- The impeller blade wakes appear in the diffuser as a pattern of positive and negative vorticity, which is convected downstream of the diffuser throat.
- Recirculating back flow from the diffuser into the impeller occurs at partload conditions, and the extent of the back flow is circumferentially nonuniform. Because of this, CFD calculations of a pump stage using a "mixing plane" approach to provide the computational interface between the rotating impeller and the stationary diffuser cannot be expected to give an accurate prediction of this important phenomena.
- The onset and location of back flow from the diffuser into the impeller has a strong influence on the stability of the pump head characteristic and accounts for the observed changes in the stage characteristic.

Acknowledgments

The authors would like to thank Sulzer Pump Ltd., Sulzer Hydro Ltd., Sulzer Turbo Ltd. and Sulzer Innotec Ltd. for their financial support of this project and for permission to publish this paper.

References

Akin, O., Rockwell, D., 1994, "Flow Structure in a Radial Flow Pumping System Using High-Image-Density Particle Image Velocimetry", ASME JOURNAL OF FLUIDS ENGINEERING Vol. 116, Sept. pp. 538, 544.

Arndt, N., Acosta, A. J., Brennen, C. E., and Kaughey, T. K., 1989, "Experimental Investigation of Rotor-Stator Interaction in a Centrifugal Pump with Several Vaned Diffusers," ASME paper 89-GT-62.

Camp, T. R., and Shin, H.-W., "Turbulence Intensity and Length Scale Measurements in Multistage Compressors," ASME Paper 94-GT-4.

Casey, M. V., 1994, "The Industrial use of CFD in the Design of Turbomachinery," Agard Lecture Series 195, May 1994.

Cumpsty, N. A., 1989, *Compressor Aerodynamics,* Longman.

Dawes, W. N., 1994, "A Simulation of the Unsteady Interaction of a Centrifugal Impeller with its Vaned Diffuser: Flows Analysis," ASME Paper 94-GT-105.

Eisele, K., Muggli, F., and Schachenmann, A. 1992, "Investigations of Flow Phenomena in Multistage Pumps," *Sixth Int. Symp. on Appl. of Laser Anem. to Fluid Mechanics* Lisbon July.

Eisele, K., Muggli, F. et al., 1993, "Pump Development with Laser and Computer," *Technical Review Sulzer,* Vol. 2, pp. 37–39.

Eisele, K., Zhang, Z., Hirt, F., Perschke, N., 1996, "High-Speed Cameras Image Flow Successfully," *Laser Focus World* May, pp. 75–83.

Grant, I., and Liu, A., 1990, "Directional Ambiguity Resolution in Particle image Velocimetry by Pulse Tagging," *Experiments in Fluids,* Vol. 10, pp. 71–76, reprinted in Selected Papers on PTV, SPIE Milestone Volume MS 99, Ian Grant.

Gülich, J. F., 1988, "Bemerkungen zur Kennlinienstabilität von Kreiselpumpen, Pumpentagung Karlsruhe.

Gülich, J. F., 1995, "Untersuchungen zur sattelförmigen Kennlinien Instabilität von Kreiselpumpen," to be published in VDI *Forschung in Ingenieurwesen.*

Gülich, J. F., and Bolleter, U. 1992, "Pressure pulsations in Centrifugal Pumps," ASME Vol. 114 pp. 272–279.

Hunziker, E., 1993 "Einfluss der Diffusorgeometrie auf die Insatabilitätsgrenze des Radialverdichters, Dissertation ETH-Zürich.

Inoue, M., and Cumpsty, N. A., 1984, "Experimental Study of Centrifugal Impeller Discharge Flow in Vaneless and Vaned Diffusers," ASME *Journal of Engineering for Gas Turbines and Power,* Vol. 106, pp 455–467.

Muggli, F., Wiss, D., Eisele, K., Zhang, Z., Casey, M. V., Galpin, P., 1996: "Unsteady Flow in the Vaned Diffuser of a Medium Specific Speed Pump," *Proc. of the 1996 Int. Gas Turbine and Aeroengine Cogress & Exhibition,* 10–13. June ASME Paper 96-GT-157, New York.

Muggli, F., Eisele, K., Zhang, Casey, M. V. Z., Gülich, J., and Schachenmann, A., 1995, "Flow Analysis in a Pump Diffuser—Part 2: Validation and Limitations of CFD for Diffuser Flows," ASME JOURNAL OF FLUIDS ENGINEERING published in this issue, pp.

Renau, L. R., Johnston, J. P. and Kline, S. J., 1967, "Performance and Design of Straight, Two-Dimensional Diffusers," ASME *Journal of Basic Engineering,* pp 141–150, Mar.

Ubaldi, M., Zunino, P., Barigozzi, G., and Cattanei, A., 1994, "An Experimental Study of Stator Induced Unsteadiness on Centrifugal Impeller Outflow," ASME paper 94-GT-5.

Zhang, Z. and Eisele, K., 1995, "Off-Axis Alignment of an LDA-Probe and the Effect of Astigmatism on Measurements" *Experiments in Fluids,* Vol. 19, pp. 89–94, Springer-Verlag.

Zhang, Z., and Eisele, K., 1997, "The Influence of Phase Averaging Window Size on the Determination of Turbulence Quantities in Unsteady Turbulent Flows," *Experiments in Fluids* Vol. 22, pp. 265–267, Springer-Verlag.

F. A. Muggli

K. Eisele

M. V. Casey

Fluid Dynamics Laboratory,
Sulzer Innotec AG,
Winterthur,
Switzerland

J. Gülich

A. Schachenmann

Sulzer Pumps,
Winterthur,
Switzerland

Flow Analysis in a Pump Diffuser—Part 2: Validation and Limitations of CFD for Diffuser Flows

This paper describes an investigation into the use of CFD for highly loaded pump diffuser flows. A reliable commercial Navier-Stokes code with the standard k-ϵ turbulence model was used for this work. Calculations of a simple planar two-dimensional diffuser demonstrate the ability of the k-ϵ model to predict the measured effects of blockage and area ratio on the diffuser static pressure recovery at low loading levels. At high loading levels with flow separation the k-ϵ model underestimates the blockage caused by the recirculation in the flow separation region and overestimates the pressure recovery in the diffuser. Three steady-state calculations of a highly loaded vaned diffuser of a medium specific speed pump have been carried out using different inlet boundary conditions to represent the pump outlet flow. These are compared to LDA measurement data of the flow field and demonstrate that although the Navier-Stokes code with the standard k-ϵ turbulence model is able to predict the presence of separation in the flow, it is not yet able to accurately predict the static pressure rise of this highly loaded pump diffuser beyond the flow separation point.

Introduction

The use of CFD codes for turbomachinery design applications has undergone a rapid transformation during the last ten years and their use is now commonplace in most turbomachinery design systems, see Casey (1994). In the design of industrial centrifugal pumps, CFD has already become a standard tool in the analysis of impellers, and a number of recent publications demonstrate its capability here, see for example, Schachenmann et al. (1993) and Gülich et al. (1997). In the design of vaned diffusers for pumps, however, CFD has not yet made the breakthrough as a standard design tool and designs still tend to be based on empirical methods, most of them going back to the classical diffuser data produced by the early workers in the field, Runstadtler et al. (1975) and Reneau et al. (1967).

There are a number of reasons why CFD methods are not yet widely used in vaned diffuser design. First, the flow at the diffuser inlet coming from the impeller is unsteady and three-dimensional so that the inlet boundary conditions for the diffuser calculations are extremely complex. The three-dimensional nature of this flow field can be estimated by using a simulation of the impeller flow field, but few CFD codes are available that can efficiently compute the flow field in a diffuser taking into account the true periodically unsteady nature of the flow from the impeller. A fully unsteady calculation of both the impeller and the diffuser in a pump would really be needed and, although this is now technically possible, see Dawes (1994), it is well beyond the capability of normal design resources in industry. Even an unsteady simulation of the diffuser only (Muggli et al., 1996), using a time periodic velocity profile at the inlet, is too time consuming for the designer of pump diffusers. For industrial calculations, the diffuser flow is generally considered as being steady and the inlet boundary conditions are taken as a time-average of the impeller outlet flow conditions, see for example Dalbert et al. (1995). Muggli et al. (1996) demonstrate that this is a reasonable approach, as the time average of the unsteady simulation is shown to be essentially the same as a steady simulation with time average inlet conditions.

Second, as in all pump CFD calculations, the diffuser blades are at high stagger angles and many CFD methods using simple H-grids with circumferential grid lines have numerical problems with the highly skewed grids that this implies. Third, it is clear that the decelerating nature of the flow in a diffuser is an extremely difficult problem for Navier-Stokes solvers, as it is known that the k-ϵ turbulence model has a number of severe weaknesses in adverse pressure gradients with flow separation, see Wilcox (1993). This is exacerbated by the fact that the diffuser designer is interested in obtaining peak pressure rise from the diffuser and this occurs very close to the condition where unsteady flow separation begins, see Reneau et al. (1967). Thus, even at the design point the flow in a well-designed diffuser is on the verge of separation and difficult to calculate, and at off-design operating points strong flow separations are even more likely. In many diffuser designs, the extreme condition imposed on the available radial extent of the blades also forces the designer to use a highly loaded diffuser with some degree of flow separation at the design point, as in the example given in this paper.

This paper describes some numerical work recently carried out with the objective of determining the extent to which modern CFD codes can be used for the design and analysis of highly loaded vaned diffusers in industrial pumps. The companion paper, Eisele et al. (1997), describes the detailed measurements that have been made on the vaned diffuser of a centrifugal pump using a dedicated pump test rig and LDA optical measurement techniques. This paper uses these measurements as test data for the comparison with predictions from a Reynolds-averaged Navier Stokes CFD code with a k-ϵ turbulence model. It should be noted that the measurements showed that the flow in the diffuser was periodically unsteady, highly turbulent (Tu $\approx$ 40 percent) and had extensive regions of flow separation, especially at off-design operating points. It should be clear from this, that this is an extremely difficult case for CFD simulations. Because of this, the CFD code is only compared with the time-

Contributed by the Fluids Engineering Division for publication in the JOURNAL OF FLUIDS ENGINEERING. Manuscript received by the Fluids Engineering Division October 12, 1995; revised manuscript received July 21, 1997. Associate Technical Editor: L. Nelik.

average steady flow field from the measurements at the best operating point of the pump. Other extensive comparisons have been made with the off-design measurement points and with unsteady data (see Muggli et al., 1996), but these are not discussed here.

Navier-Stokes Code With k-ϵ Turbulence Model

A commercial software package was used for this study, the code "TASCflow" from ASC (1994). The Reynolds-averaged Navier-Stokes equations are solved by this code in strong conservation form. The transport equations are discretized using a conservative finite-volume method. Both incompressible and compressible flows can be analyzed. Turbulence effects are modeled using the k-ϵ turbulence model. Details regarding the theoretical basis and handling of the boundary conditions of the code are reported in full by ASC (1994). Many successful reports of the application of this code to turbomachinery problems have been reported in the technical literature, for example, it has been used for pump impellers by Schachenmann et al. (1993), for a transonic compressor rotor by Dalbert and Wiss (1995), for a turbine draft tube by Drtina et al. (1992) and for a complete Francis Turbine (Keck et al., 1996).

Despite the success of the code for turbomachinery flow calculations involving impeller blade rows and inlet and outlet ducts, a fundamental examination of the use of CFD for pump diffuser flows was considered prudent. As the decelerating flows in diffusers are still a real challenge for current Navier-Stokes solvers using the k-ϵ turbulence model, the flow through a simple two-dimensional planar diffuser was calculated before the flow through a highly loaded vaned diffuser of an industrial pump was simulated.

Simulations of a Two-Dimensional Planar Diffuser

The important flow physics of diffusing flows are demonstrated by the simple two-dimensional planar diffuser, as reported by Reneau et al. (1967). Before proceeding to analyze the complex three-dimensional flow field found in a pump diffuser it was considered worthwhile to examine the ability of the CFD code on the simple two-dimensional case. To this end, some representative simulations of two-dimensional diffuser flows were run with the code using the standard k-ϵ turbulence model. For this study, the simulations were compared with the data published by Reneau et al. (1967). The simulations were performed with several diffuser opening angles leading to a range of diffuser area ratios, and for both a thin and a thick inlet boundary layer giving rise to different values of the inlet blockage.

Geometry and Grid. The geometry of the two-dimensional diffuser, as investigated by Reneau et al. (1967), consists of the inlet duct, the diffuser and the outlet duct (Fig. 1). Only one half of the diffuser was modelled in the simulations using a simple H-grid consisting of about 14000 nodes, and symmetry boundary conditions were applied to model the other half of the diffuser. Figure 1 shows the area covered by the H-grid. The y^+ values obtained with this grid are in the normal range for this kind of CFD applications.

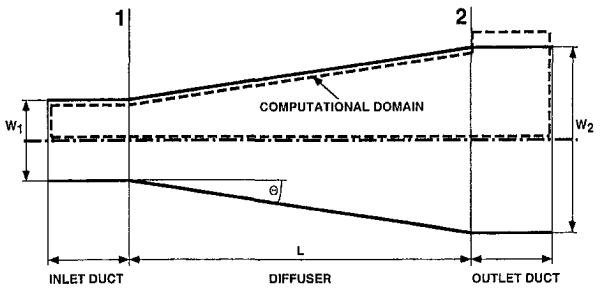

Fig. 1 Geometry and computational domain of the two-dimensional diffuser

Boundary Conditions. The walls were modeled as solid boundaries and the logarithmic law of the wall was used as a wall boundary condition. At the end of the outlet duct a constant static pressure was assumed. As the Mach number is less than 0.2 an incompressible flow could be simulated. To obtain the desired blockage at the inlet, a turbulent boundary layer velocity profile based on the $\frac{1}{7}$-power law was created on the diffuser endwalls. Values for the turbulence intensity and eddy length scale had to be estimated and were kept constant at the inlet. Variations of these two parameters in the range of 1 to 50 percent and 0.001 to 0.07, respectively, showed that they have very little or no effect on the simulated flow field in the diffuser.

Comparison With Experiments. Simulations were carried out for a thin inlet boundary layer giving a low blockage ($2\delta_1^*/W_1 = 0.007$) and a thick inlet boundary layer giving a high blockage ($2\delta_1^*/W_1 = 0.05$) covering the range of conditions typically found in turbomachinery. For both cases the diffuser opening angle was varied in eight steps between 2Θ = 4 and 24 deg. Figures 2(a) and 2(b) show the static pressure recovery c_p for the two different inlet blockages:

$$c_p = \frac{\bar{p}_2 - \bar{p}_1}{\frac{\rho}{2}\bar{u}_1^2} \tag{1}$$

The results of the simulations are compared with the data from Reneau et al. (1967) (labeled "experiment") and an ideal pressure recovery, which can be derived from the Bernoulli equation:

$$c_{p,\text{ideal}} = 1 - \left(\frac{W_1}{W_2}\right)^2 \tag{2}$$

For lightly loaded diffusers (i.e., small opening angles 2Θ)

Nomenclature

c = absolute velocity
c_p = static pressure recovery
L = diffuser axial length
p = static pressure
Re = Reynolds number Re = $u_1 W_1/\nu$
R_2 = impeller exit radius
s = centerline
Tu = turbulence intensity
u = velocity
W = diffuser width between diverging walls
Z = span
δ^* = boundary layer displacement thickness
Θ = diffuser opening angle
ν = kinematic viscosity
ρ = density
ψ = static pressure rise

Subscripts

ideal = ideal value
local = local value
rad = radial
ref = reference value
tang = tangential
1 = diffuser entrance
2 = diffuser exit

Superscripts

$-$ = average

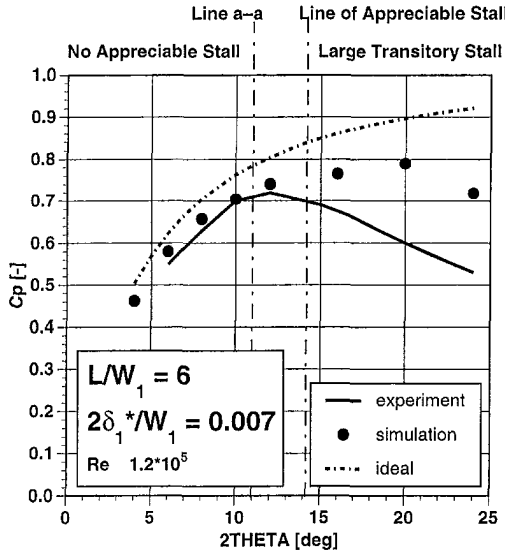

Fig. 2(*a*) Static pressure recovery c_p for thin inlet blockage in a two-dimensional diffuser

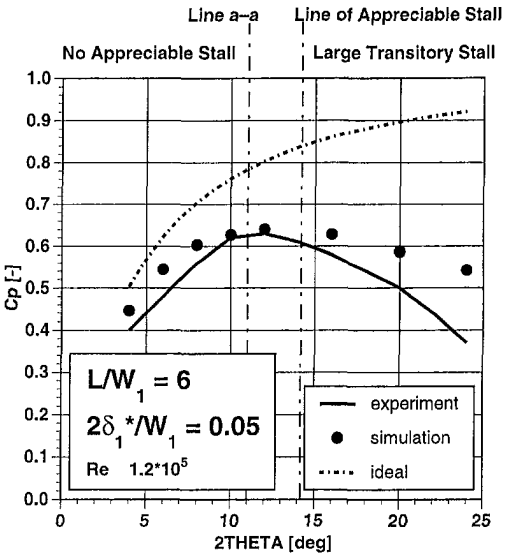

Fig. 2(*b*) Static pressure recovery c_p for thick inlet blockage in a two-dimensional diffuser

the simulations agree very well with the experiments, although there is a slight tendency to overestimate the level of the static pressure recovery. (It should be noted that the experimental data plotted in these figures has been taken from the design charts interpolated by Reneau et al. and not directly from their measurements.) As the loading is increased and the amount of flow separation becomes larger the discrepancies increase. Up to the line denoted by Kline as the "Line of Appreciable Stall," the static pressure recovery is reasonably well predicted by the code for both levels of inlet blockage. In the region of "Transitory Stall" the code fails to predict the diffuser flow correctly, and this is attributed to inadequacies of the k-ϵ turbulence model in adverse pressure gradients, see Wilcox (1993), and the steady nature of the simulation. At high loading levels the turbulence model fails to predict the size of the flow recirculation and extent of the blockage caused by the flow separation. As a consequence, the calculation overestimates the pressure rise in this region. In reality the flow is unsteady with a transitory stall which shifts from one side of the diffuser to the other. A simulation of both sides of the diffuser with many more grid points would be needed to capture the details of this unsteady flow separation.

This basic validation shows, however, that the most important aspects of diffusing flows for the designer can be well predicted by steady simulations with the Navier-Stokes code using a k-ϵ turbulence model, as long as no appreciable stall occurs in the diffuser. At low loading levels the important flow physics, such as the level of static pressure rise, the effects of diffuser area ratio and the effects of inlet blockage, can be very well calculated. At high loading levels the steady predictions are less accurate, because of the unsteady stall shown by the measurements and the inherent limitations of the k-ϵ turbulence model in an adverse pressure gradient.

Simulations of a Three-Dimensional Radial Pump Diffuser

The flow field in a highly loaded vaned diffuser of a centrifugal pump has been investigated experimentally and the optical and pneumatic measurements are described in a companion paper to this, Eisele et al. (1997). The measurements of this diffuser show that the flow is periodically unsteady, highly turbulent and has extensive flow separation. As the numerical computation of the unsteady flow in a pump diffuser is currently at the limit of the capability of current CFD methods in the design environment, the results of three steady simulations are presented here and these are compared to the time-averaged flow measurements in the diffuser. The main objective is to determine the extent to which CFD can be used to predict the flow field, recirculation and static pressure recovery in this highly loaded pump diffuser.

Geometry and Grid. The diffuser investigated is part of a test rig for a single stage radial pump. The stage design is similar to the middle stage of a multistage pump, whereby some small changes to the diffuser geometry were made to provide good optical access for LDA measurements and flow visualizations and to provide a clearly defined outlet plane for the flow simulations. Earlier work on the same test rig included detailed measurements and numerical computations of the flow in the pump impeller, Schachenmann et al. (1993). Further details of the rig and the optical measurements in the diffuser can be found in a companion paper to this paper, Eisele et al. (1997).

Figure 3 shows the area covered by the computational domain for the diffuser simulations. Depending on the inlet boundary conditions used (see below) the computational grid starts either at the radius of the impeller trailing edges or at the radius of the leading edges of the diffuser vanes and extends radially to the endwall of the casing. The flow leaves the computational domain in the axial direction, similar to the true geometry of the return channel crossover bend. For reasons of symmetry it was only necessary to model a single blade channel of the whole diffuser, which includes twelve vanes in total. The H-grid, containing 68750 nodes, generated for this study is shown in Fig. 4. Clearly visible in this figure is the three-dimensional nature of the highly loaded diffuser channel geometry, in which the area increase takes place both between the vanes due to their curvature and due to nonparallel endwalls. The hub endwall slopes in the axial direction, the slope starting at the throat of the channel and ending at the vane trailing edge.

The sloping endwall gives rise to a nonaxisymmetric hub wall and also leads to a very highly loaded diffuser design with a channel length to inlet width ratio of 4.8, an equivalent 2D diffuser opening angle of $2\Theta = 14$ deg, and an area ratio of 2.55. In the typical diffuser design charts of Reneau et al. (1967) the diffuser is just below the transition from attached flow to transitory stall.

Boundary Conditions. The pump diffuser simulations were carried out with water as the fluid, and therefore incompressible flow could be assumed. All the surfaces of the diffuser

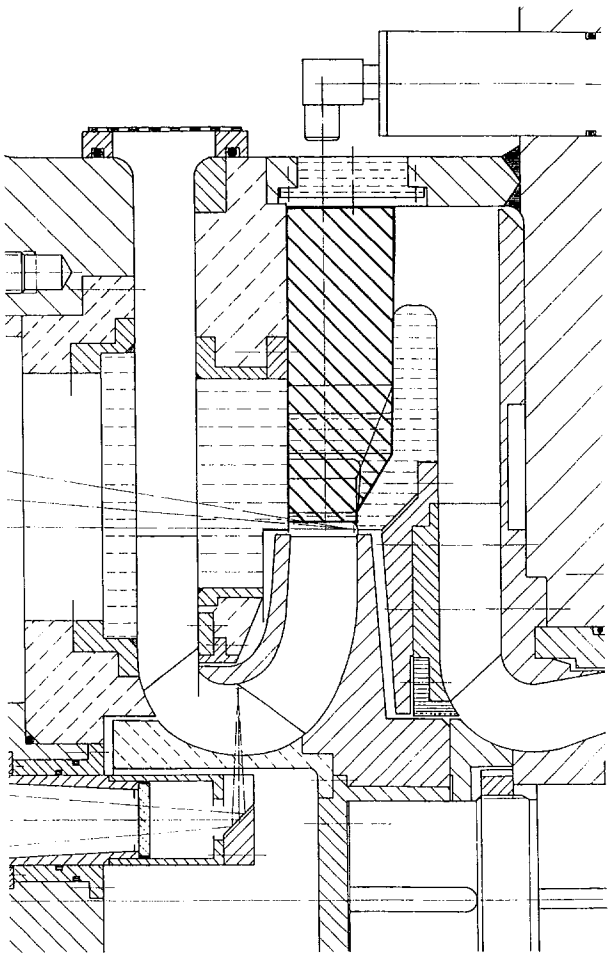

Fig. 3 Computational domain for the radial pump diffuser simulations

channel were defined as solid walls. A single diffuser channel was modeled and the adjacent regions of the full diffuser were modeled by the appropriate use of periodic boundary conditions. At the domain outflow, the mean value of the static pressure was set (the particular value is not important, since incompressible flow is simulated here and pressure differences are compared).

At the inlet, three different levels of approximation of the flow in the diffuser were studied:

Simulation 1. The flow at the inlet both in spanwise and circumferential directions, as well as the turbulence quantities, is assumed to be uniform. This calculation is typical of that which can be carried out at an early stage of the design process when the preliminary one-dimensional velocity triangles have already been determined.

Simulation 2. The circumferentially averaged flow at the outlet of the impeller, taken from a Navier-Stokes CFD simulation of the impeller alone, is taken as the inlet flow for the diffuser. This calculation is typical of that which can be carried out when the impeller design is complete and after the impeller flow field has been simulated.

Simulation 3. The inlet flow conditions for the diffuser simulation are taken from LDA measurements at the impeller outlet. The LDA measurements points are fairly sparse and do not get too close to the walls so that interpolation and extrapolation of the data was necessary to make the data suitable as inlet boundary conditions for the calculations. This kind of boundary condition is, of course, only possible, if a test rig with the measuring equipment is available. But such a simulation using measurement data is highly relevant for code validation.

The resulting velocity profiles in the radial and circumferential directions at the radius of the leading edges of the diffuser vanes ($R/R_2 = 1.058$) midway between the vane leading edges are plotted in figures 5(*a*) and 5(*b*) respectively. For simulation 3 this corresponds to the inlet boundary conditions of the calculation and for simulations 1 and 2 this is 7 mm downstream of the inlet plane of the calculation. It is clearly visible, that the data taken from the impeller simulation (simulation 2) generates profiles which are different from the measured ones, especially for the radial velocity. This is attributed to the fact that the impeller simulation used was carried out some time ago on a relatively coarse H-grid. More recent calculations of the impeller have been made with a block-structured pinched H-grid and with improved outlet boundary conditions to get improved agreement with the impeller data, but these were not available for the simulations presented here.

The computation was started by specifying a single constant value for each solved variable for the entire domain. This simple initial guess was sufficient to get converged results after about 150 time steps, which required about 9 hours CPU-time an IBM RISC/6000 workstation.

Comparison With LDA-Measurements. The LDA measurements available make possible the comparison of the measured and calculated velocity vectors in the diffuser. The velocity vectors of simulation 3 are compared directly with those of the measurements in Fig. 6. This figure shows the velocity vectors on three blade-to-blade planes, near to the hub (labeled "HUB"), on the mid-plane between hub and shroud (labeled "MIDSPAN") and near to the shroud (labeled "SHROUD").

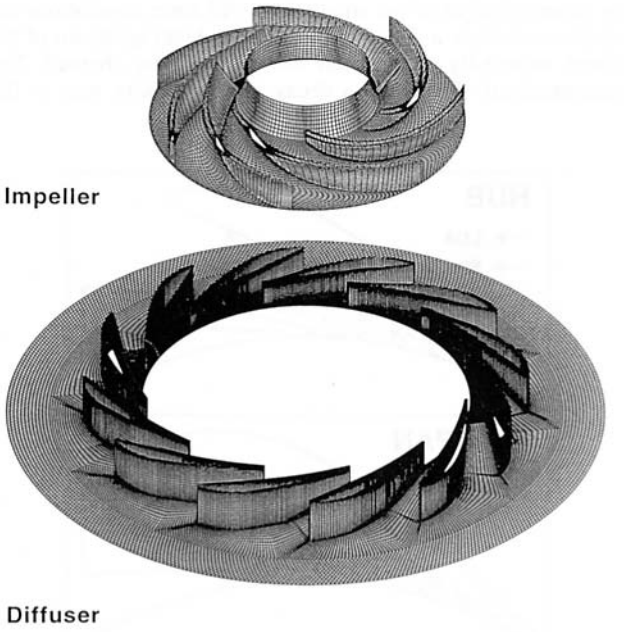

Fig. 4(*a*) Computational grids for radial pump impeller and diffuser

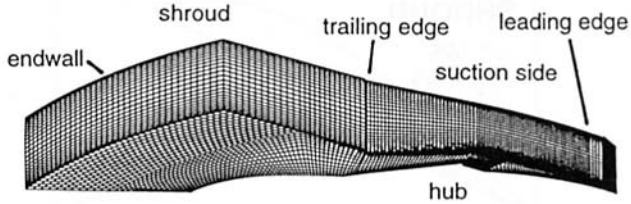

Fig. 4(*b*) H-grid (68750 NODES) for one partition of the radial pump diffuser

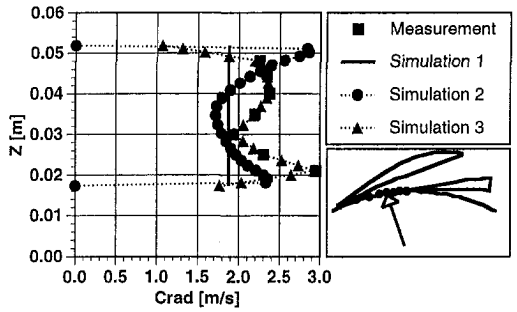

Fig. 5(*a*) Radial velocity profile at $R/R_2 = 1.058$, mid-channel

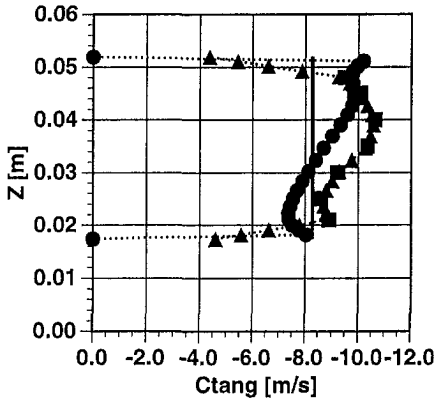

Fig. 5(*b*) Tangential velocity profile at $R/R_2 = 1.058$, mid-channel

The flow field is strongly three-dimensional at the design point and a strong separation on the hub side of the flow channel can be observed in all of the simulations. All three simulations are similar and show a decay in the velocity level upstream of the throat, especially on the hub side of the flow channel. The measurements show only a decay in the velocity near to the shroud. A recirculation is shown by all three simulations, which starts on the pressure side of the vane on the hub endwall. This is related to the conical form of the hub side diffuser wall; the separation begins at the point where the slope of the diffuser wall abruptly changes, see Figs. 3 and 4(*b*). The time-average of the LDA measurements show vectors which are almost parallel to the diffuser vanes and provides little evidence of the flow separation. Flow visualization studies with a high speed video camera, see Eisele et al. (1997), showed that in fact an unsteady flow separation was present on the blades in this region. The high turbulence level of the flow measured by the LDA system (≈40 percent) also indicates that an unsteady flow separation is present.

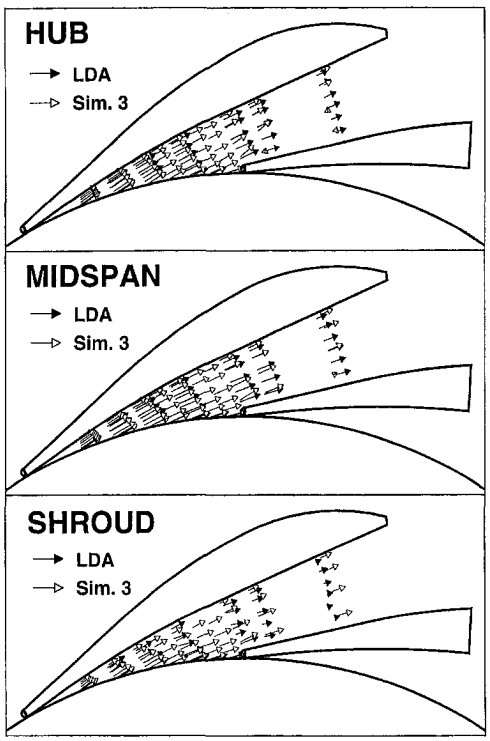

Fig. 6 Comparison of velocity vectors

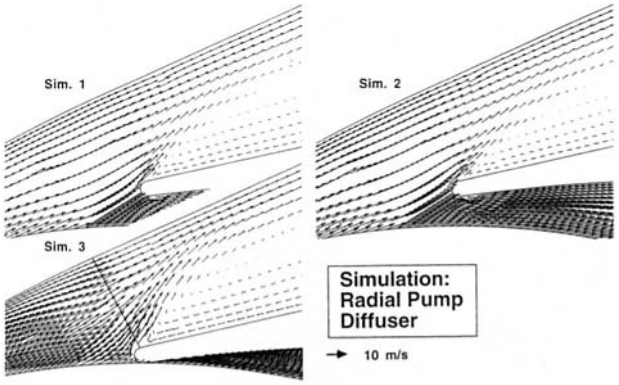

Fig. 7 Comparison of velocity vectors at HUB near the leading edge

Figure 7 shows a close-up of the vectors of all three simulations at the hub in the region of the leading edge. The simulations 1 and 2 yield quite similar flow patterns in that region. In all three cases the flow angle on to the vane is slightly different, which leads to different shapes of the recirculation zones. The different angle of attack on to the diffuser vane arises from the different inlet boundary conditions that are specified for the simulations. For simulations 1 and 2, the location of the inlet plane of the calculation is so close to the leading edge that the inlet flow defined by the boundary conditions has no time to develop before it reaches the leading edge. The different incidence levels in this region are a direct result of the velocity specification on the inlet boundary. For simulation 3, the inlet boundary conditions are actually defined from measurements made on the inlet plane.

The comparison of the velocity vectors in a spanwise plane midway between the blades, as shown in Fig. 8, shows clearly that the sharp edge at the beginning of the endwall slope on the hub side triggers the flow separation in the simulations and the resulting recirculation. Comparisons between the simulations (not presented here) show, that simulation 3, which gets its inlet boundary conditions from LDA-measurements, reveals the

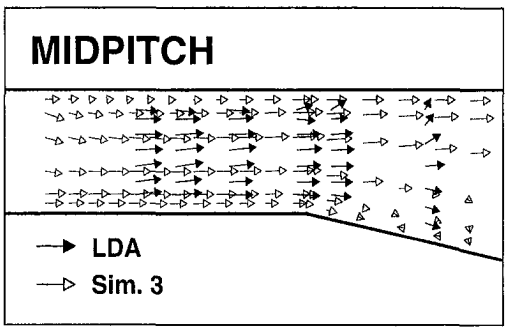

Fig. 8 Comparison of velocity vectors at midpitch

smallest recirculation zone. The LDA-vectors compare quite well with the calculated ones and the last row of vectors in streamwise direction in the plot indicates the onset of a separation. Unfortunately in the area, where the simulations show flow separation, there are no LDA-data available.

Although it is difficult to see recirculation in the LDA plots, such zones exist in the test rig, as can be shown by flow visualization, see Eisele et al. (1997). These flow separations are not steady, and are also independent of the blade passing of the impeller. They appear randomly and their shape varies, but they lie within the area predicted by the simulations. At off-design operating points the LDA measurements showed more extensive flow separation along the hub which were in better agreement with the simulations.

Comparison With Pressure-Measurements. The radial pump test rig is equipped at the hub side with seven and at the shroud side with four pressure taps along the centerline of the blade channel. The measured and calculated pressure rise in the diffuser is compared by considering the variation of the nondimensional static pressure rise coefficient ψ along the channel:

$$\psi = \frac{p_{\text{local}} - p_{\text{ref}}}{\rho \frac{u^2_{\text{impeller}}}{2}} \tag{3}$$

The reference pressure p_{ref} is located near the middle of the diffuser channel on the shroud side at the leading edge radius of the diffuser vanes. The reference speed u_{impeller} is the circumferential velocity of the impeller at the radius of the blade trailing edges.

In Figs. 9(a) and 9(b), the static pressure rise ψ along the hub and shroud side of the diffuser is compared. All of the simulations show similar tendencies for the prediction of the pressure rise but different ultimate pressure levels are attained. Due to this quite large discrepancy in the pressure prediction, the influence of the grid was investigated. The grid has been locally refined around the leading edge of the vane. The calculated pressure rise with this improved grid is shown for simulation 2 in Figs. 9(a) and 9(b) and is labeled "Simulation 2A." This comparison clearly shows, that the grid has a small influence on the pressure rise ψ in the diffuser downstream of the separation point. The pressure rise agrees fairly well with the measurement up to about $s = 0.082$ m, where the conical endwall in the flow channel on the hub side begins. From there on flow separation is predicted by the calculations and no further pressure rise takes place. In the test rig, however, there is an unsteady separation which varies in location and strength and higher pressures are attained. This phenomenon is similar to the two-dimensional diffuser simulations (see Fig. 2(a) and 2(b)), in that the predictions start to diverge from the experiments as they enter the region of "Large Transitory Stall." In the pump diffuser simulations, however, the flow separation leads to a larger flow blockage than that measured. This accelerates the flow outside the recirculation zone and reduces the static pressure rise.

Small variations of the predicted flow blockage affect the flow velocity and have a great impact on the static pressure. Because of this, the static pressure rise predictions are very sensitive to the shape and extent of the recirculation zone, and the computed values agree only qualitatively with the measurements.

Discussion

There are a number of interesting points which arise from these simulations of a highly loaded pump diffuser. First, the simulations of the two-dimensional diffuser show clearly that current CFD methods with the k-ϵ turbulence model have extreme difficulty in predicting exact diffuser performance in regions where separation has occurred. This is an important finding because the best operating point of any diffuser is usually very close to the onset of separated flow. In addition, the design constraints relating to the achievement of a maximum pressure rise in the smallest possible radial extent cause the pump designer to select highly loaded diffusers with the likelihood of separation. The flow visualization measurements of this pump diffuser show clearly that this diffuser has a strong separation even at the design point. It is clear, therefore, that the CFD simulations are going to have some difficulty in the flow prediction of this diffuser.

Second, as the flow separation in the diffuser has such a strong influence on the predicted pressure rise, there is no relevant difference between the three simulations. Simulation 1, based on simple one-dimensional inlet velocity profiles, is not substantially worse than simulations 2 and 3. Simulation 2 suffers because of the fact that the impeller simulation used does not agree in all details with the measured diffuser inlet flow. Simulation 3 using the measured inlet conditions suffers be-

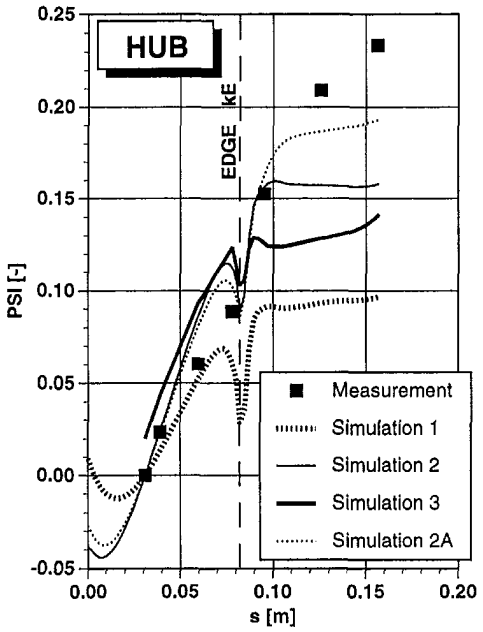

Fig. 9(a) Static pressure rise Ψ along centerline of diffuser at HUB

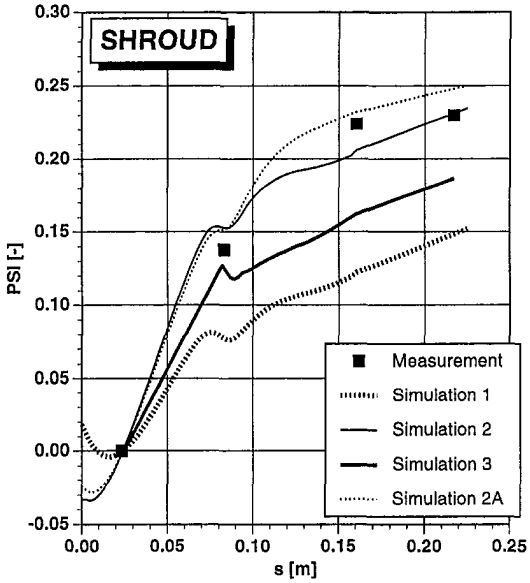

Fig. 9(b) Static pressure rise Ψ along centerline of diffuser at SHROUD

cause these are not sufficiently detailed, especially close to the blades and endwalls, to generate accurate data for the diffuser simulation. It is clear from this work that more accurate simulation of diffuser performance will require accurate information on the upstream flow from the impeller.

Third, a clear problem with such diffuser calculations is the position of the inlet boundary condition. This has to be placed in the small space between the impeller and the diffuser, in a region where the flow is relatively highly distorted. In the long run it is possible that the best simulations are likely with a full stage calculation of the impeller and diffuser with a suitable mixing plane interface at the junction between them, whereby relatively straightforward inlet boundary conditions at the inlet of the impeller can then be used.

Fourth, the flow field in the diffuser is known to have large periodic unsteadiness related to the impeller blade passing. The steady flow simulations have not included this and have been compared to the time-average of the test data. It is considered that this has not substantially contributed to the uncertainty in the comparisons between the test data and the simulations, see also Muggli et al. (1996). In this case of a very highly loaded diffuser with a strong flow separation the results are mainly influenced by this phenomenon.

Some studies of the effects of grid resolution on the predicted flow field have been carried out, but owing to the strong influence of the large flow separations predicted, the grid has little influence on the results. The main uncertainty in these calculations arises from the very difficult three-dimensional nature of the impeller outlet flow, and the limitations in the way this has been simulated. The next step in this project is to repeat these steady calculations with an inlet boundary condition based on an improved simulation of the impeller flow field, and to carry out a full stage simulation. In addition, measurements are planned on a diffuser which is slightly less highly loaded than the one here so that the regions of flow separation are reduced. It is also expected that in this case it may be easier to predict the flow than in the diffuser used here.

Conclusions

A Reynolds-averaged Navier-Stokes code with a standard k-ϵ turbulence model is able to predict the important flow physics of a two-dimensional planar diffuser, such as the well-known effects of inlet blockage and diffuser area ratio on static pressure recovery. At low loading (low area ratio) there is good agreement between measured and computed static pressure recovery. At high loading, where an unsteady transitory stall occurs, the predictions of pressure recovery are too optimistic. The static pressure rise is overestimated by the numerical computations as the k-ϵ turbulence model underestimates the blockage caused by the recirculation of the large separation region.

The flow through a highly-loaded vaned diffuser of a radial pump was simulated and the results were compared with LDA and pressure measurements. Three simulations of the diffuser flow have been carried out, with three levels of approximation for the inlet flow to the diffuser. It was found that the flow field in this highly loaded pump diffuser is strongly three-dimensional due to a flow separation on the hub side. This separation is shown by all three simulations but with somewhat different locations and recirculation strength. The simulations demonstrate that numerical computations can be useful tools to identify regions of flow separations in pump diffusers, but that in the presence of large flow separations, they are inadequate for accurate predictions of pressure rise.

At the current state of the art for CFD in highly loaded pump diffusers, more complicated inlet boundary conditions, as used for simulations 2 and 3, do not yet yield significantly better results than simple inlet condition using averaged one-dimensional velocity profiles (simulation 1). This highly loaded diffuser is influenced by the inlet boundary conditions up to the beginning of the slope at the hub side. From there on, the flow is dominated by the separations triggered by the edge of this slope and the highly loaded diffuser channel, and the simulations with the k-ϵ model are limited by their ability to predict extensive flow separations with sufficient accuracy.

References

ASC, 1994, TASCflow Documentation Version 2.3, Advanced Scientific Computing Ltd., Waterloo, Ontario, Canada.

Casey, M. V., 1994, "The Industrial Use of CFD in the Design of Turbomachinery," AGARD Lecture Series Turbomachinery design using CFD, AGARD LS-195.

Dalbert, P., and Wiss, D., 1995, "Numerical Transonic Flow Field Predictions for NASA Compressor Rotor 37," ASME Gas Turbine Conference, Houston.

Dawes, W. D., 1994, "A Simulation of the Unsteady Interaction of a Centrifugal Impeller with its Vaned Diffuser: Flow Analysis," ASME Paper 94-GT-105.

Drtina, P., Göde, E., and Schachenmann, A., 1992, "Three-Dimensional Turbulent Flow Simulation for Two Different Hydraulic Turbine Draft Tubes," First European CFD conference, Brussels, Sept. 7–11.

Eisele, K., Muggli, F., et al., 1993, "Pump Development with Laser and Computer," *Technical Review Sulzer,* 93/2, pp. 37–39.

Eisele, K., Casey, M. V., Zhang, Z., Gülich, J., and Schachenmann, A., 1997, "Flow Analysis in a pump Diffuser, Part 1: LDA and PTV Measurements of the Unsteady Flow," ASME JOURNAL OF FLUIDS ENGINEERING, published in this issue.

Eisele, K., Zhang, Z., and Muggli, F., 1994, "Investigation of the Unsteady Diffuser Flow in a Radial Pump," 7th International Symposium on Applications of Laser Techniques to Fluid Dynamics, Lisbon, Portugal, July.

Gülich, J., Favre, J.-N., and Denus, K., 1997, "An Assessment of Pump Impeller Performance Predictions by 3D-Navier-Stokes Calculations," *Proc. of the 1997 ASME Fluids Engineering Division Summer Meeting,* June 22–26.

Keck, H., Drtina, P., and Sick, M., 1996, "Numerical Hill Chart Prediction by Means of CFD Stage Simulation for a Complete Francis Turbine," *Proc. of the XVIII IAHR Symposium,* Valencia, Spain.

Muggli, F., Wiss, D., Eisele, K., Zhang, Z., Casey, M. V., Galpin, P., 1996, "Unsteady Flow in the Vaned Diffuser of a Medium Specific Speed Pump," *Proc. of the 1996 Int. Gas Turbine and Aeroengine Congress & Exhibition,* 10–13 June, ASME-Paper 96-GT-157, New York.

Renau, L. R., Johnston, J. P., and Kline, S. J., 1967, "Performance and Design of Straight, Two-Dimensional Diffusers," ASME *Journal of Basic Engineering,* pp. 141–150.

Runstadler, P. W., Dolan, F. X., and Dean, R. C., 1975, *Diffuser Data Book,* Creare Inc., TN-186, Hanover, NH.

Schachenmann, A., Muggli, F., and Gülich, J., 1993, "Comparison of three Navier-Stokes Codes with LDA-Measurements on an Industrial Radial Pump Impeller," ASME Fluids Engineering Conference, Washington D.C.

Wilcox, D. C., 1993, "Comparison of Two-Equation Turbulence Models for Boundary Layers with Pressure Gradient," *AIAA Journal,* Vol. 31, No. 8, pp. 1414–1421.

Unsteady Total Pressure Field Downstream of an Embedded Stator in a Multistage Axial Flow Compressor

N. Suryavamshi[1]

B. Lakshminarayana

J. Prato

Center for Gas Turbines and Power,
The Pennsylvania State University,
University Park, PA 16802

J. R. Fagan
Allison Engine Company,
Indianapolis, IN 46206

The results from measurements of the unsteady total pressure field downstream of an embedded stage of a three stage axial flow compressor are presented in this paper. The measurements include area traverses of a high response kulite total pressure probe and a pneumatic five hole probe downstream of stator 2 at the peak efficiency operating point for the compressor. These data indicate that both the shaft-resolved and unresolved fluctuations contribute to the unsteadiness of the total pressure field in multistage compressors. Specifically, regions associated with high levels of unsteadiness and, consequently, high levels of mixing including both the hub and casing endwalls and the airfoil wakes have significant levels of shaft resolved and unresolved unsteadiness. Temporal variations of stator exit flow are influenced by both shaft resolved and unresolved unsteadiness distributions. The limitations of state-of-the-art instrumentation for making measurements in moderate and high speed turbomachinery and the decomposition used to analyze these data are also discussed.

Introduction

Unsteady interactions are known to affect turbomachinery performance. However, almost all existing turbomachinery design methods are based on steady-state flow analysis. While the importance of including unsteady effects in the turbomachinery design process is generally accepted, the specific influence of unsteady interactions on the time averaged flow is not well understood. Consequently, it is not obvious how these effects should be integrated into turbomachinery component design systems. A more complete understanding of the unsteady flow in turbomachinery components is required to integrate these effects in current and next generation design and analysis tools.

The unsteadiness resulting from the relative motion of neighboring blade rows causes various interactions between the blade rows that may influence both the aerodynamic and structural behavior, as well as noise emission of the rotor and stator blades of the turbomachine. The potential flow fields about a blade extend both upstream and downstream of the blade, and decay exponentially with a length scale of the order of a chord. The wake interaction refers to the unsteadiness induced at a blade row by the wakes shed by the blades of an upstream blade row and convected downstream. Owing to the slow decay of the wakes, the wake interaction persists significantly farther downstream than the potential flow interaction. In the endwall, the unsteadiness caused by the secondary and leakage flows and associated vortices also contribute to the blade row interactions. All earlier investigations in a multistage compressor, with the exception of Falchetti (1992) and Cherrett and Bryce (1992), were carried out in either low speed compressors or compressors having the same number of rotor and stator blades in every blade row. Hence, there is a need for detailed understanding of the physics of the flow in a high speed multistage compressor. This is one of the goals of the Penn State program.

The unsteadiness in turbomachines has been generally categorized as being either "periodic" or "random" ("turbulent"). Flow field fluctuations at discrete frequencies (e.g., blade passing frequency, shaft frequency etc.) are termed as periodic unsteadiness. Random unsteadiness has been used as a catch-all term which includes flow-field fluctuations due to turbulence, vortex shedding, global flow-field fluctuations, random unsteadiness, and any other unsteadiness not correlated with the rotor speed. Therefore, in the absence of a more descriptive terminology for unsteady flow typical of turbomachines and to attempt to avoid confusion of terms, Suder et al. (1987), used the terms *rotor-wake-generated* unsteadiness to describe the unsteadiness generated by the rotor wake deficit, and *unresolved* unsteadiness to refer to the remaining unsteadiness. Adamczyk (1985) used density weighted averaging (temporal and ensemble averaging) in the Navier-Stokes equations to derive the average passage equations. He decomposed instantaneous velocity and thermodynamic state variables into their steady-state component, revolution periodic, revolution aperiodic, and unresolved components. These equations include terms which account for the effects of the unsteady flows. A similar decomposition of the unsteady total pressure measured downstream of a second stage stator in a three stage compressor is carried out in this paper.

Description of Test Facility, Instrumentation, and Data Acquisition System

The test compressor is a three stage axial flow compressor consisting of an inlet guidevane row and three stages of rotor and cantilevered stator blading with a rotating hub. Table 1 gives the general specifications of the research compressor. Rotors 1, 2, and 3 have 70, 72, and 74 blades, respectively, and stators 1, 2, and 3 have 71, 73, and 75 blades, respectively. The test facility is equipped with a stepper motor driven area traverse mechanism. This traverse has three degrees of freedom: radial, circumferential, and probe rotation. The probes are inserted into the compressor casing through teflon shoes and the chamber is sealed to prevent flow from recirculating through the slots. The motors are controlled by an IBM compatible 486 personal computer. Approximately 185 percent of the stator 2 blade pitch can be traversed at each radial location. Lakshminarayana et al. (1994) give a complete description of the test compressor,

[1] Present Address: Allison Engine Company, Indianapolis, IN 46206.

Contributed by the Fluids Engineering Division for publication in the JOURNAL OF FLUIDS ENGINEERING. Manuscript received by the Fluids Engineering Division April 20, 1994; revised manuscript received May 30, 1997. Associate Technical Editor: Wing Ng.

Table 1 General specifications of test compressor

Number of Stages	3
Design Corrected Rotor speed	5410 rpm
Design Corrected Mass Flow	8.609 kg/s
Design Overall Total Pressure Ratio	1.354
Mass Averaged Peak Efficiency at 100% Corrected Speed (Torque Based)	90.65%
Tip Diameter	0.6096 m
Blade Tip Mach Number	0.5
Average Reynolds Number (Based on Stator 3 chord length and axial velocity)	2.448×10^5
Average Hub-Tip Ratio	0.843
Diffusion factor (avg)	0.438
Average Flow Coefficient (V_X/U_t) (Average for a Stage)	0.509
Reaction (avg)	0.570
Space Chord Ratio (avg)	0.780
Aspect Ratio (avg)	1.500
Average Rotor Tip Clearance (static)	1.328 mm
Average Rotor Tip Clearance (dynamic)	0.667 mm
Average Stator Hub Clearance (static)	0.686 mm

associated instrumentation and the operating characteristics at three different speeds.

A subminiature five-hole probe (1.07 mm tip diameter) and a high response kulite total pressure probe (1.57 mm tip diameter) were cicumferentially and radially traversed downstream of stator 2 (at 5.6 percent stator 2 mid-span chord) at the peak efficiency operating condition at 100 percent speed. The pressure transducer is a Kulite XB-062-25A (absolute type). It has a natural frequency of 250 kHz and is electronically compensated for temperature changes from 80 to 180°F. Experimental data indicate that the kulite total pressure probe has a frequency response of approximately 40 kHz. The overall uncertainty in the instantaneous total pressure calculated with the ASME uncertainty analysis (based on 95 percent confidence intervals) is ±0.0074 psia. This translates to a maximum uncertainty of ±0.5 percent (of the local time mean C_{pt}) for both the time mean and RMS level of unsteadiness (all components) (Yavuzkurt, 1984). The high speed data was acquired using a Metrabyte DAS-50 system. The DAS-50 system was triggered using the once-per-rev pulse from an encoder mounted on the compressor shaft. A signal based upon the discretization of the rotor 2 blade passage (20 points per blade passage) obtained from a disk mounted on the same encoder is used to provide the clock frequency (approximately 130 kHz for this traverse) for the data acquisition system. At each location approximately 3.37 seconds (300 rotor revolutions) of data was acquired. Also a continuous stream of data was acquired at a few locations at a frequency of 200 kHz to conduct a spectral analysis of the data.

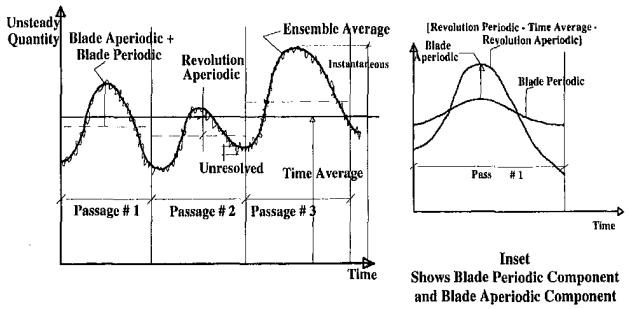

Fig. 1 Schematic of decomposition of any instantaneous quantity

A 31 by 25 mesh (31 tangential nodes and 25 radial nodes) with clustering in the endwall and the wake regions was employed to discretize the flow field. The discretization was the same as that used for the five hole probe except in the endwall regions where the smaller five hole probe could be traversed closer to the wall surface. At each radial location the kulite probe was rotated to align it in the mean direction of the mean flow as measured by the pneumatic five hole probe. In this paper, the nondimensional instantaneous total pressure is decomposed into a shaft-resolved and an unresolved component by an ensemble averaging procedure similar to the approach used by Suder et al. (1987) and Cherrett and Bryce (1992). Since these data are acquired with the use of the shaft-encoder and can be synchronized to individual rotor two blade passages, these data are further decomposed into components analogous to the decomposition used by Adamczyk (1985) for the derivation of the average passage equation.

Decomposition of Instantaneous Total Pressure

Each discrete measurement of total pressure is nondimensionalized and presented as an instantaneous total pressure coefficient $C_{pt_{ijk}}$.

$$C_{pt_{ijk}} = \frac{(P_{oijk} - \overline{P_{s1}})}{(\overline{P_{o1}} - \overline{P_{s1}})} \tag{1}$$

Here subscripts i, j, and k represent indices in ensemble averaging (i indicates the index of revolution, j the index of the blade in the row, and k the index of the point in the blade passage). The procedure of ensemble averaging is illustrated schematically in Fig. 1 and is shown for an actual experimental data set in Fig. 2 for P_o(psi) before nondimensionalization. The

Nomenclature

BPF = blade passing frequency
$C_{pt_{ijk}}$ = instantaneous total pressure coefficient (Eq. (1))
$\overline{C_{pt}}$ = time averaged total pressure coefficient (Eq. (6))
$(C_{pt_j})_{RA}$ = revolution aperiodic total pressure coefficient (Eq. (7))
$(C_{pt_{jk}})_{RP}$ = revolution periodic total pressure coefficient (Eq. (8))
$(C_{pt_{jk}})_s$ = shaft-resolved total pressure coefficient (Eq. (3))
$(C_{pt_k})_{BP}$ = blade periodic total pressure coefficient (Eq. (10))
$(C_{pt_{jk}})_{BA}$ = blade aperiodic total pressure coefficient (Eq. (11))
$(C'_{pt})_{ijk}$ = unresolved total pressure coefficient (Eq. (4))
$DS2$ = downstream of stator 2
N_b = number of blades per rotor
N_{pb} = discretization of a blade passage
N_{rev} = number of revolutions of data acquired
P_o = total pressure
PS = pressure side
P_s = static pressure
$\overline{P}_{s1}$ = mass averaged inlet casing P_s
r = radius
RMS = root mean square value
SS = suction side
V = absolute velocity
ω_z = axial component of vorticity $\omega_z = ((1/r)(\partial(rV_\theta)/\partial r)) - ((1/r)(\partial V_r/\partial\theta))$

Subscripts

1 = inlet to IGV
i = index denoting revolution
j = index denoting blade passage in revolution
k = index denoting discretization of blade
r = denotes radial direction

Superscripts

θ = denotes tangential direction
$-$ = denotes time average

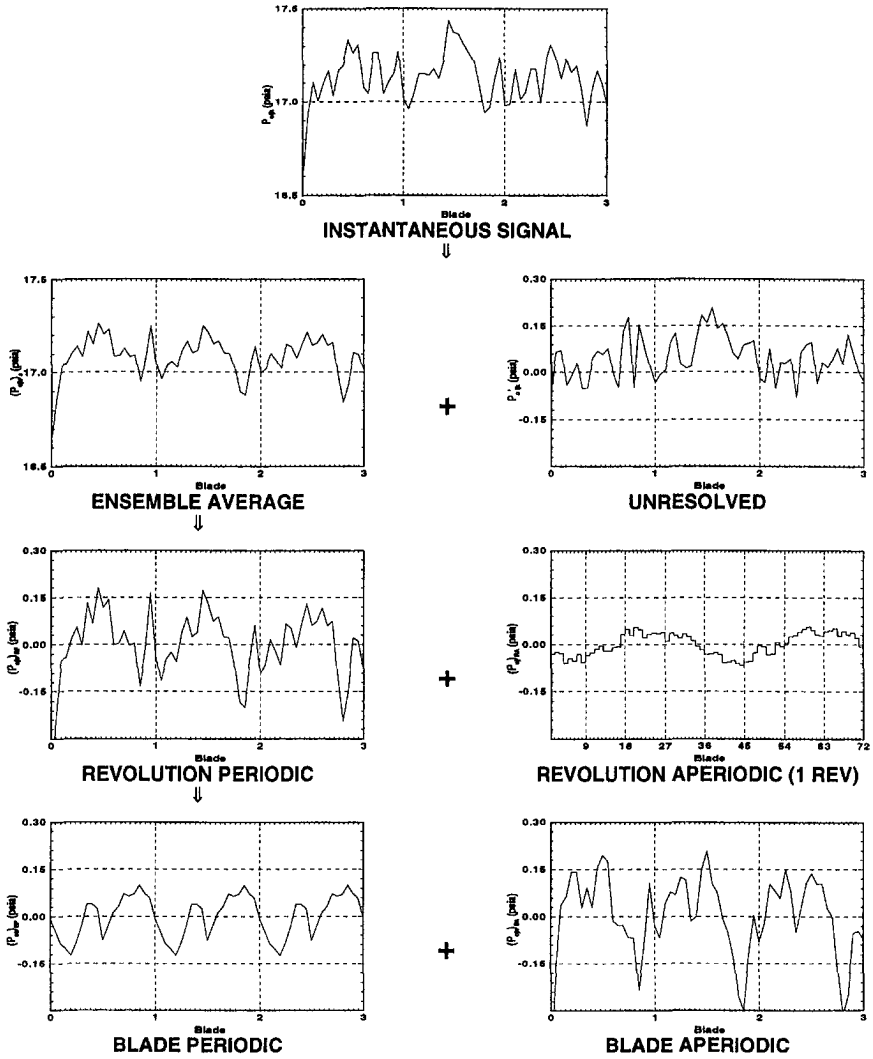

Fig. 2 Schematic of decomposition of unsteady pressure (*Cpt*) signal: actual data

instantaneous total pressure coefficient is decomposed into a shaft resolved and an unresolved component

$$C_{pt_{ijk}} = (C_{pt_{jk}})_s + C'_{pt_{ijk}} \tag{2}$$

where the shaft resolved component is obtained by ensemble averaging the instantaneous total pressure data set. The shaft resolved component is also referred to as the "deterministic" or "periodic" flow field since it is "clocked" with shaft and blade rotation.

$$(C_{pt_{jk}})_s = \frac{1}{N_{rev}} \sum_{i=1}^{N_{rev}} (C_{pt})_{ijk} \tag{3}$$

$$C'_{pt_{ijk}} = C_{pt_{ijk}} - (C_{pt_{jk}})_s \tag{4}$$

The shaft resolved component is further decomposed into a time average ($\overline{C_{pt}}$), a revolution periodic ($(C_{pt_{jk}})_{RP}$) and a revolution aperiodic ($(C_{pt_j})_{RA}$)

$$(C_{pt_{jk}})_s = \overline{C_{pt}} + (C_{pt_j})_{RA} + (C_{pt_{jk}})_{RP} \tag{5}$$

where

$$\overline{C_{pt}} = \frac{1}{N_{rev} \times N_b \times N_{pb}} \sum_{i=1}^{N_{rev}} \sum_{j=1}^{N_b} \sum_{k=1}^{N_{pb}} C_{pt_{ijk}} \tag{6}$$

$$(C_{pt_j})_{RA} = \left\{ \frac{1}{N_{pb}} \sum_{k=1}^{N_{pb}} [(C_{pt_{jk}})_s - \overline{C_{pt}}] \right\}_j \tag{7}$$

$$(C_{pt_{jk}})_{RP} = [(C_{pt_{jk}})_s - \overline{C_{pt}} - (C_{pt_j})_{RA}] \tag{8}$$

The revolution aperiodic component which is a passage to passage average (averaged across each blade passage) reflects the average condition within each rotor blade passage and thus represents the asymmetry around a rotor revolution with a time constant of one rotor 2 blade passing period (such as those arising from differences in blade count between rotors 1 and 2). The revolution aperiodic component for a typical measurement in this compressor is shown in Fig. 2. The two cycle per revolution pattern observed in this figure is consistent with the rotor blade count variations in the compressor (70, 72, 74 for rotors 1, 2, and 3, respectively). The revolution periodic component of the total pressure can then be decomposed into the blade periodic ($(C_{pt_k})_{BP}$) and the blade aperiodic ($(C_{pt_{jk}})_{BA}$) components.

$$(C_{pt_{jk}})_{RP} = (C_{pt_k})_{BP} + (C_{pt_{jk}})_{BA} \tag{9}$$

$$(C_{pt_k})_{BP} = \frac{1}{N_b} \sum_{j=1}^{N_b} [(C_{pt_{jk}})_{RP}] \tag{10}$$

$$(C_{pt_{jk}})_{BA} = [(C_{pt_{jk}})_{RP} - (C_{pt_k})_{BP}] \tag{11}$$

The blade periodic components generally represents the fluctuations of the total pressure field over an "average" rotor 2 blade passing period. The blade periodic component for a typical measurement is shown in Fig. 2. The blade aperiodic component

generally represents the asymmetry about a rotor revolution with a time constant of the sampling period. Since the decomposition of the original signal has already filtered the asymmetries with a time constant on the order of a rotor 2 blade passing period (revolution aperiodic), this component includes short term asymmetries synchronized to the passage of the individual rotor 2 blades (such as those arising from passage-to-passage variations in geometry).

For each of the unsteady components discussed above, the RMS values are calculated by:

$$\mathrm{RMS}((C_{pt})_{RP}) = 100\,\frac{\sqrt{\dfrac{1}{N_b \times N_{pb}}\sum_{j=1}^{N_b}\sum_{k=1}^{N_{pb}}(C_{pt_{jk}})^2_{RP}}}{\overline{C_{pt}}} \quad (12)$$

$$\mathrm{RMS}((C_{pt})_{RA}) = 100\,\frac{\sqrt{\dfrac{1}{N_b}\sum_{j=1}^{N_b}(C_{pt_j})^2_{RA}}}{\overline{C_{pt}}} \quad (13)$$

$$\mathrm{RMS}((C_{pt})_{BP}) = 100\,\frac{\sqrt{\dfrac{1}{N_{pb}}\sum_{k=1}^{N_{pb}}(C_{pt_k})^2_{BP}}}{\overline{C_{pt}}} \quad (14)$$

$$\mathrm{RMS}((C_{pt})_{BA}) = 100\,\frac{\sqrt{\dfrac{1}{N_b \times N_{pb}}\sum_{j=1}^{N_b}\sum_{k=1}^{N_{pb}}(C_{pt_{jk}})^2_{BA}}}{\overline{C_{pt}}} \quad (15)$$

$$\mathrm{RMS}(C'_{pt}) = 100\,\frac{\sqrt{\dfrac{\sum_{i=1}^{N_{rev}}\sum_{j=1}^{N_b}\sum_{k=1}^{N_{pb}}(C'_{pt})^2_{ijk}}{N_b \times N_{pb} \times N_{rev}}}}{\overline{C_{pt}}} \quad (16)$$

While this decomposition is mathematically rigorous (i.e., the unsteady pressure signal can be reconstructed by summing each of the components), it is premised upon the assumption that the deterministic structure correlated with shaft speed are the most relevant for turbomachinery considerations. As such, measurement of the unsteady total pressure field resulting from all other physical phenomena not correlated with shaft speed, such as vortices originating in the stationary frame of reference, will be included in the unresolved component. Additionally, variations in the magnitude of the velocity deficit, width, and spatial positions of the rotor wakes between rotor revolutions, which are clearly shaft-synchronized physical phenomena, contribute to the unresolved component due to the algebraic nature of the ensemble averaging procedure. As a consequence, the magnitude of the shaft-resolved and unresolved components of the unsteady pressure signals cannot be explicitly defined as the respective contributions to the total unsteadiness of the deterministic structures and random turbulence. The impact on the data presented and analyzed in this paper in the relative levels of the various components of shaft-resolved and unresolved unsteadiness cannot be compared due to the algebraic nature of the ensemble averaging procedure. However, these data can be used to identify in which regions of the flow field each of these components make significant contributions to the total unsteadiness and consequently flow mixing in the compressor.

Time Averaged Total Pressure Field

In this section, the time averaged total pressure field is compared with the total pressure data acquired using a pneumatic five-hole probe at the same axial location at the same operating condition (peak efficiency point). Figure 3 shows the contours of time averaged total pressure coefficient (Eq. (6)) compared with the pneumatic data. The time averaged total pressure coefficient compares very well, with the pneumatic data at most locations. The maximum discrepancy in C_{pt} (less than 4 percent) occurs near the hub. Thus the data presented in Fig. 3 do provide confidence in the data acquired from a high response probe. The second blade (marked KB in Fig. 3) shows a larger loss core near the casing. This is due to the presence of a leading edge kiel probe at the 90 percent spanwise position on the blade leading edge. The blade with the leading edge kiel probe will be referred to as the "kiel" blade (KB), while the blade with no kiel probe will be referred to as the "clean" blade (CB). Even though the measurements are acquired downstream of a stator with a leading edge kiel, all analysis and interpretations have been carried out for the flow downstream of the clean blade only. The rotor shaft resolved data presented in the next section are also for the clean blade only. In this section, focus is placed on the following important features of the flow: the stator wake regions, effect of the secondary flow and the thickening of the boundary layer near the suction surface corner in the casing region and the effect of secondary and leakage flows in the hub endwall region.

Stator Wake Region. Thin stator wakes are observed in the midspan regions at this axial location. This is consistently observed in all the data sets. Widening of the stator wakes is observed in the endwall regions (both hub and casing endwall). In the hub endwall region the wake width increases both on the pressure side and on the suction side of the stator. However, in the casing endwall region, the thickening is mainly on the suction side. Due to interaction between the stator wake flow and the hub clearance flow as well as an increase in incidences from the rotor exit flow upstream causes the thickening of the stator wakes in the hub endwall region. In the casing endwall region, the thickening is mainly due to the presence of a corner interaction with the endwall flow on the suction side. Jung and Eikelmann (1995) also document very similar features to that observed in the PSU data set in a high speed industrial compressor in so far as the wakes, casing corner flows and hub clearance flow region.

Hub Endwall Region. In the hub endwall region, the regions of interest are in the midpitch close to the hub, on the suction and pressure side of the stator wake close to the hub as well. The stagnation pressure contours near the midpitch location close to the hub indicates a region of low total pressure. In order to better explain the flow physics in this region, use is made of available five hole probe measurements at this same location. From the five hole probe data it is observed that this region also has low total velocity, high losses and a region of significant vorticity. Figure 4 shows the axial vorticity distribution close to the hub endwall. The high vorticity in the region is due to the hub leakage flow caused by clearance between the stator tip and the rotating hub. Jung and Eikelmann (1995) show a schematic of the development of the leakage flow and its subsequent rollup into a vortex for an industrial compressor with cantilevered stator blading and a rotating hub. The present data set also shows similar features and so one can conclude that the low energy field on the stator hub is indeed the hub leakage flow. The extent of this leakage flow region is around 60 percent in the pitchwise and nearly 10 percent in the spanwise directions. As a result, this endwall phenomena generates more blockage than that generated by endwall viscous fluid on the hub endwall.

Casing Endwall Region. The other region which has a complex loss region that warrants interpretation is the suction surface casing endwall corner region. This region is characterized by low total pressure and high total pressure loss. This is also a region of low efficiency and high unresolved unsteadiness (as will be observed later). From the radial velocity distribution and the axial vorticity distribution (five hole probe data) a vortex type distribution is observed in this region. Figures 5 and 6 show the axial vorticity and secondary velocity distribu-

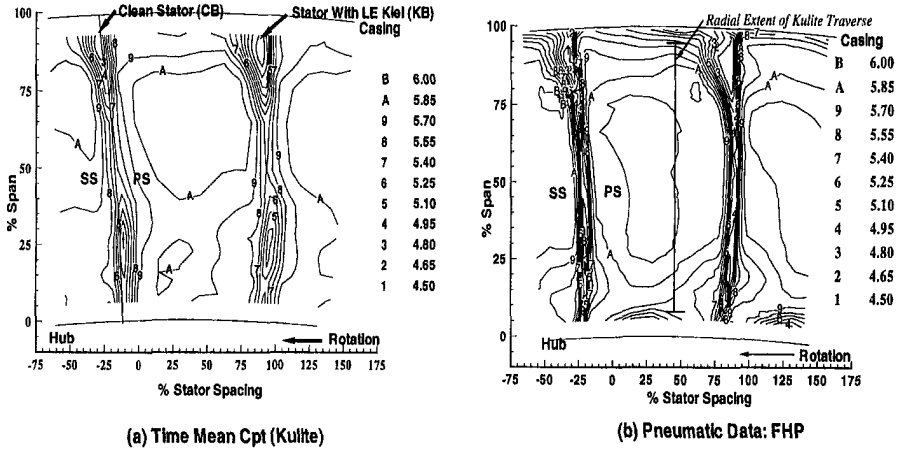

Fig. 3 Contours of time averaged total pressure coefficient: comparison with pneumatic five hole probe data

tion near the casing endwall location respectively. From Figs. 3, 4, and 6 we can observe that the vortex center and the loss core is located at approximately in the same location near the casing compared with the situation at the hub. This loss core is of a higher level than that observed at the hub region (5 percent compared to 2.5 percent at the hub). This flow arises due to a combination of various phenomena: probable casing stall, high inlet skew and casing secondary flow. The presence of an intense secondary flow feature as evidenced by radial outward flow toward the low pressure region on both the suction and pressure sides of the stator as well as flow overturning and underturning on the suction and pressure sides of the stator. The static pressure is quite low in the corner region confirming the presence of a vortex. The secondary velocity distribution shows an entrainment of flow into this region generating a large secondary vortex.

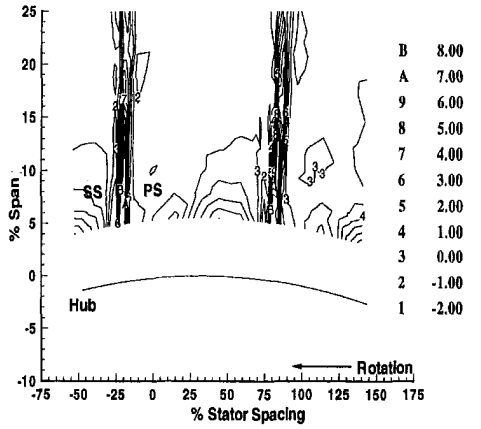

Fig. 4 Contours of axial vorticity near hub endwall: pneumatic five hole probe data

Unsteady Total Pressure Field

In this section the unsteady total pressure field is presented and analyzed. Unsteadiness at the exit of the stator exists due to interaction of at least three different mechanisms: the presence of rotor exit flow including wakes, secondary flow and leakage flow features being convected through the stator passage which have not fully mixed out, the shedding of vorticity from the stator trailing edge due to a time varying stator circulation or loading caused by the passage of the rotor flow over the stator surface, and the presence of a potential field due to the downstream rotor. By analyzing the stator exit data, it is possible to determine which of these mechanisms are dominant contributors to the unsteadiness.

The unsteady flow is viewed from two different perspectives in this section. First, attention is focused on the RMS flow field. This provides the overall information of the unsteady flow field downstream of the stator which is useful in design of future stators. Hub-to-tip contour plots of the various unsteadiness

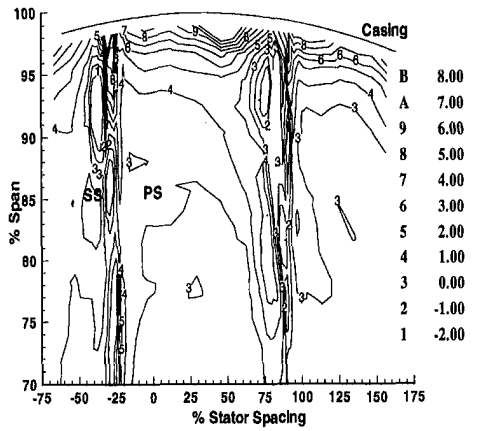

Fig. 5 Contours of axial vorticity near casing endwall: pneumatic five hole probe data

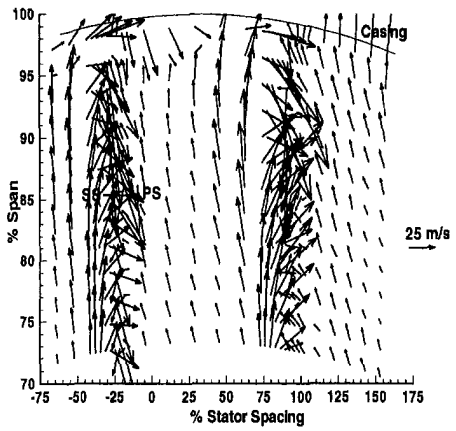

Fig. 6 Secondary flow vectors near casing endwall: pneumatic five hole probe data

components are used for this description. Attention is next focused on the temporal variation of the stator exit flow at each instant of rotor passage time. For this perspective, 6 frames of shaft resolved and unresolved unsteadiness in total pressure are used. Each frame represents one rotor 2 location with respect to the stator and 20 frames represents a complete cycle of one particular rotor blade passage as it moves across the stator passage (only six are shown for the sake of berivity and the explanation is based on all the frames). The shaft resolved and unresolved components of the total pressure coefficient are presented to illustrate flow characteristics which are due to the relative motion between the rotor and stator. This represents the perspective of one rotor blade sweeping past the stator only. A movie version of this description is also available from the authors.

Care must be taken when interpreting the unsteady data because of the frequency response limitations of the kulite probes. The most apparent limitation of these measurements is the resolution of the random (turbulent) fluctuations which are included in the unresolved component of total pressure. The actual frequency response for the kulite probe is approximately 40 kHz. Assuming a mean velocity of 100 m/s, the smallest length scale measured by the probe is given by $100/40000 = 2.5 \times 10^{-3}$m. Hence energy in turbulent eddies with length scales smaller than this is not measured by the instrument. Therefore the instrument measures all the features associated with frequencies less than 40 kHz (blade passing, shaft frequency and substantial part of random turbulence). For deterministic structure associated with the rotor blades (blade passing frequency of 6700 hz), this instrumentation can measure the first six harmonics. Although finer details of the structure may be contained in higher harmonics, beyond the measurement capability of the probe, the majority of the energy content is included in these lower harmonics.

RMS Unsteady Pressure Field. In this section the hub to tip contours of RMS values of the unsteady components of total pressure defined in Eqs. (3) through (11) are presented and analyzed. The RMS levels are calculated using Eqs. (12)–(16). Figure 7(*a*) shows the contours of rms total unsteadiness and Figs. 7(*b*)–7(*d*) show the contribution of the unresolved, revolution periodic and revolution aperiodic components to the total unsteadiness in similar plots. Much relevant information about significant features of the flow field can be discerned from these figures. Three significant regions of the flow are discussed in this section: the stator wake region, the hub endwall region, and the casing endwall region. These regions are the same as that discussed in the time averaged flow section.

Stator Wake Region. In the stator wake region, values of the shaft resolved unsteadiness (revolution periodic and revolution aperiodic) and unresolved unsteadiness are of the same order of magnitude in the mid-span regions and shaft resolved unsteadiness is lower than the unresolved unsteadiness in both the hub and casing endwall regions. On the pressure side of the stator, away from the endwalls, the levels of both the revolution periodic and unresolved unsteadiness are higher than the corresponding values on the suction side of the stator. This is certainly due to the migration of stator exit flow to the pressure side. The unsteady CFD simulations of this flow conducted by Hall (1997) very clearly show the migration of the shaft resolved rotor wake features on the pressure side of the downstream stator. The revolution aperiodic unsteadiness does not show any changes in the stator wake regions away from the endwall and the magnitudes are very low indeed. Only in the endwall regions, where there are influences of tip clearance flow and possible flow separations on the rotor suction surface hub endwall region, do the revolution aperiodic unsteadiness change and this is explained in the next section.

Hub Endwall Region. As was observed earlier, the hub endwall region is dominated by the clearance flow from the stator hub endwall and its interaction with the hub endwall fluid. The unsteadiness distributions shown in Fig. 7 do indicate that this region has significant levels of both revolution periodic and unresolved unsteadiness. However, the levels of the unresolved unsteadiness are much higher than the revolution periodic unsteadiness. This is mainly due to the propagation and decay of the hub leakage vortex which may be unresolved in nature. The revolution periodic unsteadiness is the rotor hub wake fluid which is trapped in the leakage flow and its subsequent interaction with the leakage flow. Slightly away from the leakage flow region, a region of comparable levels of revolution periodic and revolution aperiodic unsteadiness is observed on the suction side of the blade. It is surmised that there is transport of possibly separated rotor boundary fluid on the suction side close to the hub.

Casing Endwall Region. In the casing endwall region, the dominant source of unsteadiness is in the suction surface corner region and bulk of this unsteadiness is unresolved in nature. From the time averaged flow it was observed that this was due to intense secondary flow and interaction of the casing endwall fluid with the rotor leakage flow. The presence of high levels of unresolved unsteadiness indicates a dominant source of mixing to be turbulent in nature. There is significant levels of revolution periodic unsteadiness in the endwall region, but it is close to the blade on both sides of the stator whereas the unresolved unsteadiness is only on the suction side of the stator. The appearance of revolution periodic unsteadiness is probably due to the transport of the rotor tip leakage flow to the suction side of the stator passage. The unsteady CFD simulation (Hall, 1997) seems to qualify this hypothesis. The revolution aperiodic unsteadiness levels are high in these regions as well confirming the probable transport of the rotor tip leakage flow to the suction surface. Away from the blade surfaces, the levels of unresolved unsteadiness are higher than that observed in the core region, consistent with the increase in vorticity and associated turbulence production in the endwall viscous fluid.

Temporal Variation of Stator Exit Flow. In this section, the temporal variation of the stator exit flow is discussed. For the sake of brevity, the following discussion is limited to the shaft resolved and unresolved unsteadiness results only. Figure 8 contains several perspectives of the stator exit measurements (shaft-resolved and unresolved unsteadiness in total pressure) "frozen" at the same instant in time within the rotor revolution, but derived by averaging over 250 consecutive rotor revolutions. Six frames from the passage of the first rotor blade across the stator passage is shown but the interpretation is based on the analysis of 20 frames (the first blade in the revolution). A clock shown in the upper right hand corner of each picture shows the passage of the rotor blade across the stator passage (from $\tau/T = 0.0$ to $\tau/T = 1.0$). These times are arbitrary as the location of the rotor blade with respect to stator is not known. The location of the trigger is the same with respect to all locations in the stator passage. The right side blade is the clean blade, this is the blade that we will concentrate on. For detailed interpretation, it is essential to view the video depicting continuous time history of the flow field. Most of the interpretation in this section is based on the movie. The six frames shown in Fig. 8 do provide overall flow features but not the details on rotor wake, leakage flow, and corner flow transport and their features at the stator exit. *The video is available from the authors.* The discussion in focused on the following phenomena: (1) behavior of the rotor wake; (2) behavior of the stator wake; (3) behavior of the hub endwall leakage flow region; (4) behavior of the casing endwall corner region (blade suction surface and casing endwall corner); and (5) behavior of the casing endwall region away from the blade surfaces.

Behavior of the Rotor Wake. The rotor wake is identified by local increases in total pressure (both ensemble averaged and unresolved unsteadiness) above the time average. Closer

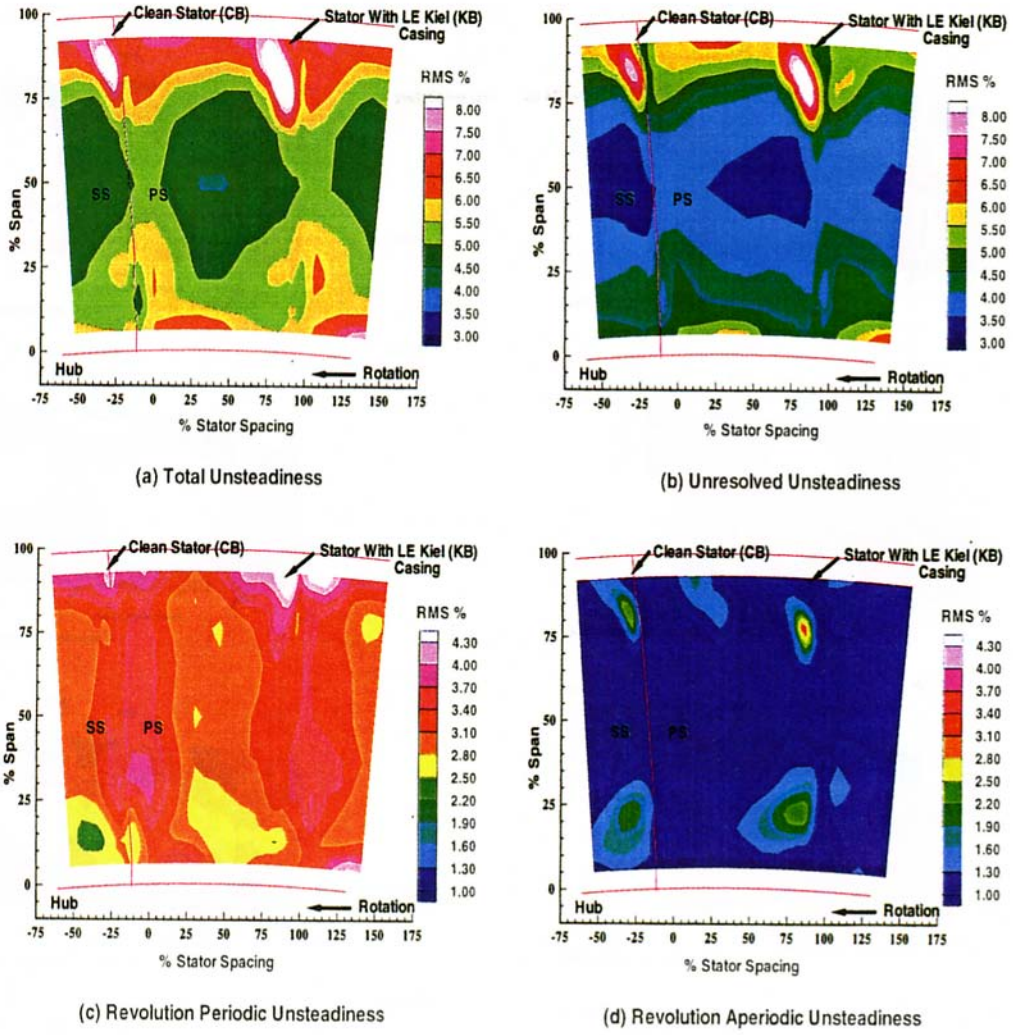

Fig. 7 Contours of RMS values of various unsteadiness in *Cpt*

examination of the rotor wake as it crosses the stator passage reveals that it becomes discontinuous either side of the stator wake. Starting with nondimensional time $\tau/T = 0.0$, one leg of the deterministic content of the rotor wake is seen on the suction side of stator and the other leg is seen approaching the pressure surface of the stator. This is because of higher convection speeds of the rotor wake on the suction surface of the downstream stator than on the pressure side. As the rotor sweeps across the stator passage, the rotor wake i is observed to be at various locations in the core flow region of the compressor until time approaches $\tau/T = 0.35$, where the wake approaches the next stator blade wake on the suction side. It is between times 0.35 and 0.5, that rotor wake $i + 1$ makes its appearance on the suction side of the stator blade CB. Since the blade count difference between rotor 2 and stator 2 is 1, part of the wake of rotor blade i is still in the stator passage when wake $i + 1$ makes its appearance. From the video animation, at time $\tau/T = 0.40$, both the rotor wakes are observed distinctly in the stator passage and this accounts for the maximum interaction between the stator and the rotor flow. This time is labeled the *maximum interaction time for rotor wake* at midspan. Unfortunately, it is not possible to correlate this time with the locations of the rotor trailing edge. If this information was available, one could correlate the direct rotor passing with the maximum and minimum interaction times.

Stator Wake Region Away From the Endwalls. As the rotor passes across the stator passage, the stator wakes show changes in their behavior. Different behaviors are observed at different radii. Near the hub, the width and depth of the total pressure wake remain almost constant (both ensemble average and unresolved unsteadiness) with rotor passing. The increase of the wake width on the pressure side of the stator is indicative of the rotor wake arrival at the measurement station. Since in the hub endwall region, there is entrainment of fluid from the suction side into the hub leakage flow due to the pressure gradient which exists from the pressure to suction side, there is no change in the wake width on the suction side. At mid-span, the pressure wake shows changes in wake width. In contrast to the situation at the hub, the wake depth also changes with blade passing. The ensemble averaged wake is widest at $\tau/T = 0.35$ and the thinnest at $\tau/T = 0.75$, whereas the unresolved unsteadiness distributions do not show too much of a change. It may be recalled here that at $\tau/T = 0.35$, the rotor wake was observed approaching the suction side of the stator and $\tau/T = 0.40$ was the "maximum interaction time" for the rotor wake. At the 81.89 percent spanwise location which is in the core of the casing vortex region, the width of the wake and its depth changes with rotor passage. The wake width is the largest at $\tau/T = 0.85$ and the smallest at $\tau/T = 1.00$. The wake depth change is not as high as in the midspan region. At the 90.44 percent spanwise location, bulk of the changes occur outside the wake. There is very little change in the wake depth and width with blade passing on the suction side of the wake. Once again, the change in wake depth is not as pronounced as it is at midspan.

It can be concluded from a detailed examination of the temporal analysis that the stator wake is adversely affected by the rotor wake passage. There is an almost periodic pulsing motion

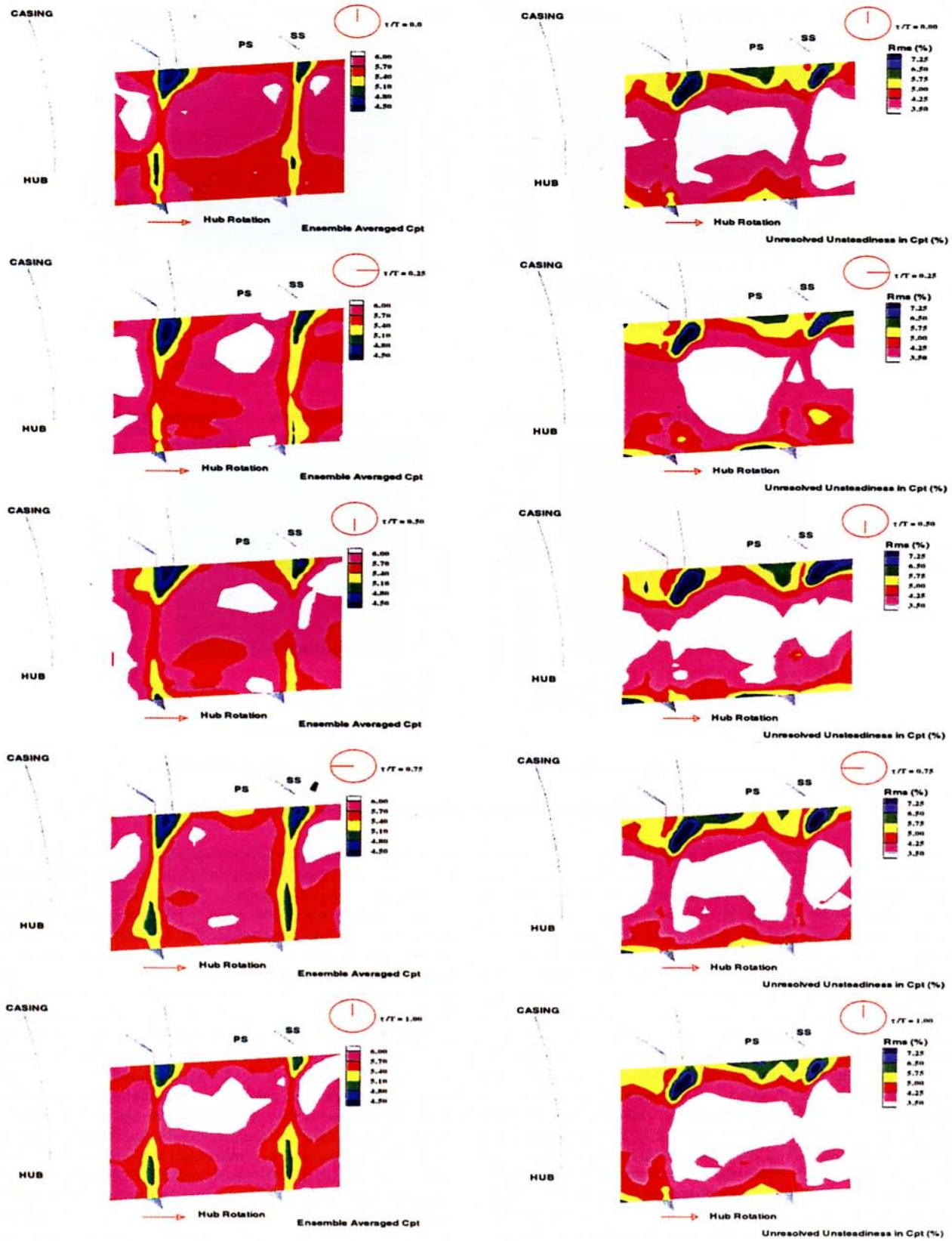

Fig. 8 Temporal variation of the stator exit flow

of the wake brought about by wake passing. This can be clearly seen in the video animation. However, this pulsing occurs at different times at various radial locations. This is most certainly due to differential wake decay and skewing of the rotor wake as it passes through the stator passage. The pulsing was the highest at around 81 percent span in the suction surface corner and the lowest near the hub. There is certainly an influence of the downstream rotor which would affect the stator wake behav-

ior through the potential influence, though it is difficult to quantify.

Behavior of the Hub Endwall Flow Region. As was observed earlier, the hub endwall region is dominated by the clearance flow from the stator endwall and its interaction with the hub endwall fluid. At $\tau/T = 0.0$, the region is spread out almost across the entire passage and as the rotor moves across the stator blade, the clearance flow grows in size in the spanwise direction while shrinking in the circumferential direction and starts moving across the passage transporting some of the hub endwall boundary layer flow toward the pressure surface of the stator blade. This can be verified by the appearance of higher levels of unsteadiness on the pressure surface of the blade with the passage of time. This is a clear indication of the scraping of the hubwall boundary layer and a presence of scraping vortex. The appearance of high unsteadiness on the pressure surface away from the hub substantiates this notion. And as the rotor blade continues further, the hub clearance region starts decreasing in size in the spanwise direction and starts spreading across the stator passage. The core of this region remains approximately at the same position with respect to the stator pitch. From Fig. 8, it is observed that the magnitude of the pressure fluctuations at the core of the leakage flow is the lowest at $\tau/T = 0.75$ and highest at $\tau/T = 0.25$.

Behavior of the Casing Endwall Suction Surface Corner Region. Like the wake region, this region also changes significantly with rotor passing. This region pulses (increases and decreases in size) as the rotor passes. Similar behavior was observed by Cherrett et al. (1994) in the hub corner flow region downstream of a stator of a single stage transonic fan. The region starts decreasing in size as the time increases from $\tau/T = 0.0$ and is the smallest at the minimum interaction time ($\tau/T = 0.35$) and then starts increasing rapidly reaching a maximum at the maximum interaction time ($\tau/T = 0.85$). As time further increases, the region starts decreasing once again in size. This is true for both the ensemble average as well as the unresolved unsteadiness. Cherrett et al. (1994) theorize that this is due to the rotor moving across the stator leading edge. The stator wake as was observed earlier was the thickest at $\tau/T = 0.85$. As the corner flow region grows in size from $\tau/T = 0.35$ to 0.85, the region is no longer confined to the suction surface region. It slowly spreads to the pressure surface and at the maximum interaction time, the region is almost the same size on either of side of the stator blade. It is also interesting to see that the corner region is observed to be "feeding" the flow in the casing region away from the endwalls as the blade passes by. This is observed very clearly in the unresolved unsteadiness distribution but not so clearly in the ensemble averaged plots. This was a region of intense secondary flow activity as seen in the time averaged flow field features seen earlier. So there is radial and circumferential transportation from both secondary flow as well as rotor wake related unsteadiness.

Behavior of the Casing Endwall Region Away From the Blade Surfaces. The ensemble average values in the casing wall region, away from the suction surface corner vary significantly. This is caused by rotor leakage flow and endwall flow interacting with the stator flow. The upstream rotor clearance flow (low pressures and higher levels of unsteadiness away from the corner regions) seems to have been smeared across the stator passage. As time progresses from 0.0, the high unsteadiness in the midpitch region (unresolved unsteadiness in total pressure), starts reducing in size circumferentially and very slightly increasing in size in the spanwise direction until time reaches the minimum interaction position. Afterwards, the region starts spreading in size in the circumferential direction as time approaches the maximum interaction point. At this time it is almost spread across the passage with feeding into this flow from the suction surface casing corner region as well. As already observed, the rotor wakes do have different wake widths and depths not only in the same revolution, but also in successive revolutions. Coupled to the fact that the wake location in the stator passage oscillates with time, tends to give the impression of smearing. As observed in the unresolved unsteadiness plots, as the rotor passes by, the clearance flow seems to be transported to the pressure surface of the stator. This shows that the rotor clearance flow is being transported through the stator passage and being deposited on the pressure surface of the stator as well.

Conclusions

Major conclusions based on an area traverse of a kulite total pressure probe downstream of the second stator of the Penn State multistage compressor are as follows:

1. Thicker stator wakes, higher levels of revolution periodic, and unresolved unsteadiness found on the pressure side of the stator confirm transport of the rotor wake toward the pressure side of the stator.
2. The flow in the hub endwall region is dominated by the stator hub clearance flow and its interaction with upstream rotor exit flow results in high unsteadiness in this region and indicates that hub clearance flow/vortex is unsteady and has contribution from both revolution periodic and unresolved unsteadiness.
3. In the casing endwall region, the dominant source of unsteadiness is in the suction surface corner region and bulk of this unsteadiness is unresolved in nature.
4. Across the span away from the endwalls, the levels of revolution periodic and unresolved unsteadiness are of the same order of magnitude. Close to the endwalls, the unresolved unsteadiness is generally higher than the revolution periodic unsteadiness.
5. As the rotor passes across the stator passage, there are changes in the stator exit flow behavior. The presence of thick stator wakes, largest extant of the casing endwall corner region, smallest influence of rotor leakage flow in the passage, and the spreading of the hub clearance flow across the entire stator passage are an indication of the maximum interaction time.
6. As the rotor passes across the stator passage, the stator wakes start increasing in size and the corner region starts reducing in size. The hub leakage flow region starts contracting in the circumferential direction and starts moving radially.

Acknowledgments

The authors wish to acknowledge United Technologies Research Center (UTRC)/Pratt & Whitney Aircraft Division of United Technologies Corporation for donating the multistage compressor facility to Penn State. This research project was supported by a grant from NASA Lewis Research Center (NAG3-1222 with Dr. A. J. Strazisar as technical monitor), Rolls Royce plc (Mr. M. A. Howard), Rolls Royce Inc. (Mr. R. Moritz) and the Allison engine company (Dr. J. R. Fagan). Helpful suggestions and discussions by these personnel are acknowledged.

References

Adamczyk, J. J., 1985, "Model Equation for Simulating Flows in Multistage Turbomachinery," ASME Paper No. 85-GT-226.

Cherrett, M. A., Bryce, J. D., and Ginder, R. B., 1995, "Unsteady 3D Flow in a Single-Stage Transonic Fan. Part II: Unsteady Stator Exit Flow Field," ASME *Journal of Turbomachinery,* Vol. 117, pp. 514–521.

Cherrett, M. A., and Bryce, J. D., 1992, "Unsteady Viscous Flow in a High Speed Core Compressor," ASME *Journal of Turbomachinery,* Vol. 114, pp. 287–294.

Falchetti, F., 1992, "Advanced CFD Simulation and Testing of Blading in the Multistage Environment," AIAA Paper No. 92-3040.

Hall, E. J., 1997, "Aerodynamic Modelling of Multistage Compressor Flow Fields; Part 1: Analysis of Rotor/Stator/Rotor Interaction; Part 2: Modeling of Deterministic Stresses," ASME Papers 97-GT-344 and 345.

Jung, M., and Eikelmann, J., 1995, "Stator Exit Flow Fields in the Multistage Environment of an Axial Compressor," ASME Paper No. 95-GT-165.

Lakshminarayana, B., Suryavamshi, N., Prato, J., and Moritz, R., 1994, "Experimental Investigation of Flow Field in a Multistage Axial Flow Compressor," ASME Paper No. 94-GT-455.

Suder, K. L., et al., 1987, "Measurements of the Unsteady Flow Fields Within the Stator Row of a Transonic Axial Flow Fan, Part I: Measurement and Analysis Technique," ASME Paper No. 87-GT-226.

Yavuzkurt, S., 1984, "A Guide to Uncertainty Analysis of Hot-Wire Data," ASME JOURNAL OF FLUIDS ENGINEERING, Vol. 106, pp. 181–186.

A Generalized Gas-Liquid-Solid Three-Phase Flow Analysis for Airlift Pump Design

D. P. Margaris
Lecturer.

D. G. Papanikas
Professor.

Fluid Mechanics Laboratory,
Department of Mechanical Engineering and Aeronautics,
University of Patras, GR-26001 Patras, Greece

The object of the present study is to access the performance of an airlift pump under predetermined operating conditions. The gas-liquid-solid three phase flow in an airlift pump is described by a system of differential equations, which derives from the fundamental conservation equations of continuity and momentum. This approach leads to a more general mathematical model which is applicable to a wide range of installations, from small airlift pumps to very large systems, suitable for deep-sea mining. For the frictional pressure drop calculation a new correlation, based on a pseudoliquid model, has been proposed. In addition, parameters such as the drag coefficient of both solid and gas phase, the shape of particles and the compressibility factor, which is very important for deep-sea mining, have been incorporated in the governing equations. The application of the computational algorithm to different geometry and flow conditions of an airlift pump leads to the optimization of the system. The numerical simulation results clearly show a very good agreement with experimental and computational data of other researchers. The analysis methods have been combined in an easily used computer code which is a very useful tool for the optimum design of airlift pump systems.

Introduction

The Air-Lift Principle is a well-established method for vertical transport of liquids and solid-liquids mixtures. It is based on the principle of injecting a compressed gas, usually air, into the conveying pipe causing thus, under special conditions, the gradual lifting of the liquid or the mixture. During the early stages, the airlift pump was used for water pumping, later on, for lifting and transporting corrosive and radio-active liquids as well as for pumping crude oil. A special application was to pump liquids with suspended solid particles and more recently to be used in deep-sea mining.

There have been numerous publications suggesting calculation procedures for the design and the satisfactory operation of an airlift pump. Among others, Pickert (1931) and Parsons (1965) developed a procedure while working in excavating metal ore. A systematic review concerning the applications and developments of the airlift pump was presented by Chaziteodorou (1977). Weber and Dedegil (1976), Weber et al. (1978), and Weber (1982) presented a calculation model for an airlift pump to be used for lifting a suspension of solids in a liquid phase. Dedegil (1986) presented the principles of airlift techniques and Bernard and Fitremann (1987) presented a model for a transient vertical three-phase flow which is the prevailing situation when using an airlift pump for lifting of solid particles. The technology of artificial lift methods has been presented by Brown (1977–1984) in a four volumes series concerning fundamental concepts and technical data needed to design the artificial lift installations. Yet all the above studies depend either on experimental data or empirical correlation factors leading to results without general validity.

In the present study, a general calculation method for the three phase flow and a design model for an airlift pump installation are presented. This method can be used in simulation of an airlift system for pumping liquids or solid-liquid mixtures. The differential form of the governing equations derives from the fundamental fluid mechanics equations, i.e., continuity and momentum, and leads to a more general mathematical model which can be extended with the equation of energy to a more complex model, applicable for two- or three-dimensional analysis of a steady or unsteady airlift pump operation. For the prediction of a three-phase flow pattern and the calculation of frictional pressure losses, a pseudoliquid model has been introduced in an analogous way already done in particulate flows by Margaris (1989). In addition to the above, provisions were made in the computational algorithm so as to take into account the influence of more specific factors such as the compressibility factor of the gas phase, the drag coefficient of both gas and solid phase as well as the shape of the solid particles.

Physical Modeling

The airlift pump consists of two vertical pipes. One for pumping liquid or a mixture of liquid and solid particles and a parallel one for the injection of the gas phase. As can be seen from Fig. 1, the main pipe is divided into three parts. First, there is the suction part L_S extended from the bottom of the pipe to the gas injection point, second, the raising part or injection depth L_I from the injection port to the free surface of the liquid in the feed tank, and last the third one and so-called discharge part L_D from the free surface of the liquid to the pipe outlet. During the operation in the suction part we can have either liquid flow or a hydraulic transport of solids and so, in the parts above the gas injection port, we can have a liquid-gas flow or a hydropneumatic transport of solids, respectively.

In normal pumping installations, high energy cost is caused by the need to increase the total pressure of the liquid in order to overcome the related pressure losses while it is transported to a higher level. These losses are mainly due to gravity and second due to friction and acceleration. In an airlift pump, at first the liquid is in balance within the pipe under an existing pressure difference. The weight reduction of the liquid column caused by the injection of a gas phase forces the fluid to move upwards in order to restore the same static equilibrium. In this manner, with a suitable and continuous feed of gas, we can manage to raise the liquid to the desired level and to discharge it from the pipe. The suspended solids at the inlet of the pipe

Contributed by the Fluids Engineering Division for publication in the JOURNAL OF FLUIDS ENGINEERING. Manuscript received by the Fluids Engineering Division February 2, 1995; revised manuscript received March 10, 1997. Associate Technical Editor: M. W. Reeks.

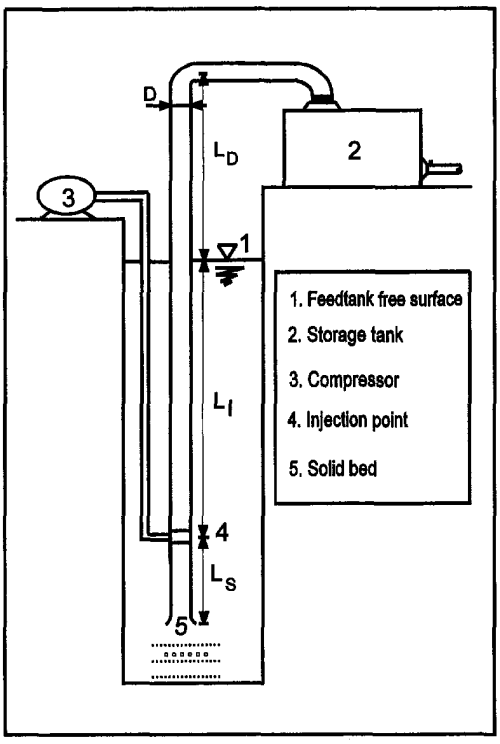

Fig. 1 Airlift pump installation

will be carried over as long as the velocity of the liquid, which tends to fill the pipe, is higher than their settling velocity.

While forming a three-phase model, it was considered that the liquid medium is always the carrier of the solid particles. As a result, the change of the gas phase velocity, will directly influence the liquid phase and indirectly the particle velocity. Because of its expansion, the gas acquires an acceleration higher than that of the liquid phase. The velocity profile thus created, develops unequal shear stresses on each solid particle causing it to revolve and move toward the lower velocity area. In this manner, eventually all the solid particles are captured in the liquid phase. This approach is valid for particles in low volume concentrations and having small dimensions.

In a two-phase flow analysis, the problem of frictional pressure drop prediction can be handled by using correlations based on the homogeneous or separated flow models. This means treating the flow as if the gas-liquid mixture is behaving like a homogeneous fluid with identical velocities of the two phases, or to treat the flow of each phase separately, taking into account the interaction forces between the phases. The fact that in a three-phase flow there are no such correlations, led some researchers to an assumption of a pure liquid on the pipe walls, taking into account only the friction of the liquid phase. In the present study, for the calculation of the frictional pressure drop, a new correlation has been introduced for a vertical gas liquid flow, similar to that proposed by Friedel (1979). In this correlation the influence of the solid particles is taken into account substituting the properties of the liquid with that of an equivalent pseudoliquid, as it is described in the mathematical modeling.

Furthermore, the following assumptions are made for the mathematical formulation of the airlift mechanism. The transport of the solid particles occurs primarily through water. The planes of equal velocity and equal pressure should be normal to the pipe axis. This makes the problem one-dimensional, which is approximately the case in practice. No particular shape of bubbles or solid particles is assumed, due to the generalized relationship used for the calculation of the drag coefficients. Flow pattern prediction for the three-phase flow can be made, applying to the gas-pseudoliquid mixture the well-known criteria of the two-phase flow, but for a first approximation no particular influence of the different flow regimes is taken into account. Finally, an isothermal change of state is assumed for air. This assumption is justified only if the three phases flow very slowly through the pipe. This seems to be the case here since air expands very little in the lower depths during rising and only for long vertical pipelines there is a critical length some meters before the exit of the pipe, where the flow has large velocities, so that a continuous heat exchange with the environment is no longer possible.

Mathematical Modeling

Conservation Equations for Separated Three Phase Flow. A useful starting point for a two-phase flow analysis is to apply the separated flow model and to write conservation equations for mass and momentum for each phase separately taking into account different velocity for each phase and the interaction forces between the phases. However, each pair of conservation equations can be added together to give an overall balance equation for the mixture, and it is the overall balance equation that has been most commonly adopted in pressure drop prediction. Following the same procedure it is possible to write an overall balance equation for a gas-liquid-solid phase flow considering that the velocity as well as the pressure will be constant, in any given pipe cross-section, which makes the problem one-dimensional.

Nomenclature

a = void fraction
A = area of the pipe
b, B = constants
C = coefficient
C_D = drag coefficient
c_m = mass concentration of particles
d = particle or bubble diameter
dx = step size
dp = pressure loss
D = pipe diameter
f = friction factor
F = force
g = acceleration of gravity
L = pipe length
m = mass flux
M = mass flow rate
N_C = consumed power
N_G = gained power
p = pressure
R = gas constant for air
Re = Reynolds number
T = temperature
u = phase velocity
v_B = bubble volume
w = interaction forces
We = Weber number
x = quality
Z = compressibility factor
Δx = calculation step
Δp = pressure loss
η = pump efficiency
μ = viscosity
ν = kinematic viscosity
ρ = density
σ = surface tension
Φ = friction multiplier

Subscripts

o = reference magnitude
1, s = solid
2, g = gas
3, l = liquid
D = discharge length
FR = friction
I = injection depth
n = nominal
O = one-phase
PS = pseudoliquid
r = relative
S = suction length
Tot = total

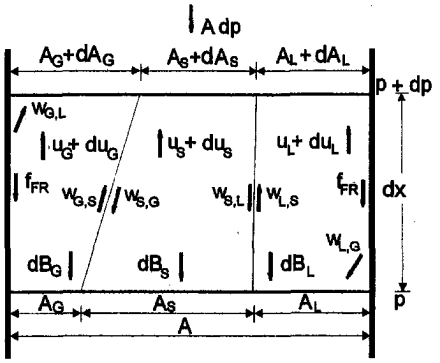

Fig. 2 Forces acting on an elementary pipe volume

For a separated flow model, one should consider the balance equations for flow through the vertical pipe element of length dx and cross-sectional area A, divided into the subareas with cross section A_S, A_G, A_L, for solid, gas and liquid phase, respectively (Fig. 2). This separated flow concept is an advanced version of the model introduced by Chaziteodorou (1977). The continuity equation for the mixture may be expressed as

$$M_t = \sum_{i=1}^{3} M_i = \sum_{i=1}^{3} \rho_i u_i A_i = \sum_{i=1}^{3} \rho_i u_i a_i A = \text{const.}$$

$$\text{with} \quad \sum_{i=1}^{3} a_i = 1 \qquad (1)$$

where $i = 1$ for solid, $i = 2$ for gas, $i = 3$ for liquid phase and ρ_i, u_i, and a_i are the density, the velocity, and the void fraction of each phase, respectively.

The momentum equations for the separate phases, resulting from the balance of forces that are exerted on each phase in the control volume, Fig. 2, can be added to give the mixture momentum equation as follows:

$$\sum F = \sum_{i=1}^{3} \left(-\rho_i a_i A dx g - \rho_i a_i A dx \frac{du_i}{dt} - a_i A dp - a_i A dp_{FR,i} + \sum_{j=1}^{3} \delta_{i,j} w_{i,j} \right) = 0 \qquad (2)$$

{Gravitational forces} {Accelerational forces} {Pressure forces} {Friction forces} {Interaction forces}

The above equation may be applied to one, two, or three phase flow, with the last term $w_{i,j}$ indicating the interaction forces between the phases, taking into account that $w_{i,j} = -w_{j,i}$ and that $\delta_{i,j} = 0$ for $i = j$ and $\delta_{i,j} = 1$ for $i \neq j$. These forces will appear in the momentum equation for each phase and will disappear in the momentum equation for the mixture. According to this and recognizing that $du_i/dt = u_i\, du_i/dx$, Eq. (2) can be rewritten for the mixture pressure drop prediction as

$$-\frac{dp}{dx} = \sum_{i=1}^{3} \left(\rho_i a_i g + \rho_i a_i u_i \frac{du_i}{dx} + \left(\frac{dp}{dx}\right)_{FR,i} \right) \qquad (3)$$

with the last term $(dp/dx)_{FR,i}$ indicating the frictional pressure drop which is the most difficult mathematical term to conceptualize.

According to the physical modeling, we assume that the liquid is the main phase and that there is no interaction forces between bubbles and solid particles. So the velocity of both gas and solid phases is expressed in relation to the velocity of the liquid phase and the relative velocity $u_{i,r}$ of the corresponding phase. That is

$$u_i = u_3 + (-1)^i u_{i,r} \quad |i = 1, 2 \qquad (4)$$

The settling velocity of the solid particles or the rising velocity of the bubbles are given by the following equations,

$$u_{i,r} = \left(\frac{4}{3} \frac{d_i a_3 g}{C_{D,i}} \left| 1 - \frac{\rho_i}{\rho_3} \right| \right)^{1/2} \quad |i = 1, 2 \qquad (5)$$

where for the rising velocity of bubbles we have to consider the change of the bubble diameter due to the expansion of the gas phase.

The calculation of the drag coefficient, $C_{D,i}$, of solid particles or the bubbles is based on a generalized form, similar to that proposed by Margaris and Papanikas (1989).

$$C_{D,i} = \sum_{j=1}^{2} B_{i,j} \mathrm{Re}_i^{b_{i,j}} \quad |i = 1, 2 \qquad (6)$$

where the slip velocity between the corresponding two phases, $u_i - u_3$, is used in the Reynolds number

$$\mathrm{Re}_i = \frac{\rho_3 |u_i - u_3| d_i}{\mu_3} \qquad (7)$$

and $B_{i,j}$ and $b_{i,j}$ are constants depending upon the shape of the particles or bubbles and the values of the Reynolds number Re_i. (For spherical particles or bubbles see Table 1 (Clift et al., 1978), for other shapes see Margaris and Papanikas (1989).

According to the airlift principle, the gas phase is supplied at the injection point under pressure p_I and it is expanded to the nominal pressure p_n of the storage tank. It can be assumed that its expansion will be done isothermally according to the following equation of state

$$\frac{p}{Z \rho_2} = RT = \text{const.} \qquad (8)$$

The compressibility factor Z for air is calculated in the present paper as a function of pressure according to the equation (Schlichting, 1958, Chaziteodorou, 1977),

$$Z(p) = 1 - 5.8198 \cdot 10^{-4} \left(\frac{p_I}{p_n} \right) + 2.809 \cdot 10^{-6} \left(\frac{p_I}{p_n} \right)^2 \qquad (9)$$

Since the gas phase is not always air, the compressibility factor Z can be calculated from any appropriate relation (Prausnitz et al., 1986), taking into consideration the composition of the gas and the properties of its components. A separate system

Table 1 Constants for the calculation of the drag coefficient of spherical particles or bubbles

Re_i	B_{11}	b_{11}	B_{12}	b_{12}	B_{21}	b_{21}	B_{22}	b_{22}
<0.2	24	−1	0	0	24	−1	0	0
0.2–989	26	0.8	0.4	0	3.6	−0.313	24	−1
989–10^4					0.44	0	0	0
10^4–2×10^5	0.4	0	0	0				
$>2 \times 10^5$	—	—	—	—	0.1	0	0	0

for prediction of transport properties, enabling the calculation of pure substances or mixtures properties, developed by Papanikas et al. (1993a), has been adopted and integrated into the computational system.

Frictional Pressure Drop Correlation Based on the Pseudoliquid Model. In order to generalize the applicability of the mathematical model taking into account the influence of solid particles on friction, irrespective of whether the flow inside the pipe is a hydraulic or a hydropneumatic transport of solids, we introduce a pseudoliquid which is formed by liquid and solid phase. The governing equations describing the behavior of this pseudoliquid are the equations for its transport properties. For the density of the pseudoliquid, ρ_{PS}, we have

$$\rho_{PS} = \left(\frac{a_1}{a_{PS}}\right)\rho_1 + \left(\frac{a_3}{a_{PS}}\right)\rho_3 = \alpha_1^*\rho_1 + \alpha_3^*\rho_3$$

$$\text{with} \quad a_{PS} = a_1 + a_3 \qquad (10)$$

where α_1^*, α_3^* the void fraction of solids and liquid, with respect to the area occupied by the two phases, and a_{PS} the void fraction of the pseudoliquid, with respect to the total area of the pipe cross-section.

For the dynamic viscosity of the pseudoliquid, μ_{PS}, we have

$$\mu_{PS} = (1 - c_m)\nu_3\rho_{PS} \quad \text{with} \quad c_m = \frac{\rho_1}{\rho_{PS}}\left(\frac{a_1}{a_{PS}}\right) \qquad (11)$$

where ν_3 is the kinematic viscosity of the liquid phase and c_m is the mass concentration of solid particles. The equivalent velocity u_{PS} of the pseudoliquid is defined by the equation

$$M_{PS} = M_1 + M_2 = u_{PS}\rho_{PS}a_{PS}A \qquad (12)$$

It is obvious that for a flow with no solid particles, the pseudoliquid behavior according to the above model will be the same as that of the liquid phase. Moreover, in most practical cases, the liquid phase appears as a mixture of more than one fluid. For example, when pumping crude oil both water and oil may form the liquid phase. It is suitable in such cases to treat the liquid phases as to be one liquid, the behavior of which may be described by the same relationships used for the pseudoliquid.

With the introduction of the pseudoliquid, any three-phase flow can be treated as a two-phase flow of a gas and a pseudoliquid. According to this the frictional pressure drop correlation, based on the separated flow model, (Hetsroni, 1982), is given by

$$\left(\frac{dp}{dx}\right)_{FR} = \Phi_{PSO}^2\left[\left(\frac{dp}{dx}\right)_{FR}\right]_{PSO} \qquad (13)$$

where Φ_{PSO} is a friction multiplier for the pseudoliquid and $((dp/dx)_{FR})_{PSO}$ is the frictional pressure gradient for a single phase flow at the same total mass velocity and with the physical properties of the pseudoliquid phase. For the calculation of the friction multiplier, the Friedel correlation for a gas-liquid flow (Friedel, 1979) is extended and applied to a gas-pseudoliquid flow substituting the liquid properties with those of the pseudoliquid. According to this correlation the friction multiplier is given by

$$\Phi_{PSO}^2 = E + \frac{3.24FH}{\text{Fr}^{0.045}\text{We}^{0.035}} \qquad (14)$$

where

$$E = (1 - x)^2 + x^2\frac{\rho_{PS}f_{2O}}{\rho_2 f_{PSO}}, \quad F = x^{0.78}(1 - x)^{0.24},$$

$$H = \left(\frac{\rho_{PS}}{\rho_2}\right)^{0.91}\left(\frac{\mu_2}{\mu_{PS}}\right)^{0.19}\left(1 - \frac{\mu_2}{\mu_{PS}}\right)^{0.7} \qquad (15)$$

$$\text{Fr} = \frac{m^2}{gD\rho_{PST}^2}, \quad \text{We} = \frac{m^2D}{\sigma\rho_{PST}},$$

$$\rho_{PST} = \left(\frac{x}{\rho_2} + \frac{1 - x}{\rho_{PS}}\right)^{-1} \qquad (16)$$

with m the total mass flux of the two phases, σ the surface tension, D the pipe diameter and x the quality or the ratio of the gas mass flux to the total mass flux, Fr is the Froude number, We is the Weber number, and ρ_{PST} is the two-phase density of the gas and pseudoliquid mixture. The friction factors, f_{2O} and f_{PSO}, for the total mass flux flowing with gas and pseudoliquid properties respectively, are calculated using the Colebrook-White (1939) nonlinear equation, which is a very accurate and valid equation for single phase flow.

For the completeness of the described analysis, it has to be noted that other two-phase flow correlations can be applied also in a similar way and this has been done in the course of this research by using an integrated computational system for a wide range of gas-liquid flows developed by Papanikas et al. (1993b).

Design Model for an Airlift Pump

A typical airlift pump installation is shown in Fig. 1. Considering the pressure at the free surface of the feed tank to be p_o and in the storage tank to be p_n, the pressure balance can be written as

$$p_o + \rho_3 g(L_S + L_I) = p_n + \Delta p_{Tot} \qquad (17)$$

where Δp_{Tot} are the total pressure losses along the three parts of the pipe, due to the frictional, accelerational and gravitational component of the pressure gradient, L_S is the suction part and L_I is the raising part or injection depth.

In the suction part, pressure losses are calculated as an integral whole according to the equation

$$\Delta p_S = \int_0^{L_S}\frac{dp}{dx}\,dx = \Delta p_{\Delta x}L_S \qquad (18)$$

In the other two sections, the pressure losses should be calculated step-by-step because of the expansion of the gas phase, using the following equation:

$$\Delta p_{I,D} = \sum_1^K\left(\frac{\Delta p}{\Delta x}\right)_K\Delta x, \quad K = \frac{L_I + L_D}{\Delta x} \qquad (19)$$

where the pressure gradient dp/dx or $\Delta p/\Delta x$ must be calculated using the system of equations described above in the mathematical modeling.

A very important quantity is the pump or lifting efficiency, which is defined as the ratio of the gained power N_G over the consumed power N_C. That is

$$\eta = \frac{N_G}{N_C} \qquad (20)$$

The power consumed due to the gas compression from pressure p_o to pressure p_I at the injection level is calculated from the integral

$$N_C = \int_{p_o}^{p_I}\frac{M_2}{\rho_2}\,dp = M_2RT\ln\left(\frac{p_I}{p_o}\right) \qquad (21)$$

On the other hand, the power gained is defined as the increase of the potential energy of the liquid phase, if the airlift pump is used for pumping liquids, or the solid phase, if it is used for pumping solids. Combining the two cases and taking into account the Archimedes principle for the case of lifting solid

particles, the power gained is given by the following general relationship

$$N_G = CM_1 g\left((L_S + L_I)\left(1 - \frac{\rho_1}{\rho_3}\right) + L_D\right) + (1 - C)gL_D M_3 \quad (22)$$

with $C = 0$ for pumping liquids and $C = 1$ for pumping solids.

Numerical Solution of a Gas-Liquid-Solid Vertical Flow

In order to design an airlift pump we have to solve the governing equations for a vertical three-phase flow. Because of the gas-phase expansion, it is necessary to calculate step-by-step the pressure gradient and the related magnitudes, such as the velocities and the void fractions of the phases. To treat this step-by-step calculation procedure, we transform the system of equations to a system of differential equations which can be solved using a suitable numerical method. That is, the momentum equation in differential form is the same with Eq. (3), so we have

$$-\frac{dp}{dx} = \sum_{i=1}^{3}\left(\rho_i a_i g + \rho_i a_i u_i \frac{du_i}{dx} + \left(\frac{dp}{dx}\right)_{FR,i}\right) \quad (23)$$

The continuity equations for the individual phases, ($i = 1, 2, 3$), in differential form are

$$u_i\rho_i \frac{da_i}{dx} + u_i a_i \frac{d\rho_i}{dx} + \rho_i a_i \frac{du_i}{dx} = 0$$

$$\text{with} \quad \frac{d\rho_1}{dx} = \frac{d\rho_3}{dx} = 0 \quad \text{and} \quad \sum_{i=1}^{3}\frac{da_i}{dx} = 0 \quad (24)$$

The absolute velocity of the solid and gas phase in differential form derives from Eq. (4)

$$\frac{du_i}{dx} = \frac{du_3}{dx} + (-1)^i \frac{du_{i,r}}{dx} \quad (25)$$

with $i = 1, 2$, while the relative velocity of particles derives from Eq. (5) for $i = 1$, that is

$$\frac{du_{1,r}}{dx} = \left(\frac{4}{3}\frac{d_1 g}{C_{D,1}}\left(\frac{\rho_1}{\rho_3} - 1\right)\right)^{1/2} \frac{1}{2a_3^{1/2}}\frac{da_3}{dx} \quad (26)$$

For the rising velocity of bubbles, we have to consider in addition the change of the bubble diameter due to the expansion of the gas-phase. Since the air volume of one bubble v_B is related to the pressure by $p/Z \sim 1/v_B$ and because of $v_B \sim d_2^3$, it follows that $p/Z \sim 1/d_2^3$. Taking also into account the isothermal expansion of gas, the rising velocity of bubbles derives from Eq. (5) for $i = 2$

$$u_{2,r} = \left(\frac{4}{3}\frac{d_{2,0}a_3 g}{C_{D,2}}\left(\frac{p_0}{Z_0}\right)^{1/3}\right)^{1/2}\left(1 - \frac{Z_0\rho_{2,0}p}{p_0\rho_3 Z}\right)^{1/2}\left(\frac{Z}{p}\right)^{1/6} \quad (27)$$

with $d_{2,0}$ the initial bubble diameter at the injection point where the pressure is p_0 and the compressibility factor is Z_0. The differential equation for the rising velocity of bubbles follows from Eq. (27)

$$\frac{du_{2,r}}{dx} = C_1\left(C_2\left(Z^{-1}\frac{dZ}{dp} - p^{-1}\right)\right)\frac{dp}{dx} + \left(\frac{\rho_3 - \rho_2}{4\rho_3 a_3^2}\right)^{1/2}\frac{da_3}{dx} \quad (28)$$

with the coefficients $C1$ and $C2$ given by the relations

$$C_1 = \left(\frac{4}{3}\frac{d_{2,0}ga_3}{C_{D,2}}\right)^{1/2}\left(\frac{p_0}{p}\frac{Z}{Z_0}\right)^{1/6}$$

$$\text{and} \quad C_2 = \frac{1}{6}\frac{\rho_3 + 2\rho_2}{(2\rho_3 - \rho_2)^{1/2}} \quad (29)$$

For the expansion of the gas phase, differentiated Eq. (8), we get

$$\frac{dZ}{dx} = \left(\frac{dp}{dx} - \frac{p}{\rho_2}\frac{d\rho_2}{dx}\right)\frac{Z}{p} \quad (30)$$

In the framework of the present paper a Runge-Kutta fourth-order method was used in order to solve the above system of differential equations for the gas-liquid-solid flow. When this system is applied to the liquid-solid flow at the lower part of an airlift system, it gives a constant pressure gradient dp/dx, which multiplied by the length L_S gives the corresponding pressure drop. Combining this result with those related to the gas phase for the relative velocity and the compressibility factor, we determine the necessary initial conditions for the Runge-Kutta method.

The variables, which must be defined, for the solution of the gas-liquid-solid flow, are the physical properties of the phases (density and viscosity of liquid and solid phase, diameter of solid particles etc.), the geometry of the pipe (diameter, total and injection depth), and the mass flow rate of solids. For these conditions, the computational algorithm calculates the necessary mass flow rate of gas. The calculation starts with the assumption that the pressure at the injection point is equal to the hydrostatic pressure outside the pipe at the same depth. An iterational procedure has been established for the correction of the pressure, taking into account the condition that at the exit of the pipe the pressure must be equal to the atmospheric. The procedure is repeated until the calculated value of pressure differs from the atmospheric one with less than 0.5 percent. This accuracy can be predetermined by the user, depending on the computing time and the final results. A lower limit will increase the computing time without dramatical improvement of the final results, so the difference of 0.5 percent is considered as an effective limit for engineering applications.

Results and Discussion

In order to validate our analysis, a large number of results were compared against both experimental and computed data by other researchers. But the existing experimental data in the literature do not cover a full range of the operational characteristic curve of an airlift pump, as they are referred every time to different conditions or to airlift pumps for pumping liquids only. Weber (1976, 1982) presented in a table a lot of experimental data obtained at the lignite open-pit mining of the Rheinische Brounkohle AG in the vicinity of Cologne, and for validation purposes he compared calculated versus measured volume flow rate of solids. There is no characteristic curve diagram because the experiments were carried out with the following varying geometry conditions: pipe diameter 300 mm, total depth 50 to 441 m, injection depth 42 to 248 m, air supply 0.22 to 0.713 m^3/s, delivered volumetric concentrations 0 to 8.6 percent and maximum out put of solid material 115 t/h. The solid materials were gravel, sand, and lignite with densities 2575, 2610, and

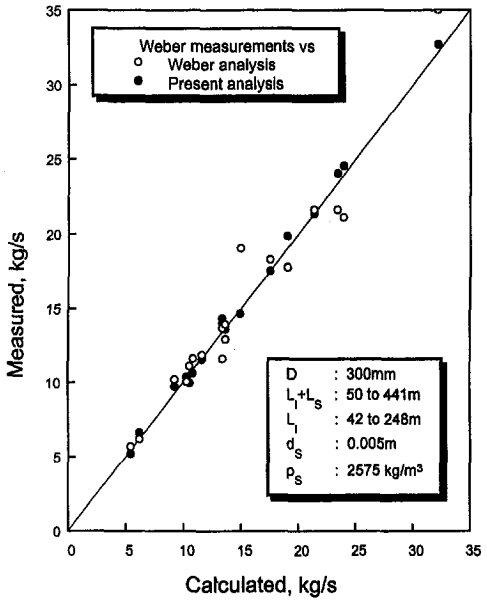

Fig. 3 Comparison between calculated and measured mass flow rate of solids

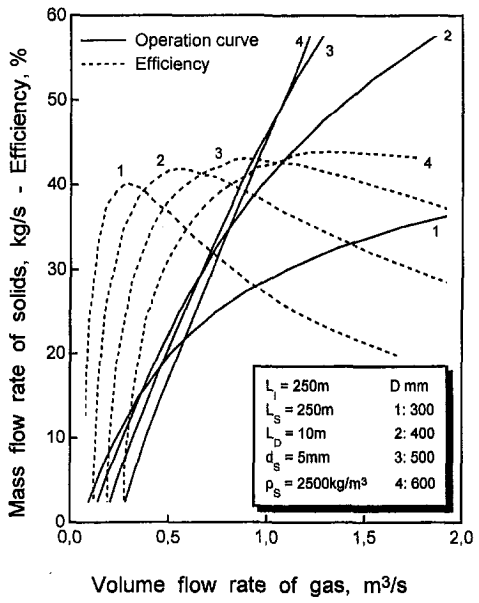

Fig. 5 Influence of the pipe diameter on the airlift pump operation

1143 kg/m^3 and particle diameter 5, 0.6 and 50 mm, respectively.

The validation of our results is presented in Figs. 3 and 4 through the comparison of our calculated results, according to the above data, versus measured and calculated by Weber, for the mass flow rate of solid and liquid. The agreement of our results with the experimental data, especially for the liquid, is obviously better than that of Weber. The average deviation of our results is 5 percent for the solid flow rate and 0.3 percent for the liquid flow rate, while the corresponding values for Weber's results are 10 percent and 15 percent, respectively. The difference is due to the fact that the analysis of Weber is based on empirical or mechanistic model, while our analysis is based on the fundamental equations of fluid mechanics.

Applying our analysis, we next present the influence of the most important parameters, such as the diameter of the pipe and the injection depth, to the airlift pump operation. In all the diagrams presented here, seawater with density of 1030 kg/m^3 is used for the liquid phase, the gas is always air with density 1.2 kg/m^3, and three solid materials with densities of 2650, 2500, and 1150 kg/m^3 are used. The initial value of the bubble diameter is 3 cm and the volumetric concentration of solids coming into the system at the lower pipe section is 5 percent, which is the proposed value by Weber (1976) for optimum capacity of the pump. The pressure at the free surface of both storage and feed tank were atmospheric and the temperature inside the pipe was considered to be 10°C. In order to be more clear we use for the magnitudes the subscripts s, g, and l for solid, gas, and liquid instead of 1, 2, 3, respectively, which are used in the mathematical equations.

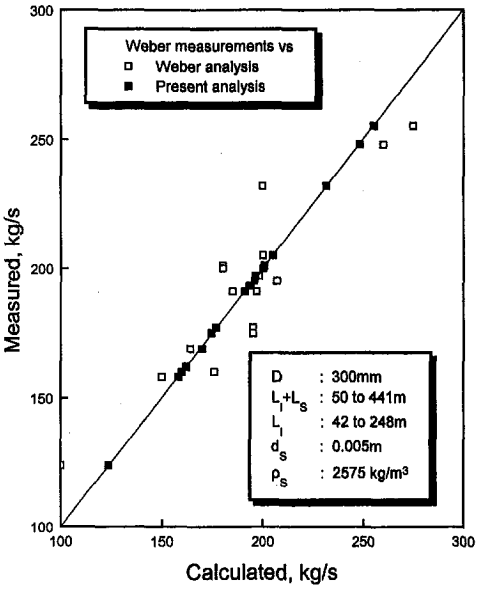

Fig. 4 Comparison between calculated and measured mass flow rate of liquid

An operation curve of an airlift pump shows mass flow rate of solids and pump efficiency as a function of gas flow rate delivered by the compressor (Fig. 5). The most significant geometric parameter is the pipe diameter and its magnitude has a great effect in the airlift efficiency. In case of relatively large quantities of the gas phase, resulting in large concentrations, undesirable flow regimes like plug, annular or mist flow is possible to appear. These flow regimes cause a very low efficiency (Chaziteodorou, 1977). This drawback can be corrected by increasing the pipe diameter thus decreasing the gas void fraction. In this manner, the flow can be bubble flow and the pump efficiency will remain at high levels. This gradual increase of the pipe diameter helps to avoid unpleasant situations in airlift pump installations.

In bubble flow, the bubbles undergo random motion in passing through the channel; from time to time, two bubbles collide and may coalesce to form a larger bubble. This process of collision and coalescence ultimately leads to plug flow. Radovcick and Moissis (1962) showed that for void fractions higher than 30 percent, collision and coalescence of bubbles becomes very rapid and bubble flow is very unstable, but at high velocities we may have bubbly flows at higher void fractions. Applying this rule to our analysis for the three-phase flow we assume a bubble flow for void fractions up to 50 percent. Above this limit, the computational algorithm will increase the pipe diameter in order to maintain the void fraction less than 50 percent.

It is obvious that an optimization of the system is important and for the installation depicted in Fig. 6, applying our analysis, the optimum diameter resulted to be 0.44 m. It should also be

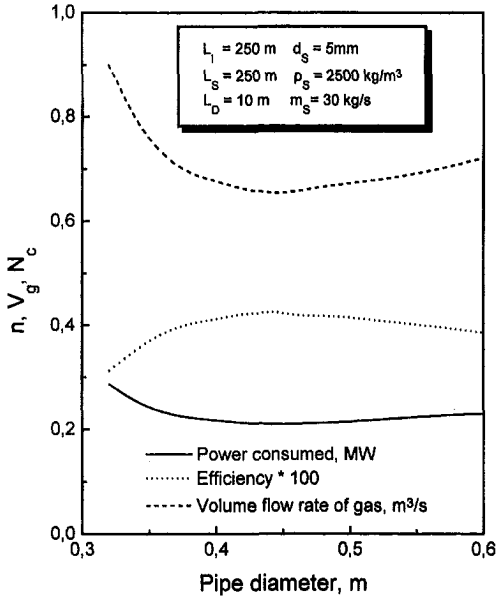

Fig. 6 Optimization of the pipe diameter of an airlift pump installation

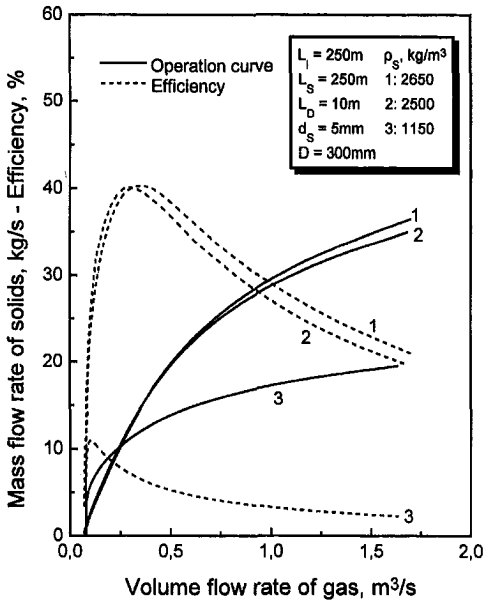

Fig. 8 Influence of solid density on the airlift pump operation

noted that for different mass flow rates of solids different optimum diameters would result. The optimum design of an airlift system should aim to obtain not always the maximum efficiency but a high enough efficiency for a wide range of applications, which means a wide range of mass flow rates of solid particles.

Another important parameter in the airlift design is the injection depth L_I of the gas phase (Fig. 7). A bad choice of gas injection depth can cause a decrease in pump efficiency due to the existence of undesirable flow regimes, such as annular flow, where the liquid flows on the wall of the tube as a film and the gas phase flows in the center. This flow regime can be caused by a large pressure difference between the gas injection port and the pressure of the storage tank. A way to overcome this phenomenon, in large scale installations, is to inject the gas phase to more than one level thus decreasing the pressure differences between the one port to the next.

Generally the increase in the gas injection depth results in an increase of the amount of solids that can be pumped followed by a parallel decrease of the maximum pump efficiency, as related to the power consumed. On the other hand, by increasing the injection depth L_I, for pumping a certain quantity of solids, we can also increase the total submerged length, $L_I + L_S$. But as the injection depth increases the suction part decreases, eventually reaching the limit where the gas injection point is at the same level with the solid bed. This phenomenon is of great importance to large scale installations, such as deep-sea mining.

Negative effects on the pump efficiency have the discharge length L_D, due to the pressure losses, the diameter of solid particles and the initial diameter of bubbles, due to the increase of their relative velocity. These magnitudes must be as small as possible, depending on the specific demands and design of the installation, in order to achieve higher efficiency of the system. Although the increase of the density of solids results in an increase of their relative velocity it has the opposite effect to that of the diameter of the solid particles. This is due to the fact that in order to pump the same quantity of solids the increase of density means lower solids volume flow rate and eventually lower liquid and gas flow rates. For example, in Fig. 8 we note that for pumping manganese nodules with mass flow rates 15 kg/s and density of 2650 kg/m^3 we need 0.4 m^3/s of gas while for lignite with density 1150 kg/m^3 we need 0.7 m^3/s of gas phase.

The purpose of the airlift designer is to combine all the above geometric and functional parameters in order to achieve at first the maximum efficiency while the solids flow rate is large enough, on the other hand, to maintain a satisfactory efficiency over a large range of gas flow rates.

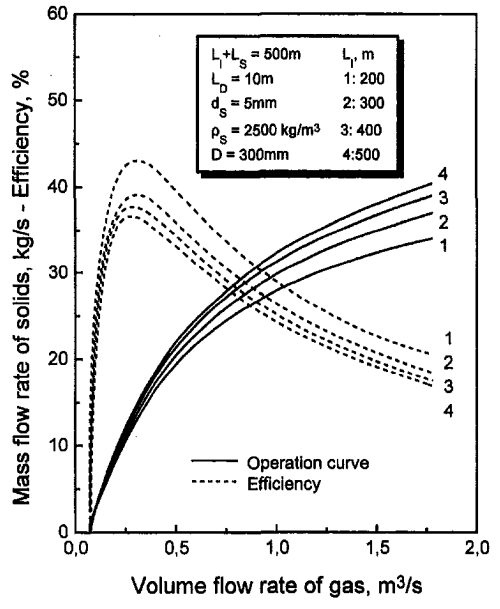

Fig. 7 Influence of the gas injection depth on the airlift pump operation

Conclusions

An applied **A**ir **L**ift **M**odel **A**nalysis for air-water-solid flow has been developed. Based on a system of differential equations, derived from the fundamental equations of continuity and momentum conservation, this model has a very good performance and a more general mathematical form, compared to other models based on a power balance and making a superposition of an air-water flow on a water-solid flow to form the three-phase flow. This model has been combined in an easily used computer code, named ALMA, which is a very useful tool for the optimum design of airlift pump installations.

The optimization of the installation is the more important feature of the code. This means that the code can calculate the

optimum value for the pipe diameter, injection depth, and the other parameters in order to minimize the energy consumption. The method can be applied to an air lift pump installation with short or long vertical pipeline system since it is independent of the flow regime in the pipe. From the injection point the flow is bubble and only in the upper part of a long vertical pipeline system we may have transition from bubble flow to annular flow, due to the expansion of the gas phase. For the present, we assume an upper limit of 50 percent for the void fraction of air, in order to avoid the transition, to maintain the flow bubble and to achieve higher efficiency of the system.

The results of the present analysis are in good agreement with the existing data in the literature, but in order to approximate the phenomenon better an extended modeling is in progress now, taking into account the flow regimes that may exist in the pipeline, as well as the influence of the solid particles to the development of the flow regimes. This extended modeling is expected to contribute more to the optimum design of the airlift pump installations.

Acknowledgments

The present study was supported in part by the Directorate General for Energy of the Commission of the European Communities Union in the framework of the THERMIE project OG/041/90.

References

Bernard, J., and Fitremann, J. M., 1987, "Gas-Liquid-Solid Transient Vertical Flow. The Gas Lifting of Polymetallic Nodules," 3rd International Conference on Multi-Phase Flow.

Brown, K. E., 1977–1984, *The Technology of Artificial Lift Methods,* Pennwell Publ. Co., Vol. 1–4.

Chaziteodorou, G., 1977, *Fundamentals of Oceanic Mining,* Dr. Riederer-Verlag, Stuttgart.

Clift, R., Grace, J. R., and Weber, M. E., 1978, *Bubbles, Drops and Particles,* Academic Press, Inc.

Colebrook, C. F., 1939, "Turbulent Flow in Pipes with Particular Reference to the Transition Region Between the Smooth and Rough Pipe Laws," *Journal of the Institution Civil Engineers,* Vol. 11, pp. 133–156.

Dedegil, Y., 1986, "Principles of Airlift Techniques," *Encyclopedia of Fluid Mechanics,* pp. 383–397.

Friedel, L., 1979, "Improved Friction Pressure Drop Correlations for Horizontal and Vertical Two Phase Pipe Flow," European Two Phase Flow Meet., Ispra, Italy, paper E2.

Hetsroni, G., 1982, *Handbook of Multiphase Systems,* Mc Graw-Hill, NY.

Margaris, D., and Papanikas, D., 1989, "Effect of Particle Drag Coefficient on the Boundary Layer of Particulate Gas Flow Over a Flat Plate," Z. Flugwis. Weltraumforschung, Band 13, Heft 2, pp. 73–79.

Margaris, D., 1989, "Gas-Particle Two Phase Flow in Closed Pipes," Dr.-Eng. thesis, Mechanical Engineering Dept., University of Patras, Greece.

Papanikas, D. G. et al., 1993a, "Transport Properties Estimation System for Natural Gas and Oil Production and Transport," Project TH/10070/89, THERMIE programme, European Union, Directorate for Energy, Brussels, Final Report 1993.

Papanikas, D. G. et al., 1993b, "Extended Modeling of Multiphase Flow in Oil and Natural Gas Pipe Systems," Project OG/041/90, THERMIE programme, European Union, Directorate for Energy, Brussels, Final Report 1993.

Parsons, S., 1965, "A Preliminary Investigation of Deep-Sea Mining Dredging by Airlift," dissertation, University of California, Berkeley.

Pickert, F., 1931, "Lifting Efficiency and Fundamental Data for the Calculation of Airlift Pumps," Thesis, University of Berlin.

Prausnitz, J., Reid, R., and Poling, B., 1986, *The Properties of Gases and Liquids,* McGraw-Hill, Fourth Edition.

Radovcick, N. A. and Moissis, R., 1962, "The Transition From Two Phase Bubble Flow to Slug Flow," M.I.T. Rept. 7-7673-22.

Schlichting, H., 1958, *Grenzschichttheorie,* 3, Aufl. Karlsruhe.

Weber, M., and Dedegil, Y., 1976, "Transport of Solids According to the Airlift Principle," Fourth International Conference on the Hydraulic Transport of Solids in Pipes, May 18–21, Alberta, Canada, paper H1.

Weber, M., 1982, "Vertical Hydraulic Conveying of Solids by Airlift," *Journal of Pipelines,* pp. 137–152.

Weber, M., Dedegil, Y., and Feldle, G., 1978, "New Experimental Results Regarding Extreme Operating Conditions in Air Lifting and Vertical Transport of Solids According to the Jet Lift Principle and its Applicability to Deep-Sea Mining," Fifth International Conference on the Hydraulic Transport of Solids in Pipes, May 8–11, Hanover, Germany, paper F7.

K. J. Ruschak
Senior Research Associate.

S. J. Weinstein
Research Associate..

Manufacturing Research and Engineering Organization, Eastman Kodak Company, Rochester, NY 14652-3701

Perturbation Solution for Flow in Two-Cavity Dies

Dies having two distribution cavities and slots are sometimes used in film-forming applications demanding high uniformity. The flow distribution in the primary slot is evened by the secondary cavity and slot. The flow equations for such a die are solved in closed form for coat-hanger and T-shaped dies by a perturbation method. Limiting cases of the solutions reveal the operating mechanism, and the use of the solutions in a design problem is demonstrated.

Introduction

Dies are used to form sheets or films of liquids in the coatings and plastics industries. In a common design, the die comprises cavities and slots to distribute the liquid (Fig. 1). Usually, liquid is supplied through a tube to the center of a primary cavity spanning the width of the film. Along its entire length (the Z direction in Fig. 1), the primary cavity adjoins a primary slot. The basic design strategy is achieving a flow resistance through the slot significantly exceeding that along the cavity to distribute the liquid to the ends of the cavities. A slot with a height that is much less than the breadth of the cavity achieves this partitioning of flow resistance. The cross-sectional area of the primary cavity is sometimes tapered from center to end to preclude stagnant regions, even though resistance to flow along the cavity increases as a result.

In a two cavity die, the primary slot adjoins a secondary cavity that in turn adjoins a secondary slot. Again, dimensions are such that flow resistance through the slot significantly exceeds that along the cavity, and the flow distribution from the primary slot is consequently evened.

Beyond gross partitioning of flow resistances, the resistance of the primary slot can be locally adjusted to compensate for pressure loss along the primary cavity. The length of the slot can be tapered from center to ends. Reduced slot length near the ends maintains flow there even though cavity pressure is below its center value.

Models for die design are essential because the hardware is expensive and intricate, and there are too many geometric and flow parameters for a purely experimental approach to be efficient. The many analyses of single-cavity dies include that for a T die (Carley, 1954) and that for a linearly tapered coat-hanger die (Liu et al., 1988). Two-cavity dies have been analyzed as well (Leonard, 1985; Lee and Liu, 1989; Sartor, 1990; Yuan, 1995; Durst et al., 1996). The analog of a resistor network has been developed for multiple cavities (Sartor, 1990). Some linearization of the flow equations has been carried out for a single-cavity die (Durst, 1994).

Most of the models proposed for flow inside dies require the numerical solution of differential equations. There are circumstances, though, for which results in closed form can be obtained. When the uniformity of the extruded film can vary by no more than a few percent, perturbation methods are applicable; the flow equations are linearized about the limiting case of perfect distribution. The analytic solutions for a Newtonian liquid obtained here enable efficient design optimization and elucidation of the operating mechanism.

In addition to strictly Newtonian liquids, the results may be applicable to emulsions, dispersions, or solutions of polymers that are sufficiently dilute or experience shear rates in the die below the onset of pseudoplasticity. As an example, the photographic industry employs aqueous solutions of bone gelatin for which the onset of shear thinning is several thousand reciprocal seconds. The perturbation method is applicable to non-Newtonian constitutive equations (Weinstein and Ruschak, 1996a), but the results are more complex.

In what follows, the geometry is described, and the governing equations are presented and solved by a perturbation method. Solutions for a coat-hanger and T-shaped dies are listed, and the results are used to explain the function of the secondary cavity and the interaction between the cavities. Following a summary of the limitations of the solutions, an example of optimized design is given.

Description of the Flow

Figure 1 is a schematic of a die comprising two cavities and slots. The die is symmetric about its center, and so only half is drawn. Liquid is fed to the center of the die at a total flow rate of $2Q_e$ dividing equally between the two sides. The cavities extend laterally a distance W from center. The primary cavity has a cross-sectional area A_i that optionally tapers from A_e at its center to a nominal value at its end. A slot of uniform height H_i connects the primary and secondary cavities. The length of this primary slot, L_i, is optionally tapered from center to end, and L_e is the length of the slot at center. The secondary cavity has a uniform cross-sectional area A_o, and the secondary slot has a uniform height H_o and length L_o. Gross partitioning of flow resistance mandates slot heights much smaller than cavity breadths.

The Z-coordinate, with origin at the center, spans the length of the cavities. The tapering of the cavity and slot is so slight and gradual that the effects of curvature are negligible.

Of primary interest is the peak-to-peak deviation of the flow rate per unit width exiting the die from uniform flow distribution, for which the volumetric flow rate per unit width is $\langle q \rangle = Q_e/W$. The details of the final flow distribution are often of no practical consequence.

Governing Equations

The disparate length scales of a die give rise to small parameters, summarized below, that enable simplifications. Flow in the primary cavity can be modeled with the results for fully developed flow in conduits of uniform cross section; in particular, the velocity profiles for fully developed flow are used.

In the analysis of the complete die that follows, the shape of the primary cavity remains constant, but its area A_i tapers according to

$$A_i = A_e\left(1 - \frac{Z}{W}\right)^{\gamma} \tag{1}$$

Contributed by the Fluids Engineering Division for publication in the JOURNAL OF FLUIDS ENGINEERING. Manuscript received by the Fluids Engineering Division September 5, 1996; revised manuscript received May 5, 1997. Associate Technical Editor: M. S. Cramer.

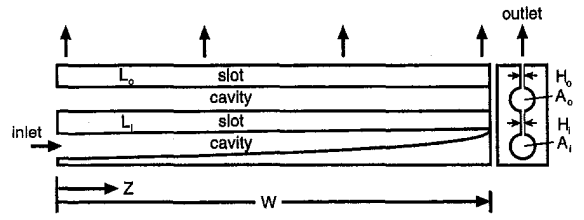

Fig. 1 Schematic of a two-cavity die

where A_e is the initial area and $0 \le \gamma < 1$ is the taper exponent.

The pressure in the primary cavity is determined by the equation (Weinstein and Ruschak, 1996b)

$$\frac{dP_i}{dZ} = -\frac{\mu Q_i}{\lambda_i A_i^2} - \frac{\rho \vartheta}{A_i}\frac{d}{dZ}\left(\frac{Q_i^2}{A_i}\right) \tag{2}$$

Here, P_i is pressure, μ viscosity, Q_i volumetric flow rate, and ρ density. The first term on the right-hand side gives the viscous pressure loss. The viscous shape factor, λ_i, depends only upon the shape of the cross-section for Newtonian and power-law liquids (Liu, 1983). Its value results in the correct pressure gradient for viscous, rectilinear flow in a conduit of uniform cross section. The second term on the right-hand side gives the inertial pressure recovery as the liquid decelerates. The momentum shape factor, ϑ, has a value such that the momentum flux in the primary cavity, computed with the fully developed velocity profile, is given by $\vartheta \rho Q_i^2/A_i$. For plug flow, $\vartheta = 1$; for curved velocity profiles ϑ exceeds 1 and equals $\frac{4}{3}$ for the parabolic velocity profile of a circular cross section. The equation of continuity for the primary cavity is

$$\frac{dQ_i}{dz} = -q_i \tag{3}$$

where q_i is the volumetric flow rate per unit width in the slot. The flow rate in the cavity diminishes as liquid is lost to the slot.

Pressure drop in the secondary cavity is determined by

$$\frac{dP_o}{dZ} = -\frac{\mu Q_o}{\lambda_o A_o^2} \tag{4}$$

where P_o is pressure and Q_o volumetric flow rate (Ruschak and Weinstein, 1997). The inertial term that appears in Eq. (2) has been dropped because the main flow direction is across rather than along the secondary cavity. For purely viscous flow the linear Stokes equation applies, the flows along and across the cavity are independent, and the shape factor in Eq. (4) relates to fully developed flow in an identical manner to that in Eq. (2). If the flow equations are nonlinear, however, because of inertial terms or a non-Newtonian constitutive equation, then the flows across and along the secondary cavity are coupled. For non-negligible inertia, λ_o can be adjusted by the method of Ruschak and Weinstein (1997). The inertia of the main flow across the cavity resists flow along the cavity, and a decrease in the value of λ_o results. Eq. (4) can be more generally modified for nonlinearities in the constitutive equation by the same method. The continuity equation for the secondary cavity is

$$\frac{dQ_o}{dZ} = q_i - q_o \tag{5}$$

where q_o is the flow rate per unit width in the secondary slot.

Flow in the slots is considered normal to the cavities because the aspect ratios of the slots, length to width, are small (Weinstein and Ruschak, 1996b). Normally the entry length (Atkinson et al., 1968) is a negligible fraction of slot length. The pressure drop across the primary slot is therefore

$$P_i - P_o = \frac{12\mu q_i L_i}{H_i^3} \tag{6}$$

The length of the primary slot, L_i, can vary in the Z direction; an advantageous form for this variation is identified as part of the solution to the problem. Similarly, the pressure drop across the secondary slot, and hence the pressure in the secondary cavity, is

$$P_o = \frac{12\mu q_o L_o}{H_o^3} \tag{7}$$

The boundary conditions specify no flow at the ends of the cavities. By symmetry, there is also no flow at the center of the secondary cavity. The flow at the center of the primary cavity equals Q_e, half the inlet flow rate.

$$Q_o = 0 \quad (Z = 0, W) \tag{8}$$

$$Q_i = 0 \quad (Z = W) \tag{9}$$

$$Q_i = Q_e \quad (Z = 0) \tag{10}$$

The cavity pressures are eliminated from the equations. In addition, the following dimensionless variables are introduced

$$f = \frac{Q_i}{Q_e}, \quad g = \frac{Q_o}{Q_e}, \quad \xi = \frac{Z}{W}, \quad a = \frac{A_i}{A_e}, \quad m = \frac{L_i}{L_e} \tag{11}$$

Here f is the dimensionless flow rate in the primary cavity, g the dimensionless flow rate in the secondary cavity, ξ the dimensionless coordinate along the cavities, a the normalized cross-sectional area of the primary cavity, and m the normalized length of the primary slot. In terms of these variables the equations to solve are

$$m\frac{d^2f}{d\xi^2} + \frac{dm}{d\xi}\frac{df}{d\xi} + rsg - \epsilon\frac{f}{a^2}\left\{1 + \vartheta\lambda_i \,\mathrm{Re}\left[2\frac{df}{d\xi} - \frac{f}{a}\frac{da}{d\xi}\right]\right\} = 0 \tag{12}$$

$$\frac{d^2f}{d\xi^2} + \frac{d^2g}{d\xi^2} - sg = 0 \tag{13}$$

$$f = 1 \quad (\xi = 0) \tag{14}$$

$$f = 0 \quad (\xi = 1) \tag{15}$$

$$g = 0 \quad (\xi = 0) \tag{16}$$

$$g = 0 \quad (\xi = 1) \tag{17}$$

$$m = 1 \quad (\xi = 0) \tag{18}$$

The dimensionless groups of parameters appearing here are

$$r = \frac{L_o H_i^3}{L_e H_o^3} \tag{19}$$

$$\epsilon = \frac{H_i^3 W^2}{12\lambda_i A_e^2 L_e} \tag{20}$$

$$s = \frac{H_o^3 W^2}{12\lambda_o L_o A_o^2} \tag{21}$$

$$\mathrm{Re} = \frac{\rho\langle q\rangle}{\mu} \tag{22}$$

The group r is the ratio of the resistance of the secondary slot to that of the primary slot. The group ϵ is the ratio of the resistance of the primary cavity to that of the primary slot and is required to be a small number in what follows; the group

arises naturally in models of dies and appears in the literature since Carley (1954) at least. The group s is analogous to ϵ but consists of parameters for the secondary cavity and slot; it is not necessarily small although a small value turns out to be advantageous. Re is a Reynolds number for flow in the slots.

These equations are general for the type of die under consideration. In order to simplify the mathematics, the taper of the primary cavity is taken to be

$$a = (1 - \xi)^{\gamma} \quad 0 \leq \gamma < 1 \tag{23}$$

The solution process makes it clear that this form is natural to the problem.

Perturbation Solution

The solution to the problem is expanded in powers of the small parameter ϵ

$$f = f_o + \epsilon f_1 + O(\epsilon^2) \tag{24}$$

$$g = g_o + \epsilon g_1 + O(\epsilon^2) \tag{25}$$

$$m = m_o + \epsilon m_1 + O(\epsilon^2) \tag{26}$$

The equations and boundary conditions determining the lowest order terms are found by formally setting ϵ to zero in Eqs. (12)–(18). The solution is

$$f_o = 1 - \xi, \quad g_o = 0, \quad m_o = 1 \tag{27}$$

At lowest order, the pressure drop along the primary cavity is negligible compared to that across the primary slot. Flow distribution in the primary slot is perfect, and no flow redistribution takes place in the secondary cavity. The linear drop of flow rate in the primary cavity is consistent with perfect distribution in the slot. The uniform length of the slot reflects the negligible loss of pressure in the cavity.

The problem at first order in ϵ is

$$\frac{d^2 f_1}{d\xi^2} - \frac{dm_1}{d\xi} + rsg_1 = (1 - \xi)^{1-2\gamma}\{1 - \vartheta\lambda_i \operatorname{Re}(2 - \gamma)\} \tag{28}$$

$$\frac{d^2 f_1}{d\xi^2} + \frac{d^2 g_1}{d\xi^2} - sg_1 = 0 \tag{29}$$

$$f_1 = 0 \quad (\xi = 0, 1) \tag{30}$$

$$g_1 = 0 \quad (\xi = 0, 1) \tag{31}$$

$$m_1 = 0 \quad (\xi = 0) \tag{32}$$

Equations (28) and (29) are combined to eliminate f_1.

$$\frac{d^2 g_1}{d\xi^2} - s(1 + r)g_1 = -\frac{dm_1}{d\xi} - [1 - \vartheta\lambda_i \operatorname{Re}(2 - \gamma)](1 - \xi)^{1-2\gamma} \tag{33}$$

To solve this problem, the variation in length of the primary metering slot must be specified. It is possible to choose this variation so that the flow distribution remains perfect at first order. If the right-hand side of Eq. (33) is zero, then the solution is $g_1 = 0$ and $f_1 = 0$. Consequently, the variation in slot length for perfect distribution is determined by

$$\frac{dm_1}{d\xi} = -[1 - \vartheta\lambda_i \operatorname{Re}(2 - \gamma)](1 - \xi)^{1-2\gamma} \tag{34}$$

Integrating Eq. (34) and applying Eq. (32) gives

$$m_1 = -\frac{[1 - \vartheta\lambda_i \operatorname{Re}(2 - \gamma)]}{(2 - 2\gamma)}\{1 - (1 - \xi)^{2-2\gamma}\} \tag{35}$$

and by Eqs. (26) and (27) the taper of the primary metering slot is

$$m = 1 - \epsilon\hat{T}[1 - (1 - \xi)^{2-2\gamma}] \tag{36}$$

in which

$$\hat{T} = \frac{1 - \vartheta\lambda_i \operatorname{Re}(2 - \gamma)}{2 - 2\gamma} \tag{37}$$

The slot taper for perfect distribution through first order depends on flow properties through Re; for purely viscous flow, the taper is independent of flow rate and viscosity.

A die has a fixed shape and may be operated over a range of Reynolds numbers. Based on the form of Eq. (36), the expression for slot length is taken to be

$$m = 1 - \epsilon T[1 - (1 - \xi)^{2-2\gamma}] \tag{38}$$

where T is a constant characterizing a specific design.

Equation (33) can be rewritten as

$$\frac{d^2 g_1}{d\xi^2} - \alpha^2 g_1 = -E(1 - \xi)^{1-2\gamma} \tag{39}$$

where E and α are combinations of parameters given by

$$E = 1 - \lambda_i\vartheta(2 - \gamma)\operatorname{Re} - (2 - 2\gamma)T = (2 - 2\gamma)(\hat{T} - T) \tag{40}$$

$$\alpha = \sqrt{s(1 + r)} \tag{41}$$

Although T is a constant, $\hat{T}$ depends upon Re through Eq. (37) and for one value of Re equals T. In that case $E = 0$ and the flow distribution remains perfect at first order as discussed. For other values of Re, E is not zero, and Eq. (39) is easily solved once a particular solution is constructed. The particular solution is especially simple in two cases of interest, $\gamma = \frac{1}{2}$ and $\gamma = 0$.

Results for a Coat Hanger Die and a T-Shaped Die. Results for $\gamma = \frac{1}{2}$, corresponding to a linear coat-hanger die, are

$$g_1 = \frac{E}{\alpha^2}\left\{1 - \frac{\sinh[\alpha(1 - \xi)] + \sinh[\alpha\xi]}{\sinh(\alpha)}\right\} \tag{42}$$

$$f_1 = \frac{Es}{\alpha^2}\left\{-\frac{r}{\alpha^2}\left[1 - \frac{\sinh[\alpha(1 - \xi)] + \sinh[\alpha\xi]}{\sinh(\alpha)}\right] + \frac{(1 - \xi)^2 - (1 - \xi)}{2}\right\} \tag{43}$$

Flow distribution from the die is given by

$$\frac{q_o}{\langle q\rangle} = 1 + \frac{\epsilon E}{1 + r} \times \left\{\frac{\cosh[\alpha\xi] - \cosh[\alpha(1 - \xi)]}{\alpha\sinh(\alpha)} + \frac{1}{2} - \xi\right\} \tag{44}$$

The distribution varies monotonically with ξ, and so the peak-to-peak variation is the difference between the flow at the center, $q_o(0)$, and that at the end, $q_o(1)$.

$$\frac{q_o(0) - q_o(1)}{\langle q \rangle} = \frac{\epsilon E}{1 + r}\left\{1 + \frac{2[1 - \cosh(\alpha)]}{\alpha \sinh(\alpha)}\right\} \quad (45)$$

Asymptotic forms of Eq. (45) for small and large values of α are

$$\frac{q_o(0) - q_o(1)}{\langle q \rangle} \approx \frac{\epsilon E s}{12} \quad (\alpha < 0.1) \quad (46)$$

$$\frac{q_o(0) - q_o(1)}{\langle q \rangle} \approx \frac{\epsilon E}{1 + r}\left(1 - \frac{2}{\alpha} + \ldots\right) \quad (\alpha \to \infty) \quad (47)$$

The corresponding results for a T-shaped die, $\gamma = 0$, are

$$g_1 = \frac{E}{\alpha^2}\left\{(1 - \xi) - \frac{\sinh[\alpha(1 - \xi)]}{\sinh(\alpha)}\right\} \quad (48)$$

$$f_1 = \frac{Es}{\alpha^2}\left\{\frac{r}{\alpha^2}\left[\frac{\sinh[\alpha(1 - \xi)]}{\sinh(\alpha)} - (1 - \xi)\right] + \frac{1}{6}[(1 - \xi)^3 - (1 - \xi)]\right\} \quad (49)$$

$$\frac{q_o}{\langle q \rangle} = 1 + \frac{\epsilon E}{1 + r}\left\{\frac{1}{\alpha^2}\left[1 - \frac{\alpha \cosh[\alpha(1 - \xi)]}{\sinh(\alpha)}\right] + \frac{1}{6}[3(1 - \xi)^2 - 1]\right\} \quad (50)$$

$$\frac{q_o(0) - q_o(1)}{\langle q \rangle} = \frac{\epsilon E}{1 + r}\left\{\frac{1 - \cosh(\alpha)}{\alpha \sinh(\alpha)} + \frac{1}{2}\right\} \quad (51)$$

$$\frac{q_o(0) - q_o(1)}{\langle q \rangle} \approx \frac{\epsilon E s}{24} \quad (\alpha < 0.1) \quad (52)$$

$$\frac{q_o(0) - q_o(1)}{\langle q \rangle} \approx \frac{\epsilon E}{2(1 + r)}\left(1 - \frac{2}{\alpha} + \ldots\right) \quad (\alpha \to \infty) \quad (53)$$

The peak-to-peak nonuniformity from the die has the form

$$\frac{q_o(0) - q_o(1)}{\langle q \rangle} = \frac{\epsilon E}{1 + r} F(\alpha, \gamma) \quad (54)$$

The function F is plotted in Fig. 2 against α for values of γ of 0 and 0.5. The graph shows that the cavity of uniform cross-sectional area ($\gamma = 0$) has an advantage that is maintained over the entire range of α. The graph also shows that the uniformity of the flow distribution steadily degrades as α increases.

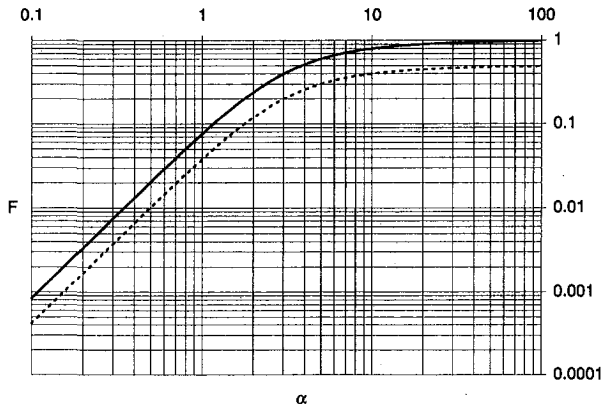

Fig. 2 Plot of the function F in the expression for the peak-to-peak nonuniformity of the flow distribution, Eq. (54). Solid line, $\gamma = 0.5$; dashed line, $\gamma = 0$.

Interpretation of the Effect of the Secondary Cavity

The flows in the primary and secondary cavities are coupled; a change in one cavity induces a change in the other. Special cases where the cavities are uncoupled are explored here to reveal the nature of this interaction.

Spatial Frequency Response of the Secondary Cavity for an Imposed Inflow. The flow distribution in the primary slot is imposed, and the alteration of this distribution by the secondary cavity is computed. The applicable differential equation follows from Eqs. (3) and (13)

$$\frac{d^2 g}{d\xi^2} - sg = \frac{1}{\langle q \rangle}\frac{dq_i}{d\xi} \quad (55)$$

Boundary conditions are given by Eqs. (16)–(17). The flow distribution in the primary slot is written as the average flow rate plus a deviation

$$\frac{q_i}{\langle q \rangle} - 1 = \theta(\xi) \quad (56)$$

The deviation, $\theta(\xi)$, is written as a Fourier series

$$\theta(\xi) = \sum_{n=1}^{\infty} k_n \cos(n\pi\xi) \quad (57)$$

$$k_n = 2\int_0^1 \theta(\xi) \cos(n\pi\xi) d\xi \quad (58)$$

The solution to Eq. (55) is

$$g = \sum_{n=1}^{\infty} \frac{n\pi}{(s + n^2\pi^2)} k_n \sin(n\pi\xi) \quad (59)$$

and the flow distribution in the secondary slot follows as

$$\frac{q_o}{\langle q \rangle} - 1 = \sum_{n=1}^{\infty} \frac{s}{(s + n^2\pi^2)} k_n \sin(n\pi\xi) \quad (60)$$

For the case where the prescribed flow distribution in the primary slot has only one component of spatial frequency, the amplitude of that component is diminished by the factor $s/(s + n^2\pi^2)$. So, flow variations of high spatial frequency are effectively damped by the secondary cavity, and small values of s increase damping by the secondary cavity.

Nearly Uniform Pressure in the Secondary Cavity. Consider the situation of uncoupled cavities arising because the pressure in the secondary cavity is essentially uniform. The flow distribution from the primary cavity can then be determined by imposing constant pressure at the outlet of the primary slot. The first-order problem for the flow in the primary cavity follows by setting $g_1 = 0$ in Eq. (28)

$$\frac{d^2 f_1}{d\xi^2} = E(1 - \xi)^{1-2\gamma} \quad (61)$$

along with Eq. (30). The solution is

$$f_1 = \frac{E}{(2 - 2\gamma)(3 - 2\gamma)}[(1 - \xi)^{3-2\gamma} - (1 - \xi)] \quad (62)$$

The resulting flow distribution in the primary slot,

$$\frac{q_i}{\langle q \rangle} = 1 + \frac{\epsilon E}{(2 - 2\gamma)(3 - 2\gamma)} \times [(3 - 2\gamma)(1 - \xi)^{2-2\gamma} - 1] \quad (63)$$

is imposed as the feed to the secondary cavity, just as in the previous case. The governing differential equation follows from Eqs. (61) and (29)

$$\frac{d^2 g_1}{d\xi^2} - s g_1 = -E(1-\xi)^{1-2\gamma} \tag{64}$$

Comparison of this equation with its counterpart in the coupled analysis, Eq. (39), shows as the only difference that $s(1+r)$ in Eq. (39) is just s here. So, the effect of coupling between the cavities is to increase the value of s in the uncoupled analysis by the factor $(1+r)$ and thereby make the secondary cavity less effective at evening the flow distribution. The group r measures the degree of coupling. If the flow resistance of the primary slot is small compared to that of the secondary slot, the degree of coupling is high, and the secondary cavity is less efficient than would be the case if the cavities did not interact.

From Eqs. (46) and (52), or from Eqs. (28)–(32), r has no effect if s is small. Therefore, the flows in the cavities uncouple for s sufficiently small.

High Flow Resistance Along the Secondary Cavity. If the secondary cavity has high flow resistance, then the secondary cavity does not influence the flow distribution in the slots. Flow redistribution in the secondary cavity can be neglected, and the slots can be considered directly connected; the two-cavity die becomes a single cavity die. The flows in the cavities are again uncoupled and can be independently determined.

The pressure in the primary cavity is determined as the sum of the pressure drops across the primary and secondary slots. Combining Eqs. (6) and (7) gives

$$P_i = 12\mu\left[\frac{L_i}{H_i^3} + \frac{L_o}{H_o^3}\right] q_i \tag{65}$$

Combining Eqs. (2) and (65) leads to the following equation for flow in the primary cavity at first order, instead of Eq. (28)

$$\frac{d^2 f_1}{d\xi^2} = \frac{E}{1+r}(1-\xi)^{1-2\gamma} \tag{66}$$

The solution to this differential equation and Eq. (30) is

$$f_1 = \frac{E}{1+r}\frac{(1-\xi)^{3-2\gamma} - (1-\xi)}{(3-2\gamma)(2-2\gamma)} \tag{67}$$

Final flow distribution and its peak-to-peak variation follow as

$$\frac{q_o}{\langle q\rangle} = 1 - \frac{\epsilon E}{1+r}\frac{1-(3-2\gamma)(1-\xi)^{2-2\gamma}}{(3-2\gamma)(2-2\gamma)} \tag{68}$$

$$\frac{q_o(0) - q_o(1)}{\langle q\rangle} = \frac{\epsilon E}{(1+r)(2-2\gamma)} \tag{70}$$

These results are identical to those obtained in the full analysis in the limit $s \to \infty$, r fixed. Therefore, the flows in the cavities uncouple for s sufficiently large. Note that in this limit a large value for r is beneficial. The term $(1+r)$ represents the total resistance to flow of the primary and secondary slots. An increase in r is favorable because the ratio of slot resistance to cavity resistance increases.

Limitations of the Solutions

The flow variation is a perturbation series in ϵ, and Weinstein and Ruschak (1996a) have estimated the error for a single-cavity die as $\epsilon^2/45$. This estimate should be conservative for a two-cavity die because the secondary cavity only improves the flow distribution. Additionally, it is prudent to verify that the flow distribution in the primary slot varies by no more than a few percent. The tapering of slot length is a first-order effect compensating for the pressure loss in the primary cavity. As such, the variation in slot length is restricted to order ϵ and should not exceed a few percent. More aggressive designs with severe tapers to compensate for larger pressure loss (ϵ not small) are beyond the applicability of the solutions given here, and the equations must be solved numerically. A design with ϵ small can be preferable because of reduced sensitivity to modeling, dimensional, rheological, and other uncertainties.

For flow in the metering slots to be effectively perpendicular to the Z-direction, the length of the cavity must greatly exceed the length of the slots, $(L_e/W)^2 \ll 1$ and $(L_o/W)^2 \ll 1$ (Weinstein and Ruschak, 1996b). For the flow in the cavities to be considered fully developed (pressure uniform over a cross section and Z-derivatives of viscous stresses negligible compared to cross derivatives), the length of the cavity must greatly exceed its width, $A_o/W^2 \ll 1$ and $A_e/W^2 \ll 1$, and pressure drops across the slots must greatly exceed those across the cavities, $H_o^3/L_oA_o \ll 1$ and $H_i^3/L_iA_i \ll 1$.

The inertial term in Eq. (2) for the primary cavity applies to fully developed flow. The decreasing velocity in the primary cavity leads to an inertial pressure recovery counteracting the viscous pressure loss. From Eq. (2) and the lowest order solution Eq. (27), the viscous pressure loss can be estimated as $\mu Q_e W/\lambda_i(2-2\gamma)A_e^2$ and the inertial pressure recovery as $[(2-\gamma)\vartheta/(1-\gamma)]\rho Q_e^2/2A_e^2$; it follows that the pressure recovery is significant in the primary cavity for Re greater than about 1. For $\mathrm{Re} > 1/(2-\gamma)\vartheta\lambda_i \approx 10$, the equations predict that the inertial recovery exceeds the viscous loss.

However, Eq. (2) in most cases over predicts the pressure recovery because it does not account for entry losses. From work on developing flow in conduits (Lundgren et al., 1964), high wall friction and a pressure gradient exceeding that of developed flow are expected in the entry region. The length of the entry region is a negligible fraction of total cavity length for purely viscous flow, but it becomes significant with the ascendancy of inertia (Wen and Liu, 1994). Developing flow typically extends over a distance $\xi \approx 0.03$ Re and generates an additional pressure loss of order $\rho Q_e^2/2A_e^2$ (Schlichting, 1979), but the precise magnitude and extent of entry losses depend upon the degree of streamlining of the inlet region. The magnitude and extent of the entrance loss is more important than its detailed variation because the secondary cavity filters out components of high spatial frequency. The most straightforward inlet configuration, a supply stream entering the cavity perpendicularly, is not streamlined and generates a stagnation pressure. For an inlet with a cross-sectional area matching that of the cavity, a local pressure increase of $\rho Q_e^2/2A_e^2$ extending over a distance $Z \approx \sqrt{A_e}$ is roughly expected.

As a practical matter, the effect of entry losses on the final peak-to-peak flow distribution is of greater consequence than the effect in the primary cavity. If undamped by the secondary cavity, a pressure perturbation of $\rho Q_e^2/2A_e^2$ in the primary cavity gives rise to a fractional change in flow rate of $\lambda_i\epsilon\ \mathrm{Re}/2(1+r)$ according to Eq. (65). By Eq. (60), a secondary cavity with $s \approx 1$ or smaller reduces the magnitude by a factor of about s/π^2 if the perturbation extends over more than a few percent of the cavity. So, because $\lambda_i \approx 0.03$, the effect on the final flow distribution does not exceed 1% if ϵs Re is less than 10. With $\epsilon < 0.1$ and $s < 10$, Re can be 10 or higher and greatly exceed the value of 1 required for significance in the primary cavity. Narrower disturbances, $\xi \ll 1$, such as the inlet stagnation pressure is likely to be, are additionally damped by a factor of about 4ξ, as follows from Eq. (60) with k_1 appropriately chosen. So, a two-cavity die is particularly effective at dampening inlet pressure spikes.

Numerical Example

The perturbation approach makes modest computational demands. This advantage is amplified in die design because the flow model is just a portion of a model of a die and because

optimization algorithms requiring repeated evaluations are used (Ruschak and Weinstein, 1996; Durst et al., 1996). For example, the design of a two-cavity die must at least consider dimensional uncertainties consisting of fabrication allowances and, perhaps, pressure- or temperature-induced mechanical deformations. The final flow distribution is particularly sensitive to uncertainties in the length and height of the secondary slot. The linearity of the perturbation equations and the simplicity of the lowest order solution make it easy to estimate the effects on flow distribution of uncertainties in dimensions. Equation (7), when linearized about the lowest order solution where pressure in the secondary cavity is uniform, predicts that the fractional change in flow rate equals the sum of the fractional change in slot length and three times the fractional change in slot height.

For a specific example, suppose the following specifications: the half length of the cavities is $W = 100$ cm; flow conditions are for small Reynolds number; the primary cavity has a circular cross section ($\lambda_i = 1/8\pi$, $\vartheta = \frac{4}{3}$); the taper parameter is $\gamma = 0.5$; and the secondary cavity has a circular cross section ($\lambda_o = 1/8\pi$). Selecting the slot taper through Eq. (35) with $\mathrm{Re} = 0$ yields perfect distribution but does not determine unique values for all dimensions. However, suppose that 8 cm is available for the cavities and slots, that the heights of the primary and secondary slots are the same ($H_i = H_o$), and that peak-to-peak fabrication tolerances are 0.00025 cm for slot height and 0.01 cm for slot length. The total flow nonuniformity will be less than the sum of the absolute values of the peak-to-peak flow nonuniformities due to the design with perfect dimensions, the fabrication tolerances for the slot height, and the fabrication tolerances for the slot length; minimizing the total nonuniformity under the given constraints determines the remaining dimensions. An additional constraint, $\epsilon < 0.05$, is added so that the perturbation model is valid. It is clear that the metering slot taper must be given by Eq. (35) so that the design with perfect dimensions makes no nonuniformity contribution; if this choice is not made a priori, the optimizing algorithm will make it. This optimization was carried out using the Solver algorithm of Microsoft® Excel with the following results: slot heights 0.065 cm; secondary metering slot length, 1.93 cm; secondary cavity diameter, 1.38 cm; primary slot length 0.91 cm at center and tapering to 95 percent at the ends; and a primary cavity diameter at center, 3.78 cm. These values give $s = 1.31$, $r = 2.12$, and for the groups required to be small, $\epsilon = 0.05$ and values less than 0.001 for the others. The peak-to-peak flow nonuniformity of at most 1.8 percent is completely attributable to fabrication tolerances.

Concluding Remark

An attractive feature of a two-cavity design is the evening of the flow distribution arriving from the primary slot and the filtering out of components of high spatial frequency. This feature extends the versatility of designs and reduces the consequences of uncertainties in the design model, such as inlet effects, or uncertainties in dimensions due to fabrication tolerances or mechanical deformations.

References

Atkinson, B., Brocklebank, M. P., and Card, C. C. H., 1968, "Low Reynolds Number Developing Flows," *AIChE Journal,* Vol. 15, pp. 548–553.

Carley, J. F., 1954, "Flow of Melts in 'Crosshead'-Slit Dies; Criteria for Die Design," *Journal of Applied Physics,* Vol. 25, pp. 1118–1123.

Durst, F., Lange, U., and Raszillier, H., 1994, "Optimization of Distribution Chambers of Coating Facilities," *Chemical Engineering Science,* Vol. 48, pp. 161–170.

Durst, F., Lange, U., and Raszillier, H., 1996, "Minimization and Control of Random Effects on Film Thickness Uniformity by Optimized Design of Coating Die Internals," *The Mechanics of Thin Film Coatings,* the Proceedings of the First European Coating Symposium, World Scientific, London.

Lee, K., and Liu, T., 1989, "Design and Analysis of a Dual-Cavity Coat-Hanger Die," *Polymer Engineering and Science,* Vol. 29, pp. 1066–1075.

Leonard, W. K., 1985, "Effects of Secondary Cavities, Inertia and Gravity on Extrusion Dies," SPE ANTEC Technical Papers, Vol. 31, pp. 144–148.

Liu, T., 1983, "Fully Developed Flow of Power-Law Liquid in Ducts," *Industrial and Engineering Chemistry Fundamentals,* Vol. 22, pp. 183–186.

Liu, T., Hong, C., and Chen, K., 1988, "Computer-Aided Analysis of a Linearly Tapered Coat-Hanger Die," *Polymer Engineering and Science,* Vol. 28, pp. 1517–1526.

Lundgren, T. S., Sparrow, E. M., and Starr, J. B., 1964, "Pressure Drop Due to the Entrance Region in Ducts of Arbitrary Cross Section," ASME *Journal of Basic Engineering,* Vol. 86, pp. 620–626.

Ruschak, K. J., and Weinstein, S. J., 1996, "Mathematical Modelling of Fluid Dies," *The Mechanics of Thin Film Coatings,* the Proceedings of the First European Coating Symposium, World Scientific, London.

Ruschak, K. J., and Weinstein, S. J., 1997, "Method for Determining the Flow Equation for the Secondary Cavity of a Two-Cavity Die," *Polymer Engineering and Science,* in press.

Sartor, L., 1990, "Slot Coating: Fluid Mechanics and Die Design," Ph.D. thesis, Univ. of Minnesota, Minneapolis.

Schlichting, H., 1979, *Boundary-Layer Theory,* McGraw-Hill, New York, p. 241.

Weinstein, S. J., and Ruschak, K. J., 1996a, "Asymptotic Analysis of Die Flow for Shear-Thinning Fluids," *AIChE Journal,* Vol. 46, pp. 1501–1513.

Weinstein, S. J., and Ruschak, K. J., 1996b, "One-Dimensional Equations Governing Single-Cavity Die Design," *AIChE Journal,* Vol. 42, pp. 2401–2414.

Yuan, S., 1995, "A Flow Model for Non-Newtonian Liquids Inside a Slot Die," *Polymer Engineering and Science,* Vol. 35, pp. 577–586.

Wen, S., and Liu, T., 1994, "Three-Dimensional Finite Element Analysis of Polymeric Fluid Flow in an Extrusion Die. Part I: Entrance Effect," *Polymer Engineering and Science,* Vol. 34, pp. 827–834.

Journal of Fluids Engineering

Technical Brief

On the Accuracy of Wall Similarity Methods in Determining Friction Velocity Over Smooth and Ribletted Surfaces

Arturo Baron[1] **and Maurizio Quadrio**[1]

1 Introduction

An accurate determination of friction velocity u_τ or, alternatively, of wall shear stress $\tau_w = \rho u_\tau^2$ is of paramount importance in many turbulent boundary layer problems. In applications concerning drag reducing flows, moreover, the wall shear stress is required to be known with high accuracy, since the amount of drag reduction achievable with passive drag reducing techniques is usually of the order of a few percent.

A direct evaluation of the gradient $\partial U/\partial y$ at the wall can but seldom be achieved because of experimental problems. Integral momentum methods for the evaluation of friction velocity are often too inaccurate and direct shear stress measurement techniques are either inaccurate or expensive. This is why to date the most widely used techniques for determining u_τ are indirect, and rely on the well-known law of the wall. Such techniques are known as wall similarity methods.

The universality of the law of the wall, which can be deduced from simple dimensional considerations, is, however, subject to many important assumptions and limitations, in particular, the boundary layer must be fully developed and must flow, in equilibrium conditions, over smooth and flat walls, with no longitudinal pressure gradient. Provided these conditions are fully satisfied, the so-called logarithmic region of the mean velocity profile (i.e., that portion where the coordinate normal to the wall is between $30\,\nu/u_\tau$ and 0.15δ, δ being the boundary layer thickness) can be expressed in dimensionless form as a function of the friction velocity u_τ (Coles, 1956):

$$\frac{U(y)}{u_\tau} = A \ln\left(\frac{y u_\tau}{\nu}\right) + B \qquad (1)$$

where y is the coordinate normal to the wall, $U(y)$ is the local mean streamwise velocity component, A and B are, respectively, the slope and the intercept of the law of the wall, which is linear when plotted in semilogarithmic coordinates. In the present work, the classical values $A = 2.44$ and $B = 5.45$ will be adopted, following the early suggestion of Patel (1965).

Besides the basic boundary layer in zero pressure gradient, there are several flows where the law of the wall, even if strictly speaking not applicable, gives nevertheless satisfactory results. This is the case, for example, of flows with mild (positive or negative) streamwise pressure gradient, and flows over ribletted surfaces. For such flows also the law of the wall can be used, provided its intercept is allowed to assume a value different from the "universal" one by a quantity ΔB (Acharya and Escudier, 1984).

In the following, four of the most widely used wall similarity methods are considered, with special emphasis on their limitations and problems that are necessarily encountered in their application to real velocity profiles, i.e., profiles affected by unavoidable scattering and experimental errors. One of these methods, the so-called slope method, is selected on the basis of its capability to treat boundary layers over both smooth and rough walls and is then modified to reduce its inherent margins of subjectivity.

It must be clear that the present work is not intended to design and propose new and better wall similarity techniques. Rather, the limits and potentialities of some widely used techniques are discussed and a modified method is proposed which has the property of greatly reducing such arbitrary choices.

2 Wall Similarity Methods

Wall similarity methods can be considered a means for calculating the friction velocity u_τ that gives the best fit between a measured velocity profile and the law of the wall (Kline et al., 1967). These methods work in the linear portion of the velocity profile plotted in semilogarithmic coordinates.

Standard wall similarity methods can be divided into two main groups, depending on the constant B in Eq. (1) being educed from the method itself or being fixed a priori. In the following, two classical methods for each group are considered: the Clauser chart method (CCM), the standard (SBM) and modified (MBM) Bradshaw methods, and the standard slope method (SSM).

CCM (Clauser, 1954) is quite independet from local measurement errors and scattering, because of their statistical compensation operated by the fitting procedure. However, this method explicitely uses the law of the wall equation, and therefore requires that a value for the constant B to be assigned a priori. SBM (Bradshaw, 1959) again requires a value of B to be assigned, and is extremely sensitive to measurement errors.

With MBM one is able to compute the values of B and u_τ at the same time, hence handling flows over rough surfaces. Last, SSM does not require any value to be imposed a priori for B, and with its linear fitting guarantees a statistical compensation for the scattering of the experimental data. The slope of the velocity profile is not affected by a possibly inaccurate evalua-

[1] Associate Professor of Fluid Dynamics and Research Assistant, respectively, Dipartimento di Ingegneria Aerospaziale del Politecnico di Milano, via C. Golgi, 40, 20133 Milano, Italy.

Contributed by the Fluids Engineering Division of THE AMERICAN SOCIETY OF MECHANICAL ENGINEERS. Manuscript received by the Fluids Engineering Division June 3, 1996; revised manuscript received June 27, 1997. Associate Technical Editor: D. P. Telionis.

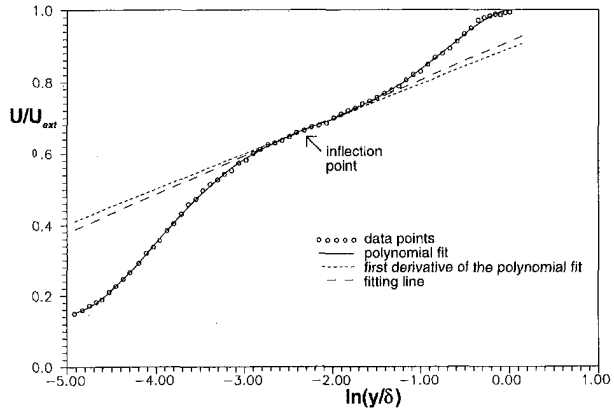

Fig. 1 Interpolation of the experimental velocity distribution with an 8th degree polynomial. The slope of the experimental profile does not coincide with the slope of the polynomial in the point of zero curvature.

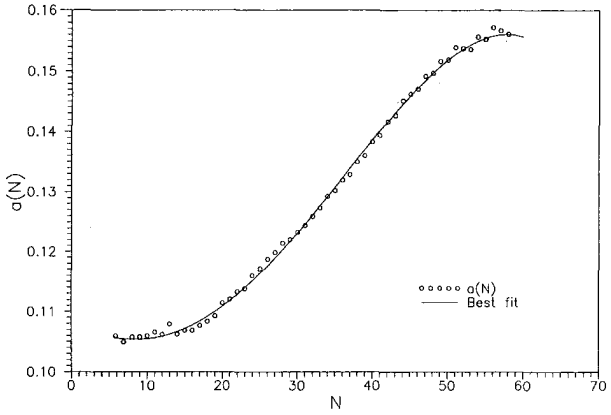

Fig. 2 Behavior of the slope *a* of the velocity profile in outer coordinates, versus the number of points *N* used for the linear regression. The center of the linear region is the inflexion point evidenced in Fig. 1. The solid line shows a polynomial fit.

tion of δ. The central problem encountereed in the use of this method on a real velocity profile is the strong lack of repeatability associated with the subjective identification of the location and width of the linear region of the fit, i.e., where and how the linear region is selected.

3 A Suggested Procedure: A Modification of the Slope Method

The classical slope method presents the advantage of wide applicability and low sensitivity to the scattering of the data; its main drawback seems to be a clear lack of repeatability. In the following, a procedure is proposed which is aimed at determining the linear region in the mean velocity profile in an automatic and repeatable way. The procedure only applies to turbulent boundary layers, and addresses the problem in two steps.

In the first step, the center of the linear region is determined. This point must coincide with a point where the curvature of the velocity profile changes its sign. The fitting of the experimental curve with an 8th degree polynomial, and the analytical calculation of the point of zero curvature, have been shown to be a dependable way for identifying the center of the linear region. The use of higher-degree polynomials changes neither the results nor the quality of the fit.

If the tangent to the polynomial at the point of zero curvature were coincident with the slope of the linear part of the velocity distribution, the entire problem could be easily solved. Unfortunately the scattering of the experimental data can be such that the local slope of the experimental distribution is often quite different from the tangent, as evident from Fig. 1 (the data set used in Figs. 1 and 2 is the same as Figs. 3 and 4). The second step, therefore, consists in determining the number of experimental points that have to be used for the linear regression.

A reliable solution to this problem can be found by plotting the behavior of the slope a of the fitting line (the same result holds for the intercept) versus the number N of points used for the linear regression analysis (Fig. 2). With the exception of the first values, obtained with too few points and consequently highly irregular because of their scattering, the slope remains quite constant (as it should be in absence of scattering), until points outside the linear region are considered and the values of the slope start getting higher and higher. A polynomial fit may be used to determine the first point of stationarity of the curve $a(N)$ versus N, and therefore to select in an exact and objective way the number of points to be used for the linear regression.

It has to be said that, unless the computed number of points is even, the choice has to be made on how to distribute them around the central one. This leads, even for the modified slope method, to some variation in the predicted values of u_τ and B.

Once the central point of the linear region and its width have been determined, it is possible to use a linear regression analysis for calculating the values of the slope a and the intercept b in the equation:

$$U/U_{\text{ext}} = a \ln y/\delta + b$$

Finally, once a and b are known, the friction velocity u_τ and the intercept B of the law of the wall are computed; all interventions, judgments, or personal visual interpretation of the experimenter have been avoided, so that repeatability of the procedure is achieved.

4 Validation

In Fig. 3, an evaluation is reported of the sensitivity of the results of the various examined wall similarity techniques to

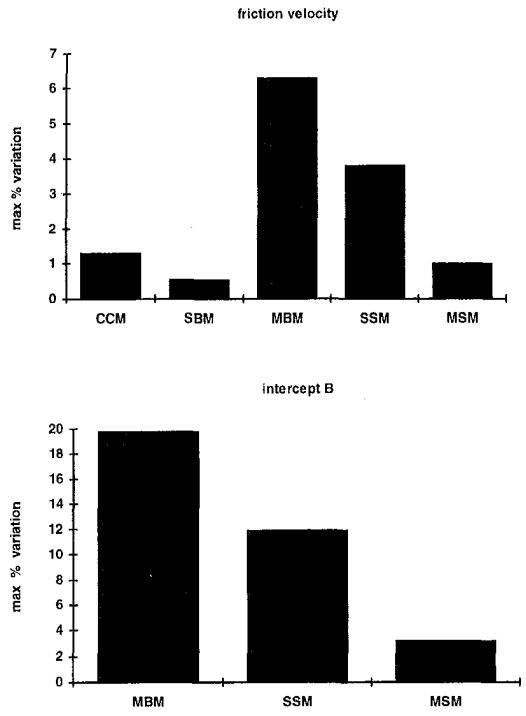

Fig. 3 Evaluation of the sensitivity of the friction velocity u_τ (left) and of the intercept B of the law of the wall (right) to the various wall similarity methods

the free choices that the experimenter has to perform during the overall data reduction process.

In the Clauser chart method (CCM), the best-fitting value of C_f has been varied in a range of ± 0.001. In the standard Bradshaw method (SBM), the height K of the point of intersection has been moved from 30 to 90 wall units (extrema of the logarithmic portion of the velocity profile). In the modified Bradshaw method (MBM) the heights K_1 and K_2 have been varied independently in the range between 30 to 60 wall units, and 60 to 90 wall units, respectively. In the standard slope method (SSM), the width of the region used for the regression analysis has been varied inside the range determinable by visual observation.

The results obtained by varying the above-mentioned free parameters in their range have been computed, and their scatter in terms of maximum percentage variation around the mean value has been reported in Fig. 3. Also computed are the predictions obtained with the modified slope method (MSM), in which, as mentioned above, a small variation is present, associated to an odd number of points to be used for the linear regression.

It can be seen that, as far as the friction velocity is concerned, CCM and SBM, which require that a value for the intercept B be assigned, and have therefore a single degree of freedom, show quite better performances, in terms of percentage variations, with respect to MBM and SSM, which have two degrees of freedom. Their results are comparable with that of MSM. On the other hand, the value of B, which is predictable only by using this last group of wall similarity methods, appears to be reliable only when educed from a procedure, such as the proposed one, which removes the influence of the choices of the experimenter.

In Fig. 4, a typical application is shown, concerning the comparison between the mean velocity distributions in law of the wall form for turbulent flows over a flat and a ribletted plate. The measurements have been performed by the authors in a low speed wind tunnel at the von Kàrmàn Institute for Fluid Dynamics. The experiment is described in detail in Baron and Quadrio (1993a).

The virtual origin of the mean velocity profile for the riblet case has been set according to the concept of longitudinal protrusion height (Bechert et al., 1989; Luchini et al., 1991) and taking into account the actual geometry of the riblet contour (Baron et al., 1993b).

The friction velocity necessary for plotting the velocity profiles in law of the wall coordinates has been computed according to the modified slope procedure (MSM) illustrated in the preceding paragraph. The slope of the linear part, as expected, remains unchanged, while the intercept B increases from 5.38 to 5.95 for the ribletted one. This upward shift ΔB, the amount of which is equal to 0.57, is in good agreement with published experimental results (e.g., those reported by Choi, 1989), and corresponds to a reduction in the friction coefficient of approximately 3–4 percent, which is consistent with the theoretical prediction one could obtain on the basis of the computed value of the protrusion height of the real geometry of the ribs.

5 Conclusions

An analysis has been performed of four widely used wall similarity methods. Particular attention has been devoted to the so-called standard slope method (SSM), because of its ability to educe the value of the constant B and, consequently, to also deal with drag reducing flows while preserving the capability of statistically compensating the scattering of the experimental data.

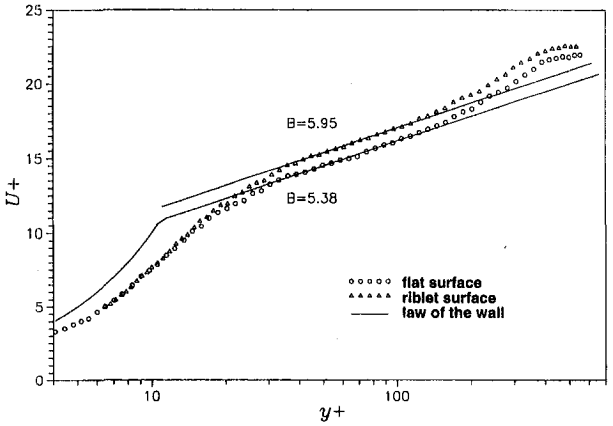

Fig. 4 Application of the modified slope method (MSM) to a real case of turbulent flow over flat and ribletted surfaces

However, the standard slope method also presents an intrinsic limitation concerning the subjectivity in the determination of the amplitude of the linear region and the location of its center. This led to the formulation of a procedure, based on some relevant properties in the velocity profile when interpolated with a polynomial, which has been eventually applied to a data set from previous experiments.

This procedure can be employed also to estimate the upward shift ΔB in the law of the wall, which can be extremely small in flows where drag reduction is achieved by passive techniques.

Acknowledgments

The present work has been partially supported by the Ministero dell'Università e della Ricerca Scientifica e Tecnologica. The authors would like to express their gratitude to Ing. Umberto Fasanotto for his substantial contribution to part of this work.

References

Acharya, M., and Escudier, M. P., 1984, "Measurements of the Wall Shear Stress in Boundary Layer Flows," *Turbulent Shear Flows,* Vol. 4, Springer-Verlag Berlin, p. 277.

Baron, A., and Quadrio, M., 1993a, "Some Preliminary Results on the Influence of Riblets on the Structure of a Turbulent Boundary Layer." *The International Journal of Heat and Fluid Flow,* Vol. 14, No. 3.

Baron, A., Quadrio, M., and Vigevano, L., 1993b, "On the Boundary Layer/Riblets Interaction Mechanism and the Prediction of Turbulent Drag Reduction," *The International Journal of Heat and Fluid Flow,* Vol. 14, No. 4.

Bechert, D. W., and Bartenwerfer, M. 1989, "The Viscous Flow on Surfaces With Longitudinal Ribs," *Journal of Fluid Mechanics,* Vol. 206, p. 105.

Bradshaw, P., 1959, "A Simple Method for Determining Turbulent Skin Friction From Velocity Profiles," *Journal of Aeronautical Science,* Vol. 26, p. 841.

Choi, K.-S., 1989, "Near-Wall Structure of a Turbulent Boundary Layer with Riblets," *Journal of Fluid Mechanics,* Vol. 208, p. 417.

Clauser, F. H., 1954, "Turbulent Boundary Layers in Adverse Pressure Gradients," *Journal of Aeronautical Science,* Vol. 21, p. 91.

Coles, D., 1956, "The Law of the Wake in the Turbulent Boundary Layer," *Journal of Fluid Mechanics,* Vol. 1, p. 191.

Kline, S. J., Reynolds, W. C., Schraub, F. A., and Runstadler, P. W., 1967, "The Structure of Turbulent Boundary Layers," *Journal of Fluid Mechanics,* Vol. 30, p. 741.

Luchini, P., Manzo, F., and Pozzi, A., 1991, "Resistance of a Grooved Surface to Parallel Flow and Cross-Flow," *Journal of Fluid Mechanics,* Vol. 228, p. 87.

Patel, V. C., 1965, "Calibration of the Preston Tube and Limitations on its Use in Pressure Gradients," *Journal of Fluid Mechanics,* Vol. 23, p. 185.